# On Characteristics and Flow Dynamics of Large Rapid Mass Movements in Glacial Environments

---

Dissertation
zur
Erlangung der naturwissenschaftlichen Doktorwürde
(Dr. sc. nat.)

Vorgelegt der
Mathematisch-naturwissenschaftlichen Fakultät
der
Universität Zürich
von

**Demian Schneider**

von
Luzern LU / Suhr AG

Promotionskomitee
Prof. Dr. Wilfried Haeberli (Vorsitz)
Dr. Christian Huggel (Leitung der Dissertation)
Dr. Brian W. McArdell
Dr. Perry Bartelt

Zürich, April 2011

# Summary

Current developments of the climate involve dramatic changes in the high-mountain cryosphere, such as glacial retreat, permafrost degradation, development of new glacial lakes, release of huge masses of friable and often steep debris, and altered precipitation patterns. Consequences are increased mass turnover rates, characterized by higher frequencies and magnitudes of rock falls, debris flows and slow slope movements, but also by large ($V > 10^6$ m$^3$) and rapid mass movements such as landslides, rock-, debris- or ice-avalanches and debris flows.

Large rapid mass movements in or from glacial and periglacial high mountain environments can be attributed by extraordinary mobility, flow transformations or chain reactions implying high hazard potentials if they are reaching populated areas such as demonstrated by a number of disastrous events during the last decades. The present study concentrates on the propagation and deposition of large rapid mass movements in glacial environments. This includes aspects from general landslide long-runout mechanisms, several case studies in volcanic and non-volcanic glacial environments, numerical runout modeling, seismic data analysis, physical flow experiments in the laboratory and an empirical analysis of specific flow characteristics of large rapid mass movements in glacial environments.

Simple empirical runout modeling of mass movements was applied for preliminary regional hazard assessments. For specific retrospective local case studies, physically-based dynamic numerical simulations were performed. Besides required geometric similarities between the modeled and real event, the rheologic model input parameters could be better constrained by fitting dynamic model output parameters to seismic data. As a result, insights into flow dynamics of rock-ice avalanches can be improved, such as by more accurate velocity estimations that is of interest for hazard mitigation measures.

Laboratory experiments in large vertically rotating drum flumes were used to quantify the influence of ice on the friction coefficient of granular gravel-ice mixtures to make conclusions on the effects of ice on the mobility of natural rock-ice avalanches. The friction coefficient was found to decrease linearly with increasing volumetric ice content by a maximum of ~20%. For longer process durations, melting ice caused partial or complete liquefaction of the mass with a consequent reduction of the friction coefficient by nearly 50%.

An empirical analysis of 64 large rock-ice avalanches has shown that the effect of the ice content is not a dominant factor in natural events. The mobility of the events revealed a correlation with the relative flow path length leading over a glacier, confirming quantitatively

that the low-friction glacier surfaces effectively contribute in extending the runout distance of rapid mass movements as hypothesized by previous authors. Furthermore, rock-ice avalanches with high water contents are often among the most mobile events. However, the most disastrous rapid mass movements from glacial environments have often shown a combination of features, such as large volumes, flow paths over glaciers or smooth bedrock, confined flow, high ice and water contents, strong material entrainment and flow transformations or chain reactions.

Despite the broad variety and complex process interactions in large rapid mass movements in glacial environments, insights to several aspects were deepened. The findings should be extended in future by similar and additional methods to serve once as a strong basis for scenario-based modeling.

# Zusammenfassung

Die heutige Entwicklung des Klimas beinhaltet dramatische Veränderungen der Hochgebirgs-Kryosphäre, beispielsweise die Bildung neuer glazialer Seen, die Freigabe grosser Mengen an lockerem, häufig steilem Schutt, sowie veränderten Niederschlagsbedingungen. Die Folgen sind verstärkte Massenumsatzraten, welche durch erhöhte Frequenzen und Magnituden von Felsstürzen, Murgängen und langsamen Hangbewegungen, jedoch auch durch grosse ($V > 10^6$ m$^3$) und schnelle Massenbewegungen wie zum Beispiel Bergstürze, Fels-, Schutt- oder Eislawinen und Murgänge in Erscheinung treten.

Grosse schnelle Massenbewegungen in oder von glazialen und periglazialen Hochgebirgsgebieten charakterisieren sich durch ausserordentliche Mobilitäten, Fliesstransformationen oder Kettenreaktionen, welche ein grosses Gefahrenpotenzial beinhalten sofern besiedelte Gebiete erreicht werden – wie es durch einige katastrophale Ereignisse in den letzten Jahrzehnten gezeigt wurde. Die vorliegende Studie konzentriert sich auf das Fliessen und die Ablagerung von grossen schnellen Massenbewegungen in glazialen Gebieten. Dies beinhaltet Aspekte allgemeiner Mechanismen für grosse Auslaufdistanzen von Bergstürzen, einige Fallstudien in vulkanischen und nicht-vulkanischen glazialen Gebieten, numerische Auslaufmodellierungen, Analysen seismischer Daten, physikalische Fliessexperimente im Labor, sowie eine empirische Analyse spezifischer Fliesseigenschaften von grossen schnellen Massenbewegungen in glazialen Gebieten.

Für vorläufige regionale Gefahrenbeurteilungen wurden einfache empirische Auslaufmodellierungen von Massenbewegungen verwendet während in spezifischen retrospektiven lokalen Fallstudien physikalisch-basierte dynamische Auslaufmodellierungen durchgeführt wurden. Neben den nötigen geometrischen Ähnlichkeiten zwischen den modellierten und den echten Ereignissen, konnten die rheologischen Eingangsparameter durch Einpassung dynamischer Modell-Ausgangsparameter an seismische Daten besser eingeschränkt werden. Das Ergebnis ist ein besserer Einblick in die Fliessdynamik von Fels-Eislawinen, wie beispielsweise genauere Geschwindigkeitsabschätzungen welche für Massnahmen der Gefahrenreduzierung von Interesse sind.

Um den Effekt von Eis auf den Reibungskoeffizienten granularer Kies-Eisgemische und damit auf den Einfluss von Eis auf die Mobilität von natürlichen Fels-Eislawinen zu quantifizieren, wurden Laborexperimente in grossen vertikal rotierenden Trommelgerinnen durchgeführt. Es wurde festgestellt, dass der Reibungskoeffizient mit steigendem volumetrischem

Eisgehalt linear bis maximal ~20% abnimmt. Bei längerer Prozessdauer verursachte schmelzendes Eis eine teilweise oder komplette Verflüssigung der Masse mit folgender Abnahme des Reibungskoeffizienten von beinahe 50%.

Eine empirische Analyse von 64 grossen Fels-Eislawinen zeigte, dass der Einfluss von Eis in natürlichen Stürzen kein dominanter Faktor ist. Die Mobilität der Ereignisse zeigte einen Zusammenhang mit der über einen Gletscher führenden relativen Fliesspfadlänge, wodurch quantitativ bestätigt wurde, dass Gletscheroberflächen mit geringer Reibung zu verlängerten Auslaufdistanzen beitragen – wie bereits von früherer Autoren angenommen. Ausserdem gehören Fels-Eislawinen mit hohem Wassergehalt häufig zu denjenigen mit den grössten Auslaufdistanzen. Die verheerendsten schnellen Massenbewegungen aus glazialen Gebieten beinhalten jedoch oftmals Kombinationen von Eigenschaften wie ein grosses Volumen, Fliesspfade über Gletscher oder glatten Fels, eingeengtes Fliessen, hoher Eis- und Wassergehalt, starke Erosion von Lockermaterial sowie Fliesstransformationen oder Kettenreaktionen.

Trotz der grossen Vielfalt und Komplexität der Prozessinteraktionen in grossen schnellen Massenbewegungen in glazialen Gebieten, konnten Einblicke in diverse Aspekte vertieft werden. Die Erkenntnisse sollten in Zukunft durch ähnliche und zusätzliche Methoden ausgeweitet werden um dereinst als fundierte Basis für Szenarien-basiertes Modellieren zu dienen.

# Table of Contents

# PART A: OVERVIEW

# PART B: PUBLICATIONS

**I** Korup, O., **Schneider, D.**, Huggel, C. and Dufresne, A. (in press): Long-runout landslides. In: Treatise on Geomorphology, edited by Shroder, J., Jr., Marston, R. and Stoffel M., Academic Press, San Diego, CA, 7, doi:10.1016/B978-0-08-088523-0.00164-7.

**II** **Schneider, D.**, Delgado Granados, H., Huggel, C. and Kääb, A. (2008): Assessing lahars from ice-capped volcanoes using ASTER satellite data, the SRTM DTM and two different flow models: case study on Iztaccíhuatl (Central Mexico). Natural Hazards and Earth System Sciences, 8(3), 559-558.

**III** Allen, S., **Schneider, D.** and Owens, I. F. (2009): First approaches towards modelling glacial hazards in the Mount Cook region of New Zealand’s Southern Alps. Natural Hazards and Earth System Sciences, 9(2), 481-499.

**IV** **Schneider, D.**, Bartelt, P., Caplan-Auerbach, J., Christen, M., Huggel, C. and McArdell, B. W. (2010): Insights into rock-ice avalanche dynamics by combined analysis of seismic recordings and a numerical avalanche model. Journal of Geophysical Research, 115(F04026), 1-20.

**V** **Schneider, D.**, Kaitna, R., Dietrich, W. E., Hsu, L., Huggel, C. and McArdell, B. W. (2011): Frictional behavior of granular gravel-ice mixtures in vertically rotating drum experiments and implications for rock-ice avalanches. Cold Regions Sciences and Technology, 69(1), 70-90.

**VI** **Schneider, D.**, Huggel, C., Haeberli, W. and Kaitna, R. (2011): Unraveling driving factors for large rock-ice avalanche mobility. Earth Surface Processes and Landforms, 36(14), 1948-1966.

# List of Abbreviations

| | |
|---|---|
| BOKU | University of Natural Resources and Applied Life Sciences, Vienna (Universität für Bodenkultur) |
| COM | Center Of Mass |
| DTM | Digital Terrain Model |
| GIS | Geographic Information System |
| LAHARZ | Empirical lahar inundation model by Iverson et al. (1998) |
| MSF | Modified single-flow-direction (numerical model by Huggel et al., 2003) |
| RAMMS | RApid Mass MovementS (dynamic physical numerical model by WSL-SLF; Christen et al., 2010) |
| SLF | WSL Institute for Snow and Avalanche Research, Davos Dorf, Switzerland |
| UCB | University of California, Berkeley |
| WSL | Swiss Federal Institute for Forest, Snow and Landscape Research, Birmensdorf, Switzerland |

# Notation

| | |
|---|---|
| $a$ | acceleration [m/s$^2$] |
| $A$ | area [m$^2$] |
| $C$ | Chézy coefficient [m$^{0.5}$/s] |
| $e$ | coefficient of restitution of solid grains [-] |
| $E$ | Energy [J] |
| $F$ | force [N] |
| $Fr$ | Froude number [-] |
| $g$ | gravitational acceleration [m/s$^2$] |
| $h$ | slope normal flow height [m] |
| $h_s$ | shear layer thickness [m] |
| $H_{com}$ | drop height of center of mass [m] |
| $H_{max}$ | maximum failure altitude [m] |
| $H_{min}$ | minimum deposition altitude [m] |
| $H'/L'$ | tangent of the slope of the high-energy cone where deposition starts (see Iverson et al., 1998) |
| $i$ | inertia |
| $k$ | hydraulic permeability [m$^2$] |
| $L$ | characteristic length [m] |
| $L_{com}$ | horizontal runout distance of centre of mass [m] |
| $L_{hor}$ | maximum horizontal runout distance [m] |
| $L_{real}$ | length of real curved path [m] |
| $m$ | mass [kg] |
| $n$ | number of particles [-] |
| $N_B$ | Bagnold number [-] |
| $N_f$ | Friction number [-] |
| $N_S$ | Savage number [-] |
| $N_m$ | Mass number [-] |
| $N_D$ | Darcy number [-] |
| $N_R$ | Reynolds number [-] |
| $r_h$ | hydraulic radius [m] |
| $R$ | random kinetic energy [J] |
| $s$ | pore water saturation [%] |
| $t$ | time [s] |
| $u$ | velocity [m/s] |
| $u_s$ | velocity difference across shear layer [m/s] |
| $V$ | volume [m$^3$] |
| $w$ | width [m] |
| $x$ | x-coordinate [m] |
| $y$ | y-coordinate [m] |
| $z$ | z-coordinate [m] |
| $\varphi$ | slope angle [°] |
| $\dot{\gamma}$ | shear rate [s$^{-1}$] |
| $\delta$ | grain size [m] |
| $\Delta H$ | vertical drop height [m] |
| $\varepsilon$ | composite mixture stiffness [Pa] |
| $\eta$ | dynamic fluid viscosity inclusive suspended fines [Pa s] |
| $\theta_{bulk}$ | bulk friction angle (static internal friction angle, ~angle of repose) [°] |
| $\theta_{bas}$ | dynamic basal friction angle [°] |
| $\lambda$ | scaling factor [-] |
| $\mu$ | friction coefficient ($\tan\theta_{bas}$) [-] |
| $\mu_{app}$ | apparent coefficient of friction ($\Delta H/L_{hor}$-ratio or $\tan\alpha$) [-] |
| $\mu_{com}$ | friction coefficient of the center of mass ($\Delta H_{com}/L_{com}$-ratio or $\tan\beta$) [-] |

| | |
|---|---|
| $\xi$ | turbulent (or 'viscous') friction coefficient [m/s$^2$] |
| $\rho$ | density [kg/m$^3$] |
| $\rho_f$ | fluid density [kg/m$^3$] |
| $\rho_s$ | solid density [kg/m$^3$] |
| $\sigma$ | normal stress [Pa] |
| $\sigma_{tot}$ | total normal stress [Pa] |
| $\tau_{bas}$ | basal shear stress [Pa] |
| $\tau_{int}$ | internal shear stress [Pa] |
| $\tau_{tot}$ | total shear stress [Pa] |
| $T$ | granular temperature [m$^2$/s$^2$] |
| $\upsilon_f$ | fluid fraction [-] |
| $\upsilon_s$ | solid fraction [-] |
| $\upsilon*$ | maximum close-packed value for the solid fraction [-] |
| *avg* | index for average value |
| *max* | index for maximum value |
| *start* | index for the start of the experiment (1st minute) or event |
| *end* | index for the end of the experiment (last minute) or event |
| *mod* | index for model |
| *prot* | index for prototype |

# PART A: OVERVIEW

# 1 Introduction

## 1.1 Motivation

Large rapid mass movements in glacial environments with volumes larger than 1 million cubic meters can have an enormous destructive potential and cause high numbers of casualties as demonstrated by a number of catastrophic events during the past decades and around the world (**Figure 1**). Considering the strong and rapid geomorphological modifications of the glacial and periglacial high mountain areas due to climate change, evidence is growing that the observed increase of mass movement activity in these highly temperature-sensitive environments is linked to the warmer temperature trends (Geertsema et al., 2006; Gruber et al., 2004; Haeberli and Hohmann, 2008).

Indeed, vanishing glaciers and degrading permafrost can reduce the strength of rock and ice in steep topography through changes in the stress regime having an important effect on slope stability (Davies et al., 2001; Gruber and Haeberli, 2007; Haeberli et al., 1997; O'Connor and Costa, 1993; Ravanel and Deline, 2010): retreating glaciers can debuttress steep valley flanks, reveal glacier lakes and leave enormous masses of unconsolidated debris that all can either be a source for mass movements or have the potential to favor process chains such as impacts into natural or artificial lakes, flood wave generation, dam overtopping, entrainment of material, and formation of debris flows (Evans and Clague, 1994; Haeberli and Hohmann, 2008; O'Connor and Costa, 1993; Rickenmann and Zimmermann, 1993).

Some of the mass movement events in the last decades are believed to be clearly linked to glacier and permafrost degradation (Fischer et al., 2006; Gruber and Haeberli, 2007; Noetzli et al., 2003). In the near future, thus, we will likely face an increasing number of mass movements involving ice, and populated areas or infrastructure could well be affected due to possible flow transformations resulting in longer runout distances than commonly assumed (Huggel, 2009). So far, a number of theoretical considerations on the mobility of large rapid mass movements have been proposed (see **Chapter 2.3**). However, the role of ice within these processes has not been systematically studied and the mechanisms leading to the typically long runout distances of such events are not well understood. An improved knowledge about the role of ice in rapid mass movements is therefore strongly needed to better assess corresponding hazards. Appropriate hazard prevention and mitigation measures must be developed particularly for regions with dense population and important economic developments that are within or close to glacial environments.

**Figure 1:** Main deposition of the Kolka-Karmadon rock-ice avalanche of September 20, 2002. The mass of approximately 130 × $10^6$ $m^3$ ice and debris detached ~20 km upstream. Photo by Igor Galushkin, September 22, 2002.

The collection of empirical data on large rapid mass movements usually remains restricted to static geometrical post-event characteristics (volume, deposition height, path length, grain size distribution, etc.). This makes it necessary that the data is complemented e.g. by physical laboratory experiments which have the advantage that individual parameters can be varied under controlled conditions and dynamic processes can be studied. However, lab experiments are subject to inadvertent scale effects, meaning that some physical processes do only occur when the event exceeds a critical size (e.g. a volume larger than $1 \times 10^6$ $m^3$) (e.g. Davies et al., 1999).

Computer based simulations are the other important methods to close the gap between real events and physical laboratory events. Thereby, physical findings as well as theoretical considerations can be tested by retrospective modeling and – if successful – used for predictive applications in hazard assessments. Expert knowledge about critical failure dispositions and empirical findings concerning the mass movement mobility play a key role for scenario developments which then can be numerically modeled. To account for the possibility that regional extreme scenarios based on empirical evidence and expert knowledge might be exceeded under current climate change induced developments (Haeberli and Beniston, 1998; Huggel, 2004), a global perspective is needed for considering worst-case scenarios. As an example, no event such as Kolka-Karmadon or Huascarán has occurred in the European Alps in historic times, but due to current changes, similar initiation conditions could be reached soon for particular settings. The improvement of knowledge about such disastrous cases can therefore help to estimate worst-case scenarios of failure mechanisms, flow propagation and reach of potential extreme events in other regions than those where observations were made. In glacial environments, the effects of ice on the dynamics of rapid mass movements can be critical and need to be considered specifically, either within simple parameterization methods or in computer simulations.

## 1.2 Objectives and research questions

In this work we focus on the propagation mechanisms and mobility of rapid mass movements from glacial environments while detailed analysis of failure mechanisms specifically related to glacial and periglacial areas have been conducted by other authors (Amitrano et al., 2010; Eberhardt et al., 2004; Fischer et al., 2010; Fischer et al., 2006; Gruber and Haeberli, 2007; Hasler et al., submitted; Krautblatter and Funk, 2010). The main research questions related to large rapid mass movements from glacial environments addressed in this thesis are:

1. *What are the effects of ice on mobility of large rapid mass movements in/from glacial environments?*

Since the constitutive work of Evans and Clague (1988) who proposed several mechanisms having potential effects on the runout dynamics of rapid mass movements in glacial environments, no systematic investigation has been performed on the effective influence of ice nor has it been quantified. This involves the contribution of ice as a part of the moving mass and as source of meltwater during the flow propagation that has been assessed in this study by laboratory experiments while the role of ice as a low friction sliding surface was analyzed on an empirical basis. Because this issue does not cover all aspects which are typical for rapid mass movements in glacial environments, the second question is wider:

2. *Which factors and situations have the potential to lead to extremely mobile events in glacial environments?*

To address this question, the work contains an attempt to unravel key driving factors for rock-ice avalanche mobility based on empirical and laboratory results. The focus thereby was set on the influence of volumes, topographic/geometric factors, ice- and water content, and on low friction surfaces such as glaciers while general theories related to rapid mass movement dynamics and excess-runout are also considered.

Retrospective case study analysis usually serves as a basis for rapid mass movement studies so that several numerical models were applied. This led to the next question:

3. *What kind of numerical tools can be applied to assess large rapid mass movements in/from glacial environments and how can the benefits from numerical modeling be maximized to enhance process understanding?*

Case studies were performed in the European Alps, Alaska, New Zealand and in Mexico where two numerical mass movement simulation models based on hydrologic flow routing and empirical assumptions were applied and a third physically-based model was used. A key method applied here was the comparison of model results to seismic data.

Finally, the consequences for hazard assessments may be of interest:

4. *What are the implications for hazard assessments?*

The study does not provide distinct guidelines for hazard assessment, but includes some empirical (semi-) quantitative diagrams that may be useful for practical applications.

During the progress of this work, these questions were not answered sequentially, but individual publications within this study contain several aspects so that all questions could be addressed to some extent. It needs to be noted that the complexity of the topic likely will never allow full explanation of all features related to large mass movements (in general and in glacial environments). However, the presented work should contribute to the understanding of relevant mechanisms for a special type of rapid mass movement, some results of which may also be transferred to other settings.

## 1.3 Structure of the thesis

The thesis comprises two main parts: an overview (Part A) and a part with six publications (Part B). **Figure 2** provides a schematic view of the two components and its contents.

**Part A** serves as a framework and synopsis of the entire study. After the current Introduction, the Scientific Background is provided (**Chapter 2**). This encloses a short review of existing knowledge and theories about relevant mechanisms in mass movements in general and some special characteristics of events in glacial environments, including potential failure situations of rock-ice avalanches. An overview over existing numerical simulation tools is provided and benefits and limits of laboratory models are discussed. Another important aspect is related to the contribution of seismic data to the understanding of rapid mass movements. Then, the main results of the individual publications are summarized (**Chapter 3**) and discussed (**Chapter 4**). Within the Conclusions and Perspectives (**Chapter 5**), the initially presented research questions are addressed and answered as far as possible. The last chapter (**Chapter 6**) is an Appendix that includes detailed plots and tables of the results from the laboratory experiments that were not published in this form.

**Part B** includes six publications (roman numbers **I**-**VI**) that have arisen within the framework of this study. For publication numbers **I** and **III**, the present author contributed significant parts as a second author. These contributions fit well into the framework of the thesis because characteristics and mechanisms of long-runout landslides (**Paper I**) are also relevant for rapid mass movements in glacial environments, and the performance of a numerical avalanche model has been tested on the basis of a case study in New Zealand (**Paper III**). The other four papers include original first author contributions on the topic which have been published in peer reviewed journals (**Papers II**, **IV**, **V** and **VI**). Their contents can be roughly divided into seven core topics and methods such as literature review, case study analysis, numerical modeling, process understanding, physical modeling, empirical analysis, and a synthesis on large rapid mass movements in glacial environments (**Figure 2**).

| **Part A:** Overview | |
|---|---|
| 1 | Introduction |
| 2 | Scientific Background |
| 3 | Summary of Research Results |
| 4 | General Discussion |
| 5 | Conclusions and Perspektives |
| 6 | Appendix |

| **Part B:** Publications | | | | | | | | |
|---|---|---|---|---|---|---|---|---|
| **Paper number** | Literature review | Case studies | Numerical modeling | Process understanding | Physical modeling | Empirical analysis | Synthesis | Titles of enclosed publications |
| **I** | ■ | | | | | | | Long-runout landslides** |
| **II** | ▨ | ■ | ■ | | | | | Assessing lahars from ice-capped volcanoes using ASTER satellite data, the SRTM DTM and two different flow models: case study on Iztaccíhuatl (Central Mexico)* |
| **III** | ▨ | ■ | ■ | | | | | First approaches towards modelling glacial hazards in the Mount Cook region of New Zealand's Southern Alps** |
| **IV** | ▨ | ■ | ■ | ■ | | | | Insights into rock-ice avalanche dynamics by combined analysis of seismic recordings and a numerical avalanche model* |
| **V** | ▨ | | | ■ | ■ | | | Frictional behavior of granular gravel-ice mixtures in vertically rotating drum experiments and implications for rock-ice avalanches* |
| **VI** | ■ | ■ | | ■ | ■ | ■ | ■ | Unraveling driving factors for large rock-ice avalanche mobility* |

**Figure 2:** Overview of the structure of the thesis (* first author papers; ** second author papers of the present author). Core topics of the publications are highlighted.

# 2 Scientific Background

The current chapter provides an overview of the scientific background of various aspects of rapid mass movements in steep high mountain areas. First, we introduce different types of rapid mass movements, including some definitions. This is followed by a discussion of current theories on long runout mechanisms, some peculiarities of rapid mass movements evolving in or from glacial environments, the possibilities of numerical and physical runout modeling, and the use of seismic signals of rapid mass movements.

## 2.1 Rapid mass movements

Different types of rapid mass movements exist and many attempts have been made to classify the unrestricted natural variability (Hungr et al., 2001; Hutchinson, 1988; Varnes, 1978). Classification can be done e.g. according to the water content, material properties, velocity of movement, failure mechanism, and volume (Hungr, 2005). Here, the term *rapid mass movements* is used as an umbrella term for landslides of very high velocity (>5 m/s according to Hungr et al., 2001) that include *rock avalanches*, *debris avalanches*, and *debris flows*. Iverson and Denlinger (2001) used the term *geophysical flow* that may be used as a synonym. The ancillary word *large* refers here to volumes larger than $1 \times 10^6$ $m^3$ where long runout effects are becoming relevant (Davies and McSaveney, 1999).

We further use the expressions *rapid mass movements in glacial environments* (including the periglacial area) and more specifically *rock-ice avalanches* that relate to the influence of ice on the flow propagation and runout dynamics. *Rock-ice avalanches* term rock- and debris avalanches which involve ice, firn or snow from the beginning of the movement or due to entrainment. The terminology underlines the role of ice in a stronger way and adverts more explicitly to the relatively dry, unconfined and turbulent avalanche-like movement type which is typical for these events but not for all flow stages, e.g. if a rock-ice avalanche develops a debris flow-like movement which is characterized by stronger channelization (Hungr et al., 2001) and higher contents of water and fines (clay and silt; <0.0625 mm) so that viscous forces increase (Higashi and Sumita, 2009; Iverson, 1997b). Therefore, *rapid mass movements in glacial environments* is an appropriate term to enclose a broader range of flow stages within an individual event, as well as mass movements over glaciers without any significant entrainment of ice.

In volcanic environments, the term *lahar* is used for a range of debris flows with usually higher concentrations of fines (Vallance, 2000; Verstappen, 1992). The difference of source and path material makes them as well as volcanic debris- and rock avalanches significantly more mobile than their non-volcanic counterparts (Dufresne et al., 2010; Korup et al., in press; Legros, 2002). Other distinctive features on volcanoes are the abundance of hydrothermally altered rock which is more susceptible to failure than non-volcanic rock (Crowley and Zimbelman, 1997; Huggel et al., 2007; Waythomas and Wallace, 2002) and the possibility of volcano-ice/-snow interactions which can release large amounts of water within a short time and lead to lahars (Julio-Miranda et al., 2008; Pierson et al., 1990; Thouret et al., 2007) or ice-slurry flows (Cole et al., 2009; Lube et al., 2009).

In terms of hazards from rapid mass movements, their mobility is among the most critical parameters and usually expressed as the apparent coefficient of friction $\mu_{app}$ which is defined as the ratio between drop height $\Delta H$ and maximum horizontal runout distance $L_{hor}$ ($\Delta H/L_{hor}$ = tangent of slope). Other authors denote mobility also as *'Fahrböschung'* (Heim, 1932) or *'angle of reach'* (Corominas, 1996). Despite the strong differences in material properties, flow behavior and mobility between different individual types of mass movements, there is a common ground from an avalanche dynamics perspective which has been pointed out by many authors (Bouchut et al., 2008; Iverson and Denlinger, 2001; McDougall and Hungr, 2005; Savage and Hutter, 1989). Therefore, various flow mechanisms (as described in **Chapter 2.3**) and numerical runout models (**Chapter 2.4**) can be considered for a broad range of rapid mass movement types, such as for rock avalanches, landslides, debris flows, ice- and snow avalanches (excl. powder avalanches) and combined events.

## 2.2 Rapid mass movements in glacial environments

On September 20, 2002, an extremely large rock-ice avalanche of approximately $130 \times 10^6$ $m^3$ devastated the Genaldon valley in the Russian Caucasus and destroyed the lower parts of the village of Karmadon causing at least ~125 fatalities (Evans et al., 2009b; Haeberli et al., 2004; Huggel et al., 2005; Kotlyakov et al., 2004; Petrakov et al., 2008). This event was not only extraordinary in terms of its size, but also with respect to the high mobility, complete failure of a glacier, strong entrainment of sediments, and the flow transformation which was involved (**Figure 3**). The mixture of ice, debris and water travelled at maximum velocities of 70-90 m/s over 19 km where it was blocked by a narrow gorge (Huggel et al., 2005). A massive debris flow formed from draining water that continued for another 17 km. The Kolka event was extremely mobile, reaching a value for $\mu_{app}$ of 0.11 for the main part of the avalanche and even 0.08 if the distal debris/mud flow is included. Petrakov et al. (2008) introduced the new term *'catastrophic glacial multi-phase mass movements'* to account for these special types of rapid mass movements from glacial environments that involved high mobility, long runout, extremely rapid movement and flow transformations.

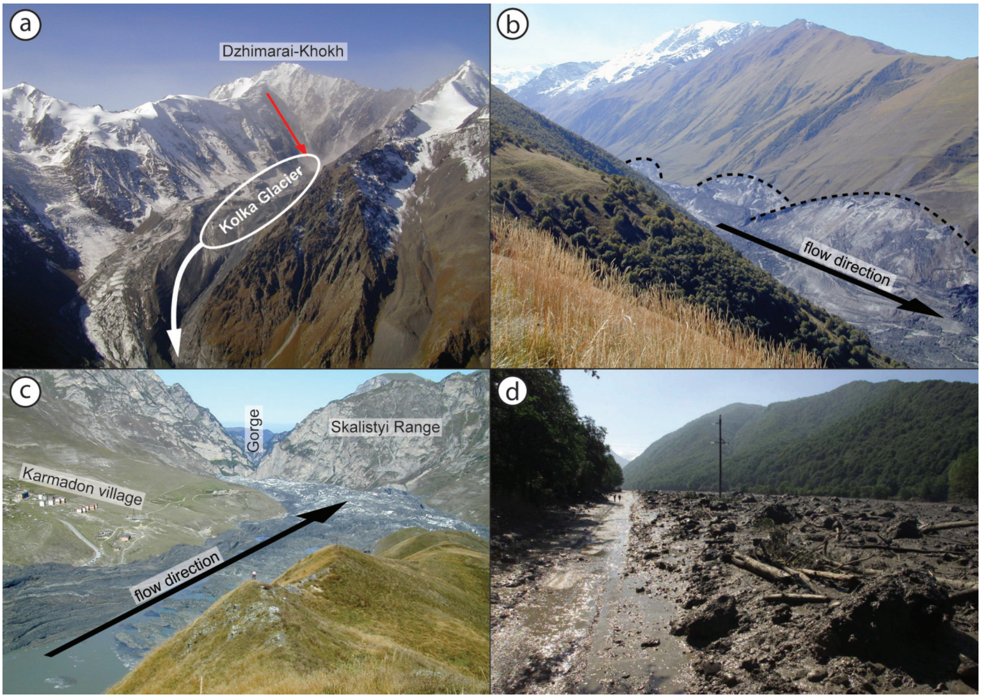

**Figure 3:** Different flow path sections of the Kolka-Karmadon rock-ice avalanche of September 20, 2002. (a) Area of rock and glacier failure. Red arrow indicates the source of rock and ice which caused failure of Kolka Glacier either directly by the impact of one major event (Haeberli et al., 2004; Huggel et al., 2005), or due to accumulation of material by high rockfall activity over months (Evans et al., 2009b). White arrow shows the area where Kolka Glacier failed. (b) Flow path showing lateral swash ('caroming', dashed lines; Hewitt et al., 2008) and entrainment of valley-fill sediments. (c) Main deposit at Karmadon depression where about half of the total number of 125 victims were killed. The mass impacted the Skalistyi Range and was blocked by the narrow gorge. (d) Distal debris/mud flow formed by squeezed-out water. Photos by Igor Galushkin, September 22, 2002.

The rock-ice avalanche of May 31, 1970, from Nevado Huascarán in the Cordillera Blanca, Peru, was among the largest rock-ice avalanches of the last decades with a volume of approximately 60 × $10^6$ $m^3$ (Evans et al., 2009a; Körner, 1983; Plafker and Ericksen, 1978). The 1970-event was preceded by a first avalanche on January 10, 1962, and the two avalanches caused a total live loss of 7,000 to 22,000 people depending on the source. This is the most tragic catastrophe related to glacial hazards known in history because a low-frequency/high-magnitude event impacted a densely populated region. Similarly to Kolka-Karmadon, the avalanches from Huascarán featured a horizontal runout of 16 km with maximum velocities above 100 m/s, and evolved from a rock-ice avalanche into a much more mobile debris-flow-like rapid mass movement (Evans et al., 2009a). While the ice content at Kolka was as high as 80-90% by volume, it was ~30% or less at Huascarán and flow transformation was probably favored by entrainment of fine grained water-saturated debris. However, at Huascarán $\mu_{app}$ was significantly higher with 0.23.

A number of rapid mass movements in glacial environments larger than 1 × $10^6$ $m^3$ were reported during the last decades in the European Alps (Alean, 1984; Bottino et al., 2002; Coaz, 1910; Deline, 2001; Deline and Kirkbride, 2009; Eisbacher and Clague, 1984; Hanke, 1966; Noetzli et al., 2003; Noetzli et al., 2006; Raymond et al., 2003; Rozman et al., 2004; Sosio et al., 2008), North America (Caplan-Auerbach et al., 2004; Crandell and Fahnestock, 1965; Delaney and Evans, 2008; Evans and Clague, 1988; Huggel et al., 2007; Iverson, 1997a; Jibson et al., 2006; Jiskoot, 2010; Lipovsky et al., 2008; Marangunic and Bull, 1968; McSaveney, 1978; Post, 1968), South America (Gordon et al., 1978; Hauser, 2002; Iribarren Anacona and Bodin, 2010), New Zealand (Korup, 2005; McSaveney, 2002) and Central Asia (Hewitt, 1988; Hewitt, 2009; Schneider, 2006; Van Der Woerd et al., 2004). Most of these events occurred in remote areas, but several passed beyond glacial limits and reached populated areas or infrastructure, causing high numbers of casualties or damage to infrastructure.

Glacial environments provide settings for rapid mass movements which differ significantly from non-glacial environments. Characteristic features can be related to increased susceptibility for detachment – particularly under conditions of a warming climate – and to effects which may increase the mobility. In comparison to non-glacial regions, the frequency and magnitude of rapid mass movements in glacial environments may be enhanced in general and with respect to climate change in terms of:

- Potentially unstable steep glaciers (transition of cold to polythermal or temperate base) (Alean, 1985; Frey et al., 2010; Huggel, 2009; Huggel et al., 2005; Pralong and Funk, 2006).
- Debuttressed slopes due to glacier retreat which could fail (Deline, 2009; Evans and Clague, 1994; Haeberli and Hohmann, 2008; Holm et al., 2004; O'Connor and Costa, 1993; Oppikofer et al., 2008).
- Permafrost degradation in steep bedrock or debris, often resulting in slope destabilization (Bottino et al., 2002; Davies et al., 2001; Deline, 2009; Dramis et al., 1995; Fischer et al., 2006; Gruber and Haeberli, 2007; Haeberli et al., 1997; Harris et al., 2003; Hasler et al., submitted; Ravanel and Deline, 2010).
- Abundance of (often steep) friable material which can be eroded such as debris, snow and ice (Evans and Clague, 1994; Huggel, 2004; Rickenmann and Zimmermann, 1993).
- Process chains such as impact waves caused by rapid mass movements into (young) glacial lakes with potentially unconsolidated and unstable moraine dams that could fail and produce subsequent debris flows and floods (Evans and Clague, 1994; Korup and Tweed, 2007).
- Volcano-ice interactions by hydrothermal or eruptive volcanic activity which can destabilize potentially frozen steep debris (Evans and Clague, 1988; Iverson, 1997a) and

glaciers (Huggel et al., 2007) or rapidly melt large volumes of ice (Julio-Miranda et al., 2008; Pierson et al., 1990; Thouret et al., 2007).

- High mass turnover rates which can successively lead to new hazard situations much faster than in non-glacial environments (Allen et al., 2009).

Indications for an intensified mass movement activity in (formerly) glacierized high mountain regions are currently increasing (Allen et al., 2010; Fischer, 2009; Huggel, 2009) and a linkage to global warming is becoming more evident (Geertsema et al., 2006; Gruber et al., 2004; Haeberli and Hohmann, 2008; Ravanel and Deline, 2010). The stability of steep rock walls in glacial environments was investigated within several recent studies. Fischer (2009) found that besides slope gradient and elevation, changes in glaciation strongly influenced recent slope failures. Additionally, many unstable zones have been observed to be close to the lower limits of permafrost (Deline et al., 2009; Fischer, 2009; Ravanel et al., 2010; Ravanel and Deline, 2010), supporting the theory that permafrost degradation can be an important factor in rock slope destabilization (Davies et al., 2001; Dramis et al., 1995; Gruber and Haeberli, 2007; Gruber et al., 2004; Haeberli et al., 1997; Harris et al., 2003). Atmospheric warming can be dissipated to subsurface either by conduction (Noetzli et al., 2007) or in a much faster way by the development of thaw corridors along fractures, enabling water to percolate advectively much deeper into the bedrock and destabilize much larger volumes than by pure conduction (Hasler et al., in revision). Huggel et al. (2010) found that several large slope failures were preceded by unusually warm periods, often followed by a sudden drop in temperature. They suppose that rapid refreezing of meltwater in rock discontinuities could strongly increase pore pressures within these joints. Given potentially unstable geological, glaciological and topographic conditions, this may be a sufficient triggering factor for rapid mass movements (see also McSaveney, 2002).

We distinguish between three general possibilities how ice can be incorporated in the moving mass while most events include combinations of them (see also **Paper VI**, Schneider et al., 2011a):

- Failure of steep glaciers (**Figure 4a**). Ice content is high to very high but debris may be eroded along the downstream path.

- Failure within bedrock or rock debris (**Figure 4b**). Ice content ranges from high if entire overlying glaciers are entrained to low if permafrost from cleft systems or pore spaces is involved.

- Entrainment of snow, ice and frozen debris by rock-/debris avalanche passing over glaciers (**Figure 4c**), snow or debris covered areas with seasonal frost or permafrost (potentially degraded). The erosion rate strongly varies depending on the internal strength of the entrained material.

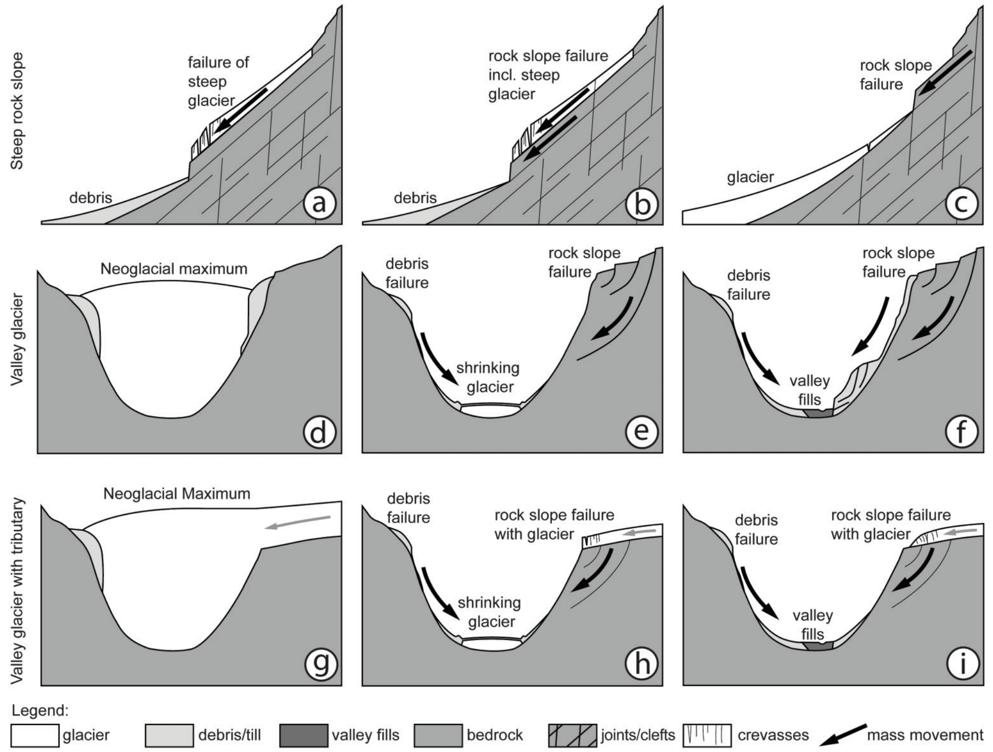

**Figure 4:** Cross section examples of rock slope and glacier failure situations where ice can be involved. Rock slope and debris failures can contain varying quantities of ice (permafrost, seasonal cleft ice, dead ice, etc.). Mass movements over glaciers and debris/till often involve entrainment of the corresponding material. Figures (d) and (f) are modified from O'Connor and Costa (1993).

Other possible predispositions for rock-ice avalanches related to debuttressing of a valley glacier with or without a tributary glacier are depicted in **Figure 4d-i**. Hewitt (2009) defined different categories of rock avalanches in glacial environments according to their origin, travel path and deposition areas in relation to the glacial basins: events occurring entirely in glacial zones, those originating in glacier basins that travel onto ice-free valley floors, and others detaching from slopes in ice-free valleys and travelling or depositing on tongues of valley glaciers.

Evans and Clague (1988) found significantly lower average apparent friction coefficients for a number of rapid mass movements in glacial environments compared to others in non-glacial settings. The higher mobility may be explained by the following possible reasons:

- Low-friction surfaces provided by glaciers (Bottino et al., 2002; Evans and Clague, 1988; Sosio et al., 2008).

- The possibility of self-lubrication in rapid mass movements by melting of overflown or incorporated ice and snow due to frictional heating that causes pore pressure effects at the base of the moving mass or fluidizes the entire flow body (Erismann and Abele, 2001; Evans and Clague, 1988; Huggel et al., 2005).
- Topographic effects due to channeling or air-launching of the debris by moraines (Evans and Clague, 1988; Nicoletti and Sorriso-Valvo, 1991; Shreve, 1966).

Bottino et al. (2002) used friction coefficients as low as 0.01 on a glacial surface for calculations of the Felik and Brenva avalanches in Northern Italy compared to 0.3-0.4 for flow over bedrock. They quantified the observed runout distances of rock-ice avalanches in glacial environments to exceed predicted ones for pure rock avalanches by 30%. Sheridan et al. (2005) applied a friction coefficient of 0.037 over ice and snow for simulations of the 1963 Little Tahoma Peak avalanche ($1 \times 10^6$ $m^3$) from Mt. Rainier, Washington USA. A compilation of typical friction values for different flow rheologies and avalanche types by Sosio et al. (2008) confirms that rock-ice avalanches exhibit the lowest friction values.

Melting of ice has been proposed by several authors to contribute to reducing friction. Erismann and Abele (2001) argue that with a melt-energy of 334 kJ/kg, ice can lubricate an overlying mass much more easily than rock (1280 kJ/kg) or evaporated water (2260 kJ/kg). They calculated that a mass with a thickness of 100 m and 1 km travel distance could melt a layer of ice as thick as 1.6 m compared to an energy-equivalent molten rock layer of only 0.15 m. Harrison and Grimm (2003) assumed that substantial parts of long-runout Martian landslides must have been saturated with ice (see also Mangold and Allemand, 2001). They used the DAN model (Hungr, 1995) to calculate that heat energy of 1 kJ/kg was produced due to friction. Based on the required melt-energy for ice (334 kJ/kg) they concluded that the energy is much too small. Based on similar assumptions, Soukhovitskaya and Manga (2006) calculated that a maximum of 10% of the total volume could have melted at the time when the Martian landslides stopped, and concluded that this amount was unlikely to have fluidized the mass. However, it is possible that the melt energy was concentrated on thinner layers and not distributed equally over the entire flow height. Legros (2002) assumed that at least a part of the ice in the landslides on Mars must have melted rapidly and remained stable within the landslide due to the pressure of the overburden, so that the mass may have been lubricated. Based on evidence for quicklime (a calcined carbonate frictionite) at the Bualtar rock-ice avalanche in the Karakoram Himalaya, Hewitt (1988) argues that strong frictional heating can only occur when the mass has attained a critical velocity, but before it disintegrates when the heat would diffuse rapidly (usually at very high velocities on irregular terrain with turbulent flow).

## 2.3 Long-runout mechanisms

It is assumed that the mobility of rapid mass movements from glacial environments involving varying portions of ice is influenced by similar effects as their non-glacial counterparts. Therefore, general mechanisms which are hypothesized or assumed to be effective in landslides and debris avalanches need to be included to assess the mobility of rock-ice avalanches. This section is based on the theoretical background in **Paper VI** (Schneider et al., 2011a). **Paper I** (Korup et al., in press) provides an additional and broader overview of long-runout landslides in volcanic and non-volcanic settings.

The question why many large landslides ($>1 \times 10^6$ m$^3$) reach runout distances exceeding those expected from conventional friction physics (Davies and McSaveney, 1999; Erismann and Abele, 2001; Heim, 1932; Hsü, 1975; Legros, 2002) has concerned scientists for decades and a variety of theories have been developed to explain this phenomenon. We first give an overview of such theories which can be relevant for rapid mass movement dynamics (including rock-ice avalanches).

### 2.3.1 Volume effect

Heim (1932) found that the apparent friction coefficients $\mu_{app}$ (see **Figure 5**) for landslides progressively decrease with increasing volumes. Many other authors extended the dataset differentiating between various types of mass movements, such as debris flows/debris avalanches/rock avalanches/landslides (Hsü, 1975; Okura et al., 2003; Rickenmann, 2005; Scheidegger, 1973), changing path conditions (Corominas, 1996), and different environmental settings like volcanic/non-volcanic (Dade and Huppert, 1998), glacial/non-glacial (Alean, 1985; Evans and Clague, 1988), subaerial/submarine (Legros, 2002), or Earth/Moon/Mars (Collins and Melosh, 2003; Harrison and Grimm, 2003), largely confirming this trend. At first sight this may seem astonishing because the runout distance in a simple sliding block model is independent of volume, however, disintegrated rapidly moving granular masses apparently behave differently.

Legros (2002) proposed that the velocity and hence the reach of a rapid granular mass movement depends on the slope and flow thickness. Indeed, flow resistance forces are determined by the slope angle, and basal and internal frictional characteristics of the interacting materials (see **Chapter 2.4.2**) which together define the shear gradient that in turn controls the rate of deposition at the base. As soon as deposition starts, the shear layer moves progressively upwards (normal to slope) to let the mass movement run out of material and stop entirely (see also Bartelt et al., 2007; Van Gassen and Cruden, 1989). In other words, the forces acting against gravitational acceleration and previously gained momentum (frictional and viscous resistance) need to stop one layer after each other from the base to the top. The stopping mechanism consequently takes more time for thicker mass movements than for thin and less voluminous ones. This time can be used to travel further and elongate the deposition lobe (Straub, 1997). In fact, the friction coefficient of the center of mass $\mu_{com}$ rather than the apparent friction coefficient $\mu_{app}$ defines the energy balance, and excess runout can only be achieved by corresponding early deposition of material (Campbell et al., 1995; Davies, 1982; Straub, 1997). Okura et al. (2000) have experimentally confirmed the decrease of $\mu_{app}$ with increasing volume but also found $\mu_{com}$ to increase, possibly due to more frequent collisions

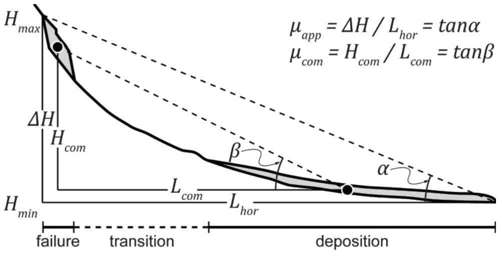

**Figure 5:** Schematic profile along a mass movement trajectory with different measures of the friction coefficients. Centers of mass (COM) are indicated by black dots. $\mu_{app}$, apparent coefficient of friction [-]; $\mu_{com}$, coefficient of friction of the center of mass [-]; $H_{max}$, maximum failure altitude [m a.s.l.]; $H_{min}$, minimum deposition altitude [m a.s.l.]; $\Delta H$, total drop height ($H_{max}$ - $H_{min}$) [m]; $L_{hor}$, maximum horizontal runout distance [m]; $H_{com}$, drop height of center of mass [m]; $L_{com}$, horizontal runout distance of center of mass [m]. Figure from Schneider et al. (2011a).

between blocks (for number $n$ of particles $1 \leq n \leq 1000$ and volumes $V$ $0.001 \leq V \leq 1$ m$^3$). While the decrease of $\mu_{app}$ with increasing volume can be widely confirmed for large natural rapid mass movements, $\mu_{com}$ remains much more difficult to determine and precise field data is largely missing.

If friction at the base is reduced by any of the mechanisms presented in the following sections, the shear gradient gets sharper (thinner shear layer) and hence its upward migration (Imre et al., 2010) that finally stops the flow is retarded. The consequence is endured preservation of the movement resulting in an enhanced runout in addition to the volume effect.

### 2.3.2 Theories related to dispersive pressure

In a granular mass that destabilizes and starts moving, the static friction coefficient reduces to a significantly lower dynamic friction (Straub, 1997; Voellmy, 1955). With increasing velocity, the mass leaves the frictional flow regime in which energy is dissipated by long-lasting frictional contacts and reaches the collisional flow regime where energy predominantly dissipates by short-lived collisional contacts between individual grains (Bagnold, 1954; Iverson and Denlinger, 2001; Savage, 1984), and the particle behavior resembles that of individual molecules in a gas (Campbell, 1990; Iverson et al., 1997). The *granular agitation* energy is causing a randomly driven dispersive pressure which is also called *granular temperature* (due to the linkage to thermodynamics; **Figure 6**) or *random kinetic energy* (Bartelt, 2007; Bartelt and Buser, 2010; Bartelt et al., 2006; Buser and Bartelt, 2009). This is expected to result in a volume increase (dilatation) and a further reduction of the internal shear resistance within the shear layer. The so-called *mechanical fluidization* (Davies, 1982) hence is driven by the avalanche movement itself (loss of potential energy) and the work done to overcome friction (frictional work rate). When the avalanche is decelerating, the production of random kinetic energy and its effect to reduce the friction coefficient starve (Bartelt et al., 2007). This also explains the often observed abrupt stopping and sharp boundaries of rapid mass movements as well as the formation of pressure ridges (Campbell, 1989; Davies, 1982; Eisbacher and Clague, 1984; Hewitt, 2002).

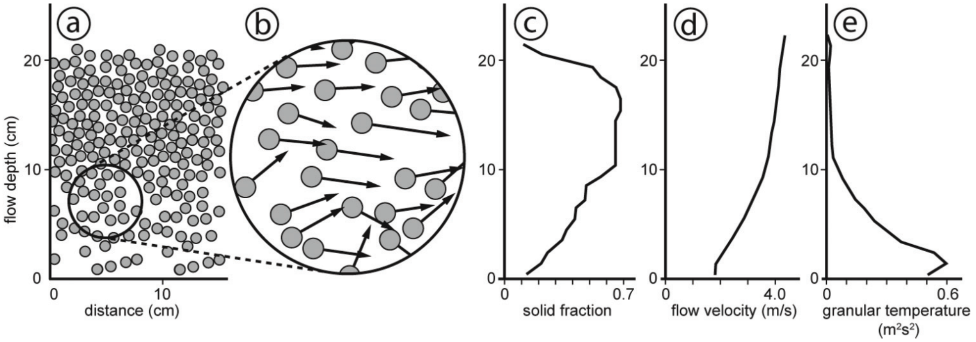

**Figure 6:** Simulation of the shear zone (height 0 – 10 cm) and plug flow (height 10 – 20 cm) of a monodisperse dry granular flow (modified from Straub, 1997). Distribution of grains (a) is magnified in (b) to indicate random movements of individual grain. (c) Solid fraction and (d) flow velocity as a function of flow height. The strength of shearing is given by the gradient of the flow velocity which is equivalent to the granular temperature shown in (e).

A similar decrease of the shear resistance due to grain dilatation may be externally induced by the oscillating ground during an earthquake, such as hypothesized by McSaveney (1978) to be a reason for the extremely long runout of the Sherman Glacier rock-avalanche during the Alaskan earthquake of 1964, and as shown by small-scale laboratory experiments by Davies (1982). However, most long runout events do not occur during earthquakes. Melosh (1979) proposed that the energy needed to cause grain fluctuations may result from an acoustic source and called the effect *acoustic fluidization*. The initial collapse and subsequent flow of the rock material are assumed to generate high-frequency pressure fluctuations which locally relieve overburden stresses, reducing frictional resistance (Collins and Melosh, 2003). The generation of the grain fluctuations is closely related to the above described *granular agitation*, *granular temperature*, and *random kinetic energy* concepts.

The *dynamic fragmentation* theory (comminution) infers that dispersive pressure can also be generated by the rapid breakage of rock particles within force chains (or so-called grain bridges; Campbell, 2002; Davies and McSaveney, 2009; Davies et al., 1999; Davies et al., 2010; Howell and Behringer, 1999; Mair and Hazzard, 2007; Taboada and Estrada, 2009). Thereby, the elastic strain energy increases until the particle fragments and the stored energy converts into kinetic energy (pressure energy) and heat (**Figure 7**). The crushed fragments move away from the original center of mass – primarily in the direction of the minimum effective stress – reducing the friction between these grains (see also Imre et al., 2010). This process seems to be possible even within a strongly confined shear layer and the resulting effective shear stress is a function of the overburden stress (flow thickness) and the strength of the intact material. That gives support to the observed volume effects as well as to the generally higher mobility of volcanic debris avalanches which comprise much more weakened material compared to non-volcanic events (Davies et al., 2010).

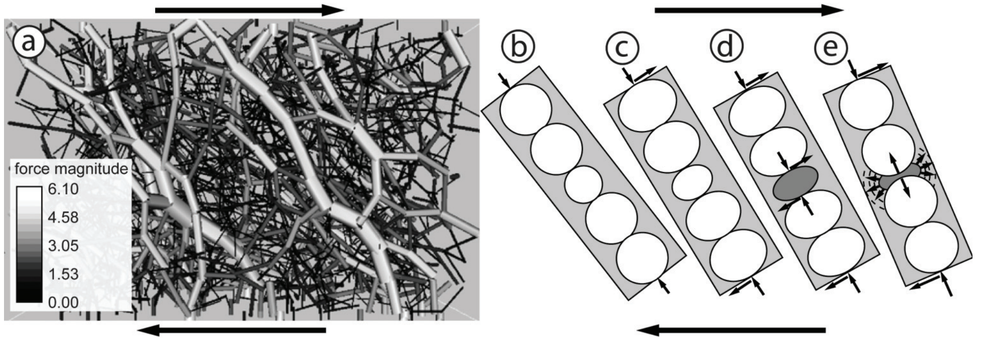

**Figure 7:** (a) Simulated force chains which are developing diagonally to shear (black arrows; modified from Mair and Hazzard, 2007). (b) – (e) are modified from Davies and McSaveney (2009) and schematically show the mechanism of dynamic fragmentation within an individual force chain. Compressive forces due to shear lead to elastic distortions of grains so that the weakest grain finally fragments (dark grey) and outwards-directed forces lead to a dispersive pressure.

All these mechanism do not require the presence of any lubricants such as water, air or molten rock, and therefore could also explain long runout landslides on Moon, Mars, Venus and other planets.

### 2.3.3 Lubrication and fluidization

On Earth, most rapid mass movements are not completely dry and the presence of liquids strongly influence flow dynamics. Thereby we distinguish *lubrication* that is restricted on a thin basal layer and *fluidization* that affects larger parts of the flow body.

Kent (1966) and Shreve (1968) proposed air lubrication where rapid landslides may slide on a thin layer of compressed air after topographic jumps. However, the dynamic air pressures needed to support the overburden stresses are unrealistically high (Erismann and Abele, 2001), and agitated particles are relatively permeable so that air is likely to leak largely unhindered through the debris. Lubrication by water is much more realistic due to its incompressibility, as well as its higher density and viscosity (Legros, 2002). High water concentrations can be reached at the base of landslides e.g. by initial shearing within a highly saturated water-rich layer, entrainment of river water, shallow lakes, or water-saturated valley-fill deposits (Dufresne et al., 2010; Hungr and Evans, 2004; Kelfoun and Druitt, 2005; McSaveney and Davies, 2007; Prager et al., 2006; Voight and Sousa, 1994). This may force pore water to support at least part of the landslide's weight and occasionally lead to hydroplaning (Voight and Sousa, 1994).

Evidence for lubrication by frictional heating was provided when layers of molten rock (frictionites) were found in several rock-avalanche deposits (De Blasio and Elverhoi, 2008; Erismann, 1979; Hewitt, 1988; Legros et al., 2000; Weidinger and Korup, 2009). Refrozen snow observed at the base of snow avalanches gave further support to the relevance of frictional heating (Bartelt et al., 2006; De Blasio and Elverhoi, 2008). Goguel (1978) even discussed steam generation along thin sliding planes which may elevate pore pressure and reduce shear resistance if permeability and diffusion rates of the overlying substrate are low enough

(Goren and Aharonov, 2007). However, measured shear layers are often much thicker than they would be required to concentrate the frictional heat energy sufficiently to enable steam production (Davies et al., 2006).

If water is not concentrated on a thin layer but affects the entire avalanche body, partial or complete saturation may evolve. Under unsaturated conditions water can stabilize soil and debris due to cohesion (particularly in combination with clays; McSaveney and Davies, 2007), but as soon as the pores get saturated, buoyancy forces strongly increase and support parts of the debris, reducing internal friction and finally fluidizing the mass. This effect can liquefy large amounts of friable material to form far reaching debris avalanches, debris flows or lahars, and has already been verified theoretically (Iverson, 2005), experimentally in artificial debris flow flumes (Iverson et al., 2010; Schneider et al., 2011b), as well as observed in natural debris flows (McArdell et al., 2007). Due to shearing of the interstitial water it can reach pressures exceeding hydrostatic pressures – so-called 'excess pore water pressure' – that contributes to fluidizing the saturated mass (Hotta and Ohta, 2000; McArdell et al., 2007). Furthermore, dynamic pore pressure fluctuations which result from grain rearrangements in rapidly shearing granular flows may reduce frictional energy dissipation (Iverson and LaHusen, 1989). Water is therefore seen as one of the most important reasons for excess runout of rapid mass movements (Legros, 2006).

## 2.4 Numerical runout modeling

Computer-based numerical modeling of rapid mass movements closes the gap between rather small-scale physical modeling and real field events where dynamic measurements are expensive or impossible. Modeling of mass movements includes tools which are specialized on the failure mechanisms (e.g. Eberhardt et al., 2004; Fischer et al., 2010; Kveldsvik et al., 2009; Stead et al., 2006) and others which concentrate on the runout of mass movements (flow propagation and deposition) some of which are introduced in the following. A more complete list of runout prediction methods is provided by Rickenmann (2005).

Numerical runout models are important tools for retrospective modeling and hazard assessments of rapid mass movements. They roughly can be divided into empirical and dynamic models. Because the focus is on rapid mass movements with high contents of solids, purely hydraulic flood routing models such as *Hec-Ras* (Brunner, 2002) are not considered.

### 2.4.1 Empirical runout models

Besides simply defining a minimum average slope for the maximum runout distance, one of the most basic runout prediction method is based on the empirical relation between volume and apparent coeffiction of friction for specific types of historical mass movements (see **Chapter 2.3.1** and **Figure 5**), meaning that the expected mobility – and hence the travel distance – can be derived from a given volume (Rickenmann, 2005). Further developments of this method such as the *MSF*-model by Huggel et al. (2003) include the implementation of a probability function to define the strength and likelihood of a flow to deviate from the steepest path according to the D8-method (O'Callaghan and Mark, 1984), allowing some lateral spreading of the flows.

Iverson et al. (1998) presented the model *LAHARZ* that follows selected paths of the stream network and calculates for each cell the cross-sectional areas which are progressively filled until a value defined by an empirical relationship for the total volume and the cross-sectional inundated area is reached. At the same time, the affected cells are summarized and the calculation is stopped when a total area defined by a volume-area relationship is obtained. The two basic equations were derived from 27 lahars from 9 volcanoes but may need adjustment if applied to regions with different conditions or other process forms (e.g. Crosta et al., 2003; Griswold and Iverson, 2007; Tang et al., 2011; Worni et al., submitted). This concept has been adapted within the *DFLOWZ* code to better account for unconfined or convex topographies – such as on debris flow fans – by introducing a third equation (mean deposition height as a function of volume) to restrict the deposition height of the part which is leaving the main channel (Berti and Simoni, 2007). Scheidl and Rickenmann (2010) introduced a Monte Carlo approach to account for lateral spreading instead of the constant cross-section assumption (*TopRunDF*). Monte Carlo random walk techniques have also been used earlier within the *dfwalk*-code by Gamma (1999) and by Hürlimann et al. (2008).

Such methods well represent the flow path and deposition areas of laterally confined debris flow-like mass movements which generally follow the natural stream path and possibly spread on a fan. To account for more rapid and larger mass movements which are often unconfined, lateral swash or runup on opposite slopes need to be considered so that dynamic models including solutions of the governing equations of motion are required.

### 2.4.2 Dynamic runout models

Dynamic runout models use analytical methods that calculate the depth-averaged movement of mass points (usually grid cells) within user-specified time steps. They are able to compute physical parameters such as time-dependent flow height, velocity, kinetic energy, momentum, frictional work rate, and flow pressure, as well as final deposition heights and maximum values. Because the simulated movements are physically-based and depend on the competition between accelerating gravitational and decelerating frictional (and viscous) forces, unconstrained flow over complex topography including lateral swash and runup on opposite valley walls can be better reproduced.

The main difference between various dynamic runout models is the implementation of the flow rheology, particularly of the law of flow resistance. Naef et al. (2006) provide an overview and comparison of eight different flow resistance relations that are applied for debris flows. In the simplest case, Coulomb friction is assumed for a flowing mass with a slope normal flow height $h$ from the analogy of an intact block sliding on an incline (Sassa, 1988; Savage and Hutter, 1989) as shown in **Figure 8**:

$$\tau_{bas} = \mu\, \sigma = \mu\, \rho\, g\, h\, cos\alpha \qquad [\mathrm{Pa}] \qquad (1)$$

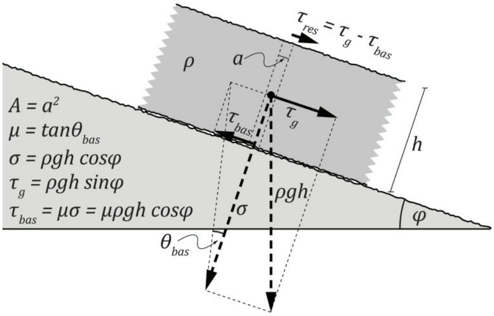

**Figure 8:** Schematic view of an accelerating flowing mass on a rough slope at inclination φ from the analogy of a sliding block. Stresses are indicated by vectors [Pa]. The resulting stress $\tau_{res}$ is the difference between the stress from gravitational acceleration $\tau_g$ and the negative frictional deceleration $\tau_{bas}$, which in this case results in a positive stress so that the mass is accelerating. Within a grid calculation domain, the cell size $A$ [m$^2$] is given by the square of the cell side length $a$ [m]. Forces can be easily calculated by multiplication of the stresses by the grid size $A$. See text for explanation of other symbols.

The parameter $\mu$ is equal to the friction coefficient $tan\theta_{bas}$ between the two interacting materials (where $\theta_{bas}$ is the dynamic basal friction angle), $\sigma$ the normal stress of the block, $\rho$ the density of the mass, $g$ the gravitational acceleration, $\varphi$ the slope angle, and hence, the flow resistance $\tau_{bas}$ (in Pascal) from basal shear stress is velocity-independent (Coulomb, 1773). However, to account for the fact that natural avalanches usually reach steady-state flow behavior on long trajectories and internal shearing with associated energy absorption, Voellmy (1955) introduced a second internal flow resistance $\tau_{int}$ which is proportional to the square of the velocity $u$, that has later been modified by Salm (1993):

$$\tau_{int} = \frac{\rho\, g\, u^2}{\xi} \qquad \text{[Pa]} \qquad (2)$$

where $\xi$ is the so-called turbulent (or 'viscous') friction coefficient. The total shear resistance $\tau_{tot}$ is defined by:

$$\tau_{tot} = \tau_{bas} + \tau_{int} = \mu\, \sigma\, + \frac{\rho\, g\, u^2}{\xi} = \mu\, \rho\, g\, h\, cos\, \varphi + \frac{\rho\, g\, u^2}{\xi} \qquad \text{[Pa]} \qquad (3)$$

The two friction-parameters $\mu$ and $\xi$ are depending on the properties of the flowing material and the surface roughness (Bartelt et al., 1999). In fact, the turbulent friction term has also a hydraulic background due to its relation to the Chézy equation from open channel hydraulics ($\xi$ equals the square of the Chézy coefficient $C$; Chow, 1959) and the assumption for shallow-water condition requiring that the flow height $h$ is relatively low compared to the width and length of the flowing mass (Gruber and Bartelt, 2007). Such models have also been developed by Russians and are widely used for avalanche runout calculations (see discussions of the Russian model in Bartelt et al., 1999; Salm, 2004). As a slight modification, Perla et al. (1980) replaced the turbulent term by a mass-to-drag ratio to account for mass entrainment along the flow path and for abrupt slope changes. Their model includes the effects of inertial resistance resulting from static particles that need to be accelerated to the avalanche velocity.

Savage and Hutter (1989) proposed two numerical finite-difference schemes (Lagrangian and Eulerian) to solve the depth-averaged equations of motion which are similar to the shallow water equations, including a Coulomb-like basal friction law. Iverson (1997b) generalized this theory to include the effects of viscous pore fluid with varying pressure in debris flows. He stated that the solid and fluid components of debris flows need to be treated separately. The two-phase rheology he proposed included the frictional resistance of enduring grain to grain friction, short-lived particle collisions (see **Chapter 2.3.2**), and fluid viscosity. Comparison between small experimental debris flows and numerical computations across three-dimensional terrain have shown that two-phase models can successfully describe the interaction between the solid and fluid phase where grain to grain friction or viscous forces dominate (Denlinger and Iverson, 2001; Iverson and Denlinger, 2001). However, the effects of particle collisions are not accounted for. An adapted version was later applied to numerically simulate dry granular avalanches on more complex terrain in laboratory (Denlinger and Iverson, 2004; Iverson et al., 2004).

Mangeney-Castelnau et al. (2003) also tested dry granular flows with the numerical model (*SHWCIN*) based on the Savage-Hutter theory (Bouchut et al., 2003) by applying constant and variable Coulomb friction angles as a function of avalanche mean velocity and flow height that was proposed by Pouliquen (1999). This model was later modified in *RASH3D* by Pirulli (2007) to account for varying earth pressure coefficients as suggested by Iverson and Denlinger (2001) that control the internal strength and hence the spreading of the avalanche. Finally, and in addition to the Pouliquen and frictional rheology, a Voellmy rheology was implemented to account for the usually overestimated velocities by the other flow resistance models (Pirulli and Mangeney, 2008; Pirulli and Sorbino, 2008). Due to variable advantages and disadvantages of each flow resistance law, a total number of six rheological relationships have been included into the *DAN*-model (Hungr, 1995) and its further development *DAN3D* (Hungr and McDougall, 2009; McDougall and Hungr, 2004): laminar, turbulent, plastic, Bingham, frictional and Voellmy rheologies.

The *TITAN2D* model for dry flows by Pitman et al. (2003a; 2003b) that was tested by Sheridan et al. (2005) and Patra et al. (2005) is based on the theory by Iverson and Denlinger (2001) assuming Coulomb friction and Newtonian fluid stresses. Bartelt et al. (2006) proposed that the random fluctuations of individual grains which possibly reduce the shear resistance within snow avalanches are a function of the frictional work rate. This concept was introduced into a Voellmy rheology where the random kinetic energy $R(x,y,t)$ at each calculation cell $x,y$ and time $t$ steers the effective values of the two friction-parameters $\mu(R)$ and $\xi(R)$ (Bartelt and Buser, 2010; Bartelt et al., 2006; Buser and Bartelt, 2009; Christen et al., 2010).

In a distinct contrast to Coulomb friction, Dade and Huppert (1998) considered a constant retarding stress of 10-100 kPa (plastic behavior) that is consistent with earthquake-induced brittle failure in tectonic faults. Such a model is capable to explain the high mobility of very large avalanche volumes (see **Chapter 2.3.1**) and according to Kelfoun and Druitt (2005) it also allows material deposition on moderate slopes. They have shown with the example of the prehistoric Socompa rock avalanche in Chile, that this concept well reproduces topographic features of the deposits and could narrow the range for the constant retarding stress to 50-100 kPa. A mechanical explanation for the low and constant values could be dynamic fragmentation as proposed by Davies et al. (2010) (see **Chapter 2.3.2**).

Two-phase models as suggested by Iverson (1997b) are physically meaningful but require a number of physical parameters that are difficult to measure or to be determined by calibration (Naef et al., 2006). Single-phase models such as the Voellmy-model which do not directly involve grain collisional flow resistance are much simpler and have been successfully applied to simulate saturated and unsaturated rapid mass movements, such as snow avalanches (Gruber and Bartelt, 2007), debris avalanches (Revellino et al., 2004), debris flows (Graf and McArdell, 2008; Rickenmann et al., 2006), rock avalanches (Crosta et al., 2007b) and landslides (Crosta et al., 2004). The problem of the omitted collisional and viscous forces can be accounted for by adapting the velocity-dependent flow resistance if necessary (Hungr, 2006; McDougall, 2006).

A variety of models make use of the Voellmy-approach or of modified versions, such as *RAMMS* (Christen et al., 2010), *DAN/DAN3D* (Hungr, 1995; Hungr and McDougall, 2009; McDougall and Hungr, 2004; McDougall and Hungr, 2005), and *RASH3D* (Pirulli and Sorbino, 2008). In the commercial and widely used *FLO-2D* mudflow model, O'Brien et al. (1993) split the velocity-dependent term into a viscous and turbulent-dispersive part of which the latter includes the Manning equation (Williams, 1970). This is an alternative for the Chézy equation and hence has some similarities to the Voellmy-Salm model (see e.g. McDougall, 2006). However, *FLO-2D* was designed to simulate completely liquefied mass flows, such as water floods, hyperconcentrated flows, mud floods/flows, and debris flows and requires a number of physically or empirically based input parameters (O'Brien et al., 1993).

The need for only two friction-parameters $\mu$ and $\xi$ within the Voellmy-model has practical advantages compared to more complex alternatives (Naef et al., 2006), but the deficiency of unlimited possibilities of parameter combinations resulting in a certain runout distance cannot be avoided (e.g. Alean, 1985; Perla et al., 1980). Therefore, calibration runs simply based on the runout distance and lateral spreading are not sufficient for full dynamic similarity between any model and the prototype. To improve the selection of adequate parameter combinations, model input parameters also need to be adapted according to other geometric characteristics (deposition thickness; Pirulli and Mangeney, 2008) and dynamic properties where seismic data can be very useful (velocities or frictional work rate; Schneider et al., 2010).

Although the Voellmy-model is prominent in this work, the reasons for the decision to its use as a dynamic model have been on the practical side. The present thesis does not aim to make comparisons between different models and flow rheologies to judge them. In fact, it needs to be considered that today's attempts for more complex models are promising in terms of accuracy of the results and process understanding as long as the input parameters can be defined precisely enough, but they do not necessarily lead to better results in terms of practical use for hazard assessements because such parameters are hardly ever known in advance of an event (Salm, 2004).

## 2.5 Physical runout experiments

### 2.5.1 Types of models and experiments

Physical laboratory modeling of (1) failure, (2) transition and (3) deposition of mass movements (see **Figure 5**) has a long history and has strongly improved the understanding of involved processes. Each model is a simplified, usually strongly downscaled analogy for the prototype (original) and can be specifically designed for one or various of the three stages (similarly to numerical models). Static models focusing on the transition and deposition of the material usually make use of an artificial sudden release of the stored mass (e.g by a trap door) without considering different failure mechanisms. The material rushes down a straight incline or a replicated terrain to hit e.g. replicates of dams, nets and other physical mitigation measures or fill retention basins, and finally deposit.

Before numerical modeling has become popular, widespread physical experiments have been a common tool for investigations and verifications of different hypothesis (e.g. Hsü, 1975; Körner, 1983; Savage, 1984). Today it is still a widely used method to either complement or directly test the capacities of numerical runout models (Denlinger and Iverson, 2004; Iverson et al., 2004; Mangeney et al., 2010; McDougall and Hungr, 2004). By means of lab experiments, a number of runs at changing and controlled settings can be performed, whereas comparisons to real events are much more time-intensive, involve high uncertainties about material properties, volumes, surface roughness, etc., and cannot be repeated.

Due to scaling problems (which are treated in the next section, **Chapter 2.5.2**), efforts have been made for larger dimensions which are closer to natural conditions, particularly if pore fluid effects are significant (Denlinger and Iverson, 2001). However, the possibility to gather more representative data from larger models stands in contrast to the difficulty of reproducibility while costs increase and the amount of data that can be gathered decreases. Iverson (1997b) and later Iverson et al. (2010) performed several experiments with different water-loam-sand-gravel-stone-mixtures in a 95 m long and 2 m wide concrete channel at a uniform slope of 31°. So far, this is the largest artificial flume for repeated experiments under largely controlled conditions. However, real-scale experiments of debris flows under marginally controlled conditions have been performed e.g. by Russians in the 1970s in Kazakhstan (Nosov et al., 2006) and recently in Austria (Hübl et al., 2009). Between 1959 and 1989, the Russians also triggered huge artificial rock avalanches in the order of $1 \times 10^5$ $m^3$ to $3 \times 10^6$ $m^3$ by explosives for the construction of debris flow retention dams, the largest of which was near the city of Almaty (Alma-Ata) in Kazakhstan (Adushkin, 2000). Extremely large rock avalanches of up to $8 \times 10^7$ $m^3$ were caused by underground nuclear explosions at the Novaya Zemlya test site, Russia (Adushkin, 2006). Even though these rock avalanches have not been the primary goals and were not reproducible (uncontrolled conditions), they have been expected and observed so that several measurements could be done (e.g. velocity measurements by filming; Adushkin, 2006).

Due to the high velocities of avalanche-like mass movements, the material transition stage within laboratory experiments usually takes only a few seconds or even less. Therefore, two other model types – so called *moving-bed channels* – have been designed to especially account for the highly interesting flow process within the transition zone:

- **Conveyor belt flumes:** The material flows on an adjustable straight incline. For steady-state flow, the conveyor belt velocity needs to be adjusted according to the inclination and rheology of the material. Side-wall friction is minimized due to the quasi stationary flow with respect to the static side walls. A problem can be the loss of material at the tail and to the sides which increases with increasing roughness of the conveyor belt (Davies, 1990; Hirano and Iwamoto, 1981; Kaitna et al., 2006).

- **Vertically rotating drum flumes:** The material moves inside the drum and automatically adjusts its mean slope according to the drum velocity and maintains steady-state flow (**Figure 9**). Side-wall friction is comparable to the one in static flume experiments and attempted to be low. Material loss occurs mainly during the first few rotations to the channel bed ('wettening' of the drum surface) but does not leave the system. The more the flow is sheared and individual grains are moving on curved paths, higher drum velocities lead to centrifugal accelerations which can affect the flow behavior by amplifying bed normal and shear stresses (Chou and Lee, 2009; Ding et al., 2002; Gray, 2001; Henein et al., 1983b; Henein et al., 1985; Hotta and Ohta, 2000; Hsu et al., 2008; Huizinga, 1996; Jain et al., 2002; Kaitna and Rickenmann, 2007; Kodama, 1994; Longo and Lamberti, 2002; Mikoš and Jaeggi, 1995; Sai et al., 1990; Schneider et al., 2011b; Sepúlveda et al., 2005; Volgger, 2007).

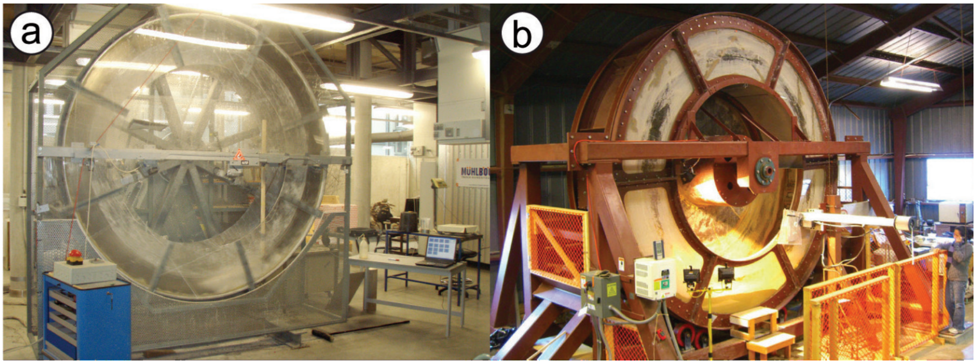

**Figure 9:** Vertically rotating drum flumes (a) at the Institute of Mountain Risk Engineering of the University of Natural Resources and Applied Life Sciences (BOKU) in Vienna, Austria, with a diameter of 2.46 m and (b) at the Richmond Field Station laboratory of the Department of Earth and Planetary Science of the University of California, Berkeley (UCB), USA, with a diameter of 4 m.

The simulation of long flow process durations has been used to gain insights about the rheologic and frictional behavior of different mixtures (Kaitna et al., 2006), different flow modes (Ding et al., 2002), bedrock erosion capacity of debris flows (Hsu et al., 2008), grain abrasion (Kodama, 1994; Mikoš and Jaeggi, 1995), grain size segregation (Henein et al., 1985; Hsu, 2010), surge development (Davies, 1988; Davies, 1990), and velocity profiles or grain trajectories (Hirano and Iwamoto, 1981; Hsu, 2010; Kaitna and Dietrich, 2009; Longo and Lamberti, 2002).

### 2.5.2 Similarity in models and scaling

A distinct problem within laboratory experiments evolves from downscaling where not all needed parameters can be adapted accordingly. From open channel hydraulics it is known, that a model needs to accomplish *geometric*, *kinematic* and *dynamic similarity* to the prototype (Henderson, 1966). In the following, a short overview on scaling and dimensionless analysis is provided. More details can be found in Henderson (1966), Davies and McSaveney (1999) and Kaitna (2006).

*Geometric similarity* can be achieved when the ratios of all characteristic lengths $L$ in the model ($_{mod}$) and the prototype ($_{prot}$) have the same geometric scaling factor $\lambda_L = L_{prot}/L_{mod}$. This consequently means that areas within the model must be scaled at $\lambda_L^2$ and volumes at $\lambda_L^3$. In rapid mass movements, length scales need to be applied e.g. for areas $A$, volumes $V$, flow height $h$, flow width $w$, and grain sizes $\delta$.

*Kinematic similarity* requires individual kinematic scaling factors $\lambda_t$ for time $t$, $\lambda_u$ for velocity $u$ and $\lambda_a$ for acceleration $a$. The scaling factor for velocity $\lambda_u$ can also be expressed as the ratio between the geometric scaling factor and the one for time ($\lambda_u = \lambda_L/\lambda_t$), and accordingly the scaling factor for acceleration as $\lambda_a = \lambda_L/\lambda_t^2$. Both, geometric and kinematic similarities are necessary but not sufficient conditions.

To accomplish full similarity, *dynamic similarity* is required too – meaning that all forces $F$ which are effective in the prototype need to be scaled by the same factor $\lambda_F$ in the model. This includes mainly forces due to gravitation, inertial and frictional forces, but also e.g. capillary forces. Concentrating on the three main forces, their scaling factors can be expressed as functions of the scaling factors for density $\lambda_\rho$, gravitational acceleration $\lambda_g$, viscosity $\lambda_\eta$, time $\lambda_t$ and length $\lambda_L$:

Gravitational forces: $$\lambda_{Fg} = \lambda_\rho \, \lambda_g \, \lambda_L^3 \tag{4}$$

Inertial forces: $$\lambda_{Fi} = \lambda_\rho \, \lambda_L^4 \, \lambda_t^{-2} \tag{5}$$

Viscous friction forces: $$\lambda_{F\eta} = \lambda_\eta \, \lambda_L^2 \, \lambda_t^{-1} \tag{6}$$

Dynamic similarity would require that at least the scaling factors of the three main forces were equal: $\lambda_{Fg} = \lambda_{Fi} = \lambda_{F\eta}$. This is not possible since usually the same densities, gravitational acceleration and viscosities are used. In that case, similarity can only be approximated by considering two of the three scaling levels. For rapid flows under turbulent conditions, viscous forces (Equation 6) are strongly reduced while forces due to gravitation and inertia dominate so that the corresponding scaling factors must be equal ($\lambda_{Fg} = \lambda_{Fi}$):

$$\lambda_\rho \, \lambda_g \, \lambda_L^3 = \lambda_\rho \, \lambda_L^4 \, \lambda_t^{-2} \qquad \text{(from \textbf{Equations 5} and \textbf{6})} \tag{7a}$$

$$\text{with} \quad \lambda_t = \frac{\lambda_L}{\lambda_u} \qquad \text{following} \tag{7b}$$

$$\lambda_g = \lambda_L \, \lambda_t^{-2} \tag{7c}$$

and hence

$$\frac{\lambda_u}{\sqrt{\lambda_g \lambda_L}} = 1 \tag{7d}$$

**Equation 7c** leads to the well known *Froude number* which characterizes the relation of inertial to gravitational forces and needs to be the same for the prototype and model:

$$\frac{u_{prot}}{\sqrt{g \, L_{prot}}} = \frac{u_{mod}}{\sqrt{g L_{mod}}} = Fr_{prot} = Fr_{mod} \tag{8}$$

where the characteristic length $L$ can be any length, e.g. the hydraulic radius $r_h$, flow height $h$, or the grain size $\delta$, but needs to be the same variable in the model as in the prototype. A Froude number $Fr < 1$ describes subcritical flow, $Fr = 0$ critical flow, and with $Fr > 1$ the flow is supercritical so that the flow velocity is larger than the velocity of disturbances such as waves.

In experiments under the same gravitational conditions (e.g. on Earth with $g \approx 9.81$ m/s$^2$) $\lambda_g = 1$ so that – following **Equation 7d** – the kinematic and dynamic similarities can be expressed in terms of the length scale $\lambda_L$. For the time scale $\lambda_t = \lambda_L^{0.5}$ results, and accordingly the velocity scale $\lambda_u = \lambda_L / \lambda_L^{0.5} = \lambda_L^{0.5}$ and the acceleration scale $\lambda_a = \lambda_L / (\lambda_L^{0.5})^2 = 1$ can be found. Furthermore, other scaling parameters such as those for the slope and discharge can be derived (**Table 1**).

If the flow is in the laminar regime and the flow resistance mainly driven by viscous forces, the scaling factors of the inertial and viscous friction forces need to be the same ($\lambda_{Fi} = \lambda_{Ff}$):

$$\lambda_\rho \, \lambda_L^4 \, \lambda_t^{-2} = \lambda_\eta \, \lambda_L^2 \, \lambda_t^{-1} \qquad \text{(from \textbf{Equations 6} and \textbf{7a})} \tag{9a}$$

$$\text{with} \quad \lambda_t = \frac{\lambda_L}{\lambda_u} \qquad \text{following} \tag{9b}$$

$$\lambda_\rho \, \lambda_L^2 \, \lambda_t^{-1} = \lambda_\eta \tag{9c}$$

and hence

$$\frac{\lambda_\rho \, \lambda_L \, \lambda_u}{\lambda_\eta} = 1 \tag{9d}$$

From **Equation 9d** follows the common *Reynolds number* $N_R$ which describes the ratio of the inertial to the viscous forces and also should be identical for the prototype and the model:

$$\frac{\rho_{prot}\, L_{prot}\, u_{prot}}{\eta_{prot}} = \frac{\rho_{mod}\, L_{mod}\, u_{mod}}{\eta_{mod}} = N_{R,prot} = N_{R,mod} \tag{10}$$

If the same fluid is used in the model as in the prototype, its density $\rho$ and viscosity $\eta$ remains unchanged and hence their scaling factors are equal to 1 ($\lambda_\rho = 1$ and $\lambda_\eta = 1$). According to **Equation 9c**, the time scale in Reynolds scaling is $\lambda_t = \lambda_L{}^2$. Consequently, the other kinematic and dynamic scaling factors do also differ from Froude scaling.

**Table 1** exemplifies that for a model where the same fluids are used as in its prototype, full dynamic similarity is not possible. However, because the majority of open channel flows (and avalanches) are turbulent, Froude scaling is the preferable scaling method for these cases.

Following the above considerations, Davies and McSaveney (1999) discuss three conditions which need to be accomplished to correctly scale a model from its prototype. (1) Geometric similarity that can be easily fulfilled for the shape of the model, surface roughness, flow heights and widths, etc., but may be troublesome in terms of the grain size: because prototypes can consist of finely crushed particles, models would require even much smaller particles where intergranular forces can cause cohesive and/or electrostatic effects which are different from the prototype. (2) The densities of the solids and fluids need to be the same, which can be accounted for by using the same material such as the same specific rock type (including similar

**Table 1:** Scaling parameters and factors according to the hydraulic Froude and Reynolds number to downscale models from prototypes by means of the length scale $\lambda_L$ under the condition that the same fluids are applied in the model and prototype (modified from Henderson, 1966; and Kaitna, 2006). Note that in the case of identical fluids, the scaling factor for density is $\lambda_\rho = 1$.

| Scaling parameter | Unit | Froude scaling (for turbulent flow where forces due to gravity and inertia dominate) | | Reynolds scaling (for laminar flow where viscous forces dominate) | |
|---|---|---|---|---|---|
| | | scale factor $\lambda_L = L_{prot}/L_{mod}$ | example $L_{prot}/L_{mod} = 500$ | scale factor $\lambda_L = L_{prot}/L_{mod}$ | example $L_{prot}/L_{mod} = 500$ |
| **Length scale $\lambda_L$** | m | $\lambda_L$ | 500 | $\lambda_L$ | 500 |
| **Area scale $\lambda_A$** | $m^2$ | $\lambda_L{}^2$ | 250,000 | $\lambda_L{}^2$ | 250,000 |
| **Volume scale $\lambda_V$** | $m^3$ | $\lambda_L{}^3$ | 125,000,000 | $\lambda_L{}^3$ | 125,000,000 |
| **Mass scale $\lambda_m$** | kg | $\lambda_\rho\, \lambda_L{}^3$ | $\lambda_\rho$ * 125,000,000 | $\lambda_\rho\, \lambda_L{}^3$ | $\lambda_\rho$ * 125,000,000 |
| **Time scale $\lambda_t$** | s | $\lambda_L{}^{0.5}$ | 22.4 | $\lambda_L{}^2$ | 250'000 |
| **Velocity scale $\lambda_u$** | m/s | $\lambda_L{}^{0.5}$ | 22.4 | $\lambda_L{}^{-1}$ | 0.002 |
| **Acceleration scale $\lambda_a$** | $m/s^2$ | 1 | 1 | $\lambda_L{}^{-3}$ | 0.000000008 |
| **Force scale $\lambda_F$** | N | $\lambda_\rho\, \lambda_L{}^3$ | $\lambda_\rho$ * 125,000,000 | $\lambda_\rho$ | $\lambda_\rho$ |
| **Energy scale $\lambda_E$** | J | $\lambda_\rho\, \lambda_L{}^4$ | $\lambda_\rho$ * $62{,}5\times10^9$ | $\lambda_\rho * \lambda_L$ | $\lambda_\rho$ * 500 |
| **Slope scale $\lambda_S$** | m/m | 1 | 1 | 1 | 1 |
| **Discharge scale $\lambda_Q$** | $m^3/s$ | $\lambda_L{}^{2.5}$ | 5,590,170 | $\lambda_L$ | 500 |

shape and grading that the bulk densities are identical), water and air in the model as in the prototype. The last condition (3) states that the drag coefficient should be equal in the model compared to the prototype, which is not possible when the densities of the fluids and solids remain constant as requested in condition (2). However, drag forces are much smaller than internal friction forces so that air drag can be neglected. Therefore, reduced-scale laboratory experiments can reproduce at least several features of their prototypes while other effects will be reduced or amplified. The only way to reduce the effects of such errors is to build models as large as possible.

The laboratory experiments within this work were performed by applying Froude scaling. More details about the finding of appropriate model characteristics can be found in **Chapter 4.3**.

### 2.5.3 Dimensionless numbers

To assess whether flow behavior in the model is comparable to prototypes, non-dimensional analysis is required. A number of dimensionless numbers describing the relations of different acting forces can be calculated; however, due to difficulties in determining the values of many of the required parameters, the non-dimensional numbers are rough estimations rather than accurate descriptions of the flow characteristics. This chapter provides the background of dimensionless numbers while the resulting values from the laboratory experiments are briefly discussed in **Chapter 4.3** and the measured values from the laboratory and several real events can be found in the **Appendix** within **Tables 3-8**.

Rapid mass movements such as debris flows, debris avalanches, rock avalanches and rock-ice avalanches usually involve mixtures of solids of different grain sizes (rock, debris or ice) and fluids (air or water) that interact in complex ways. Their flow behavior is largely driven by frictional or – if more agitated – collisional forces between individual grains; this stands in contrast to flows of very fine grained sediment that is completely suspended in water and hence shows a viscous behavior (e.g. viscous debris flows or lahars with high contents of fines or clay) (Ancey and Coussot, 1999; Iverson, 1997b).

Iverson (1997b) adapted the work of Savage (1984) and assumed that effective normal and shear stresses mainly depend on 13 variables: shear rate $\dot{\gamma}$, characteristic grain diameter $\delta$, density of the solids $\rho_s$, density of the fluid $\rho_f$, gravitational acceleration $g$, dynamic viscosity of pore fluid inclusive suspended fines $\eta$, hydraulic permeability $k$, granular temperature $T$, composite mixture stiffness $\varepsilon$, solid fraction $\upsilon_s$, fluid fraction $\upsilon_f$, *'bulk friction angle'* $\theta_{bulk}$, and coefficient of restitution of solid grains $e$ (the last four variables are already dimensionless and can be ignored for the dimensional analysis). If the grain diameter $\delta$ is the characteristic length $L$ within a [$m$, $L$, $t$]-system (mass, length, time), the characteristic mass $m$ is given by $\rho_s\delta^3$ and the characteristic time by $\dot{\gamma}^{-1}$ so that the characteristic velocity is $\delta\dot{\gamma}$. Dimensional analysis of the above variables leads to at least six dimensionless parameters which characterize the processes of energy dissipation in two-phase solid-fluid mixtures where (coarse) grains are interacting between themselves and with the (viscous) fluid matrix. **Equations 11-16** are from

Iverson (1997b) and Iverson and Denlinger (2001) and focus on shear stresses which are of much more interest than normal stresses as they drive the velocity and reach of a mass movement. They help quantifying inertial and quasi-static stresses for the solid and the fluid part of the flow, as well as direct solid-fluid interaction stresses. The dimensionless numbers thus can be used to determine the flow behavior of flow-type mass movements and should exhibit similar values for models as for prototypes.

The ratio of inertial shear stress associated with grain collisions to quasi-static shear stress associated with the weight and friction of the granular mass (from Coulomb friction) can be described by the *Savage number* that is according to Iverson and Denlinger (2001):

$$N_S = \frac{\rho_S \dot{\gamma}^2 \delta^2}{(\rho_S - \rho_f)\, g\, h} \tag{11a}$$

Note that the earlier Savage number given by Iverson (1997b) included $tan\theta_{bulk}$ in the denominator where $\theta_{bulk}$ is the *'bulk friction angle'*, which in this case is assumed to correspond to the static internal friction angle (according to Iverson, 1997b, the denominator term in Equation 11a is the 'quasi-static solid stress') that may be estimated from the angle of repose (critical slope of a static pile of the corresponding granular material; Lu et al., 2007). However, $tan\theta_{bulk}$ was not included in Iverson and Denlinger (2001; Equation 11a) and Iverson and Vallance (2001) whose version of the Savage number is preferred.

From experimental tests with glass-beads, Savage and Hutter (1989) found that steady shearing flows with $N_S$-values larger than about 0.1 correspond to the fluidized state where collisional interactions dominate. Lower values for the Savage number in turn indicate frictional-dominated flow regimes which are typical for dense geophysical flows such as debris flows, rock avalanches and pyroclastic flows (Iverson and Denlinger, 2001).

***Remark:*** *Savage and Hutter (1989) originally defined the 'number which characterizes the extent of fluidization and the importance of collisional stresses' by:*

$$N_S = \frac{\rho_S \left(\frac{u_S}{h_S}\right)^2 \delta^2}{\sigma_{tot}} \tag{11b}$$

*where* $u_s$ *is the velocity difference across the shear layer,* $h_s$ *the shear layer thickness and* $\sigma_{tot}$ *the total normal stress. Therefore, the Savage number actually needs to be calculated only for the sheared part of the flow. For the case that the flow is fully sheared, it can be assumed that the surface velocity* $u = u_s$ *and the slope normal flow height* $h = h_s$*. A practical problem relates to the fact that it is often largely unknow how a flow internally behaves.*

To assess the role of viscous fluid stresses in granular mixtures, Bagnold (1954) introduced a dimensionless number – the so called *Bagnold number* – which represents the ratio of inertial (collisional) grain stresses to viscous shear stresses from the fluid fraction (Iverson, 1997b):

$$N_B = \frac{\upsilon_S\, \rho_S\, \delta^2\, \dot{\gamma}}{(1-\upsilon_S)\, \eta} \tag{12}$$

Bagnold (1954) roughly assigned $N_B < 40$ to the 'macro viscous' regime and $N_B > 450$ to the inertial (collisional) regime, while intermediate values formed the transitional regime. However, Iverson (1997b) included $\upsilon_s/(1 - \upsilon_s)$ instead of Bagnold's factor $\lambda^{0.5}$ so that the upper threshold applies to values of $N_B > 200$ (see also Parsons et al., 2001).

The ratio of solid to fluid inertial stresses is described by the *Mass number* (Iverson, 1997b):

$$N_m = \frac{\upsilon_s \, \rho_s}{(1 - \upsilon_s) \, \rho_f} \tag{13}$$

Debris flows are usually strongly dominated by solid inertia. Assuming a rock grain density of 2700 kg/m$^3$ and clear water density of 1100 kg/m$^3$ for the fluid, the solid inertia will be larger than the fluid inertia if $\upsilon_s > 0.29$ (>29% solids content by volume). Typical solid fractions of debris flows are between 0.5 or 0.6 and 0.9 while hyperconcentrated flows including lahars can reach fluid-dominated flow conditions with solid fractions between 0.2 or 0.25 and 0.5-0.6 (Coussot and Meunier, 1996; Pierson and Scott, 1985; Vallance, 2000).

Iverson (1997b) proposed another dimensionless number which describes the tendency for pore fluid between individual moving grains to buffer grain interactions, and is called *Darcy number*:

$$N_D = \frac{\eta}{\upsilon_s \, \rho_s \, \dot{\gamma} \, k} \tag{14}$$

Iverson (1997b) reports Darcy numbers between 600 and $6 \times 10^7$ for experimental respectively natural debris flows, and earlier, Iverson and LaHusen (1989) measured dynamic pore pressure fluctuations within flume experiments, that suggest strong solid-fluid interactions. However, there is not much data available and the Darcy number is rarely used by other authors, possibly also due to the difficulty of estimating the hydraulic permeability $k$ in natural flows. Iverson et al. (2010) published values from permeameter measurements between $10^{-11}$ m$^2$ and $10^{-12}$ m$^2$ for different geophysical flows, but effective natural variability of $k$ is likely to be much larger (see also Iverson, 1997b; Iverson and Denlinger, 2001).

Following the above considerations, the ratio of fluid inertia to its viscous shear stresses can also be expressed by the ratio of the Bagnold to the Mass number, that is a version of the *Reynolds number* (Iverson, 1997b):

$$N_R = \frac{N_B}{N_m} = \frac{\rho_f \, \dot{\gamma} \, \delta^2}{\eta} \tag{15}$$

In natural geophysical flows, $N_R$ is usually in the order of $10^6$, indicating that inertial forces dominate in large flows. However, viscous forces will be more important in smaller flows.

Finally, friction dominated and viscous dominated debris flows can be separated by building the ratio of quasi-static solid stress to quasi-static fluid stress (in other words: shear stress from sustained grain contacts to viscous shear stress) which can be addressed by the *Friction number*:

$$N_f = \frac{N_B}{N_S} = \frac{\upsilon_s\,(\rho_s - \rho_f)\,g\,h}{(1-\upsilon_s)\,\dot{\gamma}\,\eta} \tag{16}$$

Parsons et al. (2001) experimentally found $N_f \approx 100$ to be the boundary for the transition from the viscous to frictional regime (this is apparently lower than earlier reports defining a boundary for $N_f$ around 2000).

## 2.6 Seismic signals in rapid mass movement analysis

Since the seismic network for earthquake detection and volcano observations is highly developed, ground vibrations from large rapid mass movements are commonly recorded by one or many seismometers and can be well distinguished from tectonic sources (Kishimura and Izumi, 1997; Weichert et al., 1994). The seismic methods described in the following generally apply for studying most types of rapid mass movements, such as snow avalanches, debris flows, lahars, pyroclastic flows, rock and ice avalanches or landslides (Suriñach et al., 2005).

Seismograms have been widely used to localize and define the exact timing of the failure of landslides or debris flows (Burtin et al., 2009; Jiskoot, 2010) and to back-calculate the approximate duration of the avalanche that serves as a basis for average velocity estimations (Crosta et al., 2007a; Lipovsky et al., 2008; McSaveney, 2002; McSaveney and Downes, 2002). Difficulties in determining the duration of an avalanche arise from the gradual increase and decrease of the signal at the beginning and end of the avalanche so that exact start and end times are diffuse (characteristic spindle-shape form of the seismogram **Figure 10**). This problem rises with increasing distance between the source and seismic station as the signal to noise-ratio is decreasing. Depending on the event size, however, the basic form of the signal can be preserved over distances of several 100 km while long-period waves of large slope failures can be detected even around the world (Huggel et al., 2008a). Deparis et al. (2008) addressed this issue by defining the start and end time as the points where 5% and 95% of the total energy has been recorded. They also pointed out, that the duration of the seismic signal increases for longer source-receiver distances due to the propagation of waves at different velocities as well as from seismic wave diffusion in the crust due to refractions, reflections and scattering at surface and ground discontinuities or heterogeneities, including topography (see also Suriñach et al., 2001). Further uncertainties are related to seismograms of progressive failures where the signals of various overlying subevents can get obscured (see also McSaveney and Downes, 2002). However, seismic recordings contain the most precise dynamic information about rapid mass movements, especially on the failure mechanism, the avalanche path topography such as slope, obstacles and lateral deflections, frictional changes or about the stopping mechanism (Kishimura and Izumi, 1997; Sabot et al., 1998; Schneider et al., 2010; Suriñach et al., 2000).

Two attempts to calibrate rheological parameters of numerical physical avalanche flow models have recently been done by the use of seismic signals. Favreau et al. (2010) modeled low-frequency seismic signals of the Thurwieser rock avalanche related to loading and unloading of the topography by the moving rock mass. They could show that applying a lower

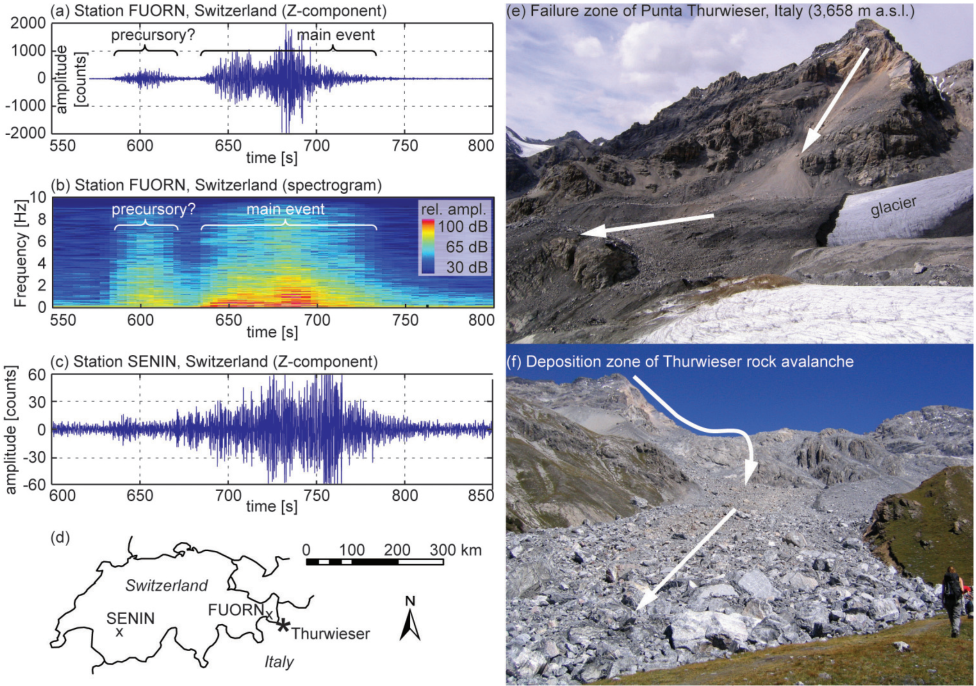

**Figure 10:** Seismograms of the vertical component (Z-component) of the 2.5 × $10^6$ $m^3$ Punta Thurwieser rock avalanche of September 18, 2004, Italy. (a) Filtered seismogram from FUORN station, at 25 km horizontal distance from the seismic source. Interpretation of first pulse around t=600s is difficult and possibly a precursory small failure. The main event is well identifiable but start and end times remain fuzzy. Note the spindle-shape signal which is typical for rapid mass movements. (b) Unfiltered spectrogram from FUORN station. The triangular shape of the frequency distribution is also characteristic. (c) Filtered seismogram from SENIN station, at 250 km distance. Note the lower amplitudes (magnified y-scale), the shift in time and prolonged signal due to differing travel times of seismic waves, and loss of signal quality with distance. Estimations of the event duration is much more difficult and attributed to the mentioned problems, however, the main characteristics have been preserved. (d) Overwiew of the two presented seismic stations and the Thurwieser rock avalanche. (e) Failure zone of the rock avalanche that travelled and partially deposited on Zebrù glacier. (f) Deposits of highly fragmented rock clasts (mainly limestone). Note person for scale; individual boulders were up to several meters large and the original stratification was not preserved in that case (highly turbulent movement, similar to a powder snow avalanche). Seismic data from '*IRIS SeismiQuery*' and pictures taken on September 11, 2006 by D. Schneider.

friction for the glacier surface that was passed by the rock masses produced a better fit between modeled and measured long-period seismic signals and that the deposition geometry of that run did also better reflect the real deposits. Schneider et al. (2010) assumed that the rate of seismic energy that is lost by a rapid mass movement and parts of which are recorded by a seismometer must be related to the frictional work rate. Frictional work rates from different rheological parameters have been modeled using a dynamic numerical runout model (RAMMS). The results fitted well to the total seismic energy described by the seismic envelope of nearby stations (for source-receiver distances < 100 km) so that they could be used for model calibration if the slope failures were not multiple-failure events that timely overlapped.

Cole et al. (2009) were able to distinguish the flow rheology of water-rich lahars from the one of snow-slurry flows at Ruapehu volcano, New Zealand, by means of seismic amplitudes and frequency distributions. Accordingly, water-rich highly turbulent flows exhibit stronger collisional interactions between particles that are reflected by a broader frequency range in the seismic signature. Similarly, Vilajosana et al. (2007) found variable total amounts of dissipated seismic energy for different flow types of snow avalanches. Brodsky et al. (2003) were able to calculate the apparent coefficient of friction $\mu_{app}$ that is another rheologic factor. They used long-period signals of large landslides from teleseismic stations (stations that are at distances greater than 1000 km from the source); however, the values for $\mu_{app}$ could only be constrained to a broad range of 0.2-0.6.

Estimations of landslide volumes by the means of seismic magnitudes would be helpful because current methods are either unprecise (estimations from punctual thickness measurements and expert knowledge) or expensive (differences between high-resolution pre- and post-event DTMs). Deparis et al. (2008) analyzed rock-falls with volumes between $10^4$ and $10^5$ in the French Alps, but no correlation between volume and magnitude could be found. However, better correlations were found between volumes and peak amplitudes for several events from the nearly identical source site, suggesting that site and path effects can significantly influence the peak amplitude (Dammeier et al., 2010). They also found that the volume correlated with the area of the seismic velocity envelope that previously was extrapolated to a common distance of 30 km. Therefore, volume estimations may be possible but site and path effects as well as different seismic behavior directly related to the flowing mass (turbulency, flowing material; see Cole et al., 2009) will pose difficulties to any such method (Suriñach et al., 2001).

Seismic and acoustic methods – including infrasound – are common tools for monitoring and early warning of debris flows (Arattano, 1999; Badoux et al., 2009; Kogelnig et al., 2011; Suriñach et al., 2005), lahars (Huggel et al., 2009; Kumagai et al., 2009; Lavigne et al., 2000) or pyroclastic flows (De Angelis et al., 2007; Ripepe et al., 2009) and empirical threshold values can be defined for specific seismic magnitudes to trigger alarm. Such systems base on the seismicity that is emitted when the mass is already moving, and hence, time spans for early warning are extremely short. In contrast to this, precursory seismic signals have been repeatedly detected up to 2 hours before massive failure of ice at the rock-ice interface from Iliamna volcano, Alaska (Caplan-Auerbach and Huggel, 2007; Caplan-Auerbach et al., 2004; Huggel et al., 2007). Due to the unusual high-frequency and high-magnitude ice-rock avalanches, Iliamna volcano is an excellent place to study large avalanche flow behavior. However, precursory signals may be typical but unique to ice avalanches (Huggel et al., 2007). E.g. in Switzerland, Faillettaz et al. (2008) also observed increased seismic activity three days prior to the failure of large ice masses from Weisshorn and Mönch hanging glaciers, so that real time monitoring focusing on the precursory seismic activity could be a promising predictive tool for populated regions that are prone to ice avalanche hazards.

# 3 Summary of Research Results

This chapter provides summaries of the six research papers that are enclosed in **Part B**. The abstracts include a short overview and the main research results of the individual studies.

## Paper I:

Korup, O., **Schneider, D.**, Huggel, C. and Dufresne, A. (in press): Long-runout landslides. In: Treatise on Geomorphology, edited by Shroder, J., Jr., Marston, R. and Stoffel M., Academic Press, San Diego, CA, 7, doi:10.1016/B978-0-08-088523-0.00164-7.

This paper provides a review of volcanic and non-volcanic large ($> 10^6$ $m^3$) long-runout landslides which are usually characterized by high velocities, large release and deposit volumes, and excess runout. The chapter concludes with an overview of consequences and implications for hazard assessment:

- Both volcanic and non-volcanic long-runout landslides are generally associated with high velocities and large release and deposit volumes; excess runout is mainly associated to landslides $> 10^6$ $m^3$.
- The relation between landslide volume and affected area differs significantly between volcanic and non-volcanic landslides owing to differences in runout topography, material properties, and water content.
- Despite a number of mechanistic theories, there is no common agreement on the explanation of excess runout. Any such unifying theory may want to consider the superposition of processes such as dynamic fragmentation, material bulking, and partial lubrication. In fact, the diversity of processes involved with long-runout landslides suggests that no single explanation is fully sufficient. However, water as a lubricant seems to play only a minor or limited role given the ample evidence of dry excess runout.

- Numerical models based on shallow-water equations provide some of the best means to realistically simulate rapid flow- and avalanche-like motion over 3D terrain, given that physical experiments suffer from inadvertent scale effects. However, numerical runout models critically depend on realistic initial conditions, such as failure volume and scar, material properties, and runout topography.
- Large, long-runout landslides are very rare events and pose substantial challenges to quantitative hazard assessments. Empirical magnitude-frequency relationships derived from landslide inventories provide a means to at least constrain the probability of occurrence for a given region to an order of magnitude.

# Paper II

---

**Schneider, D.**, Delgado Granados, H., Huggel, C. and Kääb, A. (2008): Assessing lahars from ice-capped volcanoes using ASTER satellite data, the SRTM DTM and two different flow models: case study on Iztaccíhuatl (Central Mexico). Natural Hazards and Earth System Sciences, 8(3), 559-558.

---

This case study investigates the lahar hazard potential from the glacier-clad Iztaccíhuatl volcano (5230 m a.s.l.) in Central Mexico. Due to the abundance of friable volcanic material and steep terrain, water has been identified to be the critical predisposition factor for lahar formation. Several scenarios for water release have been considered, such as (1) heavy rainstorms, (2) eruptive activity volcano-ice interaction on Iztaccíhuatl leading to rapid melting of ice, (3) reduced glacier albedo and intensified melting due to ash deposition from its southern neighbour Popocatépetl volcano, and (4) slow formation of sub-, supra- or proglacial water reservoirs forced by geothermal volcanic activity or climatically induced that are prone for sudden outbursts.

Because outbursts of water bodies have been frequently observed in volcanic and non-volcanic glacial environments, the study focuses on potential lahars related to the glaciers on Iztaccíhuatl. An evaluation of the glacial extents over the past ~150 years by means of geomorphological features (moraines), previous work and remote sensing data was used to project the future developments of the glaciers.

Potential lahars were calculated with two empirical GIS-based flow routing models: *MSF* and *LAHARZ* where scenarios of involved water and debris volumes depended on the size of the glaciers. The influence of the DTM source and resolution on the lahar path calculations was assessed by applying the SRTM DTM (90 m resolution) and ASTER DTMs (60 m and 30 m resolution).

The main results of the study are:

- The glacial recession on Iztaccíhuatl volcano has been intensified over the past decades and total deglaciation is likely to develop before ~2020 AD. Hazards from volcano-ice interactions are therefore assumed to decline in a long-term view while new hazards, such lake as development, destabilization of over-steepened flanks due to glacial recession and permafrost thawing could develop and increase temporally the hazard for lahars or landslides.
- The rapid glacier retreat can be attributed to atmospheric warming, but may also be a consequence of increased volcanic heat flux and changes in the hydrothermal system. However, Iztaccíhuatl volcano is not necessarily ready to become active again.

- The formerly glacierized areas exhibit huge masses of friable material on steep slopes that could be mobilized by heavy precipitation (if heavy rains reach these altitudes).

- In terms of lahar hazards, the safety of the surrounding villages is reduced on the volcano's west side, because ravines are leading directly to populated areas. On the east side, communities are largely situated on higher ground while the streams are deeply incised.

- The SRTM DTM generally represents the drainage channels in a better way than the ASTER DTM and hence provides more realistic results for the lahar modeling. Problems with the ASTER DTM mainly occur in narrow ravines which lead to incorrect deflection of the modeled lahar.

- Due to different resolutions and sources, lahars modeled with LAHARZ on different DTMs can have much longer or shorter runout distances. Because this is crucial for hazard assessment, DTMs from various sources should be applied for that model. The MSF-model is much less affected by this effect.

A more detailed evaluation of the MSF and LAHARZ models on ASTER and SRTM DTMs at Iztaccíhuatl's active southern neighbor Popocatépetl volcano is provided by Huggel et al. (2008b).

## Paper III

---

Allen, S., **Schneider, D.** and Owens, I. F. (2009): First approaches towards modelling glacial hazards in the Mount Cook region of New Zealand's Southern Alps. Natural Hazards and Earth System Sciences, 9(2), 481-499.

---

This integrative work makes use of remote sensing based terrain mapping, GIS and flow path modeling with the MSF and RAMMS model to preliminarily assess the glacier-related hazard potential in the Aoraki/Mount Cook region, New Zealand. The Aoraki/Mount Cook region is a typical glacial environment that is characterized by high mass turnover rates. Numerous smaller to very large rapid mass movements have occurred during the last decades while the touristic utilization has been intensified and the high sensitivity of valley glaciers to climate forcing is currently demonstrated by the rapid development of large proglacial lakes. The dramatic changes in glacial environments induced by climate change can lead to shifted or new hazard situations without historical precedence. This includes ice avalanches, glacial floods, debris flows, large bedrock failures and surge type glacier movements, however, the most catastrophic events often involved chain reactions (e.g. ice- or rock-avalanches into glacial lakes; flood wave generation; erosion of moraine dam; subsequent debris flow or flood) or flow transformations of rock- or debris avalanches into more mobile debris flows that may have the potential to threaten people and affect local touristic infrastructure.

The regional-scale hazard assessment of lake outburst floods included mapping of the glacial lakes, empirical water volume estimations, dam characteristics (debris covered/vegetated/bedrock; slope gradient), and – depending on the slope – flood wave or debris flow modeling. While potential flood wave propagation was modeled by MSF until the great lakes Tekapo and Pukaki, debris flows were calculated with MSF according to empirical threshold values for the angle of reach (analogously to $\mu_{app}$ in **Figure 5**). Steep glacial ice as possible detachment zones for ice avalanches was identified and due to their abundance, potential ice avalanches were again calculated with the simple MSF model, applying empirical thresholds for ice avalanche mobility. Finally, the potential of rock avalanche modeling with the physically based RAMMS model was assessed on a local-scale by retrospective modeling of three specific recent rock avalanches.

The main results within this first approach to model glacial hazards in the Aoraki Mount Cook region (NZ) are:

- Several large volume moraine- or gravel- dammed lakes have formed during recent decades in proglacial areas below 1000 m a.s.l. In these cases, gentle and vegetated slopes around the outlet channels indicate relatively stable conditions, suggesting that catastrophic dam failure and flooding is unlikely. However, impacts from ice-, debris- or rock-avalanches could lead to flood waves, particularly where lakes are forming directly beneath steep slopes.

- A number of smaller cirque lakes are dammed by steep morainic debris so that debris flow scenarios need to be considered. But maximum probable runouts in these instances were well short of affecting any infrastructure.
- Runout paths of potential debris flows from glacial sediment accumulations (steep moraines and talus slopes) intersected with human activity in many instances when worst-case runout distances were considered.
- There is often a large discrepancy between empirical worst-case runout distances of debris flows and maximum runout distances expected on the basis of the size of catchment area above the debris source.
- Direct impacts from potential high-magnitude ice avalanches are limited to walking tracks and some huts or shelters located in close proximity to steep ice. Though numerous lakes are positioned within the runout paths from even smaller magnitude events, providing hazard potential for displacement waves and flooding.
- Longer term glacial recession and lake expansion will increase the potential for ice-, debris- or rock-avalanche impacts into most lakes across the region. The rapidly expanding Mueller Lake is thereby one example in close proximity to tourist and residential infrastructure.
- Physically based numerical modeling with RAMMS for more detailed local-scale analyses of rock avalanche events is a useful tool for establishing more accurate avalanche dynamics including runups, flow heights and velocities, as well as maximum reach. For predictive purposes, further calibration studies will be needed.
- For a full hazard assessment, further local-scale studies of rapid mass movement processes are required. Considering the facts of an unstable geological setting within a seismically active zone, relatively high precipitation rates, and strong impacts by climate change, a broader approach considering topographic, geological and glacial factors relating to bedrock failure susceptibility is encouraged.

## Paper IV

**Schneider, D.**, Bartelt, P., Caplan-Auerbach, J., Christen, M., Huggel, C. and McArdell, B. W. (2010): Insights into rock-ice avalanche dynamics by combined analysis of seismic recordings and a numerical avalanche model. Journal of Geophysical Research, 115(F04026), 1-20.

This paper presents a novel approach to relate seismic data and numerical model results. While seismograms have already been extensively used for average velocity calculations of rapid mass movements, the described method opens new perspectives to determine dynamic avalanche parameters much more accurately. We used the physically based numerical runout model RAMMS to compare computed dynamic avalanche parameters with seismograms of large rock-ice avalanches. Two case studies were included: One from Iliamna volcano, Alaska, having simple runout path geometry, and a second one from Aoraki/Mt. Cook, New Zealand, that is characterized by a much more complex topography.

The RAMMS simulations of the events were geometrically calibrated to fit the maximum runout distances and lateral expansion of the avalanches. However, within a two-parameter model, several combinations of friction-parameters that influence the flow dynamics are possible. Therefore, total avalanche momentum, kinetic energy, and frictional work rates calculated by the RAMMS model were used for comparison with seismograms of the corresponding events.

Seismic information well serves as independent data to better constrain the range of appropriate input parameters of a numerical avalanche model – besides geometrical aspects also from a dynamic point of view. Higher reliability of the model results in turn can lead to better insights into rock-ice avalanche dynamics (e.g. maximum velocity, flow heights, entrainment behavior). The most important findings of the study are as follows:

- Model optimization and evaluation (e.g., determination of appropriate friction-parameters) should be done systematically using geometric, energetic, and dynamic aspects of the avalanche.
- For very large avalanches, seismic recordings are often the only data available for characterizing dynamic aspects. Such data may be obtained even for remote areas and are largely independent of weather conditions.
- Dynamic model results should be compared to the seismic pattern of an avalanche event so that the model results are dynamically consistent with the seismic data over the entire displacement process and not only in the final resting state (deposition geometry and total duration).

- Among different dynamic parameters, the total frictional work rate was found to best correlate with the absolute seismic amplitude. The frictional work rate describes the rate of energy loss by the avalanche due to friction, suggesting that the energy captured by the seismograph represents a small but proportional fraction of this energy loss.
- Due to attenuation of the high-frequency signal content in the seismograms with increasing source-receiver distance, the signal of the closest (unsaturated) station should be used. However, because the bulk of the seismic energy generated by rapid mass movements is low-frequency, seismograms from large avalanches ($> 10^6$ $m^3$) of more than 100 km distance can be useful.
- Differences between the seismic data and the modeled total frictional work rate indicate source site, path, and recorder site effects, or departures of the model from reality (e.g., multiple failures, different frictional properties). Such findings can in turn be used to assess the model quality or to optimize the choice of frictional parameters and other variables used for modeling.

# Paper V

---

**Schneider, D.**, Kaitna, R., Dietrich, W. E., Hsu, L., Huggel, C. and McArdell, B. W. (2011): Frictional behavior of granular gravel-ice mixtures in vertically rotating drum experiments and implications for rock-ice avalanches. Cold Regions Sciences and Technology, 69(1), 70-90.

---

This study is based on the observation that rapid mass movements in glacial environments travel significantly further downslope than rock avalanches that consist only of rock. They also can transform into debris flows as the ice melts when travelling downstream and while water from the stream network or water-saturated debris is incorporated. Ice and snow are thought to affect rapid mass movements in three different ways: 1) reduction of the internal friction when ice is a part of the moving mass, 2) reduction of the internal shear resistance of the flowing material due to rising pore water pressures by continuous melting water supply, and 3) reduced basal friction if the mass travels over a glacier surface. So far, any quantitative data on these factors is largely missing.

Laboratory experiments have been performed to test the role of the first two mechanisms when ice is a part of the moving mass. Two large vertically rotating drums (diameters 2 and 4 m) have been used and granular mixtures of varying proportions of ice and rock were applied in Vienna, Austria, and in Berkeley, USA (see **Figure 9**). Flow behavior was recorded with flow depth, normal force, shear force, pore water pressure, and temperature sensors. The key findings from the laboratory experiments are:

- The bulk friction coefficient of the gravel-ice mixture linearly decreases with increasing ice content by approximately 20% for pure cold granular ice compared to dry gravel only. Grain size and shape have some influence on this value but the general trend remains comparable.
- Bulk friction coefficients of rock-ice mixtures may be estimated if the friction coefficient of the rock fraction is known. A 50% ice content (by volume) therefore leads to a reduction of the friction coefficient by 10%.
- During an intermediate phase of the experiments (between 5 and 15 minutes), an intergranular water film developed and cohesion effects led to a slight increase of the friction coefficient.
- Runs with initial ice contents higher than 40% by volume were entirely liquefied due to increasing water content during the later phase, around 15 minutes after the beginning of the experiments. The flow phase transformation evolved from a dry granular mass to a debris flow and finally into a hyperconcentrated flow and was accompagnied by an additional continuous reduction of the bulk friction coefficient.

- Measured bulk friction coefficients were relatively high compared to empirical apparent friction coefficients. Apparently, other effects that reduce the friction of a rapid mass movement, such as sliding on low friction surfaces (e.g. glacier ice), volume effects, fluidization, and the concentration of lubricants (e.g. water) to thin layers need to be considered additionally. However, the relative change of the friction coefficient may also be roughly valid for much larger natural rock-ice avalanches.
- The results reveal that the presence of ice in the moving mass is important as a part of the moving material as well as a supplier of water for the flow itself. In natural events, the melting of ice can be induced by frictional heating as well as by mixing with air and eroded surface material that is warmer than 0°C.
- Numerical modeling of rapid mass movements can account for the ice content by applying generally lower friction coefficients compared to non-glacial events. The rheologic changes from melting ice can be addressed by continuous spatial and/or temporal variation of the friction coefficients.

## Paper VI

---

**Schneider, D.**, Huggel, C., Haeberli, W. and Kaitna, R. (2011): Unraveling driving factors for large rock-ice avalanche mobility. Earth Surface Processes and Landforms, 36(14), 1948-1966.

---

This paper includes an empirical analysis of 64 documented rock-ice avalanches with volumes $> 10^6$ $m^3$ distributed over glacierized high mountain regions all around the world, focusing on different factors that are likely to affect their mobility. The empirical data is presumably the most complete dataset on rock-ice avalanches to date, and synthesized with the results from the laboratory experiments (Paper V).

The influence of avalanche volume, topography, ice and water content and low-friction surface on the apparent coefficient of friction as a measure of mobility was systematically assessed. The findings for each of the individual factors are:

- *Volumes:* Larger volumes tend to increase mobility (confirming findings of many other studies) but scatter is large due to the high variability of flow and surface characteristics.
- *Topography:* Downstream topography was not found to significantly influence mobility but is still likely to be a key factor because the path deviation index as parameterized in the present study probably underestimates the effects of strong impacts. Lateral confinement is also a relevant factor for mobility but difficult to quantify. The presented width to length ratio is an attempt to measure channelization but quantification on the basis of the hydraulic radius concept for individual channel sections may lead to more representative results.
- *Ice content:* According to the laboratory experiments, the ice content in the moving mass reduced bulk friction by 20%. This effect is not visible in the empirical data so that it might not be a dominant but more likely a secondary factor in reducing bulk friction that is blurred by other effects.
- *Water content:* We found in laboratory experiments that the bulk friction coefficient is reduced by nearly 50% for completely liquefied flows compared to dry granular masses. Empirical data confirms that events with high water contents reach much further while those with low water contents are often less mobile. However, the runout of dry rapid mass movements can also be extended by other factors.
- *Low-friction surfaces:* Glaciers as low-friction surfaces have significant effects in extending runout distances. Debris cover of glaciers is not much relevant, probably due to rapid entrainment of the debris layer. Low-friction surfaces may also be provided by smooth

bedrock planes and multi-phase flows reach high mobilities without extended glacial trajectories.

This leads to some more general conclusions:

- Most of the analyzed parameters may be significantly enhanced by improvements of the dataset. A reduction of uncertainties may help in separating individual factors which are influencing rapid mass movement mobility.
- Dispersive pressure-related mechanisms and corresponding friction reduction need to be considered in addition to the presented parameters. They are much more difficult to be quantified but seismic data may provide deeper insights to these mechanisms in future (see Paper IV).
- For hazard assessments of future events, dynamic avalanche models should be adjusted to fit empirical apparent coefficients of friction from events having similarities to the considered scenario. **Figures 6, 7, 9, 10, and 11 in Paper VI** provide a first semi-quantitative basis to assess the mobility of potential large rock-ice avalanches with given characteristics.
- Scenarios beyond historical evidence need to be considered to account for new hazard situations from glacial and periglacial areas due to climate change. Reduced slope stability can be related to permafrost degradation and glacial debuttressing while new glacial lake formations provide a potential for chain reactions such as avalanche impact waves leading to subsequent debris flows (flow transformations).
- Large rock-ice avalanches passing glacial limits often evolve to events with multi-phase flow behavior reaching much further and having an extremely destructive potential. They involve many factors that enhance mobility, such as high volumes, water and ice contents, glacial trajectories or smooth bedrock, and lateral confinement (catastrophic glacier multi-phase mass movements).

# 4 General Discussion

The study includes a broad variety of methods and combines them in different ways to enhance the benefits from individual findings on large rapid mass movements in glacial environments. **Figure 11** exemplifies the strong connections of individual methods.

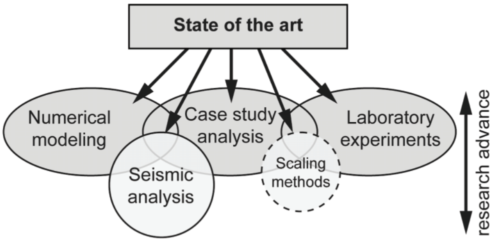

**Figure 11:** Relations of the core methods that were used within the thesis. The methods roughly correspond to the steps presented in the overview in **Figure 2**. Besides geometrical aspects, seismic analysis was the main method to connect numerical modeling to case study events. In contrast to the other elements, the scaling methods were not subject to specific investigations and research advances but necessary to elaborate a connection between real events and the laboratory results.

In the following, main results including several benefits and difficulties are briefly discussed. The chapters roughly follow the methods and work flow presented in **Figure 2** and **Figure 11** while more detailed discussions of specific results can be found in the individual papers in **Part B**.

## 4.1 Numerical modeling based on case studies

Regional-scale first-order hazard assessments including numerical modeling have been done within case studies around Iztaccíhuatl volcano in Mexico (**Paper II:** Schneider et al., 2008) and in the Mount Cook region in New Zealand (**Paper III:** Allen et al., 2009). Choosing appropriate modeling tools and elevation data depending on the extent and detail of the analysis is crucial (van Westen et al., 2006). Due to the volcanic and glacial setting in Mexico, as well as the preliminary regional-scale approach, an empirical lahar inundation model was applied (LAHARZ) that has been used before at different volcanoes in that region (e.g. Davila et al., 2007; Hubbard et al., 2006).

The main obstacle for the lahar calculations was determining appropriate values to define the uppermost points in the flow paths where deposition starts, and finding realistic flow volumes. Volumes were chosen according to lahars that occurred during the 1997 and 2001 eruptive phases of Iztaccíhuatl's southern neigbour Popocatépetl (Delgado Granados et al., 2007; Julio Miranda et al., 2005; Palacios et al., 1998). The volumes of these lahars were modified to larger and smaller sizes and set into relation to current and future glacier extents. This was the only reasonable method due to the scarcity of historical data about magnitudes and frequencies of lahars from Izatccíhuatl. However, because Iztaccíhuatl is not active in contrast to Popocatépetl, the calculations remain somewhat hypothetic in terms of lahars triggered by volcano-ice interactions while conditions for rain-triggered lahars are comparable between the two volcanoes. The rapid changes of the subtropical glacial setting suggest new hazard situations in near future, but the question whether the scenarios are adequate is still remaining. In any case, the calculated flow paths roughly represent a qualitative likelihood concerning the areas that could be affected if lahars of similar sizes occurred. Basic morphological differences related to the hazard situation at specific sites can be easily identified between the eastern and western flank of the volcano by means of the calculated deposition areas of lahars and corresponding DTMs. However, deviations between calculations on different DTMs can be significant so that effects from the source and resolution of the elevation data need to be considered in hazard assessments (see also Huggel et al., 2008b; Muñoz-Salinas et al., 2009; Stolz and Huggel, 2008).

Similar problems arose for the $\Delta H/L_{hor}$-values (that are called simply $H/L$ ratio in **Paper II** and $tan\alpha$ in **Paper III**) which were chosen for the MSF model calculations to define the maximum reach. In the case of Iztaccíhuatl they were adjusted according to empirical analysis of debris flows and several case studies from other volcanoes while different empirical values have been chosen for floods, debris flows and ice avalanches in the Mount Cook region in New Zealand (**Paper III**). Empirical values are always affected by the natural variability of mass movement phenomena such as differences in the flow rheology and uncertainties about the respective variables. Additionally, the $\Delta H/L_{hor}$ ratio of a past event can be well determined but the volume, water content and viscosity that strongly define mobility of the event can only roughly be estimated. Therefore, empirical data usually are affected by large scatters that can be typically up to one order of magnitude (Rickenmann, 1999). However, worst-case scenarios based on empirical $\Delta H/L_{hor}$ ratios for specific mass movement types provide an objective basis for possible maximum runout distance calculations. Different event magnitude scenarios (such as minimal, medium and extreme scenarios; see Margreth and Funk, 1999), various types of mass movements (e.g. according to water content and rheology, such as for granular or viscous debris flows, lahars or hyperconcentrated flows) or intensity/probability-relations (Lateltin et al., 2005; Raetzo et al., 2002) can be created by corresponding adjustments of the $\Delta H/L_{hor}$ ratios.

Difficulties with parameter calibration increase with each variable that is included in more complicated models. For instance, the RAMMS model which includes the simple two-parameter Voellmy rheology is much more time-intensive to be calibrated and requires more computational resources so that it is more difficult to be applied at many sites on a regional-scale. Its potential to represent flow paths and deposition areas of individual rock-avalanches has been demonstrated by retrospectively modeling in **Papers III** and **IV**, but uncertainty about the input values remain, such as starting volumes (Huggel et al., 2004), or different possible combinations of the two friction-parameters to reach a given runout distance (see **Chapter 2.4.2**; Alean, 1985; Perla et al., 1980). Retrospectively regionally calibrated values may be applied for similar volumes and types of mass movements, but material and flow path conditions can strongly vary within short distances. As a consequence, the presented preliminary hazard assessments in **Papers II** and **III** that included simple empirical runout models are largely of a qualitative nature. They can be seen as a relative indication of the spatial probability to be affected by the indicated type of rapid mass movement (van Westen et al., 2006) that could serve as a solid basis for the elaboration of more detailed hazard maps.

While climate-induced changes in Mexico are largely restricted to the potential starting zones of rapid mass movements, in New Zealand, major changes also affect the lower slopes which can serve as deposition zones for rock and ice avalanches or debris flows. The rapid growth of large proglacial lake in the Aoraki/Mt. Cook area increases the hazard for impacts of rapid mass movements and flood wave generation. Due to the flat terrain surrounding the lakes, moraine breaching and debris flow generation is unlikely, but flood waves could reach far downstream. Permafrost degradation is considered as a potential trigger for destabilizing bedrock slopes but the seismically active region also suggests that strong earthquakes could have severe consequences and trigger numerous large landslides simultaneously as shown by the March 27, 1964 Alaskan earthquake (Post, 1968).

## 4.2 Benefits from seismic signals

Seismic signals can help with a more accurate determination of rheologic parameters, but again only in a retrospective manner (**Paper IV**). The basis of characteristic empirical values and the general process understanding can be well improved in certain cases. In the following, we discuss several findings and problems having general validity on the basis of a specific example, the January 18, 1997 Brenva avalanche in the Mont Blanc region in Italy.

If available, the total seismic energy is best represented by the average filtered absolute amplitude of all three seismic components (E = east; N = north; Z = vertical), while the basic characteristics are also well represented by only the Z-component (**Figure 12a** and **b**). Topographic features within the avalanche path are well reflected in the seismograms (Favreau et al., 2010) but a critical factor is the source-receiver distance. The rapid degradation of the seismic waves with distance weakens the information content of the recorded signal about its origin – the mass movement (Deparis et al., 2008).

Comparison of the filtered seismic absolute amplitude in **Figure 12b** with the modeled work rates in **Figure 12c** exemplifies that differences appear at larger distances while the basic shape is still comparable. The seismic station Bardonecchia in Italy is at 85 km distance from the source (Brenva) so that alone the differences in propagation speed of P- (~5.55 km/s) and S-waves (~3.25 km/s) lead to an extension of the seismogram of more than 10 seconds. This obliterates the dynamic avalanche information, suggesting a longer process duration with smaller average velocities, such as they would be related to by lower combinations of $\mu$ and $\xi$ ($\mu = 0.12$, $\xi = 700\ \mathrm{m/s^2}$ in **Figure 12c**). However, the relative amplitudes of the two main peaks fit better for higher combinations of $\mu$ and $\xi$ ($\mu = 0.20$, $\xi = 2000\ \mathrm{m/s^2}$). Therefore, we can conclude that the most appropriate parameters are likely to lie in between these boundaries, but also that there might have been other relevant differences between the model and reality.

Deviations of the modeled work rates and the seismic data can have many reasons. Besides variable frictional conditions along the flow path, it is possible that estimated starting and

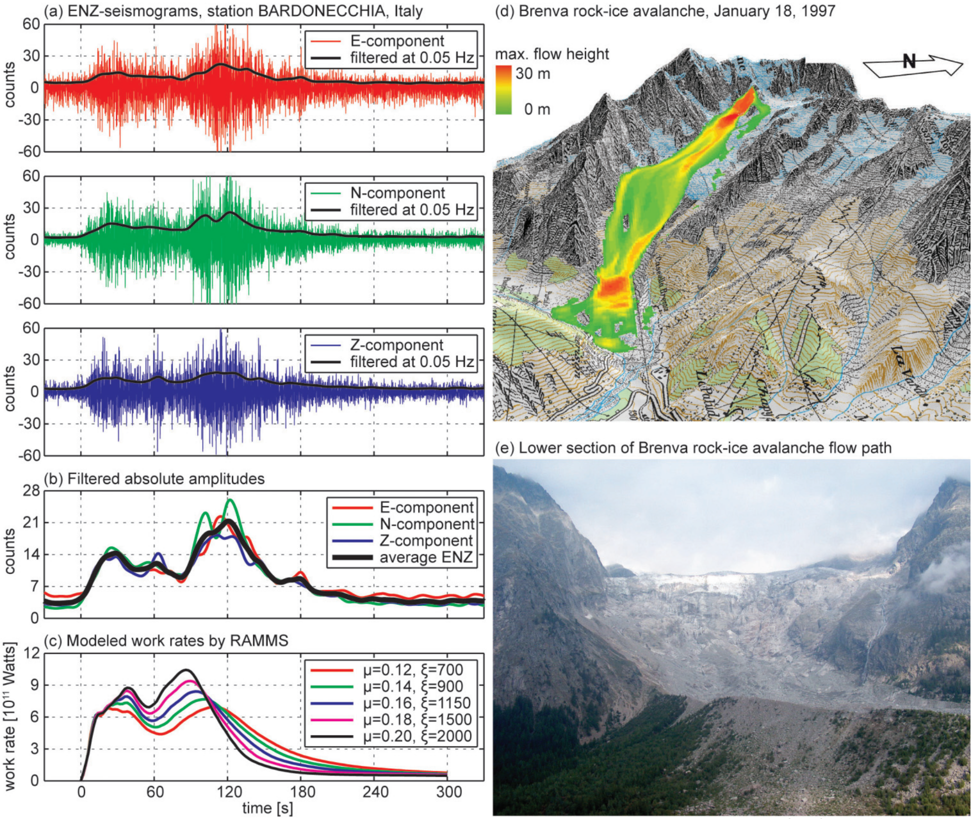

**Figure 12:** (a) Seismograms of the east, north and vertical component of the $6.5 \times 10^6\ \mathrm{m}^3$ Brenva rock-ice avalanche of January 18, 1997 (Italy). Black lines are the filtered absolute amplitudes of each component. (b) Calculation of the average filtered absolute amplitude of the three components. (c) RAMMS calculations of the frictional work rates for different friction parameter combinations resulting in similar runout paths. (d) Maximum flow heights as calculated by RAMMS (topographic map reproduced by permission of swisstopo BA081843). (e) Picture of lower avalanche path section of the 1997 Brenva event. Little ice age moraine was overflown on the orographically right side (note that this is also the case in the simulation). Photo by L. Fischer.

entrainment volumes which were used in the model differ by up to ±50% from reality (Schneider et al., 2011a). In the case of Brenva, the failure volume in the model was set to ~$3 \times 10^6$ $m^3$ (mainly rock) and the avalanche entrained another ~$3.5 \times 10^6$ $m^3$ of ice and debris to result in a total avalanche volume of ~$6.5 \times 10^6$ $m^3$ that well fits the reported values by Deline (2009). Differing starting volumes and entrainment rates would lead to somewhat modified frictional work rate plots. Moreover, the material in the RAMMS model was entrained depending on the avalanche velocity and flow height (see momentum-dependent erosion in Schneider et al., 2010) along the entire avalanche track. If most of the material has been eroded from the glacier within the upper part, momentum-transfer might have decelerated the avalanche in that section (see experiments by Mangeney et al., 2010). In the model, this would lead to a delay and accentuation of the second peak because a larger volume would be travelling somewhat later down the steep cliffs to the deposition area and the calculated frictional work rate may better fit the seismic data. For such a precise calibration, however, comparison to seismic data at 85 km distance is too speculative and data from closer stations would be preferred.

Average and maximum velocity estimations can be strongly improved by seismic analysis. The seismograms in **Figure 12a** suggest a total duration of nearly 240 seconds for the entire event, resulting in an average velocity of ~24 m/s for the horizontal distance of ~5800 m, although much of the later ground shaking might be attributed to continuous minor mass movements around the source area and at the tail of the avalanche. As an average of the different RAMMS calculations, the avalanche front reaches close to the maximum runout distance already after ~150 seconds, leading to a much higher average velocity of 39 m/s. Additionally, the maximum velocities of the avalanche can be extracted from the model results, reaching 50-60 m/s depending on the friction-parameter combination (on the central Brenva glacier part and at the toe of the steep cliffs above the deposition area).

As shown within this discussion and in **Paper IV**, seismic signals provide an excellent possibility to enhance the dynamic understanding of rapid mass movements and the maximum benefit can be extracted in combination with dynamic numerical models. Other promising possibilities related to seismic data currently evolve for monitoring and predictive purposes as presented in **Chapter 2.6** but were not included in this study.

## 4.3 Insights from laboratory experiments and event-based analysis

The advantages of experimental runs under controlled laboratory conditions were used to assess the influence of ice – and associated effects of increasing pore water pressure – on the friction coefficient (**Paper V**). Scale effects are unavoidable. However, they can at least be roughly assessed by dimensional analysis.

A main problem was to find appropriate volumes, flow heights, grain sizes and flow velocities. The size of the rotating drums restricted the maximum flow height $h$ to a few decimeters. Applying Froude similarity (Reynolds similarity using identical fluids as in nature would require impossible experimental velocities 1000 times faster than the real events; see **Chapter 2.5.2**), the clearly supercritical flow of many natural rapid mass movements ($Fr >> 1$) required either high rotational velocities $u$ or low flow heights $h$ (applied for the characteristic length $L$ in **Equation 8**). However, velocity was restricted by technical and mechanical limits of the rotating drum (including that centripetal effects should be minimized) and flow depth should not be too low, so that the maximum flow height did not decrease below ~10 particle diameters. Furthermore, wide grain size distributions and small uniform particles (ice or gravel) led to stick-slip effects (Higashi and Sumita, 2009) after a few rotations, probably related to increasing intergranular forces (cohesive and/or electrostatic effects; see Davies and McSaveney, 1999). Consequently, we chose the fastest velocity where a stable flow behavior developed (1.64 in the smaller drum and 2.09 m/s in the larger drum, corresponding to the rolling to cascading mode after Henein et al., 1983a), uniform grain sizes of several millimeters to a few centimeters, and a low percental fill of the drum leading to flow depths that were 10-20 times higher than the average grain size for most of the experiment time (**Figure 13**).

The main result from the laboratory experiments is that the friction coefficient of a dry granular mass does linearly decrease with increasing ice content and can be reduced by up to 20% for pure ice compared to gravel only (**Paper V**). The effects of increasing pore water pressure for longer time spans can further reduce the friction coefficients by up to ~50%. The difficulty remains in transferring these results to natural events. The measured effects were similar for both rotating drums but the geometric scaling factor $\lambda_L$ between the models is only 1.6 compared to ~1000 between the models and reality.

A rheologic analysis by means of the dimensionless numbers presented in **Chapter 2.5.3** revealed that the majority of the values are within a similar range for the natural events as for the laboratory experiments. **During the dry stage at the beginning of the experiments**,

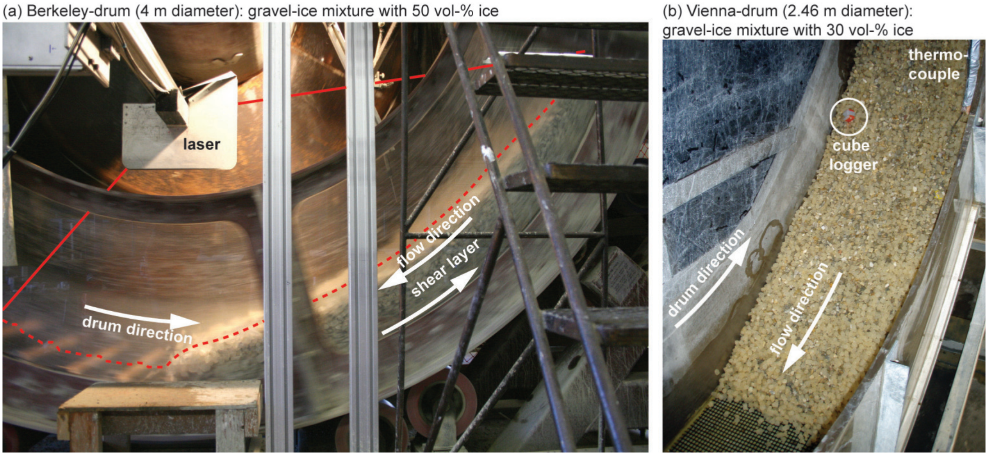
(a) Berkeley-drum (4 m diameter): gravel-ice mixture with 50 vol-% ice

(b) Vienna-drum (2.46 m diameter): gravel-ice mixture with 30 vol-% ice

**Figure 13:** Side view (a) and oblique view (b) of the two used rotating drums in Berkeley and Vienna. Red straight and dashed lines in (a) indicate the range and profile line of the laser. The cube logger and thermocouple that are indicated in (b) were both used for temperature measurements. Both pictures were taken during the first 5 minutes of the experiments when the material was still largely dry.

differences mainly arise for the Reynolds number $N_R$ which is much lower in the laboratory experiments compared to prototypes (**Tables 3-8** in the **Appendix**), confirming that viscosity of the pore 'fluid' (that is air in the dry flow) is more effective than in natural events as suggested by Iverson (1997b). This effect is inevitable when the same materials are used in the model as in nature (rock and air). Moreover, the dimensionless numbers $N_B$, $N_R$ and $N_F$ indicate that fluid viscosity is of secondary importance for the flows in the rotating drums and natural events as long as they are dry. The Savage numbers in the experiments and prototypes $N_S$ refer to the frictional-dominated flow regime but most values are close to the transitional regime and in several cases collisional interactions may already dominate.

Flow behavior strongly changes for those mixtures that get saturated with water towards the end of the experiments. **The late and saturated stage** of flows with higher ice contents is characterized by Mass numbers $N_M$ reducing to zero. This is because the fluid inertial stresses increase and can get larger than solid inertial stresses if the sediment content is low. In such cases, the Bagnold numbers $N_B$ also drops to much lower values close to zero, indicating that viscous stresses are becoming important.

Such flow transformations from relatively dry avalanches to completely saturated flows are typical for many large rapid mass movements from glacial environments (Petrakov et al., 2008). The evolution of the pore water pressure in the drum started from the tail of the flow and moved progressively to the front. At the same time, the friction coefficient was reduced linearly. If a similar process is active in nature (e.g. large rapid mass movements which are increasingly fluidizing while they are travelling downstream), the reduction of the friction coefficient may compensate the decreasing slope gradient and lead to much longer runout distances in cases where the slope is very close to the friction angle.

The initial ice content reduces the original dry friction during the early stage and later contributes in reducing friction by providing melt water. The flow behavior of a rapid mass movement during the early stage is of special importance because a reduced friction in typically steep starting zones strongly increases flow velocities which in turn enhances the erosion capacities within areas where steep friable material usually is abundant (erosion is largely limited by the availability of erodible material: Hungr et al., 2005; Mangeney et al., 2010). This can lead to strong entrainment and a significant volume increase having again a critical effect on the runout distance.

The empirical parameters that were extracted from recent large rock-ice avalanche events (apparent coefficient of friction, topographic characteristics, ice and water content, and the trajectory leading over glacier surface) show high variabilities representing natural peculiarities of specific events but also included uncertainties related to the parameter collection method. Extracting individual influence factors on rapid mass movement mobility is extremely difficult due to the complex interlacing of the individual mechanisms. On the one hand, the effect of ice to reduce friction – as observed in the laboratory experiments – was not visible in nature. The reasons therefore may lie in inaccurate estimations of the ice content, but mainly in obliteration of the effects of ice by other factors. On the other hand, the water content and the part of the avalanche trajectory leading over glaciers have shown some (semi-) quantitative negative correlation with the apparent friction coefficient, suggesting that these factors significantly steer rapid mass movement mobility.

A common feature between the performed laboratory experiments and natural large-scale rapid mass movements is the strongly variable flow behavior – in space and time. Therefore it is difficult to characterize the flow behavior in general. As an example, water content varies from the tail to the front (e.g. dry front of debris flows Iverson et al., 2010; McArdell et al., 2007) and may increase or decrease as a flow propagates along its path. Dimensionless numbers as described in **Chapter 2.5.3**, **Chapter 4.3** and in **Tables 3-8** in the **Appendix** in fact strongly vary along the flow profiles in the rotating drum and in real events. Therefore, a rapid mass movement can flow at supercritical conditions within the fast and moderately deep front, followed by a main body having lower or even subcritical Froude numbers. Moreover, in the drum, the tail of the flow is artificially kept at the same velocities as the front. The consequence of the reduced flow height towards the tail of the mass by constant effective velocities is a strongly increasing Froude number and shear rate. For such reasons, flows also tend more to the collisional regime at the very front (Jop et al., 2006) where 'grain spray' can be observed (Jop et al., 2006; Major and Iverson, 1999) – and in the special case of vertically rotating drums also at the tail.

# 5 Conclusions and Perspectives

## 5.1 Conclusions

Governing flow mechanisms which are effective in large landslides, rock- or debris avalanches are assumed to be also relevant for events within or from glacial environments. However, additional effects are caused by the presence of ice and need to be considered. The broad variability of these events is a challenge to perform adequate characterization. Moreover, material entrainment or deposition, particle comminution and melting of ice can modify the rheologic behavior on the way downstream, significantly affecting flow dynamics. Conditions for positive feedback mechanisms that lead to extreme events are often very close to negative feedbacks resulting in a low mobility. Within terraced topographies, or on slopes at angles very close to the friction angle of a rapid mass movement, a minor reduction of the shear resistance may strongly increase the runout distance.

To improve hazard assessments, it is necessary to know how different factors contribute to mass movement mobility and how practical tools such as numerical models need to be calibrated. However, numerical methods should still be critically reviewed by experts because they consider only much simplified mechanisms.

In the following, the four main research questions raised in **Chapter 1.2** are addressed:

1. *What are the effects of ice on mobility of large rapid mass movements in/from glacial environments?*

   - In the laboratory experiments, dry granular ice has a dynamic friction coefficient which is about 20% lower than the one of angular gravel. Despite that this effect could not clearly be identified in empirical data of large rock-ice avalanches and limitations in projecting small-scale laboratory results to natural events, a similar relative reduction of the friction coefficient by incorporated ice needs to be considered also in larger rock-ice avalanches.

   - Ice serves as a continuous supplier of melt water due to frictional heating, conduction and advection (heat assimilation from warmer surrounding). Increasing water contents reduced the friction coefficient by additional 50% for completely saturated flows compared to dry mixtures in the rotating drums. This effect could be even larger in natural flows where the spectrum of grain size distribution is much wider and suspended fines can increase the fluid density. In fact, natural events with high water contents are often among the most mobile events.

- Rapid mass movements with flow paths leading over glacial surfaces have significantly higher mobilities. For relatively dry events, the apparent coefficient of friction correlates with the proportion of the trajectory over glacial surface. However, low-friction surfaces can also be provided by smooth bedrock (e.g. former glacier beds).
- Snow, firn and ice are more susceptible to erosion compared to bedrock so that mass movements over glaciers can entrain large amounts of ice. Larger volumes in turn lead to increased mobilities (similarly, the abundance of friable steep debris in formerly glacierized areas sets nearly no limits to entrainment that is strongly supply-dependent).

2. *Which factors and situations have the potential to lead to extremely mobile events in glacial environments?*

- The most mobile events usually involve many individual factors. Their sum can lead to exceptionally high mobility. However, complex interactions are extremely difficult to understand.
- The above effects of ice can be among these factors while the basis for high mobility is usually provided by the volume (including entrainment), topography, material properties and long-runout mechanisms such as dispersive pressure effects, lubrication and/or fluidization (see details in **Chapter 2.3**).
- Glacial environments – particularly if affected by increasing temperatures – provide ideal conditions for large rapid mass movements. This mainly concerns the initiation and early propagation of the avalanches when entrainment can be significant, but also later flow phases if ice was incorporated in the mass.
- A higher frequency of rapid mass movements in changing environments also increases the number of events where individual factors achieve ideal constellations for long-runout that are usually rare.
- Flow transformations have a high potential to increase mobility and can evolve progressively by entrainment of water-saturated substrates or surface water from streamlets and by melting of incorporated ice.
- The most critical hazard situations often result from process chains, such as rapid mass movements into glacial or landslide-dammed lakes, flood wave generation, dam overtopping, consequent erosion of the dam, and formation of a debris flow or flood.

3. *What kind of numerical tools can be applied to assess large rapid mass movements in/from glacial environments and how can the benefits from numerical modeling be maximized to enhance process understanding?*

    - Existing empirical and physically-based dynamic runout simulation models are useful tools to assess rapid mass movements in glacial environments and need to be chosen according to the most relevant processes and an appropriate scale (regional or local).
    - Empirical models can rapidly give a rough overview of areas that may be potentially affected by rapid mass movements on the basis of historical data. They can be easily adjusted to consider future scenarios.
    - Dynamic physical models can well reproduce the typically unconfined flow behavior and features such as overtopping of lateral ridges and run-up on opposite slopes. Such models should be calibrated in retrospective modeling using geometric, energetic and dynamic aspects.
    - Seismic data is usually available for large rapid mass movements and can be used for dynamic calibration of dynamic runout models. The basic seismic characteristics of large avalanches can be sustained for source-receiver distances up to ~100 km.
    - The frictional work rate of an avalanche – which depends on the frictional rheology and can be calculated by dynamic models – correlates with the absolute seismic amplitude and is therefore well suited to calibrate the model. With this method, event duration and flow velocities can be determined much better.
    - Deviations between models and seismograms indicate model deficiencies, other processes being active at the mass movement, or may result from modifications of the seismic energy on its way between the source and receiver (path effects).
    - On the one hand parameters such as flow heights, velocities and pressures can be determined more accurately by seismic analysis, that are of importance e.g. in case of planned mitigation measures and for hazard assessments. On the other hand, the process understanding can be much improved, such as identification of different failure mechanisms (single or multiple/progressive failures), interactions of the avalanche with obstacles, and changes in rheology or basal friction.

4. *What are the implications for hazard assessments?*

    - An important problem is that due to rapidly changing climatic conditions, large rapid mass movements in/from glacial environments are increasingly affecting areas going beyond historical precedence. Scenarios can therefore not be built simply on the basis of local empirical data. Instead, a global perspective is necessary and worst-case scenarios should be considered.

- The study confirms on a (semi-) quantitative basis that hazard assessments in glacial environments need to account for enhanced mobility effects of rapid mass movements resulting from interaction with ice, that was part of the conclusions by Evans and Clague (1988), by adding considerable detail to the understanding of individual mechanisms.

- Individual factors to be considered according to their presence/likelihood and the strength of the total effects can only be roughly estimated for given volumes. The diagrams provided in **Paper VI** may help to roughly determine appropriate apparent coefficients of friction.

- The values of a potential $\mu_{app}$ can be used in a second step to adjust scenario calculations of a dynamic runout model so that lateral expansion, flow heights and velocities may be roughly determined.

The study made use of a multidisciplinary integrative approach by means of case studies, numerical modeling (retrospective and scenario-based), seismic analysis, and physical experiments in rotating drums to improve the understanding of characteristics and flow dynamics of rapid mass movements in glacial environments. The unique measurements of the friction coefficients and pore water pressure in granular rock-ice mixtures as well as the successful combination of seismic data with numerical model results thereby build the core elements of the work.

## 5.2 Perspectives

This thesis aims at contributing to the developing field of landslide seismology (particularly in relation to dynamic numerical models), at providing first measurements of the effects of ice on dynamic friction coefficients and presenting detailed empirical data on rock-ice avalanches, and at serving as a basis for improving hazard assessments in glacial environments. The understanding of rapid mass movements in general and of the ice content in particular is still in its infancy and the complexity of the processes poses major obstacles for enhanced or full comprehension. The following topics related to the current work are seen to be of major importance for further research:

- The experimental series with gravel-ice mixtures should be extended to include other particle sizes, wider grain size distributions and different velocities. The experiments may be performed in a cold room at subzero temperatures or in a more isolated system so that an estimation of frictional heating will be possible (thermodynamic considerations).

- Ice could be substituted by another material having also a clearly different internal friction coefficient but which does not melt at room temperatures. Effects of varying fractions of two materials with different internal friction coefficients could be assessed more easily in this way.
- The contribution of ice as a low-strength material to increase runout distance due to intensified comminution may be considered in analogy to hydrothermally altered weak volcanic material where long-runout is amplified (see Davies et al., 2010).
- Effects from increasing pore water pressure should be addressed in more detail, such as excess pore water pressure (McArdell et al., 2007) and pore water pressure fluctuations (Iverson and LaHusen, 1989). The experiments from the gravel-ice mixture experiments provide ideal data in terms to study such effects.
- Pressure melting of ice was not considered but could be relevant in very large events. Centrifuge experiments may help to investigate this issue (e.g. Imre et al., 2010).
- Datasets of past events need to be improved to enhance the quality of empirical information. This will be difficult with respect to most parameters (e.g. water and ice content), but others like volumes may be enhanced by new technologies, such as by subtraction of high resolution DTMs (e.g. Scheidl et al., 2008).
- Seismic data needs more attention as it usually contains the only dynamic information on rapid mass movements. Besides many other applications in landslide seismology, studies need to be intensified in terms of the relation between the energy that is lost by the mass movement due to friction and the signal that is recorded at a seismic station as well as the effects that modify the seismic waves when they propagate through the ground.
- The high-frequency content of nearby seismic stations could include important information about the granular agitation of mass movements that may be useful to estimate the strength of the corresponding effect of dispersive pressure.
- For practical use, more detailed guidelines and strategies are required to address the growing challenge of changing hazard situations and increasing likelihoods for worst-case events.

# 6 References

Adushkin, V.V., 2000. Explosive initiation of creative processes in nature. Combustion, Explosion, and Shock Waves, 36(6): 695-703.

Adushkin, V.V., 2006. Mobility of rock avalanches triggered by underground nuclear explosions. In: S.G. Evans, G. Scarascia Mugnozza, A.L. Strom and R.L. Hermanns (Editors), Landslides from massive rock slope failures. Springer Netherlands, 267-284.

Alean, J., 1984. Ice avalanches and a landslide on Grosser Aletschgletscher. Zeitschrift für Gletscherkunde und Glazialgeologie, 20: 9-25.

Alean, J., 1985. Ice avalanches: some empirical information about their formation and reach. Journal of Glaciology, 31(109): 324-333.

Allen, S., Schneider, D. and Owens, I.F., 2009. First approaches towards modelling glacial hazards in the Mount Cook region of New Zealand's Southern Alps. Natural Hazards and Earth System Sciences, 9(2): 481-499.

Allen, S.K., Cox, S.C. and Owens, I.F., 2010. Rock avalanches and other landslides in the central Southern Alps of New Zealand: a regional study considering possible climate change impacts. Landslides, 8(1): 1-16.

Amitrano, D., Arattano, M., Chiarle, M., Mortara, G., Occhiena, C., Pirulli, M. and Scavia, C., 2010. Microseismic activity analysis for the study of the rupture mechanisms in unstable rock masses. Natural Hazards and Earth System Sciences, 10(4): 831-841.

Ancey, C. and Coussot, P., 1999. Transition frictionnelle/visqueuse pour une suspension granulaire. Comptes Rendus de l'Academie des Sciences - Series IIB - Mechanics-Physics-Astronomy, 327(5): 515.

Arattano, M., 1999. On the use of seismic detectors as monitoring and warning systems for debris flows. Natural Hazards, 20(2): 197-213.

Badoux, A., Graf, C., Rhyner, J., Kuntner, R. and McArdell, B., 2009. A debris-flow alarm system for the Alpine Illgraben catchment: design and performance. Natural Hazards, 49(3): 517-539.

Bagnold, R.A., 1954. Experiments on a gravity-free dispersion of large solid spheres in a Newtonian fluid under shear. Royal Society of London, 225: 49-63.

Bartelt, P., 2007. Work minimisation in rock and snow avalanches: the competition between random kinetic energy and heat, BOKU Vienna (oral presentation).

Bartelt, P. and Buser, O., 2010. Frictional relaxation in avalanches. Annals of Glaciology, 51(54): 98-104.

Bartelt, P., Buser, O. and Platzer, K., 2006. Fluctuation-dissipation relations for granular snow avalanches. Journal of Glaciology, 52(179): 631-643.

Bartelt, P., Buser, O. and Platzer, K., 2007. Starving avalanches: Frictional mechanisms at the tails of finite-sized mass movements. Geophysical Research Letters, 34(L20407): 1-6.

Bartelt, P., Salm, B. and Gruber, U., 1999. Calculating dense-snow avalanche runout using a voellmy-fluid model with active/passive longitudinal straining. Journal of Glaciology, 45(150): 242-254.

Berti, M. and Simoni, A., 2007. Prediction of debris flow inundation areas using empirical mobility relationships. Geomorphology, 90: 144-161.

Bottino, G., Chiarle, M., Joly, A. and Mortara, G., 2002. Modelling rock avalanches and their relation to permafrost degradation in glacial environments. Permafrost and Periglacial Processes, 13(4): 283-288.

Bouchut, F., Fernández-Nieto, E.D., Mangeney, A. and Lagrée, P.-Y., 2008. On new erosion models of Savage-Hutter type for avalanches. Acta Mechanica, 199(1-4): 181-208.

Bouchut, F., Mangeney-Castelnau, A., Perthame, B. and Vilotte, J.-P., 2003. A new model of Saint Venant and Savage-Hutter type for gravity driven shallow water flows. Comptes Rendus Mathematique, 336(6): 531-536.

Brodsky, E.E., Gordeev, E. and Kanamori, H., 2003. Landslide basal friction as measured by seismic waves. Geophysical Research Letters, 30(24): 2236.

Brunner, G.W., 2002. HEC-RAS River analysis system application guide, US Army Corps of Engineers, Hydrologic Engineering Center, Davis, California, USA.

Burtin, A., Bollinger, L., Cattin, R., Vergne, J. and Nábělek, J.L., 2009. Spatiotemporal sequence of Himalayan debris flow from high-frequency seismic noise analysis. Journal of Geophysical Research, 114(F04009): 1-15.

Buser, O. and Bartelt, P., 2009. Production and decay of random kinetic energy in granular snow avalanches. Journal of Glaciology, 55(189): 3-12.

Campbell, C.S., 1989. Self-lubrication for long runout landslides. The Journal of Geology, 97(6): 653-665.

Campbell, C.S., 1990. Rapid granular flows. Annual Review of Fluid Mechanics, 22: 57-92.

Campbell, C.S., 2002. Granular shear flows at the elastic limit. Journal of Fluid Mechanics, 465: 261-291.

Campbell, C.S., Cleary, P.W. and Hopkins, M., 1995. Large-scale landslide simulations: Global deformation, velocities and basal friction. Journal of Geophysical Research, 100(B5): 8267-8283.

Caplan-Auerbach, J. and Huggel, C., 2007. Precursory seismicity associated with frequent, large ice avalanches on Iliamna volcano, Alaska, USA. Journal of Glaciology, 53(180): 128-140.

Caplan-Auerbach, J., Prejean, S. and Power, J.A., 2004. Seismic recordings of ice and debris avalanches of Iliamna Volcano, Alaska. Acta Vulcanologica, 16(1-2): 9-20.

Chou, H.-T. and Lee, C.-F., 2009. Cross-sectional and axial flow characteristics of dry granular material in rotating drums. Granular Matter, 11: 13-32.

Chow, V.T., 1959. Open-Channel Hydraulics. McGraw-Hill, Inc., 700 pp.

Christen, M., Kowalski, J. and Bartelt, P., 2010. RAMMS: Numerical simulation of dense snow avalanches in three-dimensional terrain. Cold Regions Science and Technology, 63: 1-14.

Coaz, J.W.F., 1910. Statistik und Verbau der Lawinen in den Schweizeralpen. Stämpfli, Bern, Switzerland, 126 pp.

Cole, S.E., Cronin, S.J., Sherburn, S. and Manville, V., 2009. Seismic signals of snow-slurry lahars in motion: 25 September 2007, Mt Ruapehu, New Zealand. Geophys. Res. Lett., 36(9): L09405.

Collins, G.S. and Melosh, H.J., 2003. Acoustic fluidization and the extraordinary mobility of sturzstroms. Journal Of Geophysical Research, 108(B10): 2473-2487.

Corominas, J., 1996. The angle of reach as a mobility index for small and large landslides. Canadian Geotechnical Journal, 33: 260-271.

Coulomb, C.A., 1773. Sur une application des règles de maximis & minimus a quelques problèmes de statique, relatifs a l'architecture, Memoires de Mathématique et de Physique. Imp. R. Acad. Sci., Paris., Presentes à l'Académie Royale des Sciences, Paris, 343-384.

Coussot, P. and Meunier, M., 1996. Recognition, classification and mechanical description of debris flows. Earth-Science Reviews, 40(3-4): 209-227.

Crandell, D.R. and Fahnestock, R.K., 1965. Rockfalls and avalanches from Little Tahoma Peak on Mount Rainier Washington, Geological Survey Bulletin, 30 pp.

Crosta, G.B., Chen, H. and Lee, D.F., 2004. Replay of the 1987 Val Pola Landslide, Italian Alps. Geomorphology, 60: 127-146.

Crosta, G.B., Cucchiaro, S. and Frattini, P., 2003. Validation of semiempirical relationships for the definition of debris-flow behaviour in granular materials. In: D. Rickenmann and C.-l. Chen (Editors), Debris Flows Hazards Mitigation: Mechanics, Prediction, and Assessment. Millpress, Rotterdam, 821-831.

Crosta, G.B., Frattini, P. and Fusi, N., 2007a. Fragmentation in the Val Pola rock avalanche, Italian Alps. Journal of Geophysical Research, 112: 1-23.

Crosta, G.B., Hungr, O., Sosio, R. and Frattini, P., 2007b. Dynamic analysis of the Thurwieser rock avalanche, Italian Alps. Geophysical Research Abstracts, 9(09602): 1.

Crowley, J.K. and Zimbelman, D.R., 1997. Mapping hydrothermally altered rocks on Mount Rainier, Washington, with Airborne Visible/Infrared Imaging Spectrometer (AVIRIS) data. Geology, 25(6): 559-562.

Dade, W.B. and Huppert, H.E., 1998. Long-runout rockfalls. Geology, 26(9): 803-806.

Dammeier, F., Moore, J.R., Haslinger, F. and Loew, S., 2010. The seismic signature of rockslides: a review of events in the Central Alps, AGU, San Francisco.

Davies, M.C.R., Hamza, O. and Harris, C., 2001. The effect of rise in mean annual temperature on the stability of rock slopes containing ice-filled discontinuities. Permafrost and Periglacial Processes, 12: 137-144.

Davies, T.R.H., 1982. Spreading of rock avalanche debris by mechanical fluidization. Rock Mechanics, 15(1): 9-24.

Davies, T.R.H., 1988. Debris flow surges - a laboratory investigation. Mitteilungen der Versuchsanstalt für Wasserbau, Hydrologie und Glaziologie an der Eidgenössischen Technischen Hochschule, 96, 122 pp.

Davies, T.R.H., 1990. Debris-flow surges - experimental simulation. New Zealand Journal of Hydrology, 29(1): 18-46.

Davies, T.R.H. and McSaveney, M.J., 1999. Runout of dry granular avalanches. Canadian Geotechnical Journal, 36: 313-320.

Davies, T.R.H. and McSaveney, M.J., 2009. The role of rock fragmentation in the motion of large landslides. Engineering Geology, 109: 67-79.

Davies, T.R.H., McSaveney, M.J. and Beetham, R.D., 2006. Rapid block glides: slide-surface fragmentation in New Zealand's Waikaremoana landslide. Quarterly Journal of Engineering Geology and Hydrogeology, 39: 115-129.

Davies, T.R.H., McSaveney, M.J. and Hodgson, K.A., 1999. A fragmentation-spreading model for long-runout rock avalanches. Canadian Geotechnical Journal, 36: 1096-1110.

Davies, T.R.H., McSaveney, M.J. and Kelfoun, K., 2010. Runout of the Socompa volcanic debris avalanche, Chile: a mechanical explanation for low basal shear resistance. Bulletin of Volcanology, 72: 933-944.

Davila, N., Capra, L., Gavilanes-Ruiz, J.C., Varley, N., Norini, G. and Vazquez, A.G., 2007. Recent lahars at Volcan de Colima (Mexico): Drainage variation and spectral classification. Journal of Volcanology and Geothermal Research, 165(3-4): 127-141.

De Angelis, S., Bass, V., Hards, V. and Ryan, G., 2007. Seismic characterization of pyroclastic flow activity at Soufrière Hills Volcano, Montserrat, 8 January 2007. Natural Hazards and Earth System Sciences, 7: 467-472.

De Blasio, F.V. and Elverhoi, A., 2008. A model for frictional melt production beneath large rock avalanches. Journal of Geophysical Research, 113(F02014): 1-13.

Delaney, K.B. and Evans, S.G., 2008. Application of digital cartographic techniques in the characterization and analysis of catastrophic landslides; the case of the 1997 Mount Munday rock avalanche, British Columbia. In: J. Locat, D. Perret, D. Turmel, D. Demers and S. Leroueil (Editors), 4th Canadian Conference on Geohazards: From Cause to Management. Presse de l'Université Laval, University Laval, Québec, Canada, 141-146.

Delgado Granados, H., Huggel, C., Julio Miranda, P., Cárdenas Gonzalez, L., Ortega del Valle, S. and Alatorre Ibargüengoitia, M.A., 2007. Chronicle of a death foretold: extinction of the small-size tropical glaciers of Popocatépetl volcano (Mexico). Global and Planetary Change, 56: 13-22.

Deline, P., 2001. Recent Brenva rock avalanches (Valley of Aosta): new chapter in an old story? Geografia Fisica e Dinamica Quaternaria, Supplemento V: 55-63.

Deline, P., 2009. Interactions between rock avalanches and glaciers in the Mont Blanc massif during late Holocene. Quaternary Science Reviews, 28(11-12): 1070-1083.

Deline, P. and Kirkbride, M.P., 2009. Rock avalanches on a glacier and morainic complex in Haut Val Ferret (Mont Blanc Massif, Italy). Geomorphology, 103(1): 80-92.

Deline, P., Kirkbride, M.P., Ravanel, L. and Ravello, M., 2009. The Tré-la-Tête rockfall onto the glacier de la Lex Blanche (Mont Blanc massif, Italy) in September 2008. Geografia Fisica e Dinamica Quaternaria, 31: 251-254.

Denlinger, R.P. and Iverson, R.M., 2001. Flow of variably fluidized granular masses across three-dimensional terrain - 2. Numerical predictions and experimental tests. Journal of Geophysical Research, 106(B1): 553-566.

Denlinger, R.P. and Iverson, R.M., 2004. Granular avalanches across irregular three-dimensional terrain: 1. Theory and computation. Journal of Geophysical Research, 109(F01014): 1-14.

Deparis, J., Jongmans, D., Cotton, F., Baillet, L., Thouvenot, F. and Hantz, D., 2008. Analysis of rock-fall and rock-fall avalanche seismograms in the French Alps. Bulletin of the Seismological Society of America, 98(4): 1781-1796.

Ding, Y.L., Forster, R., Seville, J.P.K. and Parker, D.J., 2002. Granular motion in rotating drums: bed turnover time and slumping-rolling transition. Powder Technology, 124(1-2): 18-27.

Dramis, F., Govi, M., Guglielmin, M. and Mortara, G., 1995. Mountain permafrost and slope instability in the Italian Alps: the Val Pola landslide. Permafrost and Periglacial Processes, 6(1): 73-81.

Dufresne, A., Davies, T.R. and McSaveney, M.J., 2010. Influence of runout-path material on emplacement of the Round Top rock avalanche, New Zealand. Earth Surface Processes and Landforms, 35(2): 190-201.

Eberhardt, E., Stead, D. and Coggan, J.S., 2004. Numerical analysis of initiation and progressive failure in natural rock slopes--the 1991 Randa rockslide. International Journal of Rock Mechanics and Mining Sciences, 41(1): 69.

Eisbacher, H. and Clague, J.J., 1984. Destructive mass movements in high mountains: hazard and management. Geological Survey of Canada Paper 84-16, Ottawa, 230 pp.

Erismann, T.H., 1979. Mechanics of large landslides. Rock Mechanics, 12 (1): 15-46.

Erismann, T.H. and Abele, G., 2001. Dynamics of Rockslides and Rockfalls. Springer, Heidelberg, 316 pp.

Evans, S.G., Bishop, N.F., Smoll, L.F., Valderrama Murillo, P., Delaney, K.B. and Oliver-Smith, A., 2009a. A re-examination of the mechanism and human impact of catastrophic mass flows originating on Nevado Huascarán, Cordillera Blanca, Peru in 1962 and 1970. Engineering Geology, 108(1-2): 96-118.

Evans, S.G. and Clague, J.J., 1988. Catastrophic rock avalanches in glacial environments. In: C. Bonnard (Editor), Landslides - Proceedings of the fifth international symposium on landslides, Lausanne, Switzerland, 1153-1158.

Evans, S.G. and Clague, J.J., 1994. Recent climatic change and catastrophic geomorphic processes in mountain environments. Geomorphology, 10(1-4): 107-128.

Evans, S.G., Tutubalina, O.V., Drobyshev, V.N., Chernomorets, S.S., McDougall, S., Petrakov, D. and Hungr, O., 2009b. Catastrophic detachment and high-velocity long-runout flow of Kolka Glacier, Caucasus Mountains, Russia in 2002. Geomorphology, 105: 314-321.

Faillettaz, J., Pralong, A., Funk, M. and Deichmann, N., 2008. Evidence of log-periodic oscillations and increasing icequake activity during the breaking-off of large ice masses. Journal of Glaciology, 54(187): 725-737.

Favreau, P., Mangeney, A., Lucas, A., Crosta, G. and Bouchut, F., 2010. Numerical modeling of landquakes. Geophysical Research Letters, 37(L15305).

Fischer, L., 2009. Slope instabilites on perennially frozen and glacierised rock walls: multi-scale observations, analyses and modelling, University of Zurich, Zurich, 81 pp.

Fischer, L., Amann, F., Moore, J.R. and Huggel, C., 2010. Assessment of periglacial slope stability for the 1988 Tschierva rock avalanche (Piz Morteratsch, Switzerland). Engineering Geology, 2010: 32-43.

Fischer, L., Kääb, A., Huggel, C. and Noetzli, J., 2006. Geology, glacier retreat and permafrost degradation as controlling factors of slope instabilities in a high-mountain rock wall: the Monte Rosa east face. Natural Hazards and Earth System Sciences, 6: 761-772.

Frey, H., Haeberli, W., Linsbauer, A., Huggel, C. and Paul, F., 2010. A multi-level strategy for anticipating future glacier lake formation and associated hazard potentials. Natural Hazards and Earth System Sciences, 10: 339-352.

Gamma, P., 1999. dfwalk - Ein Murgang-Simulationsprogramm zur Gefahrenzonierung. PhD Thesis, University of Berne, Switzerland, 144 pp.

Geertsema, M., Clague, J.J., Schwab, J.W. and Evans, S.G., 2006. An overview of recent large catastrophic landslides in northern British Columbia, Canada. Engineering Geology, 83: 120-143.

Goguel, J., 1978. Scale-dependent rockslide mechanisms, with emphasis on the role of pore fluid vaporization. In: B. Voight (Editor), Rockslides and Avalanches, 1: Natural Phenomena. Elsevier, Amsterdam, 693-705.

Gordon, J.E., Birnie, R. and Timmis, R., 1978. A major rockfall and debris slide on the Lyell Glacier, South Georgia. Arctic and Alpine Research, 10: 49-60.

Goren, L. and Aharonov, E., 2007. Long runout landslides: The role of frictional heating and hydraulic diffusivity. Geophysical Research Letters, 34(L07301): 1-7.

Graf, C. and McArdell, B.W., 2008. Simulation of debris flow runout before and after construction of mitigation measures: an example from the Swiss Alps. In: S.S. Chernomorets (Editor), Debris Flows: Disaster, Risk, Forecast, Protection. Sevkavgiprovodkhoz Institute, Pyatigorsk, Pyatigorsk, Russia, 233-236.

Gray, J.M.N.T., 2001. Granular flow in partially filled slowly rotating drums. Journal of Fluid Mechanics, 441: 1-29.

Griswold, J.P. and Iverson, R.M., 2007. Mobility statistics and automated hazard mapping for debris flows and rock avalanches, Scientific investigations report 2007-5276. USGS, Reston, Virginia, 59 pp.

Gruber, S. and Haeberli, W., 2007. Permafrost in steep bedrock slopes and its temperature-related destabilization following climate change. Journal of Geophysical Research, 112(F02S18): 1-10.

Gruber, S., Hoelzle, M. and Haeberli, W., 2004. Permafrost thaw and destabilization of Alpine rock walls in the hot summer of 2003. Geophysical Research Letters, 31(L13504): 1-4.

Gruber, U. and Bartelt, P., 2007. Snow avalanche hazard modelling of large areas using shallow water numerical methods and GIS. Environmental Modelling & Software, 22(10): 1472-1481.

Haeberli, W. and Beniston, M., 1998. Climate change and its impacts on glaciers and permafrost in the Alps. Ambio, 27(4): 258-265.

Haeberli, W. and Hohmann, R., 2008. Climate, glaciers and permafrost in the Swiss Alps 2050: scenarios, consequences and recommendations. In: D.L. Kane and K.M. Hinkel (Editors), Ninth International Conference on Permafrost. University of Alaska, Fairbanks, Fairbanks, Alaska, 607-612.

Haeberli, W., Huggel, C., Kääb, A., Zgraggen-Oswald, S., Polkvoj, A., Galushkin, I., Zotikov, I. and Osokin, N., 2004. The Kolka-Karmadon rock/ice slide of 20 September 2002: an extraordinary event of historical dimensions in North Ossetia, Russian Caucasus. Journal of Glaciology, 50(171): 533-546.

Haeberli, W., Wegmann, M. and Vonder Mühll, D., 1997. Slope stability problems related to glacier shrinkage and permafrost degradation in the Alps. Eclogae Geologicae Helveticae, 90: 407-414.

Hanke, H., 1966. Gletscherkatastrophen. Der Bergsteiger, 33.

Harris, C., Vonder Muhll, D., Isaksen, K., Haeberli, W., Sollid, J.L., King, L., Holmlund, P., Dramis, F., Guglielmin, M. and Palacios, D., 2003. Warming permafrost in European mountains. Global and Planetary Change, 39(3-4): 215-225.

Harrison, K.P. and Grimm, R.E., 2003. Rheological constraints on martian landslides. Icarus, 163(2): 347-362.

Hasler, A., Gruber, S. and Beutel, J., submitted. Kinematics of steep bedrock permafrost. Journal of Geophysical Research: 1-20.

Hasler, A., Gruber, S., Font, M. and Dubois, A., in revision. Advective heat transport in frozen rock clefts - conceptual model, laboratory experiments and numerical simulation. Permafrost and Periglacial Processes.

Hauser, A., 2002. Rock avalanche and resulting debris flow in Estero Parraguirre and Río Colorado, Región Metropolitana, Chile. In: S.G. Evans and J.V. DeGraff (Editors), Catastrophic landslides: Effects, occurrence, and mechanisms. Geological Society of America Reviews in Engineering Geology, Boulder, Colorado, 135-148.

Heim, A., 1932. Bergsturz und Menschenleben. Beiblatt zur Vierteljahrsschrift der Naturforschenden Gesellschaft Zürich, 20: 217.

Henderson, F.M., 1966. Open channel flow. Macmillan Publishing Co., Inc. , New York, 522 pp.

Henein, H., Brimacombe, J.K. and Watkinson, A.P., 1983a. Experimental study of transverse bed motion in rotary kilns. Metallurgical and Materials Transactions B, 14(2): 191-205.

Henein, H., Brimacombe, J.K. and Watkinson, A.P., 1983b. The modeling of transverse solids motion in rotary kilns. Metallurgical and Materials Transactions B, 14(2): 207-220.

Henein, H., Brimacombe, J.K. and Watkinson, A.P., 1985. An experimental study of segregation in rotary kilns Metallurgical and Materials Transactions B, 16(4): 763-774.

Hewitt, K., 1988. Catastrophic landslide deposits in the Karakoram Himalaya. Science, 242: 64-67.

Hewitt, K. (Editor), 2002. Styles of rock-avalanche depositional complexes conditioned by very rugged terrain, Karakoram Himalaya, Pakistan. Reviews in Engineering Geology, XV. The Geological Society of America, Boulder, Colorado, pp 345-377.

Hewitt, K., 2009. Rock avalanches that travel onto glaciers and related developments, Karakoram Himalaya, Inner Asia. Geomorphology, 103: 66-79.

Hewitt, K., Clague, J.J. and Orwin, J.F., 2008. Legacies of catastrophic rock slope failures in mountain landscapes. Earth-Science Reviews, 87: 1-38.

Higashi, N. and Sumita, I., 2009. Experiments on granular rheology: Effects of particle size and fluid viscosity. Journal of Geophysical Research, 114(B04413).

Hirano, M. and Iwamoto, M., 1981. Measurement of debris flow and sediment-laden flow using a conveyor belt flume in a laboratory. Erosion and Sediment Transport Measurement. Proceedings of the Florence Symposium, June 1981. International Association of Hydrological Sciences Publication, 133: 225-230.

Holm, K., Bovis, M.J. and Jakob, M., 2004. The landslide response of alpine basins to post-Little Ice Age glacial thinning and retreat in southwestern British Columbia. Geomorphology, 57: 201-216.

Hotta, N. and Ohta, T., 2000. Pore-Water pressure of debris flows. Physics and Chemistry of the Earth, Part B: Hydrology, Oceans and Atmosphere, 25(4): 381-385.

Howell, D. and Behringer, R.P., 1999. Stress fluctuations in a 2D granular Couette experiment: a continuous transition. Physical Review Letters, 82(26): 5241-5244.

Hsü, K.J., 1975. Catastrophic debris streams (Sturzstroms) generated by rockfalls. Geological Society of America Bulletin, 86: 129-140.

Hsu, L., 2010. Bedrock erosion by granular flow, University of California, Berkeley, 190 pp.

Hsu, L., Dietrich, W.E. and Sklar, L.S., 2008. Experimental study of bedrock erosion by granular flows. Journal of Geophysical Research, 113(F02001): 1-21.

Hubbard, B.E., Sheridan, M.F., Carrasco-Nunez, G., Diaz-Castellon, R. and Rodriguez, S.R., 2006. Comparative lahar hazard mapping at Volcan Citlaltepetl, Mexico using SRTM, ASTER and DTED-1 digital topographic data. Journal of Volcanology and Geothermal Research, 160(1-2): 99-124.

Hübl, J., Suda, J., Proske, D., Kaitna, R. and Scheidl, C., 2009. Debris flow impact estimation. In: C. Popovska and M. Jovanovski (Editors), Eleventh International Symposium on Water Management and Hydraulic Engineering, 1-5 September 2009, Ohrid, Macedonia, 137-148.

Huggel, C., 2004. Assessment of Glacial Hazards based on Remote Sensing and GIS Modeling. PhD Thesis, University of Zurich, Zurich, 75 pp.

Huggel, C., 2009. Recent extreme slope failures in glacial environments: effects of thermal perturbation. Quaternary Science Reviews, 28: 1119-1130.

Huggel, C., Caplan-Auerbach, J., Waythomas, C.F. and Wessels, R.L., 2007. Monitoring and modeling ice-rock avalanches from ice-capped volcanoes: A case study of frequent large avalanches on Iliamna Volcano, Alaska. Journal of Volcanology and Geothermal Research, 168(1-4): 114-136.

Huggel, C., Gruber, S., Caplan-Auerbach, J., Wessels, R.L. and Molnia, B.F., 2008a. The 2005 Mt. Steller, Alaska, rock-ice avalanche: What does it tell us about large slope failures in cold permafrost? In: D.L. Kane and K.M. Hinkel (Editors), Ninth International Conference on Permafrost. University of Alaska, Fairbanks, Fairbanks, Alaska, 747-752.

Huggel, C., Kääb, A., Haeberli, W. and Krummenacher, B., 2003. Regional-scale GIS-models for assessment of hazards from glacier lake outbursts: evaluation and application in the Swiss Alps. Natural Hazards and Earth System Sciences, 3: 647-662.

Huggel, C., Kääb, A. and Salzmann, N., 2004. GIS-based modeling of glacial hazards and their interactions using Landsat-TM and IKONOS imagery. Norsk Geografisk Tidsskrift-Norwegian Journal of Geography, 58: 61-73.

Huggel, C., Khabarov, N., Obersteiner, M. and Ramírez, J.M., 2009. Implementation and integrated numerical modeling of a landslide early warning system: a pilot study in Colombia. Natural Hazards, 52: 1-18.

Huggel, C., Salzmann, N., Allen, S., Caplan-Auerbach, J., Fischer, L., Haeberli, W., Larsen, C., Schneider, D. and Wessels, R., 2010. Recent and future warm extreme events and high-mountain slope stability. Philosophical Transactions of the Royal Society A, 368: 2435-2459.

Huggel, C., Schneider, D., Julio, P., Delgado, H. and Kääb, A., 2008b. Evaluation of ASTER and SRTM DEM data for lahar modeling: a case study on lahars from Popocatépetl Volcano, Mexico. Journal of Volcanology and Geothermal Research, 170(1-2): 99-110.

Huggel, C., Zgraggen-Oswald, S., Haeberli, W., Kääb, A., Polkvoj, A., Galushkin, I. and Evans, S.G., 2005. The 2002 rock/ice avalanche at Kolka/Karmadon, Russian Caucasus: assessment of extraordinary avalanche formation and mobility, and application of QuickBird satellite imagery. Natural Hazards and Earth System Sciences, 5: 173-187.

Huizinga, R.J., 1996. Verification of vertically rotating flume using non-newtonian fluids. Journal of Hydraulic Engineering, 122(8): 456-459.

Hungr, O., 1995. A model for the runout analysis of rapid flow slides, debris flows, and avalanches. Canadian Geotechnical Journal, 32: 610-623.

Hungr, O., 2005. Classification and terminology. In: M. Jakob and O. Hungr (Editors), Debris-flow hazards and related phenomena. Springer, Berlin Heidelberg, 9-23.

Hungr, O., 2006. Rock avalanche occurrence, process and modelling. In: S.G. Evans, G. Scarascia-Mugnozza, A. Strom and R. Hermanns (Editors), Advanced Research Workshop: Landslides from massive rock slope failure. NATO Science Series, IV Earth and Environmental Sciences, Celano, Italy, June 16-21, 2002. Springer, Heidelberg, 243-266.

Hungr, O. and Evans, S.G., 2004. Entrainment of debris in rock avalanches: An analysis of a long run-out mechanism. GSA Bulletin, 116(9/10): 1240-1252.

Hungr, O., Evans, S.G., Bovis, M.J. and Hutchinson, J.N., 2001. A review of the classification of landslides of the flow type. Environmental & Engineering Geoscience, 7(3): 221-238.

Hungr, O. and McDougall, S., 2009. Two numerical models for landslide dynamic analysis. Computers & Geosciences, 35: 978-992.

Hungr, O., McDougall, S. and Bovis, M., 2005. Entrainment of material by debris flows. In: M. Jakob and O. Hungr (Editors), Debris-flow hazards and related phenomena. Springer, Berlin Heidelberg, 135-158.

Hürlimann, M., Rickenmann, D., Medina, V. and Bateman, A., 2008. Evaluation of approaches to calculate debris-flow parameters for hazard assessment. Engineering Geology, 102: 152-163.

Hutchinson, J.N., 1988. Catastrophic rock avalanches in glacial environments. In: C. Bonnard (Editor), Landslides - Proceedings of the fifth international symposium on landslides, Lausanne, Switzerland, 3-36.

Imre, B., Laue, J. and Springman, S.M., 2010. Fractal fragmentation of rocks within sturzstroms: insight derived from physical experiments within the ETH geotechnical drum centrifuge. Granular Matter, 12: 267-285.

Iribarren Anacona, P. and Bodin, X., 2010. Geomorphic consequences of two large glacier and rock glacier destabilizations in the Central and Northern Chilean Andes. EGU General Assembly 2010, 12(7162-5): 1.

Iverson, R., 1997a. Mount Adams, Washington 1997 debris avalanches. Internet source: http://vulcan.wr.usgs.gov/Volcanoes/Adams/DebrisAval/DebrisAval1997/framework.html (last access March 15, 2011).

Iverson, R.M., 1997b. The physics of debris flows. Reviews of Geophysics, 35(3): 245-296.

Iverson, R.M., 2005. Regulation of landslide motion by dilatancy and pore pressure feedback. Journal of Geophysical Research, 110(F02015): 1-16.

Iverson, R.M. and Denlinger, R.P., 2001. Flow of variably fluidized granular masses across three-dimensional terrain - 1. Coulomb mixture theory. Journal of Geophysical Research, 106(B1): 537-552.

Iverson, R.M. and LaHusen, R.G., 1989. Dynamic pore-pressure fluctuations in rapidly shearing granular materials. Science, 246(4931): 796-799.

Iverson, R.M., Logan, M. and Denlinger, R.P., 2004. Granular avalanches across irregular three-dimensional terrain: 2. Experimental tests. Journal of Geophysical Research, 109(F01015): 1-16.

Iverson, R.M., Logan, M., LaHusen, R.G. and Berti, M., 2010. The perfect debris flow? Aggregated results from 28 large-scale experiments. Journal of Geophysical Research, 115(F03005): 1-29.

Iverson, R.M., Reid, M.E. and LaHusen, R.G., 1997. Debris-flow mobilization from landslides. Annual Review of Earth and Planetary Sciences, 25: 85-138.

Iverson, R.M., Schilling, S.P. and Vallance, J.W., 1998. Objective delineation of lahar-inundation hazard zones. GSA Bulletin, 110(8): 972-984.

Iverson, R.M. and Vallance, J.W., 2001. New views of granular mass flows. Geology, 29(2): 115-118.

Jain, N., Ottino, J.M. and Lueptow, R.M., 2002. An experimental study of the flowing granular layer in a rotating tumbler. Physics of fluids, 14(2): 11.

Jibson, R.W., Harp, E.L., Schulz, W. and Keefer, D.K., 2006. Large rock avalanches triggered by the M 7.9 Denali Fault, Alaska, earthquake of 3 November 2002. Engineering Geology, 83(1-3): 144-160.

Jiskoot, H., 2010. Long-runout rockslide on glacier at Tsar Mountain, Canadian Rocky Mountains: potential triggers, seismic and glaciological implications. Earth Surface Processes and Landforms, 36(2): 203-216.

Jop, P., Forterre, Y. and Pouliquen, O., 2006. A constitutive law for dense granular flows. Nature, 441: 727-730.

Julio-Miranda, P., Delgado-Granados, H., Huggel, C. and Kääb, A., 2008. Impact of the eruptive activity on glacier evolution at Popocatepetl Volcano (México) during 1994-2004. Journal of Volcanology and Geothermal Research, 170: 86-98.

Julio Miranda, P., Gonzalez-Huesca, A.E., Delgado Granados, H. and Kääb, A., 2005. Glacier melting and lahar formation during January 22, 2001 eruption, Popocatépetl volcano (Mexico). Zeitschrift für Geomorphologie, 140: 93-102.

Kaitna, R., 2006. Debris flow experiments in a rotating drum. PhD Thesis, Universität für Bodenkultur, Vienna, 170 pp.

Kaitna, R. and Dietrich, W., 2009. Measuring velocity profiles in large scale debris flow experiments, From Volcanoes to Vineyards: Living with Dynamic Landscapes. Abstracts with Programs. Geological Society of America, Annual meeting, Portland, Oregon, 18-21 Octobre 2009, 609 pp.

Kaitna, R. and Rickenmann, D., 2007. A new experimental facility for laboratory debris flow investigation. Journal of Hydraulic Research, 45(6): 797-810.

Kaitna, R., Rickenmann, D. and Schneiderbauer, S., 2006. Comparative rheologic investigations in a vertically rotating flume and a 'moving-bed' conveyor belt flume. In: G. Lorenzini, C.A. Brebbia and D.E. Emmanouloudis (Editors), Monitoring, simulation, prevention and remediation of dense and debris flows. WIT Press, Rhodos, 89-98.

Kelfoun, K. and Druitt, T.H., 2005. Numerical modeling of the emplacement of Socompa rock avalanche, Chile. Journal of Geophysical Research, 110: 1-13.

Kent, P.E., 1966. The transport mechanism in catastrophic rock falls. Journal of Geology, 74: 79-83.

Kishimura, K. and Izumi, K., 1997. Seismic signals induced by snow avalanche flow. Natural Hazards, 15: 89-100.

Kodama, Y., 1994. Experimental study of abrasion and its role in producing downstream fining in gravel-bed rivers. Journal of Sedimentary Research, A64(1): 76-85.

Kogelnig, A., Hübl, J., Suriñach, E., Vilajosana, I. and McArdell, B., 2011. Infrasound produced by debris flow: propagation and frequency content evolution. Natural Hazards, in press.

Körner, H.J., 1983. Zur Mechanik der Bergsturzströme vom Huascarán, Perú. In: G. Patzelt (Editor), Die Berg- und Gletscherstürze vom Huascarán, Cordillera Blanca, Perú. Universitätsverlag Wagner, Innsbruck, 71-110.

Korup, O., 2005. Distribution of landslides in southwest New Zealand. Landslides, 2: 43-51.

Korup, O., Schneider, D., Huggel, C. and Dufresne, A., in press. Long-runout landslides. In: J. Shroder, R. Marston and M. Stoffel (Editors), Treatise on Geomorphology. Academic Press, Elsevier, San Diego, CA, doi:10.1016/B978-0-08-088523-0.00164-7.

Korup, O. and Tweed, F., 2007. Ice, moraine, and landslide dams in mountainous terrain. Quaternary Science Reviews, 26(25-28): 3406-3422.

Kotlyakov, V.M., Rototaeva, O.V. and Nosenko, G.A., 2004. The September 2002 Kolka Glacier Catastrophe in North Ossetia, Russian Federation: Evidence and Analysis. Mountain Research and Development, 24(1): 78-83.

Krautblatter, M. and Funk, D., 2010. A rock-/ice mechanical model for the destabilisation of permafrost rocks and first laboratory evidence for the "reduced friction hypothesis", Proceedings of the 3rd European Conference on Permafrost, Svalbard, Spitsbergen, 205 pp.

Kumagai, H., Palacios, P., Maeda, T., Castillo, D.B. and Nakano, M., 2009. Seismic tracking of lahars using tremor signals. Journal of Volcanology and Geothermal Research, 183: 112-121.

Kveldsvik, V., Kaynia, A.M., Nadim, F., Bhasin, R., Nilsen, B. and Einstein, H.H., 2009. Dynamic distinct-element analysis of the 800 m high Åknes rock slope International Journal of Rock Mechanics and Mining Sciences, 46(4): 686-698

Lateltin, O., Haemmig, C., Raetzo, H. and Bonnard, C., 2005. Landslide risk management in Switzerland. Landslides, 2(4): 313-320.

Lavigne, F., Thouret, J.C., Voight, B., Young, K., LaHusen, R., Marso, J., Suwa, H., Sumaryono, A., Sayudi, D.S. and Dejean, M., 2000. Instrumental lahar monitoring at Merapi Volcano, Central Java, Indonesia. Journal of Volcanology and Geothermal Research, 100(1-4): 457-478.

Legros, F., 2002. The mobility of long-runout landslides. Engineering Geology, 63: 301-331.

Legros, F., 2006. Landslide mobility and the role of water. In: S.G. Evans, G. Scarascia Mugnozza, A.L. Strom and R.L. Hermanns (Editors), Advanced Research Workshop: landslides from massive rock slope failure. NATO Science Series, IV Earth and Environmental Sciences, June 16-21, 2002, Celano, Italy. Springer, 233-242.

Legros, F., Cantagrel, J.-M. and Bertrand, D., 2000. Pseudotachylyte (frictionite) at the base of the Arequipa volcanic landslide deposit (Peru): Implications for emplacement mechanisms. The Journal of Geology, 108: 601-611.

Lipovsky, P.S., Evans, S.G., Clague, J.J., Hopkinson, C., Couture, R., Bobrowsky, P., Ekström, G., Demuth, M.N., Delaney, K.B., Roberts, N.J., Clarke, G. and Schaeffer, A., 2008. The July 2007 rock and ice avalanches at Mount Steele, St. Elias Mountains, Yukon, Canada. Landslides, 5(4): 445-455.

Longo, S. and Lamberti, A., 2002. Grain shear flow in a rotating drum. Experiments in Fluids, 32(3): 313-325.

Lu, K., Brodsky, E.E. and Kavehpour, H.P., 2007. Shear-weakening of the transitional regime for granular flow. Journal of Fluid Mechanics, 587: 347-372.

Lube, G., Cronin, S.J. and Procter, J.N., 2009. Explaining the extreme mobility of volcanic ice-slurry flows, Ruapehu volcano, New Zealand. Geology, 37(1): 15-18.

Mair, K. and Hazzard, J.F., 2007. Nature of stress accommodation in sheared granular material: Insights from 3D numerical modeling. Earth and Planetary Science Letters, 259(3-4): 469-485.

Major, J. and Iverson, R.M., 1999. Debris-flow deposition: effects of pore-fluid pressure and friction concentrated at flow margins. Geological Society of America Bulletin, 110: 1424-1434.

Mangeney-Castelnau, A., Vilotte, J.P., Bristeau, M.O., Perthame, B., Bouchut, F., Simeoni, C. and Yerneni, S., 2003. Numerical modeling of avalanches based on Saint Venant equations using a kinetic scheme. Journal of Geophysical Research, 108(B11): 2527.

Mangeney, A., Roche, O., Hungr, O., Mangold, N., Faccanoni, G. and Lucas, A., 2010. Erosion and mobility in granular collapse over sloping beds. Journal of Geophysical Research, 115(F03040): 1-21.

Mangold, N. and Allemand, P., 2001. Topographic analysis of features related to ice on Mars. Geophysical Research Letters, 28(3): 407-410.

Marangunic, C. and Bull, C., 1968. The landslide on the Sherman Glacier, The Great Alaska Earthquake of 1964, Hydrology. National Academy of Sciences, Washington D.C., 383-394.

Margreth, S. and Funk, M., 1999. Hazard mapping for ice and combined snow/ice avalanches -- two case studies from the Swiss and Italian Alps. Cold Regions Science and Technology, 30(1-3): 159-173.

McArdell, B.W., Bartelt, P. and Kowalski, J., 2007. Field observations of basal forces and fluid pore pressure in a debris flow. Geophysical Research Letters, 34(L07406).

McDougall, S., 2006. A new continuum dynamic model for the analysis of extremely rapid landslide motion across complex 3D terrain. PhD Thesis, The University of British Columbia, 253 pp.

McDougall, S. and Hungr, O., 2004. A model for the analysis of rapid landslide motion across three-dimensional terrain. Canadian Geotechnical Journal, 41: 1084-1097.

McDougall, S. and Hungr, O., 2005. Dynamic modelling of entrainment in rapid landslides. Canadian Geotechnical Journal, 42: 1437-1448.

McSaveney, M.J., 1978. Sherman Glacier rock avalanche, Alaska, U.S.A. In: B. Voight (Editor), Rockslides and Avalanches, 1; Natural Phenomena. Elsevier, Amsterdam, 197-258.

McSaveney, M.J., 2002. Recent rockfalls and rock avalanches in Mount Cook National Park, New Zealand. In: S.G. Evans and J.V. DeGraff (Editors), Catastrophic landslides: effects, occurrence and mechanism. Geological Society of America, Reviews in Engineering Geology. Geological Society of America Reviews in Engineering Geology, Boulder, Colorado, 35-70.

McSaveney, M.J. and Davies, T.R.H., 2007. Rockslides and their motion. In: K. Sassa, H. Fukuoka, F. Wang and G. Wang (Editors), Progress in Landslide Science. Springer, 113-133.

McSaveney, M.J. and Downes, G., 2002. Application of landslide seismology to some New Zealand rock avalanches. In: J. Rybář, J. Stemberk and P. Wagner (Editors), Landslides. Swets & Zeitlinger, Lisse, 649-654.

Mikoš, M. and Jaeggi, M.N.R., 1995. Experiments on motion of sediment mixtures in a tumbling mill to study fluvial abrasion. Journal of Hydraulic Research, 33(6): 751-772.

Muñoz-Salinas, E., Castillo-Rodríguez, M., Manea, V. and Palacios, D., 2009. Lahar flow simulations using LAHARZ program: Application for the Popocatépetl volcano, Mexico. Journal of Volcanology and Geothermal Research, 182: 13-22.

Naef, D., Rickenmann, D., Rutschmann, P. and McArdell, B.W., 2006. Comparison of flow resistance relations for debris flows using a one-dimensional finite element simulation model. Natural Hazards and Earth System Sciences, 6: 155-165.

Nicoletti, P.G. and Sorriso-Valvo, M., 1991. Geomorphic controls of the shape and mobility of rock avalanches. Geological Society of America Bulletin, 103: 1365-1373.

Noetzli, J., Gruber, S., Kohl, T., Salzmann, N. and Haeberli, W., 2007. Three-dimensional distribution and evolution of permafrost temperatures in idealized high-mountain topography. Journal of Geophysical Research, 112(F02S13): 1-14.

Noetzli, J., Hoelzle, M. and Haeberli, W., 2003. Mountain permafrost and recent Alpine rock-fall events: a GIS-based approach to determine critical factors. In: M. Phillips, S. Springman and L. Arenson (Editors), 8th International Conference on Permafrost. Swets & Zeitlinger, Lisse, Zurich, 827-832.

Noetzli, J., Huggel, C., Hoelzle, M. and Haeberli, W., 2006. GIS-based modelling of rock-ice avalanches from Alpine permafrost areas. Computational Geosciences, 10(2): 161-178.

Nosov, K.N., Chernomorets, S.S., Tutubalina, O.V. and Zaporozhchenko, E.V., 2006. Debris flow research in Russia and the former Soviet Union: history and perspectives. WIT Transaction on Ecology and the Environment, 90.

O'Brien, J.S., Julien, P.Y., Fullerton, W.T. and Members, A., 1993. Two-dimensional water flood and mudflow simulation. Journal of Hydraulic Engineering, 119: 244-261.

O'Callaghan, J.F. and Mark, D.M., 1984. The extraction of drainage networks from digital elevation data. Computer Vision, Graphics, and Image Processing, 28(3): 323-344.

O'Connor, J.E. and Costa, J.E., 1993. Geologic and hydrologic hazards in glacierized basins in North America resulting from 19th and 20th century global warming. Natural Hazards, 8(2): 121-140.

Okura, Y., Kitahara, H., Kawanami, A. and Kurokawa, U., 2003. Topography and volume effects on travel distance of surface failure. Engineering Geology, 67(3-4): 243.

Okura, Y., Kitahara, H., Sammori, T. and Kawanami, A., 2000. The effects of rockfall volume on runout distance. Engineering Geology, 58(2): 109.

Oppikofer, T., Jaboyedoff, M. and Keusen, H.-R., 2008. Collapse at the eastern Eiger flank in the Swiss Alps. Nature Geoscience, 1(8).

Palacios, D., Zamorano, J.J. and Parrilla, G., 1998. Proglacial debris flow in Popocatepetl north face and their relation to 1995 eruption. Zeitschrift für Geomorphologie, 42(3): 273-295.

Parsons, J.D., Whipple, K.X. and Simoni, A., 2001. Experimental study of the grain-flow, fluid-mud transition in debris flows. The Journal of Geology, 109(4): 427-447.

Patra, A.K., Bauer, A.C., Nichita, C.C., Pitman, E.B., Sheridan, M.F., Bursik, M., Rupp, B., Webber, A., Stinton, A.J., Namikawa, L.M. and Renschler, C.S., 2005. Parallel adaptive numerical simulation of dry avalanches over natural terrain. Journal of Volcanology and Geothermal Research, 139: 1-21.

Perla, R., Cheng, T.T. and McClung, D.M., 1980. A two-parameter model of snow-avalanche motion. Journal of Glaciology, 26(94): 197-207.

Petrakov, D.A., Chernomorets, S.S., Evans, S.G. and Tutubalina, O.V., 2008. Catastrophic glacial multi-phase mass movements: a special type of glacial hazard. Advances in Geosciences, 14: 211-218.

Pierson, T.C., Janda, R.J., Thouret, J.-C. and Borrero, C.A., 1990. Perturbation and melting of snow and ice by the 13 November 1985 eruption of Nevado del Ruiz, Colombia, and consequent mobilization, flow and deposition of lahars. Journal of Volcanology and Geothermal Research, 41: 17-66.

Pierson, T.C. and Scott, K.M., 1985. Downstream dilution of a lahar: transition from debris flow to hyperconcentrated streamflow. Water Resources Research, 21(10): 1511-1524.

Pirulli, M., Bristeau, M.-O., Mangeney, A. and Scavia, C., 2007. The effect of the earth pressure coefficients on the runout of granular material. Environmental Modelling & Software(22): 1437-1454.

Pirulli, M. and Mangeney, A., 2008. Results of Back-Analysis of the Propagation of Rock Avalanches as a Function of the Assumed Rheology. In: G. Barla (Editor), Rock Mechanics and Rock Engineering. Springer Wien, 59-84.

Pirulli, M. and Sorbino, G., 2008. Assessing potential debris flow runout: a comparison of two simulation models. Natural Hazards and Earth System Sciences, 8: 961-971.

Pitman, E.B., Nichita, C.C., Patra, A., Bauer, A., Sheridan, M.F. and Bursik, M., 2003a. Computing granular avalanches and landslides. Physics of Fluids, 15(12): 3638-3646.

Pitman, E.B., Nichita, C.C., Patra, A.K., Bauer, A.C., Bursik, M. and Webb, A., 2003b. A model of granular flows over an erodible surface. Discrete and Continuous Dynamical Systems-Series B, 3(4): 589-599.

Plafker, G. and Ericksen, G.E., 1978. Nevados Huascarán avalanches, Peru. In: B. Voight (Editor), Rockslides and Avalanches, 1: Natural Phenomena. Elsevier, Amsterdam, 277-314.

Post, A., 1968. Effects on Glaciers, The Great Alaska Earthquake of 1964, Hydrology. National Academy of Sciences, Washington D.C., 266-308.

Pouliquen, O., 1999. Scaling laws in granular flows down rough inclined planes. Physics of Fluids, 11(3): 542-548.

Prager, C., Krainer, K., Seidl, V. and Chwatal, W., 2006. Spatial features of holocene sturzstrom-deposits inferred from subsurface investigations (Fernpass rockslide, Tyrol, Austria). Geo.Alp, 3: 147-166.

Pralong, A. and Funk, M., 2006. On the instability of avalanching glaciers. Journal of Glaciology, 52: 31-48.

Raetzo, H., Lateltin, O., Bollinger, D. and Tripet, J.P., 2002. Hazard assessment in Switzerland - codes for practice for mass movements. Bulletin of Engineering Geology and the Environment, 61(3): 263-268.

Ravanel, L., Allignol, F., Deline, P., Gruber, S. and Ravello, M., 2010. Rock falls in the Mont Blanc Massif in 2007 and 2008. Landslides, 7: 493-501.

Ravanel, L. and Deline, P., 2010. Climate influence on rockfalls in high-Alpine steep rockwalls: The north side of the Aiguilles de Chamonix (Mont Blanc massif) since the end of the 'Little Ice Age'. The Holocene, 21(2): 357-365.

Raymond, M., Wegmann, M. and Funk, M., 2003. Inventar gefährlicher Gletscher in der Schweiz, Laboratory of hydraulics, hydrology and glaciology, Zurich, VAW reports, 182: 368 pp.

Revellino, P., Hungr, O., Guadagno, F.M. and Evans, S.G., 2004. Velocity and runout simulation of destructive debris flows and debris avalanches in pyroclastic deposits, Campania region, Italy. Environmental Geology, 45(3): 295-311.

Rickenmann, D., 1999. Empirical Relationships for Debris Flows. Natural Hazards, 19: 47-77.

Rickenmann, D., 2005. Runout prediction methods. In: M. Jakob and O. Hungr (Editors), Debris-flow hazards and related phenomena. Springer, Berlin Heidelberg, 305-324.

Rickenmann, D., Laigle, D., McArdell, B.W. and Hübl, J., 2006. Comparison of 2D debris-flow simulation models with field events. Computational Geosciences, 10: 241-264.

Rickenmann, D. and Zimmermann, M., 1993. The 1987 debris flows in Switzerland: documentation and analysis. Geomorphology, 8: 175-189.

Ripepe, M., De Angelis, S., Lacanna, G., Poggi, P., Williams, C., Marchetti, E., Delle Donne, D. and Ulivieri, G., 2009. Tracking pyroclastic flows at Soufrière Hills Volcano. EOS, 90(27): 229-230.

Rozman, J., Rožič, A., Budkovič, A. and Budkovič, T., 2004. Rockfall in the southern wall of Punta Thurwieser (Italy) on September 18, 2004. Geologija, 47(2): 221-232.

Sabot, F., Naaim, M., Granada, F., Suriñach, E., Planet, P. and Furdada, G., 1998. Study of avalanche dynamics by seismic methods, image-processing techniques and numerical models. Annals of Glaciology, 26: 319-323.

Sai, P.S.T., Surender, G.D., Damodaran, A.D., Suresh, V., Philip, Z.G. and Sankaran, K., 1990. Residence time distribution and material flow studies in a rotary kiln. Metallurgical and Materials Transactions B, 21(6): 1005-1011.

Salm, B., 1993. Flow, flow transition and runout distances of flowing avalanches. Annals of Glaciology, 18: 221-226.

Salm, B., 2004. A short and personal history of snow avalanche dynamics. Cold Regions Science and Technology, 39(2-3): 83-92.

Sassa, K., 1988. Geotechnical model for the motion of landslides, Proc. 5th International Symposium on Landslides. Balkema, Rotterdam, Lausanne, 37-55.

Savage, S.B., 1984. The mechanics of rapid granular flows. Advances in Applied Mechanics, 24: 289-366.

Savage, S.B. and Hutter, K., 1989. The motion of a finite mass of granular material down a rough incline. Journal of Fluid Mechanics, 199: 177-215.

Scheidegger, A.E., 1973. On the Prediction of the Reach and Velocity of Catastrophic Landslides. Rock Mechanics, 5: 231-236.

Scheidl, C. and Rickenmann, D., 2010. Empirical prediction of debris-flow mobility and deposition on fans. Earth Surface Processes and Landforms, 35: 157-173.

Scheidl, C., Rickenmann, D. and Chiari, M., 2008. The use of airborne LiDAR data for the analysis of debris flow events in Switzerland. Natural Hazards and Earth System Sciences, 8: 1113-1127.

Schneider, D., Bartelt, P., Caplan-Auerbach, J., Christen, M., Huggel, C. and McArdell, B.W., 2010. Insights into rock-ice avalanche dynamics by combined analysis of seismic recordings and a numerical avalanche model. Journal of Geophysical Research, 115(F04026): 1-20.

Schneider, D., Delgado Granados, H., Huggel, C. and Kääb, A., 2008. Assessing lahars from ice-capped volcanoes using ASTER satellite data, the SRTM DTM and two different flow models: case study on Iztaccíhuatl (Central Mexico). Natural Hazards and Earth System Sciences, 8(3): 559-558.

Schneider, D., Huggel, C., Haeberli, W. and Kaitna, R., 2011a. Unraveling driving factors for large rock-ice avalanche mobility. Earth Surface Processes and Landforms, 36(14), 1948-1966.

Schneider, D., Kaitna, R., Dietrich, W.E., Hsu, L., Huggel, C. and McArdell, B.W., 2011b. Frictional behavior of granular gravel-ice mixtures in vertically rotating drum experiments and implications for rock-ice avalanches. Cold Regions Science and Technology, 69(1), 70-90.

Schneider, J.F., 2006. Risk assessment of remote geohazards in Western Pamir, GBAO, Tajikistan. In: W. Haeberli et al. (Editors), Proceedings of the International Conference on High Mountain Hazard Prevention, Vladikavkaz/Moscow, 252-267.

Sepúlveda, N., Krstulovic, G. and Rica, S., 2005. Scaling laws in granular continuous avalanches in a rotating drum. Physica A, 356: 178-183.

Sheridan, M.F., Stinton, A.J., Patra, A., Pitman, E.B., Bauer, A. and Nichita, C.C., 2005. Evaluating Titan2D mass-flow model using the 1963 Little Tahoma Peak avalanches, Mount Rainier, Washington. Journal of Volcanology and Geothermal Research, 139(1-2): 89-102.

Shreve, R.L., 1966. Sherman Landslide, Alaska. Science, 154(3757): 1639-1643.

Shreve, R.L., 1968. Leakage and fluidization in air-layer lubricated avalanches. Geological Society of America Bulletin, 79: 653-658.

Sosio, R., Crosta, G.B. and Hungr, O., 2008. Complete dynamic modeling calibration for the Thurwieser rock avalanche (Italian Central Alps). Engineering Geology, 100: 11-26.

Soukhovitskaya, V. and Manga, M., 2006. Martian landslides in Valles Marineris: Wet or dry? Icarus, 180(2): 348-352.

Stead, D., Eberhardt, E. and Coggan, J.S., 2006. Developments in the characterization of complex rock slope deformation and failure using numerical modelling techniques. Engineering Geology, 83(1-3): 217-235.

Stolz, A. and Huggel, C., 2008. Debris flows in the Swiss National Park: the influence of different flow models and varying DEM grid size on modeling results. Landslides, 5(3): 311-319.

Straub, S., 1997. Predictability of long runout landslide motion: implications from granular flow mechanics. Geologische Rundschau, 86(2): 415-425.

Suriñach, E., Furdada, G., Sabot, F., Biescas, B. and Vilaplana, J.M., 2001. On the characterization of seismic signals generated by snow avalanches for monitoring purposes. Annals of Glaciology, 32: 268-274.

Suriñach, E., Sabot, F., Furdada, G. and Vilaplana, J.M., 2000. Study of seismic signals of artificially released snow avalanches for monitoring purposes. Phys. Chem. Earth, 25(9): 721-727.

Suriñach, E., Vilajosana, I., Khazaradze, G., Biescas, B., Furdada, G. and Vilaplana, J.M., 2005. Seismic detection and characterization of landslides and other mass movements. Natural Hazards and Earth System Sciences, 5(6): 791-798.

Taboada, A. and Estrada, N., 2009. Rock-and-soil avalanches: Theory and simulation. Journal of Geophysical Research, 114(F03004): 1-23.

Tang, C., Zhu, J., Chang, M., Ding, J. and Qi, X., 2011. An empirical-statistical model for predicting debris-flow runout zones in the Wenchuan earthquake area. Quaternary International, In Press, Corrected Proof: 1-11.

Thouret, J.C., Ramírez, J., Gibert-Malengrau, B., Vargas, C.A., Naranjo, J.L., Vandemeulebrouck, J., Valla, F. and Funk, M., 2007. Volcano-glacier interactions on composite cones and lahar generation: Nevado del Ruiz, Colombia, case study. Annals of Glaciology, 45: 115-127.

Vallance, J.W., 2000. Lahars. In: H. Sugurdsson (Editor), Encyclopedia of Volcanoes. Academic Press, 601-616.

Van Der Woerd, J., Owen, L.A., Tapponnier, P., Xiwei, X., Kervyn, F., Finkel, R.C. and Barnard, P.L., 2004. Giant, ~M8 earthquake-triggered ice avalanches in the eastern Kunlun Shan, northern Tibet: characteristics, nature and dynamics. GSA Bulletin, 116(3/4): 394-406.

Van Gassen, W. and Cruden, D.M., 1989. Momentum transfer and friction in the debris of rock avalanches. Canadian Geotechniqual Journal, 26: 623-628.

van Westen, C.J., van Asch, T.W.J. and Soeters, R., 2006. Landslide hazard and risk zonation—why is it still so difficult? Bulletin of Engineering Geology and the Environment, 65(2): 167-184.

Varnes, D.J., 1978. Slope movement types and processes. Landslides, Analysis and Control, Special Report 176, Transportation Research Board, National Academy of Sciences, Washington, DC: 11-33.

Verstappen, H.T., 1992. Volcanic hazards in Colombia and Indonesia: lahars and related phenomena. In: G.J.H. McCall, D.J.C. Laming and S.C. Scott (Editors), Geohazards - Natural and man-made. Chapman & Hall, 33-42.

Vilajosana, I., Suriñach, E., Khazaradze, G. and Gauer, P., 2007. Snow avalanche energy estimation from seismic signal analysis. Cold Regions Science and Technology, 50(1-3): 72-85.

Voellmy, A., 1955. Über die Zerstörungskraft von Lawinen. Schweizerische Bauzeitung, 73(15): 212-217.

Voight, B. and Sousa, J., 1994. Lessons from Ontake-san: A comparative analysis of debris avalanche dynamics. Engineering Geology, 38: 261-297.

Volgger, C., 2007. Numerische Simulation zum Fliessverhalten von Muren: Studie in einer vertikal rotierenden Trommel. Diploma Thesis Thesis, Leopold-Franzens-Universitaet Innsbruck, Innsbruck, 85 pp.

Waythomas, C.F. and Wallace, K.L., 2002. Flank collapse at Mount Wrangell, Alaska, recorded by volcanic mass-flow deposits in the Copper River lowland. Canadian Journal of Earth Sciences, 39(8): 1257-1279.

Weichert, D., Horner, R.B. and Evans, S.G., 1994. Seismic signatures of landslides: the 1990 Brenda mine collapse and the 1965 Hope rockslides. Bulletin of the Seismological Society of America, 84(5): 1523-1532.

Weidinger, J.T. and Korup, O., 2009. Frictionite as evidence for a large Late Quaternary rockslide near Kanchenjunga, Sikkim Himalayas, India -- Implications for extreme events in mountain relief destruction. Geomorphology, 103(1): 57-65.

Williams, G.P., 1970. Manning Formula—a misnomer? Journal of the Hydraulics Division, 96(1): 193-200.

Worni, R., Huggel, C., Stoffel, M. and Pulgarín, B., submitted. Challenges of modeling current very large lahars at Nevado del Huila Volcano, Colombia. Bulletin of Volcanology.

# 7 Personal Bibliography

## 7.1 Peer reviewed publications

Korup, O., Schneider, D., Huggel, C. and Dufresne, A. (in press): Long-runout landslides. In: Treatise on Geomorphology, edited by Shroder, J., Jr., Marston, R. and Stoffel M., Academic Press, San Diego, CA, 7, doi:10.1016/B978-0-08-088523-0.00164-7.

Schneider, D., Huggel, C., Haeberli, W. and Kaitna, R. (2011): Unraveling driving factors for large rock-ice avalanche mobility. Earth Surface Processes and Landforms, 36(14), 1948-1966.

Schneider, D., Kaitna, R., Dietrich, W. E., Hsu, L., Huggel, C. and McArdell, B. W. (2011): Frictional behavior of granular gravel-ice mixtures in vertically rotating drum experiments and implications for rock-ice avalanches. Cold Regions Sciences and Technology, 69(1), 70-90.

Schneider, D., Bartelt, P., Caplan-Auerbach, J., Christen, M., Huggel, C. and McArdell, B. W. (2010): Insights into rock-ice avalanche dynamics by combined analysis of seismic recordings and a numerical avalanche model. Journal of Geophysical Research, 115(F04026): 1-20.

Huggel, C., Fischer, L., Schneider, D. and Haeberli, W. (2010): Research advances on climate-induced slope instability in glacier and permafrost high-mountain environments, Geographica Helvetica, 65(2): 146-156.

Huggel, C., Salzmann, N., Allen, S., Caplan-Auerbach, J., Fischer, L., Haeberli, W., Larsen, C., Schneider, D. and Wessels, R. (2010): Recent and future warm extreme events and high-mountain slope stability, Philosophical Transactions of the Royal Society A, 368: 2435-2459.

Allen, S., Schneider, D. and Owens, I. F. (2009): First approaches towards modelling glacial hazards in the Mount Cook region of New Zealand's Southern Alps. Natural Hazards and Earth System Sciences, 9(2): 481-499.

Huggel, C., Schneider, D., Julio, P., Delgado, H. and Kääb, A. (2008): Evaluation of ASTER and SRTM DEM data for lahar modeling: a case study on lahars from Popocatépetl Volcano, Mexico. Journal of Volcanology and Geothermal Research, 170: 99-110.

Schneider, D., Delgado Granados, H., Huggel, C. and Kääb, A. (2008): Assessing lahars from ice-capped volcanoes using ASTER satellite data, the SRTM DTM and two different flow models: case study on Iztaccíhuatl (Central Mexico). Natural Hazards and Earth System Sciences, 8(3): 559-558.

Kääb, A., Huggel, C., Fischer, L., Guex, S., Paul, F., Roer, I., Salzmann, N., Schlaefli, S., Schmutz, K., Schneider, D., Strozzi, T. and Weidmann, Y. (2005): Remote sensing of glacier- and permafrost-related hazards in high mountains: an overview. Natural Hazards and Earth System Sciences, 5: 527-554.

## 7.2 Conference proceedings and other publications

Schneider J. F., Mergili, M., Amon, H. Bauer, T., Gruber, F., Kleinbauer, I., Kopf, C., Mühlböck, F., Müllebner, B., Straka, W., Andres, N., Schneider, D., Worni, R., Ishuk, A., Ishuk, N., Saidulloyev, U., Homidov, A., Pirov, A., Shodmonov, M., Tagoybekov, A., Karimov, F., Nazarkhudoev, F., Shobekov, S. and Samiev, M. (2010): Remote geohazards in high mountain areas of Tajikistan. Assessment of hazards connected to lake outburst floods and large landslide dams in selected areas of the Pamir and Alai mountains. Final report, IAG-BOKU, Vienna, 342 pp.

Mergili, M., Schneider, D., Worni, R. and Schneider, J. F. (2011): Glacial lake outburst floods in the Pamir of Tajikistan: challenges in prediction and modelling. *Conference Proceedings of the 5th International Conference on Debris-Flow Hazards Mitigation: Mechanics, Prediction and Assessment*, University of Padova, Italy, June 14-17, 2011, 973-982.

Huggel, C., Fischer, L. and Schneider, D. (2008): Gletscher- und Permafrost-Naturgefahren in der Perspektive sich ändernder Umweltbedingungen. Fachsektionen Ingenieurgeologie D, A & CH. Sonderheft zur 18. Bodenseetagung, Allensbach, October 17-18, 2008, 66: 39-40.

Kääb, A., Huggel, C., Guex, S., Paul, F., Salzmann, N., Schmutz, K., Schneider, D. and Weidmann, Y. (2005): Glacier hazard assessment in mountains using satellite optical data. EARSeL eProceedings: 79-93.

Schneider, D. (2005): Modeling of lahar hazard potentials on glacier covered volcanoes: Iztaccíhuatl, Mexico. Diploma thesis, University of Zurich-Irchel, Zurich, 92 pp.

## 7.3 Conference contributions (first author only)

Schneider, D., Caplan-Auerbach, J., Huggel, C. and Bartelt, P. (November 11, 2009): Iliamna Volcano (Alaska): a field laboratory for large rock-ice avalanche modelling. International workshop: Glacier hazards, permafrost hazards and GLOFs in mountain areas: processes, assessment, prevention, mitigation, Vienna, Austria, November 10-13, 2009. Poster presentation.

Schneider, D. (April 20, 2009): Rock-ice avalanches and the effects of ice on the mobility. Monday Geomorphology Seminar, Department for Earth & Planetary Science, Berkeley. Oral presentation.

Schneider, D. (October 14, 2008): Fels-/Eislawinen: Beispiele und Modellierungen. Invited talk. BOKU-IAN Institut für Alpine Naturgefahren. Oral presentation.

Schneider, D. (November 14, 2008): (Rock-ice) avalanche modelling with RAMMS model. GriaAlp workshop: measuring and modelling instability factors of permafrost-affected bedrock, Zurich, Switzerland, November 13-14, 2008. Oral presentation.

Schneider, D., Huggel, C., Caplan-Auerbach, J. and Bartelt, P. (September 24, 2008): Using seismic data to validate numeric simulation of large rock-ice avalanches. International conference debris flows: disaster, risk, forecast, protection, Pyatigorsk, Russia, September 22-28, 2008. Oral presentation.

Schneider, D., Huggel, C., Caplan-Auerbach, J., Waythomas, C., Wessels, R., Bartelt, P. and McArdell, B.W. (August 18, 2008): Dynamic modelling of large rock-ice avalanches from active volcanoes: case study at Iliamna volcano, Alaska. IAVCEI general assembly, Reykjavik, Iceland, August 18-22, 2008. Oral presentation.

Schneider, D., Allen, S., Christen, M., Huggel, C., McArdell, B.W. and Bartelt, P. (April 17, 2008): Application of the RAMMS model to recent and potential rock-ice avalanches in the Mount Cook region (New Zealand). European Geoscience Union, General Assembly 2008, Vienna, Austria, April 14-18, 2008. Oral presentation.

Schneider, D., Huggel, C., McArdell, B.W., Bartelt, P. and Haeberli, W. (August 28, 2007): The influence of ice on the mobility of rapid rock-ice mass movements: a concept for systematic research. 6th International NCCR Climate Summer School, Land Surface – Atmosphere Interactions in a Changing Climate, Grindelwald, Switzerland, August 26-31, 2007. Poster presentation.

Schneider, D., Huggel, C., McArdell, B.W., Bartelt, P. and Haeberli, W. (April 17, 2007): The influence of ice on the mobility of rapid rock-ice mass movements: a concept for systematic research. European Geoscience Union, General Assembly 2007, Vienna, Austria, April 16-20, 2007. Poster presentation.

Schneider, D., Delgado Granados, H., Huggel, C. and Kääb, A. (June 21, 2006): Modeling and assessing lahar hazards under a rapid glacier-melting scenario at Iztaccíhuatl volcano (Central Mexico). International Glaciological Society, Volcano-ice interactions, Reykjavík, Iceland, June 19-23, 2006. Oral presentation.

Schneider, D., Delgado Granados, H., Huggel, C. and Kääb, A. (April 3, 2006): Modeling potential laharic hazards related to ice-melting in case of unrest of Iztaccíhuatl volcano (Central Mexico). European Geoscience Union, General Assembly 2006, Vienna, Austria, April 2-7, 2006. Oral presentation.

# 8 Acknowledgments

I have experienced many unforgettable moments on the way of my PhD and was accompanied by many people at very different sites, nearly all around the world. My greatest thanks go to Wilfried Haeberli who gave me the opportunity to work on a highly interesting topic in a very interdisciplinary field. His enthusiasm was a main reason that I found the way to Physical Geography and he significantly formed and widened my view in geoscience.

Very special thanks go to Christian Huggel who supervised my thesis on the entire journey. We had many discussions which strongly influenced and contributed to the current work. He always kept the overview and helped to redirect me when I started to get lost in details. His positive attitudes were strongly motivating many times.

Brian McArdell gave me the opportunity to work at WSL during the early stage of the PhD and was a very helpful supervisor for many aspects and particularly for the laboratory experiments. He also established the contact to Berkeley and I'm very grateful for all his contributions.

Perry Bartelt supported me as a supervisor and strongly helped during the work with the RAMMS model. I highly acknowledge the interesting discussions about avalanche dynamics and the feedbacks to papers and conference contributions.

The basis for the work was already laid during my diploma thesis in Mexico, where I had the opportunity to climb Central America's highest peak Pico de Orizaba and the somewhat lower Iztaccíhuatl volcano. Therefore, I would like to thank Andi Kääb, Hugo Delgado, Patricia Julio-Miranda and Eduardo Rubio-Herrera, Helios Rodriguez for having strongly supported my work and let me have a great time in Mexico. Conferences brought me twice to Iceland where I could admire the active geology and extraordinary co-existence of fire and ice for a few days. Another conference in the Russian Caucasus was followed by an impressive trip via the Baksan river valley to Mt. Elbrus. The devastating power of glacial debris flows has been strikingly demonstrated at the debris-flow barrier above the city of Tyrnyauz which has been destroyed in 1999 and 2000, and a proglacial lake which is prone for outburst was visited on a side trip to Bashkara glacier. Many thanks go to Sergey Chernomorets, Olga Tutubalina and Dmitri Petrakov for their great organization and hospitality.

Various stays in Vienna – for conferences and mainly for the rotating drum experiments – gave me the opportunity to become acquainted with that beautiful city and I met a lot of very nice persons. My greatest thanks are indebted to Roland Kaitna, who gave me the opportunity

to work with the rotating drum. He invested a tremendous amount of time in explaining me details about the sensor system and thinking about many issues. We had many intensive and interesting discussions in the office or while having a beer, and temporally established a 'Skype-Hotline' between Zurich and Vienna to work on specific problems. The great joint time in Berkeley was supplemented by several short trips to the surroundings of Berkeley and especially by the crazy 18-hour-non-stop-drive within a field trip to the Henry Mountains region in Utah to assist river geomorphology colleagues from Berkeley in field work.

Many thanks go to Fritz Zott who helped me many times when devices and sensors needed to be installed in the rotating drum in Vienna or when other technical problems arose. Johannes Hübl is acknowledged to enable me staying at the Institute of Mountain Risk Engineering at the BOKU-University in Vienna. I thank all colleagues of the group in Vienna for the very friendly hospitality; the working atmosphere was just great! I especially thank Christian Scheidl and Michael Chiari for the many moments we shared in- and outside the University. Dieter Rickenmann is also acknowledged for his support to work with the rotating drum and for the interesting discussions.

I thank Jean Schneider, Martin Mergili, Wolfgang Straka, Raphael Worni, Norina Andres and all other students from the Institute of Applied Geology for the good collaboration within the 'TajHaz'-project and the nice excursion to the Aosta Valley in Italy. The study on Glacial Lake Outburst Floods (GLOFs) in Tajikistan was an interesting task where I could well extend my experience in natural hazards from glacial environments.

The months in the United States have been extremely intensive and I'll never forget this time. My deepest gratitude goes to Bill Dietrich and Leslie Hsu. They enabled me to stay in Berkeley, California, and to use their extraordinarily large rotating drum at the Richmond Field Station and supported my work in many aspects. Leslie introduced me to work in the lab and helped a lot with data process and Matlab codes. Bill invested a lot of time to listen and answer my questions and gave important inputs for the laboratory experiments. His enthusiasm about geomorphologic processes was highly infectious. I would further like to thank Stuart Foster who helped a lot in the laboratory. Without his aid I would not have been able to perform all the experiments within the short time of three months. Many thanks go also to Leonard Sklar from the San Francisco State University (SFSU) whose cold room I could use and who gave me the unique chance to join field work in Utah where we had a great time and many scientific and non-scientific discussions.

Besides work, I had the chance to join the UCB Windsurf Club where I met a lot of nice people across all scientific disciplines. Many great rides in the fresh breeze from the Pacific Ocean and in front of the Golden Gate Bridge gave me new power in the evenings after having sieved and shuvelled tons of gravel and performed experiments. Thanks go also to Megan and Mike Kirkwood for their great hospitality and to my housemate Konrad Linnemann.

Very special thanks go to Jackie Caplan-Auerbach, her husband Mike and their two children who warmly included me in their family during my two-week stay in Bellingham, Washington (USA). Jackie gave me the possibility to work at the Western Washington University in

Bellingham and provided strong support in handling and interpreting seismic data. This was an aspect of the work that fascinated me exceedingly and I highly appreciate Jackie's engagement.

I wish to express the most special thanks to Marc Christen who helped me extensively with technical issues related to the RAMMS model and spent hours to adapt the model code to special desires from my side. Julia Kowalski is deeply acknowledged for her support in mathematical and physical questions. Moreover many thanks go to all colleagues within the 'Avalanches, Debris Flows and Rockfall' and 'Mountain Hydrology and Torrents' groups at WSL.

Many other people provided material or contributed in fruitful discussions. I'd like to specifically thank Oliver Korup, Steve Evans, Chris Waythomas, Bruce Molnia, Ian Owens, Igor Galushkin and Michael Krautblatter.

Very helpful discussions concerning the use of seismic data also arose through intensive e-mail discussions with Mauri McSaveney. He strongly improved my comprehension of landslide seismology and I'd like to sincerely acknowledge his contributions to **Paper IV**. Tim Davies and Philip Deline are acknowledged for providing external reviews of this work.

Many thanks go to my colleagues in the 3G-group at my home-base in Zurich. Despite my many travels, this was where I always felt home. Scientific and non-scientific discussions during coffee breaks supported me on the way during this work, even though my breaks got shorter towards the end of the thesis. I'd like to express my special gratitude to my great officemates Luzia Fischer, Andreas Linsbauer, Lorenz Böckli, Joel Fiddes, and for a while Simon Allen. The working atmosphere in H68 and in general at the Institute was always highly enjoyable! Further thanks go to Lisbeth Nietlisbach and Helene Grüter for their support of administrative work.

The warmest thanks are addressed to Barbara, my parents Jean and Ines, and to my brother Linus. They all supported me strongly during good and sometimes quite though times. They gave me the necessary strength for heading forward and to keep balance between science and social life. At this point I'd also like to mention all my long lasting friends in Baden and at other places in Switzerland.

The major part of the work was supported by the Swiss National Foundation grant NF 200021-121823/1 (Rock-ice avalanches: a systematic investigation of the influence of ice) and a part of the time was financed through University-internal funds. During 2009/2010, the PhD thesis was accompanied by the 'TajHaz'-project in cooperation with the Institute of Applied Geology from the BOKU-University. Funding of that project was through the FOCUS Humanitarian Assistance, an affiliate of the Aga Khan Development Network, by the Swiss Agency for Development and Cooperation (SDC), and the British Department for International Development (DFID).

# 9 Appendix

## 9.1 Details of laboratory experiments

Laboratory experiments with gravel-ice mixtures in vertically rotating drums have been started at the *Institute of Mountain Risk Engineering of the University of Natural Resources and Applied Life Sciences (BOKU)* in Vienna, Austria, between September and November 2008 (**Figure 9**). Different ice types (ice-shards, cubes and granular ice), gravel grain sizes and grain size distributions have been tested. From April to June 2009, gravel-ice avalanche experiments have been performed with the larger vertically rotating drum at the Richmond field station of the *Department of Earth and Planetary Science of the University of California, Berkeley (UCB)*, USA. Finally, a complete serie with gradual steps of 10% ice by volume has been prepared in November 2009, and completed in January/February 2010 again in the smaller drum in Vienna. This second series in Vienna was directly scaled from the Berkeley experiments to hold as many parameters as possible comparable.

**Table 2** provides an overview of the 25 experiments that have been performed with varying ice contents and grain sizes. Further details about the laboratory experiments can be found in **Paper V**. Preliminary test runs from the Vienna-drum are not included here.

**Table 2:** Overview of performed experiments and some characteristics of the used gravel and velocities in the smaller and larger drums.

| grain size $D_{50}$ [mm] | rot. veloc. $u_{drum}$ [m/s] | lithology | shape | ice content [vol-%] | | | | | | | | | | |
|---|---|---|---|---|---|---|---|---|---|---|---|---|---|---|
| | | | | 0 | 10 | 20 | 30 | 40 | 50 | 60 | 70 | 80 | 90 | 100 |
| **Smaller drum (Vienna)** | | | | | | | | | | | | | | |
| **9.1** | ~1.64 | quartz | ■ | V09-000 | V08-010 | V06-020 | V05-030 | V02-040 | V01-050<br>V10-050 | V03-060 | V04-070 | V07-080 | V11-090 | V12-100 |
| **Larger drum (Berkeley)** | | | | | | | | | | | | | | |
| **6** | ~2.09 | basalt | ■ | | B04-010 | | B02-030 | | B01-050 | | B03-070 | | B05-090 | |
| **5.6** | ~2.09 | basalt | ● | | | | | B07-040 | B06-050 | B08-060 | | | | |
| **16** | ~2.09 | d. bas. | ■ | | | | | B11-040 | B09-050 | B10-060 | B12-070 | | | |
| **16** | ~1.27 | d.bas. | ■ | | | | | | B13-050 | | | | | |

d. bas. = dacitic basalt; ■ = angular gravel; ● = rounded gravel; 'V' in labeling relates to 'Vienna' and 'B' to 'Berkeley'; experiments are numbered chronologically, followed by a second number relating to the ice content in percents by volume.

## 9.2 Plots from the Vienna-drum experiments

The following figures present all measurements during every experimental run. The smaller drum in Vienna included flow height (laser), normal and shear stress sensors (force plates) as main measurement devices. The individual measurements are enclosed in subplots (a), (c) and (e) while the corresponding standard deviations are plotted on the right side in subplots (b), (d) and (f). Each line in every graph represents an average profile of one minute. All points that were recorded during that minute were binned at steps of one angular degree.The black lines correspond to the first minute that is followed by the next minute with increasing color values (full-tone colors consequently correspond to the last minute of the experiment).

The local basal friction profiles in (g) were calculated by the ratios of shear to normal stresses for each angular degree and minute and the apparent local bulk density profiles in (i) by the ratio of the flow height to the normal stress. It is called 'apparent' because the the normal stress measurements (and shear stress) are affected by centripetal acceleration from grains that are moving on curved paths along the drum bottom. The maximum possible centripetal acceleration at the used velocity is 2.19 m/s$^2$ or 22% of the earth's gravitational acceleration. As simply a fraction of the grains moves at the full drum velocity, the bulk densities might be only slightly overestimated due to the higher normal stresses (see details in **Paper V**).

Temperature measurements were performed by 1-4 freely moving in-flow temperature loggers (h) and by two thermocouples (k): one recording the laboratory temperature and one dipping statically into the flow to measure the in-flow temperature. While the cube loggers were freezed to -10°C with the ice and gravel before each experiment, the thermocouples were fixed in the laboratory at room temperatures. When the warmer needle of the thermocouple dipped into the icy mass, some melt water might have formed around the needle. This was likely the reason that the thermocouple measured 0°C-temperatures as long there was ice present. The following temperature increase was used as an indicator that all ice has melted, and the experiment was generally stopped when the temperature rised to ~3°C. As a consequence, experiments with low ice contents are shorter. However, the runs with very high ice contents (90 and 100% by volume) have shown flow instabilities such as stick-slip effects after a few minutes and therefore were stopped earlier.

Each run was started by a total volume of 0.0856 m$^3$ (note that the bulk volumes were only calculated for the ice- and gravel-fractions separately and not as mixtures). In contrast, back-calculated values indicated volumes around 0.1000 m$^3$ at the beginning of each experiment (**Table 3** and **4**) that might be related to dilatation effects from agitated grains. All runs but the one without ice were affected by volume losses during time. This was because the ice melted and was absorbed within the pore spaces of the gravel. However, as some water drained continuously from the smaller drum in Vienna, the runs with higher ice contents (respectively water when melted) exhibited not only strong volume reductions but also significant mass losses for longer running times (e.g. **Figure 21** to **Figure 23** and **Table 3** and **4**). Therefore, only the first 5 minutes when mass loss was irrelevant were included in the analysis of the friction coefficient in **Paper V**.

## Run V09-000 (0 vol-% ice):

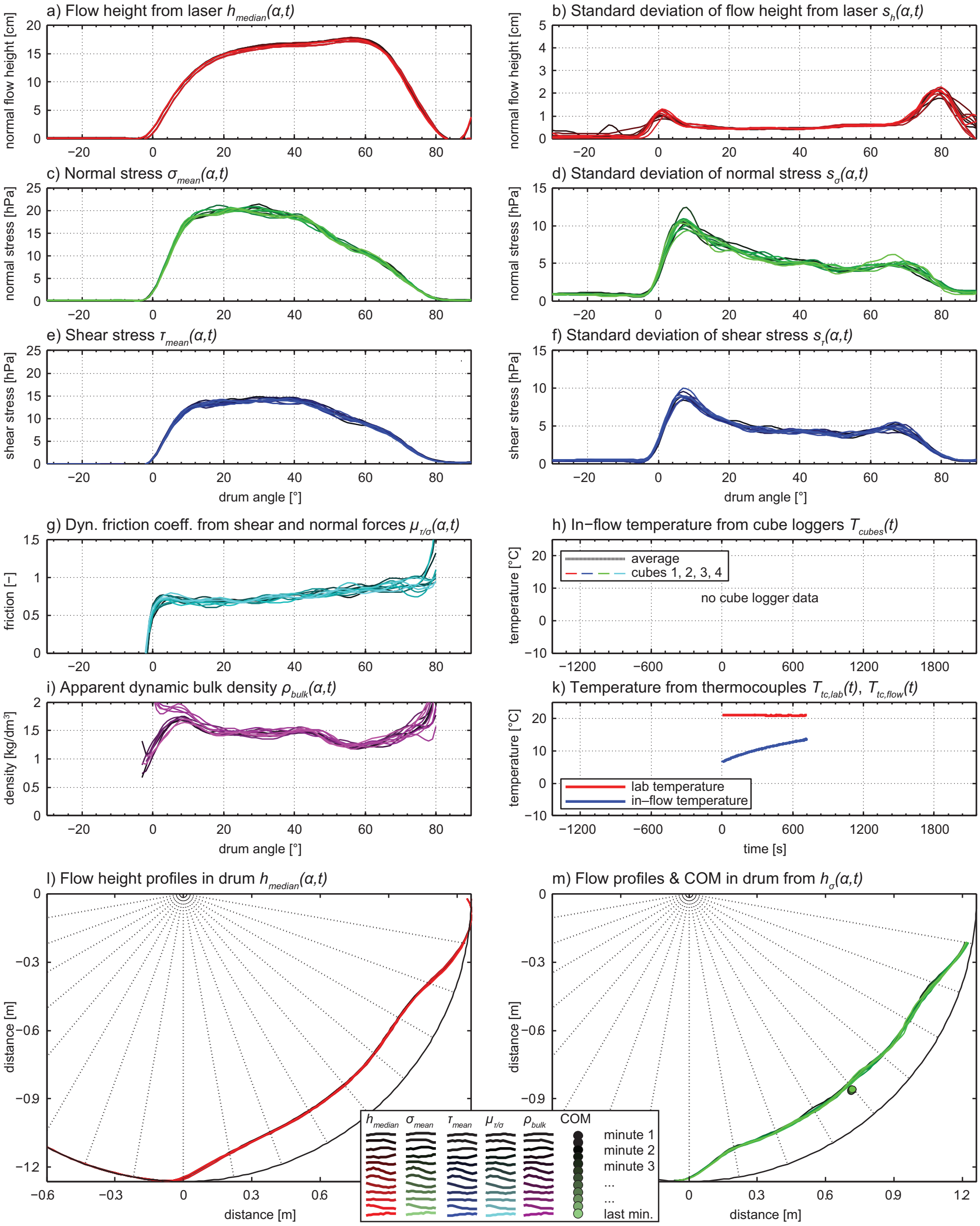

**Figure 14:** Vienna-experiment V09-000. The gravel of the pure gravel run was not specifically cooled before the run and cube logger measurements were abandoned. The run was held short (12 minutes) because no significant changes were expected due to the absence of ice and water and unnecessary wear of the drum surface roughness should be avoided.

## Run V08-010 (10 vol-% ice):

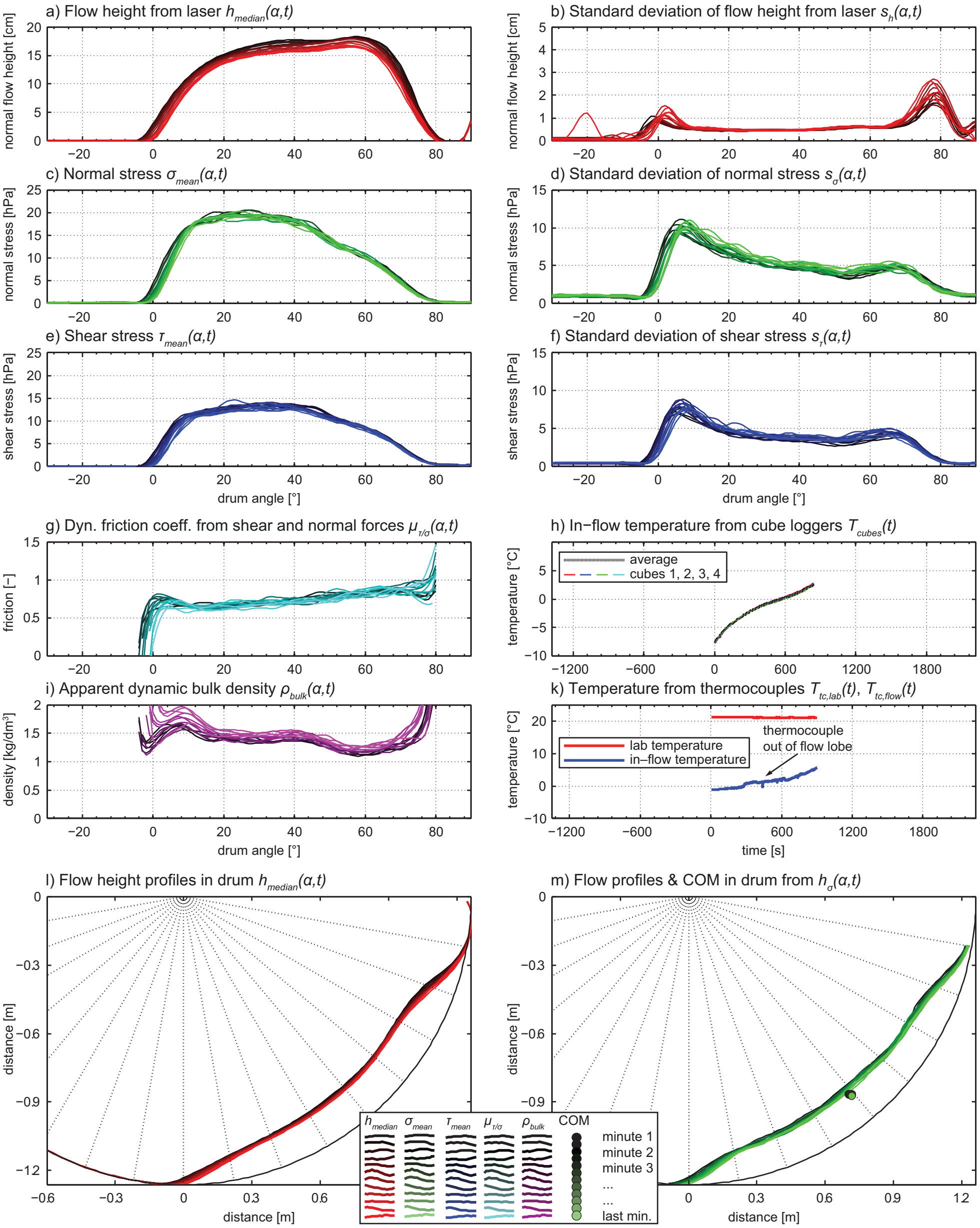

**Figure 15:** Vienna-experiment V08-010. All ice has melted within less than the 15 minutes of the experiment.

## Run V06-020 (20 vol-% ice):

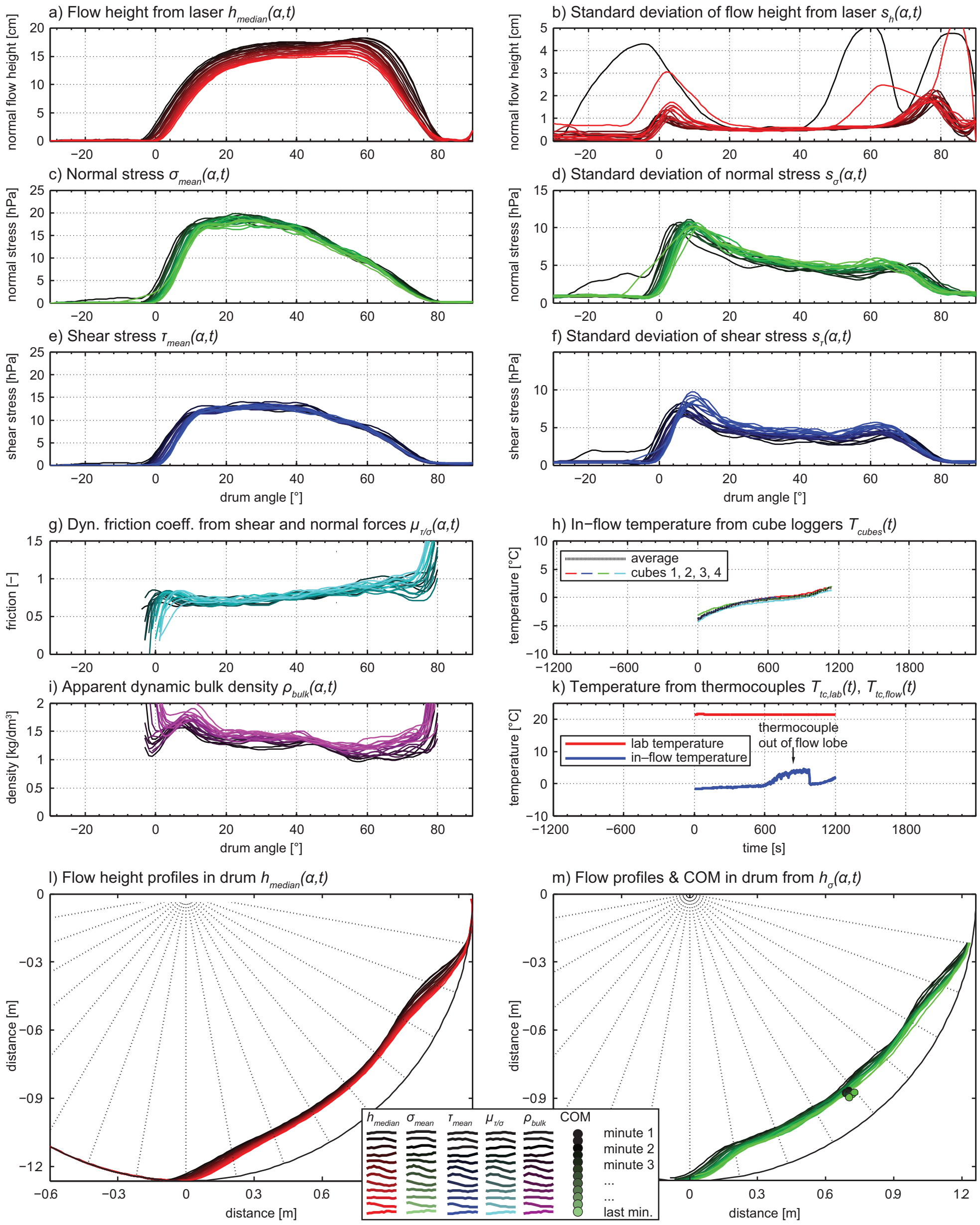

a) Flow height from laser $h_{median}(\alpha,t)$

b) Standard deviation of flow height from laser $s_h(\alpha,t)$

c) Normal stress $\sigma_{mean}(\alpha,t)$

d) Standard deviation of normal stress $s_\sigma(\alpha,t)$

e) Shear stress $\tau_{mean}(\alpha,t)$

f) Standard deviation of shear stress $s_\tau(\alpha,t)$

g) Dyn. friction coeff. from shear and normal forces $\mu_{\tau/\sigma}(\alpha,t)$

h) In–flow temperature from cube loggers $T_{cubes}(t)$

i) Apparent dynamic bulk density $\rho_{bulk}(\alpha,t)$

k) Temperature from thermocouples $T_{tc,lab}(t)$, $T_{tc,flow}(t)$

l) Flow height profiles in drum $h_{median}(\alpha,t)$

m) Flow profiles & COM in drum from $h_\sigma(\alpha,t)$

**Figure 16:** Vienna-experiment V06-020. Note that in subfigure (k) the thermocouple was temporally not dipped into the moving mass (at time 600 s to 900 s).

## Run V05-030 (30 vol-% ice):

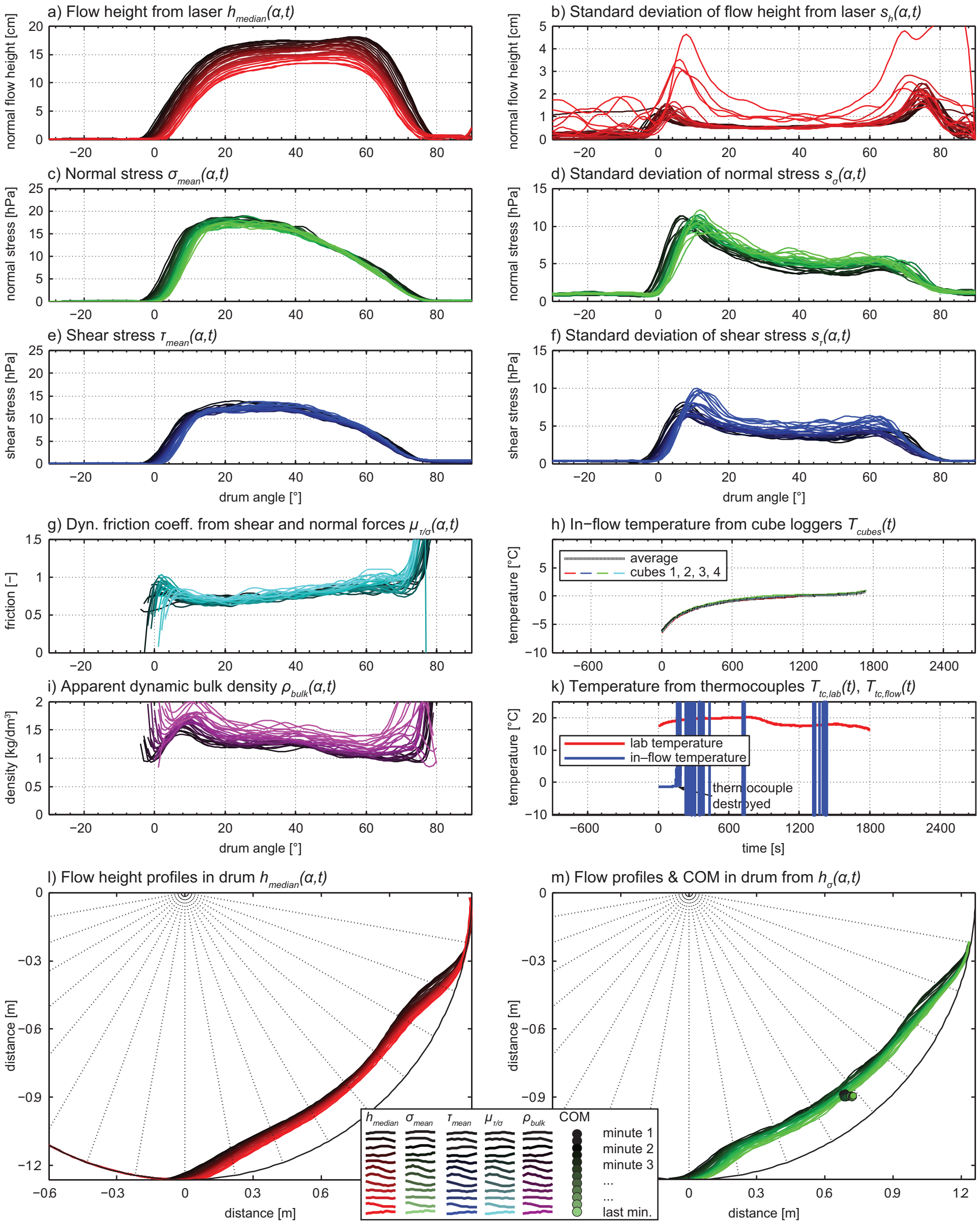

**Figure 17:** Vienna-experiment V05-030. Note that in subfigure (k) the thermocouple was destroyed due to abrasion of the measurement needle.

## Run V02-040 (40 vol-% ice):

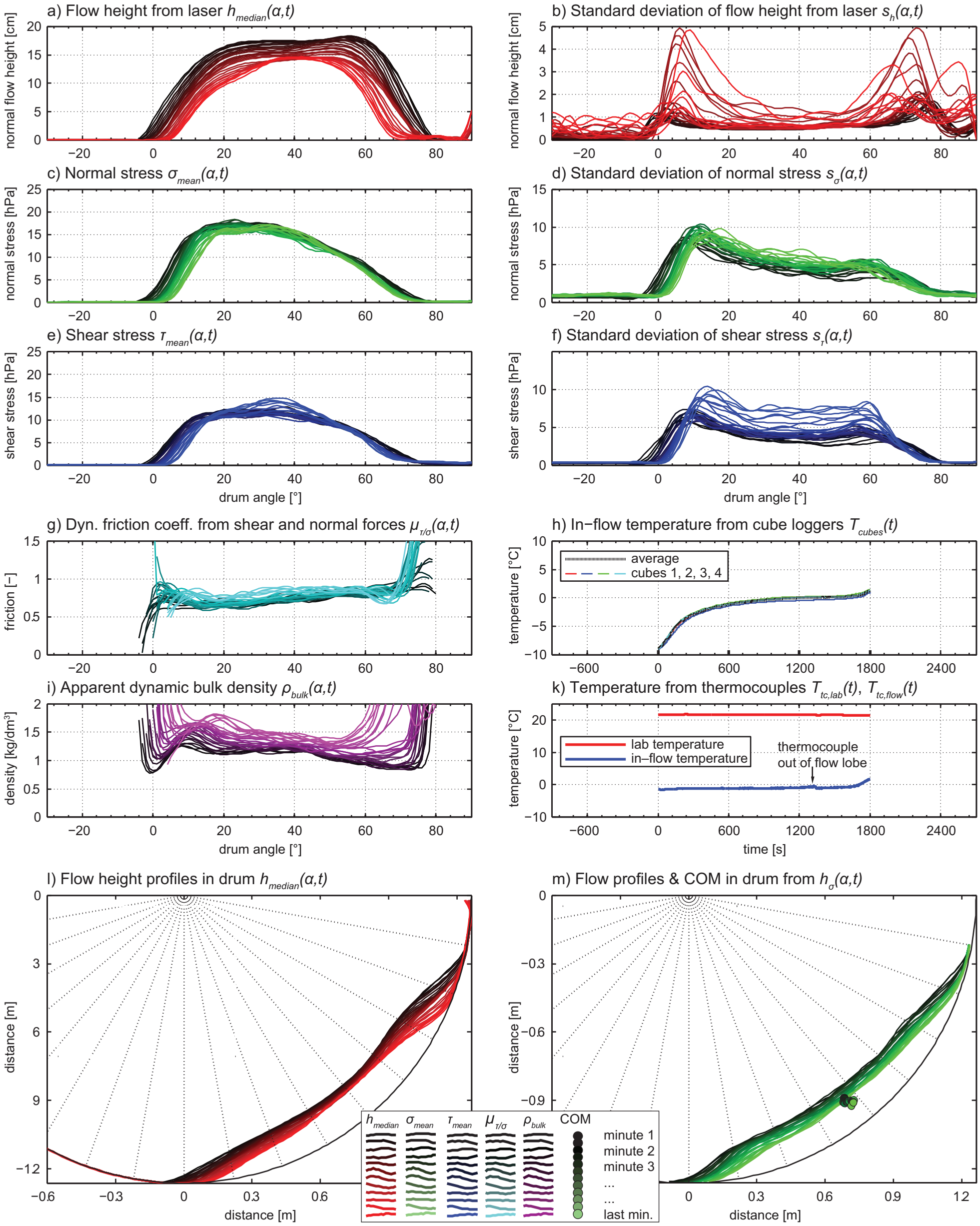

**Figure 18:** Vienna-experiment V02-040.

## Run V01-050 (50 vol-% ice):

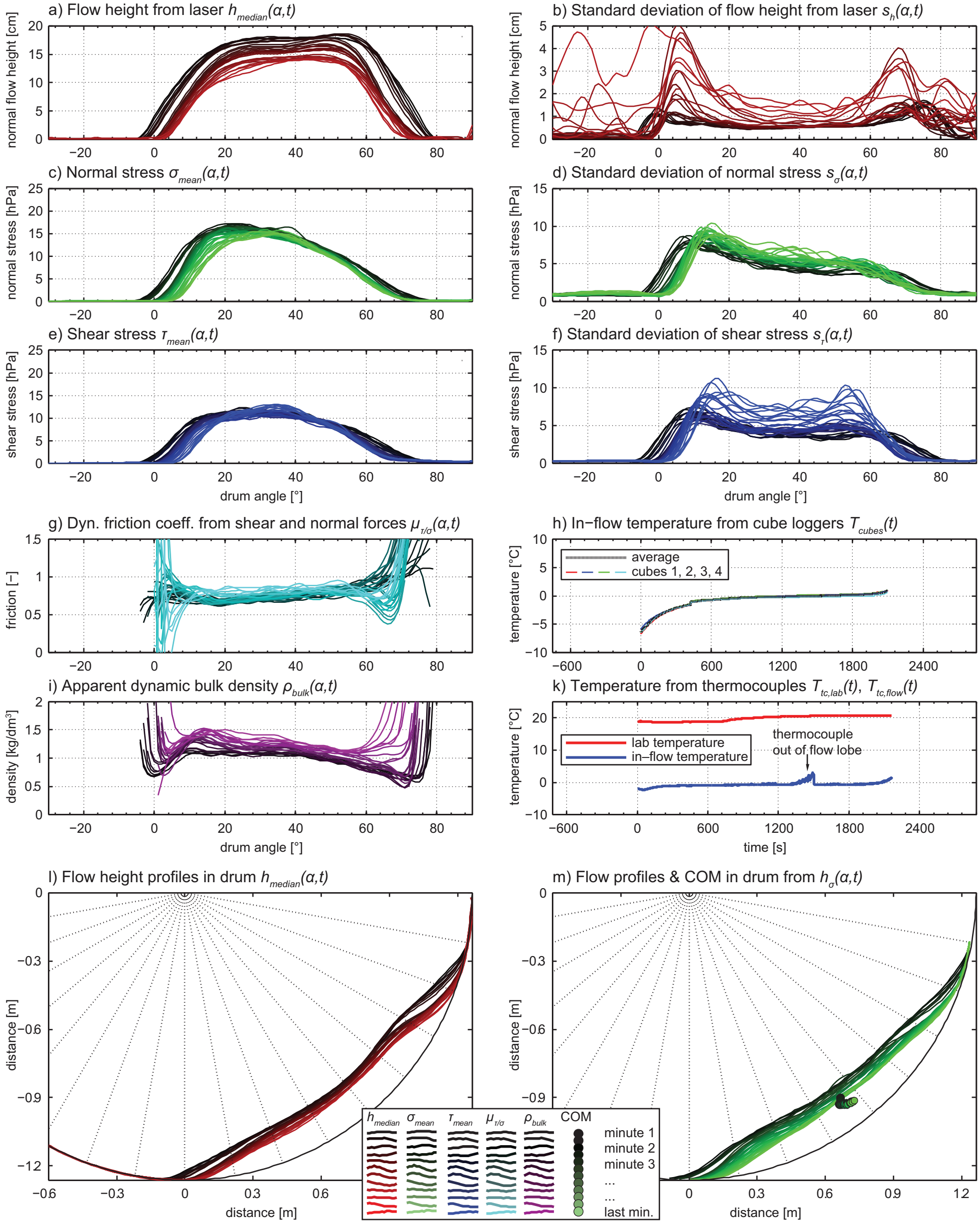

**Figure 19:** Vienna-experiment V01-050.

## Run V10-050 (50 vol-% ice):

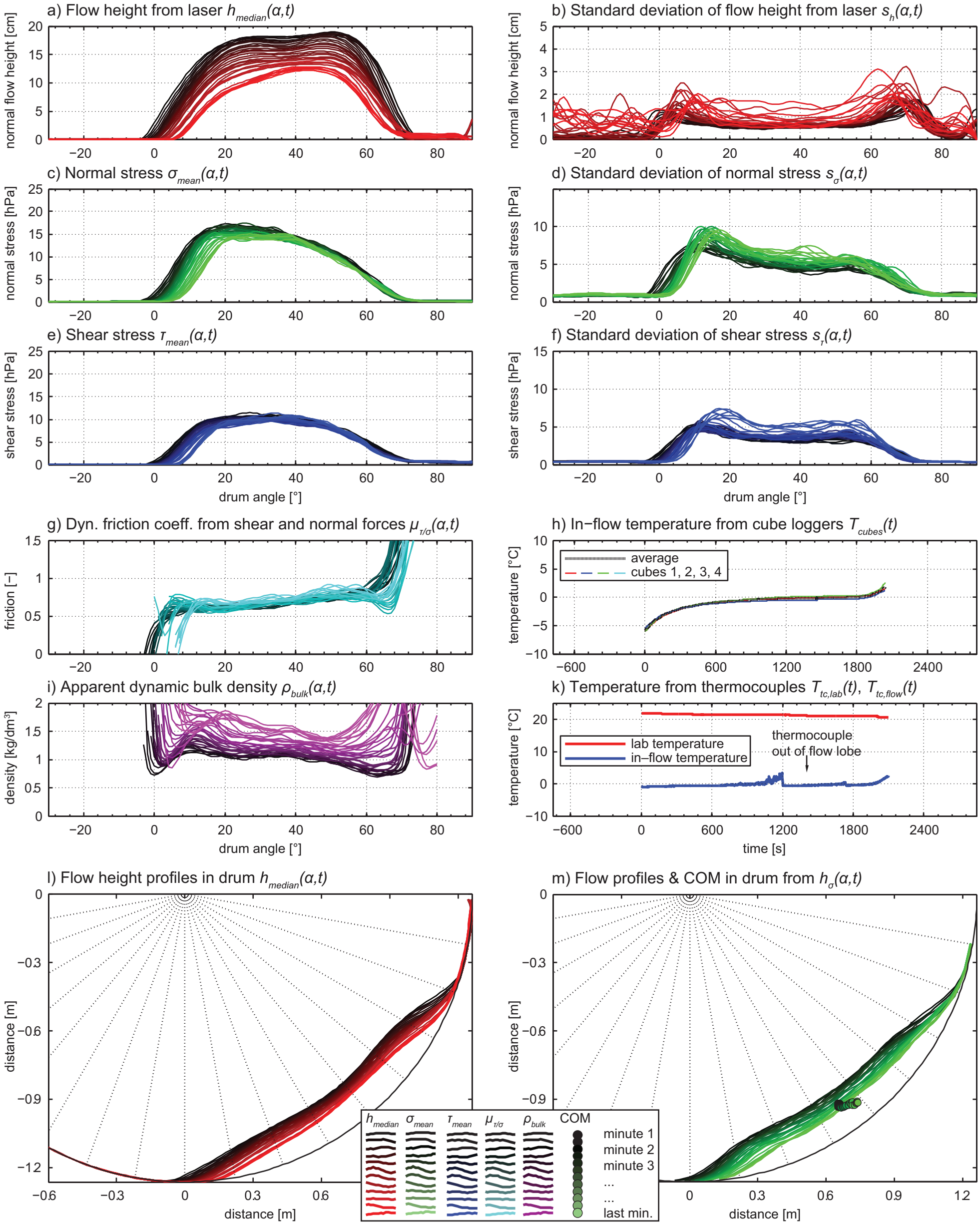

**Figure 20:** Vienna-experiment V10-050.

## Run V03-060 (60 vol-% ice):

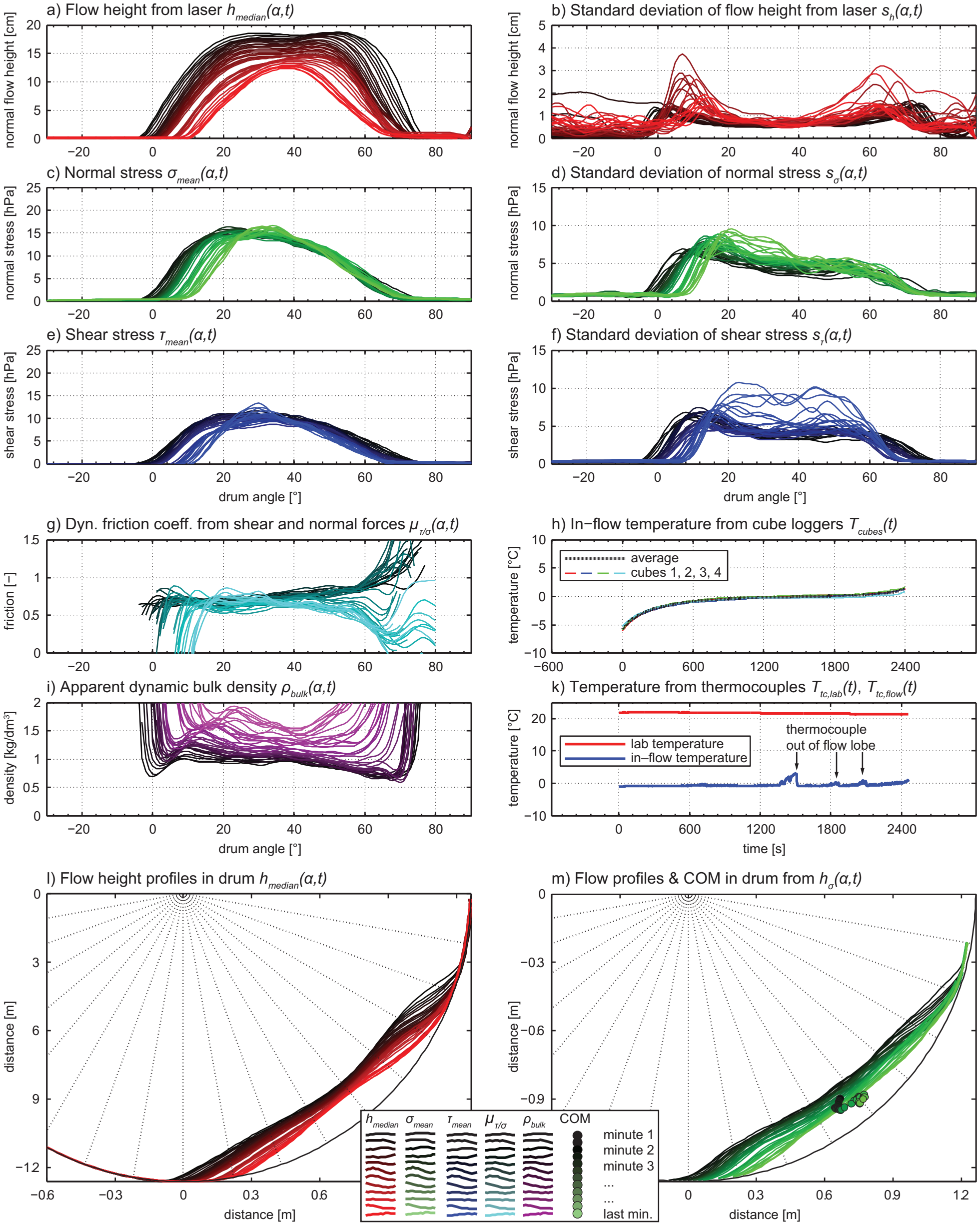
a) Flow height from laser $h_{median}(\alpha,t)$

b) Standard deviation of flow height from laser $s_h(\alpha,t)$

c) Normal stress $\sigma_{mean}(\alpha,t)$

d) Standard deviation of normal stress $s_\sigma(\alpha,t)$

e) Shear stress $\tau_{mean}(\alpha,t)$

f) Standard deviation of shear stress $s_\tau(\alpha,t)$

g) Dyn. friction coeff. from shear and normal forces $\mu_{\tau/\sigma}(\alpha,t)$

h) In−flow temperature from cube loggers $T_{cubes}(t)$

i) Apparent dynamic bulk density $\rho_{bulk}(\alpha,t)$

k) Temperature from thermocouples $T_{tc,lab}(t)$, $T_{tc,flow}(t)$

l) Flow height profiles in drum $h_{median}(\alpha,t)$

m) Flow profiles & COM in drum from $h_\sigma(\alpha,t)$

**Figure 21:** Vienna-experiment V03-060.

## Run V04-070 (70 vol-% ice):

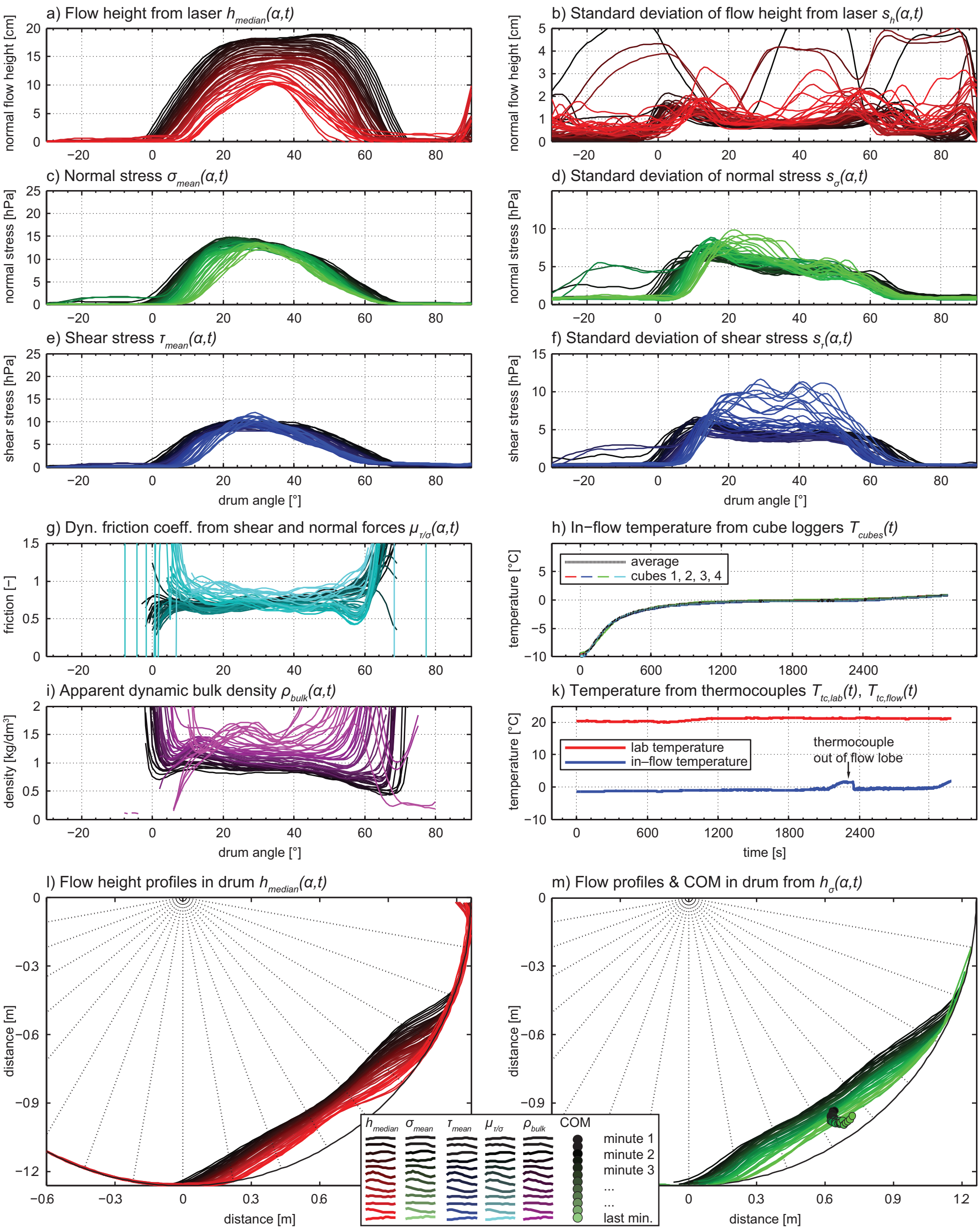

**Figure 22:** Vienna-experiment V04-070.

## Run V07-080 (80 vol-% ice):

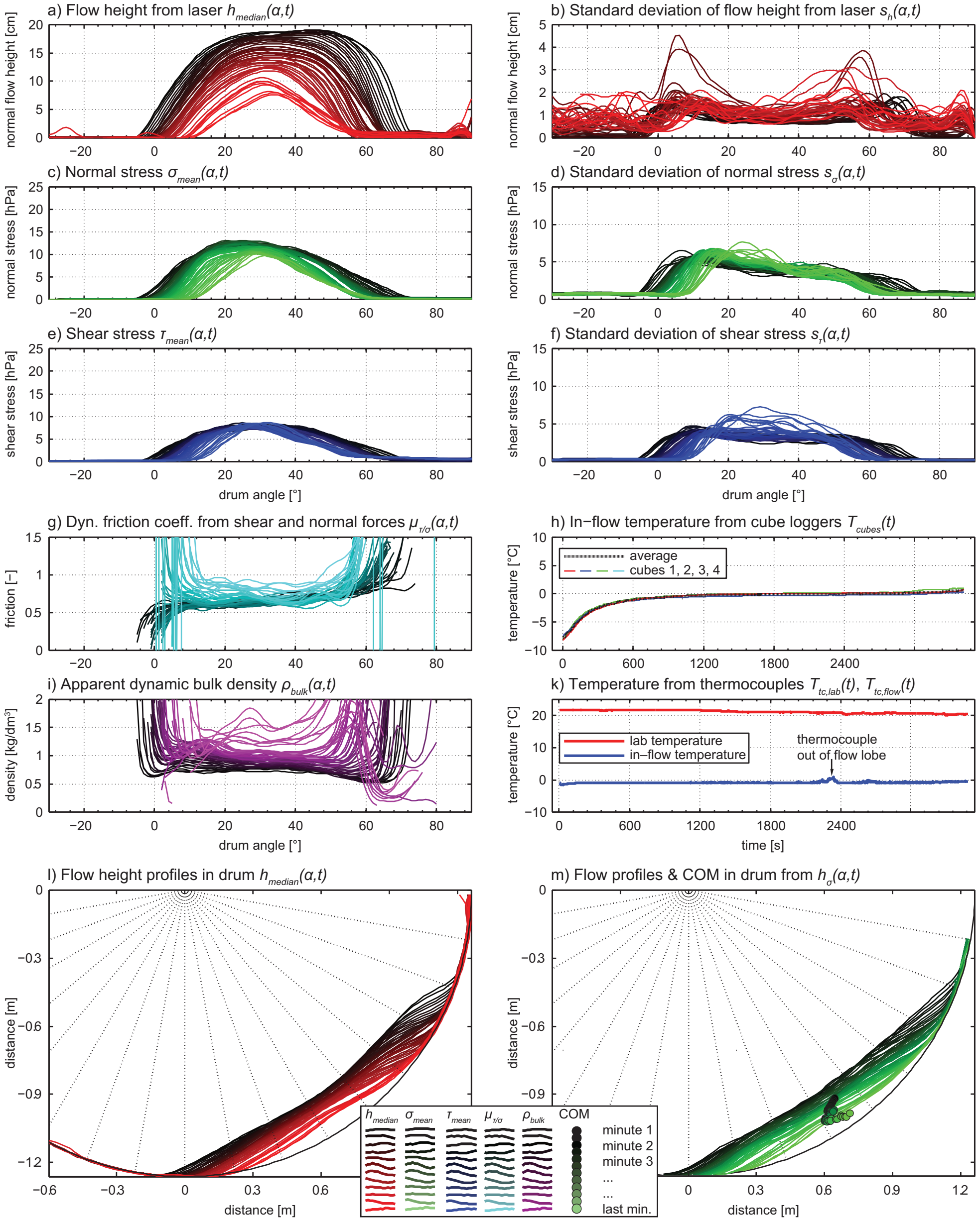

**Figure 23:** Vienna-experiment V07-080.

## Run V11-090 (90 vol-% ice):

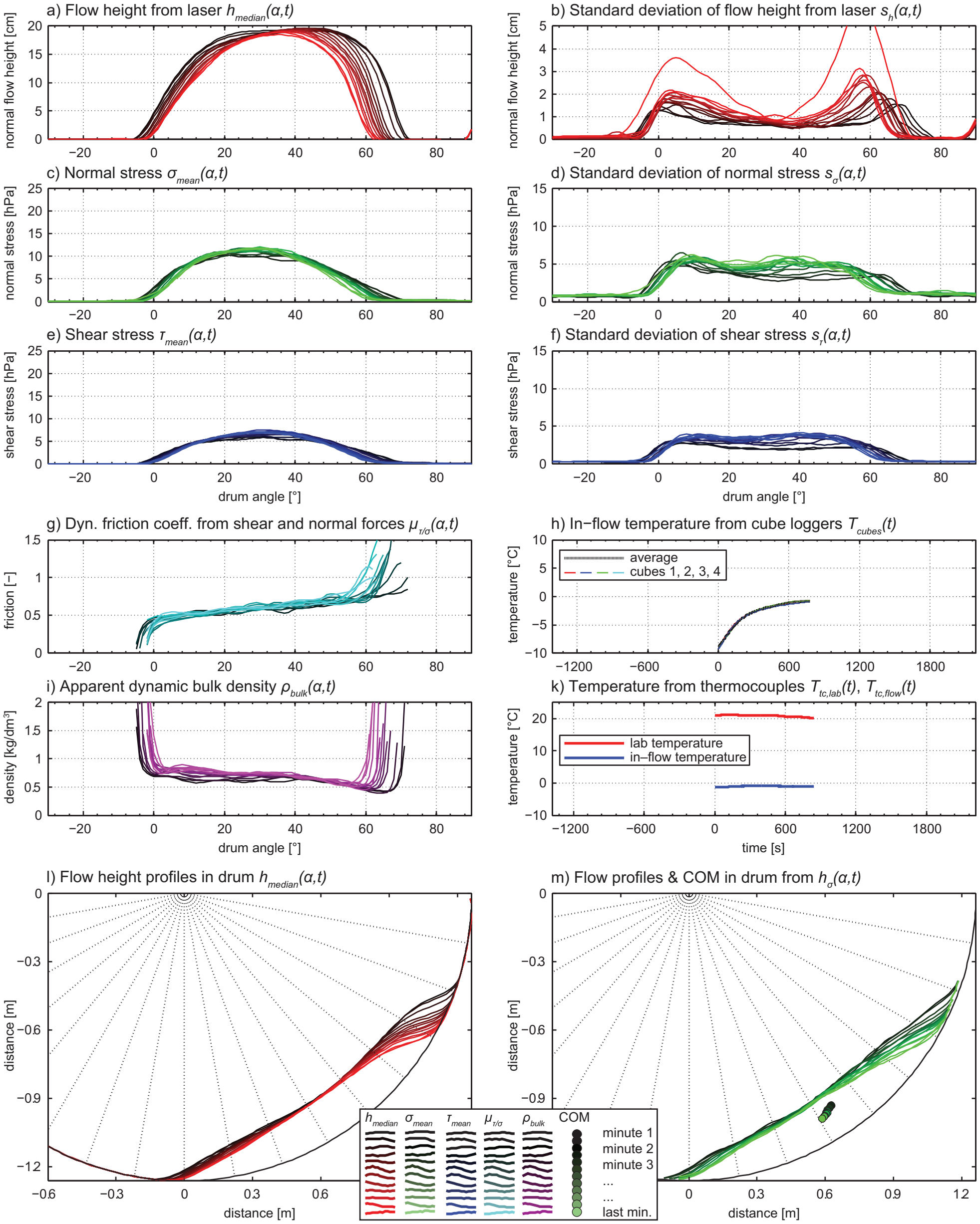

**Figure 24:** Vienna-experiment V11-090. The experiment was stopped after 14 minutes because the ice sticked together and the mass became unstable (stick-slip effects).

## Run V12-100 (100 vol-% ice):

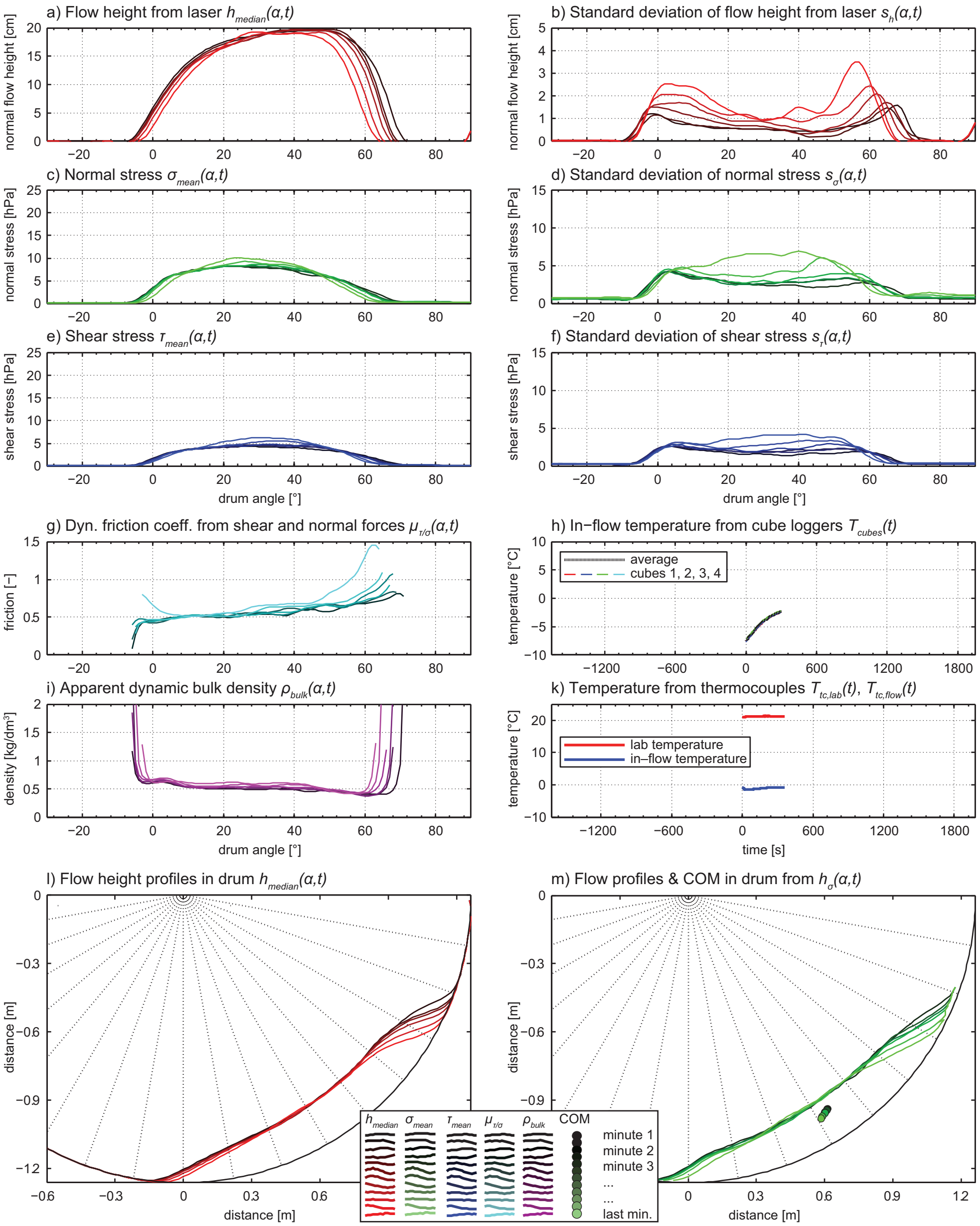

**Figure 25:** Vienna-experiment V12-100. The experiment was stopped already after 6 minutes because the ice sticked together and the mass became unstable (stick-slip effects).

## 9.3 Plots from the Berkeley-drum experiments

In the following, the direct measurement results from the Berkeley experiments are presented. The larger drum in Berkeley included flow height (laser), normal stress (force plates) and two pore water pressure sensors – one at the center and one at the side of the drum – as main measurement devices. The individual measurements are enclosed in subplots (a), (c), (e) and (g) while the corresponding standard deviations are plotted on the right side in subplots (b), (d), (f) and (h). As in Vienna, each line in every graph represents an average profile of one minute where the black lines correspond to the first minute and the full-tone colored lines to the last minute of the experiment. The laser profiles end around the angular positions of 60 to 70° because a curtain covered the rear part to protect the laser mirror from splashes.

Due to the lack of a shear stress sensor, no friction profiles could be calculated directly, but the apparent local bulk density profiles were again formed by the ratio of the flow height to the normal stress (i). Except the slower run B13-050, all Berkeley-runs were affected by the identical maximum centripetal acceleration of 2.19 $m/s^2$ as in the smaller drum in Vienna (22% of the earth's gravitational acceleration). A slight overestimation of the normal stresses and apparent bulk densities can therefore also be expected (see **Chapter 9.2**).

Temperature measurements were performed as in Vienna but by only 1-2 freely moving in-flow temperature loggers of the same type (k). Because thermocouples could not be easily attached to the sensor system, independent control measurements were done with a thermostat that was temporally dipped into the mass to manually check the temperature and stop the run wenn positive temperatures around ~3°C were detected. However, these temperatures could not be recorded.

The runs in the larger drum were all intended to perform at volumes of 0.4000 $m^3$. However, back-calculated values varied much more and at largely lower volumes despite agitation (0.2940 – 0.4265 $m^3$). This can have several reasons: (1) the difference in the grain size of the gravel and ice led to a denser package of the mixture, (2) a certain amount of material was lost to the drum bottom and drop-protection roof, (3) inaccurate calculation of the volume because the laser profile was incomplete at the tail of the flow where it needed to be extrapolated (linearly to the angular position of 85°).

Water loss was irrelevant over longer time periods in the Berkeley-drum, so that the water content continuously increased while ice melted. The evolution of the pore water pressure from the tail to the front and from the center to the sides can well be observed in all runs with ice contents of 40 vol-% and more (**Figure 28** to **Figure 38**).

## Run B04-010 (10 vol-% ice, angular fine gravel ($D_{50}$ = 6 mm), $u_{drum}$ ≈ 2.09 m/s):

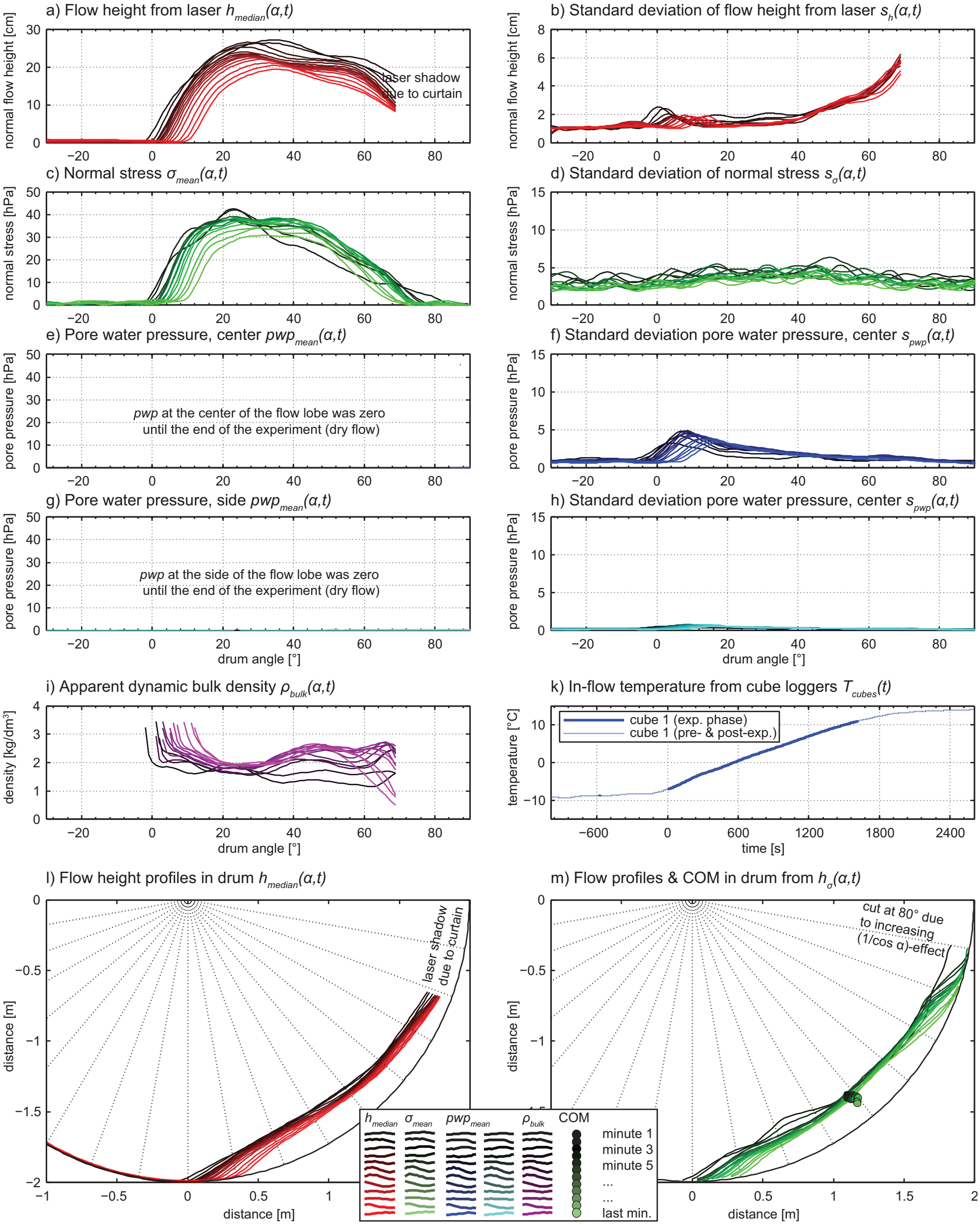

**Figure 26:** Berkeley-experiment B04-010.

## Run B02-030 (30 vol-% ice, angular fine gravel ($D_{50}$ = 6 mm), $u_{drum}$ ≈ 2.09 m/s):

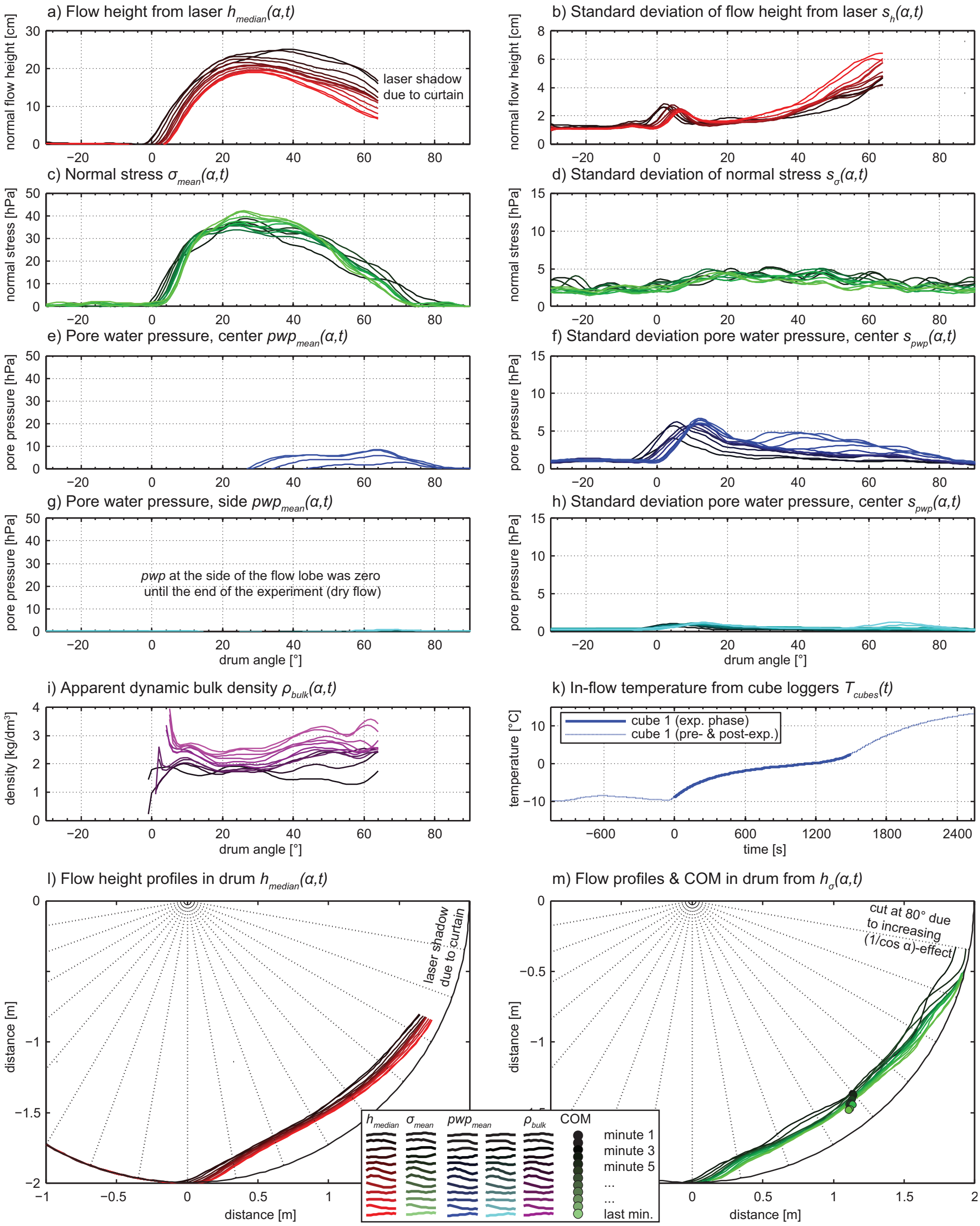

**Figure 27:** Berkeley-experiment B02-030.

### Run B01-050 (50 vol-% ice, angular fine gravel ($D_{50}$ = 6 mm), $u_{drum}$ ≈ 2.09 m/s):

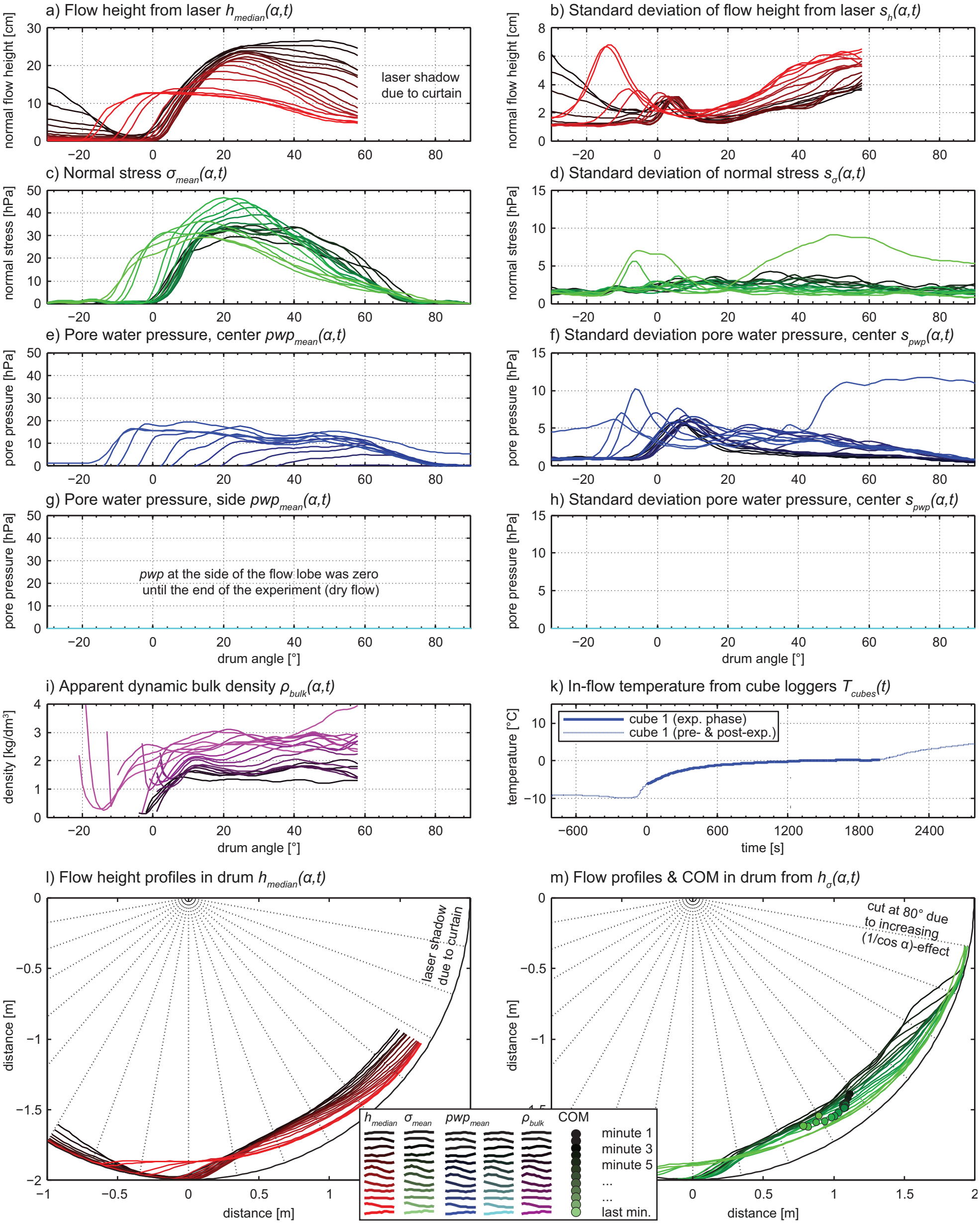

**Figure 28:** Berkeley-experiment B01-050.

**Run B03-070 (70 vol-% ice, angular fine gravel ($D_{50}$ = 6 mm), $u_{drum}$ ≈ 2.09 m/s):**

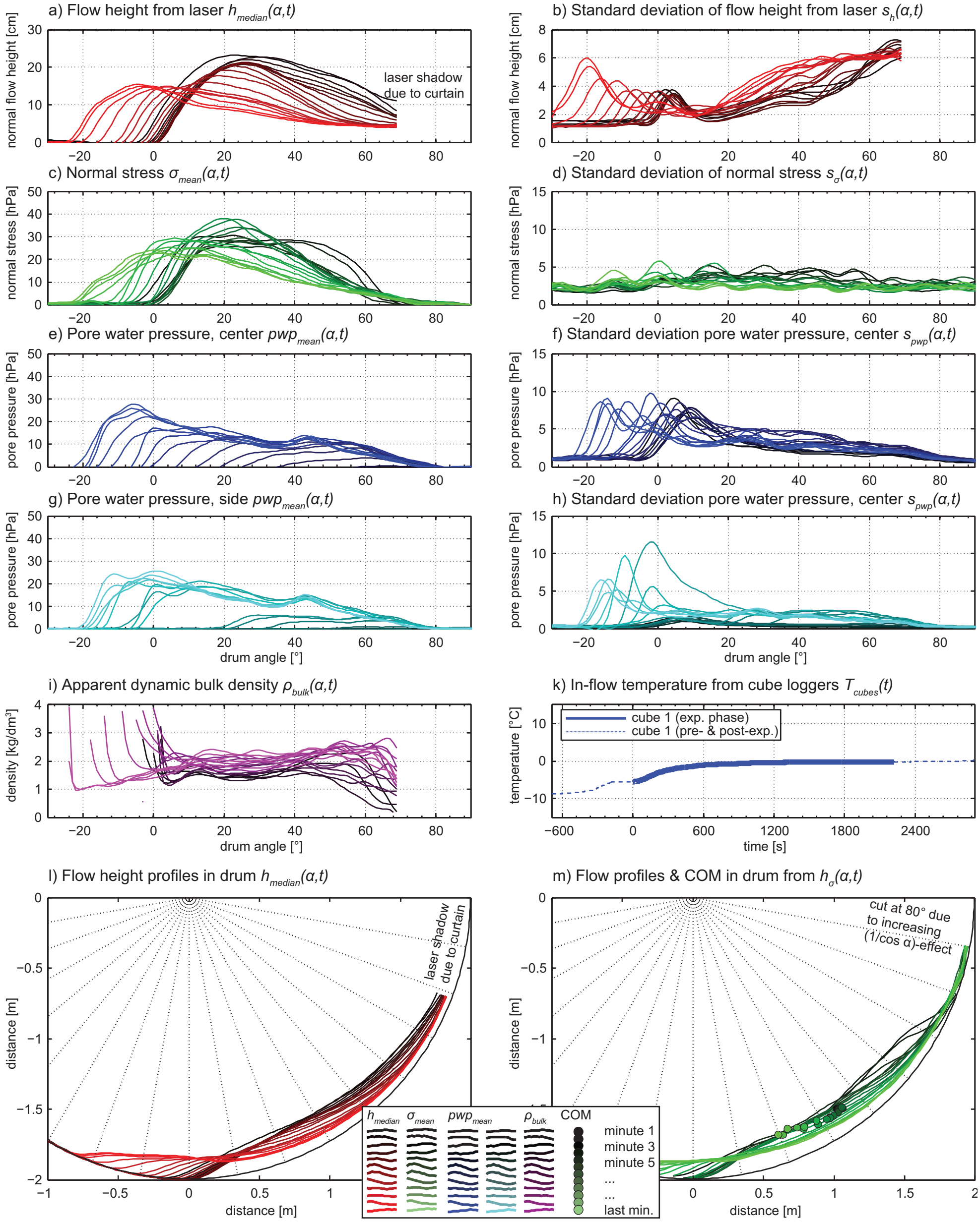

**Figure 29:** Berkeley-experiment B03-070.

## Run B05-090 (90 vol-% ice, angular fine gravel ($D_{50}$ = 6 mm), $u_{drum}$ ≈ 2.09 m/s):

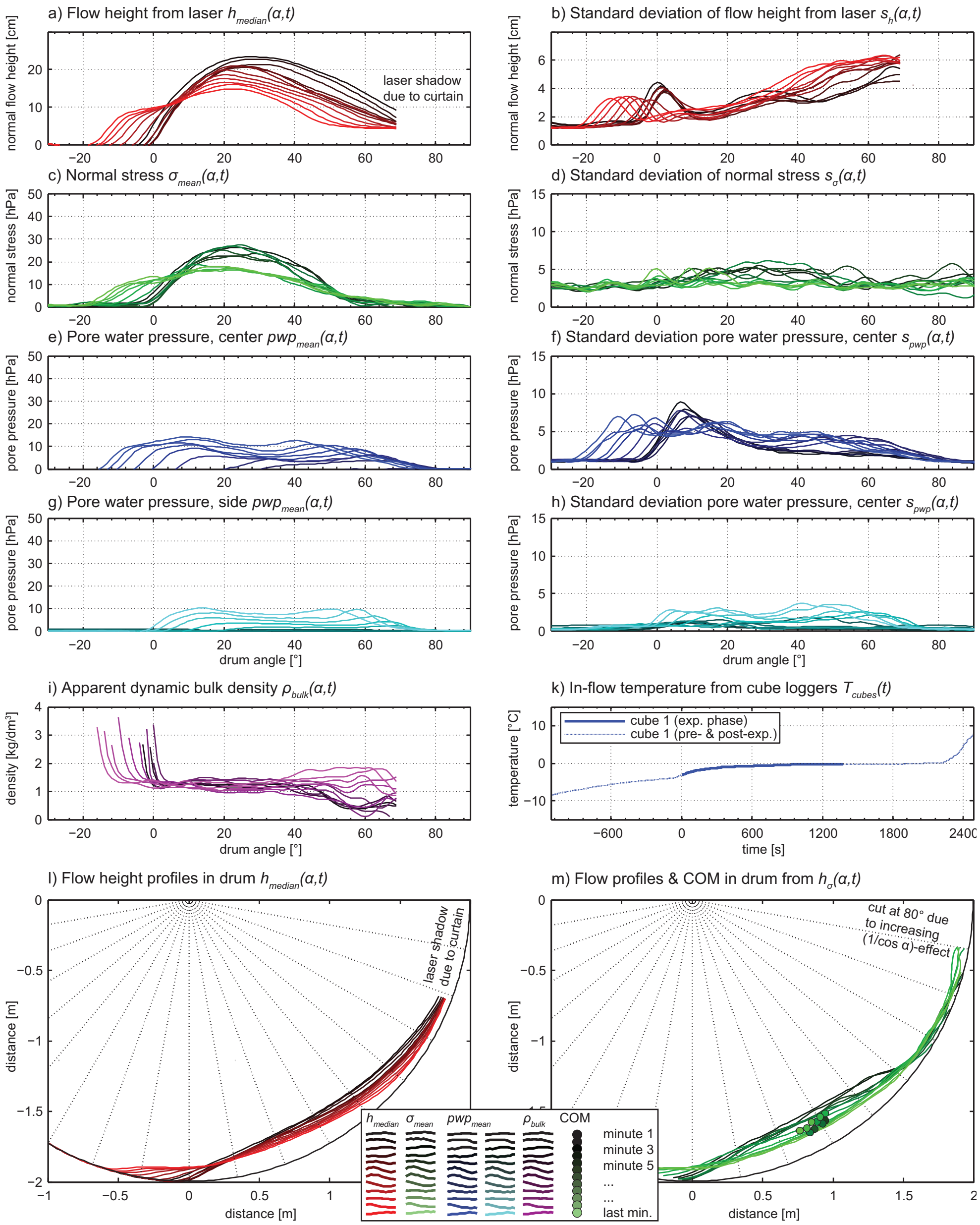

**Figure 30:** Berkeley-experiment B05-090.

### Run B07-040 (40 vol-% ice, rounded fine gravel ($D_{50}$ = 5.6 mm), $u_{drum}$ ≈ 2.09 m/s):

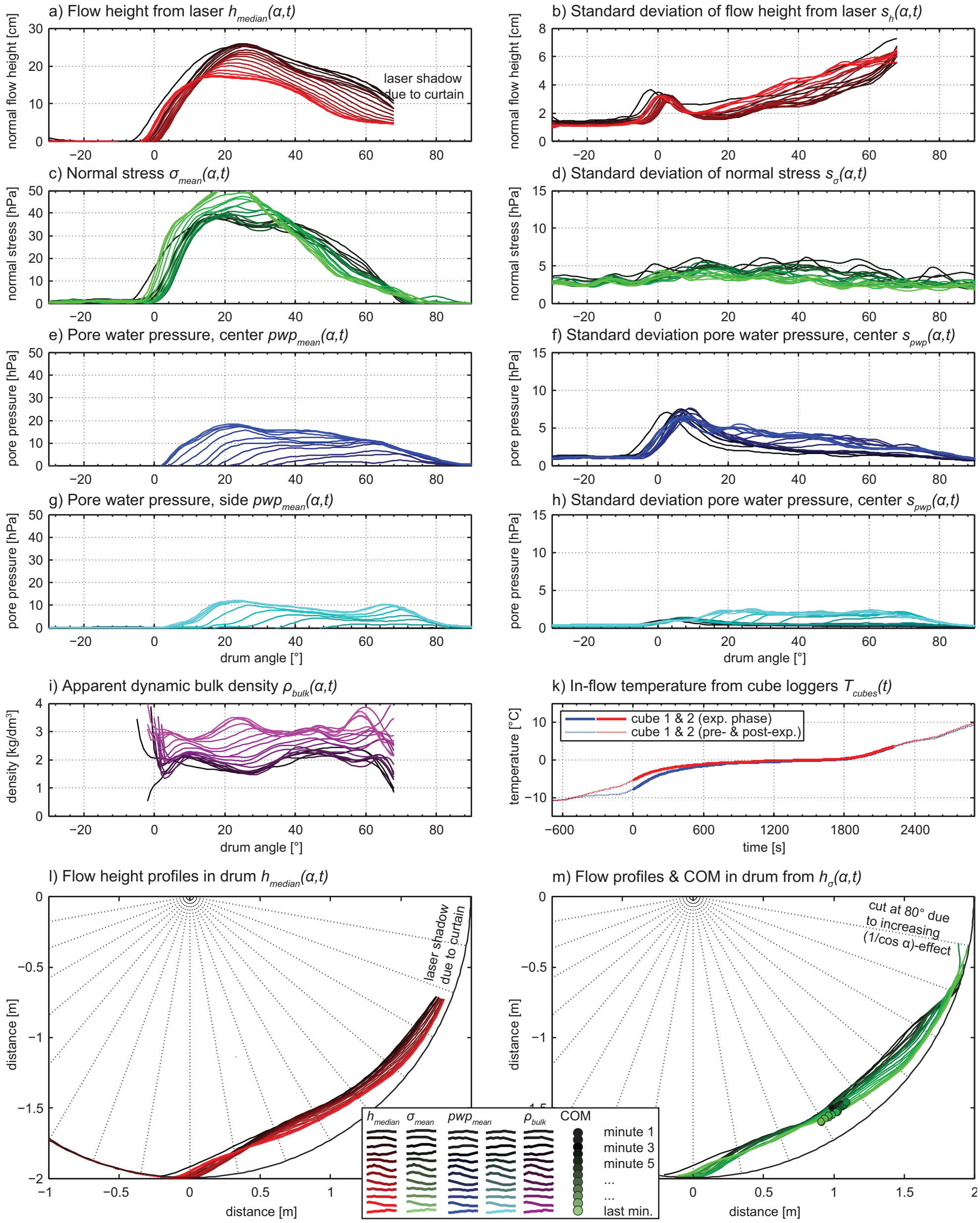

**Figure 31:** Berkeley-experiment B07-040.

## Run B06-050 (50 vol-% ice, rounded fine gravel ($D_{50}$ = 5.6 mm), $u_{drum}$ ≈ 2.09 m/s):

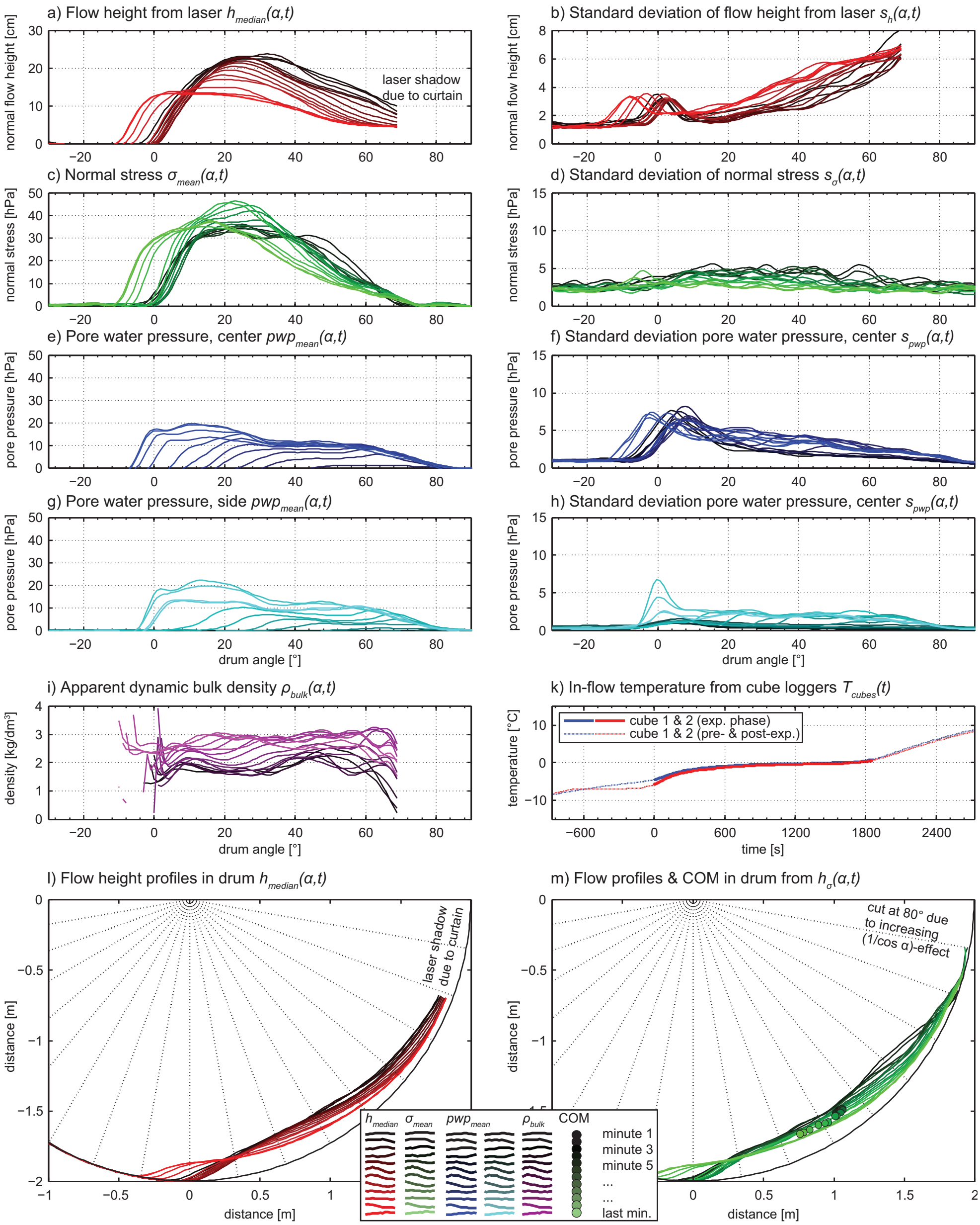

**Figure 32:** Berkeley-experiment B06-050.

## Run B08-060 (60 vol-% ice, rounded fine gravel ($D_{50}$ = 5.6 mm), $u_{drum}$ ≈ 2.09 m/s):

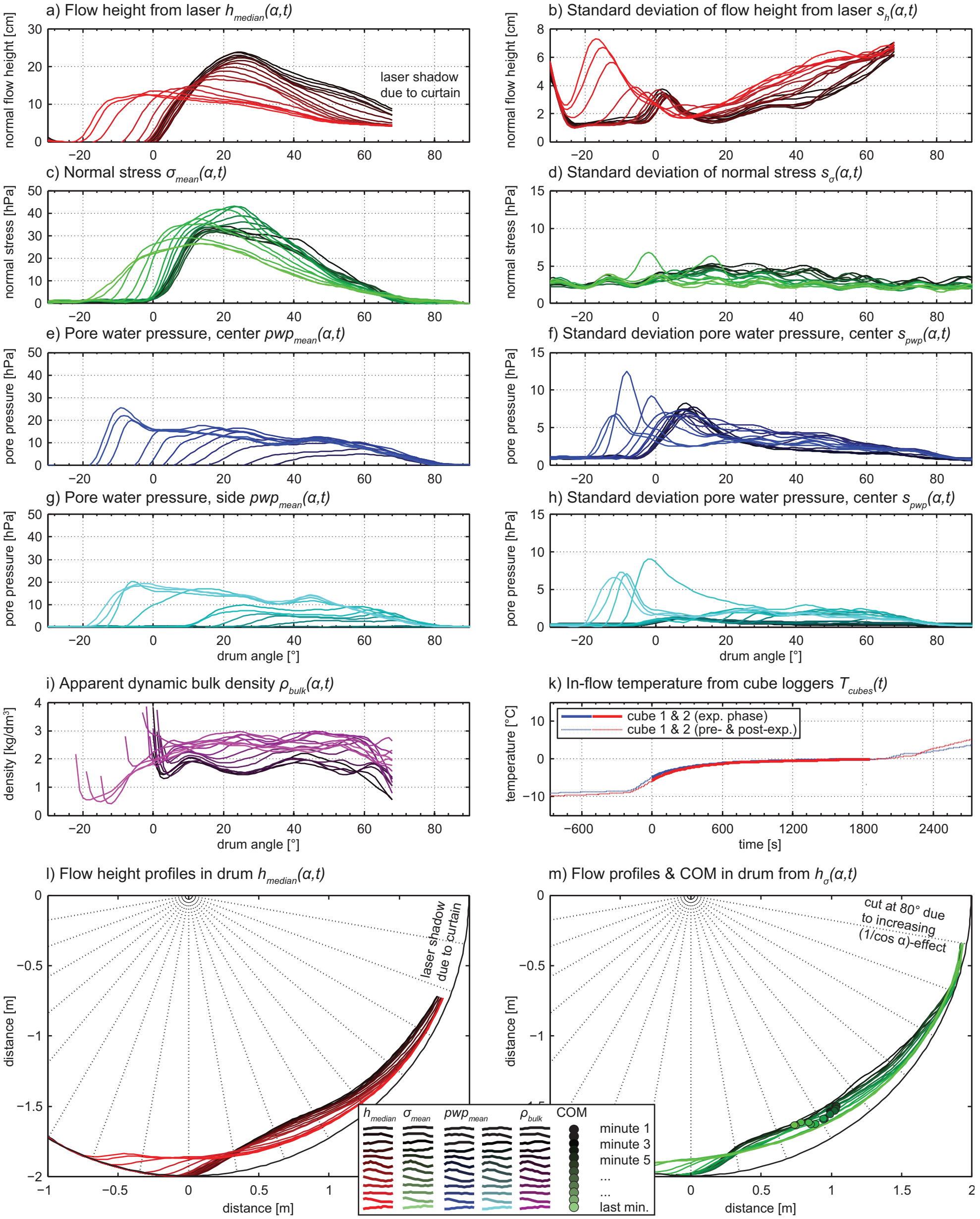

**Figure 33:** Berkeley-experiment B08-060.

## Run B11-040 (40 vol-% ice, angular coarse gravel ($D_{50}$ = 16 mm), $u_{drum}$ ≈ 2.09 m/s):

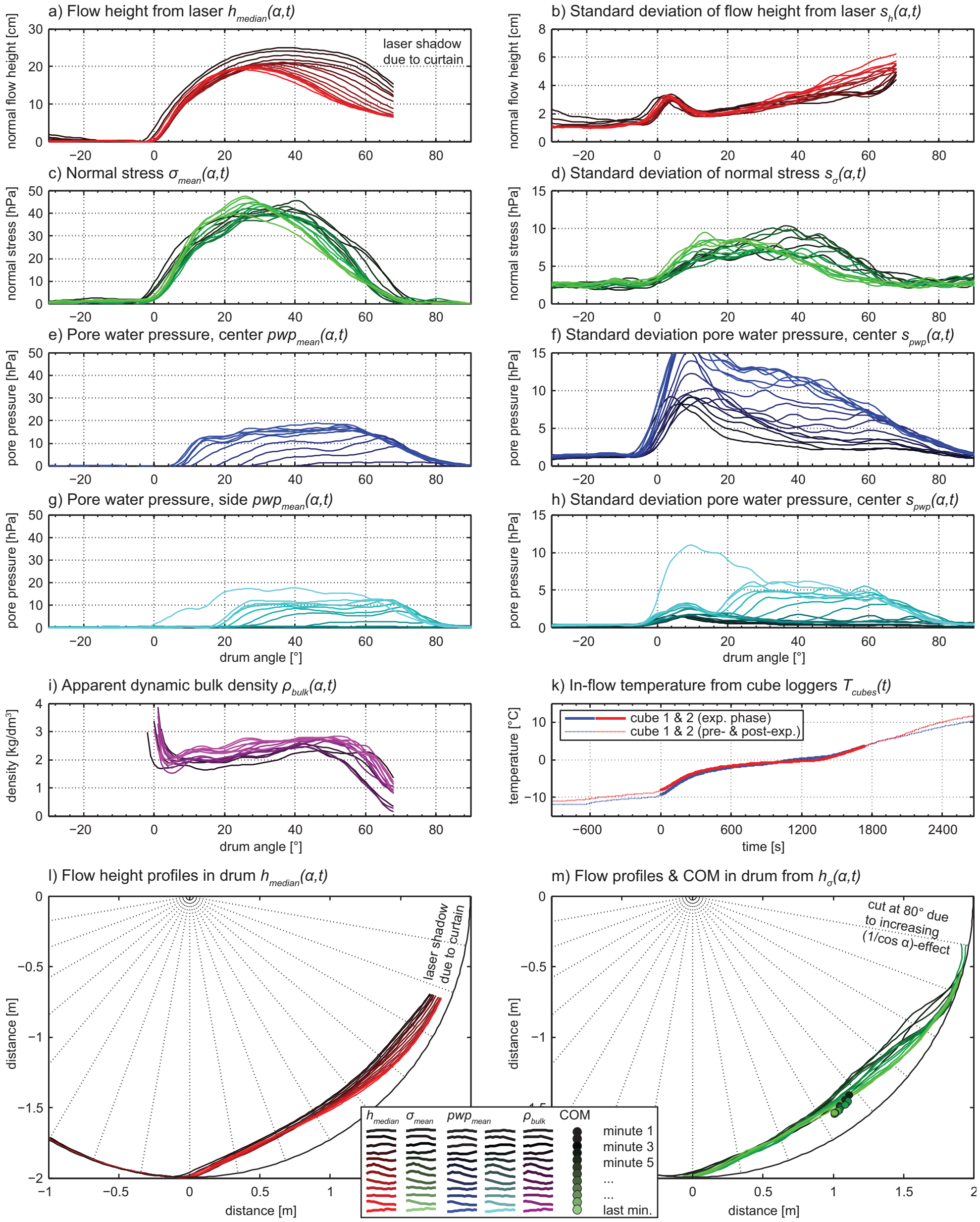

**Figure 34:** Berkeley-experiment B11-040.

## Run B09-050 (50 vol-% ice, angular coarse gravel ($D_{50}$ = 16 mm), $u_{drum}$ ≈ 2.09 m/s):

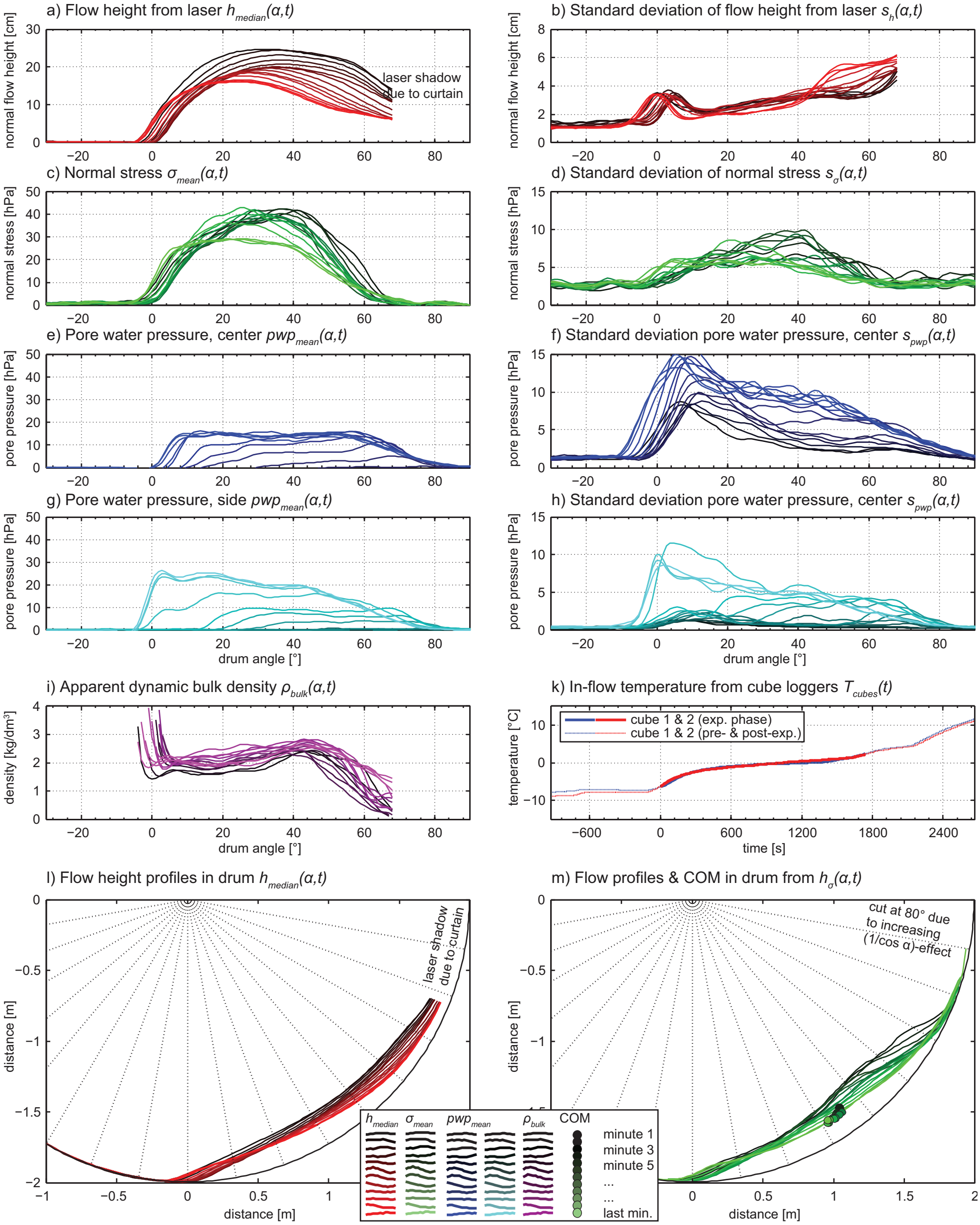

**Figure 35:** Berkeley-experiment B09-050.

## Run B10-060 (60 vol-% ice, angular coarse gravel ($D_{50}$ = 16 mm), $u_{drum}$ ≈ 2.09 m/s):

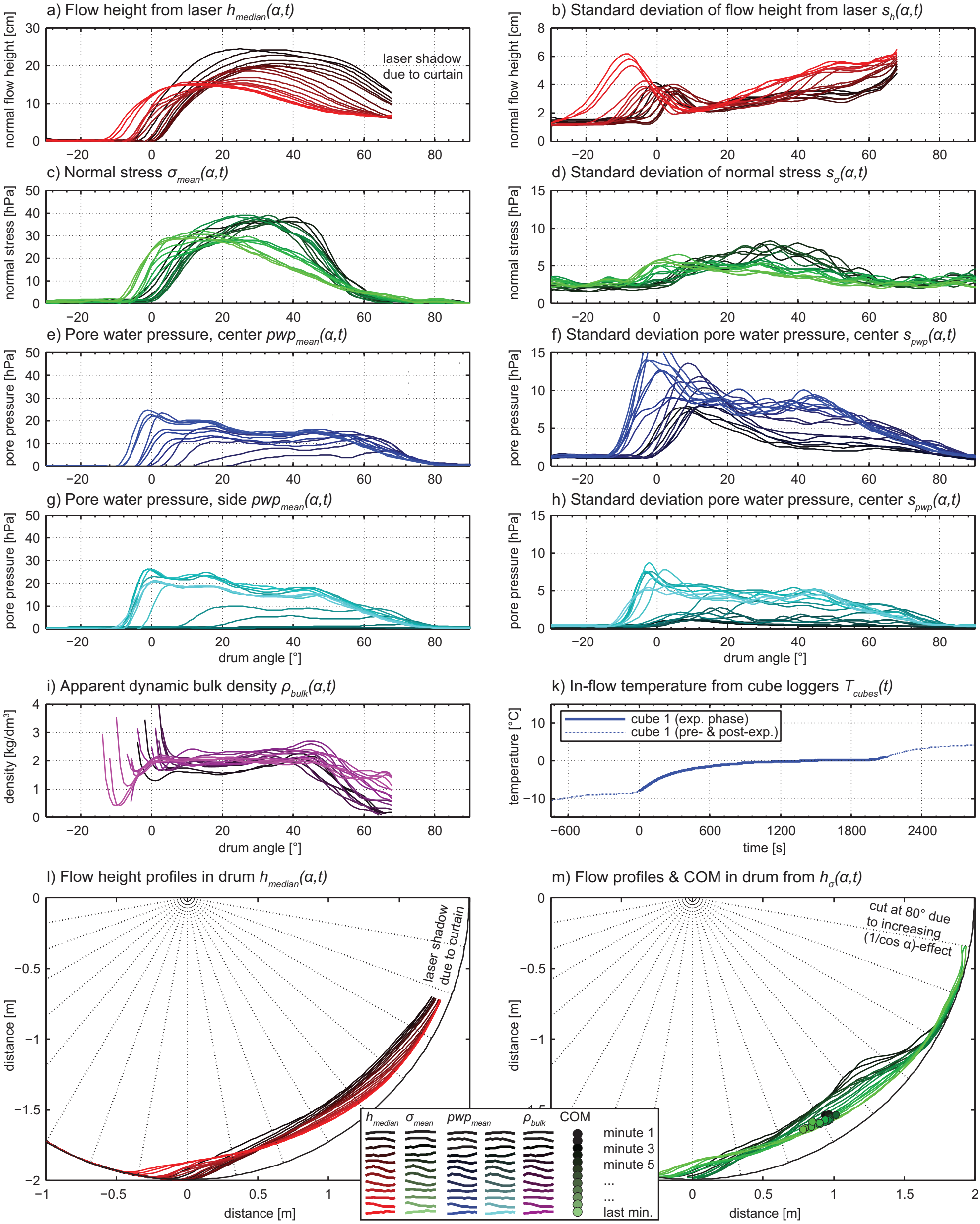

**Figure 36:** Berkeley-experiment B10-060.

## Run B12-070 (70 vol-% ice, angular coarse gravel ($D_{50}$ = 16 mm), $u_{drum}$ ≈ 2.09 m/s):

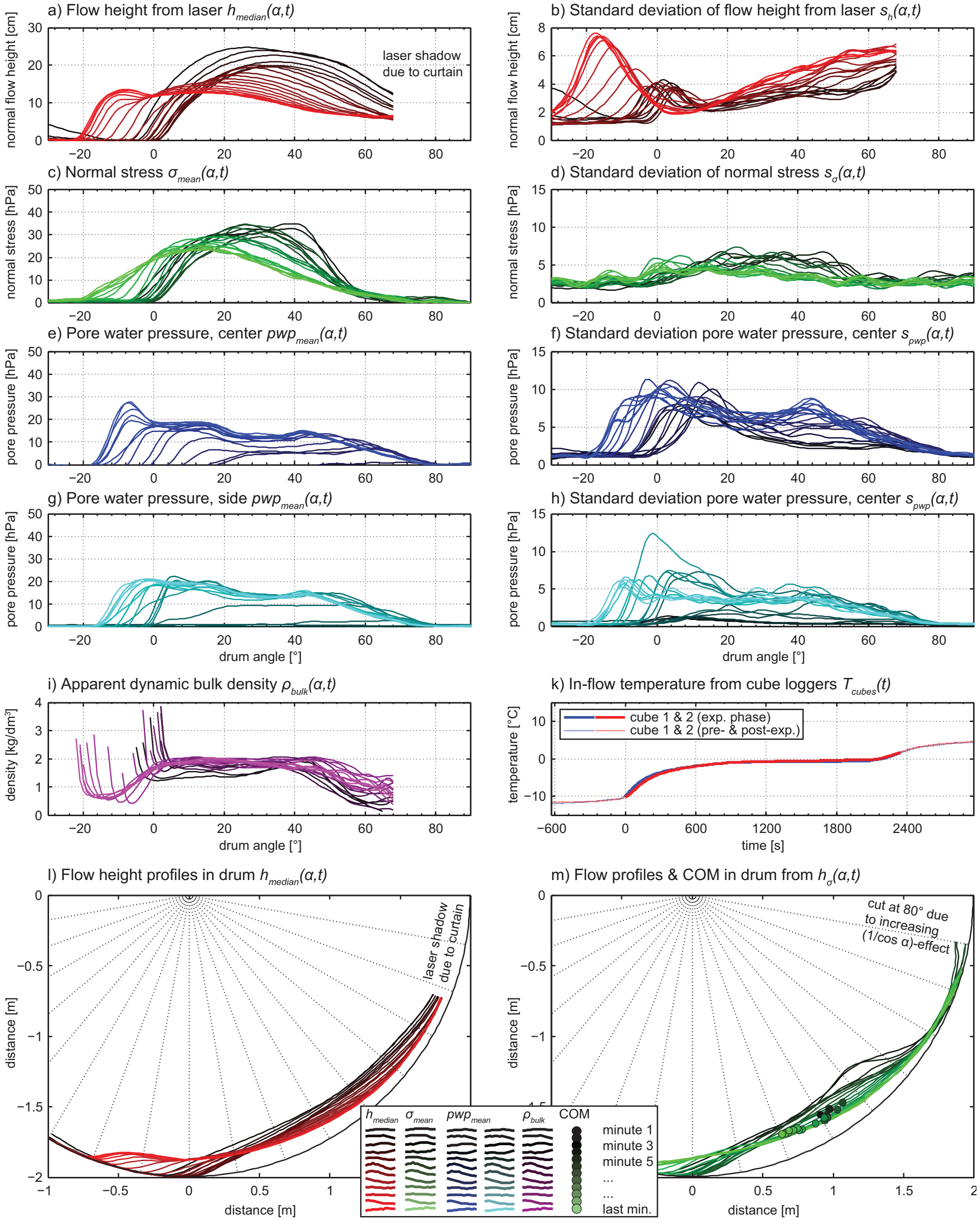

**Figure 37:** Berkeley-experiment B12-070.

## Run B13-050 (50 vol-% ice, angular coarse gravel ($D_{50}$ = 16 mm), $u_{drum}$ ≈ 1.27 m/s):

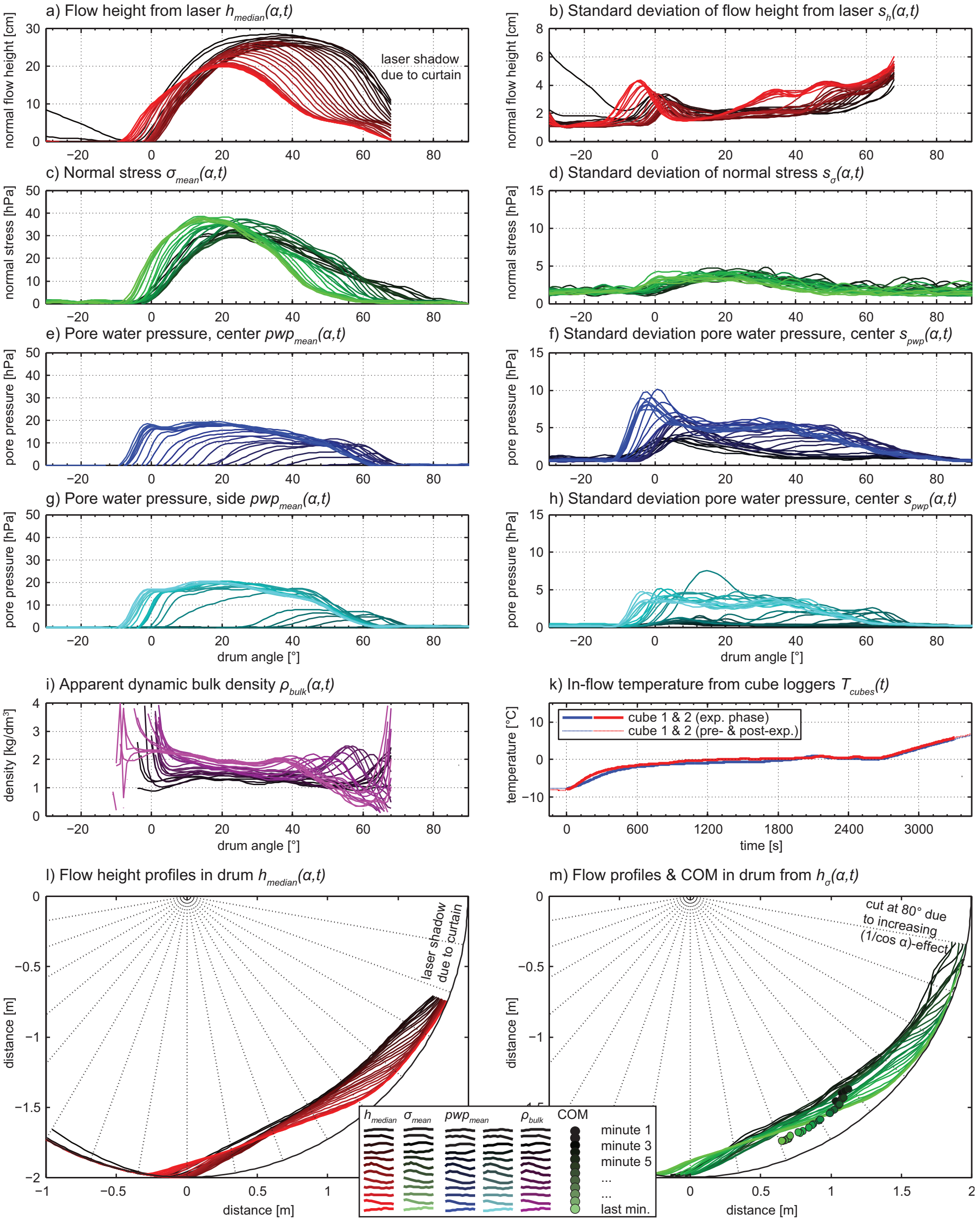

**Figure 38:** Berkeley-experiment B13-050. This was the only run at a lower velocity and hence lower Froude numbers that were subcritical at the beginning (0.88) and increased to supercritical at the end of the run (1.18) for average flow depths (**Table 7**).

## 9.4 Laboratory experiments: Tables

The following **Tables 3-7** provide an overview of several parameters which were directly measured before and during the experiments, calculated from other parameters or estimated. Note that the volume fractions of ice $\upsilon_{ice}$ and gravel $\upsilon_{gravel}$ relate to the unmixed fractions. For example in the larger drum in Berkeley and for a run with 70 vol-% ice we used 28 buckets (with a volume of 20 liters) of granular ice and 12 buckets of gravel.

The maximum theoretic pore water saturation $s_{end}$ indicates an upper boundary for the water saturation if all ice has melted and not water would be lost during the experiments. However, real values are significantly lower. The masses and weighted densities result from the proportions of ice and gravel in the mixtures. Because the runs were dry at the beginning and increasingly saturated during the experiments, pure air and water were used as the end-members for fluid densities and viscosities. Similarly, the characteristic grain sizes needed to be calculated from the median grain sizes of gravel and ice that were weighted for the beginning of the experiments and reduced to the somewhat smaller gravel size at the end of the experiment when all ice melted.

Maximum and average flow heights were calculated from the flow height profiles. Because the laser profile ended around the 70°-position, the adjusted height profiles from the normal stress sensor as shown in the **Subfigures (m)** of **Figures 14-38** was used to calculate the average flow heights. The shear rate was calculated under the simplified assumption of a mirrored linear triangular shear profile where the grains at the center of the flow height would be quasi-static.

From these values, the dimensionless numbers as described in **Chapter 2.5.3** were calculated for the dry start and the end of the experiments where all ice has melted and the fluid fraction was made of water and air.

For comparison, data for several real events was estimated in **Table 8**. Not all values could be derived specifically for the start and end of the events so that values representing the entire event were taken.

**Table 3:** Measured (bold) and calculated parameters from the experiments in the **smaller rotating drum in Vienna** with varying volumetric ice contents and **angular quartz gravel ($D_{50}$ = 9.1 mm)**. Due to water leakage from the Vienna-drum, the end-values in the grey cells need to be considered under reserve. The same experimental series is continued in **Table 4**.

| Description of variable | Symbol | Unit | V09-000 | V08-010 | V06-020 | V05-030 | V02-040 | V01-050 |
|---|---|---|---|---|---|---|---|---|
| volume fraction ice | $\upsilon_{ice}$ | % | 0 | 10 | 20 | 30 | 40 | 50 |
| volume fraction gravel | $\upsilon_{gravel}$ | % | 100 | 90 | 80 | 70 | 60 | 50 |
| experiment end time | $t_{end}$ | min | **12** | **15** | **20** | **29** | **29** | **25** |
| start volume (measured during 1st minute) | $V_{start}$ | $m^3$ | **0.1022** | **0.1061** | **0.1079** | **0.1043** | **0.1039** | **0.1044** |
| end volume (measured during $T_{end}$) | $V_{end}$ | $m^3$ | **0.0999** | **0.0912** | **0.0801** | **0.0672** | **0.0574** | **0.0617** |
| maximum theoretic pore water saturation (end) | $s_{end}$ | % | 0 | 13 | 29 | 50 | 78 | >100 |
| total mass (start) | $m_{tot}$ | kg | 153.3 | 148.8 | 140.8 | 125.9 | 115.3 | 105.7 |
| density of dense rock | $\rho_{rock}$ | $kg/m^3$ | **2,710** | **2,710** | **2,710** | **2,710** | **2,710** | **2,710** |
| density of dense ice | $\rho_{ice}$ | $kg/m^3$ | 910 | 910 | 910 | 910 | 910 | 910 |
| weighted density of solids (gravel & ice) | $\rho_s$ | $kg/m^3$ | 2,710 | 2,530 | 2,350 | 2,170 | 1,990 | 1,810 |
| density of fluids (air, start) | $\rho_{f.a.start}$ | $kg/m^3$ | 1.2 | 1.2 | 1.2 | 1.2 | 1.2 | 1.2 |
| weighted density of fluids (water & air, end) | $\rho_{f.a.w.end}$ | $kg/m^3$ | 1.2 | 131 | 291 | 501 | 780 | 1000 |
| dynamic bulk density of gravel-ice mixt. (start) | $\rho_{dyn.start}$ | $kg/m^3$ | **1,057** | **995** | **917** | **902** | **834** | **770** |
| dynamic bulk density of gravel-ice mixt. (end) | $\rho_{dyn.end}$ | $kg/m^3$ | **1,058** | **1,061** | **1,096** | **1,205** | **1,227** | **1,043** |
| grain size of gravel (≈ median grain size $D_{50}$) | $\delta_r$ | m | 0.0091 | 0.0091 | 0.0091 | 0.0091 | 0.0091 | 0.0091 |
| grain size of ice (≈ median grain size $D_{50}$) | $\delta_i$ | m | 0.0110 | 0.0110 | 0.0110 | 0.0110 | 0.0110 | 0.0110 |
| weighted grain size (gravel & ice, start) | $\delta_{av}$ | m | 0.0091 | 0.0093 | 0.0095 | 0.0097 | 0.0099 | 0.0101 |
| volume fraction of solids (gravel & ice, start) | $\upsilon_{s.start}$ | - | 0.55 | 0.55 | 0.56 | 0.56 | 0.56 | 0.56 |
| volume fraction of fluids (air, start) | $\upsilon_{f.start}$ | - | 0.45 | 0.45 | 0.44 | 0.44 | 0.44 | 0.44 |
| volume fraction of solids (gravel, end) | $\upsilon_{s.end}$ | - | 0.55 | 0.55 | 0.55 | 0.55 | 0.55 | 0.52 |
| volume fraction of fluids (water or air, end) | $\upsilon_{f.end}$ | - | 0.45 | 0.45 | 0.45 | 0.45 | 0.45 | 0.48 |
| fluid viscosity (air at 0°C) | $\eta_{start}$ | Pa s | 0.000017 | 0.000017 | 0.000017 | 0.000017 | 0.000017 | 0.000017 |
| fluid viscosity (water at 0°C) | $\eta_{water}$ | Pa s | 0.001787 | 0.001787 | 0.001787 | 0.001787 | 0.001787 | 0.001787 |
| weighted fluid viscosity (air & water, at 0°C) | $\eta_{end}$ | Pa s | 0.000017 | 0.000247 | 0.000531 | 0.000902 | 0.001398 | 0.001787 |
| maximum flow height (start) | $h_{max.start}$ | m | **0.177** | **0.183** | **0.182** | **0.178** | **0.176** | **0.180** |
| maximum flow height (end) | $h_{max.end}$ | m | **0.175** | **0.168** | **0.150** | **0.134** | **0.144** | **0.140** |
| average flow height (start) | $h_{av.start}$ | m | **0.131** | **0.134** | **0.136** | **0.133** | **0.131** | **0.134** |
| average flow height (end) | $h_{av.end}$ | m | **0.129** | **0.120** | **0.106** | **0.097** | **0.095** | **0.095** |
| drum velocity (rounds per minute) | $u_d$ | RPM | **12.73** | **12.27** | **12.50** | **12.58** | **12.42** | **12.42** |
| tangential drum velocity | $u_{d.t}$ | m/s | **1.64** | **1.58** | **1.61** | **1.62** | **1.60** | **1.60** |
| effective velocity due to shearing (2 * $u_{d.t}$) | $u_{eff}$ | m/s | 3.28 | 3.16 | 3.22 | 3.24 | 3.20 | 3.20 |
| average shear rate (with $h_{av.start}$) | $\dot{\gamma}_{av.start}$ | $s^{-1}$ | 25.04 | 23.58 | 23.68 | 24.36 | 24.43 | 23.88 |
| average shear rate (with $h_{av.end}$) | $\dot{\gamma}_{av.end}$ | $s^{-1}$ | 25.43 | 26.33 | 30.38 | 33.40 | 33.68 | 33.68 |
| **Dimensionless numbers calc. from average flow heights $h_{av}$ during the first (start) and last (end) minute of the experiments** | | | | | | | | |
| **Froude number** | $Fr_{start}$ | - | 1.45 | 1.38 | 1.39 | 1.42 | 1.41 | 1.40 |
| | $Fr_{end}$ | - | 1.46 | 1.46 | 1.58 | 1.66 | 1.66 | 1.66 |
| **Reynolds number** | $N_{R.start}$ | - | 143 | 141 | 147 | 157 | 164 | 167 |
| | $N_{R.end}$ | - | 146 | 1,155 | 1,379 | 1,535 | 1,557 | 1,561 |
| **Savage number** | $N_{S.start}$ | - | 0.0404 | 0.0365 | 0.0378 | 0.0426 | 0.0452 | 0.0438 |
| | $N_{S.end}$ | - | 0.0423 | 0.0513 | 0.0823 | 0.1191 | 0.1416 | 0.1598 |
| **Bagnold number** | $N_{B.start}$ | - | 401,198 | 368,909 | 359,662 | 357,183 | 343,340 | 319,241 |
| | $N_{B.end}$ | - | 401,684 | 29,193 | 15,704 | 10,155 | 6,610 | 4,507 |
| **Mass number** | $N_{M.start}$ | - | 2,799 | 2622 | 2445 | 2268 | 2091 | 1914 |
| | $N_{M.end}$ | - | 2,760 | 25.28 | 11.39 | 6.62 | 4.25 | 2.89 |
| **Darcy number** | $N_{D.av.start}$ | - | 46 | 52 | 56 | 59 | 64 | 72 |
| | $N_{D.av.end}$ | - | 46 | 675 | 1351 | 2263 | 3791 | 5682 |
| **Friction number** | $N_{F.av.start}$ | - | $9{,}9 \times 10^6$ | $10{,}1 \times 10^6$ | $9{,}5 \times 10^6$ | $8{,}4 \times 10^6$ | $7{,}6 \times 10^6$ | $7{,}3 \times 10^6$ |
| | $N_{F.av.end}$ | - | $9{,}5 \times 10^6$ | 569,525 | 190,768 | 85,270 | 46,688 | 28,209 |

**Table 4:** Continued from **Table 3**.
* no value (division by zero due to absence of solid components $\upsilon_{s.end}$ at the end of the experiment)

| Description of variable | Symbol | Unit | V10-050 | V03-060 | V04-070 | V07-080 | V11-090 | V12-100 |
|---|---|---|---|---|---|---|---|---|
| volume fraction ice | $\upsilon_{ice}$ | % | 50 | 60 | 70 | 80 | 90 | 100 |
| volume fraction gravel | $\upsilon_{gravel}$ | % | 50 | 40 | 30 | 20 | 10 | 0 |
| experiment end time | $t_{end}$ | min | **35** | **39** | **52** | **57** | **14** | **6** |
| start volume (measured during 1st minute) | $V_{start}$ | $m^3$ | **0.0994** | **0.1056** | **0.0970** | **0.1025** | **0.1044** | **0.1041** |
| end volume (measured during $T_{end}$) | $V_{end}$ | $m^3$ | **0.0489** | **0.0387** | **0.0285** | **0.0183** | **0.0750** | **0.0845** |
| maximum theoretic pore water saturation (end) | $s_{end}$ | % | >100 | >100 | >100 | >100 | >100 | >100 |
| total mass (start) | $m_{tot}$ | kg | 100.6 | 96.6 | 79.3 | 73.8 | 65.0 | 54.7 |
| density of dense rock | $\rho_{rock}$ | $kg/m^3$ | **2,710** | **2,710** | **2,710** | **2,710** | **2,710** | **2,710** |
| density of dense ice | $\rho_{ice}$ | $kg/m^3$ | 910 | 910 | 910 | 910 | 910 | 910 |
| weighted density of solids (gravel & ice) | $\rho_s$ | $kg/m^3$ | 1,810 | 1,630 | 1,450 | 1,270 | 1,090 | 910 |
| density of fluids (air, start) | $\rho_{f.a.start}$ | $kg/m^3$ | 1.2 | 1.2 | 1.2 | 1.2 | 1.2 | 1.2 |
| weighted density of fluids (water & air, end) | $\rho_{f.a.w.end}$ | $kg/m^3$ | 1,000 | 1,000 | 1,000 | 1,000 | 1,000 | 1,000 |
| dynamic bulk density of gravel-ice mixt. (start) | $\rho_{dyn.start}$ | $kg/m^3$ | **799** | **688** | **623** | **552** | **477** | **403** |
| dynamic bulk density of gravel-ice mixt. (end) | $\rho_{dyn.end}$ | $kg/m^3$ | **1,193** | **1,377** | **1,194** | **1,371** | **610** | **488** |
| grain size of gravel (≈ median grain size $D_{50}$) | $\delta_r$ | m | 0.0091 | 0.0091 | 0.0091 | 0.0091 | 0.0091 | 0.0091 |
| grain size of ice (≈ median grain size $D_{50}$) | $\delta_i$ | m | 0.0110 | 0.0110 | 0.0110 | 0.0110 | 0.0110 | 0.0110 |
| weighted grain size (gravel & ice, start) | $\delta_{av}$ | m | 0.0101 | 0.0102 | 0.0104 | 0.0106 | 0.0108 | 0.0110 |
| volume fraction of solids (gravel & ice, start) | $\upsilon_{s.start}$ | - | 0.56 | 0.56 | 0.56 | 0.57 | 0.57 | 0.58 |
| volume fraction of fluids (air, start) | $\upsilon_{f.start}$ | - | 0.44 | 0.44 | 0.44 | 0.43 | 0.43 | 0.42 |
| volume fraction of solids (gravel, end) | $\upsilon_{s.end}$ | - | 0.52 | 0.42 | 0.32 | 0.21 | 0.11 | 0.00 |
| volume fraction of fluids (water or air, end) | $\upsilon_{f.end}$ | - | 0.48 | 0.58 | 0.68 | 0.79 | 0.89 | 1.00 |
| fluid viscosity (air at 0°C) | $\eta_{start}$ | Pa s | 0.000017 | 0.000017 | 0.000017 | 0.000017 | 0.000017 | 0.000017 |
| fluid viscosity (water at 0°C) | $\eta_{water}$ | Pa s | 0.001787 | 0.001787 | 0.001787 | 0.001787 | 0.001787 | 0.001787 |
| weighted fluid viscosity (air & water, at 0°C) | $\eta_{end}$ | Pa s | 0.001787 | 0.001787 | 0.001787 | 0.001787 | 0.001787 | 0.001787 |
| maximum flow height (start) | $h_{max.start}$ | m | **0.183** | **0.186** | **0.189** | **0.187** | **0.193** | **0.195** |
| maximum flow height (end) | $h_{max.end}$ | m | **0.122** | **0.124** | **0.102** | **0.076** | **0.184** | **0.193** |
| average flow height (start) | $h_{av.start}$ | m | **0.136** | **0.139** | **0.136** | **0.138** | **0.145** | **0.144** |
| average flow height (end) | $h_{av.end}$ | m | **0.078** | **0.070** | **0.058** | **0.038** | **0.122** | **0.134** |
| drum velocity (rounds per minute) | $u_d$ | RPM | **12.27** | **12.73** | **12.42** | **12.42** | **12.42** | **12.50** |
| tangential drum velocity | $u_{d.t}$ | m/s | **1.58** | **1.64** | **1.60** | **1.60** | **1.60** | **1.61** |
| effective velocity due to shearing (2 * $u_{d.t}$) | $u_{eff}$ | m/s | 3.16 | 3.28 | 3.20 | 3.20 | 3.20 | 3.22 |
| average shear rate (with $h_{av.start}$) | $\dot{\gamma}_{av.start}$ | $s^{-1}$ | 23.24 | 23.60 | 23.53 | 23.19 | 22.07 | 22.36 |
| average shear rate (with $h_{av.end}$) | $\dot{\gamma}_{av.end}$ | $s^{-1}$ | 40.51 | 46.86 | 55.17 | 84.21 | 26.23 | 24.03 |
| **Dimensionless numbers calc. from average flow heights $h_{av}$ during the first (start) and last (end) minute of the experiments** | | | | | | | | |
| **Froude number** | $Fr_{start}$ | - | 1.37 | 1.40 | 1.39 | 1.38 | 1.34 | 1.35 |
| | $Fr_{end}$ | - | 1.81 | 1.98 | 2.12 | 2.62 | 1.46 | 1.40 |
| **Reynolds number** | $N_{R.start}$ | - | 162 | 171 | 177 | 181 | 178 | 187 |
| | $N_{R.end}$ | - | 1,877 | 2,171 | 2,557 | 3,902 | 1,215 | 1,114 |
| **Savage number** | $N_{S.start}$ | - | 0.0409 | 0.0429 | 0.0452 | 0.0448 | 0.0401 | 0.0429 |
| | $N_{S.end}$ | - | 0.2815 | 0.4196 | 0.7021 | 2.4965 | 0.0754 | 0.0576 |
| **Bagnold number** | $N_{B.start}$ | - | 310,615 | 297,276 | 276,295 | 250,433 | 215,584 | 193,383 |
| | $N_{B.end}$ | - | 5,421 | 4,195 | 3,189 | 2,855 | 398 | 0 |
| **Mass number** | $N_{M.start}$ | - | 1,915 | 1,738 | 1,562 | 1,385 | 1,209 | 1,034 |
| | $N_{M.end}$ | - | 2.89 | 1.93 | 1.25 | 0.73 | 0.33 | 0 |
| **Darcy number** | $N_{D.av.start}$ | - | 74 | 80 | 90 | 104 | 126 | 148 |
| | $N_{D.av.end}$ | - | 4,724 | 5,622 | 7,087 | 7,860 | 57,963 | - * |
| **Friction number** | $N_{F.av.start}$ | - | $7{,}6 \times 10^6$ | $6{,}9 \times 10^6$ | $6{,}1 \times 10^6$ | $5{,}6 \times 10^6$ | $5{,}4 \times 10^6$ | $4{,}5 \times 10^6$ |
| | $N_{F.av.end}$ | - | 19,257 | 9,996 | 4,542 | 1,144 | 5,277 | 0 |

**Table 5:** Measured (bold) and calculated parameters from the experiments in the **larger rotating drum in Berkeley** with varying volumetric ice contents and **angular fine basalt gravel ($D_{50}$ = 6 mm)**.

| Description of variable | Symbol | Unit | B04-010 | B02-030 | B01-050 | B03-070 | B05-090 |
|---|---|---|---|---|---|---|---|
| volume fraction ice | $\upsilon_{ice}$ | % | 10 | 30 | 50 | 70 | 90 |
| volume fraction gravel | $\upsilon_{gravel}$ | % | 90 | 70 | 50 | 30 | 10 |
| experiment end time | $t_{end}$ | min | **27** | **23** | **25** | **35** | **23** |
| start volume (measured during 1st minute) | $V_{start}$ | $m^3$ | **0.4265** | **0.3965** | **0.4223** | **0.3323** | **0.3343** |
| end volume (measured during $T_{end}$) | $V_{end}$ | $m^3$ | **0.2283** | **0.2248** | **0.2155** | **0.2109** | **0.2176** |
| maximum theoretic pore water saturation (end) | $s_{end}$ | % | 16 | 60 | >100 | >100 | >100 |
| total mass (start) | $m_{tot}$ | kg | 599.9 | 483.5 | 436.0 | 281.0 | 220.1 |
| density of dense rock | $\rho_{rock}$ | $kg/m^3$ | **2,800** | **2,800** | **2,800** | **2,800** | **2,800** |
| density of dense ice | $\rho_{ice}$ | $kg/m^3$ | 910 | 910 | 910 | 910 | 910 |
| weighted density of solids (gravel & ice) | $\rho_s$ | $kg/m^3$ | 2,611 | 2,233 | 1,855 | 1,477 | 1,099 |
| density of fluids (air, start) | $\rho_{f.a.start}$ | $kg/m^3$ | 1.2 | 1.2 | 1.2 | 1.2 | 1.2 |
| weighted density of fluids (water & air, end) | $\rho_{f.a.w.end}$ | $kg/m^3$ | 161 | 600 | 1000 | 1000 | 1000 |
| dynamic bulk density of gravel-ice mixt. (start) | $\rho_{dyn.start}$ | $kg/m^3$ | **1,152** | **1,192** | **1,002** | **1,373** | **923** |
| dynamic bulk density of gravel-ice mixt. (end) | $\rho_{dyn.end}$ | $kg/m^3$ | **1,553** | **2,225** | **2,328** | **1,659** | **1,215** |
| grain size of gravel (≈ median grain size $D_{50}$) | $\delta_r$ | m | 0.0060 | 0.0060 | 0.0060 | 0.0060 | 0.0060 |
| grain size of ice (≈ median grain size $D_{50}$) | $\delta_i$ | m | 0.0200 | 0.0200 | 0.0200 | 0.0200 | 0.0200 |
| weighted grain size (gravel & ice, start) | $\delta_{av}$ | m | 0.0074 | 0.0102 | 0.0130 | 0.0158 | 0.0186 |
| volume fraction of solids (gravel & ice, start) | $\upsilon_{s.start}$ | - | 0.54 | 0.55 | 0.56 | 0.57 | 0.60 |
| volume fraction of fluids (air, start) | $\upsilon_{f.start}$ | - | 0.46 | 0.45 | 0.44 | 0.43 | 0.40 |
| volume fraction of solids (gravel, end) | $\upsilon_{s.end}$ | - | 0.58 | 0.58 | 0.50 | 0.30 | 0.11 |
| volume fraction of fluids (water or air, end) | $\upsilon_{f.end}$ | - | 0.42 | 0.42 | 0.50 | 0.70 | 0.89 |
| fluid viscosity (air at 0°C) | $\eta_{start}$ | Pa s | 0.000017 | 0.000017 | 0.000017 | 0.000017 | 0.000017 |
| fluid viscosity (water at 0°C) | $\eta_{water}$ | Pa s | 0.001787 | 0.001787 | 0.001787 | 0.001787 | 0.001787 |
| weighted fluid viscosity (air & water, at 0°C) | $\eta_{end}$ | Pa s | 0.000301 | 0.001079 | 0.001787 | 0.001787 | 0.001787 |
| maximum flow height (start) | $h_{max.start}$ | m | **0.315** | **0.267** | **0.273** | **0.241** | **0.281** |
| maximum flow height (end) | $h_{max.end}$ | m | **0.206** | **0.176** | **0.183** | **0.130** | **0.137** |
| average flow height (start) | $h_{av.start}$ | m | **0.196** | **0.181** | **0.204** | **0.168** | **0.163** |
| average flow height (end) | $h_{av.end}$ | m | **0.136** | **0.120** | **0.100** | **0.078** | **0.085** |
| drum velocity (rounds per minute) | $u_d$ | RPM | **9.93** | **9.99** | **10.01** | **10.05** | **10.07** |
| tangential drum velocity | $u_{d.t}$ | m/s | **2.08** | **2.09** | **2.10** | **2.10** | **2.11** |
| effective velocity due to shearing (2 * $u_{d.t}$) | $u_{eff}$ | m/s | 4.16 | 4.18 | 4.19 | 4.21 | 4.22 |
| average shear rate (with $h_{av.start}$) | $\dot{\gamma}_{av.start}$ | $s^{-1}$ | 21.22 | 23.11 | 20.55 | 25.05 | 25.87 |
| average shear rate (with $h_{av.end}$) | $\dot{\gamma}_{av.end}$ | $s^{-1}$ | 30.59 | 34.86 | 41.93 | 53.94 | 49.60 |
| **Dimensionless numbers calc. from average flow heights $h_{av}$ during the first (start) and last (end) minute of the experiments** | | | | | | | |
| **Froude number** | $Fr_{start}$ | - | 1.50 | 1.57 | 1.48 | 1.64 | 1.67 |
| | $Fr_{end}$ | - | 1.80 | 1.93 | 2.12 | 2.41 | 2.31 |
| **Reynolds number** | $N_{R.start}$ | - | 80 | 166 | 240 | 432 | 619 |
| | $N_{R.end}$ | - | 590 | 698 | 845 | 1,087 | 999 |
| **Savage number** | $N_{S.start}$ | - | 0.0128 | 0.0313 | 0.0357 | 0.0951 | 0.1449 |
| | $N_{S.end}$ | - | 0.0268 | 0.0473 | 0.1004 | 0.2130 | 0.1653 |
| **Bagnold number** | $N_{B.start}$ | - | 204,079 | 372,114 | 465,884 | 712,129 | 846,811 |
| | $N_{B.end}$ | - | 14,168 | 4,497 | 2,330 | 1,321 | 330 |
| **Mass number** | $N_{M.start}$ | - | 2,540 | 2,239 | 1,940 | 1,647 | 1,369 |
| | $N_{M.end}$ | - | 24.02 | 6.44 | 2.76 | 1.22 | 0.33 |
| **Darcy number** | $N_{D.av.start}$ | - | 58 | 62 | 82 | 82 | 102 |
| | $N_{D.av.end}$ | - | 649 | 2,390 | 4,630 | 7,408 | 31,097 |
| **Friction number** | $N_{F.av.start}$ | - | $15,9 \times 10^6$ | $11,9 \times 10^6$ | $13,1 \times 10^6$ | $7,5 \times 10^6$ | $5,8 \times 10^6$ |
| | $N_{F.av.end}$ | - | 529,007 | 95,049 | 23,216 | 6,204 | 1,995 |

**Table 6:** Measured (bold) and calculated parameters from the experiments in the **larger rotating drum in Berkeley** with varying volumetric ice contents and **slightly rounded fine basalt gravel ($D_{50}$ = 5.6 mm)**.

| Description of variable | Symbol | Unit | B07-040 | B06-050 | B08-060 |
|---|---|---|---|---|---|
| volume fraction ice | $\upsilon_{ice}$ | % | 40 | 50 | 60 |
| volume fraction gravel | $\upsilon_{gravel}$ | % | 60 | 50 | 40 |
| experiment end time | $t_{end}$ | min | **37** | **31** | **31** |
| start volume (measured during 1st minute) | $V_{start}$ | m³ | **0.3568** | **0.3216** | **0.2940** |
| end volume (measured during $T_{end}$) | $V_{end}$ | m³ | **0.2234** | **0.2039** | **0.2140** |
| maximum theoretic pore water saturation (end) | $s_{end}$ | % | 95 | >100 | >100 |
| total mass (start) | $m_{tot}$ | kg | 401.8 | 332.1 | 276.1 |
| density of dense rock | $\rho_{rock}$ | kg/m³ | **2,800** | **2,800** | **2,800** |
| density of dense ice | $\rho_{ice}$ | kg/m³ | 910 | 910 | 910 |
| weighted density of solids (gravel & ice) | $\rho_s$ | kg/m³ | 2,044 | 1,855 | 1,666 |
| density of fluids (air, start) | $\rho_{f.a.start}$ | kg/m³ | 1.2 | 1.2 | 1.2 |
| weighted density of fluids (water & air, end) | $\rho_{f.a.w.end}$ | kg/m³ | 950 | 1,000 | 1,000 |
| dynamic bulk density of gravel-ice mixt. (start) | $\rho_{dyn.start}$ | kg/m³ | **1,533** | **1,515** | **1,447** |
| dynamic bulk density of gravel-ice mixt. (end) | $\rho_{dyn.end}$ | kg/m³ | **2,595** | **2,301** | **1,772** |
| grain size of gravel (≈ median grain size $D_{50}$) | $\delta_r$ | m | 0.0056 | 0.0056 | 0.0056 |
| grain size of ice (≈ median grain size $D_{50}$) | $\delta_i$ | m | 0.0200 | 0.0200 | 0.0200 |
| weighted grain size (gravel & ice, start) | $\delta_{av}$ | m | 0.0114 | 0.0128 | 0.0142 |
| volume fraction of solids (gravel & ice, start) | $\upsilon_{s.start}$ | - | 0.55 | 0.56 | 0.56 |
| volume fraction of fluids (air, start) | $\upsilon_{f.start}$ | - | 0.45 | 0.44 | 0.44 |
| volume fraction of solids (gravel, end) | $\upsilon_{s.end}$ | - | 0.57 | 0.50 | 0.40 |
| volume fraction of fluids (water or air, end) | $\upsilon_{f.end}$ | - | 0.43 | 0.50 | 0.60 |
| fluid viscosity (air at 0°C) | $\eta_{start}$ | Pa s | 0.000017 | 0.000017 | 0.000017 |
| fluid viscosity (water at 0°C) | $\eta_{water}$ | Pa s | 0.001787 | 0.001787 | 0.001787 |
| weighted fluid viscosity (air & water, at 0°C) | $\eta_{end}$ | Pa s | 0.001699 | 0.001787 | 0.001787 |
| maximum flow height (start) | $h_{max.start}$ | m | **0.234** | **0.242** | **0.222** |
| maximum flow height (end) | $h_{max.end}$ | m | **0.192** | **0.151** | **0.134** |
| average flow height (start) | $h_{av.start}$ | m | **0.169** | **0.162** | **0.148** |
| average flow height (end) | $h_{av.end}$ | m | **0.104** | **0.088** | **0.075** |
| drum velocity (rounds per minute) | $u_d$ | RPM | **10.01** | **10.04** | **10.06** |
| tangential drum velocity | $u_{d.t}$ | m/s | **2.10** | **2.10** | **2.11** |
| effective velocity due to shearing (2 * $u_{d.t}$) | $u_{eff}$ | m/s | 4.19 | 4.21 | 4.21 |
| average shear rate (with $h_{av.start}$) | $\dot{\gamma}_{av.start}$ | $s^{-1}$ | 24.80 | 25.97 | 28.46 |
| average shear rate (with $h_{av.end}$) | $\dot{\gamma}_{av.end}$ | $s^{-1}$ | 40.30 | 47.80 | 56.15 |
| **Dimensionless numbers calc. from average flow heights $h_{av}$ during the first (start) and last (end) minute of the experiments** | | | | | |
| **Froude number** | $Fr_{start}$ | - | 1.63 | 1.67 | 1.75 |
| | $Fr_{end}$ | - | 2.07 | 2.26 | 2.45 |
| **Reynolds number** | $N_{R.start}$ | - | 221 | 294 | 399 |
| | $N_{R.end}$ | - | 707 | 839 | 985 |
| **Savage number** | $N_{S.start}$ | - | 0.0479 | 0.0696 | 0.1132 |
| | $N_{S.end}$ | - | 0.0756 | 0.1291 | 0.2091 |
| **Bagnold number** | $N_{B.start}$ | - | 462,151 | 570,574 | 715,138 |
| | $N_{B.end}$ | - | 2,762 | 2,314 | 1,835 |
| **Mass number** | $N_{M.start}$ | - | 2,089 | 1,940 | 1,793 |
| | $N_{M.end}$ | - | 3.91 | 2.76 | 1.86 |
| **Darcy number** | $N_{D.av.start}$ | - | 62 | 65 | 65 |
| | $N_{D.av.end}$ | - | 3,618 | 4,061 | 4,783 |
| **Friction number** | $N_{F.av.start}$ | - | $9{,}6 \times 10^6$ | $8{,}2 \times 10^6$ | $6{,}3 \times 10^6$ |
| | $N_{F.av.end}$ | - | 36,550 | 17,921 | 8,777 |

**Table 7:** Measured (bold) and calculated parameters from the experiments in the **larger rotating drum in Berkeley** with varying volumetric ice contents and **angular coarse dacitic basalt gravel ($D_{50}$ = 16 mm)**. Note that the drum rotation velocity of experiment B13-050 was with 1.25 m/s much slower compared to the ~2.10 m/s for all other Berkeley-runs.

| Description of variable | Symbol | Unit | B11-040 | B09-050 | B10-060 | B12-070 | B13-050 |
|---|---|---|---|---|---|---|---|
| volume fraction ice | $\upsilon_{ice}$ | % | 40 | 50 | 60 | 70 | 50 |
| volume fraction gravel | $\upsilon_{gravel}$ | % | 60 | 50 | 40 | 30 | 50 |
| experiment end time | $t_{end}$ | min | **39** | **29** | **35** | **31** | **55** |
| start volume (measured during 1st minute) | $V_{start}$ | $m^3$ | **0.3735** | **0.3695** | **0.3677** | **0.3731** | **0.4557** |
| end volume (measured during $T_{end}$) | $V_{end}$ | $m^3$ | **0.2454** | **0.2276** | **0.2328** | **0.2454** | **0.2193** |
| maximum theoretic pore water saturation (end) | $s_{end}$ | % | 99 | >100 | >100 | >100 | >100 |
| total mass (start) | $m_{tot}$ | kg | 431.8 | 390.7 | 352.6 | 321.1 | 481.9 |
| density of dense rock | $\rho_{rock}$ | $kg/m^3$ | **2,740** | **2,740** | **2,740** | **2,740** | **2,740** |
| density of dense ice | $\rho_{ice}$ | $kg/m^3$ | 910 | 910 | 910 | 910 | 910 |
| weighted density of solids (gravel & ice) | $\rho_s$ | $kg/m^3$ | 2,008 | 1,825 | 1,642 | 1,459 | 1,825 |
| density of fluids (air, start) | $\rho_{f.a.start}$ | $kg/m^3$ | 1.2 | 1.2 | 1.2 | 1.2 | 1.2 |
| weighted density of fluids (water & air, end) | $\rho_{f.a.w.end}$ | $kg/m^3$ | 990 | 1,000 | 1,000 | 1,000 | 1,000 |
| dynamic bulk density of gravel-ice mixt. (start) | $\rho_{dyn.start}$ | $kg/m^3$ | **1,563** | **1,488** | **1,326** | **1,148** | **941** |
| dynamic bulk density of gravel-ice mixt. (end) | $\rho_{dyn.end}$ | $kg/m^3$ | **1,951** | **1,755** | **1,611** | **1,376** | **1,744** |
| grain size of gravel (≈ median grain size $D_{50}$) | $\delta_r$ | m | 0.0160 | 0.0160 | 0.0160 | 0.0160 | 0.0160 |
| grain size of ice (≈ median grain size $D_{50}$) | $\delta_i$ | m | 0.0200 | 0.0200 | 0.0200 | 0.0200 | 0.0200 |
| weighted grain size (gravel & ice, start) | $\delta_{av}$ | m | 0.0176 | 0.0180 | 0.0184 | 0.0188 | 0.0180 |
| volume fraction of solids (gravel & ice, start) | $\upsilon_{s.start}$ | - | 0.58 | 0.58 | 0.58 | 0.59 | 0.58 |
| volume fraction of fluids (air, start) | $\upsilon_{f.start}$ | - | 0.42 | 0.42 | 0.42 | 0.41 | 0.42 |
| volume fraction of solids (gravel, end) | $\upsilon_{s.end}$ | - | 0.61 | 0.51 | 0.41 | 0.31 | 0.51 |
| volume fraction of fluids (water or air, end) | $\upsilon_{f.end}$ | - | 0.39 | 0.49 | 0.59 | 0.69 | 0.49 |
| fluid viscosity (air at 0°C) | $\eta_{start}$ | Pa s | 0.000017 | 0.000017 | 0.000017 | 0.000017 | 0.000017 |
| fluid viscosity (water at 0°C) | $\eta_{water}$ | Pa s | 0.001787 | 0.001787 | 0.001787 | 0.001787 | 0.001787 |
| weighted fluid viscosity (air & water, at 0°C) | $\eta_{end}$ | Pa s | 0.001769 | 0.001787 | 0.001787 | 0.001787 | 0.001787 |
| maximum flow height (start) | $h_{max.start}$ | m | **0.283** | **0.313** | **0.333** | **0.283** | **0.299** |
| maximum flow height (end) | $h_{max.end}$ | m | **0.188** | **0.160** | **0.164** | **0.188** | **0.210** |
| average flow height (start) | $h_{av.start}$ | m | **0.185** | **0.185** | **0.176** | **0.185** | **0.205** |
| average flow height (end) | $h_{av.end}$ | m | **0.118** | **0.096** | **0.089** | **0.118** | **0.114** |
| drum velocity (rounds per minute) | $u_d$ | RPM | **10.00** | **10.03** | **10.06** | **10.06** | **5.98** |
| tangential drum velocity | $u_{d.t}$ | m/s | **2.09** | **2.10** | **2.11** | **2.11** | **1.25** |
| effective velocity due to shearing (2 * $u_{d.t}$) | $u_{eff}$ | m/s | 4.19 | 4.20 | 4.21 | 4.21 | 2.50 |
| average shear rate (with $h_{av.start}$) | $\dot{\gamma}_{av.start}$ | $s^{-1}$ | 22.63 | 22.70 | 23.93 | 22.77 | 12.22 |
| average shear rate (with $h_{av.end}$) | $\dot{\gamma}_{av.end}$ | $s^{-1}$ | 35.48 | 43.75 | 47.33 | 35.70 | 21.97 |
| **Dimensionless numbers calc. from average flow heights $h_{av}$ during the first (start) and last (end) minute of the experiments** | | | | | | | |
| **Froude number** | $Fr_{start}$ | - | 1.55 | 1.56 | 1.60 | 1.56 | 0.88 |
| | $Fr_{end}$ | - | 1.95 | 2.16 | 2.25 | 1.96 | 1.18 |
| **Reynolds number** | $N_{R.start}$ | - | 485 | 508 | 560 | 556 | 274 |
| | $N_{R.end}$ | - | 5,082 | 6,268 | 6,780 | 5,114 | 3,148 |
| **Savage number** | $N_{S.start}$ | - | 0.0875 | 0.0921 | 0.1124 | 0.1011 | 0.0241 |
| | $N_{S.end}$ | - | 0.4359 | 0.8195 | 1.0341 | 0.4438 | 0.1740 |
| **Bagnold number** | $N_{B.start}$ | - | $1{,}1 \times 10^6$ | $1{,}1 \times 10^6$ | $1{,}1 \times 10^6$ | 972,331 | 573,360 |
| | $N_{B.end}$ | - | 22,001 | 17,614 | 12,802 | 6,269 | 8,845 |
| **Mass number** | $N_{M.start}$ | - | 2,270 | 2,095 | 1,921 | 1,748 | 2,095 |
| | $N_{M.end}$ | - | 4.33 | 2.81 | 1.89 | 1.23 | 2.81 |
| **Darcy number** | $N_{D.av.start}$ | - | 66 | 72 | 76 | 89 | 134 |
| | $N_{D.av.end}$ | - | 4,071 | 4,420 | 5,637 | 11,100 | 8,802 |
| **Friction number** | $N_{F.av.start}$ | - | $12{,}6 \times 10^6$ | $11{,}6 \times 10^6$ | $9{,}6 \times 10^6$ | $9{,}6 \times 10^6$ | $23{,}8 \times 10^6$ |
| | $N_{F.av.end}$ | - | 50,474 | 21,494 | 12,379 | 14,125 | 50,828 |

**Table 8:** Estimated and calculated parameters from **real events**.

| Description of variable | Symbol | Unit | Mt. Cook | Iliamna | Kolka | Brenva | Elm |
|---|---|---|---|---|---|---|---|
| volume fraction ice | $\upsilon_{ice}$ | % | 50 | 60 | 90 | 70 | 0 |
| volume fraction gravel | $\upsilon_{gravel}$ | % | 50 | 40 | 10 | 30 | 100 |
| - | - | - | - | - | - | - | - |
| volume | $V$ | m³ | 60 × 10⁶ | 16 × 10⁶ | 130 × 10⁶ | 6.5 × 10⁶ | 10 × 10⁶ |
| - | - | - | - | - | - | - | - |
| maximum estimated pore water saturation (end) | $s_{end}$ | % | 50 | 80 | 100 | 50 | 0 |
| total mass | $m_{tot}$ | T | 70 × 10⁶ | 15 × 10⁶ | 72 × 10⁶ | 5 × 10⁶ | 28 × 10⁶ |
| density of dense rock | $\rho_{rock}$ | kg/m³ | 2,800 | 2,800 | 2,800 | 2,800 | 2,800 |
| density of dense ice | $\rho_{ice}$ | kg/m³ | 910 | 910 | 910 | 910 | 910 |
| weighted density of solids (rock & ice) | $\rho_s$ | kg/m³ | 1,855 | 1,666 | 1,099 | 1,477 | 2,800 |
| density of fluids (dusty air, start) | $\rho_{f.a.start}$ | kg/m³ | 2 | 2 | 2 | 2 | 2 |
| weighted density of fluids (water & air, end) | $\rho_{f.a.w.end}$ | kg/m³ | 501 | 800 | 1000 | 501 | 2 |
| dynamic bulk density of gravel-ice mixture | $\rho_{dyn}$ | kg/m³ | 1100 | 1000 | 950 | 975 | 1500 |
| - | - | - | - | - | - | - | - |
| grain size of rock | $\delta_r$ | m | 0.3 | 0.2 | 1.0 | 0.4 | 1.0 |
| grain size of ice | $\delta_i$ | m | 0.3 | 0.2 | 1.0 | 0.4 | 1.0 |
| weighted grain size (rock & ice, start) | $\delta_{av}$ | m | 0.3 | 0.2 | 1.0 | 0.4 | 1.0 |
| volume fraction of solids (rock & ice, start) | $\upsilon_{s.start}$ | - | 0.60 | 0.60 | 0.60 | 0.60 | 0.60 |
| volume fraction of fluids (air, start) | $\upsilon_{f.start}$ | - | 0.40 | 0.40 | 0.40 | 0.40 | 0.40 |
| volume fraction of solids (rock, end) | $\upsilon_{s.end}$ | - | 0.60 | 0.60 | 0.60 | 0.60 | 0.60 |
| volume fraction of fluids (water or air, end) | $\upsilon_{f.end}$ | - | 0.40 | 0.40 | 0.40 | 0.40 | 0.40 |
| fluid viscosity (dusty air) | $\eta_{start}$ | Pa s | 0.000020 | 0.000020 | 0.000020 | 0.000020 | 0.000020 |
| fluid viscosity (muddy water at 0°C) | $\eta_{water}$ | Pa s | 0.005000 | 0.005000 | 0.010000 | 0.005000 | - |
| weighted fluid viscosity (air & water, at 0°C) | $\eta_{end}$ | Pa s | 0.002510 | 0.004004 | 0.010000 | 0.002510 | 0.000020 |
| maximum flow height | $h_{max}$ | m | 60 | 30 | 80 | 30 | 20 |
| - | - | - | - | - | - | - | - |
| average flow height (≈ $h_{max}$ /2) | $h_{av}$ | m | 30 | 15 | 40 | 15 | 10 |
| - | - | - | - | - | - | - | - |
| - | - | - | - | - | - | - | - |
| - | - | - | - | - | - | - | - |
| average flow velocity | $u$ | m/s | 55 | 50 | 50 | 40 | 50 |
| average shear rate ($u/h_{av}$) | $\dot{\gamma}_{av}$ | $s^{-1}$ | 1.83 | 3.33 | 1.25 | 2.67 | 5.00 |
| - | - | - | - | - | - | - | - |
| **Dimensionless numbers calc. from average flow heights $h_{av}$ at the start and end of the experiments** | | | | | | | |
| **Froude number** | $Fr_{start}$ | - | 3.2 | 4.1 | 2.5 | 3.3 | 5.1 |
| | $Fr_{end}$ | - | 3.2 | 4.1 | 2.5 | 3.3 | 5.1 |
| **Reynolds number** | $N_{R.start}$ | - | 16,500 | 13,333 | 125,000 | 42,667 | 500,000 |
| | $N_{R.end}$ | - | 32,934 | 26,653 | 125,000 | 85,163 | 500,000 |
| **Savage number** | $N_{S.start}$ | - | 0.0010 | 0.0030 | 0.0040 | 0.0070 | 0.2314 |
| | $N_{S.end}$ | - | 0.0013 | 0.0042 | 0.0062 | 0.0085 | 0.2314 |
| **Bagnold number** | $N_{B.start}$ | - | 23,0 × 10⁶ | 16,7 × 10⁶ | 103 × 10⁶ | 47,3 × 10⁶ | 1,050 × 10⁶ |
| | $N_{B.end}$ | - | 276,096 | 139,860 | 525,000 | 713,944 | 1,050 × 10⁶ |
| **Mass number** | $N_{M.start}$ | - | 1,391 | 1250 | 824 | 8 | 2,100 |
| | $N_{M.end}$ | - | 8.4 | 5.3 | 4.2 | 8.4 | 2,100 |
| **Darcy number** (using $k = 10^{-11}$ m²) | $N_{D.av.start}$ | - | 980 | 600 | 2,426 | 846 | 238 |
| | $N_{D.av.end}$ | - | 123,009 | 120,168 | 1,2 × 10⁶ | 106,212 | 238 |
| **Friction number** | $N_{F.av.start}$ | - | 22,309 × 10⁶ | 5,509 × 10⁶ | 25,828×10⁶ | 6,726 × 10⁶ | 4,536 × 10⁶ |
| | $N_{F.av.end}$ | - | 221 × 10⁶ | 33 × 10⁶ | 85 × 10⁶ | 84 × 10⁶ | 4,537 × 10⁶ |

# PART B: PUBLICATIONS

# Paper I

# 7.22 Long-Runout Landslides

**O Korup,** University of Potsdam, Potsdam, Germany
**D Schneider and C Huggel,** University of Zurich, Zurich, Switzerland
**A Dufresne,** University of Freiburg, Freiburg, Germany

## Glossary

**Avalanche** Generic term describing the flow-like motion of mass movements of varying materials, i.e., snow, ice, debris, rock; originally (and often still) associated with snow.

**Carapace** A surface layer of boulder-sized rocks that typically covers a much thicker deposit of much finer, pervasively fragmented rock particles.

**Frictionite** Partly molten, glass-like, and heavily fragmented rock material found at the base of some large landslide deposits.

**Hazard** The (annual) probability of a potentially adverse landslide occurrence within a specified area and period.

**Risk** A quantitative measure of the annual expected loss from a given landslide impact.

**Rock-mass strength** A composite measure rating the overall quality of rock comprising, among others, properties of intact strength, cracks, and groundwater circulation.

**Runout** The maximum distance a given landslide has traveled, usually measured in the horizontal.

## Abstract

This chapter provides an overview of large ($>10^6$ m$^3$) volcanic and nonvolcanic long-runout landslides characterized by high velocities, large release and deposit volumes, and excess runout. Large long-runout landslides are very rare events and pose substantial challenges to quantitative hazard assessments. Despite several mechanistic theories, there is no commonly agreed-upon explanation of excess runout, which would also entail superposition of processes such as dynamic fragmentation, material bulking, and partial lubrication. Water as a lubricant plays only a minor or limited role given the ample evidence of dry excess runout. Numerical models based on shallow water equations provide some of the best means to realistically simulate rapid flow- and avalanche-like motion over three-dimensional terrain. However, such models critically depend on reliable initial conditions, such as failure volume and scar, material properties, and runout topography.

## 7.22.1 Introduction

The purpose of this chapter is to provide an overview of long-runout landslides: their characteristics, causes, and triggers; and theories on long-runout dynamics. We summarize insights from laboratory tests and numerical modeling and conclude with an overview of consequences and implications for hazard assessment. The scope of this chapter precludes detailed accounts about individual long-runout landslides. Rather, we focus on recent developments and persistent research gaps in the field, especially those concerning rock and debris avalanches that involve $10^6$ m$^3 < V_L < 10^{10}$ m$^3$ in mountainous and volcanic terrain. These are rare compared to the thousands to hundreds of thousands of smaller landslides recorded in various landslide inventories: only five long-runout landslides with $V_L > 10^9$ m$^3$ occurred in the twentieth century (Korup et al., 2007), three of which were linked to volcanic eruptions (Siebert, 1984), that is, Mount St. Helens 1980, USA; Bezymianny 1956, Kamchatka; and Kharimkotan 1933, Kuriles, Russia.

Long-runout landslides involve the rapid down- and outward-motion of hillslope soil and rock materials over distances significantly longer than Coulomb friction would

---

Korup, O., Schneider, D., Huggel, C., Dufresne, A., 2012. Long-runout landslides. In: Shroder, J., Jr., Marston, R., Stoffel, M. (Eds.), Treatise on Geomorphology. Academic Press, San Diego, CA, vol. 7, pp. xx–xx. [Please replace 'xx' by correct page number when available.]

doi:10.1016/B978-0-08-088523-0.00164-7

predict (e.g., Heim, 1932; Corominas, 1996; Legros, 2002). Several mobility indices based on landslide geometry have been suggested to characterize these long-runout slope failures. For example, Scheidegger (1973) proposed that the ratio of total landslide drop height $H$ versus maximum runout length $L$, one of the most common measures in landslide studies, reflected the 'apparent' or 'effective coefficient of friction' $\tan\phi$ during landslide motion. Most terrestrial long-runout landslides have values of $H/L < 0.5$, with $L$ attaining $10^0$–$10^2$ km, and velocities $>10^2$ m s$^{-1}$ (Table 1). Hsü (1975) proposed a measure of excess runout

$$L_e = L - H/\tan 32^\circ \qquad [1]$$

assuming that $\phi = 32^\circ$ aptly represented a typical angle of friction in most rock masses. Another mobility index derives

**Table 1** Documented long-runout landslides with the highest mobility indices

| *Location* | *Latitude* | *Longitude* | *Type*[a] | *Mobility* | *Reference* |
|---|---|---|---|---|---|
| *Volcanic* | | | | | |
| Nevado de Colima, Mexico | 19.56° | −103.61° | VDA-DF | Runout $L$ ~120 km; Deposit area $A_L$ ~2200 km$^2$ | Capra and Macías (2002) |
| Pico de Orizaba, Mexico | 19.03° | −97.28° | VDA | Runout ~95 km | Carrasco-Nunez et al. (2006) |
| Asama, Japan | 36.40° | 138.53° | VDA | Excess runout $L_e$ ~87.4 km; $H/L$ ~0.02 | Siebert (1984) |
| Mawenzi, Tanzania | −3.07° | 37.25° | VDA | $A_L/V_L^{2/3}$ ~311 | Hayashi and Self (1992) |
| *Nonvolcanic* | | | | | |
| Tsergo Ri, Nepal | 28.25° | 85.58° | RSRA | Runout $L$ ~30 km; Excess runout $L_e$ ~24.6 km | Schramm et al. (1998) |
| Lluta, Chile | −18.33° | −69.87° | RS | Deposit area $A_L$ ~600 km$^2$ | Wörner et al. (2002) |
| Belbek, Ukraine | 44.67° | 33.73° | LS | $H/L$ ~0.05 | Panek et al. (2008) |
| Buldar, Pakistan | N/A | N/A | RA | $A_L/V_L^{2/3}$ ~282 | Hewitt (2009) |
| Rondu-Mendi A, Pakistan | 35.63° | 75.12° | RA | Swash ~1100 m | Hewitt et al. (2008) |

[a] VDA, volcanic debris avalanche; DF, debris flow; RSRA, rock slide-rock avalanche; RS, rock slide; LS, lateral spread; RA, rock avalanche.

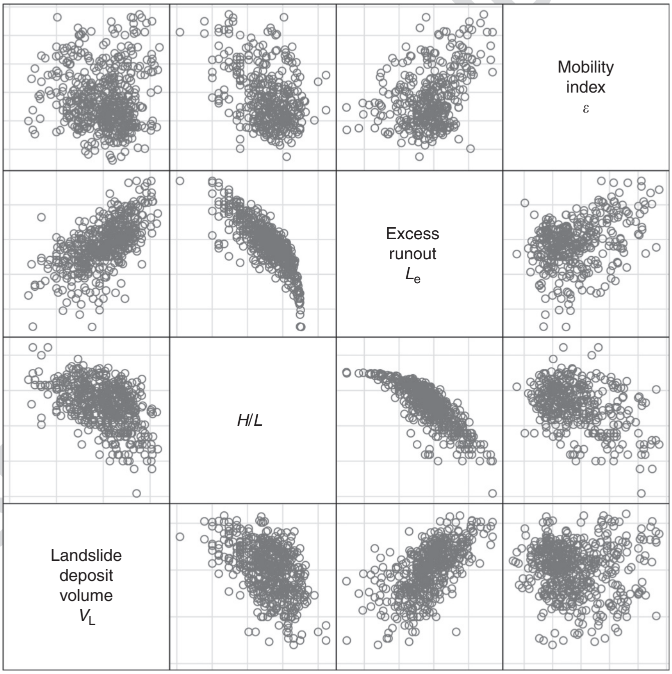

**Figure 1** Scatter–plot matrix of landslide deposit volume $V_L$ and three mobility indices ($H/L$, $L_e$, and $\varepsilon$) for long-runout landslides documented throughout the world. Axes are log–log scaled. Note that $H/L$ and $L_e$ are spuriously correlated given that they use both $H$ and $L$.

from the principle of energy conservation, based on the relationship between landslide-affected area $A_L$ and deposit volume $V_L$,

$$\phi = A_L / V_L^{2/3} \qquad [2]$$

and accounting for possible effects of isometric scaling (Dade and Huppert, 1998). Though useful for initial characterization and comparison (**Figure 1**), these indices are essentially empirical, based on a number of gross simplifications, and fall short of explaining the underlying mechanisms of long runout. Moreover, not a single quantitative descriptor of long-runout landslides is commonly agreed on.

Long-runout landslides comprise extremely rapid rockslides – rock, debris, and ice avalanches, as well as mixed events with water-saturated flow phases (*see* Chapter 7.18 Processes, Transport, Deposition and Landforms: Flow (00160)) – and occur in terrestrial, submarine, and extraterrestrial settings, frequently involving $V_L > 10^6$ m$^3$. Numerous historic accounts underline the destructiveness of long-runout landslides in terms of incurred fatalities and damage worldwide (Heim, 1932; Abele, 1974; Eisbacher and Clague, 1984). For example, recent rock and rockslide debris avalanches in Pakistan and the Philippines each killed >1000 people (Harp and Crone, 2006; Lagmay et al., 2006). Long-runout landslides triggered during the 2008 Wenchuan, China, earthquake ($M_w$ 8.3) caused the death of ~20 000 people, that is, about roughly a third of the total number of lives lost during this earthquake (Qi et al., 2011; **Figure 2**).

## 7.22.2 Catastrophic Long-Runout Landslides

### 7.22.2.1 Types and Characteristics of Long-Runout Landslides

Most long-runout landslides are of the flow or avalanche type (Cruden and Varnes, 1996). Submarine landslides aside, nearly two-thirds of the documented largest catastrophic landslides are rock or debris avalanches (Korup et al., 2007). 'Rock avalanches' and 'volcanic debris avalanches' involve the extremely rapid (>30 m s$^{-1}$), flow-like movement of large volumes (>10$^6$ m$^3$) of initially intact rock masses that are becoming increasingly fragmented during motion. Such comminution may also occur at the base of large coherent rock or block slides (Davies and McSaveney, 2002, 2009).

Importantly, large rock avalanches may travel without significant aid of water. Like many other long-runout landslides, they may be part of multiphase mass movements, for example, evolving from incipient sliding, toppling, or falling of

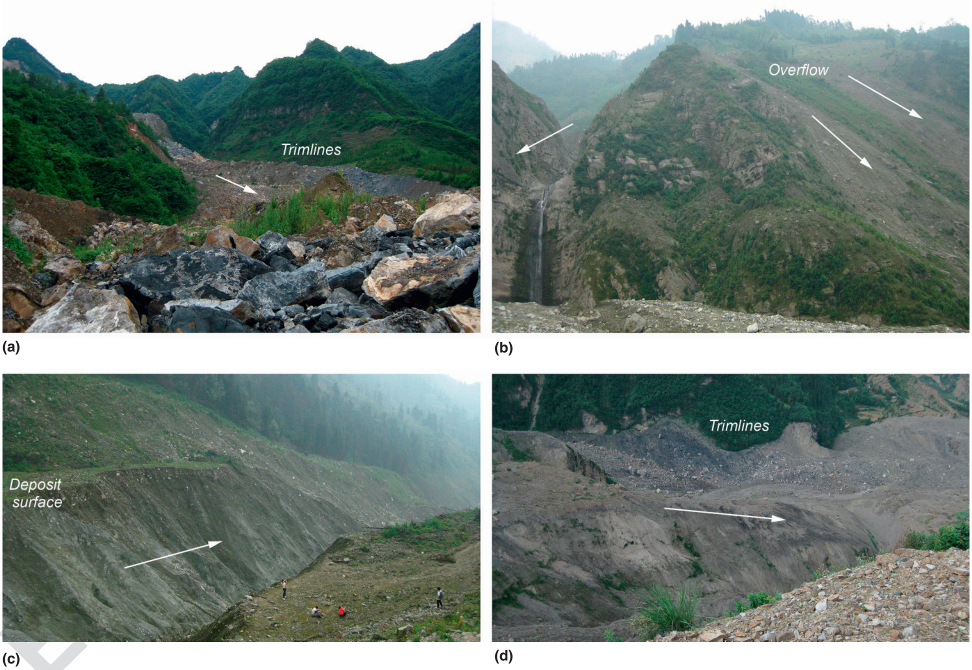

**Figure 2** Deposits from catastrophic long-runout landslides ($V_L > 10^7$ m$^3$) triggered during the 2008 Wenchuan Earthquake, Sichuan, China; photos taken approximately 1 year after the event. Arrows indicate flow direction; note vegetation trimlines. (a) Note moraine-like ~20-m-high lateral ridge below vegetation trimline. Waterfall in (b) is *c.* 20-m high. Note how some of the debris has bypassed the valley exit to the right of the waterfall (arrows); note persons in (c) and terraced slopes in (d) for scale.

coherent rock masses, and subsequently transforming into debris flows. Entrainment (= *bulking*) of valley-fill sediments, snow or glacier ice, as well as catastrophic displacement of water bodies may cause such flow transformations and modulate runout dynamics, spreading, and morphology (Hungr and Evans, 2004; Jibson et al., 2006; Dufresne et al., 2009). The disastrous 1962/70 ice-rock avalanches from Huascarán, Peru, and Karmadon, Russia, in 2002 exemplified extreme runout ($L \sim 19$ km) from substantial ice content (Huggel et al., 2005). Moreover, rock avalanches may run up (or 'swash') against obstacles, juxtaposed hillslopes, or even overtop small interfluves with vertical swash heights of up to ~1 km (Evans, 1989; Hewitt, 1998; **Figure 2(b)**). Swash marks and trimlines indicating lateral super-elevation along the flow path allow estimates of the maximum velocity during motion (**Figure 3**).

The key morphological and depositional features of rock avalanches were summarized by Hewitt (1999) who also pointed out several similarities with glacial sediments. Rock-avalanche deposits are elongate and fan-, lobe-, or tongue-shaped debris sheets with or without lateral levees and may cover up to $10^1$ km$^2$ of valley floors and lower hillslopes. Hummocky deposit surfaces typically feature multiple sets of longitudinal and transverse ridges and swales, whereas raised distal margins are sharply defined, indicating sudden termination of rapid-flow motion. Longitudinal-flow bands occur on the deposit surfaces of high-velocity rock and debris avalanches (Dufresne et al., 2009; **Figure 4**). Depressions may be occupied by ponds and sediments where reworking of debris has helped seal the deposit surface.

Rock-avalanche deposits contain chaotic (mega-)breccias characterized by tightly interlocked, poorly sorted, angular debris. Distinctive features include inverse grading topped by a bouldery *carapace* (Dunning et al., 2006). Below this surface armor, the particle-size distribution of rock-avalanche debris is roughly fractal down to silt size (Crosta et al., 2007). Microfractures $< 10^{-3}$ m further support the notion of pervasive fragmentation during flow. Although morphologically intact, large clasts are distinctly fractured in a characteristic 'jigsaw structure' (e.g., Shreve, 1968) with next to nil detectable void space.

### 7.22.2.2 Peculiarities of Volcanic Long-Runout Landslides

Volcanic debris avalanches are long-runout landslides resulting from catastrophic failure of volcanic flanks or edifices (e.g., Siebert, 1984; Hayashi and Self, 1992) and are, on average, much more mobile than their nonvolcanic counterparts (Stoopes and Sheridan, 1992; Capra and Macías, 2002; Legros, 2002; **Table 1**). Debris-avalanche deposits feature a 'block facies' consisting of coherent $10^{-2}$–$10^2$ m clasts of the source volcano. A 'matrix facies', often found in the lower parts of the deposit, consists of fine-grained, crushed material of a composition identical to the block facies (Ui and Glicken, 1986). The deposits may contain 'toreva blocks', exceptionally large fragments that remained largely intact during motion (Ponomareva et al., 2006; Dufresne et al., 2009). Despite many similarities in morphological appearance, interior structures, rapid emplacement, and excess runout, the gross geometry and material characteristics may differ markedly. **Figure 5** plots $A_L$ against $V_L$ for volcanic versus nonvolcanic avalanche deposits, illustrating that volcanic debris avalanches spread over larger areas. This scaling differs substantially between the two major types of long-runout landslides, partly owing to differing material properties: rock avalanches initiate on dry (unsaturated), massive, and variably jointed rock slopes, whereas volcanic debris avalanches are made up of a mixture of loose debris and solid rock fragments with a generally higher water content. For example, 13% of the release volume of the 1980 Mount St. Helens debris avalanche was water (Glicken, 1996). Volcanoes further host hydrothermally altered and mechanically weak clay minerals and tephra (Reid, 2004), and debris-avalanche deposits composed of such materials may be substantially thinner than those containing fresh debris (Belousov et al., 1999). The differing $A_L$–$V_L$ scaling also reflects the topographically less-confined runout of

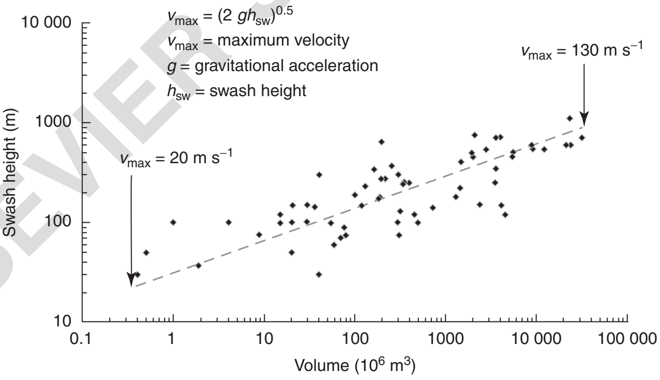

**Figure 3** Swash (= run-up) heights $h_{sw}$ of $n = 65$ long-runout rock avalanches as a function of their deposit volumes $V_L$ (Korup et al., 2007). Using the simple principle of energy conservation, and neglecting additional frictional or fragmentation energies, allows us to estimate the maximum velocity $v_{max}$ of these landslides; $v_{max}$ tends to systematically increase with total volume with an order-of-magnitude variability in $h_{sw}$ for a given $V_L$.

**Figure 4** Morphological similarities of deposits of volcanic debris avalanches and rock avalanches. (a) Large conical hummocks in the deposit of the Jocotitlán, Mexico, volcanic edifice failure. (b) Hummocky topography of the Morimotu debris avalanche, Ruapehu volcano, New Zealand. (c) Medial–distal hummocks of the Round Top rock avalanche deposit, New Zealand.

volcanic debris avalanches onto ring plains and broad inter-edifice valleys filled with volcaniclastic, lacustrine, and fluvial sediments. Narrow bedrock valleys ubiquitous in nonvolcanic mountainous terrain, on the other hand, often serve to obstruct or channelize debris from rock avalanches (Nicoletti and Sorriso-Valvo, 1991).

## 7.22.3 Causes and Triggers

The number of case studies and inventories of long-runout landslides has been growing throughout the world (e.g., Korup et al., 2007). At the same time, the underlying causes and triggers of many prehistoric examples remain unresolved. From the documented cases, however, the most prominent causes of long-runout landslides include:

- gravitational and topographically enhanced stress along (but not limited to) major rock-mass discontinuities such as fault zones and joint systems;
- gradual weakening of rock-mass strength, for example, through repeated earthquake shaking along fault zones, magma chamber inflation, hydrothermal alteration, or rock-mass shattering in hanging walls of reverse and thrust faults (Korup, 2004);
- slope debuttressing and dilatation in landslide scar areas following precursory slope failure or during deglaciation, melting of alpine permafrost ice in jointed rock slopes (Huggel, 2009) or slope loading by incoming materials; and
- incision-driven loss of internal cohesion or lateral support, including weathering, fluvial or artificial slope undercutting.

Given the depths of failure surfaces of most long-runout landslides ($>10$ m), the role of vegetation and root strength is negligible. Many of the above causes are catered for in tectonically active orogens (Hewitt et al., 2008), fault-bounded escarpments (Hermanns and Strecker, 1999), and volcanic arcs and islands (Coombs et al., 2007). Notably, high relief or

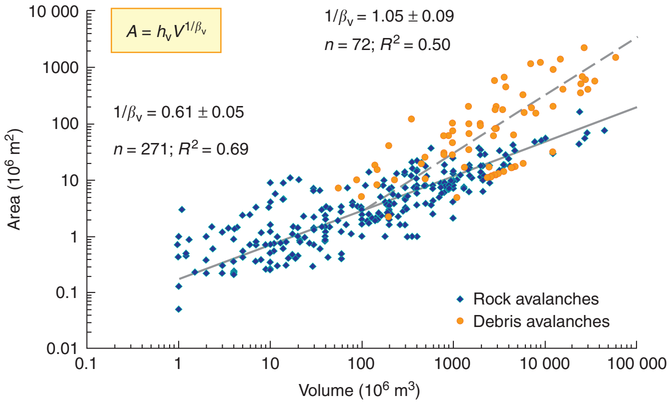

**Figure 5** Relationship between landslide deposit area $A_L$ as a measure of deposit spreading and landslide deposit volume $V_L$ as a measure of size for long-runout landslides throughout the world ($n = 271$ rock avalanches; $n = 72$ volcanic debris avalanches). The independent variable is $V_L$, underlining substantial differences in scaling exponent $1/\beta_v$ because of, among others, landslide material (volcanic vs. nonvolcanic) and runout topography (unconfined volcanic plains vs. narrow mountainous bedrock valleys).

slope steepness is a sufficient, but not necessary, precondition for long-runout landslides (Korup et al., 2007; Panek et al., 2008). One of the world's largest prehistoric rockslide/rock avalanches at Seidmarreh, Iran ($V_L \sim 2.4 \times 10^{10}$ m$^3$), has occurred in rather moderate relief ($<1$ km; defined here as the maximum elevation difference in a 10-km radius). Large rock avalanches are also common in mountainous regions on passive continental margins, where rapid-surface uplift due to postglacial isostatic rebound of the order of $10^1$ mm yr$^{-1}$ causes stress release and rock-slope dilatation (e.g., Osmundsen et al., 2009).

The most frequently reported triggers of large long-runout landslides include:

- large earthquakes;
- volcanic eruptions;
- heavy rainstorms; and
- slope undercutting by fluvial, coastal, and/or anthropogenic processes.

Based on empirical data from the United States, long-runout lateral spreads, debris flows, and rotational and translational rockslides have been triggered by $M \geq 5$ earthquakes, whereas catastrophic long-runout rock avalanches in mountainous terrain have occurred at $M \geq 6$ (Keefer, 1999). Numerous smaller long-runout debris flows or flow slides have been triggered by high-intensity rainstorms, sometimes in conjunction with excessive snowmelt (*see* Chapter 7.18 Processes, Transport, Deposition and Landforms: Flow (00160)). Many long-runout landslides have occurred without any observed triggers (Eisbacher and Clague, 1984; McSaveney, 2002). In these cases, failure may have resulted from exceeded intrinsic stress thresholds such as catastrophic culmination of prior large-scale, rock-slope creep (*sackung*; Radbruch-Hall, 1978; Chigira et al., 2003). Recent investigations of long-runout landslides in glacial environments of Alaska, the European Alps, and the New Zealand Southern Alps found that some failures were preceded by extraordinarily warm periods, followed by rapid drops in temperature. Current hypotheses propose that enhanced meltwater percolation into open-cleft systems during exceptionally warm periods may be blocked by sudden refreezing of the outlets, hence creating high water pressures that promote failure (Huggel et al., 2010).

### 7.22.3.1 Theories and Dynamics of Long Runout

Scientists have been concerned for decades with the question why landslides, particularly those with $V_L > 10^6$ m$^3$, have attained runouts that well exceeded predictions from conventional friction physics (Heim, 1932; Hsü, 1975; Legros, 2002). Several theories have attempted to explain whether and how processes near the landslide base and, to some degree, interaction with the terrain are central to understanding long-runout mechanisms.

In traditional models, water has been argued to reduce friction in two ways, that is, hydrodynamic fluidization and viscous lubrication. 'Hydrodynamic fluidization' refers to pore-fluid pressures that arise when pore spaces become saturated. Similar to debris flows, persistent pore-fluid pressures can reach hydrostatic and higher values at the landslide base (Major and Iverson, 1999; McArdell et al., 2007), linearly decreasing to zero at the surface (Iverson and Denlinger, 2001). This significantly reduces internal friction and shear strength, with rock fragments becoming partially or completely fluidized (Hsü, 1975; Kelfoun and Druitt, 2005). In glacial environments, melting of entrained snow and ice supplies water and helps maintain high pore-water pressures. Depending on entrainment and deposition dynamics, degree of water saturation, and geological characteristics of the substrate, hydrodynamic fluidization can be maintained over $10^0$-km-length scales. Yet in the case of large, catastrophic rock avalanches, the available amount of water is often insufficient to saturate large parts of the moving mass, and the theory fails to explain the long runout of dry (unsaturated) rock avalanches in arid environments (Shreve, 1968; Erismann and Abele, 2001).

'Viscous lubrication' may occur if water is entrained and concentrated along a thin shear layer, for example, during motion over saturated valley-fill deposits or glaciers, forcing pore water to support at least part of the landslide's weight (Voight and Sousa, 1994; Huggel et al., 2005; Prager et al., 2006). Localized 'frictional heating' of water in the shear zone may further elevate pore pressures, given sufficiently low permeability and diffusion rates (Goren and Aharonov, 2007). If snow and ice are part of the landslide mass, the basal melting of frozen water from friction is referred to as 'self-lubrication' (De Blasio and Elverhoi, 2008). In large bedrock landslides, significant but highly localized frictional heating along basal shear bands $10^{-1}$-m thick has been inferred from partial melting of minerals, which produced glassy, pumice-like 'frictionites' (=hyalomylonites) that resemble fault gouge (Legros et al., 2000; Erismann and Abele, 2001; Weidinger and Korup, 2009). Such melting of basal rock layers may also contribute to reducing total shear stress.

'Air lubrication' (Kent, 1966; Shreve, 1968) proposes that rapid landslides may slide on a thin layer of compressed air after topographic jumps, similar to water lubrication. This theory cannot explain the occurrence of long-runout landslide deposits on the Moon (Hsü, 1975). Unrealistically high dynamic air pressure would be necessary to support the overburden stresses involved (Erismann and Abele, 2001; Legros, 2002). Also unclear is how air can be entrapped without escaping immediately through the moving landslide mass (Goguel, 1978). Hence, although reduction of the basal shear strength by air cannot be ruled out, air lubrication is unlikely to be the principal mechanism responsible for long runout (Legros, 2002).

Melosh (1979) advocated 'acoustic fluidization' as a possible long-runout mechanism, by which high-frequency pressure fluctuations generated during the initial collapse and subsequent flow of a mass of rock debris may locally relieve overburden stresses, thereby reducing the frictional resistance (Collins and Melosh, 2003). This mechanism could allow long-runout landslides on Moon, Mars, Venus, and other celestial bodies without the need to invoke further lubricants.

Another model infers 'dynamic rock fragmentation' through rapid breakage of intact rock particles from high strain rates during emplacement with dominant grain-to-grain contact (Davies et al., 1999). Accordingly, elastic strain energy increases until particles fail and the energy converts into kinetic and thermal energy. The broken fragments moving away from the original center of mass also generate a dispersive pressure in the shear layer and lower frictional resistance (Davies and McSaveney, 2009). Numerous accounts of pervasively fragmented debris in large rock slides and rock avalanches armored at the surface by a boulder carapace lend support to this theory (Pollet and Schneider, 2004; Dunning et al., 2006; Crosta et al., 2007; Weidinger and Korup, 2009).

'Granular agitation', originally described for dense snow avalanches by Bartelt et al. (2006), is among the most recent explanations of long runout. In the frictional flow regime, grains move relatively slowly and dissipate energy through long-lasting frictional contacts. The more rapid collisional flow regime leads to stronger agitated grains, which dissipate energy through short-lived collisional contacts (Savage and Hutter, 1991; Iverson and Denlinger, 2001). The individual particles in the collisional regime move chaotically in all directions, with collisions generating dispersive pressure. The energy of the randomly moving particles is called 'granular temperature' or 'random kinetic energy'. A continuous supply of fluctuation energy near the landslide base, where most of the shearing occurs, helps reduce viscous shear resistance of the flowing mass while the upper part behaves like a rigid plug (Bartelt et al., 2006). This model explains early deposition at avalanche tails on steeper slopes as well as their long frontal runout (Bartelt et al., 2007), and has been successfully tested with a dynamic runout model based on shallow-water equations (Preuth et al., 2010) An example of the dynamic evolution and flow characteristics of a long-runout landslide along a channel profile is shown in **Figure 6**.

### 7.22.3.2 Experimental and Numerical Insights

Long-runout landslides are rare and their occurrence is still mostly unanticipated; hence, few observations provide insight

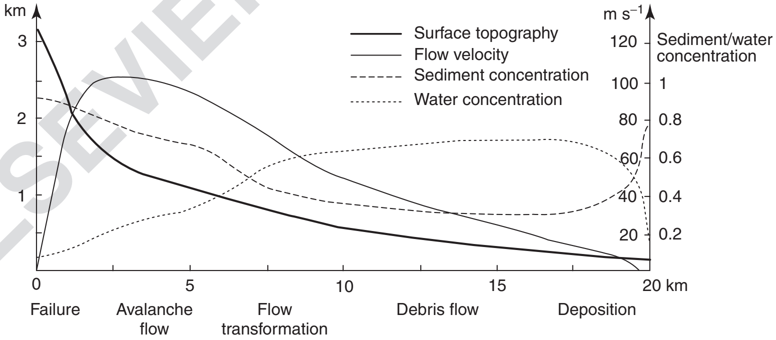

**Figure 6** Simplified longitudinal distribution of flow characteristics for a hypothetical long-runout landslide with given topography and range of flow regimes and transformation, based on the 2002 Kolka-Karamdon event (Huggel et al., 2005).

into their dynamics. Nevertheless, repeated empirical analyses of landslide geometries, laboratory experiments, and numerical modeling demonstrate that, although $H/L$ roughly scales with $V_L$, this ratio inadequately represents the coefficient of friction as proposed originally (Legros, 2002; Okura et al., 2003). Both $H$ and $L$ not only increase with $V_L$, but also add substantial scatter as data-density increases (Figures 1 and 7), thus limiting any universal prediction of landslide runout (Kilburn and Sørensen, 1998; Legros, 2002). Besides, volumetric variations along runout paths from bulking (by either material comminution and/or entrainment of substrate) and redeposition remain difficult to quantify (Hungr and Evans, 2004; Crosta et al., 2009). For example, the 1991 Aoraki/Mt. Cook rock-ice avalanche, New Zealand, had a release volume of $\sim 12 \times 10^6$ m$^3$ compared to a deposition volume of up to $80 \times 10^6$ m$^3$ (McSaveney, 2002). Substrate erosion and bulking on slopes close to the friction angle may further increase runout relative to distances expected from the release volume (Mangeney et al., 2007). This mainly occurs if the amount of material entrained constitutes $>20\%$ of the final deposit volume and if entrainment happens on a sufficiently steep failure slope compared to the terminal, lower runout zone (Dufresne et al., 2009). Conversely, erosion generally also absorbs energy when static grains and blocks have to be accelerated to avalanche velocity (McDougall and Hungr, 2005; Crosta et al., 2009). 'Substrate erodibility' is, thus, a key factor, though entrainment potential and rate might also depend on avalanche velocity, kinetic energy, momentum, frictional work rate, pore-fluid pressure gradient, basal porosity, and other influencing factors (Schneider et al., 2010). These controls remain poorly understood and further research is needed to constrain the parameters most vital in landslide–substrate interaction, substrate response to landslide impact, and, in return, its feedback on mobility.

The destructive power of long-runout landslides renders any 'in-flow measurements' intractable such that the bulk of data typically derive from postevent remote-sensing and field studies. For more recent landslides, availability of pre- and postevent digital topography enables accurate calculation of the volumes involved, as well as the amounts of erosion and

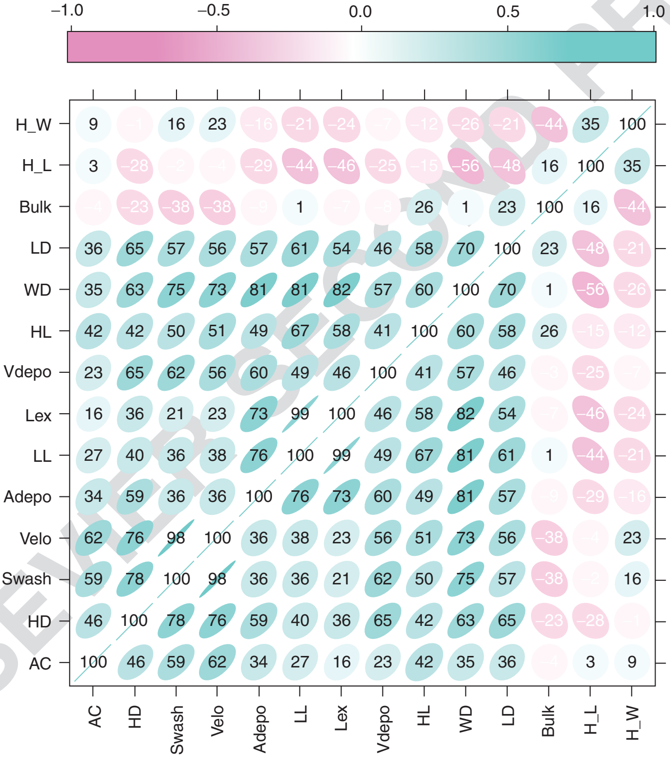

**Figure 7** Corrgram of selected parameters of long-runout landslides throughout the world. Numbers are correlation coefficients (%) superimposed on best-fit ellipses. Note that data have not been log transformed. H_W, height–width ratio of deposit; H_L, $H/L$; bulk, bulking ratio; LD, maximum length of deposit across valley floor; WD, maximum width of deposit along valley floor; HL, maximum drop height; Vdepo, $V_L$; Lex, $L_e$; LL, runout; Adepo, $A_L$; Velo, maximum velocity; Swash, swash height; HD, maximum deposit thickness; AC, upstream catchment area.

deposition (Hancox et al., 2005). In few cases, such as the 2004 Thurwieser rock avalanche, Italy (Sosio et al., 2008) or the rock avalanches triggered by underground nuclear explosion tests at Novaya Zemlya, Russia (Adushkin, 2006), photographs or videos can be used to quantify runout velocities and event durations. Seismic recordings are among the most widely available data containing information about process duration, average velocity, volume, and failure mechanism. However, the interpretation of seismic data to calculate these parameters is complex and not fully understood. Yet, recent time-series matching for some case studies demonstrate promising calibrating possibilities for numerical runout models (Schneider et al., 2010; Figure 8).

'Physical laboratory experiments' help determine certain parameters by direct measurements, including angle of friction, flow depth, front velocity, pore fluid pressure, and erosion given apt control of volume, material, and grain-size distribution (e.g., Mangeney et al., 2010). Such studies have seen a wide range of applications that have been used for

- validating numerical and mathematical codes (e.g., Hutter et al., 1995);
- simulating surface evolution of granular flows (e.g., Aranson et al., 2006);
- back-analyses of field cases (e.g., Körner, 1983; Davies et al., 2006);
- qualitative analyses of dry granular runout on rigid slopes and runout paths (e.g., Iverson et al., 2004; Manzella and Labiouse, 2009);
- dimensionless comparison between analog and natural geometric parameters of avalanches (e.g., Davies and McSaveney, 1999; Shea and van Wyk de Vries, 2009);
- testing the effect of thin layers of erodible material on an otherwise rigid, nonerodible runout path (e.g., Mangeney et al., 2007); and
- investigating effects of erodible, deformable runout-path materials of varying mechanical properties and thicknesses (Dufresne, 2009).

Some of the persistent problems of laboratory experiments relate to size effects, which increase with the ratio of event over experiment scale. Not all aspects of natural long-runout landslides such as dynamic fragmentation in rock avalanches can be represented accordingly in downscaled models. Nevertheless, these restrictions of small-scale laboratory experiments are greatly outweighed by the advantages of systematic control of boundary conditions and parameters to determine their individual or combined contributions to the simulation results (Figure 9). Thus, physical experiments are well suited to detect and measure relative changes in flow rheology by varying among others the grain size distribution; clay, water, and ice content; topography; and terrain roughness. Physical models are generally the only possibility to acquire quantitative physical data, enabling comparison of dynamic and geometric parameters with natural prototypes through proper scaling and model assumptions.

'Numerical models' close the gap of missing data and help improve process understanding, particularly that of initial failure and landslide motion. Most models are mainly used to back-analyze past events. Prognostic modeling of future events, particularly the prediction of areas likely to be affected by landslides, is only possible if detailed scenarios and knowledge of the failure type, volume, erosion, flow transformation, material properties, and friction coefficients are available. These requirements are critical and usually difficult to achieve because of considerable uncertainty tied to a high number of variables. Hence, the inevitable need for simplification yields predictions that must remain partly speculative unless calibrated for a specific case study. In their most advanced form, dynamic runout models based on shallow-water equations simulate transport and deposition of the moving mass over three-dimensional (3D) terrain, involving parameters such as flow depth, deposition height, erosion, velocities, kinetic energy, frictional work rate, and flow pressure (e.g., Hungr and McDougall, 2009; Christen et al., 2010).

### 7.22.3.3 Geomorphic Consequences

Because of their enormous volume, the larger, long-runout landslides produce geomorphic effects over $10^0$- to $10^3$-km-length scales. With increasing volume, the probability of significant geomorphic 'interference with the drainage network', and, thus, spatial and temporal translation of geomorphic impact, also increases. This issue is understated in many state-of-the-art, landslide hazard assessments, and the potential for any adverse off-site or long-term effects are not readily addressed. Valley filling with subsequent lake damming is a common geometric and hydrologic effect of long-runout landslide emplacement. For example, the earthquake-triggered ($M$ 7.4) 1911 Usoi rockslide-rock avalanche ($V_L \sim 2.2 \times 10^9$ m$^3$) in the Tajik Pamir, formed a 600-m-high natural dam across the Murgab River in 1911 at the former site of the Usoi village, impounding Lake Sarez, which has grown to $>60$ km in length and now contains $\sim 17$ km$^3$ of water. Failure of the dam would release a catastrophic outburst flow that would affect five million people living $>2000$ km downstream (Schuster and Alford, 2004).

In glaciated terrain, ice and rock avalanches entering proglacial or otherwise naturally dammed lakes cause displacement waves that may lead to dam overtopping and subsequent catastrophic dam failure (Schuster and Alford, 2004; Hubbard et al., 2005; Korup and Tweed, 2007). Known as 'aluviones' in South America, such process cascades are exemplified by the catastrophic mass movement that originated from the peak of Nevados Huascaran, Peruvian Andes, in the wake of the 1970 $M_s$ 7.8 earthquake (Evans et al., 2009a). The event initiated as a rockfall containing substantial amounts of glacier ice and entrained significant amounts of snow and glacial deposits. The mass movement then transformed into a highly mobile debris flow that obliterated the town of Yungay, killing thousands of inhabitants, before sweeping farther for several kilometers, causing temporary damming of the Rio Santa and recurrent flooding downstream.

Where mountainous terrain sustains thick loess cover, earthquakes may trigger extremely mobile and potentially highly destructive loess flows that may originate on hillslopes with moderate to low inclinations and readily interfere with the drainage network, causing ephemeral natural dams ($<15°$; Zhang and Wang, 2007). Evans et al. (2009b) reconstructed exceptionally large and long-runout rock fall/loess

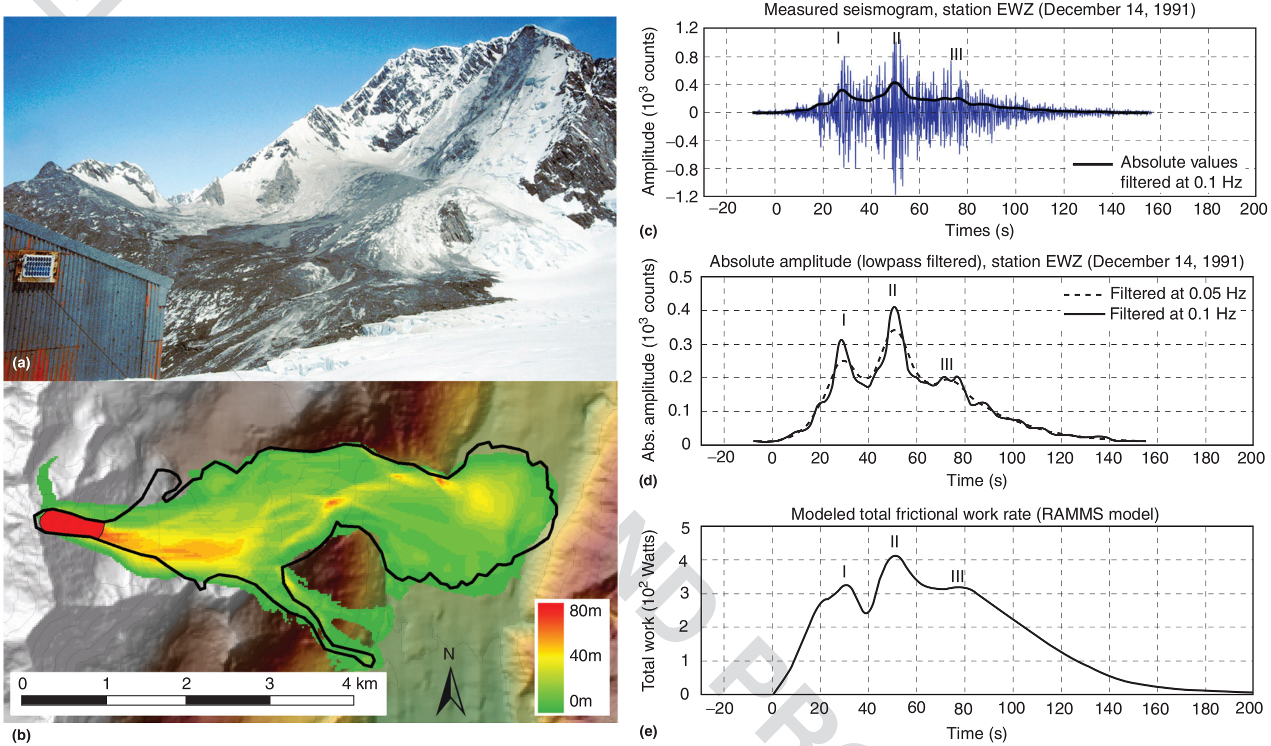

**Figure 8** Example of numerical modeling of a long-runout landslide: 1991 Aoraki/Mt. Cook rock-ice avalanche, New Zealand, had a release volume of 12 × $10^6$ $m^3$, and deposited an estimated 40–80 × $10^6$ $m^3$. (a) Overview of source zone and upper travel path. Note run-up on left ridge and traces of snow/ice entrainment as well as deposited material (photo taken 16 December 1991 by I Owens). (b) Calculated maximum flow heights from numerical model. Red area is detachment zone; deposition is to the right; black outline is mapped extent from field visits (McSaveney, 2002). (c) Seismogram of the event from seismic station EWZ located 58 km east of source area. (d) Detail of filtered absolute seismic amplitude shown in (c). (e) Total frictional work rate as calculated by the numerical model. Note identical time axis and consistence of major peaks I, II, and III that can be used to calibrate numerical model (Schneider et al., 2010).

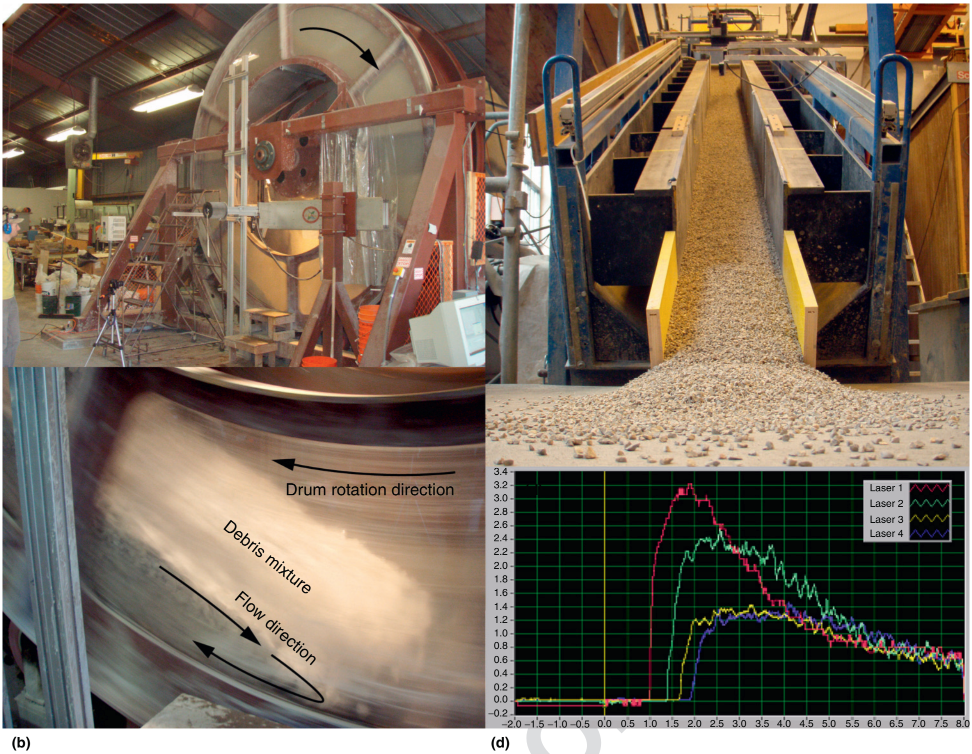

**Figure 9** Experimental setups for physical modeling of long-runout landslides. (a) Vertically clockwise rotating drum with 4-m diameter at the Richmond Field Station, UC Berkeley, USA. (b) Detail of the standing bulk of flowing debris in the drum. (c) Dry gravel avalanche experiment in a straight chute at the Swiss Federal Institute for Forest, Snow and Landscape Research WSL, Birmensdorf, Switzerland. (d) Laser measurements at different positions.

flow triggered by the 1949 Khait earthquake, Tajikistan, which moved at average travel angles of as low as 2° (*see* Chapter 7.18 Processes, Transport, Deposition and Landforms: Flow (00160)).

### 7.22.3.4 Hazard Implications

Determining the hazard of long-runout landslides in a meaningful way requires quantitative estimates of the failure location, runout path, and depositional area, as well as the probability of occurrence for a given event size or larger. Despite the significant damage potential of catastrophic long-runout landslides in many parts of the world, strategies for quantifying and managing associated hazards and risks are not equally well developed. In countries where such landslides occur frequently (e.g., Canada, New Zealand, China, and Japan), a number of studies have explicitly estimated hazard levels. This especially applies to volcanic debris avalanches in Alaska, the Pacific Northwest of the USA, and Japan, given that potential detachment areas are spatially limited to volcanic edifices and partly known beforehand on the basis of geomorphic and stratigraphic evidence (e.g., Waythomas et al., 2000). At the other end of the spectrum, practical management has rarely considered long-runout landslides other than as residual or acceptable risks. This is largely because standard engineering countermeasures that modulate or reduce physical impact forces of smaller landslides and debris flows are largely inefficient for large long-runout failures (Crosta et al., 2006). Further key challenges include estimating the probability of their occurrence for a given size (usually $A_L$ or $V_L$) as a prerequisite for quantitative hazard assessment. Statistical analyses of landslide-size distributions of substantially complete inventories for a given region have become a popular method (e.g., Malamud et al., 2004). Alternatively, first-order hazard estimates of long-runout landslides may use magnitude–frequency distributions of their triggers such as earthquakes as a surrogate, which relies heavily on empirical thresholds (Keefer, 1999).

Despite featuring up to tens of thousands of individual landslides, most inventories remain limited to $V_L \ll 10^7$ m$^3$, thus possibly missing out on a large number of long-runout

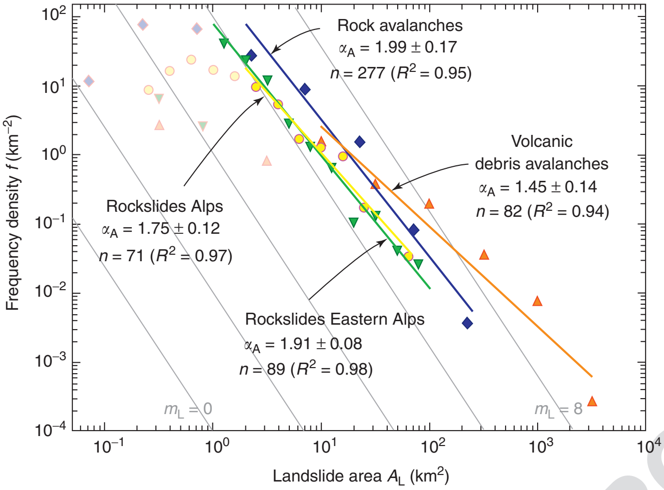

**Figure 10** Estimated frequency density as a function of $A_L$ of $n = 277$ rock avalanches, and $n = 82$ volcanic debris avalanches collected from worldwide data (Korup et al., 2007). Also shown are subsets of $n = 71$ large (and mainly catastrophic) long-runout rockslides in the European Alps, and $n = 89$ rockslides of a more detailed regional inventory in the eastern Alps. Semitransparent data points show rollovers and were excluded because of likely undersampling (note that most substantially complete landslide inventories rarely feature landslides with $A_L > 10^0$ km$^2$). Straight color-coded lines indicate best fit of inverse power-law models valid over two orders of magnitude. Note that scaling exponents $\alpha_A$ for rock-avalanche data overlap within one standard deviation ($\pm 1\sigma$) despite the differing timescales, tectonic and climatic regimes, and topographic characteristics encompassed by these data; $m_L$ is the landslide-magnitude scale (Malamud et al., 2004), highlighting deviations of trends from an inverse gamma model used to approximate substantially complete landslide inventories; grey lines are power-law tails of this distribution with values of $m_L$.

slope failures (Figure 10). Exceptions confirm this rule (e.g., Dussauge et al., 2003) and show that quantifying probabilities of occurrence of rare events require inventories that span $> 10^3$ years (e.g., Whitehouse and Griffiths, 1983; Figure 11). Obvious limitations to this approach include the diminishing preservation potential of landslide deposits with size and emplacement age (e.g., Korup and Clague, 2009; Figure 12), particularly in actively eroding landscapes. This results in inventories containing landslide samples rather than nearly complete populations, which, in turn, may weigh heavily on the robustness of derived magnitude–frequency statistics (Figure 10).

Identifying source areas for potential long-runout landslides is a further challenge, and early warning is rarely feasible without any prior detection and detailed monitoring of suspected failure sites (Crosta and Agliardi, 2002). In such ideal cases, failure volumes may be estimated or simply assumed for scenario-based, runout simulations. The potential of predictability increases where long-runout landslides are preceded by slow-moving, deep-seated slope deformation, although such low-activity phases may extend from $10^1$–$10^{3-}$ years prior to catastrophic 'creep rupture' (Radbruch-Hall, 1978). Recent progress has been achieved by ground-based and spaceborne interferometric synthetic aperture radar (InSAR; e.g., Strozzi et al., 2010), which may detect surface deformation at an accuracy of $10^{-3}$–$10^{-1}$ m over large areas. Likewise, ground- or air-based light detection and ranging (LiDAR) measurements yield similarly detailed digital terrain models for detecting large slope instabilities (e.g., Lipovsky et al., 2008). Despite these technological advances, it remains demanding to reliably predict the timing, magnitude, and type of failure (Crosta and Agliardi, 2002).

Although InSAR and LiDAR techniques are typically applied years to days before failure, recent studies analyzing seismic signals seem promising for immediate early warning in the future. For example, long-runout rock-ice avalanches with $V_L \sim 10^7$ m$^3$ have episodically detached from Iliamna volcano, Alaska. Together with several ice failures, they were associated with a sequence of small earthquakes 0.5–2 h prior to failure (Caplan-Auerbach and Huggel, 2007). If such precursory seismic signals could be analyzed in real time and unambiguously recognized as initiating failure processes, they could be an important tool for early warning of rock-ice avalanches.

## 7.22.4 Conclusions and Outlook

The chapter concludes with an overview of consequences and implications for hazard assessment:

- Both volcanic and nonvolcanic long-runout landslides are generally associated with high velocities and large release and deposit volumes; excess runout is reserved mainly for landslides $> 10^6$ m$^3$.

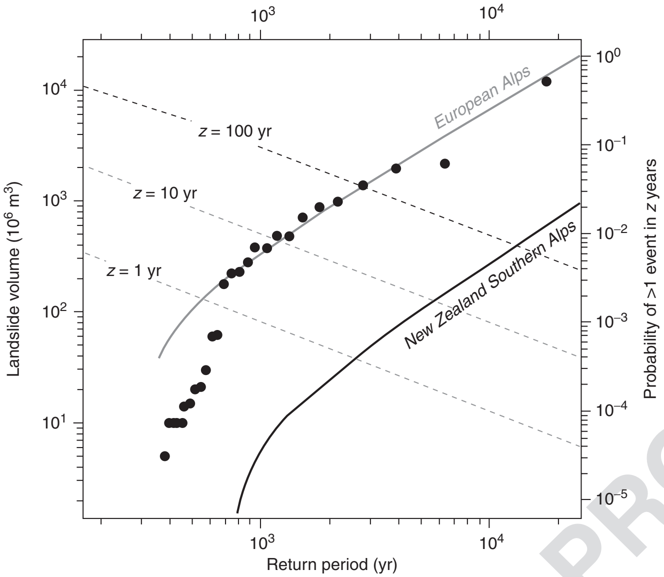

**Figure 11** Landslide volume $V_L$ as a function of its return period estimated from a dataset of $n = 31$ (black dots and grey line) compared to Weibull model fitted to $n = 14$ Holocene long-runout rock avalanches (black line) with $V_L > 20 \times 10^6$ m$^3$ in the European Alps and in the central Southern Alps, New Zealand (Whitehouse and Griffiths, 1983; Korup et al., 2007). Right-hand $y$-axis shows exceedance probability of occurrence (i.e., hazard) of a rock avalanche of known return period within $z = 1$, 10, and 100 years (dashed lines).

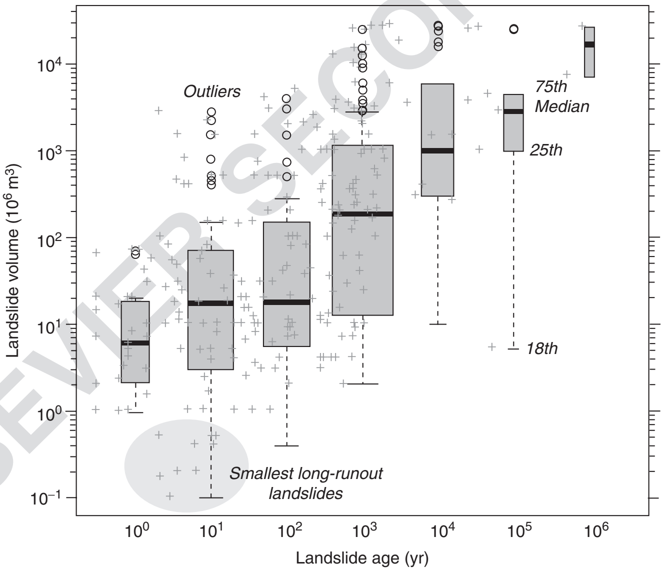

**Figure 12** Box and whisker plot shows the age–size distribution of $n = 273$ long-runout rock and debris avalanches throughout the world (grey crosses are raw data; note several historic long-runout landslides with volumes $< 10^6$ m$^3$). Box width is proportional to square root of sample number log-binned by time interval. The distinct lack of smaller deposits of greater age indicates that geomorphic and stratigraphic evidence of larger landslides tends to persist in the landscape much longer than those of smaller events, despite the broad range of climatic and tectonic settings and the erosion rates that the data encompass (after Korup and Clague, 2009).

- The scaling between landslide volume and affected area differs significantly between volcanic and nonvolcanic landslides owing to differences in runout topography, material properties, and water content.
- Despite a number of mechanistic theories, there is no common agreement on the explanation of excess runout. Any such unifying theory may want to consider the superposition of processes such as dynamic fragmentation, material bulking, and partial lubrication. In fact, the diversity of processes involved with long-runout landslides suggests that no single explanation is fully sufficient. However, water as a lubricant plays only a minor or limited role given the ample evidence of dry excess runout.
- Numerical models based on shallow-water equations provide some of the best means to realistically simulate rapid-flow- and avalanche-like motion over 3D terrain, given that physical experiments suffer from inadvertent scale effects. However, numerical runout models critically depend on realistic initial conditions, such as failure volume and scar, material properties, and runout topography.
- Large, long-runout landslides are very rare events and pose substantial challenges to quantitative hazard assessments. Empirical magnitude–frequency relationships derived from landslide inventories provide a means to at least constrain the probability of occurrence for a given region to an order of magnitude.

## References

Abele, G., 1974. Bergstürze in den Alpen–ihre Verbreitung, Morphologie und Folgeerscheinungen. Wissenschaftliche Alpenvereinshefte 25. Dt. Alpenverein, München, 230 pp.

Adushkin, V.V., 2006. Mobility of rock avalanches triggered by underground nuclear explosions. In: Evans, S.G., Scarascia Mugnozza, G., Strom, A., Hermanns, R.L. (Eds.), Landslides from Massive Rock Slope Failures. Springer, Dordrecht, pp. 267–284.

Aranson, I.S., Malloggi, F., Clément, E., 2006. Transverse Instability of Avalanches in Granular Flows Down An Incline. Physical Review E-Statistical, Nonlinear, and Soft Matter Physics, 73, 4 pp.

Bartelt, P., Buser, O., Platzer, K., 2006. Fluctuation–dissipation relations for granular snow avalanches. Journal of Glaciology 52, 631–643.

Bartelt, P., Buser, O., Platzer, K., 2007. Starving avalanches: frictional mechanisms at the tails of finite-sized mass movements. Geophysical Research Letters 34, L20407.

Belousov, A., Belousova, M., Voight, B., 1999. Multiple edifice failures, debris avalanches and associated eruptions in the Holocene history of Shiveluch volcano, Kamchatka, Russia. Bulletin of Volcanology 61, 324–342.

Caplan-Auerbach, J., Huggel, C., 2007. Precursory seismicity associated with frequent, large ice avalanches on Iliamna volcano, Alaska, USA. Journal of Glaciology 53, 128–140.

Capra, L., Macías, J.L., 2002. The cohesive Naranjo debris-flow deposit (10 km$^3$): a dam breakout flow derived from the Pleistocene debris-avalanche deposit of Nevado de Colima Volcano (Mexico). Journal of Volcanology and Geothermal Research 117, 213–235.

Carrasco-Nunez, G., Diaz-Castellon, R., Siebert, L., Hubbard, B., Sheridan, M.F., Rodriguez, S.R., 2006. Multiple edifice-collapse events in the Eastern Mexican Volcanic Belt: the role of sloping substrate and implications for hazard assessment. Journal of Volcanology and Geothermal Research 158, 151.

Chigira, M., Wang, W.N., Furuya, T., Kamai, T., 2003. Geological causes and geomorphological precursors of the Tsaoling landslide triggered by the 1999 Chi–Chi earthquake, Taiwan. Engineering Geology 68, 259–273.

Christen, M., Kowalski, J., Bartelt, P., 2010. RAMMS: numerical simulation of dense snow avalanches in three-dimensional terrain. Cold Regions Science and Technology 63, 1–14.

Collins, G.S., Melosh, H.J., 2003. Acoustic fluidization and the extraordinary mobility of sturzstroms. Journal of Geophysical Research 108(B10), 2473.

Coombs, M.L., White, S.M., Scholl, D.W., 2007. Massive edifice failure at Aleutian arc volcanoes. Earth and Planetary Science Letters 256, 403–418.

Corominas, J., 1996. The angle of reach as a mobility index for small and large landslides. Canadian Geotechnical Journal 33, 260–271.

Crosta, G.B., Agliardi, F., 2002. How to obtain velocity thresholds for large rockslides. Physics and Chemistry of the Earth 27, 1557–1565.

Crosta, G.B., Chen, H., Frattini, P., 2006. Forecasting hazard scenarios and implications for the evaluation of countermeasure efficiency for large debris avalanches. Engineering Geology 83, 236–253.

Crosta, G.B., Frattini, P., Fusi, N., 2007. Fragmentation in the Val Pola rock avalanche, Italian Alps. Journal of Geophysical Research 112, F011006.

Crosta, G.B., Imposimato, S., Roddeman, D., 2009. Numerical modelling of entrainment/deposition in rock and debris-avalanches. Engineering Geology 109, 135–145.

Cruden, D.M., Varnes, D.J., 1996. Landslide types and processes. In: Turner, A.K., Schuster, R.L. (Eds.), Landslides, Investigation and Mitigation. Special Report 247. Transportation Research Board, National Research Council, Washington, DC, pp. 36–75.

Dade, W.B., Huppert, H.E., 1998. Long-runout rockfalls. Geology 26, 803–806.

Davies, T.R., McSaveney, M.J., 1999. Runout of dry granular avalanches. Canadian Geotechnical Journal 36, 313–320.

Davies, T.R., McSaveney, M.J., 2002. Dynamic simulation of the motion of fragmenting rock avalanches. Canadian Geotechnical Journal 39, 789–798.

Davies, T.R., McSaveney, M.J., 2009. The role of rock fragmentation in the motion of large landslides. Engineering Geology 109, 67–79.

Davies, T.R., McSaveney, M.J., Beetham, R.D., 2006. Rapid block glides: slide-surface fragmentation in New Zealand's Waikaremoana landslide. Quarterly Journal of Engineering Geology and Hydrogeology 39, 115–129.

Davies, T.R.H., McSaveney, M.J., Hodgson, K.A., 1999. A fragmentation-spreading model for long-runout rock avalanches. Canadian Geotechnical Journal 36, 1096–1110.

De Blasio, F.V., Elverhoi, A., 2008. A model for frictional melt production beneath large rock avalanches. Journal of Geophysical Research 113, F02014.

Dufresne, A., 2009. Influence of runout path material on rock and debris avalanche mobility: field evidence and analogue modelling. Ph.D. thesis, University of Canterbury, Christchurch, New Zealand.

Dufresne, A., Davies, T.R., McSaveney, M.J., 2009. Influence of runout-path material on emplacement of the Round Top rock avalanche, New Zealand. Earth Surface Processes and Landforms 35, 190–201.

Dunning, S.A., Rosser, N.J., Petley, D.N., Massey, C.R., 2006. Formation and failure of Tsatichhu landslide dam, Bhutan. Landslides 3, 107–113.

Dussauge, C., Grasso, J.R., Helmstetter, A.S., 2003. Statistical analysis of rockfall volume distributions: implications for rockfall dynamics. Journal of Geophysical Research 108(B6), 2286.

Eisbacher, G.H., Clague, J.J., 1984. Destructive Mass Movements in High Mountains–Hazard and Management. Geological Survey of Canada Paper 84-16, 230 pp.

Erismann, T.H., Abele, G., 2001. Dynamics of Rockslides and Rockfalls. Springer, Heidelberg, 316 pp.

Evans, S.G., 1989. Rock avalanche run-up record. Nature 340, 271.

Evans, S.G., Bishop, N.F., Fidel Smoll, L., Valderrama Murillo, P., Delaney, K.B., Oliver-Smith, A., 2009a. A re-examination of the mechanism and human impact of catastrophic mass flows originating on Nevado Huascarán, Cordillera Blanca, Peru in 1962 and 1970. Engineering Geology 108, 96–118.

Evans, S.G., Roberts, N.J., Ischuk, A., Delaney, K.B., Morozova, G.B., Tutubalina, O., 2009b. Landslides triggered by the 1949 Khait earthquake, Tajikistan, and associated loss of life. Engineering Geology 109, 195–212.

Glicken, H., 1996. Rockslide: Debris Avalanche of May 18, 1980, Mount St. Helens volcano, Washington. US Geological Survey Open-File Report 96-677, 90 pp.

Goguel, J., 1978. Scale-dependent rockslide mechanisms, with emphasis on the role of pore fluid vaporization. In: Voight, B. (Ed.), Rockslides and Avalanches, 1: Natural Phenomena. Elsevier, Amsterdam, pp. 693–705.

Goren, L., Aharonov, E., 2007. Long runout landslides: the role of frictional heating and hydraulic diffusivity. Geophysical Research Letters 34, L07301. doi:10.1029/2006GL028895.

Hancox, G.T., McSaveney, M.J., Manville, V.R., Davies, T.R.H., 2005. The October 1999 Mt Adams rock avalanche and subsequent landslide dam-break flood and effects in Poerua River, Westland, New Zealand. New Zealand Journal of Geology and Geophysics 48, 683–705.

Harp, E.L., Crone, A.J., 2006. Landslides triggered by the October 8, 2005. Pakistan earthquake and associated landslide-dammed reservoirs. US Geological Survey Open-File Report 2006-1052, 13 pp.

Hayashi, J.N., Self, S., 1992. A comparison of pyroclastic flow and debris avalanche mobility. Journal of Geophysical Research 97(B6), 9063–9071.

Heim, A., 1932. Bergsturz und Menschenleben. Beiblatt zur Vierteljahresschrift der Naturforschenden Gesellschaft 20. Zürich, 217 pp.

Hermanns, R.L., Strecker, M.R., 1999. Structural and lithological controls on large Quaternary rock avalanches sturzstroms in arid northwestern Argentina. Geological Society of America Bulletin 111, 934–948.

Hewitt, K., 1998. Catastrophic landslides and their effects on the Upper Indus streams, Karakoram Himalaya, northern Pakistan. Geomorphology 26, 47–80.

Hewitt, K., 1999. Quaternary moraines vs catastrophic rock avalanches in the Karakoram Himalaya, northern Pakistan. Quaternary Research 51, 220–237.

Hewitt, K., Clague, J.J., Orwin, J.F., 2008. Legacies of catastrophic rock-slope failures in mountain landscapes. Earth-Science Reviews 87, 1–38.

Hsü, K.J., 1975. Catastrophic debris streams (sturzstroms) generated by rockfalls. Geological Society of America Bulletin 86, 129–140.

Hubbard, B., Heald, A., Reynolds, J.M., et al., 2005. Impact of a rock avalanche on a moraine-dammed proglacial lake: Laguna Safuna Alta, Cordillera Blanca, Peru. Earth Surface Processes and Landforms 30, 1251–1264.

Huggel, C., 2009. Recent extreme slope failures in glacial environments: effects of thermal perturbation. Quaternary Science Reviews 28, 1119–1130.

Huggel, C., Salzmann, N., Allen, S., et al., 2010. Recent and future warm extreme events and high-mountain slope stability. Philosophical Transactions of the Royal Society A 368, 2435–2459.

Huggel, C., Zgraggen-Oswald, S., Haeberli, W., Kääb, A., Polkvoj, A., Galushkin, I., Evans, S.G., 2005. The 2002 rock/ice avalanche at Kolka/Karmadon, Russian Caucasus: assessment of extraordinary avalanche formation and mobility, and application of QuickBird satellite imagery. Natural Hazards and Earth System Sciences 5, 173–187.

Hungr, O., Evans, S.G., 2004. Entrainment of debris in rock avalanches: an analysis of a long run-out mechanism. Geological Society of America Bulletin 116, 1240–1252.

Hungr, O., McDougall, S., 2009. Two numerical models for landslide dynamic analysis. Computers and Geosciences 35, 978–992.

Hutter, K., Koch, T., Pluss, C., Savage, S.B., 1995. The dynamics of avalanches of granular material from initiation to runout. Part II: Experiments. Acta Mechanica 109, 127–165.

Iverson, R.M., Denlinger, R.P., 2001. Flow of variably fluidized granular masses across three-dimensional terrain–1. Coulomb mixture theory. Journal of Geophysical Research 106(B1), 537–552.

Iverson, R.M., Logan, M., Denlinger, R.P., 2004. Granular avalanches across irregular three-dimensional terrain: 2. Experimental tests. Journal of Geophysical Research 109, F01015. doi:10.1029/2003JF000084.

Jibson, R.W., Harp, E.L., Schulz, W., Keefer, D.K., 2006. Large rock avalanches triggered by the *M*7.9 Denali Fault, Alaska, earthquake of 3 November 2002. Engineering Geology 83, 144–160.

Keefer, D.K., 1999. Earthquake-induced landslides and their effects on alluvial fans. Journal of Sedimentary Research 69, 84–104.

Kelfoun, K., Druitt, T.H., 2005. Numerical modeling of the emplacement of Socompa rock avalanche, Chile. Journal of Geophysical Research 110, B12202. doi:10.1029/2005JB003758.

Kent, P.E., 1966. The transport mechanism in catastrophic rock falls. Journal of Geology 74, 79–83.

Kilburn, C.R., Sørensen, S.A., 1998. Runout length of sturzstroms: the control of initial conditions and of fragment dynamics. Journal of Geophysical Research 103(B8), 17877–17884.

Körner, H.J., 1983. Zur Mechanik der Bergsturzströme vom Huascaran, Peru. In: Patzelt, G. (Ed.), Die Berg- und Gletscherstürze vom Huascaran, Cordillera Blanca, Peru. Universitätsverlag Wagner, Innsbruck, pp. 71–110.

Korup, O., 2004. Geomorphic implications of fault zone weakening: slope instability along the Alpine Fault, South Westland to Fiordland. New Zealand Journal of Geology and Geophysics 47, 257–267.

Korup, O., Clague, J.J., 2009. Natural hazards, extreme events, and mountain topography. Quaternary Science Reviews 28, 977–990.

Korup, O., Clague, J.J., Hermanns, R.L., Hewitt, K., Strom, A.L., Weidinger, J.T., 2007. Giant landslides, topography, and erosion. Earth and Planetary Science Letters 261, 578–589.

Korup, O., Tweed, F., 2007. Ice, moraine, and landslide dams in mountainous terrain. Quaternary Science Reviews 26, 3406–3422.

Lagmay, A.M.A., Ong, J.B.T., Fernandez, D.F.D., et al., 2006. Scientists investigate recent Philippine landslide. EOS Transactions 87, 121–124.

Legros, F., 2002. The mobility of long-runout landslides. Engineering Geology 63, 301–331.

Legros, F., Cantagrel, J.M., Bertrand, D., 2000. Pseudotachylyte (frictionite) at the base of the Arequipa volcanic landslide deposit (Peru): implications for emplacement mechanisms. Journal of Geology 108, 601–611.

Lipovsky, P.S., Evans, S.G., Clague, J.J., et al., 2008. The July 2007 rock and ice avalanches at Mount Steele, St. Elias Mountains, Yukon, Canada. Landslides 5, 445–455.

Major, J., Iverson, R.M., 1999. Debris-flow deposition: effects of pore-fluid pressure and friction concentrated at flow margins. Geological Society of America Bulletin 110, 1424–1434.

Malamud, B.D., Turcotte, D.L., Guzzetti, F., Reichenbach, P., 2004. Landslide inventories and their statistical properties. Earth Surface Processes and Landforms 29, 687–711.

Mangeney, A., Roche, O., Hungr, O., Mangold, N., Faccanoni, G., Lucas, A., 2010. Erosion and mobility in granular collapse over sloping beds. Journal of Geophysical Research 115, F03040.

Mangeney, A., Tsimring, L.S., Volfson, D., Aranson, I.S., Bouchut, F., 2007. Avalanche mobility induced by the presence of an erodible bed and associated entrainment. Geophysical Research Letters 34, L22401.

Manzella, I., Labiouse, V., 2009. Flow experiments with gravel and blocks at small scale to investigate parameters and mechanisms involved in rock avalanches. Engineering Geology 109, 146–158.

McArdell, B.W., Bartelt, P., Kowalski, J., 2007. Field observations of basal forces and fluid pore pressure in a debris flow. Geophysical Research Letters 34, L07406.

McDougall, S., Hungr, O., 2005. Dynamic modelling of entrainment in rapid landslides. Canadian Geotechnical Journal 42, 1437–1448.

McSaveney, M.J., 2002. Recent rockfalls and rock avalanches in Mount Cook National Park New Zealand. In: Evans, S.G., DeGraff, J.V. (Eds.), Catastrophic Landslides: Effects, Occurrence, and Mechanisms. Geological Society of America Reviews in Engineering Geology XV. Geological Society of America, Boulder, CO, pp. 35–70.

Melosh, H.J., 1979. Acoustic fluidization: a new geologic process? Journal of Geophysical Research 84(B13), 7513–7520.

Nicoletti, P.G., Sorriso-Valvo, M., 1991. Geomorphic controls of the shape and mobility of rock avalanches. Geological Society of America Bulletin 103, 1365–1373.

Okura, Y., Kitahara, H., Kawanami, A., Kurokawa, U., 2003. Topography and volume effects on travel distance of surface failure. Engineering Geology 67, 243–254.

Osmundsen, P.T., Henderson, I., Lauknes, T.R., Larsen, Y., Redfield, T.F., Dehls, J., 2009. Active normal fault control on landscape and rock-slope failure in northern Norway. Geology 37, 135–138.

Panek, T., Hradecky, J., Smolkova, V., Silhan, K., 2008. Gigantic low-gradient landslides in the northern periphery of the Crimean Mountains (Ukraine). Geomorphology 95, 449–473.

Pollet, N., Schneider, J.L.M., 2004. Dynamic disintegration processes accompanying transport of the Holocene Flims sturzstrom (Swiss Alps). Earth and Planetary Science Letters 221, 433–448.

Ponomareva, V.V., Melekestsev, I.V., Dirksen, O.V., 2006. Sector collapses and large landslides on late Pleistocene–Holocene volcanoes, Kamchatka, Russia. Journal of Volcanology and Geothermal Research 158, 117–138.

Prager, C., Krainer, K., Seidl, V., Chwatal, W., 2006. Spatial features of Holocene sturzstrom-deposits inferred from subsurface investigations (Fernpass rockslide, Tyrol, Austria). Geo. Alp 3, 147–166.

Preuth, T., Bartelt, P., Korup, O., McArdell, B., 2010. A random kinetic energy model for rock avalanches: eight case studies. Journal of Geophysical Research 115, F03036. doi:10.1029/2009JF001640.

Qi, S., Xu, Q., Zhang, B., Zhou, Y., Li, L., 2011. Source characteristics of long runout rock avalanches triggered by the 2008 Wenchuan earthquake, China. Journal of Asian Earth Sciences 40, 896–906.

Radbruch-Hall, D.H., 1978. Gravitational creep of rock masses on slopes. In: Voight, B. (Ed.), Rockslides and Avalanches 1. Elsevier, Amsterdam, pp. 607–657.

Reid, M.E., 2004. Massive collapse of volcano edifices triggered by hydrothermal pressurization. Geology 32, 373–376.

Savage, S.B., Hutter, K., 1991. The dynamics of avalanches of granular materials from initiation to runout. Part I: Analysis. Acta Mechanica 86, 201–223.

Scheidegger, A.E., 1973. On the prediction of the reach and velocity of catastrophic landslides. Rock Mechanics 5, 231–236.

Schneider, D., Bartelt, P., Caplan-Auerbach, J., Christen, M., Huggel, C., McArdell, B.W., 2010. Insights into rock-ice avalanche dynamics by combined analysis of seismic recordings and a numerical avalanche model. Journal of Geophysical Research 115. doi:10.1029/2010JF001734.

Schramm, J.M., Weidinger, J.T., Ibetsberger, H.J., 1998. Petrologic and structural controls on geomorphology of prehistoric Tsergo Ri slope failure, Langtang Himal, Nepal. Geomorphology 26, 107–121.

Schuster, R.L., Alford, D., 2004. Usoi landslide dam and Lake Sarez, Pamir Mountains, Tajikistan. Environmental and Engineering Geoscience 10, 151–168.

Shea, T., van Wyk de Vries, B., 2009. Structural analysis and analogue modelling of the kinematics and dynamics of rockslide avalanches. Geosphere 4, 657–686.

Shreve, R.L., 1968. Leakage and fluidization in air-layer lubricated avalanches. Geological Society of America Bulletin 79, 653–658.

Siebert, L., 1984. Large volcanic debris avalanches: characteristics of source areas, deposits, and associated eruptions. Journal of Volcanology and Geothermal Research 22, 163–197.

Sosio, R., Crosta, G.B., Hungr, O., 2008. Complete dynamic modeling calibration for the Thurwieser rock avalanche (Italian central Alps). Engineering Geology 100, 11–26.

Stoopes, G.R., Sheridan, M.F., 1992. Giant debris avalanches from the Colima Volcanic Complex, Mexico: implications for long-runout landslides ($>$100 km) and hazard assessment. Geology 20, 299–302.

Strozzi, T., Delaloye, R., Kääb, A., Ambrosi, C., Perruchoud, E., Wegmüller, U., 2010. Combined observations of rock mass movements using satellite SAR interferometry, differential GPS, airborne digital photogrammetry, and airborne photography interpretation. Journal of Geophysical Research 115(F1), F01014. doi:10.1029/2009JF001311.

Ui, Z., Glicken, H., 1986. Internal structural variations in a debris-avalanche deposit from ancestral Mount Shasta, California, USA. Bulletin of Volcanology 48, 189–194.

Voight, B., Sousa, J., 1994. Lessons from Ontake-san: a comparative analysis of debris avalanche dynamics. Engineering Geology 38, 261–297.

Waythomas, C.F., Miller, T.P., Beget, J.E., 2000. Record of late Holocene debris avalanches and lahars at Iliamna volcano, Alaska. Journal of Volcanology and Geothermal Research 104, 97–130.

Weidinger, J.T., Korup, O., 2009. Frictionite as evidence for a large Late Quaternary rockslide near Kanchenjunga, Sikkim Himalayas, India – implications for extreme events in mountain relief destruction. Geomorphology 103, 57–65.

Whitehouse, I.E., Griffiths, G.A., 1983. Frequency and hazard of large rock avalanches in the central Southern Alps. Geology 11, 331–334.

Wörner, G., Uhlig, D., Kohler, I., Seyfried, H., 2002. Evolution of the West Andean escarpment at 18° S (N. Chile) during the last 25 Ma: uplift, erosion and collapse through time. Tectonophysics 345, 183–195.

Zhang, D., Wang, G., 2007. Study of the 1920 Haiyuan earthquake-induced landslides in loess (China). Engineering Geology 94, 76–88.

## Biographical Sketch

**Oliver Korup** is a geomorphologist interested in quantitatively studying the coupling of Earth surface processes in active mountain belts. This entails investigating feedbacks with tectonic, climatic, and anthropogenic processes, and has direct applications for understanding landscape evolution and appraising natural hazards.

As a physical geographer, **Demian Schneider** is specialized on natural hazards, particularly on rapid mass movements in glacial and volcanic mountain environments. His focus is on enhancing the understanding of process interactions in a changing landscape as a key to improve hazard mapping and mitigation measures.

**Christian Huggel** has a PhD in physical geography. He is a senior scientist at the University of Zürich as well as at the University of Geneva. His research interests are in climate change impacts in high mountains, associated hazards and risks, as well as adaptation and prevention thereof.

**Anja Dufresne** is a geoscientist interested in the processes of rapid geomorphological changes within mountainous terrains. A central focus of her research is the application of laboratory analog models to investigate the processes and influencing factors, particularly of runout path materials, involved in rock-avalanche emplacement.

# Paper II

Nat. Hazards Earth Syst. Sci., 8, 559–571, 2008
www.nat-hazards-earth-syst-sci.net/8/559/2008/

Natural Hazards and Earth System Sciences

# Assessing lahars from ice-capped volcanoes using ASTER satellite data, the SRTM DTM and two different flow models: case study on Iztaccíhuatl (Central Mexico)

**D. Schneider**[1], **H. Delgado Granados**[2], **C. Huggel**[1], **and A. Kääb**[3]

[1]Glaciology, Geomorphodynamics and Geochronology, Department of Geography, University of Zurich, Switzerland
[2]Instituto de Geofísica, Universidad Nacional Autónoma de México (UNAM), Mexico City, Mexico
[3]Department of Geosciences, University of Oslo, Norway

Received: 14 December 2007 – Revised: 19 May 2008 – Accepted: 19 May 2008 – Published: 17 June 2008

**Abstract.** Lahars frequently affect the slopes of ice-capped volcanoes. They can be triggered by volcano-ice interactions during eruptions but also by processes such as intense precipitation or by outbursts of glacial water bodies not directly related to eruptive activity. We use remote sensing, GIS and lahar models in combination with ground observations for an initial lahar hazard assessment on Iztaccíhuatl volcano (5230 m a.s.l.), considering also possible future developments of the glaciers on the volcano. Observations of the glacial extent are important for estimations of future hazard scenarios, especially in a rapidly changing tropical glacial environment. In this study, analysis of the glaciers on Iztaccíhuatl shows a dramatic retreat during the last 150 years: the glaciated area in 2007 corresponds to only 4% of the one in 1850 AD and the glaciers are expected to survive no later than the year 2020. Most of the glacial retreat is considered to be related to climate change but in-situ observations suggest also that geo- and hydrothermal heat flow at the summit-crater area can not be ruled out, as emphasized by fumarolic activity documented in a former study. However, development of crater lakes and englacial water reservoirs are supposed to be a more realistic scenario for lahar generation than sudden ice melting by rigorous volcano-ice interaction. Model calculations show that possible outburst floods have to be larger than $\sim 5\times 10^5$ m$^3$ or to achieve an H/L ratio (Height/runout Length) of 0.2 and lower in order to reach the populated lower flanks. This threshold volume equals 2.4% melted ice of Iztaccíhuatl's total ice volume in 2007, assuming 40% water and 60% volumetric debris content of a potential lahar. The model sensitivity analysis reveals important effects of the generic type of the Digital Terrain Model (DTM) used on the results. As a consequence, the predicted affected areas can vary significantly. For such hazard zonation, we therefore suggest the use of different types of DTMs and flow models, followed by a careful comparison and interpretation of the results.

## 1 Introduction

Lahars are mixtures of water and volcanic debris of varying size and solids fraction, which frequently affect the steep, unconsolidated slopes of volcanoes. Lahars represent one of the most far-reaching threats in volcanic terrains. They may occur not only prior to or during eruptions, but also years later, and can be triggered by torrential storms, lake outbursts and earthquakes (Verstappen, 1992; Pierson, 1998; Vallance, 2000). Stream flows are muddy water streams with a sediment concentration below 20% in volume. Lahars however, can be further separated according to their sediment concentration: into hyperconcentrated flows between 20 and 50–60% in volume, and into debris flows if the volumetric sediment concentration is higher than 50–60% (Pierson and Scott, 1985; Pierson, 1986; Smith and Lowe, 1991; Coussot and Meunier, 1996; Vallance, 2000; Lavigne and Thouret, 2002). The lahars simulated in this study represent debris flow types with sediment concentrations similar to the observed ice-melt-triggered lahars on Popocatépetl in 1997 and 2001 (Julio Miranda and Delgado Granados, 2003; Capra et al., 2004; Julio Miranda et al., 2005).

Satellite remote sensing has been widely used in volcanic studies (Kerle and Oppenheimer, 2002; Pieri and Abrams, 2004) while GIS tools and computer based models became increasingly important during the past years, for example, for calculating the runout paths of potential lahars (Iverson et

---

*Correspondence to:* D. Schneider
(demian.schneider@geo.uzh.ch)

Published by Copernicus Publications on behalf of the European Geosciences Union.

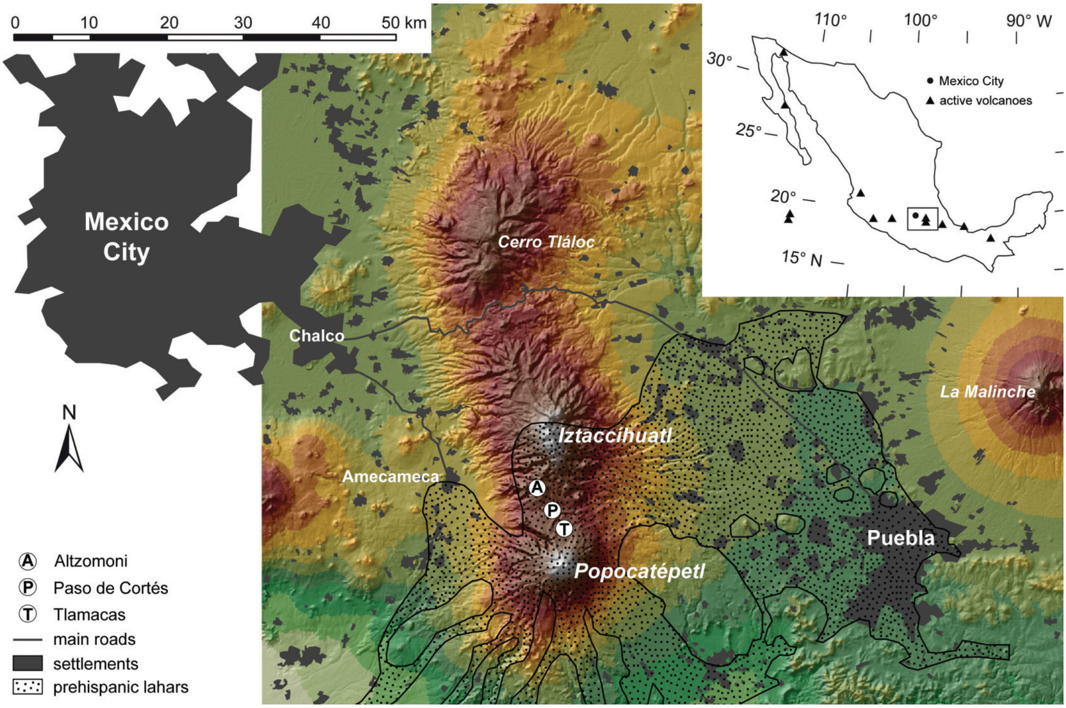

**Fig. 1.** Upper right: Location of the most active volcanoes and the study area within Mexico. The coloured shaded relief showing Mexico City, the study area and Puebla is derived from SRTM3 elevation model. The dotted area shown as 'prehispanic lahars' represent the approximate extent of areas flooded by repeated lahar events from Popocatépetl, Iztaccíhuatl and La Malinche after Siebe et al. (1996).

al., 1998; Julio Miranda and Delgado Granados, 2003; Sheridan et al., 2005; Walder et al., 2005; Hubbard et al., 2006; Davila et al., 2007; Huggel et al., 2008). By applying such tools to Iztaccíhuatl volcano in Mexico, we show how an initial hazard evaluation can be carried out relatively fast and at low cost.

### 1.1 Iztaccíhuatl volcano: setting and background

Iztaccíhuatl (5230 m a.s.l.) is a major Quaternary volcanic complex within the Trans-Mexican Volcanic Belt (TMVB) consisting of various craters, with the principal volcanic vents aligned along a N-NW to S-SE axis (Figs. 1 and 2). The volcanic activity has been variously characterized as essentially extinct (Siebe and Macías, 2006), dormant (Nixon, 1989) or active (Delgado Granados et al., 2005). According to Nixon (1989), the last activity with dacite flows took place at the northern flank at approximately 80 000 years BP. A major structural failure producing a giant debris avalanche to the E-SE side occurred several thousand years ago, just south of La Panza at the site of Las Rodillas (Siebe et al., 1995). Delgado Granados et al. (2005) reported diffuse gas emissions at La Panza of Iztaccíhuatl. Based on this and the fact that lava flows from Iztaccíhuatl overlie volcanic deposits from Popocatépetl which are younger than 5000 years (Siebe et al., 1995), these authors considered Iztaccíhuatl to be an active volcano, following the definition that volcanoes with eruptive activity within the last 10 000 years are active.

After Pico de Orizaba (also known as Citlaltépetl, 5675 m a.s.l.) and Popocatépetl (5452 m a.s.l.), Iztaccíhuatl is the third highest peak in Mexico and, like the other two volcanoes, is still covered by ice (Delgado Granados, 2007). The presence of glaciers in Mexico is noteworthy because at this latitudinal range there are no other glaciers worldwide. In reference to the silhouette of the volcanic edifice (similar to the shape of a woman lying on her back) the two main glacier systems are called El Pecho (the chest) at the summit and La Panza (the belly) 1 km to S-SE (Fig. 2 and Fig. 4). All the glaciers on Iztaccíhuatl have shown extensive retreat during the past 150 years.

Hazard evaluation for ice-volcano interactions is crucial at Mexico's active ice-covered volcanoes. Since 1994, when the recent eruptive activity of Popocatépetl volcano began, lahars related to ice melting developed in 1997 and 2001. Both events reached the nearby village of Santiago Xalitzintla, which is located 14 km away from the summit (Julio Miranda and Delgado Granados, 2003; Capra et al., 2004; Julio Miranda et al., 2005; Andrés et al., 2007).

In prehistoric time, the area around Popocatépetl and Iztaccíhuatl volcanoes was extensively inundated by lahars which destroyed various human settlements (Fig. 1; Siebe et al., 1996). The material (essentially ash and pumice from Popocatépetl) was released from the flanks of Popocatépetl, Iztaccíhuatl and La Malinche volcano, and flooded over 2600 km$^2$ (GIS calculation from the map in Siebe et al., 1996). If we assume an average thickness of the deposits of 2–5 m and a volumetric sediment content of 60%, the total lahar volume including water is about 9–22 km$^3$ during numerous events over many years. These lahars are assumed to have been mainly related to heavy precipitation, but also to volcano-ice interactions (see Sect. 1.3).

### 1.2 Predisposition for lahars on Iztaccíhuatl

For the generation of lahars, the following three conditions are important: (1) availability of potentially erodible soil and debris (including thickness of source deposits and their physical characteristics), (2) critical slope and channel gradient, (3) availability and amount of water.

Loose rock material is abundant at most of the summit areas of Iztaccíhuatl, consisting mainly of eroded dacites that are accumulated in large rock talus and moraines (Nixon, 1989). Pyroclastic material is observed on several parts of the volcano. At the lower and southernmost part (<4000 m a.s.l.), tephras from Popocatépetl volcano deposited over the last 5000 years can be found. Above 4300 m a.s.l., old and loose tephras from ancient eruptive activity from Iztaccíhuatl are abundant. Vegetation is lacking, so that the ground is not stabilized by plant matter. Permafrost can be found at northern expositions above 4900 m a.s.l. (Palacios et al., 2007).

A digital terrain model (DTM) derived from the shuttle radar topography mission (SRTM) data of February 2000, reveals inclinations of >35–45° (70–100%) around the summit area. Although the angle of repose of loose tephra has not been evaluated, we assume conditions close to the stability limits. Given that criteria (1) and (2) are fulfilled at the summit area of Iztaccíhuatl, the availability of water has to be the deciding factor for lahar formation. On Iztaccíhuatl volcano it can be released by precipitation or melting of the available ice and snow deposits.

### 1.3 Rain-triggered and glacier-related lahars

Frequency of lahars and precipitation intensity are often strongly correlated (Lavigne and Thouret, 2002; Van Westen and Daag, 2005). On the slopes of Iztaccíhuatl and Popocatépetl, small lahars occur commonly during the rainy season. For instance, a rain-triggered lahar occurred on 20 June 1994 (six months prior to the initiation of the current eruptive activity at Popocatépetl volcano). After a heavy rainfall, a relatively small lahar reached, entered, and deposited volcanic ash and debris on the streets of the village Santiago Xalitzintla, situated at the confluence of outlets from Iztaccíhuatl and Popocatépetl (Fig. 3). The material was mainly tephra from past eruptions of Popocatépetl but deposited on the southeastern flanks of Iztaccíhuatl and then remobilized by the heavy precipitation event.

The highest climate station around Iztaccíhuatl which delivered data for many years was at about 4000 m a.s.l. on the western slope, but the data were not available for this study. In 1970 the 'Instituto de Geografía de la UNAM' published a climate map at a scale of 1:500 000, showing that September is the rainiest month. It is notable that at elevations above 5000 m a.s.l. precipitation can be >1000 mm/year with an

**Fig. 2.** The silhouette of Iztaccíhuatl resembling a lying woman as believed by indigenous Mexican people, seen from the west: La Cabeza (head), El Pecho (chest), La Panza (belly), Las Rodillas (knees) and Los Pies (feet). El Pecho and La Panza are still glacier clad. Picture taken on 21 November 2004 by D. Schneider.

**Fig. 3.** View of the streets of Santiago Xalitzintla showing the deposit of a rain-triggered lahar generated on Iztaccíhuatl's southeastern flanks with deposits erupted from Popocatépetl. Picture taken on 20 June 1994 by H. Delgado Granados.

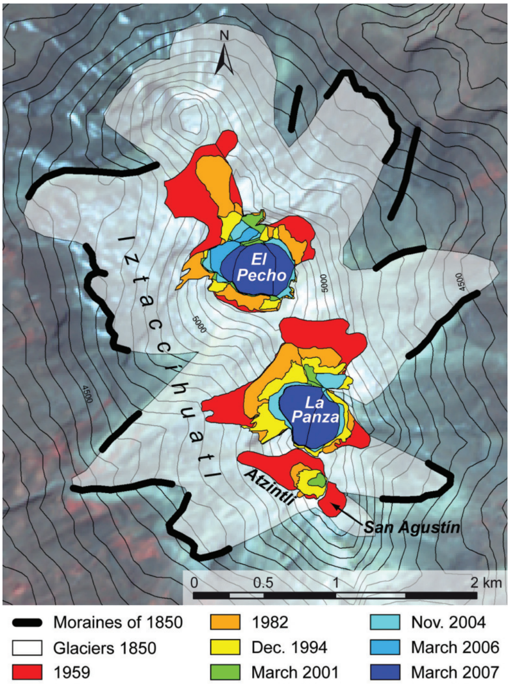

**Fig. 4.** Glacier outlines for eight different dates. Contour line interval is 50 m and the background image is the ASTER VNIR scene of March 2001.

average of 950 mm/year (Guerra-Acevedo, 2006).

Scenarios for water release from ice and snow leading to a potential lahar generation on Iztaccíhuatl can be:

1. An eruptive activity interaction at Iztaccíhuatl volcano.
2. An eruptive activity interaction from Popocatépetl volcano.
3. A non-eruptive volcanic and/or a climatically related interaction.

Scenario 1 may have the highest impact but the probability of occurrence is low as Iztaccíhuatl is considered to be active but dormant. Deposition of ash from Popocatépetl onto the glaciers of Iztaccíhuatl as proposed in scenario 2 is a possibility that could occur at any future eruptive event at Popocatépetl if the wind direction is heading northwards as it occurred in the past (Siebe et al., 1996). This could lead to intensified melting of the glaciers and possibly triggering of lahars. The third scenario includes local melting of snow, ice and permafrost connected to geothermal volcanic influence (Abramov et al., 2008 in press) or seasonal melting. This can lead to subglacial, supraglacial or proglacial water reservoirs and moraine dammed lakes which are prone to outbursts. Such observations have repeatedly been made in volcanic (Russell and Knudsen, 2002) and non-volcanic glacial environments (Haeberli, 1983).

The importance of ice, firn, snow and permafrost in lahar formation at Iztaccíhuatl has not yet been investigated and there are no records of such events. In order to provide a related initial hazard assessment we modelled hypothetical flows originating from the glaciated areas. By establishing scenarios using different volumetric lahar magnitudes and DTMs of 30–90 m resolution, we can approximately define the areas around the entire Iztaccíhuatl edifice that could be affected in case of sufficient water release from Iztaccíhuatl's glaciers.

## 2 Data and methods

We used the following data and methods to analyze the glacier dynamics for evaluation of present and future ice conditions for lahar generation at Iztaccíhuatl. The satellite imagery used was acquired by the Advanced Spaceborne Thermal Emission and Reflection Radiometer (ASTER) onboard the NASA Terra satellite. ASTER scenes consist of 3 visible and near infrared channels (VNIR; bands 1/2/3N; 0.52–0.86 $\mu$m), a back-looking channel (band 3B; 0.76–0.86 $\mu$m), 6 short wave infrared channels (SWIR; bands 4–9; 1.6–2.43 $\mu$m), and 5 thermal infrared channels (TIR; bands 10–14; 8.13-11.65 $\mu$m) (Toutin, 2002). In false colour composite images (channels 3N/2/1; 9/4/3N and 10/9/4, corresponding to red/green/blue) of an ASTER scene from 17 March 2001, the large Little Ice Age (LIA) moraines are easily visible (White, 2002). Together with the LIA moraines shown in the 1:50 000 geologic map by Nixon (1989) and the 1:50 000 topographic map published by INEGI (1995), the moraines were mapped and the last glacial maximum extent was reconstructed (Fig. 4). The exact year of the LIA maximum for Mexican glaciers is not known but is assumed to be around 1850/1860 AD as is the case for comparable tropical glaciers in the Andes (Ramírez et al., 2001; Ceballos et al., 2006).

The oldest detailed map of the glaciers on Iztaccíhuatl was made by Lorenzo (1959). However, there remains an uncertainty concerning the exact year of data collection. Lorenzo (1959) used aerial photographs taken in 1945 as a guide but the field work was probably carried out in 1958. Therefore, the glacier extent derived from Lorenzo (1959) is assumed to represent the situation at around 1959. Additionally, there exists a 1:20 000 scale orthophoto map, published by INEGI (1983). The photographs used were taken in 1982 and one of the authors (H. Delgado) manually mapped the glacier extent for the same year. The best available data for glacier mapping consisted of aerial photographs, taken on 27 December 1994. They were orthorectified by the authors of this contribution and the glaciers were mapped with a GIS. Discrimination of snow and ice was simplified by analogue stereo interpretation.

The ASTER data with its medium spatial resolution (VNIR 15 m, SWIR 30 m, TIR 90 m; Toutin, 2002), is often not useful for repeated mapping of the changes in glacier extent at a high temporal resolution. However, within periods of several years, these low-cost images are adequate if the changes in glacial extent are significantly larger than the pixel size (15 m in this case). In our study, the time span between the aerial images from December 1994 to the ASTER-scene of March 2001, and the corresponding glacier retreat turned out to be sufficient to quantify changes. To get a distinct classification of the glaciers, band ratio images were calculated by dividing the VNIR channel 3N through the SWIR channel 4. This method takes advantage of the strong decrease of reflectance of snow and ice between the near-infrared channel 3N and the shortwave-infrared channel 4 as compared to other materials (Paul et al., 2002). The resulting ratio images depict ice and snow in bright contrast to the dark grey values for debris and rocks.

In late November 2004, two field visits were carried out. On 23 November 2004, the glaciers were mapped with the aerial photograph of 1994 as a reference. Due to inaccessibility and invisibility from the top, the glacier tongues at the steepest parts in the NW and E of El Pecho could not be mapped exactly. At these areas, the glacier extent mapped from the ASTER image of 2001 was taken as a maximum extent for 2004. However, the glacier tongues very likely retreated during the intervening 3.5 years, so that the glaciated area given for 2004 represents an upper limit for the real area in 2004.

Finally, the time series has been extended by two more recent ASTER-scenes from 15 March 2006 and 2 March 2007. Surprisingly, significant changes on El Pecho glacier could be detected even in the 1 year period between these two most recent images.

The DTM used in this study was taken from the Shuttle Radar Topography Mission (SRTM), acquired in February 2000 at approximately 30 m and 90 m resolution (Rabus et al., 2003). Here, the SRTM version with 3 arcsec spatial resolution, that is approximately 90 m, was used (SRTM3). In order to have a second DTM with a potentially better spatial resolution and to analyse the influence of the DTM accuracy on the modelled flows, DTMs with a grid size of 30 m and 60 m respectively were processed from the March 2001 Terra/ASTER channels 3N (nadir looking) and 3B (looking 27.6° back from nadir; Kääb, 2005; Kääb et al., 2005). The spatial resolutions of 90 m, 60 m and 30 m for terrain elevation data is considered to be adequate for an initial, large-scale hazard assessment of the entire Iztaccíhuatl edifice.

**Table 1.** Glacier areas in km$^2$ and percentaged in relation to the 1850 extent. The area listed as 'Iztaccíhuatl' is the sum of the individual 'El Pecho' and 'La Panza' glacier systems.

| Year | Iztaccíhuatl | El Pecho | La Panza | Area left |
|---|---|---|---|---|
| 1850 | 6.369 | – | – | 100% |
| 1959 | 1.369 | 0.623 | 0.746 | 21.5% |
| 1982 | 0.863 | 0.432 | 0.431 | 13.6% |
| 1994 | 0.612 | 0.276 | 0.336 | 9.6% |
| 2001 | 0.435 | 0.233 | 0.202 | 6.8% |
| 2004 | 0.391 | 0.207 | 0.184 | 6.1% |
| 2006 | 0.305 | 0.171 | 0.134 | 4.8% |
| 2007 | 0.273 | 0.140 | 0.133 | 4.3% |

## 3 Past and future development of the glaciers on Iztaccíhuatl

### 3.1 Glaciated area

Comparison of the collected data reveals strong changes in glacier extent during the past decades on Iztaccíhuatl. Figures 4 and 5 show the glacier retreat, and in Table 1 the corresponding absolute and relative values are given. As a simplification, the different glaciers were grouped into two systems: El Pecho and La Panza. The areas of the smaller glaciers Atzintli and San Agustín (now disappeared) south of La Panza are counted into the La Panza system. If one takes the 1850 extent (6 369 000 m$^2$) as a reference, only 4.3% (273 000 m$^2$) of the glaciated area remained in March 2007. During the more recent 48-year period between 1959 (1 369 000 m$^2$) and 2007 (273 000 m$^2$), around 80% of the glaciers disappeared. This is in accordance with the general worldwide trend of glacier shrinkage (Zemp et al., 2007) but the retreat rate is extraordinarily high compared to the global average. Kaser and Osmaston (2002) made similar observations specifically on tropical and subtropical glaciers around the world. The observations emphasize the higher sensitivity of glaciers in lower latitudes to global atmospheric warming. A regional influence on climate at Iztaccíhuatl by the significant emissions of the megacity of Mexico City (at a distance of only ∼40 km to the NW) might also play a role.

### 3.2 Glacier altitude and thickness

Along with the glacier area shrinkage, the former convex glacier shape on El Pecho has changed now to a thin ice body with a concave surface. Photographs from the mid-20th century show the crater of El Pecho summit covered by a massive convex ice cap. The altitude at the highest part of the glacier was formerly indicated as 5286 m a.s.l. (Lorenzo, 1959), but the current official altitude is 5,230 m a.s.l. (INEGI, 1995). If one excludes a change of the surveying height basis, this difference in elevation can be indicative of the decrease in glacier thickness. Within the last

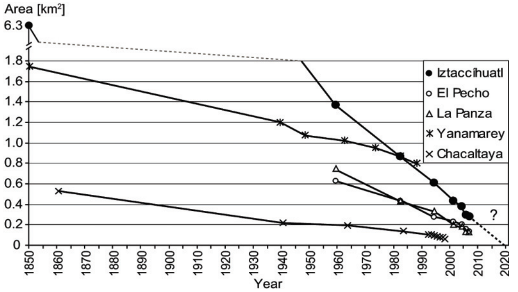

**Fig. 5.** Decreasing glacier extent at Iztaccíhuatl (Mexico, 19° N) compared to the glaciers Yanamarey (Peruvian Cordillera Blanca, 16° S; data from Kaser and Osmaston, 2002) and Chacaltaya (Bolivia, 9° 40′ S; data from Ramírez et al., 2001) through time (years AD). On Iztaccíhuatl volcano, the two glaciated parts 'El Pecho' and 'La Panza' are shown separately and summarized as 'Iztaccíhuatl'. These two parts were connected in 1850 AD and hence there is no separate data for 'El Pecho' and 'La Panza' for that date. Note the break in the y-axis and the possible future development of the glaciated area (dotted line).

decades, the height of the original peak, which was in the centre of the glacier, decreased greatly. In 2004, the crater rims on the south and north of the El Pecho glacier emerged from the melting ice and finally became the new peaks of Iztaccíhuatl (A and B in Fig. 6). Handheld GPS measurements in November 2004 yielded a height of 5210 m a.s.l. (vertical accuracy in the order of tens of meters) for both crater rims and 5195 m a.s.l. for the centre of the glacier, where the main peak of the volcano was formerly located. The maximum height of this point on the SRTM3 DTM is 5211 m a.s.l. for the date of the acquisition in February 2000, with an absolute vertical accuracy of ±16 m (Smith and Sandwell, 2003). The ASTER DTMs reveal maximum values of 5196 and 5176 m a.s.l. in March 2001 for the 30 m and 60 m DTM grids, respectively, with a vertical accuracy in mountainous terrain generally being at ±30 m (Eckert et al., 2005; Kääb et al., 2005). Considering that the summit area of El Pecho is represented as an almost flat region, a fact that often improves the height accuracy, and all the above independent measurements, we arbitrarily choose 5200 m a.s.l. ±15 m as an approximate reference for the altitude of the centre of the El Pecho glacier between the years 2000 and 2004. The altitude in 2007 could be several meters lower due to further thinning of the ice on El Pecho.

Analysing the contour lines on Lorenzo's glacier map of 1959, we derive a height of 5270 m a.s.l. for the peak in the centre of the glacier. Compared to the value of ∼5200 m a.s.l. around the year 2004, the difference is 70 m within a ∼45 year period, corresponding to more than 1.5 m vertical decrease of ice per year. The loss of ice thickness on La Panza, situated 200 m lower in elevation, is also remarkable. During the same period, there is a vertical decrease of 30 m or 0.7 m per year. This value is confirmed by photographs of a large rock buried in the ice, which was barely visible in early photographs. Today it extends ∼25 m above the ice surface.

### 3.3 Climatic influence

In order to estimate the climatic influence on their retreat, Iztaccíhuatl's glaciers should be compared to similar Mexican glaciers. Unfortunately, this is difficult because there are only two other ice-clad volcanoes and both are not adequate for comparison:

- The glaciers of Iztaccíhuatl's southern neighbour Popocatépetl (5452 m a.s.l.) have been strongly affected by the eruptive activity since 1994, in particular in 1997 and 2001 (Julio Miranda and Delgado Granados, 2003; Julio Miranda et al., 2005).
- The glaciers of Pico de Orizaba are much larger, reach up to 5675 m a.s.l. and therefore still benefit from an intact accumulation area (White, 2002; Delgado Granados, 2007).

Hence, we show in Fig. 5 the retreat of two tropical glaciers on the southern hemisphere with similar climatic conditions, comparable size and altitude range: Yanamarey glacier is situated in the Peruvian Cordillera Blanca at 9°40′S at an altitude between 4750 and 5000 m a.s.l. (Kaser and Osmaston, 2002) while Chacaltaya glacier is at 16° S between 5140 and 5360 m a.s.l. in Bolivia (Ramírez et al., 2001). The area of Iztaccíhuatl's individual glacier systems El Pecho and La Panza lies in between the two other glaciers shown, while the total glaciated area on Iztaccíhuatl is similar to the area of Yanamarey glacier during the past few decades. Although the glaciated area of the latter was a fourth of the one on Iztaccíhuatl in 1850 AD, during recent times Iztaccíhuatl's glaciers became smaller than Yanamarey. Chacaltaya glacier also shows a slower retreat than Iztaccíhuatl's glaciers. However, caution is needed for this comparison, because many basic factors such as high altitude precipitation and solar radiation due to cloud cover, etc. are not the same in these different regions.

### 3.4 Volcanic influence

The fact that the higher El Pecho glacier has a vertical melting rate approximately twice as fast as the lower La Panza glacier (1.5 m/yr. and 0.7 m/yr. respectively; see Sect. 3.2) leads to the hypothesis that – beyond climatic effects – at least a part of the very fast vertical downwasting of the glacier on El Pecho could be induced by geo- or hydrothermal volcanic heat flow.

In the southern part of El Pecho glacier a notable feature was observed. On aerial images from 1977 a small dark point appears on the glacier of El Pecho. On the airphotos from 1994 there is a large pit at the same location, which was also observed during fieldwork in 2001. In 2004 the pit had developed into a crevasse-like opening of about 50 m in length (Fig. 6). The feature is situated in the middle of the glacier in a concave area where shear and extensional stresses in the ice are expected to be minor. This atypical location for crevasse development suggests that the form could be related to a locally confined heat source, e.g. a fumarole beneath the glacier, where geothermal heat flux is considerably higher (Welch et al., 2007). No vapour or sulfur smell was observed at this location but the influence of volcanic heat flow on glacier retreat at El Pecho is supposed to contribute to the ablation. The glacier may serve here as a giant calorimeter, as has been reported for example at Mt. Wrangell, Alaska, by Benson and Motyka (1978) and Benson et al. (2007).

Close to La Panza, Delgado Granados et al. (2005) installed a volatile trap in 1999 and measured $Na^+$, $K^+$, $Ca^+$, $Mg^+$, $SiO_2$, $SO_4^{2-}$, as well as $F^-$, which suggest a magmatic source of the vapours. A strong sulfur odour could also be detected at two points around La Panza during field trips in November 2004. Delgado Granados et al. (2005) further report earthquakes that have been measured by seismic stations of the National Seismological Service (NSS) at Altzomoni and Tlamacas (A and T in Fig. 1). The origin of these seismic events was identified to lie beneath Iztaccíhuatl volcano (J. Pacheco, former head of the NSS; personal communication). Delgado Granados et al. (2005) reported temperature measurements between 0–10°C at the ground and 0.1 m below the surface at La Panza region, and glacier-ice temperatures ranging from −2.0°C and up to 0.5°C at depths between −6 m and 0 m beneath the glacier's surface. The measurements indicate an increased volcanic heat flow and temperate glacier bed conditions. The existence of liquid water in englacial water reservoirs has already been reported by Álvarez and Delgado (2002) who carried out GPR (ground penetrating radar) profile measurements through La Panza glacier.

### 3.5 Current and future hazard scenarios

Observations of ablation and accumulation area over the past years indicated that the equilibrium line altitude (ELA) rose above the top of El Pecho, transforming the entire glaciers into an ablation area. The ELA only sinks for a short time period below the summit, and throughout the year ablation dominates on all the parts of the glaciers. If we linearly extrapolate the down-wasting trend of the ice, the glaciers will survive no longer than 2020 (Fig. 5). In a long term view this may reduce the risk of any volcano-ice interaction and subsequent lahar formation. Seasonal snow cover, permafrost, and some relict ice fields may however be preserved beyond this date. Firn and snow can be even more important for lahar formation than ice in case of interaction with eruptive volcanic activity (Pierson et al., 1990).

An eruption of Iztaccíhuatl volcano is currently unlikely. More probable is the development of hazards directly or indirectly related to glacier shrinkage, such as formation of a crater lake during or following glacier recession, release of sediment from basal moraines, slope destabilization by glacial retreat and permafrost thawing. For more detailed assessment of these factors, further data, including detailed GPR profiles of the El Pecho area and precipitation data of the summit region, should be collected.

**Fig. 6.** El Pecho Glacier from south to north with the southern crater crest line **(A)** and the former ice clad northern crest line **(B)**. A large crevasse is situated in the middle of the crater glacier **(C)**. Note the current concave glacier shape in contrast to the former convex reconstructed surface of 1959, indicated by the dashed black line. The height difference at the centre of the glacier is around 70 m. Picture taken on 22 November 2004 by D. Schneider.

## 4 Lahar modelling

### 4.1 Lahar model description

Two different flow models were used to simulate the potential lahar flow paths. The first one is the modified single-flow-direction (MSF) model by Huggel et al. (2003), which is further developed from the D8 flow direction method (Marks et al., 1984). Model input parameters are the starting cell location, a DTM and an empirical value for the H/L ratio (see below). The flow direction is calculated from each cell to one of its eight neighbours (D8), either adjacent or diagonal, in the direction of the steepest descent. In order to prevent stream width being represented by only one pixel, Huggel et al. (2003) implemented a function that enables flow diversion from the steepest flow direction. The more the flow diverts from the steepest descent direction, the higher the corresponding flow resistance. The resistance values are transformed into a semi-quantitative likelihood for each cell being affected by the lahar (Fig. 7). The modelled flow stops when it reaches a specified average slope value. This slope value is defined as the ratio between the vertical drop H at the flow initiation area and the horizontal distance L along the curving flow path to the lowest deposit (H/L; Fig. 8; Huggel et al., 2003). Actually, depending on the sediment concentration, lahars can be highly mobile and show rather attenuat-

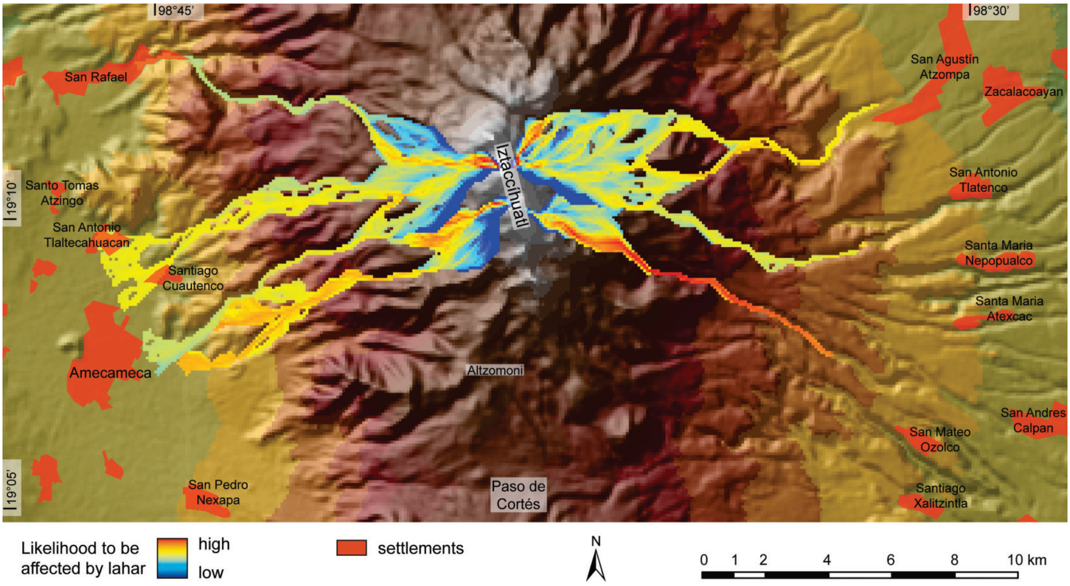

**Fig. 7.** MSF model (Huggel et al., 2003) with an H/L of 0.19 (see Fig. 8) on the colour shaded SRTM3 DTM. Lahars were only modelled from the glaciers on El Pecho and La Panza to the east and west side so that the flows only represent lahars related to the glaciers.

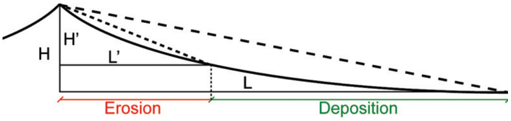

**Fig. 8.** Schematic view of a volcano and the difference between the H/L ratio used in the MSF model and the H'/L' required for LAHARZ. The division into a higher part where lahars erode material and a lower section where deposition dominates is needed to define the high-energy cone used in LAHARZ.

ing flow characteristics than abrupt stopping as granular debris flows. In the MSF model this is usually accounted for by choosing a minimum H/L value corresponding to a maximum flow reach.

The second model applied in this study was LAHARZ by Iverson et al. (1998). They examined 27 lahar paths on nine volcanoes and derived two semi-empirical equations predicting the inundated valley cross-sectional areas and the planimetric areas as a function of the lahar volume. The model assumes the simplification that there is only erosion above the limit of a 'high-energy cone' and only deposition below it (notwithstanding, erosion and deposition usually occur in conjunction). Similarly to MSF, the high-energy cone has to be defined by an H'/L' ratio which differs from the H/L used for MSF. The H'/L' ratio is the height and length from the highest point down to the limit of the high-energy cone where deposition starts, but not as far as to the lowest deposit (Fig. 8). As soon as the flow exceeds the limit of the high-energy cone, the model starts to calculate 3 valley cross-sections (at angles of 45°, 90° and 135° to the flow direction) which are filled corresponding to the first semi-empirical equation (Iverson et al., 1998). All inundated cells are marked as potentially affected by a lahar and added up until an area defined by the second semi-empirical equation is reached and the flow stops. The input parameters are potential lahar volumes, an appropriate H'/L' ratio for the border of the high energy cone, and a DTM. The ratio of sediment to water content of the simulated lahars corresponds to an average of those 27 examined lahars, from which the most diluted ones were excluded (Iverson et al., 1998). Hence, LAHARZ simulates typical debris flow-type lahars and the water content can not be varied.

## 4.2 Results of the MSF model

The MSF model was first run using the SRTM3 DTM from the glaciers on El Pecho and La Panza to the west and east side. H/L ratios for the lahar modelling between 0.2 and 0.15 were used, corresponding to published case studies (Siebe et al., 1996; Vallance et al., 2001; Capra et al., 2004). The volumes of debris flows correlate with the H/L ra-

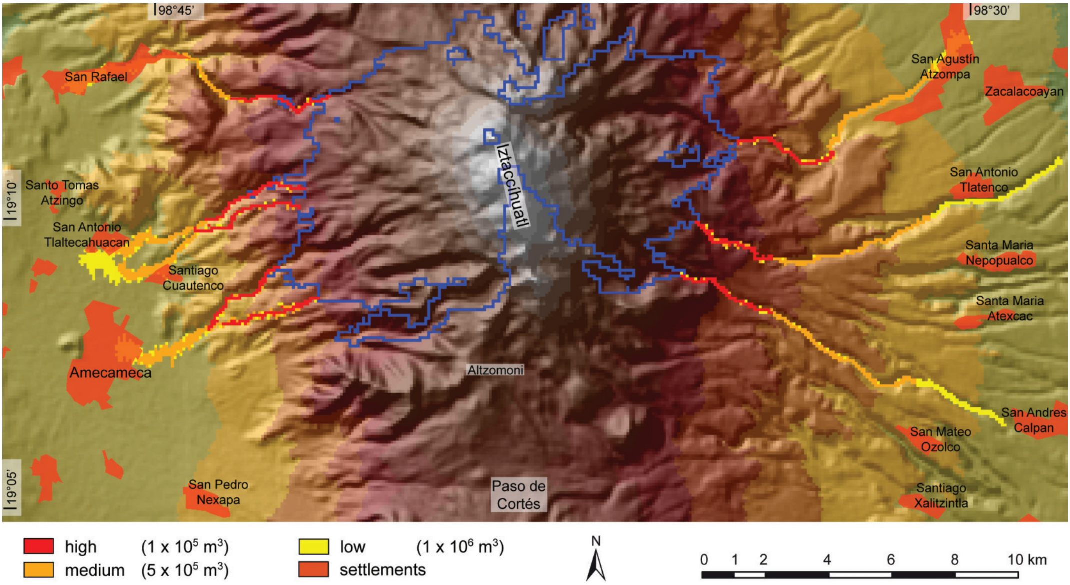

**Fig. 9.** LAHARZ (Iverson et al., 1998) model on the colour shaded SRTM3 DTM. The dark blue line around the summit is the high-energy cone with an H'/L' of 0.28 (see Fig. 8). The lahars were modelled for the same drainage paths as with the MSF model. Red, orange and yellow represent different lahar volumes with corresponding degree of hazard (high, medium, low). LAHARZ does not model erosion in the upper part above the high-energy cone.

tio as demonstrated for lahars at Popocatépetl volcano by Huggel et al. (2008). That means that the greater the volume of a debris flow, the smaller is the corresponding H/L ratio (Legros, 2002). After the relation given by Huggel et al. (2008), the chosen values approximately represent volumes between $1\times10^5$ m$^3$ and $1\times10^7$ m$^3$.

Above 3700 m a.s.l., the results show a strong flow divergence, with high probabilities that the main drainage paths would be affected, and only low probabilities that broader lateral extents would be inundated. Below 3700 m a.s.l., the flows are channelized in deep ravines heading towards populated areas. On the west side the lahars reach some settlements at an H/L of 0.2 (namely San Rafael, San Antonio Tlaltecahuacán and Santiago Cuautenco), whereas the city of Amecameca would be affected with an H/L lower than 0.19. On the east side only San Agustín Atzompa would be hit partially if the H/L value falls below 0.17 (Fig. 7).

### 4.3 Results of the LAHARZ model

For the LAHARZ model the H'/L' ratio, which defines the border of the high-energy cone, had to be determined (Fig. 8). To this end, we analysed the lahars at Popocatépetl which occurred during its eruptions in 1997 and 2001. In both cases, the village of Santiago Xalitzintla SE of Iztaccíhuatl (Fig. 9) was hit by the lahars with volumes of about $4\times10^5$ m$^3$ (Capra et al., 2004; Julio Miranda et al., 2005). We calculated several high-energy cones to ascertain that the modelled LAHARZ flow of $4\times10^5$ m$^3$ just reached the village of Santiago Xalitzintla as it happened in 1997 and 2001. Within these simulations we obtained a best-fit-value of 0.28 for the H'/L' at Popocatépetl. Assuming similar conditions at Iztaccíhuatl, we used the same H'/L' value for the LAHARZ model runs on Iztaccíhuatl. For comparison, Iverson et al. (1998) used an H'/L' of 0.23 at Mount Rainier in the US, and Davila et al. (2007) used a much lower value of 0.04 for Colima volcano in Mexico. The latter value is probably more appropriate for hyperconcentrated flows than for debris-flow-like lahars. With such a value the high-energy cone would lie completely in the alluvial plane and hence, it seems far too low for Iztaccíhuatl volcano.

We assume an average ice thickness of 30 m (GPR data from Delgado Granados et al., 2005) over the whole glaciated area. Consequently, the total ice volume in 2007 was roughly $8.2\times10^6$ m$^3$. On the basis of ice availability, as well as the volume of the 1997 Popocatépetl lahar ($4\times10^5$ m$^3$; Julio Miranda et al., 2005), we defined hypothetical lahar volumes at Iztaccíhuatl as $1\times10^5$ m$^3$, $5\times10^5$ m$^3$ and $1\times10^6$ m$^3$. These volumes correspond to flows generated from melting of 0.5, 2.4 and 4.9% of the total ice volume on Iztaccíhuatl, assuming a 40% water content in volume (boundary between debris flows and hyperconcentrated flows; Pierson and Scott, 1985; Pierson, 1986; Vallance, 2000; Lavigne and Thouret, 2002). The mass of ice lost is typically larger than the amount of water contributing to a possible lahar because not all meltwater is incorporated into the flows (Thouret, 1990; Julio Miranda et al., 2005). These volumes are plausible for the possible scenarios without any additional water from rainfall (as described in 1.3.) and lie within the range of modelled lahar volumes at Concepción Volcano in Nicaragua (Vallance et al., 2001) and at Colima in Mexico (Davila et al., 2007). Larger or more diluted lahars, which also may reach farther, are assumed to develop only as a combination of glacier-volcano interaction processes and rainfall events with shallow landsliding and additional sediment entrainment. This case seems to have a low probability. For that reason and the fact, that the sediment content can not be varied in LAHARZ (see Sect. 4.1), we do not present model results for lahars larger than $10^6$ m$^3$.

On the west side, the LAHARZ-flows reach San Rafael, San Antonio Tlaltecahuacan and Santiago Cuautenco with volumes less than $5\times10^5$ m$^3$ while Amecameca would only be reached with more than $5\times10^5$ m$^3$. In the eastern part, the same effect as with the MSF model is observed. The material stays in the deep and narrow channels but as a consequence, the flows travel farther. Lahar volumes greater than $5\times10^5$ m$^3$ reach San Agustín Atzompa in the NE. The affected town is situated at the mouth of a valley that drains from Iztaccíhuatl, similarly to Santiago Xalitzintla, which is situated completely in an erosion trench. However, most of the towns in the east are situated safely on the terraces in between the canyons, such that the ravines build a reasonable protection from lahars up to hypothetical volumes of $1\times10^7$ m$^3$.

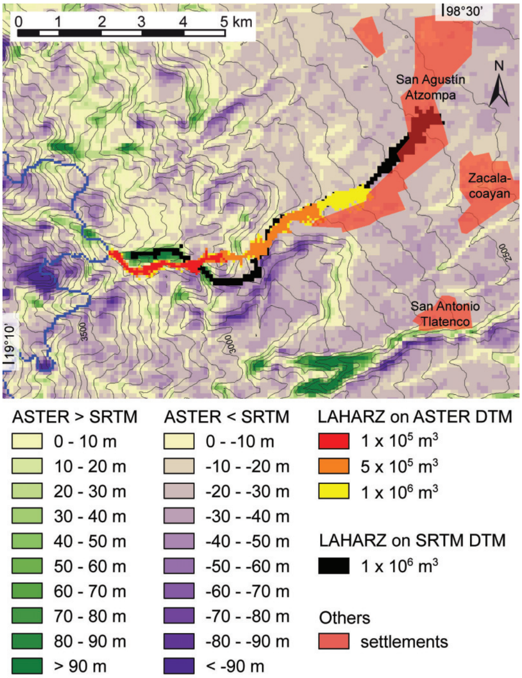

**Fig. 10.** Height difference of ASTER and SRTM DTM (ASTER – SRTM). Green cells indicate areas where the ASTER DTM is higher than the SRTM DTM and the blue cells vice versa. Contour lines are derived from the SRTM DTM at an interval of 50 m. The black lahar was modelled on the SRTM DTM while the blue line (high energy cone with an H'/L' of 0.28) and the colored lahars were calculated on the ASTER DTM. Problems with the ASTER DTM mainly occur in narrow ravines which lead to incorrect deflection of the modelled lahar.

### 4.4 Influence of the DTM on lahar models

Huggel et al. (2008) have shown that the quality and resolution of the DTM can have an important effect on the flow paths and runout distances of simulated lahars. For the MSF model, the changes of the runout distance between the runs on the SRTM-DTM and the ASTER-DTM are minor. However, small differences in the model terrain morphology can determine if a flow will find a way over a moraine or a narrow crest line. If on one DTM the flow takes a different path than on the other DTM, the subsequent flow inundates a formerly unaffected valley providing completely different results. In this study, significant differences resulted from flows modelled on the ASTER DTMs with 30 m and 60 m resolution. They were of an unsatisfying quality, mainly due to large data gaps which had to be interpolated. The modelled lahars flowing through these interpolated areas are mostly of limited practical value. Comparison of individual parts of the ASTER-DTMs to the topographic maps and to the SRTM3 DTM helped however to locate a number of crucial points where the natural sidewalls of the downstream valleys are low or narrow, and larger lahars effectively could break through.

Concerning flow channel deviation, the LAHARZ model generally has fewer problems than the MSF because only the lower parts below the high-energy cone are simulated. There, the ravines are wider and better represented by the SRTM3 and ASTER DTMs than the areas in the summit region. However, analysis of the calculated lahars on the SRTM3 and ASTER DTMs revealed significant variations in the flow path at a problematic zone on the east side of Iztaccíhuatl (Fig. 10). To assess the quality of each DTM, contour lines were derived and compared to the topographic map and the ASTER VNIR image. It was found that the ASTER DTM is defective in this area (mainly due to stereo image matching problems), forcing the modelled lahar on a wrong flow path. This is visible in the subtraction DTM of the ASTER- and SRTM-data (Fig. 10). Two erroneous areas with exaggerated heights up to 100 m (green) fall directly within the flow path, deflecting the lahar stream. Despite the abbreviation of the path, the lahar modelled on the ASTER DTM is still stopping earlier. This effect was observed for each modelled flow and we interpret grid cell size to be an important influence on runout distance calculated by the LAHARZ model. The flows inundate a wider path on the ASTER DTM (60 m) than on the SRTM3 DTM (90 m) and hence on the ASTER DTM, less material is transported downwards. This leads to significantly shorter distal hazard zone boundaries. A lahar modelled on the SRTM3 DTM at the northeastern slope and with a volume of $1\times10^6$ m$^3$ affects the central part of San Agustín Atzompa while the same volume on the ASTER DTM stops 2.5 km upstream and represents no hazard for the settlement (Fig. 9 and 10; this effect was also observed by Huggel et al., 2008). Stevens et al. (2002) found similar effects concerning the flow length on different DTMs but not to that extent. Their terrain data were derived from topographic maps and an airborne SAR (TOPSAR by NASA) with 20 m and 10 m horizontal resolution respectively. In contrast to this, the hazard zonation of Davila et al. (2007) at Colima volcano in Mexico reveals higher lateral spreading and a 1.5 km shorter runout distance for the coarser DTM. Therefore we deduce that the behaviour of the LAHARZ model is highly dependent not only on the spatial resolution, but also on the acquisition method of the DTM.

## 5 Conclusions

The glacial recession on Iztaccíhuatl has been pronounced over the past decades and is likely to lead to total deglaciation within few decades, probably before ∼2020 AD. This trend is in accordance with observed worldwide glacier retreat in tropical regions that is attributed to atmospheric warming. In the case of Iztaccíhuatl glacier retreat may also be affected by an increase in the volcanic heat flow. The crevasse-like opening on El Pecho glacier may be the chimney of an active geo- or hydrothermal vent and should be investigated further, as should the diffuse degassing fields on La Panza. Gas emission measurements, GPR profiles (which have only been performed for one glacier on La Panza by Delgado Granados et al., 2005), and ground temperature measurements could provide a better understanding of the volcanic activity of Iztaccíhuatl, which has been under dispute during the last decades. The volcano is not necessarily ready to become active again but there appear to be some changes in the volcano's hydrothermal system taking place. This could promote the development of subglacial water reservoirs and their possible outbursts may provide a sufficient amount of water for lahar formation. Within a 15 km radius of the summit, a population of approximately 210 000 lives that could be affected by lahars, depending on the lahar volume.

Glacier-related hazards at Iztaccíhuatl are expected to decline over the next decade due to the rapid loss in glacier area and volume, or even total glacier disappearance. However, seasonal snow will still pose a hazard in the case of interaction with the volcano, and several new hazards are not related to volcanic activity: (1) the development of a crater lake at El Pecho due to climate related glacier retreat, which may be prone for outbursts and (2) destabilization of the over-steepened upper flanks due to glacial recession and permafrost thawing, which both could favour the initiation of lahars or landslides. The large amounts of unconsolidated debris which have been revealed by the retreat of the glaciers could be mobilized by heavy precipitation during the rainy season. Accurate precipitation data from the summit of Iztaccíhuatl do not currently exist, but a meteorological station will be installed soon by one of the authors. However, rain-triggered lahars are more common on lower slopes (Scott et al., 2001). The hazard potential of this individual trigger mechanism should be investigated in a separate study, especially concerning a future eruption of Popocatépetl with following ash deposition on the slopes of Iztaccíhuatl that could be remobilized by heavy precipitation.

Concerning the safety of the surrounding villages, there is an important morphological difference between the western and eastern flank. Deep incised valleys serve as natural stream channels, and therefore the location of villages relative to the channel is crucial. On the west side, the ravines directly lead to the populated alluvial plane, while on the east side most of the villages are built on the higher, and hence safer, terraces between the ravines. More detailed studies are necessary to evaluate the need for mitigation measures such as deflection dams, retention basins or a warning system that would increase the safety of the settlements around Iztaccíhuatl.

The SRTM3 DTM represents the main drainage channels in a way that is sufficient for a large scale hazard assessment. In the present case, it provides more realistic results than the ASTER DTMs. However, the coarse resolution of the SRTM3 DTM allows less lateral deposition of material, a fact leading to exaggerated runout distances of the LAHARZ flows. As a consequence, for lahar hazard assessment, we emphasize the necessity of using different flow models in conjunction with mid- and high-resolution DTM data from various sources. Flow modelling on high-resolution DTMs would be helpful for detailed mapping of the hazard zone boundaries on the basis of the presented initial hazard assessment, but each simulation should be critically compared to results based on calculations on other DTMs.

*Acknowledgements.* Funding from CONACyT (grant 45433 to Hugo Delgado Granados) is acknowledged and we are indebted to Wilfried Haeberli for general support of this study. Essential assistance in Mexico was offered by Patricia Julio-Miranda, Isaac A. Farraz and Eduardo Rubio-Herrera. We are grateful for the constructive and careful reviews by Sarah Fagents and David Palacios.

Edited by: J. Marti
Reviewed by: S. Fagents and D. Palacios

## References

Abramov, A., Gruber, S., and Gilichinsky, D.: Mountain permafrost on active volcanoes: field data and statistical mapping, Klyuchevskaya Volcano Group, Kamchatka, Russia, Permafr. P. P., 19, 1–17, 2008 in press.

Álvarez, R. and Delgado, H.: Characterization of a tropical ice body on Iztaccíhuatl volcano, Mexico, Proceedings of the Ninth International Conference on Ground Penetrating Radar, 4758, 438–442, 2002.

Andrés, N., Zamorano, J. J., Sanjosé, J. J., Atkinson, A., and Palacios, D.: Glacier retreat during the recent eruptive period of Popocatépetl volcano, Mexico, Ann. Glaciol., 45, 73–82, 2007.

Benson, C. S. and Motyka, R. J.: Glacier – volcano interactions on Mt. Wrangell, Alaska, Annual Report, Geophysical Institute, University of Alaska, Fairbanks, 25 pp., 1978.

Benson, C., Motyka, R., McNutt, S., Lüthi, M., and Truffer, M.: Glacier-volcano interactions in the North Crater of Mt. Wrangell, Alaska, Ann. Glaciol., 45, 48–57, 2007.

Capra, L., Poblete, M. A., and Alvarado, R.: The 1997 and 2001 lahars of Popocatépetl volcano (Central Mexico): textural and sedimentological constraints on their origin and hazards, J. Volcanol. Geoth. Res., 131, 351–369, 2004.

Ceballos, J. L., Euscátegui, C., Ramírez, J., Cañon, M., Huggel, C., Haeberli, W., and Machguth, H.: Fast shrinkage of tropical glaciers in Colombia, Ann. Glaciol., 43, 1, 194–201, 2006.

Coussot, P. and Meunier, M.: Recognition, classification and mechanical description of debris flows, Earth-Sci. Rev., 40, 209–227, 1996.

Davila, N., Capra, L., Gavilanes-Ruiz, J. C., Varley, N., Norini, G., and Vazquez, A. G.: Recent lahars at Volcan de Colima (Mexico): Drainage variation and spectral classification, J. Volcanol. Geoth. Res., 165, 3–4, 127–141, 2007.

Delgado Granados, H.: Climate change vs. volcanic activity: Forcing Mexican glaciers to extinguish and related hazards. Proceedings of the First International Conference on the Impact of Climate Change on High-Mountain Systems, Instituto de Hidrología, Meteorología y Estudios Ambientales, Bogotá, Colombia, 153–168, 2007.

Delgado Granados, H., Julio Miranda, P., Álvarez, R., Cabral-Cano, E., Cárdenas Gonzalez, L., Correa Mora, F., Luna Alonso, M., and Huggel, C.: Study of Ayoloco Glacier at Iztaccíhuatl volcano (Mexico): hazards related to volcanic activity – ice cover interactions, Z. Geomorphol., 140, 181–193, 2005.

Eckert, S., Kellenberger, T., and Itten, K.: Accuracy Assessment of automatically derived digital elevation models from ASTER data in mountainous terrain, Int. J. Remote Sens., 26, 9, 1943–1957, 2005.

Guerra-Acevedo, B.: Estudios de balance hidrológico en la ladera oriental del volcán Iztaccíhuatl, Master thesis, Universidad Autónoma de Chihuahua, Mexico, 154 pp., 2006.

Haeberli, W.: Frequency and characteristics of glacier floods in the Swiss Alps, Ann. Glaciol., 4, 85–90, 1983.

Haeberli, W., Frauenfelder, R., Hoelzle, M., and Maisch, M.: On rates and acceleration trends of global glacier mass changes, Geogr. Ann. A, 81A, 4, 585–591, 1999.

Hubbard, B. E., Sheridan, M. F., Carrasco-Nunez, G., Diaz-Castellon, R., and Rodriguez, S. R.: Comparative lahar hazard mapping at Volcan Citlaltepetl, Mexico using SRTM, ASTER and DTED-1 digital topographic data, J. Volcanol. Geoth. Res., 160, 1–2, 99–124, 2006.

Huggel, C., Kääb, A., Haeberli, W., and Krummenacher, B.: Regional-scale GIS-models for assessment of hazards from glacier lake outbursts: evaluation and application in the Swiss Alps, Nat. Hazards Earth Syst. Sci., 3, 647–662, 2003, http://www.nat-hazards-earth-syst-sci.net/3/647/2003/.

Huggel, C., Schneider, D., Julio Miranda, P., Delgado Granados, H., and Kääb, A.: Evaluation of ASTER and SRTM DEM data for lahar modeling: a case study on lahars from Popocatépetl Volcano, Mexico, J. Volcanol. Geoth. Res., 170, 99–110, 2008.

Instituto de Geografía de la UNAM: Carta de climas, Veracruz, 1:500 000, map no. 14Q-VI, 1970.

Instituto Nacional de Estadística Geografía e Informática INEGI: Orthophoto map, 1:20 000, map no. E14B42-A, 1983.

Instituto Nacional de Estadística Geografía e Informática INEGI: Topographic map, Huejotzingo, 1:50 000, map no. E14B42, 1995.

Iverson, R. M., Schilling, S. P., and Vallance, J. W.: Objective delineation of lahar-inundation hazard zones, GSA Bulletin, 110, 8, 972–984, 1998.

Julio Miranda, P. and Delgado Granados, H.: Fast hazard evaluation employing digital photogrammetry: Popocatépetl glaciers, Mexico, Geofísica Internacional, 42, 2, 275–283, 2003.

Julio Miranda, P., Gonzalez-Huesca, A. E., Delgado Granados, H., and Kääb, A.: Glacier melting and lahar formation during January 22, 2001 eruption, Popocatépetl volcano (Mexico), Z. Geomorphol., 140, 93–102, 2005.

Kääb, A.: Combination of SRTM3 and repeat ASTER data for deriving alpine glacier flow velocities in the Bhutan Himalaya, Remote Sens. Environ., 94, 463–474, 2005.

Kääb, A., Huggel, C., Fischer, L., Guex, S., Paul, F., Roer, I., Salzmann, N., Schlaefli, S., Schmutz, K., Schneider, D., Strozzi, T., and Weidmann, W.: Remote sensing of glacier- and permafrost-related hazards in high mountains: an overview, Nat. Hazards Earth Syst. Sci., 5, 527–554, 2005

Kaser, G. and Osmaston, H.: Tropical Glaciers, International Hydrology Series, Press Syndicate of the University of Cambridge, Cambridge, 207 pp., 2002.

Kerle, N. and Oppenheimer, C.: Satellite remote sensing as a tool in lahar disaster management, Disasters, 26, 2, 140–160, 2002.

Lavigne, F. and Thouret, J.-C.: Sediment transportation and deposition by rain-triggered lahars at Merapi Volcano, Central Java, Indonesia, Geomorphology, 49, 45–69, 2002.

Legros, F.: The mobility of long-runout landslides, Eng. Geol., 63, 301–331, 2002.

Lorenzo, J. L.: Los Glaciares de México, Monografías del Instituto de Geofísica, Universidad Nacional Autónoma de México, México D. F., 114 pp., 1959.

Marks, D., Dozier, J., and Frew, J.: Automated basin delineation from digital elevation data, Geo Processing, 2, 299–311, 1984.

Nixon, G. T.: The geology of Iztaccíhuatl Volcano and adjacent areas of the Sierra Nevada and Valley of Mexico, The Geological Society of America, Special Paper 219, 58 pp., 1989.

Palacios, D., Zamorano, J. J., and Andrés, N.: Permafrost distribution in tropical stratovolcanoes: Popocatépetl and Iztaccíhuatl volcanoes (Mexico), Geophys. Res. Abstr., 9, 05615, 2007.

Paul, F., Kääb, A., Maisch, M., Kellenberger, T., and Haeberli, W.: The new remote-sensing-derived Swiss glacier inventory: I. Methods, Ann. Glaciol., 34, 1, 355–361, 2002.

Pieri, D. and Abrams, M.: ASTER watches the world's volcanoes: a new paradigm for volcanological observations from orbit, J. Volcanol. Geoth. Res., 135, 13–28, 2004.

Pierson, T. C.: Flow behaviour of channelized debris flows, Mount St. Helens, Washington, in: Hillslope Processes, edited by: Abrahams, A. D., Allen and Unwin, Winchester, 269–296, 1986.

Pierson, T. C.: An empirical method for estimating travel times for wet volcanic mass flows, B. Volcanol., 60, 2, 98–109, 1998.

Pierson, T. C. and Scott, K. M.: Downstream dilution of a lahar: transition from debris flow to hyperconcentrated streamflow, Water Resour. Res., 21, 10, 1511–1524, 1985.

Pierson, T. C., Janda, R. J., Thouret, J.-C., and Borrero, C. A.: Perturbation and melting of snow and ice by the 13 November 1985 eruption of Nevado del Ruiz, Colombia, and consequent mobilization, flow and deposition of lahars, J. Volcanol. Geoth. Res., 41, 17–66, 1990.

Rabus, B., Eineder, M., Roth, A., and Bamler, R.: The shuttle radar topography mission – a new class of digital elevation models acquired by spaceborne radar, ISPRS Journal of Photogrammetry and Remote Sensing, 57, 241–262, 2003.

Ramírez, E., Francou, B., Ribstein, P., Descloitres, M., Guérin, R., Mendoza, J., Gallaire, R., Pouyaud, B., and Jordan, E.: Small glaciers disappearing in the tropical Andes: a case-study in Bolivia: Glaciar Chacaltaya (16°S), J. Glaciol., 47, 157, 187–194, 2001.

Russell, A. J. and Knudsen, Ó.: The effects of glacier-outburst flood flow dynamics on ice-contact deposits: November 1996 jökulhlaup, Skeidarársandur, Iceland, Spec. Publ. Int. Ass. Sediment., 32, 67–83, 2002.

Scott, K. M., Macías, J. L., Naranjo, J. A., Rodríguez, S., and McGeehin, J. P.: Catastrophic debris flows transformed from landslides in volcanic terrains: mobility, hazard assessment, and mitigation strategies, U.S. Geological Survey, Professional Paper 1630, 59 pp., 2001.

Sheridan, M. F., Stinton, A. J., Patra, A., Pitman, E. B., Bauer, A., and Nichita, C. C.: Evaluating Titan2D mass-flow model using the 1963 Little Tahoma Peak avalanches, Mount Rainier, Washington, J. Volcanol. Geoth. Res., 139, 1–2, 89–102, 2005.

Siebe, C., Abrams, M. and Macías, J. L.: Derrumbes gigantes, depositos de avalancha de escombros y edad del actual cono del volcan Popocatépetl, in: Volcan Popocatépetl – Estudios Realizados durante la crisis de 1994/95, edited by: Comite cientifico asesor CENAPRED-UNAM, 195–220, 1995.

Siebe, C., Abrams, M., Macías, J. L., and Obenholzner, J.: Repeated volcanic disasters in Prehispanic time at Popocatépetl, central Mexico: Past key to the future?, Geology, 24, 5, 399–402, 1996.

Siebe, C. and Macías, J. L.: Volcanic hazards in the Mexico City metropolitan area from eruptions at Popocatépetl, Nevado de Toluca, and Jocotitlán stratovolcanoes and monogenetic scoria cones in the Sierra Chichinautzin Volcanic Field, in: Neogene-Quaternary continental margin volcanism: a perspective from México, edited by: Siebe, C., Macías, J. L., and Aguirre-Díaz, G. J., The Geological Society of America, Boulder, Colorado, Special Paper 402, 253–329, 2006.

Smith, B. and Sandwell, D.: Accuracy and resolution of shuttle radar topography mission data, Geophys. Res. Lett., 30, 9, 1467–1470, 2003.

Smith, G. and Lowe, A.: Lahars: volcano–hydrologic events and deposition in the debris-flow – hyperconcentrated flow continuum, in: Sedimentation in Volcanic Settings, edited by: Fisher, R. V. and Smith, G., SEPM Special Publication, 45, 59–70, 1991.

Stevens, N. F., Manville, V., and Heron, D. W.: The sensitivity of a volcanic flow model to digital elevation model accuracy: experiments with digitised map contours and interferometric SAR at Ruapehu and Taranaki volcanoes, New Zealand, J. Volcanol. Geoth. Res., 119, 89–105, 2002.

Thouret, J.-C.: Effects of the November 13, 1985 eruption on the snow pack and ice cap of Nevado del Ruiz volcano, Colombia, in: Nevado del Ruiz Volcano, Colombia, edited by: Williams, S. N., J. Volcanol. Geoth. Res., 41, 177–201, 1990.

Toutin, T.: Three-dimensional topographic mapping with ASTER stereo data in rugged topography, IEEE-TGARS, 40, 10, 2241–2247, 2002.

Vallance, J. W.: Lahars, in: Encyclopedia of Volcanoes, edited by: Sugurdsson, H., Academic Press, 601–616, 2000.

Vallance, J. W., Schilling, S. P., Devoli, G., and Howell, M. M.: Lahar Hazards at Concepción Volcano, Nicaragua, U.S. Geological Survey, 1–13 pp., 2001.

Van Westen, C. J. and Daag, A. S.: Analysing the relation between rainfall characteristics and lahar at Mount Pinatubo, Philippines, Earth Surf. Proc. Land., 30, 1663–1674, 2005.

Verstappen, H. T.: Volcanic hazards in Colombia and Indonesia: lahars and related phenomena, in: Geohazards – Natural and manmade, edited by: McCall, G. J. H., Laming, D. J. C., and Scott, S. C., Chapman and Hall, 33–42, 1992.

Walder, J. S., LaHusen, R. G., Vallance, J. W., and Schilling, S. P.: Crater glaciers on active volcanoes: hydrological anomalies, EOS, Transactions, American Geophysical Union, 86, 50, 521/528, 2005.

Welch, B. C., Dwyer, K., Helgen, M., Waythomas, C. F., and Jacobel, R. W.: Geophysical survey of the intra-caldera icefield of Mt. Veniaminof, Alaska, Ann. Glaciol., 45, 58–65, 2007.

White, S. E.: Glaciers of México, in: Satellite image atlas of glaciers of the world, edited by: Williams, R. S., Ferrigno, J. G., US Geological Survey, Professional Paper 1386-J-3, 383–405, 2002.

Zemp, M., Haeberli, W., Bajracharya, S., Chinn, T. J., Fountain, A. G., Hagen, J. O., Huggel, C., Kääb, A., Kaltenborn, B. P., Karki, M., Kaser, G., Kotlyakov, V. M., Lambrechts, C., Li, Z., Molnia, B. F., Mool, P., Nellemann, C., Novikov, V., Osipova, G. B., Rivera, A., Shrestha, B., Svoboda, F., Tsvetkov, D. G., and Yao, T.: Glaciers and ice caps, in: Global outlook for ice and snow, edited by: UNEP, 115-152, 2007.

# Paper III

Nat. Hazards Earth Syst. Sci., 9, 481–499, 2009
www.nat-hazards-earth-syst-sci.net/9/481/2009/

Natural Hazards
and Earth
System Sciences

# First approaches towards modelling glacial hazards in the Mount Cook region of New Zealand's Southern Alps

**S. K. Allen**[1], **D. Schneider**[2,3], **and I. F. Owens**[1]

[1]Department of Geography, University of Canterbury, Christchurch, 8140, New Zealand
[2]Glaciology, Geomorphodynamics and Geochronology, Dept. of Geography, University of Zurich-Irchel, 8057, Switzerland
[3]WSL Institute for Snow and Avalanche Research, SLF, Davos Dorf, 7250, Switzerland

Received: 11 September 2008 – Revised: 15 December 2008 – Accepted: 24 March 2009 – Published: 31 March 2009

**Abstract.** Flood and mass movements originating from glacial environments are particularly devastating in populated mountain regions of the world, but in the remote Mount Cook region of New Zealand's Southern Alps minimal attention has been given to these processes. Glacial environments are characterized by high mass turnover and combined with changing climatic conditions, potential problems and process interactions can evolve rapidly. Remote sensing based terrain mapping, geographic information systems and flow path modelling are integrated here to explore the extent of ice avalanche, debris flow and lake flood hazard potential in the Mount Cook region. Numerous proglacial lakes have formed during recent decades, but well vegetated, low gradient outlet areas suggest catastrophic dam failure and flooding is unlikely. However, potential impacts from incoming mass movements of ice, debris or rock could lead to dam overtopping, particularly where lakes are forming directly beneath steep slopes. Physically based numerical modeling with RAMMS was introduced for local scale analyses of rock avalanche events, and was shown to be a useful tool for establishing accurate flow path dynamics and estimating potential event magnitudes. Potential debris flows originating from steep moraine and talus slopes can reach road and built infrastructure when worst-case runout distances are considered, while potential effects from ice avalanches are limited to walking tracks and alpine huts located in close proximity to initiation zones of steep ice. Further local scale studies of these processes are required, leading towards a full hazard assessment, and changing glacial conditions over coming decades will necessitate ongoing monitoring and reassessment of initiation zones and potential impacts.

---

*Correspondence to:* S. K. Allen
(simon.allen@pg.canterbury.ac.nz)

## 1 Introduction

Glacial hazards have been defined as any glacial or glacier-related feature or process that adversely affect human activities (Reynolds, 1992). These hazards are a concern for many high mountain regions of the world and can have severe resource management implications relating to water availability and hydro-power generation (Reynolds, 1992; Richardson and Reynolds, 2000). Glaciers are highly sensitive to climate forcing, and in many regions glacial retreat during the past century has now continued beyond any known historical positions, drastically altering the geomorphic process activity of the environment and shifting zones of hazard initiation (Kääb et al., 2005). Glacial hazards include ice avalanches, glacial floods, and debris flows, although the most catastrophic events have involved complex chain reactions or transformation of mass movements or floods into rapid debris flows (e.g., Huggel et al., 2005). Other hazards can develop directly from surge type glacial movements (Haeberli et al., 2002), while large bedrock failures are increasingly being studied in relation to changing glacial and permafrost conditions (Harris, 2005). Fundamental research into phenomena such as ice avalanches (Alean, 1985), glacier-related debris flows (Rickenmann, 1999) and flooding (Clague and Evans, 2000; Haeberli, 1983; Maizels and Russel, 1992) has come from Canada, Central Europe and Iceland, where populated villages and transport infrastructure extend into the glacial environment. Understanding of such processes and potential impacts in the Mount Cook region of New Zealand is comparatively limited, despite recognition of 20th century glacial recession (Chinn, 1996), associated destabilisation of surrounding terrain and lake formation (Blair, 1994; Hochstein et al., 1995), and the potential for large magnitude chain reaction events involving mass movements into glacial lakes (McSaveney, 2002).

Published by Copernicus Publications on behalf of the European Geosciences Union.

This paper aims to use remote sensing, geographic information system (GIS) capabilities and flow path modelling to identify potential initiation zones and explore the spatial distribution of potential ice avalanches, debris flows and catastrophic outburst floods in the Mount Cook region of New Zealand. In addition, the first results from numerical modelling of recent rock avalanches are introduced, providing a tool for assessing future impacts from large bedrock failures in the region. The emphasis of this study is on events originating from the current glacierised and recent paraglacial landscape, which is inferred here to be terrain uncovered since the Little Ice Age (LIA) maximum was reached (see Sect. 3). It is beyond the scope of this contribution to provide a hazard assessment. Instead, the primary objective here is to apply conservative, worst-case scenario modelling of potential events, thereby directing future studies towards locations where infrastructure and human activities may be exposed to mass movements and/or flood inundation. Limitations of the approach will be discussed, and the impact of changing glacial conditions will be considered in relation to future event processes.

## 2 Background

Glacial floods refer to the sudden discharge of a water reservoir that has formed either underneath, at the side, in front, within, or at the surface of a glacier (Richardson and Reynolds, 2000). For reservoirs developing as lakes on or at the margin of glaciers, remote sensing at suitable spatial and temporal resolution is an appropriate tool for monitoring hazardous developments (e.g., Huggel et al., 2002). Floods are the most far reaching of all glacial hazards, often initiating from the catastrophic failure of moraine dammed lakes, for which the term glacial lake outburst flood (GLOF) has been adopted (Richardson and Reynolds, 2000). GLOFs frequently transform into hyperconcentrated or debris flow events following the entrainment of paraglacial debris, and are a well documented hazard for Central Asia (Ding and Liu, 1992; Quincey et al., 2007), the Andes (Reynolds, 1992), Canada (Clague and Evans, 2000), and Europe (e.g., Haeberli, 1983). Ice avalanches occur when large masses of ice detach from steep cliff or ramp type glaciers (Alean, 1985) as frontal block failures, slab failures, or deeper failures at the ice/bedrock interface (Richardson and Reynolds, 2000). Relative to glacial floods, ice avalanches typically travel shorter distances and directly affected areas are normally restricted to densely populated alpine regions (Salzmann et al., 2004). However, far reaching disasters have resulted from process interactions involving combined ice/rock avalanches and transformations into debris or mudflows, such as the 1970 Huascaran disaster in Peru (Carey, 2005), or the more recent 2002 Kolka-Karmadon avalanche in the Caucasus (Huggel et al., 2005). Periglacial and recently uncovered paraglacial environments are prone to debris flow initiation because they are characterised by large accumulations of unconsolidated sediment, in the form of moraine deposits and talus slopes (Evans and Clague, 1994). For example, over 50% of debris flows observed during one particularly severe year in the Swiss Alps initiated from zones that had deglaciated within the previous 150 years (Zimmermann and Haeberli, 1992). Unlike debris flows on lowland hillslopes, glacier-related events can become activated via several mechanisms, including snow or ice melt and high intensity rainfall (Chiarle et al., 2007; Rickenmann and Zimmermann, 1993), permafrost degradation (Harris, 2005), or from catastrophic entrainment within glacial floodwaves (Clague and Evans, 1994; O'Connor et al., 2001).

Although New Zealand has significant areas of mountainous terrain, the population is almost entirely located in lowland areas, and therefore floods and mass movements occurring in high mountain regions have received comparatively less scientific attention. Studies have described flood hazard problems from Franz Josef and Fox Glaciers where the sudden release of sub- or en-glacial reservoirs can mobilise large amounts of sediment (Davies et al., 2003; Goodsell et al., 2005). Debris flow activity initiated during storm events is known to potentially endanger infrastructure within the Mount Cook Village (Skermer et al., 2002; Whitehouse, 1982), and the catastrophic downwasting of large valley glaciers is resulting in widespread moraine wall failure and the destruction of backcountry huts and tracks (Blair, 1994). Ice avalanche activity in the Mount Cook region predominates as low magnitude ($<1000\,\mathrm{m}^3$), high frequency events (1–8 events/h) from steep cliff-type glaciers (Iseli, 1991), producing a significant hazard on many of the well known climbing routes during the summer ablation season (Irwin et al., 2002). Large bedrock failures from glaciated areas of the Southern Alps have received greater scientific attention (e.g., Korup, 2005a; Whitehouse and Griffiths, 1983), partly because road infrastructure can be at risk (Paterson, 1996), downstream chain reactions can endanger lowland areas (e.g., Davies and Scott, 1997; Hancox et al., 2005), and recent glacial changes appear to be increasing the frequency of high magnitude events and likelihood of impacts into glacial lakes (McSaveney, 2002).

An important development in glacial hazard research has been the implementation of multi-hazard approaches within a GIS environment, integrating remote sensing detection of individual ice, debris and flood hazard sources with combined empirical and hydrological approaches to event path modelling (Huggel et al., 2004). Despite the implied suitability of these approaches to large scale, regional applications, to date, results have mainly been illustrated for case-study type scenarios within the European Alps. The Mount Cook region of New Zealand's Southern Alps provides an opportunity to implement GIS based procedures across a large, dynamic and diverse region where the primary objective is to gain first order knowledge of glacial hazard potential and recognition of affected areas. Particular emphasis is given to glacial lake flooding, and exploring the use of combined remote sensing/GIS methods to distinguish lakes formed within steep morainic debris. In recognition of the importance of large bedrock failures in the region (e.g., McSaveney, 2002; Whitehouse and Griffiths, 1983) this study is expanded beyond GIS based modelling of glacial lake floods, debris flows and ice avalanches, to include a numerical modelling approach that may be used to simulate potential rock avalanche impacts at a more detailed level of investigation.

## 3 The Mount Cook region

The Mount Cook region is broadly defined here to encompass the Aoraki Mount Cook National Park, extending west of the main divide into the Westland National Park and further south towards the Ben Ohau Range, with a total land area of over 3500 km$^2$ (Fig. 1). The region includes the highest mountains and the most heavily glacierised terrain of New Zealand's Southern Alps. Permanent snow covered peaks are found between 2500 and 3754 m, with local relief in the order of 1000–2700 m (McSaveney, 2002). Moist westerly airflow generates high orographic precipitation about the main divide ($>12\,\mathrm{m\,y^{-1}}$), but an extreme leeward gradient produces $<4\,\mathrm{m\,y^{-1}}$ only 20 km further to the southeast (Henderson and Thompson, 1999). The timing of the LIA maximum varied across the region, but between 1750 and 1890 widespread retreat had begun, becoming most evident during the mid 20th century, and in total, a 49% loss in ice area has been estimated, although some highly responsive glaciers have advanced recently owing to short term climate variations (Chinn, 1996). The Alpine Fault is a major active fault traversing the northwestern edge of the study area, on which most of the ongoing tectonic movement between the Australian Plate (to the northwest) and the Pacific Plate (to the southeast) is concentrated. Plate convergence across the Australian-Pacific plate causes continued uplift of the Southern Alps in the order of $10\,\mathrm{mm\,y^{-1}}$, which is approximately in balance with regional erosion (Koons, 1990). The last major (M 8) earthquake on the Alpine Fault has been dated at 1717, although the expectation is for episodic shaking from high-magnitude (M7-8) events every 200–300 years, (Wells et al., 1999).

The Mount Cook Village is the main service and accommodation centre for visitors that access the region from the east, with a small permanent population of ∼100 and a larger seasonal component linked to tourism activities in the region. West of the main divide, the largest tourist and residential centres are Franz Josef and Fox Glacier Villages, with ∼300 permanent residents housed in each village. Figures provided by the Department of Conservation indicate that backcountry hut and camp ground usage in the Mount Cook National Park averaged nearly 10 000 bed-nights per year during the monitoring period 1982 to 2002. In the Westland National Park, 4500 visitors walked the Copland Valley track in 2007 (Fig. 1), and 250 000 made the short walk to the terminus of the Fox Glacier (FX), with these numbers slowly increasing over recent years. Main roads connect to all tourist and residential areas, but the nearest transalpine passes are 80 km to the southwest and 150 km to the northeast. Numerous unsealed vehicle tracks give access to more remote areas and farm buildings.

## 4 Regional hazard modelling

### 4.1 Modelling strategy

Allen et al. (2008b) applied remote sensing based methods to map the distribution of glacial lakes, ice, and debris accumulations across the Mount Cook region. These procedures used visible, near infrared (NIR) and shortwave infrared (SWIR) bands of the Advanced Spaceborne Thermal Emission and Reflection Radiometer (ASTER) satellite sensor, and were based upon an orthorectified scene of 24 January 2006. The inclusion of topographic information from the Landcare Research L2, 25 m gridded South Island digital elevation model (DEM) enables detection of steep, potentially unstable surfaces on the basis of empirically derived values describing critical slope gradients (Table 1). The DEM is derived from stereographic analyses of 1:50 000 aerial photography captured in 1986, and although errors are strongly related to landform, a root mean square error of 5–8 m has been calculated for hilly and steep terrain (Barringer et al., 2002).

Potential debris flow, ice avalanche, and flood events were modelled at the regional scale using the modified single flow (MSF) routing algorithm developed by Huggel et al. (2003). Simple GIS spatial queries could then identify where event paths potentially intersect with infrastructure or where interactions such as ice impacts into glacial lakes might occur (Table 2). The MSF model is based on the D8 flow direction algorithm, modified to provide a quasi-qualitative likelihood that a given cell will be affected by the flow path based on distance from the source area, and allowing for deviation of up to the 45° either side from the path of steepest descent. However, it must be noted that this should not be interpreted as a hazard probability because event frequency and timing is not considered. In addition, the MSF model has no physical basis, and therefore cannot represent more complex behavior of mass movements such as barrier run-up and overtopping. Despite these obvious limitations, the MSF model has proven a useful tool for early recognition of hazard potential, and is particularly well suited for use at larger spatial scales where multiple source areas are identified, and direct field observations may be difficult (e.g., Huggel et al., 2004; Schneider et al., 2008). As with previous studies, a worst-case scenario approach is used, whereby modelled flow paths are continued

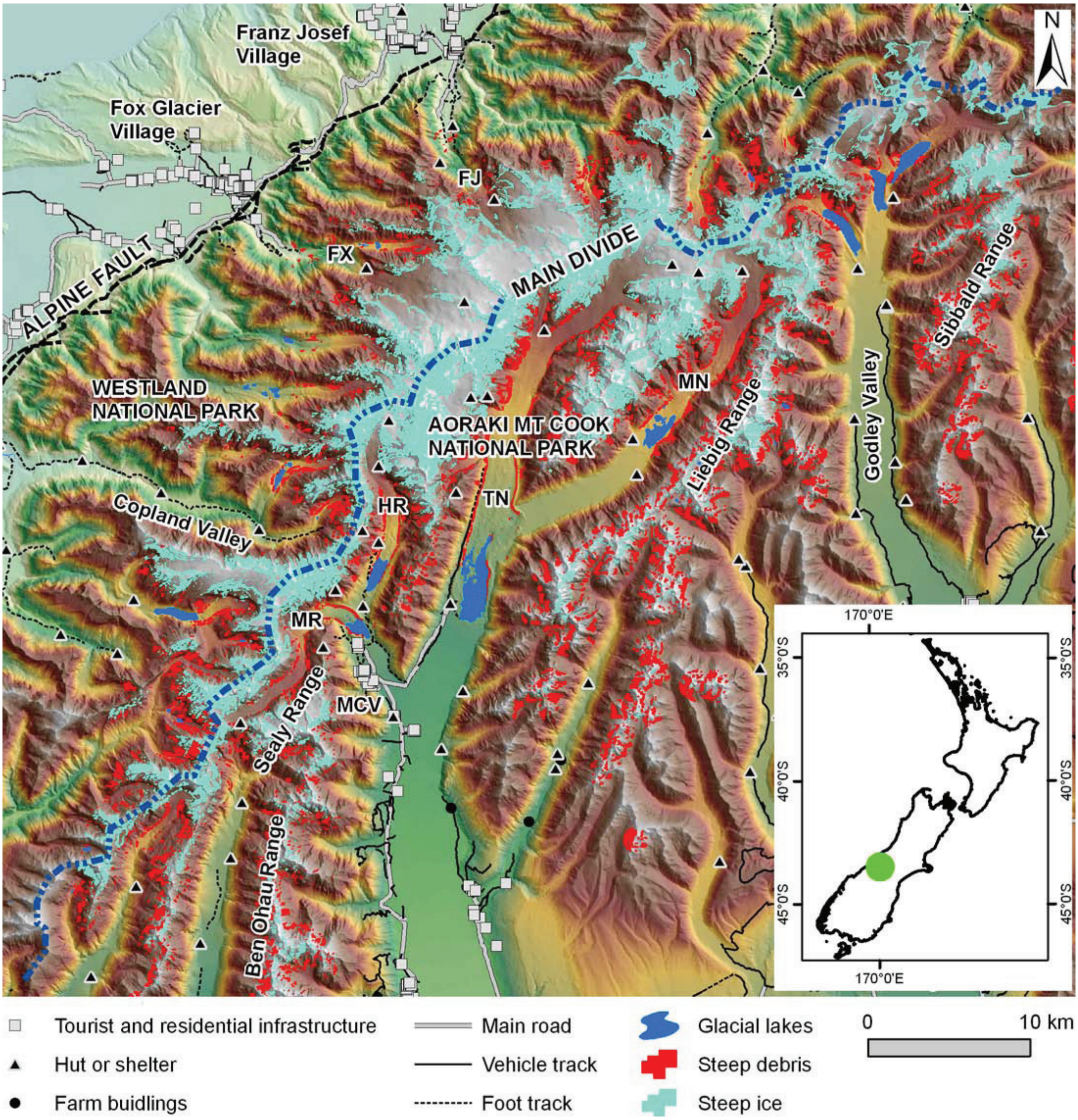

**Fig. 1.** Overview of the Mount Cook study region showing distribution of road, track, and built infrastructure. Main villages, including the Mount Cook Village (MCV) are identified. Glaciers (abbreviated), river valleys, and mountain ranges referred to in the text are also given. The base image is the colour-shaded relief from the NZ 25 m DTM, with terrain surfaces classified from ASTER satellite imagery, January 2006.

until a probable maximum runout is reached. This maximum runout is described by an angle of reach $\alpha$, which defines the average slope of a line between the starting and end points of a mass movement (Table 1).

## 4.2 Glacial lake floods

Glacial lakes were mapped with ASTER using the Normalised Difference Vegetation Index (NDVI) (NIR3-RED2)/(NIR3+RED2), and an additional threshold of

**Table 1.** Parameters used to identify potential source areas and defining the maximum probable runout of glacial lake floods, debris flows, and ice avalanches.

| | Glacial lake floods | Debris flows | Ice avalanches |
|---|---|---|---|
| Surface characteristics | – Lakes on or at the margins of a glacier<br>– Expanding lake area<br>– Steep moraine dammed lakes | – Debris accumulations occurring within glacial, or recent glacial zones | Steep glacial ice |
| Critical slope gradient | Sediment entrainment and hyperconcentration:<br>– 10°<br>(Clague and Evans, 1994; Hungr et al., 2005) | Flow initiation:<br>– 25–38°<br>(Hungr et al., 1984; Rickenmann and Zimmermann, 1993; Takahashi, 1991) | Temperate ice:<br>– 25°<br>Cold ice:<br>– 45°<br>(Alean, 1985) |
| Maximum probable runout | Clear water flood:<br>– May exceed 200 km and attain angle of reach <3°<br>GLOF triggered debris flow:<br>– 11° angle of reach<br>(Huggel et al., 2002; McKillop and Clague, 2007) | – 11° angle of reach<br>(Rickenmann, 2005; Rickenmann and Zimmermann, 1993) | – 17° angle of reach<br>(Alean, 1985; Huggel et al., 2004) |

RED2/GREEN1, providing a useful distinction of all water bodies in the region regardless of turbidity levels (Allen et al., 2008b). In total, 65 glacial lakes were identified but some were small interlinked supraglacial lakes and ponds. To exclude the smallest lakes from the flood modelling, a lake area threshold of 1500 $m^2$ was used, leaving 54 remaining lakes. The majority of lake water exists at low elevations (750–1000 m), where large proglacial lakes have formed on the Murchison (MN), Tasman (TN), Hooker (HR) and Mueller (MR) glaciers east of the main divide (Figs. 1 and 2). Because bathymetric measurements have been limited to piecemeal observations, estimation of lake volumes across the wider region must rely upon relationships describing lake volume as a function of surface area, derived from measurements in Canada, North America, Nepal, Central Europe, and South America (O'Connor et al., 2001; Huggel et al., 2002). The available measurements from the Mount Cook region enable some local validation of these relationships (Table 3). Because it results in significantly smaller errors, the relationship of Huggel et al. (2002) is preferred, albeit with the understanding that actual volumes of large proglacial lakes may be underestimated by ~20–50% because of the exceptional depths (>55 m) of these lakes compared with the sample from which the relationship was established. The Mueller Lake appears an anomaly, with very shallow depths possibly relating to greater sedimentation into the lake and/or the younger development phase of the lake. The majority of lakes are estimated to have relatively small volumes (modal volume of $0.05\times10^6$ $m^3$) but 14 lakes have estimated volumes larger than $1\times10^6$ $m^3$, with the Tasman Lake containing more than $200\times10^6$ $m^3$ (Fig. 3a).

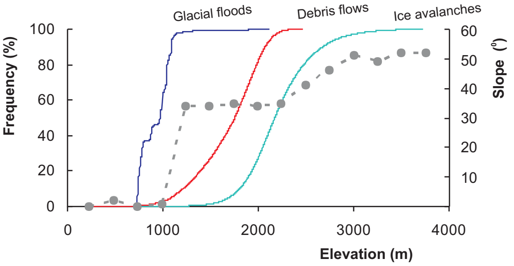

**Fig. 2.** Cumulative frequency distributions describing source areas for glacial flood and mass movements in the Mount Cook region as a function of elevation. Glacial lake water, steep debris accumulations and steep ice predominate within distinct altitudinal zones, and are compared with the modal topographic slope gradient calculated within 250 m elevation increments.

Because the majority of glacial lake water in the Mount Cook region is located at lower elevations characterized by gentle slope gradients (Fig. 2), it is considered inappropriate to assume lake failures will transform into debris flow events. Therefore, potential flood events were initially modelled as clear water floodwaves, for which flood attenuation was allowed to continue until the great lakes of Tekapo or Pukaki were reached in the east, or until the ocean was reached in the west. In fact, travel distances in excess of 200 km have been recorded in the Karakorum Himalaya from glacial floodwaves (Hewitt, 1982). In a second step, the modelled flood paths were analysed to identify outlet channel areas

**Table 2.** Summary of MSF modelling results, giving the extent of human infrastructure intersecting with modelled flow paths for the worst-case probable maximum runout. Also provided is the number of glacial lakes positioned within incoming flow paths, giving an indication of where potential flow transformations or impact waves might be initiated. Modelling was repeated for reduced runout scenarios, with minimum $\alpha$ increased by 50 and 100%.

| | Tourist or residential dwellings | Remote buildings | Main roads | Vehicle tracks | Foot tracks | Power/phone | Lake impacts |
|---|---|---|---|---|---|---|---|
| Glacial Floods | | | | | | | |
| i) Clear water | Mount Cook Village (MCV) and airport.<br>Floodplains southwest of Fox Glacier village. | 3 huts | 17 km | 29 km | 3 km | 12 km | 6 lakes |
| ii) Debris flows<br>11° ($\tan\alpha$=0.19) | NIL | NIL | NIL | NIL | NIL | NIL | NIL |
| Debris Flows | | | | | | | |
| 11° ($\tan\alpha$=0.19) | MCV and locations along main access road.<br>Glentanner Airport. | 17 huts<br>1 shelter<br>1 farm bld | 17 km | 33 km | 37 km | 3 km | 41 lakes |
| +50%<br>16.5° ($\tan\alpha$=0.30) | MCV | 13 huts<br>1 farm bld | 8 km | 22 km | 31 km | 2 km | 34 lakes |
| +100%<br>22° ($\tan\alpha$=0.40) | MCV | 10 huts<br>1 farm bld | 2 km | 16 km | 21 km | NIL | 25 lakes |
| Ice Avalanches | | | | | | | |
| 17° ($\tan\alpha$=0.31) | NIL | 10 huts<br>2 shelters | NIL | 1 km | 30 km | NIL | 36 lakes |
| +50%<br>25.5° ($\tan\alpha$=0.48) | NIL | 7 huts<br>1 shelter | NIL | NIL | 23 km | NIL | 26 lakes |
| +100%<br>34° ($\tan\alpha$=0.67) | NIL | NIL | NIL | NIL | 4 km | NIL | 11 lakes |

characterized by steep debris, and if appropriate, runout distances could then be re-evaluated for possible debris flow scenarios. A secondary output from the MSF model provides the horizontal distance along the flood path from the lake source. For floods originating from moraine breaches in the Three Sisters Range, Oregon, O'Connor et al. (2001) established 500 m as the horizontal distance in which floodwaves transformed into debris flow via sediment entrainment. This distance will be highly variable depending on local topography and channel morphology, but 500 m is taken here to arbitrarily encompass the dam and surrounding outlet channel areas for all glacial lakes (Fig. 4a).

ASTER-based methods were used to map debris and vegetation coverage within the lake outlet areas, supported by higher resolution satellite imagery and field photography. Large debris accumulations across the region have previously been identified and distinguished from bedrock using an image texture algorithm (Allen et al., 2008b). This idea stems from novel approaches developed with higher resolution imagery in the Swiss Alps (Huggel et al., 2004) and recognizes the uniformity of a debris surface compared to the rough, angular appearance of bedrock. The success of the procedure becomes more limited when applied with lower resolution ASTER imagery, but larger talus slopes, moraine deposits and outwash gravels were all identified. Vegetated surfaces were mapped using the NDVI. In a first step, outlet areas containing less than a combined 20% coverage of vegetation or debris were considered to be non-debris. For all other outlets, a larger presence of vegetation or non-vegetated debris was considered to indicate alluvium or moraine composition. If the vegetation abundance relative to non-vegetated debris exceeded 75%, the outlet area was categorized as 'vegetated' otherwise the outlet was categorized as "debris". A mean slope threshold of 10° was used to further distinguish steep outlet areas in which sediment entrainment is considered likely, based on debris flow studies of Hungr et al. (1984) and observations of GLOF events in Canada (Clague and Evans, 1994).

**Table 3.** Comparison between measured and estimated proglacial lake volumes in the Mount Cook region using two different empirical relationships.

| Lake | Observation year | Reference | Area ($m^2$ $10^6$) | Mean depth (m) | Volume ($m^3$ $10^6$) | Estimated volume[1] ($m^3$ $10^6$) | Estimated volume[2] ($m^3$ $10^6$) | Error[1] (%*) | Error[2] (%*) |
|---|---|---|---|---|---|---|---|---|---|
| Tasman | 1993 | Hochstein et al. (1995) | 2.0 | 71 | **139** | 89 | 647 | −36 | 365 |
| | 2002 | Röhl (2005) | 3.5 | 75 | **263** | 205 | 2075 | −22 | 689 |
| Hooker | 1995 | Warren and Kirkbride (1998) | 0.7 | 55 | **41** | 23 | 95 | −44 | 132 |
| | 2002 | Röhl (2005) | 0.9 | 65 | **59** | 30 | 140 | −49 | 137 |
| Mueller | 2002 | Röhl (2005) | 0.5 | 9 | **4.3** | 12 | 40 | 340 | 830 |
| Maud | 1994 | Warren and Kirkbride (1998) | 1.3 | 62 | **78** | 48 | 271 | −38 | 247 |
| Godley | 1994 | Warren and Kirkbride (1998) | 1.7 | 62 | **102** | 70 | 464 | −31 | 355 |

[1] Estimate based on the equation of Huggel et al. (2002), where lake volume ($V$) in $m^3$ is expressed by the relationship:

$V = 0.104A^{1.42}$.

[2] Estimate based on the equation of O'Connor et al. (2001) where lake volume ($V$) in $m^3$ is expressed by the relationship:

$V = 3.114\,A + 0.0001685A^2$ where ($A$) is lake area in $m^2$.

* Error is calculated as the difference between measured and estimated volumes, divided by the measured volume.

The majority of outlet areas were classified as "debris", with only one non-debris (bedrock) outlet identified. Lakes formed within debris mantled glacial ice could not be automatically excluded from the classification. These lakes have small volumes, and occur on low gradient supraglacial areas of the larger valley glaciers. Nearly 70% of terrain contained within outlet channel areas is characterized by slope gradients less than 10° (Fig. 3b), but several examples of lakes formed within steep vegetated and non-vegetated morainic debris occur in cirque basins primarily east of the main divide. In these instances, potential debris flow initiation is considered possible, and paths were therefore remodelled using a maximum runout defined by an 11° angle of reach recognized from GLOF triggered debris flow observations in the European Alps and Canada (Huggel et al., 2002; McKillop and Clague, 2007). Relative to modelled clear water floodwaves, flood triggered debris flows all appear to terminate well before huts, vehicle tracks, or other infrastructure are reached (Fig. 5, Table 2). Because the MSF model does not consider wave height and barrier overtopping cannot be simulated, the modelled floodwave down the Godley River is initially confined within a shallow channel leading from the lake outlet. However, evidence from a flood event which occurred from a rock avalanche impact in 1992 indicated that a 7–10 m high wave completely inundated the flat area surrounding the lake outlet before rapidly dispersing downstream on the wide braided river plains (McSaveney, 2002).

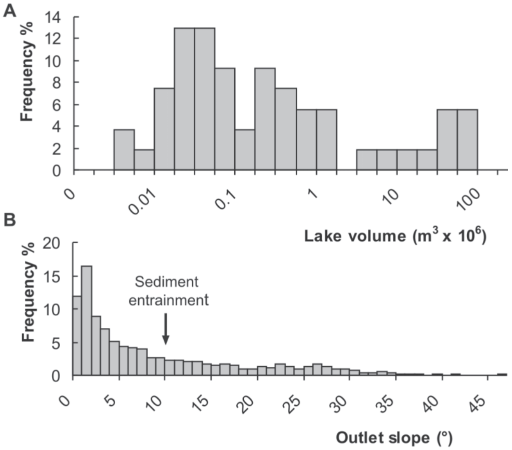

**Fig. 3.** **A** Frequency distribution of glacial lake volumes in the Mount Cook region, January 2006, estimated from ASTER mapped lake areas using an empirical relationship between lake area and volume (after Huggel et al., 2002). **B** Frequency distribution of slope gradients for all pixels contained within and surrounding lake outlet channel areas.

Vegetated outlet areas characterize most large proglacial lakes which have formed within low gradient moraine and outwash gravels during the past two decades (e.g., Figs. 4c and 7b). The presence of vegetation implies some longer term stability of the outlet area, given that no recent disturbances are likely to have occurred. This is exemplified by the Maud Glacier lake (Fig. 4b), where the current lack of vegetation provides evidence of the flood event that occurred 26 years previously. Also, vegetation can reduce the

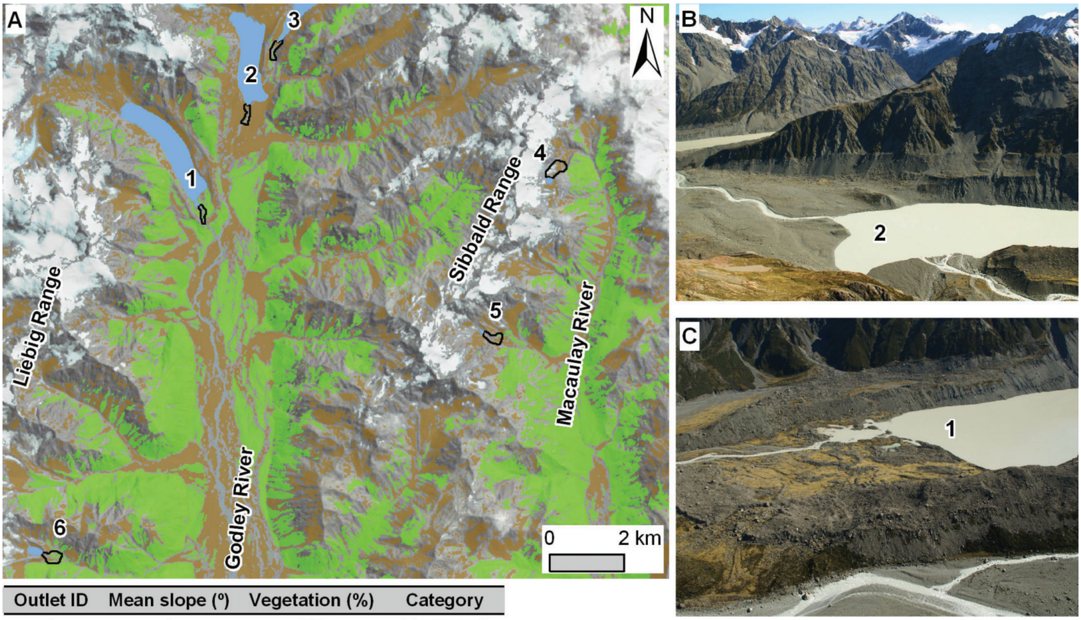

| Outlet ID | Mean slope (°) | Vegetation (%) | Category |
|---|---|---|---|
| 1 | 1 | 100 | Vegetated |
| 2 | 3 | 0 | Debris |
| 3 | 6 | 32 | Debris |
| 4 | 20 | 2 | Steep debris |
| 5 | 24 | 10 | Steep debris |
| 6 | 17 | 65 | Steep debris |

**Fig. 4.** **A** Classification of lake outlet areas (black outline) using ASTER based mapping of debris (brown) and vegetated surfaces (green). Unclassified areas predominantly represent bedrock, glacial ice, and river water. Vegetation coverage (%) is calculated relative to unvegetated debris. **B** The outlet area of the Maud Lake has been scoured of vegetation following the 1992 Mt Fletcher rock avalanche initiated floodwave, while at the Classen Lake **C** the presence of grass and tussock suggests no recent disturbances have occurred (photos: S. Winkler, April 2008).

erodibility of the channel area, limiting the likelihood of natural dam failure. However, when considering worst-case scenarios, future dam overtopping from displacement waves generated by mass movement impacts cannot be excluded. This would be most concerning where permanent building and road infrastructure are positioned within the flood plains of larger volume lakes, which occurs on the West Coast southwest of Fox Glacier Village, and along the road leading into Mount Cook Village (Table 2).

### 4.3 Debris flows

Steep ASTER classified debris accumulations that might give rise to a flow event were distinguished within a 25–38° slope range. Although specific to the source lithology involved and the associated angle of repose, this slope range typifies starting conditions observed internationally for debris flow events (e.g., Hungr et al., 1984; Rickenmann and Zimmermann, 1993), and corresponds to slope gradients measured for talus slopes in the Southern Alps of New Zealand (Dunning, 1996; Whitehouse and McSaveney, 1983). Steep debris accumulations are widespread across the region, but the emphasis of this study is towards situations where current and recent glacial processes directly influence debris accumulation and where ice or perennial snow melt can lead to flow initiation. To achieve this focus, a GIS buffer was used, extracting all debris accumulations within a maximum distance of 750 m from ASTER mapped glacial ice, including manually digitized debris covered ice. This distance is based upon average glacial length changes observed throughout the Southern Alps since the LIA, and also encompasses the likely extent of vertical recession over this time (Chinn, 1996). To remove isolated pixels, debris accumulations used as input into the MSF model were restricted to a minimum area of $1\times2$ pixels, or $\sim$1250 m$^2$, representing areas of lateral moraine above the downwasting valley glaciers, terminal moraine deposits from

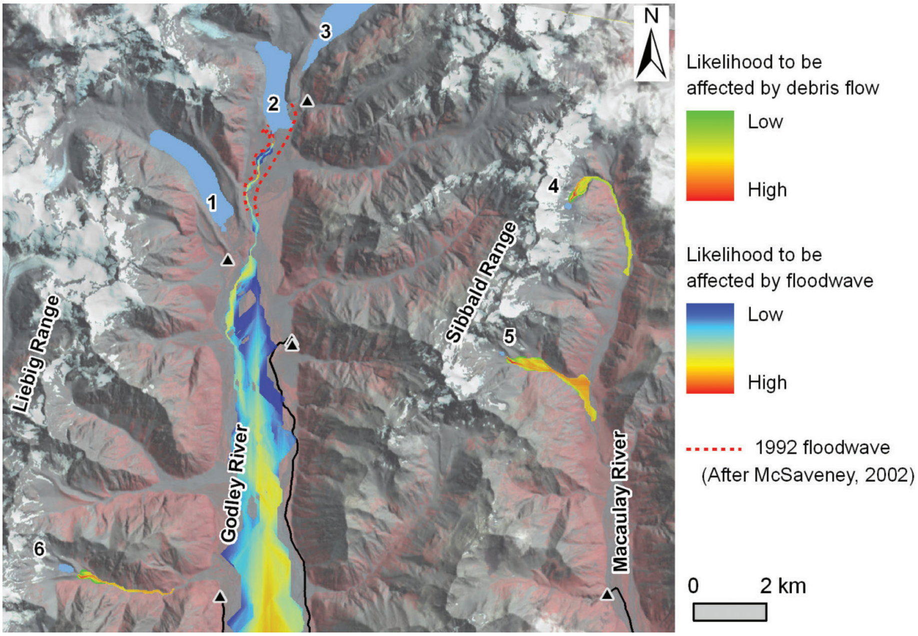

**Fig. 5.** MSF modelling of potential GLOF triggered debris flow events from 3 unnamed lakes where the dam area and outlet channel is formed within steep morainic debris (see Fig. 4). Also modelled is the most likely path for a floodwave initiating from the Maud Glacier lake (2). In 1992, a rock avalanche from Mt Fletcher produced a displacement wave from this lake. The background is provided by a 2006 ASTER image.

steeper glaciers, cirque glacial moraines, and talus slopes beneath glaciers or large perennial snow patches (Fig. 1).

The most comprehensive observations of debris flow travel distances in alpine terrain comes from the Swiss Alps, where a minimum $\alpha$=11° (tan $\alpha$=0.19) has been recognized for coarser grained flows (Rickenmann and Zimmermann, 1993), and subsequently used to define the maximum runout for modelled periglacial events (Huggel et al., 2004). Application of this worst-case scenario to potential events in the Mount Cook region identifies large sections of roading, tracks, huts, shelters and farm buildings positioned within modelled debris flow paths (Table 2). This is particularly evident east of the main divide, where a drier climate favours extensive talus development (Whitehouse, 1988) and vehicle tracks extend higher into the headwaters of braided river valleys (Fig. 1). Built infrastructure located within the Mount Cook Village, and nearby roading appears to intersect with potential paths originating from high on the Sealy Range where remnant cirque glaciers and perennial snow remain (Fig. 6). However, the maximum probable runout distance for these events exceeds any recognized threat to the village (McSaveney and Davies, 2005) and appears to overestimate flow propagation far beyond the composite fans upon which infrastructure is located. Minimum and maximum slope gradients observed on these fans range from <2 to 7°. West of the main divide, narrow steep gorges transport potential flows originating in the glacierised catchments down towards, but stopping short of directly reaching the state highway. In these instances, temporary blockage, dambreak, and remobilization of debris are possible within the confines of a steep gorge, and hence, a far reaching hazard potential may exist to not only the road, but villages such as Franz Josef located nearby (e.g., Davies and Scott, 1997).

Application of the MSF for multiple events at the regional level allows only a single worst-case maximum runout parameter, but an alternative estimate for individual events might consider available catchment area ($A_c$) above the debris source. For this purpose, $\tan\alpha=0.20\,A_c^{-0.26}$ has been used to describe the minimum $\alpha$ observed for debris flows in alpine areas of Switzerland and Canada (Rickenmann, 2005). Based on catchment areas calculated using ArcGIS watershed function, a significantly reduced maximum runout is estimated for modelled events affecting the Mount Cook Village and nearby areas (Fig. 6). For example, with a catchment area of ~0.09 km$^2$, a potential event originating from talus debris in the upper reaches of Kitchener Creek establishes a minimum tan $\alpha$=0.37, although this reach is still in excess of 300–500 m beyond any recent aggradation visi-

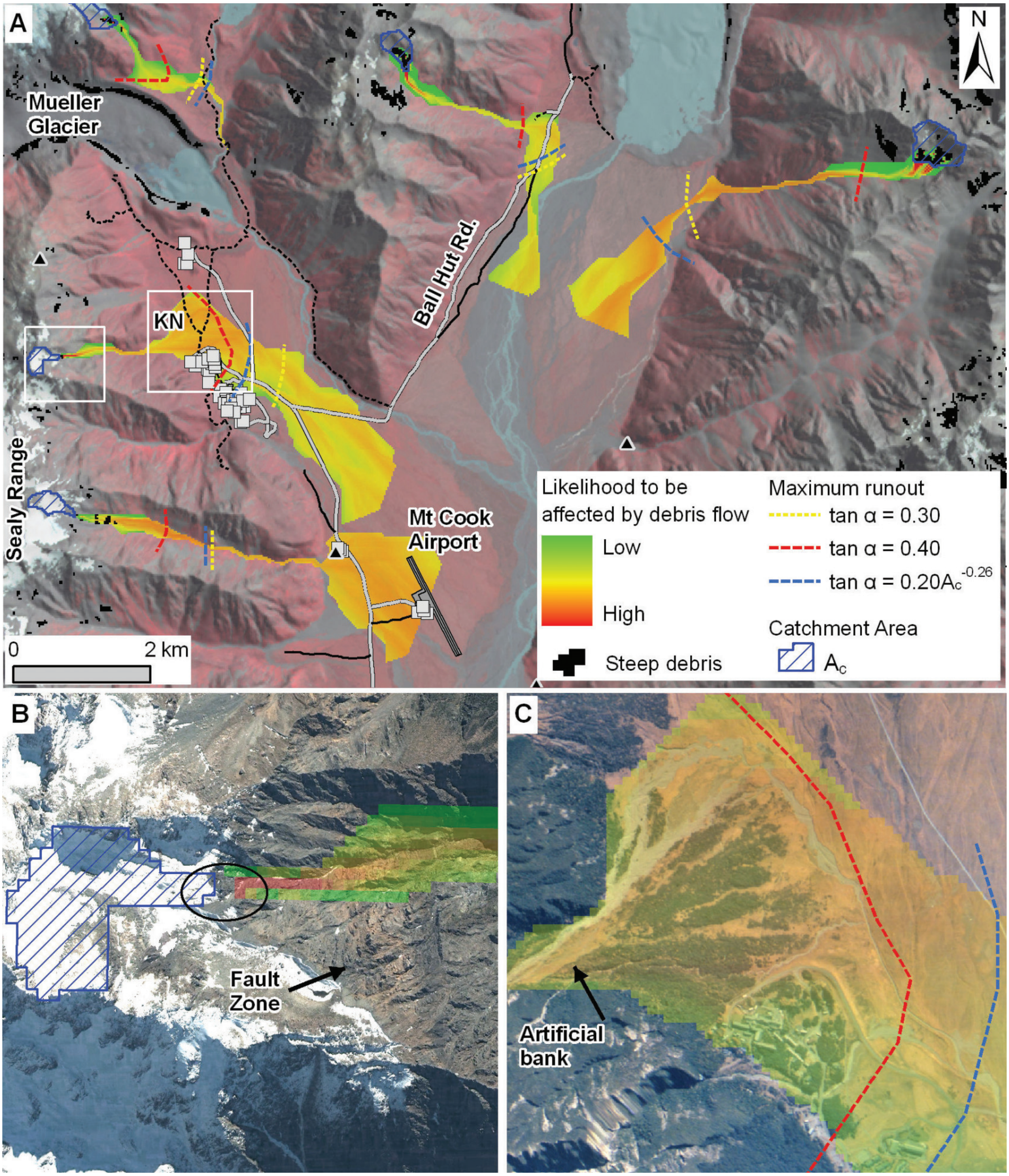

**Fig. 6.** **A** MSF modelling of selected debris flows initiating from glacial zones. The flow paths are terminated using the maximum probable runout defined by a minimum $\alpha$=11° (tan $\alpha$=0.19). Additional runout distances are indicated, corresponding to a minimum $\alpha$ increase of 50% (tan $\alpha$=0.30) and 100% (tan $\alpha$=0.40), and also using a minimum $\alpha$ related to catchment area (after Rickenmann, 2005). **B** Closer inspection of a potential source area from a snow covered talus slope at the head of Kitchener Creek (KN), and **C** deposition area with village infrastructure located towards lower right. High resolution QuickBird image is from 4 May 2006.

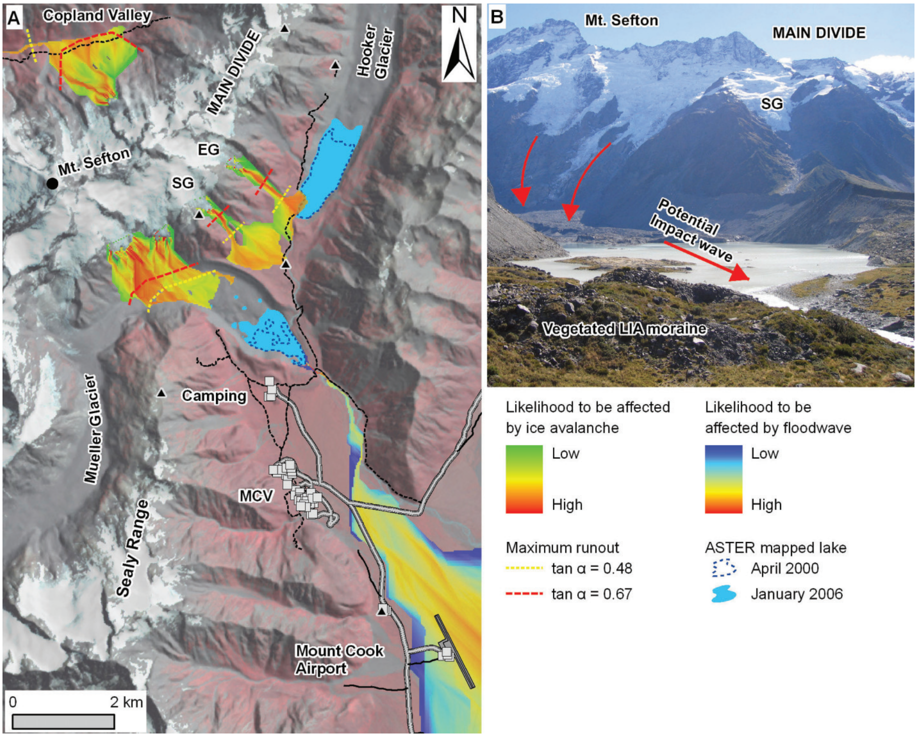

**Fig. 7.** **A** MSF modelling of selected ice avalanches affecting the lower Mueller and Hooker Glaciers, and upper Copland Valley. The flow paths are terminated using the maximum probable runout defined by a minimum $\alpha$=17° ($\tan\alpha$=0.31). Additional runout distances are indicated, corresponding to a minimum $\alpha$ increase of 50% ($\tan\alpha$=0.48) and 100% ($\tan\alpha$=0.67). A potential flood path propagating from the Mueller Lake is also shown. **B** Outlet area of the Mueller Lake looking towards the main divide, indicating potential ice avalanche trajectories towards the lake from beneath Mt Sefton (photo: S. Allen, April 2008).

ble on the stream fan (Fig. 6b, c). Artificial banks have constrained the recent flow of Kitchener creek to the north, but this was only considered a temporary measure and unlikely to mitigate a high magnitude debris flow event (McSaveney and Davies, 2005). While the $A_c$ approach provides a secondary estimate with which the static $\tan\alpha$=0.19 scenario can be quickly compared, it makes no consideration of geological, hydrological, and glaciological conditions which ultimately govern debris flow potential within an alpine catchment (Rickenmann and Zimmermann, 1993). For example, faults dissecting the Sealy range and many other steep slopes throughout the region form zones of weak shattered rock, from which enhanced sediment delivery can be expected (Korup, 2004). The future loss of remaining glacial ice and perennial snow in these ranges will expose new rock masses to weathering, and uncover further accumulations of morainic debris.

### 4.4 Ice avalanche and lake interactions

ASTER-based mapping of glacial ice has been achieved using a single band ratio (NIR3/SWIR4), providing the best distinction of glacial surfaces in steep, rocky terrain (Allen et al., 2008b). Debris covered tongues are not included within the automated classification, but these areas occur predominantly on low elevation gentle slopes and are therefore unlikely to be significant in relation to avalanche hazard. Modelling potential ice instabilities originating from $>400\,\mathrm{km}^2$ of glacier covered terrain is extremely difficult because important indicators such as crevasse patterns, ice displacements, hydrological and thermal conditions are best established through local scale analyses and field studies (e.g., Wegmann et al., 2003). At the regional scale, approaches have applied fundamental empirical observations from the Swiss Alps relating ice instability to topographic slope gradient (Alean, 1985), with a slope threshold of 25° used to classify potentially unstable steep ice (Huggel et al., 2004;

Salzmann et al., 2004). In reality, cold based ice, as occurs on steep cliffs and beneath the frontal section of many hanging glaciers at elevations where ground temperature remains <0°C (above ∼2500–3000 m) (Allen et al., 2008a), should remain stable at higher slope gradients (Table 1). However, the application of a single slope threshold is considered an appropriate worst-case scenario where polythermal glaciers are likely to occur. Steep glacial ice in the region predominates above 2000 m where modal slope gradients significantly increase (Fig. 2). To restrict the analyses to the largest potential events and exclude isolated seasonal snow, only glacial areas $>2500\,\mathrm{m}^2$ were used as input to the MSF model. The modelled avalanche runouts were terminated when a minimum $\alpha=17°$ ($\tan\alpha=0.31$) was achieved, corresponding to observed values in the Swiss Alps (Alean, 1985).

The smaller reach of ice avalanches combined with initiation zones which are generally located higher within the alpine valleys, excludes potential events from reaching any village infrastructure or major roads, and only a small section of the Ball Shelter vehicle track is located within the path of a far reaching event (Table 2). However, backcountry huts/shelters, and foot tracks located in closer proximity to starting zones are intersected by ice avalanche paths, as evident in the lower areas of the Hooker and Mueller Glaciers (Fig. 7). In these instances, events originating from the tongues of the Stocking (SG) and Eugenie (EG) Glaciers must travel the maximum probable distance to reach areas of human activity, while in the upper Copland Valley, smaller travel distances are sufficient to reach the walking track. Ice avalanches from the steep cliff glaciers beneath Mount Sefton frequently deposit onto the lower Mueller Glacier (Iseli, 1991), but these low magnitude events do not exceed a runout beyond a minimum $\tan\alpha=0.67$. However, a proglacial lake is currently expanding towards the ice cliffs, increasing the future potential for displacement waves, particularly from a larger magnitude event, with direct implications for adventure tourism activities operating on or near to the lake.

Ice avalanches on the lower Mueller Glacier are one example of the potential (current or future) for mass movements of ice, rock or debris to produce displacement waves, and lake flooding. A large proportion of lakes in the region show potential for interaction with incoming mass movements from ice and debris (Table 2), and bedrock instabilities are common from steep slopes of the main divide (e.g., McSaveney, 2002). The potential hazard from mass movements of ice (and/or rock) depositing into the Mueller Lake is exemplified because of the rapid enlargement of the lake over recent years, close proximity to the Mount Cook Village, and visitor infrastructure surrounding the lake (Fig. 7). In addition, incoming mass movements from the main divide can enter the Mueller Lake in line with the longitudinal axis of the lake, enabling wave energy to propagate directly towards the outlet channel. At other large proglacial lakes, on the Tasman, Hooker, and Murchison Glaciers, lakes have formed parallel to the mountain slopes, so that incoming mass movements are possible only from the lake sides, in which case, significant wave energy will be dissipated on the opposing bank. The Mueller Lake has formed within LIA moraines, which extend up to 150 m higher than the lake level on the true right hand side, providing a natural defense structure for the camping area and village located in behind. Nearer the outlet channel, the moraine is only 10–30 m higher than the lake level, and following some initial confinement, the modelled floodwave quickly disperses on the low gradient alluvial fan, intersecting with main roads and infrastructure of the Mount Cook airport, from where tourist flights operate. Low slope gradients in all the braided river valleys suggest that transformations into debris flows within the flood path from any larger proglacial lake are unlikely.

## 5 Rock avalanche modelling

Most steep rock walls in the Mount Cook region are heavily fractured and dilated, while many have become oversteepened as a result of glacial plucking and subsequent late Holocene ice retreat from their lower flanks (McSaveney, 2002). Given the possibility for rock avalanches to deposit into expanding proglacial lakes, and the potential for rivers to become blocked, leading to catastrophic dam failure and secondary mass movement hazards (Davies and Scott, 1997; Korup, 2005b), appropriate methods at a reduced spatial scale are needed to assess rock avalanche impacts. For simulating individual avalanche events, advanced two-dimensional mass movement modelling approaches are well suited for recognition of detailed flow patterns and dynamics. A numerical rapid mass movement model (RAMMS) developed by the WSL Institute for Snow Avalanche Research, Davos Dorf, Switzerland, meets these requirements, and the simulated output is easily integrated into a GIS environment (Christen et al., 2008). This physically based dynamic model uses a finite volume scheme to solve the 2-D shallow water equations for granular flows. The frictional resistance $S_{fx}$ in x-direction and $S_{fy}$ in y-direction which is acting against gravitational acceleration, is described by using a Voellmy approach which incorporates a dry Coulomb friction $\mu$ and a turbulent friction $\xi$ (Bartelt et al., 1999):

$$S_{fx}=\left[gH\mu\cos\alpha+\frac{g\cos\alpha(U_x^2+U_y^2)}{\xi}\right]\frac{U_x}{\sqrt{U_x^2+U_y^2}} \qquad (1)$$

$$S_{fx}=\left[gH\mu\cos\alpha+\frac{g\cos\alpha(U_x^2+U_y^2)}{\xi}\right]\frac{U_y}{\sqrt{U_x^2+U_y^2}} \qquad (2)$$

where $g$ is the gravitational acceleration, $H$ the flow height, $\alpha$ the slope angle, and $U_x$ and $U_y$ the velocity components in x- and y-direction respectively. Details concerning momentum balance and mass conservation equations, including the matter of erosion are described by Christen et al. (2008).

The RAMMS code is based on extensive experiments within snow avalanche chutes (Kern et al., 2004) and field-based measurements (Sovilla et al., 2006), but the model is also intended to simulate mass movements other than pure snow avalanches, including large rock/ice avalanche events. Here, these model capabilities are illustrated for the first time in relation to a large rock-ice avalanche event which led to lake outburst flooding, and two smaller recent rock avalanches in the Mount Cook region.

In May and September of 1992, two separate rock avalanches with a combined volume of $\sim 11\times10^6\,\mathrm{m}^3$ fell from the summit area of Mount Fletcher, depositing into a nearby proglacial lake, producing floodwaves that traveled 35 km down the Godley Valley, damaging a vehicle track. Both events followed a similar path, and for numerical modelling an initial starting volume of $8\times10^6\,\mathrm{m}^3$ was selected, corresponding to estimates completed for the May event (McSaveney, 2002). Average density was set to $2200\,\mathrm{kg\,m^{-3}}$ representing typical greywacke bedrock ($2650\,\mathrm{kg\,m^{-3}}$) mixed with minor amounts of ice and firn ($500$–$900\,\mathrm{kg\,m^{-3}}$) which were present in the source area. The density remains constant in the model, so that any desegregation of the material during the flow process and within the deposition volume should be considered when interpreting the results. Furthermore, entrainment was not included as there was no data available to support the likely magnitude involved. However, erosion of glacial ice might have played a significant role, especially during the first impact of the rock material on the glacial surface, which possibly increased the avalanche volume in the order of $10^5$–$10^6\,\mathrm{m}^3$.

Unlike simple hydrologically driven GIS approaches such as the MSF model, RAMMS is able to reflect the physical energetic characteristics of the moving mass, including barrier run-up, overtopping, and deflection, which are all important considerations for local scale modelling. This is most evident midway along the rock avalanche path where the flow travels ~350 m up the true left flank of the valley, before the majority of the mass deflects back towards the opposite wall, and then down the glacier into the lake (Fig. 8). A component of the mass reaches and overtops the ridge crest, spilling towards but stopping just short of the adjacent Godley Lake. This spillover and other lateral spreading characteristics at the lower section of the flow were used to calibrate the model geometrically. Velocity calibration was achieved on the basis of available seismic data, although the exact duration of the avalanche (~180 s) was not clearly derived from the seismogram as the collapse was progressive (McSaveney, 2002). The best fit frictional parameters for the Mt. Fletcher avalanche were achieved using $\mu$=0.19 and $\xi$=$2100\,\mathrm{m\,s^{-2}}$.

Modelled maximum flow heights correspond well with areas of run-up and the general flow direction as indicated by McSaveney (2002), although the initial run-up height and spillover extent is slightly overestimated by the model. Exaggerated spread of the flow from the initiation area results from the modelled release of the detachment mass on top of the topography, rather than from within the rock face as occurs in reality. Modelled maximum flow velocities of $102\,\mathrm{m\,s^{-1}}$ below the area of initial run-up corresponds to estimates of $\sim 120\,\mathrm{m\,s^{-1}}$ made by McSaveney (2002), while modelled mass entry into the lake occurred at a maximum velocity of $20\,\mathrm{m\,s^{-1}}$. By isolating the area of the flow that intersects with the lake and observing the maximum flow heights from within this zone, an estimation of the volume deposited into the lake was made. For the $8\times10^6\,\mathrm{m}^3$ event, only $0.76\times10^6\,\mathrm{m}^3$ was calculated to enter the lake. Although no measurement of the actual deposit into the lake has been possible, given the absence of any dam freeboard height (Fig. 4b) and the seiching effect of the impact wave, it is not unexpected that a displaced water volume several orders of magnitude greater than the incoming mass was recorded.

The capability of RAMMS to simulate avalanches at a much reduced volumetric magnitude was tested by modelling the two recent Vampire Peak rock avalanches described by Cox and Allen (2009). These events occurred in early summer 2003 and January 2008, with both having similar failure volumes of $1$–$2\times10^5\,\mathrm{m}^3$, and deposition volumes approaching $3\times10^5\,\mathrm{m}^3$. The initiation areas were located between 2500 and 2600 m, and were separated by a horizontal distance of less than 150 m. Average density was set to $2650\,\mathrm{kg\,m^{-3}}$ for both events, as there was no surface ice present in the source areas. The modelled flow paths accurately reflect the stronger run-up of the 2008 event, as it rose up to 80 m across a spur above the Bannie icefall (Fig. 9). Wider lateral spread of the 2008 flow immediately below the detachment resulted in reduced maximum flow heights, compared to the straighter, more direct path of the 2003 event. The runout distance of the 2008 event was also smaller, most probably relating to altered surface friction resulting from the presence of the earlier avalanche deposit. In the RAMMS model these differences were addressed using altered frictional input parameters. While the Coulomb friction $\mu$ was set to 0.14 for both avalanches, the turbulent friction $\xi$ was set to $3000\,\mathrm{m\,s^{-2}}$ for the 2003 event and to $2000\,\mathrm{m\,s^{-2}}$ for the 2008 event. With the lower $\xi$-value for the second event, the avalanche mobility is sufficiently reduced, terminating ~400 m earlier then the 2003 event.

The limitations of using a 25 m resolution DEM for modelling low volume avalanche events were partially solved by resampling the elevation data to a 10 m grid. Although this method does not improve the underlying DEM accuracy, it does enable a higher level of precision in dynamic avalanche modelling. However, the results must be evaluated carefully considering that the geometry of actual flow paths can be affected by small differences in topography which are not represented in such a resampled DEM. For example, both modelled paths show a third lobe deviating over the medial moraine from the right hand edge of the flow as it traveled through the lower Bannie icefall, but this phenomenon was not evident in either of the mapped deposits. This model artifact may result from a failure of the DEM to represent the

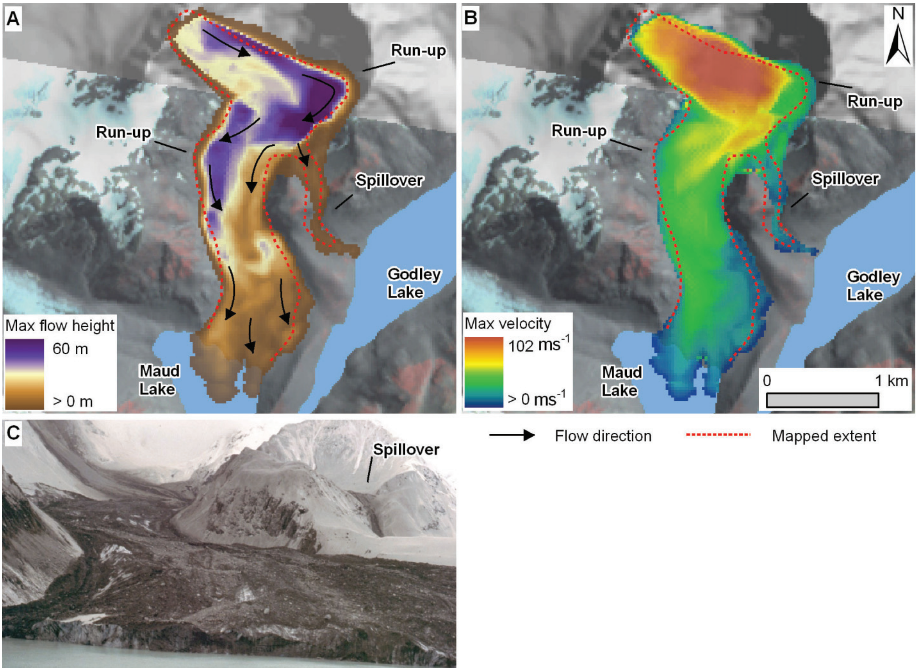

**Fig. 8.** **A** RAMMS simulation of the 1992 Mount Fletcher rock avalanche showing maximum flow heights and **B** maximum velocity. Mapped avalanche extent is after McSaveney (2002). **C** View of the avalanche path observed from the glacial lake where partial deposition occurred, resulting in a displacement wave and flooding (photo: M. McSaveney, September 1992).

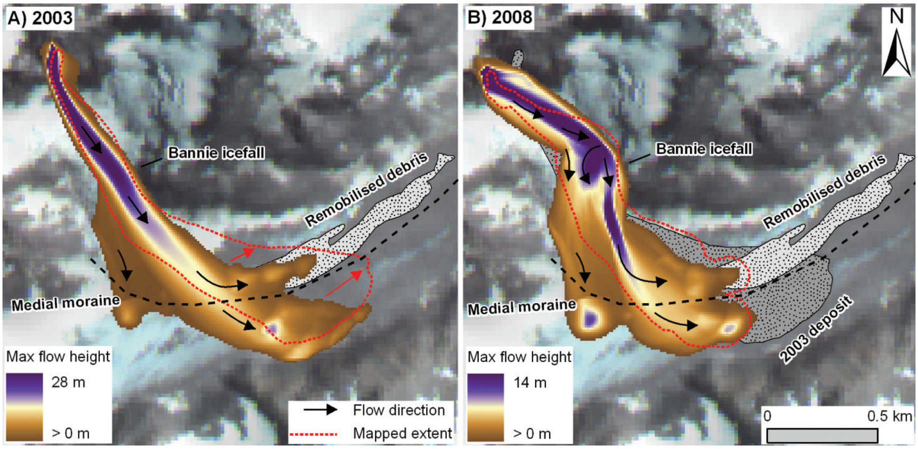

**Fig. 9.** RAMMS simulations of the **A** 2003, and **B** 2008 rock avalanches from Vampire Peak, Mueller Glacier, showing maximum flow heights. The 2003 avalanche and remobilised debris deposits are reconstructed from satellite imagery from January 2006 (Cox and Allen, 2009). As indicated by the red arrows, significant displacement of the avalanche deposit down the glacier is likely to have occurred between 2003 and 2006.

micro-topography of the steep, chaotic icefall, the effects of different surface friction within the icefall that were not accounted for in the model run, or potential changes in the icefall topography that have occurred since the elevation data was captured in 1986.

Calibrating model simulations to reconstruct past events requires that the modelled flow paths fit geometrically in three dimensions as well as in time. The examples presented here form a small component of a calibration initiative for various rock/ice avalanche events from different glacial environments around the world, establishing an initial range of best fit frictional input parameters (Fig. 10) that may be used to simulate potential events where hazardous scenarios are recognized. This range of values encompass volumetric differences of two orders of magnitudes, unequal fractions of ice and water content and extremely variable topography. The development and expansion of this dataset over time, is expected to provide an indispensable basis for future model evaluation and scenario simulations with RAMMS.

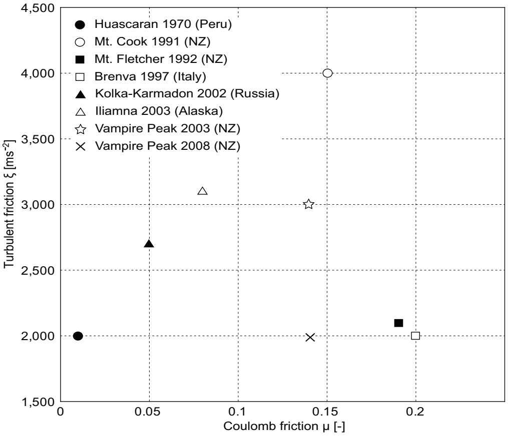

**Fig. 10.** Turbulent and coulomb friction best fit parameters established from simulating rock avalanche events in New Zealand (NZ) and other glacial regions using RAMMS. These values were iteratively found with the RAMMS program and should not be confused with the physical properties of the material as the internal and basal coefficients of friction. The Coulomb friction also can not directly be transformed to the widely used ratio of fall height to runout length (H/L). In a Voellmy model, the final runout distance also depends on the turbulent friction term (see Eqs. 1 and 2).

## 6 Discussion

A first order GIS approach to glacial hazard modelling in the Mount Cook region allows non-specialist local authorities involved in regional management to quickly identify situations or locations where more detailed and comprehensive studies should be directed. With all GIS-based procedures, the reliability of the output is determined by the accuracy and characteristics of the input data used, model assumptions and limitations. Hazard sources used as input to the MSF model were derived on the basis of satellite terrain mapping and slope gradient thresholds, where the main limitations relate to the 25 m resolution of the DEM, and filtering procedures that operate across several pixel values further increasing the minimum size of recognized surface features (Allen et al., 2008b). In addition, the New Zealand 25 m DTM is developed from 1986 aerial photography, and significant topographic changes have occurred within the glacial landscape over recent decades, most evidently surrounding the larger valley glaciers, where ice surfaces have lowered up to 4 m per year (Blair, 1994). Elevation data computed from ASTER stereo imagery (Kääb et al., 2002) or the 90 m resolution shuttle radar topography mission (SRTM) (Schneider et al., 2008), can keep pace with changing environmental conditions, but provide reduced topographic detail and can have severe errors in steep terrain. For more advanced numerical models, such as RAMMS, topographic sensitivity becomes more pronounced, and therefore a lack of recent high resolution elevation data from the Southern Alps remains a limiting factor in representing complex flow dynamics.

The limitations of the MSF model are well documented by the developer (Huggel et al., 2003), and in the context of the Mount Cook region where empirical information is lacking, specifically relate to the inability of the model to give any direct information regarding potential flow magnitudes, erosion capabilities, and deposition volumes. At the next level of hazard investigation, this information may be calculated using combined empirical relationships and field observations (e.g., McKillop and Clague, 2007; Rickenmann, 1999). Preferably, calculations will be verified using physically based flood and mass movement models such as FLO-2D (O'Brien et al., 1993) or DAN/DAN3D (Hungr, 1995), while the capabilities of RAMMS have been introduced for rock avalanche modeling in glacial environments. Greater input and computational requirements make these models best suited for local scale modelling of individual events or scenarios.

Empirical relationships represent a simplification of complex natural processes but remain useful for initial investigations and are most suitable for integration into GIS and remote sensing based approaches (Huggel et al., 2004). However, numerous climatic, topographic, geological, and glaciological factors differentiate the physical characteristics of processes occurring in one alpine region from another. Therefore, while often necessary, the extrapolation of well grounded empirical relationships must be treated cautiously and may not always be appropriate. Although not unique to New Zealand, the active tectonic setting and extreme precipitation gradient occurring across the Southern Alps has a paramount influence on geomorphic processes in the region, and related natural hazards. In particular, sediment yields may be several orders of magnitude higher than other regions (Fitzsimons and Veit, 2001) and locally enhanced by landslide activity and fault proximity (Hovius et al., 1997; Korup, 2004), while high intensity triggers (rain or earthquake) of mass movements may occur more frequently. As a consequence, there will be uncertainties associated with any attempt to quantify the longer term influence of climate and glacial change on event frequency and/or magnitude in this region. In addition, events initiating from glacial origins are only one component of mass movement processes in this mountainous region, where failure of hillslopes, river damming, debris and clear water floods not directly linked to glacial processes remain the most recognized threats to lowland populations (e.g., Davies and Scott, 1997; Korup, 2005b). Predicted climatic change, potentially bringing even greater rainfall in the west and dryer conditions in the east (Mullan et al., 2001), adds to the complexities that scientists must consider in relation to future mass movement and flood hazards in the Southern Alps.

A comparison of twentieth century glacial changes in the New Zealand and European Alps reveals comparable reductions in ice extent although New Zealand glaciers may be more sensitive to future climate warming (Hoelzle et al., 2007). However, lower equilibrium line altitudes and therefore restricted ablation zones in the Southern Alps means that lake development and moraine destabilization associated with glacial mass wastage has so far been limited to lower elevation zones east and west of the main divide. The steeper topographic expression of the Southern Alps inhibits lake development or significant moraine deposition at higher elevations. In contrast, glacial retreat in the European Alps has resulted in lake formation and unstable moraines in high elevation hanging valleys or cirque basins, often with populated valleys located below (e.g., Huggel et al., 2003). In addition, permafrost and its climate induced degradation is expected to cause further destabilization of unconsolidated moraine deposits and talus slopes, leading to increased debris flow potential in the European Alps (Harris, 2005). Results presented here suggest this is not a concern in the Mount Cook region, given that no potential debris flow source areas were identified at elevations above 2500 m where permafrost is expected on steeper slopes (Allen et al., 2008a). Permafrost degradation in the Southern Alps is therefore most relevant concerning a possible role in destabilization of high elevation bedrock slopes (e.g., Cox and Allen, 2009). This is alarming given the potential for impact induced floodwaves as many proglacial lakes in the region continue to expand. Furthermore, the expected probability of a large earthquake (>M7) striking the region during the next 50 years may be as high as 35% (Cox and Barrell, 2007), providing a trigger for future large magnitude movements of ice and rock, and possible floodwave initiation.

## 7 Conclusions

GIS based procedures were applied to gain first order knowledge of glacial flood, debris flow, and ice avalanche potential across the Mount Cook region of New Zealand's Southern Alps. Large volume lakes dammed by moraine and Quaternary gravels occur in proglacial areas below 1000 m where gentle slope gradients and well vegetated outlet channels indicate relatively stable conditions. Where smaller cirque lakes are dammed by steep morainic debris, debris flow scenarios were considered, but maximum probable runouts in these instances were well short of affecting any infrastructure. Potential debris flows were also modelled from glacial and recent paraglacial sediment accumulations, and in many instances runout paths intersected with human activity. However, examples illustrated near the Mount Cook village indicated a large discrepancy is possible between the static worst-case approach to runout modelling and maximum runout distances expected on the basis of catchment area available above the debris source. Direct impacts from potential high magnitude ice avalanches do not extend beyond walking tracks and some huts/shelters located in close proximity to steep ice, although numerous lakes are positioned within the runout paths from even smaller magnitude events, providing potential for displacement waves and flooding. The rapidly expanding Mueller Lake was illustrated as one example in close proximity to tourist and residential infrastructure, but longer term glacial recession and lake expansion will increase the potential for ice, debris or rock impacts into most lakes across the region. Physically based rock avalanche modelling with RAMMS provides a useful tool for recognizing detailed flow patterns, calculating potential flow magnitudes and velocities, and the application of this model for predictive purposes will benefit from further calibration studies. Further investigations are required at the local scale, assessing the likelihood of high magnitude flood, ice and debris hazards, and providing a comprehensive assessment of possible climate change impacts. Given an unstable geological setting and high potential for both seismic and rainfall triggered slope failures, a broader approach considering topographic, geological and glacial factors relating to bedrock failure susceptibility is encouraged. Uncertainty related to climate change and its influence on remote glacial regions should be met with robust methods for early recognition and monitoring of potential impacts.

*Acknowledgements.* This project is funded by a University of Canterbury doctoral scholarship. Quickbird imagery was sponsored by Digitial Globe$^{TM}$. RAMMS was kindly made available by the WSL Institute for Snow and Avalanche Research, SLF, Davos, Switzerland and we are greatly indebted to the support of Perry Bartelt, Marc Christen and Julia Kowalski. Christian Huggel is gratefully acknowledged for allowing access to the MSF modelling code and for providing a comprehensive review of the initial manuscript. Data provided by the Department of Conservation is appreciated. We are most thankful for the constructive suggestions provided by two anonymous reviewers.

Edited by: J. M. Vilaplana
Reviewed by: two anonymous referees

## References

Alean, J.: Ice avalanches: some empirical information about their formation and reach, J. Glaciol., 31, 324–333, 1985.

Allen, S., Owens, I., and Huggel, C.: A first estimate of mountain permafrost distribution in the Mount Cook region of New Zealand's Southern Alps, in: Ninth International Conference on Permafrost, edited by: Kane, D. L. and Hinkel, K. M., Institute of Northern Engineering, University of Alaska, Fairbanks, 37–42, 2008a.

Allen, S., Owens, I., and Sirguey, P.: Satellite remote sensing procedures for glacial terrain analyses and hazard assessment in the Aoraki Mount Cook region, New Zealand, New Zeal. J. Geol. Geop., 51, 73–87, 2008b.

Barringer, J. R. F., McNeill, S. J., and Pairman, D.: Progress on assessing the accuracy of a high–resolution digital elevation model for New Zealand, 5th International Symposium on Spatial Accuracy Assessment in Natural Resources and Environmental Sciences, Melbourne, Australia, 10–12 July 2002,

Bartelt, P., Salm, B., and Gruber, U.: Calculating dense-snow avalanche runout using a Voellmy-fluid model with active/passive longitudinal straining, J. Glaciol., 45, 242–254, 1999.

Blair Jr., R. W.: Moraine and valley wall collapse due to rapid deglaciation in Mount Cook National Park, New Zealand, Mt. Res. Dev., 14, 347–358, 1994.

Carey, M.: Living and dying with glaciers: people's historical vulnerability to avalanches and outburst floods in Peru, Global Planet. Change, 47, 122–134, 2005.

Chiarle, M., Iannotti, S., Mortara, G., and Deline, P.: Recent debris flow occurrences associated with glaciers in the Alps, Global Planet. Change, 56, 123–136, 2007.

Chinn, T. J. H.: New Zealand glacier responses to climate change in the past century, New Zeal. J. Geol. Geop., 39, 415–428, 1996.

Christen, M., Bartelt, P., Kowalski, J., and Stoffel, L.: Calculation of dense snow avalanches in three-dimensional terrain with the numerical simulation program RAMMS, Proceedings of the International Snow Science Workshop, Whistler, BC, Canada, 709–716, 2008.

Clague, J. J. and Evans, S. G.: Formation and failure of natural dams in the Canadian Cordillera, Geological Survey of Canada Bulletin 464, 35 pp., 1994.

Clague, J. J. and Evans, S. G.: A review of catastrophic drainage of moraine-dammed lakes in British Columbia, Quaternary Sci. Rev., 19, 1763–1783, 2000.

Cox, S. and Barrell, D. J. A. (compilers): Geology of the Aoraki Area, New Zealand, Institute of Geological & Nuclear Sciences 1:250 000 geological map 15, GNS Science, Lower Hutt, New Zealand, 1 sheet+71 pp., 2007.

Cox, S. C. and Allen, S. K.: Vampire rock avalanches of January 2008 and 2003, Southern Alps, New Zealand, Landslides, doi:10.1007/s10346-009-0149-4, in press, 2009.

Davies, T. R. and Scott, B. K.: Dambreak flood hazard from the Callery River, Westland, New Zealand, J. Hydrol. (New Zealand), 36, 1–13, 1997.

Davies, T. R., Smart, C. C., and Turnbull, J. M.: Water and sediment outbursts from advanced Franz Josef Glacier, New Zealand, Earth Surface Processes and Landforms, 28, 1081–1096, 2003.

Ding, Y., and Liu, J.: Glacial lake outburst flood disasters in China, Ann. Glaciol., 16, 180–184, 1992.

Dunning, J. S.: Form and process of alpine talus, Arthurs Pass, Southern Alps, New Zealand, unpublished Ph.D. thesis, Department of Geography, Univeristy of Canterbury, Christchurch, 133 pp., 1996.

Evans, S. G. and Clague, J. J.: Recent climatic change and catastrophic geomorphic processes in mountain environments, Geomorphology, 10, 107–128, 1994.

Fitzsimons, S. J. and Veit, H.: Geology and geomorphology of the European Alps and the Southern Alps of New Zealand, Mountain Research and Development, 21, 340–349, 2001.

Goodsell, B., Anderson, B., Lawson, W. J., and Owens, I. F.: Outburst flooding at Franz Josef Glacier, South Westland, New Zealand, New Zeal. J. Geol. Geop., 48, 95–104, 2005.

Haeberli, W.: Frequency and characteristics of glacier floods in the Swiss Alps, Ann. Glaciol., 4, 85–90, 1983.

Haeberli, W., Kääb, A., Paul, F., Chiarle, M., Mortara, G., Mazza, A., Deline, P., and Richardson, S.: A surge-type movement at Ghiacciaio del Belvedere and a developing slope instability in the east face of Monte Rosa, Macugnaga, Italian Alps, Norwegian Journal of Geography, 56, 104–111, 2002.

Hancox, G. T., McSaveney, M. J., Manville, V. R., and Davies, T. R.: The October 1999 Mt Adams rock avalanche and subsequent landslide dam-break flood and effects in Poerua River, Westland, New Zealand, New Zeal. J. Geol. Geop., 48, 683–705, 2005.

Harris, C.: Climate Change, Mountain Permafrost Degradation and Geotechnical Hazard, in: Global Change and Mountain Regions, An Overview of Current Knowledge, edited by: Huber, U. M., Bugmann, H. K. M., and Reasoner, M. A., Springer, Dordrecht, 215–224, 2005.

Henderson, R. D. and Thompson, S. M.: Extreme Rainfalls in the Southern Alps of New Zealand, J. Hydrol. (New Zealand), 38, 309–330, 1999.

Hewitt, K.: Natural dams and outburst floods in the Karakorum Himalaya., IAHS Publication, 138, 259–269, 1982.

Hochstein, M. P., Claridge, D., Henrys, S. A., Pyne, A., Nobes, D., and Leary, S. F.: Downwasting of the Tasman Glacier, South Island, New Zealand: changes in the terminus region between 1971 and 1993., New Zeal. J. Geol. Geop., 38, 1–16, 1995.

Hoelzle, M., Chinn, T., Stumm, D., Paul, F., Zemp, M., and Haeberli, W.: The application of glacier inventory data for estimating past climate change effects on mountain glaciers: A comparison between the European Alps and the Southern Alps of New Zealand, Global Planet. Change, 56, 69–82, 2007.

Hovius, N., Stark, C. P., and Allen, P. A.: Sediment flux from a mountain belt derived from landslide mapping, Geology, 25, 231–234, 1997.

Huggel, C., Kääb, A., Haeberli, W., Teysseire, P., and Paul, F.: Remote sensing based assessment of hazards from glacier lake outbursts: a case study in the Swiss Alps, Can. Geotech. J., 39, 316–330, 2002.

Huggel, C., Kääb, A., Haeberli, W., and Krummenacher, B.: Regional-scale GIS-models for assessment of hazards from glacier lake outbursts: evaluation and application in the Swiss Alps, Nat. Hazards Earth Syst. Sci., 3, 647–662, 2003, http://www.nat-hazards-earth-syst-sci.net/3/647/2003/.

Huggel, C., Kääb, A., and Salzmann, N.: GIS-based modeling of glacial hazards and their interactions using Landsat-TM and IKONOS imagery, Norwegian Journal of Geography, 58, 61–73, 2004.

Huggel, C., Zgraggen-Oswald, S., Haeberli, W., Kääb, A., Polkvoj, A., Galushkin, I., and Evans, S. G.: The 2002 rock/ice avalanche at Kolka/Karmadon, Russian Caucasus: assessment of extraordinary avalanche formation and mobility, and application of QuickBird satellite imagery, Nat. Hazards Earth Syst. Sci., 5, 173–187, 2005, http://www.nat-hazards-earth-syst-sci.net/5/173/2005/.

Hungr, O., Morgan, G. C., and Kellerhals, P.: Quantitative analysis of debris hazards for design of remedial measures, Can. Geotech. J., 21, 663–677, 1984.

Hungr, O.: A model for the runout analysis of rapid flow slides, debris flows, and avalanches, Can. Geotech. J., 32, 610–623, 1995.

Hungr, O., McDougall, S., and Bovis, M.: Entrainment of material by debris flows, in: Debris-flow hazards and related phenomena, edited by: Jakob, M., and Hungr, O., Springer – Praxis, Berlin Heidelberg, 135–155, 2005.

Irwin, D., MacQueen, W., and Owens, I.: Avalanche Accidents in Aotearoa New Zealand, N.Z. Mountain Safety Council, Wellington, 153 pp., 2002.

Iseli, J. G.: Ice avalanche activity in Mount Cook National Park, unpublished M.Sc. thesis, Department of Geography, University of Canterbury, Christchurch, 151 pp., 1991.

Kääb, A., Huggel, C., Paul, F., Wessels, R., Raup, B., Kieffer, H., and Kargel, J.: Glacier monitoring from ASTER imagery: accuracy and applications, Proceedings of EARSel-LISSIG-Workshop Observing our Cryosphere from Space, Bern, 43–53, 2002.

Kääb, A., Reynolds, J. M., and Haeberli, W.: Glacier and Permafrost Hazards in High Mountains, in: Global Change and Mountain Regions. An Overview of Current Knowledge, edited by: Huber, U. M., Bugmann, H. K. M., and Reasoner, M. A., Springer, Dordrecht, 225–234, 2005.

Kern, M., Tiefenbacher, F., and McElaine, J.: The rheology of snow in large chute flows, Cold Reg. Sci. Technol., 39, 181–192, 2004.

Koons, P. O.: The two-sided orogen: Collision and erosion from the sandbox to the Southern Alps, New Zealand, Geology, 18, 679–682, 1990.

Korup, O.: Geomorphic implications of fault zone weakening: slope instability along the Alpine Fault, South Westland to Fiordland, New Zeal. J. Geol. Geop., 47, 257–267, 2004.

Korup, O.: Distribution of landslides in southwest New Zealand, Landslides, 2, 43–45, 2005a.

Korup, O.: Geomorphic hazard assessment of landslide dams in South Westland, New Zealand: Fundamental problems and approaches, Geomorphology, 66, 167–188, 2005b.

Maizels, J. and Russel, A. J.: Quaternary perspectives on Jokulhlaup prediction, Quaternary Proceeedings, 2, 133–152, 1992.

McKillop, R. J. and Clague, J. J.: A procedure for making objective preliminary assessments of outburst flood hazard from moraine-dammed lakes in southwestern British Colombia, Nat. Hazards, 41, 131–157, 2007.

McSaveney, M. J.: Recent rockfalls and rock avalanches in Mount Cook National Park, New Zealand, Geology Society of America, Reviews in Engineering Geology, XV, 35–69, 2002.

McSaveney, M. J. and Davies, T. R.: Engineering for debris flows in New Zealand, in: Debris-flow hazards and related phenomena, edited by: Jakob, M. and Hungr, O., Praxis Publishing, Chichester, 635–658, 2005.

Mullan, A. B., Wratt, D. S., and Renwick, J. A.: Transient model scenarios of climate changes for New Zealand, Weather and Climate, 21, 3–34, 2001.

O'Brien, J. S., Julien, P. Y., and Fullertone, W. T.: Two-dimensional water flood and mudflow simulation, J. Hydraul. Eng.-ASCE, 119, 244–261, 1993.

O'Connor, J. E., Hardison, J. H., and Costa, J. E.: Debris flows from failures of Neoglacial-Age moraine dams in the Three Sisters and Mount Jefferson wilderness areas, Oregon, US Geological Survey Professional Paper, 1606, 93 pp., 2001.

Paterson, B. R.: Slope instability along state highway 73 through Arthur's Pass, South Island, New Zealand, New Zeal. J. Geol. Geop., 39, 339–351, 1996.

Quincey, D. J., Richardson, S. D., Luckman, A., Lucas, R. M., Reynolds, J. M., Hambrey, M. J., and Glasser, N. F.: Early recognition of glacial lake hazards in the Himalaya using remote sensing datasets, Global Planet. Change, 56, 137–152, 2007.

Reynolds, J. M.: The identification and mitigation of glacier-related hazards: examples from the Cordillera Blanca, Peru, in: Geohazards natural and man–made, edited by: McCall, G. J. H., Laming, D. J. C., and Scott, S. C., Chapman and Hall, London, 143–157, 1992.

Richardson, S. D. and Reynolds, J. M.: An overview of glacial hazards in the Himalayas, Quatern. Int., 65/66, 31–47, 2000.

Rickenmann, D. and Zimmermann, M.: The 1987 debris flows in Switzerland: documentation and analysis, Geomorphology, 8, 175–189, 1993.

Rickenmann, D.: Empirical relationships for debris flows, Nat. Hazards, 19, 47–77, 1999.

Rickenmann, D.: Runout prediction methods, in: Debris-flow hazards and related phenomena, edited by: Jakob, M. and Hungr, O., Springer – Praxis, Berlin Heidelberg, 305–321, 2005.

Röhl, K.: Behaviour of lake-terminating glacier margins, unpublished Ph.D. thesis, Department of Geography, University of Otago, Dunedin, 390 pp., 2005.

Salzmann, N., Kaab, A., Huggel, C., Allgower, B., and Haeberli, W.: Assessment of the hazard potential of ice avalanches using remote sensing and GIS-modelling, Norwegian Journal of Geography, 58, 74–84, 2004.

Schneider, D., Delgado Granados, H., Huggel, C., and Kääb, A.: Assessing lahars from ice-capped volcanoes using ASTER satellite data, the SRTM DTM and two different flow models: case study on Iztacchuatl (Central Mexico), Nat. Hazards Earth Syst. Sci., 8, 559–571, 2008, http://www.nat-hazards-earth-syst-sci.net/8/559/2008/.

Skermer, N. A., Rawlings, G. E., and Hurley, A. J.: Debris flow defences at Aoraki Mount Cook Village, New Zealand, Q. J. Eng. Geol. Hydroge., 35, 19–24, 2002.

Sovilla, B., Burlando, P., and Bartelt, P.: Field experiments and numerical modeling of mass entrainment in snow avalanches, J. Geophys. Res., 111, 1–16, 2006.

Takahashi, T.: Debris Flow, A. A. Balkema, Rotterdam, 165 pp., 1991.

Warren, C. R. and Kirkbride, M.: Temperature and bathymetry of ice–contact lakes in Mount Cook National Park, New Zealand, New Zeal. J. Geol. Geop., 41, 133–143, 1998.

Wegmann, M., Funk, M., Flotron, A., and Keusen, H.: Movement studies to forecast the time of breaking off of ice and rock masses, in: Early Warning Systems for Natural Disasters Reduction, edited by: Zschau, J. and Küppers, A., Springer Verlag, Berlin, 565–568, 2003.

Wells, A., Duncan, R. P., Stewart, G. H., and Yetton, M. D.: Prehistoric dates of the most recent Alpine Fault earthquakes, New Zealand, Geology, 27, 995–998, 1999.

Whitehouse, I. E.: Erosion on Sebastopol, Mt Cook, New Zealand, in the last 85 years, New Zealand Geographer, 38, 77–80, 1982.

Whitehouse, I. E. and Griffiths, G. A.: Frequency and hazard of large rock avalanches in the central Southern Alps, New Zealand, Geology, 11, 331–334, 1983.

Whitehouse, I. E. and McSaveney, M. J.: Diachronous talus surfaces in the Southern Alps, New Zealand, and their implications to talus accumulation, Arctic Alpine Res., 15, 53–64, 1983.

Whitehouse, I. E.: Geomorphology of the central Southern Alps, New Zealand, Z. Geomorphol., 69, 105–116, 1988.

Zimmermann, M. and Haeberli, W.: Climatic change and debris flow activity in high mountain areas: a case study in the Swiss Alps, Catena Supplement, 22, 49–72, 1992.

# Paper IV

JOURNAL OF GEOPHYSICAL RESEARCH, VOL. 115, F04026, doi:10.1029/2010JF001734, 2010

# Insights into rock-ice avalanche dynamics by combined analysis of seismic recordings and a numerical avalanche model

Demian Schneider,[1] Perry Bartelt,[2] Jacqueline Caplan-Auerbach,[3] Marc Christen,[2]
Christian Huggel,[1] and Brian W. McArdell[4]

Received 31 March 2010; revised 12 August 2010; accepted 30 August 2010; published 2 December 2010.

[1] Rock-ice avalanches larger than $1 \times 10^6$ m$^3$ are high-magnitude, low-frequency events that may occur in all ice-covered, high mountain areas around the world and can cause extensive damage if they reach populated regions. The temporal and spatial evolution of the seismic signature from two events was analyzed, and recordings at selected stations were compared to numerical model results of avalanche propagation. The first event is a rock-ice avalanche from Iliamna volcano in Alaska which serves as a "natural laboratory" with simple geometric conditions. The second one originated on Aoraki/Mt. Cook, New Zealand Southern Alps, and is characterized by a much more complex topography. A dynamic numerical model was used to calculate total avalanche momentum, total kinetic energy, and total frictional work rate, among other parameters. These three parameters correlate with characteristics of the seismic signature such as duration and signal envelopes, while other parameters such as flow depths, flow path and deposition geometry are well in agreement with observations. The total frictional work rate shows the best correlation with the absolute seismic amplitude, suggesting that it may be used as an independent model evaluation criterion and in certain cases as model calibration parameter. The good fit is likely because the total frictional work rate represents the avalanche's energy loss rate, part of which is captured by the seismometer. Deviations between corresponding calculated and measured parameters result from site and path effects which affect the recorded seismic signal or indicate deficiencies of the numerical model. The seismic recordings contain additional information about when an avalanche reaches changes in topography along the runout path and enable more accurate velocity calculations. The new concept of direct comparison of seismic and avalanche modeling data helps to constrain the numerical model input parameters and to improve the understanding of (rock-ice) avalanche dynamics.

**Citation:** Schneider, D., P. Bartelt, J. Caplan-Auerbach, M. Christen, C. Huggel, and B. W. McArdell (2010), Insights into rock-ice avalanche dynamics by combined analysis of seismic recordings and a numerical avalanche model, *J. Geophys. Res.*, *115*, F04026, doi:10.1029/2010JF001734.

## 1. Introduction

[2] Large rock avalanches, ice avalanches, and mixed events have been documented for many of the glaciated regions of the world [*Deline*, 2001; *Evans and Clague*, 1988, 1998; *Giani et al.*, 2001; *Hewitt*, 1999, 2009; *Huggel et al.*, 2005, 2007, 2008a; *Kääb et al.*, 2005; *Korup*, 2005; *Lipovsky et al.*, 2008; *Margreth and Funk*, 1999; *McSaveney*, 2002; *Schneider*, 2006; *Sosio et al.*, 2008]. Due to incomplete data for historical events, it is difficult to quantify the frequency of large rock-ice avalanches, but it is possible that increases in event occurrence and magnitude can be expected due to changes in permafrost thermal state and the water cycle in connection with climate and glacier changes [*Bottino et al.*, 2002; *Davies et al.*, 2001; *Fischer and Huggel*, 2008; *Gruber and Haeberli*, 2007; *Haeberli and Hohmann*, 2008; *Huggel et al.*, 2008b]. The events with the most catastrophic consequences during the last decades were the Huascarán (Peru, 1962: 650 casualties; 1970: 6000 casualties) [*Evans et al.*, 2009a; *Körner*, 1983; *Plafker and Ericksen*, 1978] and the Kolka-Karmadon rock-ice avalanches (2002: 120 casualties) [*Haeberli et al.*, 2004; *Huggel et al.*, 2005; *Kotlyakov et al.*, 2004]. Most rock-ice avalanches occur in remote regions with no or marginal infrastructure. However, population pressure, winter tourism development, and climate change can dramatically increase the risk for catastrophic events.

[3] Numerical models that calculate the flow path and deposition zones, or runout, are important tools for the investigation and back analysis of past events. They provide

---

[1] Department of Geography, University of Zurich, Zurich, Switzerland.
[2] WSL Institute for Snow and Avalanche Research SLF, Davos-Dorf, Switzerland.
[3] Geology Department, Western Washington University, Bellingham, Washington, USA.
[4] Swiss Federal Institute for Forest, Snow and Landscape Research WSL, Birmensdorf, Switzerland.

0148-0227/10/2010JF001734

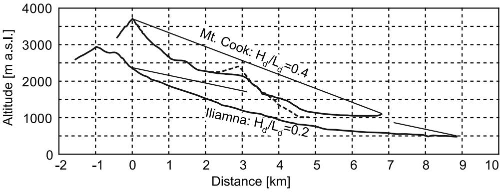

**Figure 1.** Comparison of height profiles from the 2003 Red Glacier avalanche at Iliamna volcano, Alaska, and the 1991 Aoraki/Mt. Cook avalanche, New Zealand. $H_d/L_d$ is the height to length ratio, and the straight line marks the start and end points of the avalanches. While the Iliamna profile approximates a parabola, the profile at Aoraki/Mt. Cook is much more complicated, with alternating steep and flat areas, runup on adverse slopes, and bifurcation of the runout path (dashed line is the secondary flow path).

insight into the complex processes occurring especially in large avalanches, which unlike snow avalanches [*Sovilla et al.*, 2006; *Suriñach et al.*, 2000] are problematic to trigger artificially and to perform in-flow measurements (we did not consider the artificial triggering of rock avalanches by nuclear explosions in this study [*Adushkin*, 2006]). There is a variety of different numerical mass movement models which can be roughly divided into empirical and physical models. For the current analysis, we need a physical model. These models are usually adapted to simulate the characteristic processes for a certain type of mass movement, e.g., for snow avalanches, rock slides, rock avalanches or debris flows. The events described in this study are challenging because at times they show flow characteristics similar to all of these processes, however, we call them generally "rock-ice avalanches." The choice of an appropriate model is difficult because none of the available models are able to simulate complex events with process transformations and interactions. Nevertheless, many authors pointed out similarities between flow types [e.g., *Bouchut et al.*, 2008; *Iverson and Denlinger*, 2001; *McDougall and Hungr*, 2005]. The Voellmy rheology [*Voellmy*, 1955] was originally developed for the simulation of snow avalanches and already satisfyingly applied in several case studies of retrospective modeling of rock avalanches [e.g., *Crosta et al.*, 2004; *Hungr and Evans*, 1996] and debris flows [e.g., *Armento et al.*, 2008; *Pirulli and Sorbino*, 2008]. We used the two-dimensional dynamic physical model RAMMS (Rapid Mass Movements) which is based on the 2-D shallow water equations for granular flows and the Voellmy frictional rheology and test if it is able to reproduce the flow and deposition geometry as well as dynamic aspects of large rock-ice avalanches.

[4] Seismic stations in the vicinity to an avalanche event (approximately <100 km) can be used for early warning due to precursory seismicity in certain cases [*Caplan-Auerbach et al.*, 2004], and many authors make use of seismograms of mass movement events to back-calculate total avalanche duration and velocity [*Crosta et al.*, 2007; *Lipovsky et al.*, 2008; *McSaveney*, 2002; *McSaveney and Downes*, 2002; *Sosio et al.*, 2008]. However, seismograms do also contain valuable information about energetic and dynamic characteristics of the mass movement [*Suriñach et al.*, 2005].

[5] The objective of this paper is to present a new approach for the combination of computational model results with seismic data to enhance the understanding of the dynamic (rock-ice) avalanche processes and to improve model calibration with a focus on geometric, energetic and dynamic characteristics of the modeled avalanche and the observed event. The paper indicates a possible linkage between modeled avalanche parameters and seismic data without the pretension to consider all aspects of the complexity of different mass movement types and seismic wave propagation. In particular, we explore the use of the seismic data to provide a physically based constraint on the frictional work rate predicted by the runout model, thereby resulting in a more realistic calibration of the model.

[6] First we give a short overview of the data and methods including the relationship between the computational runout model and the seismic data. Then, two avalanche events are presented as examples with very different topographic characteristics (Figure 1). The first is the 2003 Red Glacier avalanche at Iliamna volcano, Alaska, with a simple topography of a volcanic cone. There, runout is mostly straight and unconfined, with no significant vertical steps, runup, or lateral deflection of the avalanche. The second event is the Aoraki/Mt. Cook avalanche of 1991 in the Southern Alps of New Zealand. This runout was characterized by various topographic steps, extensive runup, and strong lateral deflection, and we expect a more complex seismic signal. For both study areas we discuss the model input variables and problems related to different parameter combinations. Then we link the seismic records to the physical parameters calculated with the runout model (total momentum, total kinetic energy and total frictional work rate).

## 2. Data

### 2.1. Topographic and Satellite Data

[7] Both study areas are remote, necessitating the use of remote sensing data to estimate topography and the geometry of the avalanche path and deposits. The digital terrain model (DTM) for Iliamna Volcano in Alaska, was provided by the Shuttle Radar Topography Mission (SRTM) of February 2000 at a 1 arc second (~30 m) resolution. The overall absolute vertical error of the SRTM-1 DTM is less than 16 m while the relative error which is relevant for the simulations is only 6 m [*Rabus et al.*, 2003]. A map showing absolute vertical errors on all continents published by *Farr et al.* [2007] indicates errors of only 4 m for the Iliamna region. Despite possible rapid topographic changes in glacial environments, we assume that this data set adequately represents the preevent topography for the 2003 avalanche. We also used a satellite scene from the Advanced Spaceborne Thermal Emission and Reflection Radiometer (ASTER), dating from 9 August 2003, only 15 days after a large avalanche occurred on Red Glacier; outlines could be easily extracted. Oblique air photos taken during a USGS gas measurement flight at Iliamna volcano by Rick Wessels on 1 August 2003 were also helpful. Failure and deposit volumes were estimated by *Caplan-Auerbach and Huggel* [2007] and *Huggel et al.* [2007].

[8] For the Aoraki/Mt. Cook region in New Zealand, we used the NZ 25 m DTM derived from the NZ260 topographic map series at a scale of 1:50,000 which for the Aoraki/Mt.

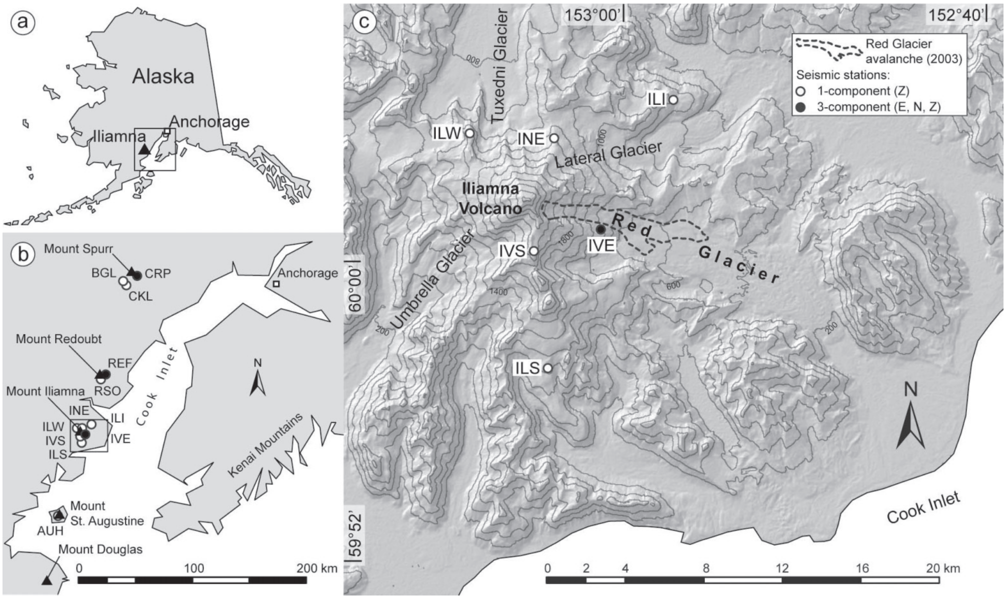

**Figure 2.** (a) Setting of Iliamna volcano in Alaska. (b) Location of the Alaska Volcano Observatory seismic network stations which were used in this study. Stations recording only vertical (Z) ground motion are shown with a white circle (one-component stations). Those recording east (E), north (N), and vertical (Z) movements are marked with a black circle (three-component stations). (c) Overview of the Iliamna region and the closest seismic stations. Dashed line shows the flow path outlines of the 25 July 2003 Red Glacier avalanche. Background map is the hillshaded SRTM-1 DTM.

Cook area is largely derived from 1986 imagery. The exception is the summit area of Aoraki/Mt. Cook, which is derived from January 1992 imagery specifically taken to correctly portray the new topography of the modified summit after the avalanche event. The topographic maps (1:50,000) and a more recent ASTER image of 24 January 2006 helped to localize the initiation area. The outlines of the 1991 rock-ice avalanche were digitized from *McSaveney* [2002]. Most of the information about erosion, dynamic behavior and deposition was taken from the same publication.

## 2.2. Seismic Recordings

[9] The Iliamna 2003 Red Glacier avalanche was recorded by the Alaska Volcano Observatory seismic network following approximately an hour of discrete earthquakes and a continuous tremor-like ground shaking. The ~3 min long broadband signal saturated all of the six seismometers on Iliamna, which are situated within epicentral distances less than 8 km at a broad azimuth range [*Caplan-Auerbach and Huggel*, 2007] (Figures 2 and 3). The avalanche signal exhibits a classic spindle shape with broadband (1–20 Hz) frequency content. The waveform envelope includes a small initial pulse lasting ~20 s followed by a stronger signal that rises, saturates, and tapers over ~100 s. Seismograms recorded at epicentral distances of 51 (RSO) and 55 km (REF) on Redoubt volcano and at four more distant stations which are not saturated suggest a gradual increase and decrease for the part of the signal that is saturated at the Iliamna stations. For this study we focus on the vertical component station ILS because it is the station with the smallest degree of saturation which is still situated on Iliamna, and approximately 7 km perpendicular (south) of the center of the Red Glacier avalanche flow path. We evaluated whether the recordings between $t = 40$ s to $t = 80$ s were amplified due to the avalanche's passing closer to the seismometer [*Suriñach et al.*, 2000], but note that a similar increase in amplitude is observed on all stations, suggesting that the signal strength is a source rather than path effect. Station ILI is symmetrically situated on the opposite side of the avalanche path, and the seismogram is almost identical, suggesting that for this case, the path effects are negligible or at least homogeneously distributed over different directions and within a distance of 7–8 km. Seismograms of a series of geometrically similar large avalanches in 1997, 2000, 2003, and 2008 on Red Glacier [see *Huggel et al.*, 2007] show very similar waveform envelopes. As *Suriñach et al.* [2000] state for artificially released snow avalanches, this indicates that large rock-ice avalanches of similar size following the same path and recorded at the same site produce similar seismic signals.

[10] The 1991 Aoraki/Mt. Cook avalanche was well detected up to distances exceeding 200 km (Figures 4 and 5). The nearest seismometer to the avalanche was short-period seismic station EWZ, located 58 km to the east of the mountain. The direction of the station is the same as the direction of avalanche movement, so we assume that during the event the signal amplitude increases continuously as the

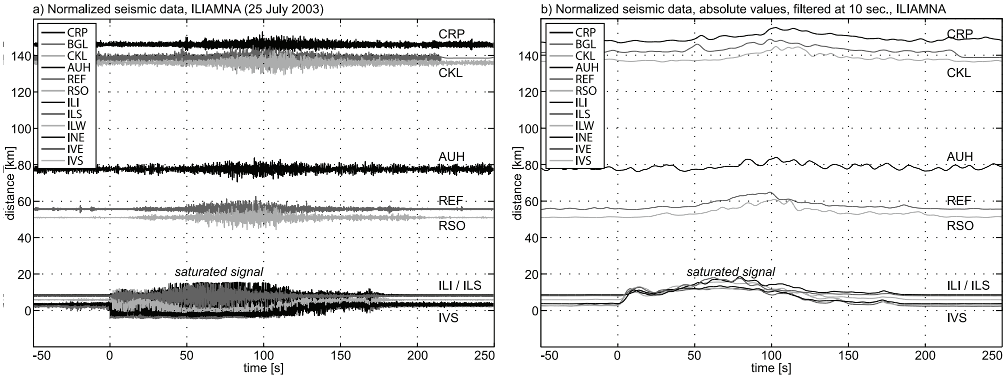

**Figure 3.** (a) Seismograms of the 25 July 2003 Red Glacier avalanche at Iliamna (Alaska) plotted against linearly increasing distance ($y$ axis). Signal amplitude is given by normalized counts of the seismograph. (b) Amplitude envelopes of the data shown in Figure 3a. Absolute signal amplitude was low-pass filtered at 10 s (0.1 Hz) to show long-period change in signal strength. Time $t = 0$ s is set to the arrival of the assumed first avalanche-induced seismic waves at station ILS. The shift in time of the seismographs with increasing distance is due to the travel time of the seismic waves in the ground. Station AUH is situated on Augustine volcano at 890 m asl on a very windy place, which might explain the high noise content.

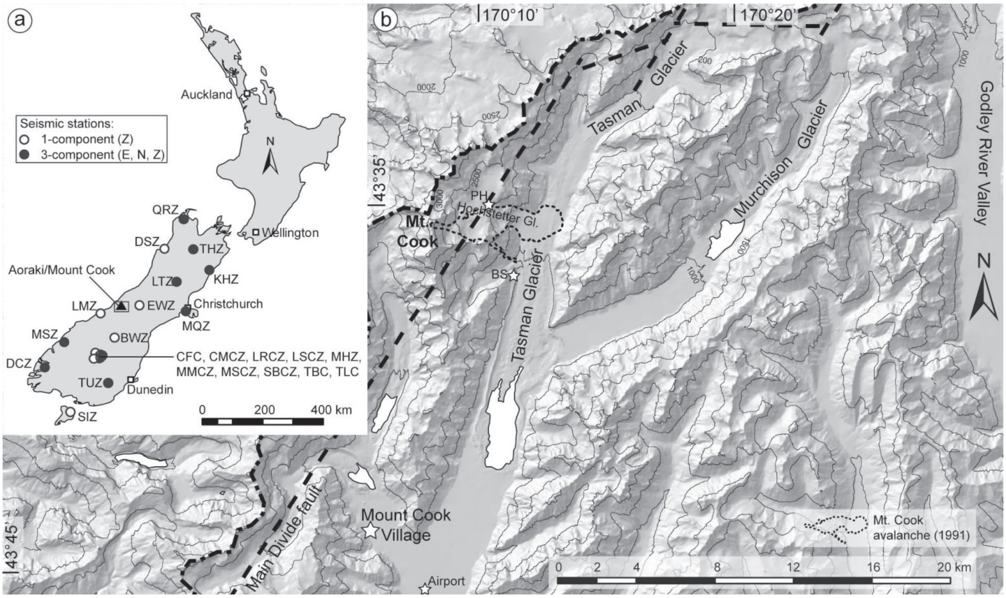

**Figure 4.** (a) New Zealand seismic network stations which were used in this study. Stations recording only vertical (Z) ground motion are shown with a white circle (one-component stations). Those recording east (E), north (N) and vertical (Z) movements are marked with a black circle (three-component stations). (b) Setting of Aoraki/Mt. Cook (3754 m asl) and the 14 December 1991 rock-ice avalanche. White areas are (glacial) lakes mapped from the ASTER image from 24 January 2006. Dash-dotted line marks the Main Divide, and the dashed line marks the Main Divide fault. Note that the shape and size of the glacial lakes can change rapidly. Ball Shelter (BS) and the Plateau Hut (PH) are marked with white stars. Background map is the hillshaded NZ 25 m DTM.

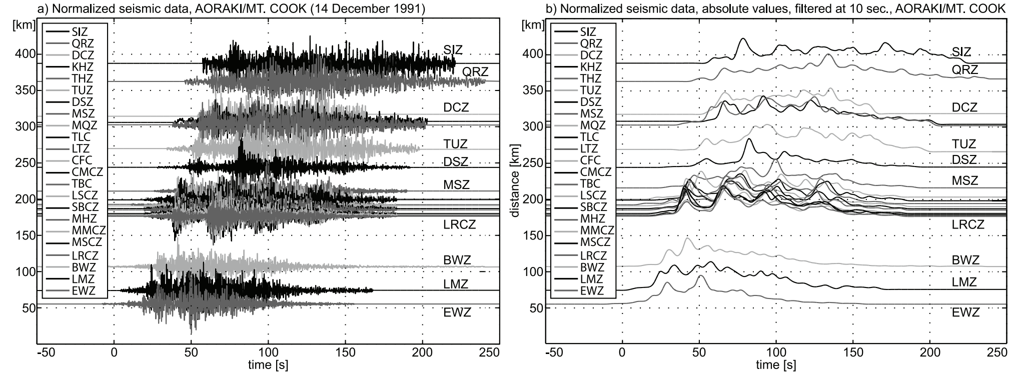

**Figure 5.** (a) Seismograms of the 14 December 1991 Aoraki/Mt. Cook avalanche (New Zealand) plotted against linearly increasing distance ($y$ axis). Signal amplitude is given by normalized counts of the seismograph. (b) Amplitude envelopes of the data shown in Figure 5a. Absolute signal amplitude was also low-pass filtered at 10 s (0.1 Hz) like in Figure 3b. Note that the straight line part of each seismogram is the centerline of the corresponding signal and the original data is missing there. Time $t = 0$ s is set to the arrival of the assumed first avalanche-induced seismic waves at station EWZ.

avalanche approaches the seismograph, however, due to the source-receiver distance this increase is likely negligible. Like the Iliamna signal, the Aoraki/Mt. Cook avalanche manifests as a spindle-shaped seismogram comprising several smaller pulses of energy. The duration of the signal at EWZ is ~2 min but the exact initiation and end times are difficult to determine. While station EWZ recorded only the vertical component of ground shaking, more distant stations were three-component (Figure 4). These stations show roughly equal amplitudes on all channels, suggesting that analysis of the vertical component at EWZ (and ILS for Iliamna) is a reasonable proxy for the total ground motion; however, some differences in amplitudes between horizontal and vertical components cannot be excluded [see also *Suriñach et al.*, 2001]. The impacts of the avalanche on the topographic steps have generated bursts of high-frequency seismic energy which were more rapidly attenuated with increasing distance than the low-frequency signal portion. Energy distribution in the recorded spectra therefore changes with increasing distance, with the lower frequencies being better preserved. However, because the bulk of seismic energy generated by avalanches is low frequency [e.g., *Caplan-Auerbach et al.*, 2004; *Huggel et al.*, 2008a] the loss of high-frequency energy does not significantly affect our interpretations. The signal becomes also more extended in time, since S waves travel more slowly than P waves and wave distortions, reflections, scatterings and dispersions affect the envelope of the seismogram [*Aki and Chouet*, 1975]. These effects are visible in Figure 5, and therefore, the closest station EWZ is expected to best serve as the reference station for comparison with avalanche simulation data.

[11] At Iliamna, stations RSO and REF at distances of 51 and 55 km support the assumption that the (vertical) seismic signal still contains the basic source characteristics at least over a distance of around 60 km (Figure 3). We tried to identify specific phases within the waveform, but the nearest unsaturated three-component station RSO was at 55 km epicentral distance and exhibited a poor signal-to-noise ratio so that we were unable to identify them.

[12] The New Zealand stations which are further away from Aoraki/Mt. Cook than station BWZ (107 km) show high consistency between adjacent stations, but substantially more variation in the waveforms with growing distance, suggesting that path effects are larger. Because the only broadband station in New Zealand at that time was not digital, these data are not available and an analysis of the seismic energy generated by a possible rebound of the unloaded source as described by *McSaveney* [2002] (mainly long-period waves) was not considered in this study.

## 3. Method

### 3.1. Numerical Simulation of Gravitationally Driven Mass Movements

#### 3.1.1. Governing Differential Equations

[13] To model (rock-ice) avalanche movement, the numerical model RAMMS (Rapid Mass Movements) solves the depth-integrated equations governing mass and momentum conservation in a two-dimensional, rectangular $x$, $y$ coordinate system [*Christen et al.*, 2010b]. RAMMS has been used extensively in Switzerland to predict snow avalanche runout and flow velocities in general mountain terrain. We only describe the governing equations, a detailed presentation of the model and case studies are provided by *Christen et al.* [2010a, 2010b], and the second-order numerical solution of the governing differential equations is discussed by *Kowalski* [2008]. The mass balance of the avalanche at any position $x$, $y$ and time $t$ is given by

$$\partial_t H + \partial_x(HU_x) + \partial_y(HU_y) = \dot{Q}(x, y, t) \qquad (1)$$

where $U(x, y, t) = (U_x(x, y, t), U_y(x, y, t))^T$ with $T$ standing for the transpose of the matrix is the depth-averaged avalanche velocity, $H(x, y, t)$ the flow depth, and $\dot{Q}(x, y, t)$ the entrainment rate in m s$^{-1}$. The volumetric entrainment rate in m$^3$ s$^{-1}$ can be calculated by multiplying $\dot{Q}$ with the cell area $A$, and if entrainment is absent, $\dot{Q}$ equals zero. A constant bulk flow density $\rho_a$ is assumed and the momentum balance is given by

$$\partial_t(HU_x) + \partial_x\left(HU_x^2 + \frac{g_z H^2}{2}\right) + \partial_y(HU_xU_y) = S_{gx} - S_{fx} \quad (2a)$$

and

$$\partial_t(HU_y) + \partial_y\left(HU_y^2 + \frac{g_z H^2}{2}\right) + \partial_x(HU_xU_y) = S_{gy} - S_{fy} \quad (2b)$$

where $g_z$ is the gravitational acceleration component perpendicular to the slope, $S_{gx}$ and $S_{gy}$ the slope-parallel gravitational acceleration forces and $S_{fx}$ and $S_{fy}$ the deceleration forces, respectively. Because the avalanche density $\rho_a$ is constant, the mass is represented by the flow depth $H$ and $S_{gx}$ and $S_{gy}$ are given by:

$$S_{gx} = g_x H \quad (3a)$$

and

$$S_{gy} = g_y H \quad (3b)$$

Although large rock-ice avalanches can reach flow depths $H$ of several decameters, they meet “shallow water” conditions since their horizontal extension is generally much larger.

### 3.1.2. Frictional Resistance Model

[14] The slope-parallel frictional deceleration forces $S_{fx}$ and $S_{fy}$ in $x$ and $y$ directions are given by the Voellmy model which combines dry Coulomb friction (coefficient $\mu$) with a velocity-squared dependent turbulent friction (coefficient $\xi$ [m s$^{-2}$]) [*Voellmy*, 1955]:

$$S_{fx} = \frac{U_x}{\sqrt{U_x^2 + U_y^2}}\left[g_z H \mu + \frac{g(U_x^2 + U_y^2)}{\xi}\right] \quad (4a)$$

and

$$S_{fy} = \frac{U_y}{\sqrt{U_x^2 + U_y^2}}\left[g_z H \mu + \frac{g(U_x^2 + U_y^2)}{\xi}\right] \quad (4b)$$

The Voellmy model can therefore be used to simulate different stages of the avalanche motion, e.g., when the avalanche is moving slowly in the runout zone in a block-like motion (Coulomb friction dominates) or as a highly sheared, turbulent fluid in the acceleration zone (velocity-squared friction dominates).

[15] Although the Voellmy model is in widespread application in snow avalanche dynamics, its use remains somewhat in debate [*Bartelt et al.*, 1999]. Despite efforts to physically quantify the values of $\mu$ and $\xi$ [*Salm*, 1993], they have not been experimentally verified. Calibrated values for extreme avalanches are available, but these are based on back calculation of events [*Buser and Frutiger*, 1980]. The Coulomb friction values used in numerical simulations are usually much smaller than the static, internal friction angle of the flow material. Similar problems arise in the application of the Voellmy model to rock avalanches [see *Körner*, 1976; *Kelfoun and Druitt*, 2005]. However, independent experimental verification of Voellmy parameters has been reported from the snow avalanche community. *Bartelt and Buser* [2009] related the decrease in apparent Coulomb friction to the kinetic energy associated with the random movements of the snow granules and ice fragments which compose snow avalanches. They showed how the evolution of shearing within the avalanche body [*Kern et al.*, 2009] can be modeled by accounting for the production and dissipation of the random kinetic energy [*Bartelt et al.*, 2007; *Buser and Bartelt*, 2009]. At the head of the avalanche $\mu$ and $\xi$ values were found matching well accepted values for large avalanches ($\mu = 0.155$ and $\xi = 2000$ m s$^{-2}$) [*Bartelt and Buser*, 2009]. At the avalanche tail, higher friction values were found which describes how avalanches run out of material (starve) or stop on steep slopes [*Bartelt et al.*, 2007]. Because the Voellmy parameters seem to capture the movement of the avalanche front, they concluded that the Voellmy model can be applied to model runout distance and maximum flow velocity, but will have difficulties capturing the motion of the avalanche tail and thus modeling the spatial distribution of avalanche deposits.

[16] The Voellmy model, including the internal kinetic energy considerations described above, has been implemented in RAMMS together with a random kinetic energy extension [*Buser and Bartelt*, 2009] and successfully applied for different types of mass movements including snow avalanches [*Christen et al.*, 2010a] and large rock avalanches [*Preuth et al.*, 2010]. By setting the parameter for the production of random kinetic energy to zero, the frictional resistance reduces to the Voellmy model described in equations (4a) and (4b) [*Christen et al.*, 2010b]. Because the focus of this paper is on the comparison between seismic data and modeled avalanche results, we concentrate on the well known and widely used Voellmy model [*Bartelt et al.*, 1999].

### 3.1.3. Entrainment of Material

[17] The total moving volume of an avalanche usually does not remain constant: entrainment and deposition of material must be considered to correctly model the overall mass balance of a particular event. Large and rapid mass movements can cause extreme frontal and basal erosion leading to deposition volumes significantly larger than the failure volume [*Fagents and Baloga*, 2006; *McDougall and Hungr*, 2005; *McSaveney*, 2002]. In certain cases, the presence of an erodible ground layer can strongly increase the mobility of granular material [*Mangeney et al.*, 2007], while in other cases the runout distance might be reduced due to momentum transfer from the moving mass to the static underlying erodible ground [*McDougall and Hungr*, 2005]. *Crosta et al.* [2009] made investigations focused on the water content of the entrained material. They found that eroded dry material generally reduces the total runout distance of debris avalanches while erosion of highly saturated material has more complex consequences. RAMMS includes the possibility to account for entrainment of a user specified potentially erodible ground layer of depth $h$, however, any resulting changes in surface topography are not considered.

[18] According to *Hungr and McDougall* [2009], entrainment can depend on slope, flow velocity, path curvature, surface roughness, or on characteristics and quantity of the erodible material (also proposed, e.g., by *Sovilla et al.* [2006] and *Bouchut et al.* [2008]). In their model DAN the erosion

rate increases in proportion to the flow depth [*Hungr and McDougall*, 2009; *McDougall and Hungr*, 2005]. Others attribute erosion to the shear forces in the shear layer [*Mangeney et al.*, 2007], fracture toughness [*Cherepanov and Esparragoza*, 2008] or, in the case of bedrock erosion of debris flows, to stresses due to granular interactions at the snout, strongly depending on the characteristic grain size [*Hsu et al.*, 2008]. However, no definitive solution for a universal erosion model is available and implementation of different entrainment relationships in a numerical model as proposed by *Hungr and McDougall* [2009] is a reasonable approach to account for different entrainment types.

[19] In field studies of snow avalanche entrainment, the increase in mass was found to depend mainly on the avalanche velocity $U(x, y, t)$ and on the availability of snow mass [*Sovilla et al.*, 2006, 2007]. Assuming a snow avalanche of constant flow density $\rho_a$ entraining an erodible snow layer of known depth $h$ and density $\rho_e$, the velocity-dependent entrainment rate $\dot{Q}_U$ is calculated as

$$\dot{Q}_U = \frac{\rho_e}{\rho_a} k_1 U \tag{5a}$$

[20] The erosion factor $k_1$ (dimensionless) needs to be calibrated to observations and controls the rate at which the erodible snow layer is incorporated and accelerated to the avalanche velocity. This regulates the mass uptake and time delay to accelerate the mass to the avalanche velocity. Details of the entrainment process and the numerical solution are presented by *Christen et al.* [2010b]. For snow avalanches, typically values between $k_1 = 0.2$ and 0.7 are used to match observed snow cover removal rates [*Sovilla et al.*, 2006].

[21] Within a series of test runs with RAMMS we found that for snow, ice and rock avalanches larger than $10^6$ m$^3$ which travel on potentially erodible layers much thicker than seasonal snow cover (e.g., entire glaciers or thick accumulations of loose debris in a glacier forefield) velocity-dependent erosion entrains too much material at the avalanche's tail. This effect is reduced by introducing the flow depth $H$ as an additional factor for scaling the entrainment rate as proposed by *Fagents and Baloga* [2006]. This results in an alternative momentum-dependent erosion $\dot{Q}_p$:

$$\dot{Q}_p = \frac{\rho_e}{\rho_a} k_2 H U \tag{5b}$$

$\dot{Q}_p$ is called "momentum-dependent" erosion because the mass $m$ which is needed to calculate the momentum $p = mU$ is explicitly given by the product of the flow depth $H(x, y, t)$, the constant avalanche density $\rho_a$ and the calculation cell area $A$. Alternatively $\dot{Q}_p$ can also be called "discharge-dependent"; however, this terminology would more relate to dilute hyperconcentrated flows that are not investigated here. The erosion factor $k_2$ can be calibrated to field observations, but has the unit [m$^{-1}$] in this case. We found values between 0.14 m$^{-1}$ and 0.25 m$^{-1}$ to end in the desired deposition volumes. This approach has the advantage that erosion is concentrated in areas where avalanches have large flow depths and are moving relatively fast, such as the avalanche front where plowing can be a dominant mechanism [*McDougall and Hungr*, 2005; *Sovilla et al.*, 2006]. Erosion is consequently attenuated behind the head of the avalanche, where flow depths and velocities are smaller, representing progressive basal erosion [*Sovilla et al.*, 2006].

[22] Herein we compared the modeled erosion to field photographs and aerial and satellite images, as well as to reports concerning erosion and deposition in published field studies [e.g., *Hungr and Evans*, 2004]. The entrainment parameter $k_2$ for the momentum-driven erosion was iteratively calibrated to match the desired final deposition volume, and was thereafter held constant for each simulation.

#### 3.1.4. Total and Moving Volumes

[23] The total volume $V_{tot}$ is the volume of the avalanche at each time step $t$ including the volume of eroded and already deposited material. The moving volume $V_{mov}$ is the amount of material that is still moving at a certain time step, according to a threshold value for the flow depth $H_i(t)$ and the flow velocity $U_i(t)$ (where $H_i(t) \geq 0.1$ m and $U_i(t) \geq 1$ ms$^{-1}$) at each affected cell $i$:

$$V_{tot}(t) = A \sum_{i=1}^{n} H_i(t) \tag{6a}$$

$$V_{mov}(t) = A \sum_{i=1}^{n} H_i(t) \tag{6b}$$

where $n$ is the number of cells affected by the avalanche at time $t$ and $A$ the area of a single cell. If either the flow depth $H_i(t)$ or the flow velocity $U_i(t)$ falls below the threshold value, the material in the affected cell is defined to be not moving anymore.

#### 3.1.5. Model Evaluation and Optimization

[24] For a given runout distance, there are various possible combinations of the friction parameters $\mu$ and $\xi$, as already shown by *Perla et al.* [1980] and *Alean* [1984] for the two-dimensional case and by *Pirulli and Sorbino* [2008] for three-dimensional terrain. We used a $\mu$ value from previous works (e.g., $\mu = 0.05$) [*Hungr and Evans*, 1996; *Lipovsky et al.*, 2008; *Sosio et al.*, 2008], and iteratively searched for a $\xi$ value such that the modeled avalanche reaches the real runout distance. Then, we increase and decrease $\mu$ systematically in 0.01 steps to find the corresponding $\xi$ values. Possible $\mu\xi$ combinations that fit the runout distance describe an exponential function (Figure 6).

[25] We distinguished between geometry and dynamics of the results to assess the performance of the model. Geometry includes the avalanche release and deposition volumes, flow depths, the spatial extent of the avalanche path and thickness of deposited or eroded material. Model dynamics are restricted to the evolution of the avalanche's momentum and kinetic energy, work rate, the stopping characteristics, mean and maximum velocities, and special attributes such as runup, backflow, centrifugal effects, overtopping and flow bifurcation. The validation is complicated by the sparse data, making a strictly quantitative assessment not feasible. Instead, the model results have to be assessed to optimize the match between the modeled event and the limited amount of real avalanche data.

### 3.2. Avalanche Model: Seismic Data Relation

[26] The basic concept of linking the calculated model parameters and seismic data is that in a (rock-ice) avalanche potential energy is converted into kinetic energy, part of

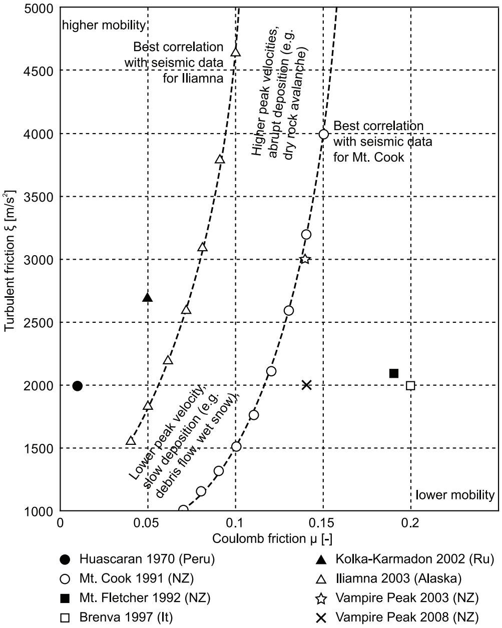

**Figure 6.** Graph modified after *Allen et al.* [2009]. Possible $\mu$ and $\xi$ input parameters for RAMMS model leading to the runout distance of the corresponding real event. For Iliamna and Aoraki/Mt. Cook, all parameter combinations that geometrically matched the observed flow path are shown on the dashed line which also indicates the exponential relationship of corresponding $\mu$ and $\xi$. The smaller the value of $\mu$ and the larger the value of $\xi$, the longer is the avalanche runout distance and vice versa. Smaller $\mu\xi$ combinations lead to slower deposition where decelerating avalanche parts keep moving with a very slow motion up to minutes. Larger $\mu\xi$ combinations show stronger acceleration during the early phase of the movement with higher peak velocities and a more abrupt stopping behavior.

which in turn is transformed into seismic energy due to interaction of the flowing mass of rock and ice with the ground [*Brodsky et al.*, 2003; *Davies and McSaveney*, 1999; *Deparis et al.*, 2008; *Kanamori and Given*, 1982; *Kawakatsu*, 1989; *Sabot et al.*, 1998; *Suriñach et al.*, 2001; *Weichert et al.*, 1994]. Because the seismometer is not situated directly at the shear layer of the moving avalanche, the recorded seismic waves are transformed between source and receiver. We distinguish between the seismic source signal and a variety of source and path effects:

[27] 1. Seismic source signal: This is the seismic signal produced by the avalanche directly at the site of the event. The strength of the produced signal is related to the total momentum, respectively total kinetic energy of the avalanche (which in turn depend on mass and velocity, and hence also on entrainment [*Suriñach et al.*, 2001, 2005]). Furthermore, the production of seismic energy is affected by the surface properties of the avalanche path which include surface roughness (on a millimeter to decameter scale), but also centrifugal and impact effects caused by minor and major obstacles, topographic steps and lateral deflections [*McSaveney and Downes*, 2002; *Sabot et al.*, 1998; *Suriñach et al.*, 2001]. All these components control the rate at which kinetic energy is transformed into heat, particle fragmentation [*Crosta et al.*, 2007; *Davies et al.*, 2007; *Locat et al.*, 2006] and seismic waves.

[28] 2. Local source site effects: The substrate below the shear plane or at an impact site can have a strong effect on the efficiency of seismic wave transmission into the ground, e.g., moraine material, snow or glacier ice might attenuate the seismic signal compared to cohesive rock [*Deparis et al.*, 2008].

[29] 3. Seismic path effects: Seismic waves can be attenuated, dispersed, scattered, refracted and reflected as they travel, in a manner dependent upon the characteristics of the material through which they propagate. This degrading effect is strongly dependent on the distance between source and receiver [*Deparis et al.*, 2008] and the frequency of the seismic waves. The seismic waveform is also changed along the path due to variations in travel path of different seismic phases; because waves travel at a range of velocities their arrivals disperse at more distant stations [*Aki and Chouet*, 1975].

[30] 4. Local recorder site effects: As at the source, the seismic station can be affected by site specific effects which are controlled by the underlying ground (lithology, topography) [*Suriñach et al.*, 2001].

[31] To compare the recorded seismograms of large and rapid mass movements with numerical simulation results, the described site and path effects in the seismic data should be as small as possible. This is possible by using a case study with a simple topography such as Iliamna volcano, and by selecting the closest seismic stations (but which still are not completely saturated). Iliamna's simple topography prevents problems in quantifying the influence of steps, obstacles, lateral deflections, and changing surface roughness on the efficiency of seismic wave generation and we therefore assume that the seismic efficiency is more or less constant (this is clearly not the case for many other mass movements and has to be considered when analyzing the seismic signal). If the avalanche loses such a constant portion of its energy in the form of seismic waves to the ground, the recorded seismic signal of the avalanche should also be approximately proportional to the instantaneous total momentum $p_{tot}(t)$, and, respectively, total kinetic energy $k_{tot}(t)$, which in the RAMMS model is calculated by

$$p_{tot}(t) = A\rho_a \sum_{i=1}^{n} H_i(t)U_i(t) \tag{7a}$$

$$k_{tot}(t) = A\rho_a \sum_{i=1}^{n} H_i(t)U_i(t)^2 \tag{7b}$$

In a strict sense, the seismic signal reflects the loss of avalanche power, not the remaining energy. The loss of power is described by the instantaneous total frictional work rate $\dot{W}_{tot}$,

$$\dot{W}_{tot}(t) = A\rho_a g \sum_{i=1}^{n} U_i(t)\left[\mu H_i(t) + \frac{U_i(t)^2}{\xi}\right] \tag{7c}$$

**Figure 7.** Oblique aerial view of the 25 July 2003 Red Glacier avalanche at Iliamna Volcano, Alaska. Dark color is evidence for basal rock entrainment from the upper part of the avalanche and remobilized debris from older rock-ice avalanche deposits on the glacier surface. Note lateral swashing in the orographically left central part of the avalanche. Photo by R. Wessels, USGS (1 August 2003).

where $g$ is the gravitational acceleration (9.81 m $s^{-2}$). Equation (7c) depends on the applied frictional resistance model, which in this case is the Voellmy model with the friction parameters $\mu$ and $\xi$. The simple Voellmy model lumps all energy consuming processes into two simple constitutive parameters. It does not consider the kinetic energy of particle fluctuations and therefore the particle interaction with the basal boundary, which is the producer of seismic energy. However, because the momentum transfer between the avalanche and the ground is given by the total frictional work rate, we assume that the seismic energy generation is proportional to the total frictional work rate given by the Voellmy model. If the seismic signal is not strongly modified on its way to a seismometer (path effects), the measured seismic signal still should be proportional to the total frictional work rate of the avalanche.

[32] We compare all calculated parameters (from equations (7a), (7b), and (7c)) of a simulated avalanche to the absolute filtered amplitudes of the corresponding recorded seismic avalanche data. Major differences between these data sets may indicate differences in the energy consuming processes (e.g., the surface roughness) or local source and recorder site effects, as well as seismic path effects. Strong differences between modeled and recorded data can also indicate progressive and multiple failures of mass, which are much more complex and cannot be modeled accordingly.

## 4. Iliamna Red Glacier 2003 Avalanche (Alaska)

### 4.1. Setting and Characteristics of Event

[33] Iliamna volcano (3053 m above sea level (asl)) is an andesitic stratovolcano of the Aleutian arc in the Cook Inlet region of Alaska [*Caplan-Auerbach and Huggel*, 2007] (Figure 2). The volcanic edifice has developed over older plutonic rocks of Jurassic age [*Detterman and Reed*, 1980]. Field investigations by *Waythomas et al.* [2000] have shown that Iliamna has erupted at least twice during the last 300 years. On the east face, there is a zone of hydrothermally altered rocks with sulfurous fumaroles and frequent steam emissions [*Huggel*, 2009; *Waythomas et al.*, 2000]. Directly below this area, Red Glacier extends from 2300 m asl to about 150 m asl. The lower boundary of Red Glacier is not clearly detectable because it is covered by debris and many small water bodies. *Trabant* [1999] estimated for Red Glacier a total ice volume of 4.7 $km^3$ and an area of 52.5 $km^2$.

[34] Since 1960, frequent and large ice-rock avalanches between $1 \times 10^6$ $m^3$ and $3 \times 10^7$ $m^3$ with return periods of only 2–4 years have been observed on the slopes of Iliamna volcano. The largest ones occurred on Red Glacier, all having a similar flow and deposition geometry [*Caplan-Auerbach and Huggel*, 2007; *Huggel et al.*, 2007]. The best documented event, which took place on 25 July 2003, was selected for investigation. During this event, approximately $6 \times 10^6$ $m^3$ of rock and ice detached at the upper boundary of Red Glacier at 2300 m asl (Figure 7). The average failure depth was estimated to be 10–15 m with the failure zone partly in ice, rock, and mostly at the ice-rock interface. The presence of rock in the initial mass is indicated by the dark color of the avalanche path and deposit (Figure 7). It is estimated that another 6–14 × $10^6$ $m^3$ of ice and debris deposits of older rock-ice avalanches were eroded on the way down where finally 12–20 × $10^6$ $m^3$ rock and ice debris were deposited [*Huggel et al.*, 2007]. The vertical height difference $H_d$ of the avalanche path is 1800 m while the horizontal distance along the curved main avalanche path $L_d$ is 8800 m, corresponding to an $H_d/L_d$ ratio of 0.2 (Figure 1 and Table 1). $H_d$ and $L_d$ are both related to the vertical and horizontal distance between the uppermost point of the detachment area and the lowest and most distant point of the avalanche deposit.

**Table 1.** Observed Characteristics of the Iliamna Red Glacier Avalanche (25 July 2003) and the Aoraki/Mt. Cook Avalanche (14 December 1991)[a]

| Avalanche | Failure Elevation (m) | Drop Height $H_d$ (m) | Runout Length $L_d$[b] (m) | $H_d/L_d$ | Initial Volume ($10^6$ $m^3$) | Entrained Volume ($10^6$ $m^3$) | Total Volume ($10^6$ $m^3$) | Time to Farthest Point (s) | Average Velocity (m $s^{-1}$) | Ice and Snow (vol %) |
|---|---|---|---|---|---|---|---|---|---|---|
| Iliamna | 2300 | 1800 | 8800 | 0.2 | ~6 | 6–14 | 12–20 | ~180 | ~48 | ~80[c] |
| Aoraki/Mt. Cook | 3754 | 2720 | 6800 | 0.4 | ~12 | 48–68 | 60–80 | ~120 | ~55 | 10–80[d] |

[a] All data are measurements and estimates according to *Caplan-Auerbach and Huggel* [2007] and *McSaveney* [2002].

[b] Runout length $L_d$ is measured horizontally along the central flow path line.

[c] Ice and snow content at the initiation of the avalanche and in the deposited material.

[d] Range of ice and snow content from initiation of the avalanche to the deposited material.

**Table 2.** Model Input Parameters for the Iliamna Red Glacier (Alaska) 2003 Avalanche and the Aoraki/Mt. Cook (New Zealand) 1991 Avalanche[a]

| Input Parameter | Iliamna Red Glacier, 2003 | Aoraki/Mt. Cook, 1991 |
|---|---|---|
| DTM (grid) | SRTM–1 30 m | NZ 25 m |
| Release density/avalanche density ($\rho_a$) | 1000 kg m$^{-3}$ | 1100 kg m$^{-3}$ |
| Release volume | 6.2 × 10$^6$ m$^3$ | 11.8 × 10$^6$ m$^3$ |
| Coulomb friction ($\mu$) | 0.04–0.11 | 0.06–0.15 |
| Turbulent friction ($\xi$) | 1550–6000 m s$^{-2}$ | 900–7000 m s$^{-2}$ |
| Max. erosion depth ($h_i$) | 10 m | 40 m |
| Average density of erodible layer ($\rho_e$) | 600 kg m$^{-3}$ | 600 kg m$^{-3}$ |
| Erosion factor ($k_2$) | 0.14 m$^{-1}$ | 0.25 m$^{-1}$ |

[a]These parameters were constant for all calculations, except $\mu$ and $\xi$, which were systematically varied according to the indicated ranges (Figure 6).

### 4.2. Model Application

[35] The release area was reconstructed using airborne oblique photographs and the slope normal release thickness was set to 10.5 m with a resulting initial volume of 6.2 × 10$^6$ m$^3$, similar to the volume estimated by *Caplan-Auerbach and Huggel* [2007] (Table 2). The avalanche density was set to an average of 1000 kg m$^{-3}$ for a mix of predominantly snow, firn and ice, and a minor amount of rock and the density of the erodible layer to 600 kg m$^{-3}$ for a mix of snow, firn, and ice. A few calibration runs were needed to find the erosion factor $k_2$ = 0.14 leading to the desired total eroded volume of approximately 10 × 10$^6$ m$^3$, in the middle of the range of entrainment volumes estimated by *Caplan-Auerbach and Huggel* [2007].

[36] We used constant friction values for the entire flow path starting with $\mu = 0.05$ and found $\xi = 1850$ m s$^{-2}$ to match the observed runout distance. According to the parameter range of 0.03–0.10 for $\mu$ suggested, e.g., by *Sosio et al.* [2008], we varied the $\mu$ value by 0.01 increments and determined $\xi$ values between 1550 and 4650 m s$^{-2}$ to fit the observed runout distance (Figure 6).

### 4.3. Model Results and Relation to Seismic Data

[37] All four modeled examples show a good fit to the mapped avalanche outline while the geometrical fit of the calculations with smaller $\mu\xi$ values is marginally better than those with larger values (Figure 8). Topographically induced lateral deflection of the flow direction is enhanced with lower $\mu\xi$ combinations, resulting in a more distinct smaller flow lobe on the orographically right side and a better fit of the swashing on the left side (Figures 7 and 8).

[38] The maximum flow depths for the model runs are 50 m for the upper narrow section where the material converges, around 15 m for the central flow part, and rapidly reduce to 1–3 m in the lower lateral sections (Figure 8). The modeled main debris deposits extend from the central avalanche part 4 km east of the initiation area to the lowest point of the avalanche and the thickness of the deposited material generally is 1–10 m. The available photographs suggest that the modeled deposition thickness lies within a reasonable range, but this comparison is of qualitative character.

[39] Erosion of snow, firn, ice and surface debris from Red Glacier concentrates along the central flow line of the avalanche where flow depth, flow velocities and hence the momentum are larger. There, modeled erosion depth has a maximum value of 8 m and is not larger than 1–2 m for the lateral zones, decreasing to zero in the lower section of the avalanche runout path. These values are plausible in relation to the event size, and traces of erosion and deposition on the images generally

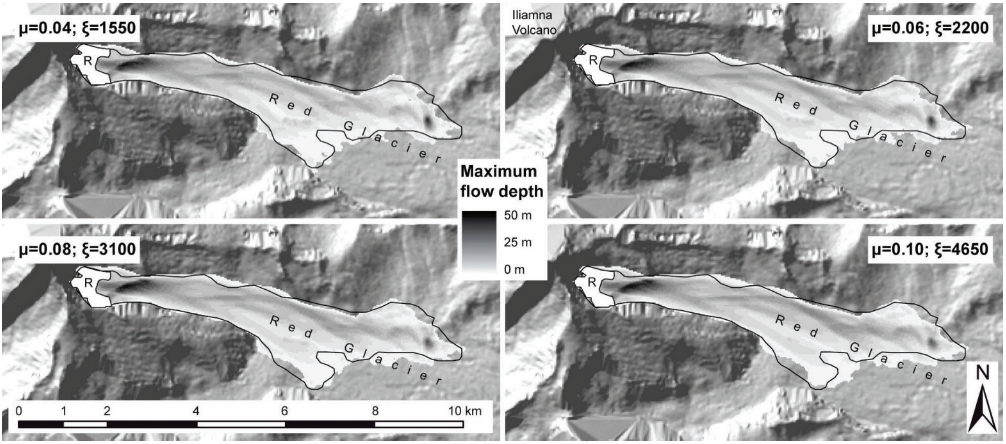

**Figure 8.** RAMMS output of maximum flow depth reached at each cell after 240 s. The four individual simulations show that it is possible to model a given runout distance with different $\mu\xi$ combinations. Minor differences mainly concern the maximum reach of the orographically right smaller branch of the flow. Flow direction is from left to right, and the black line represents the mapped outline shape of the 25 July 2003 Red Glacier avalanche. The runs with smaller $\mu\xi$ combinations have a lateral extension that is closer to the outline geometry. The letter “R” marks the release area.

correspond well with the model predictions, however, detailed conclusions about the fit of modeled erosion are not possible. For a comparison of the dynamic characteristics of the real and simulated avalanches, we use the seismic data described in the following.

[40] We compared the original seismic signal and seismic envelope of the Iliamna Red Glacier 2003 avalanche to different model output parameters that all indicate a noticeable similarity with the seismic counterpart (Figure 9). The total momentum, kinetic energy, and frictional work rate distributions over time depend on the combination of $\mu$ and $\xi$. For the $\mu$–$\xi$ combinations with larger values, the peaks are pronounced and during the run out of the avalanche, the curves decrease faster. The large amplitude of the signal between 0 and 15 s may be due to initial breakage of ice and rock combined with low attenuation because the movement takes place on bedrock where no energy absorbing snow and glacier ice is present. This effect is not unique to the 2003 avalanche and can be observed in the seismic data for all available recorded large avalanches on Red Glacier (1997, 2000, 2003 and 2008).

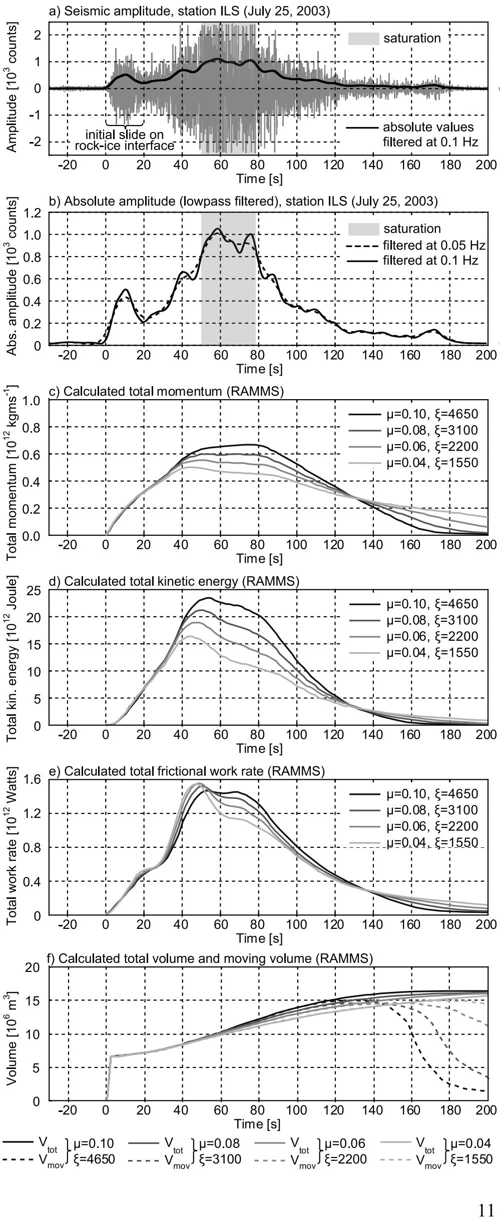

**Figure 9.** Comparison of seismic records of the 25 July 2003 Red Glacier avalanche at Iliamna Volcano with RAMMS model calculations. (a) Seismogram for station ILS and filtered absolute values. The stronger signal at $t$ = 0–15 s is possibly referred to the initial slide on the rock-ice interface and a more efficient transmission of energy into the ground. The signal is saturated for $t$ = 50–78 s. (b) Absolute amplitude low-pass filtered at 0.1 Hz (10 s) and 0.05 Hz (20 s). (c) Total momentum, (d) total kinetic energy, and (e) total frictional work rate for different $\mu\xi$ combinations calculated with RAMMS. (f) Evolution of the total volume of the avalanche due to erosion and the part which is still moving according to a defined threshold value. Most plots in Figures 9c, 9d, and 9e have a strong similarity to the filtered absolute amplitude in Figure 9b.

[41] We tested how well the normalized curves of the total momentum, kinetic energy and frictional work rate of the calculated avalanche correlate with the normalized curve of the absolute filtered amplitude of the seismogram. Correlation coefficients $R^2$ were calculated between the total momentum, kinetic energy or frictional work rate of each model run (Table 3) and the seismic data filtered at 0.1 Hz (10 s) and 0.05 Hz (20 s). The total momentum has the lowest correlation coefficients ($R^2$ between 0.692 and 0.811). The correlation of the total kinetic energy is clearly higher ($R^2$ between 0.789 and 0.888). The best correlation is reached with the total frictional work rate ($R^2$ values between 0.782 and 0.904, Figure 10) which can be used for independent model calibration.

[42] In contrast to the planform outline geometry (Figure 8), the correlation analysis indicates a better agreement of the larger $\mu\xi$ combinations with the filtered seismic data. This conflict reveals the problem that looking at the geometry of a static avalanche calculation result (e.g., maximum flow depth or deposit) is possibly misleading from a dynamic and energetic point of view. Analysis of moving and total mass (Figure 9f) show that during the initial 140 s, the release volume of $6.2 \times 10^6$ m$^3$ erodes another 10–11 × $10^6$ m$^3$ and depending on the $\mu\xi$ combination, material starts to be deposited after 140–160 s. The larger the values of the $\mu\xi$ combination, the more abruptly the avalanche stops. Despite that, e.g., for $\mu = 0.08$ and $\xi = 3100$ m s$^{-2}$ at $t = 180$ s still 50% of the mass is moving, yet the total momentum at this time is only 7% of the maximum total momentum. This can be explained by many "flowing" cells having either very small flow depths or small flow velocities, resulting in a small total kinetic energy (<1% of the maximum kinetic energy at $t$ = 180 s). In the case of lower $\mu\xi$ combinations, the modeled

**Table 3.** Correlation Analysis of RAMMS Modeling Results and Seismic Data From Figures 9 and 12[a]

| | Total Momentum | | Total Kinetic Energy | | Total Frictional Work Rate | |
|---|---|---|---|---|---|---|
| | 0.1 Hz (m) | 0.05 Hz (m) | 0.1 Hz | 0.05 Hz ($10^6$ m$^3$) | 0.1 Hz ($10^6$ m$^3$) | 0.05 Hz |
| Iliamna runs | | | | | | |
| $\mu$ = 0.04, $\xi$ = 1550 | 0.692 | 0.699 | 0.789 | 0.808 | 0.782 | 0.805 |
| $\mu$ = 0.06, $\xi$ = 2200 | 0.738 | 0.750 | 0.820 | 0.840 | 0.835 | 0.860 |
| $\mu$ = 0.08, $\xi$ = 3100 | 0.765 | 0.780 | 0.844 | 0.866 | 0.868 | 0.893 |
| $\mu$ = 0.10, $\xi$ = 4650 | 0.794 | 0.811 | 0.863 | 0.888 | 0.879 | 0.904[b] |
| Aoraki/Mt. Cook runs | | | | | | |
| $\mu$ = 0.09, $\xi$ = 1300 | 0.357 | 0.384 | 0.545 | 0.574 | 0.651 | 0.675 |
| $\mu$ = 0.11, $\xi$ = 1750 | 0.435 | 0.460 | 0.571 | 0.605 | 0.733 | 0.762 |
| $\mu$ = 0.13, $\xi$ = 2600 | 0.495 | 0.524 | 0.592 | 0.631 | 0.799 | 0.833 |
| $\mu$ = 0.15, $\xi$ = 4000 | 0.537 | 0.569 | 0.607 | 0.647 | 0.826 | 0.862[b] |

[a] Normalized total momentum, total kinetic energy, and total frictional work rate of modeled $\mu\xi$ combinations are compared to the normalized absolute count values of the seismogram filtered at 0.1 Hz (10 s) and 0.05 Hz (20 s). All values of the correlation analysis represent the correlation coefficient $R^2$ of the modeled (RAMMS) and measured (seismometer) data between $t$ = 0 s and $t$ = 200 s.

[b] Correlation diagrams of these best fit values are shown in Figures 11 and 15.

avalanche reaches lower peak velocities but takes much more time to come to rest at a given runout distance.

[43] The simulated avalanches need between 170 and 186 s to reach the lowest point at a distance of 8800 m resulting in a horizontal average velocity of 47–52 m s$^{-1}$ which is in good agreement with the mean velocity of ~50 m s$^{-1}$ reported by *Caplan-Auerbach and Huggel* [2007]. The simulations show peak velocities between 70 and 100 m s$^{-1}$ for the central part of the avalanche and the kinetic energy at $t$ = 180 s is clearly less than 15% of its maximum for all calculations.

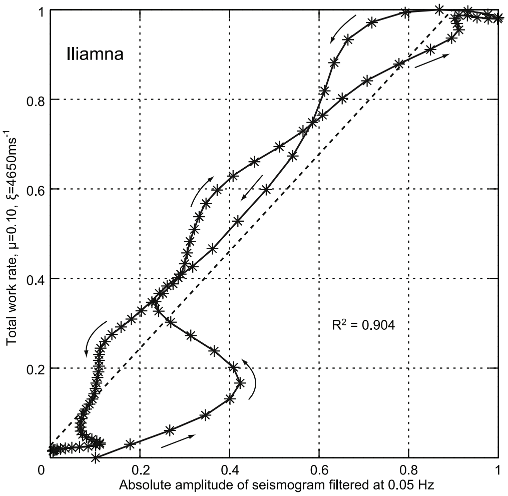

**Figure 10.** Plot of the best fit result from the correlation analysis between normalized seismic data and simulated avalanche parameters of Iliamna from Table 3 (sampled to 2 s steps between $t$ = 0 s and $t$ = 200 s). Best fit results are achieved for comparisons of the seismograms filtered at 0.05 Hz (20 s) with the total frictional work rate that was modeled with relatively high $\mu$–$\xi$ parameter values ($\mu$ = 0.10, $\xi$ = 4650). Arrows indicate the time direction, and the start and end are situated at the lower left. The initial increase in seismic energy which was not observed in the model is recognizable by the stronger deviation from the solid linear regression line in the lower left corner. The linear regression is shown by the dashed line.

## 5. Aoraki/Mt. Cook 1991 Avalanche (NZ)

### 5.1. Setting and Characteristics of Event

[44] Aoraki/Mt. Cook (3754 m asl) is the highest peak in New Zealand's Southern Alps, and situated at the Main Divide on the Main Divide fault, which is a parallel secondary fault of the 15 km northwestern Alpine fault (Figure 4). The closest settlement, Mount Cook village, is located 16 km to the south. The only infrastructure within several kilometers is Ball Shelter behind a lateral moraine of Tasman Glacier, and the Plateau Hut at 2200 m asl that serves as shelter for climbers (Figure 11).

[45] At 00:11 h local time on 14 December 1991, an avalanche of rock and ice occurred from High Peak, the uppermost part of Aoraki/Mt. Cook. The initial avalanche volume of approximately 12 × $10^6$ m$^3$ rapidly increased due to massive erosion of snow and ice, and passed within 300 m of the

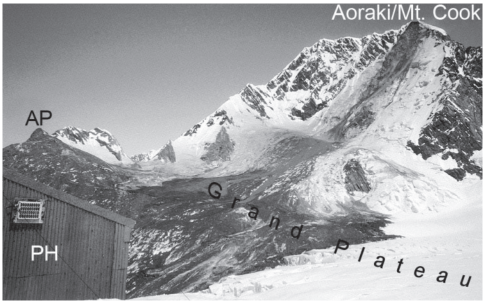

**Figure 11.** Upper and central part of the Aoraki/Mt. Cook avalanche of 14 December 1991. Detachment area is on the upper right. The flow path is well recognizable by the dark areas where massive erosion of ice and deposition of debris took place. The avalanche ran up for 200 m and overrode Anzac Peak (AP). Plateau Hut (PH) was missed by only 300 m. Photo by I. Owens (16 December 1991).

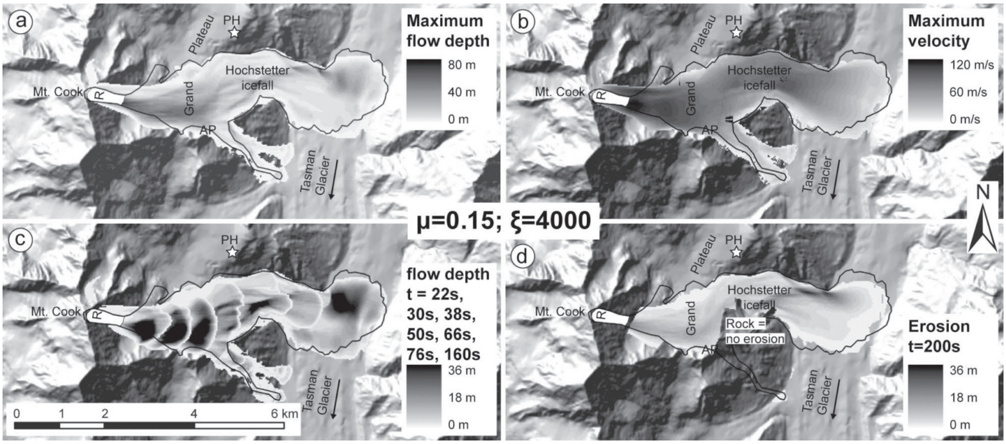

**Figure 12.** Various RAMMS results from a single simulation of the 14 December 1991 rock-ice avalanche from Aoraki/Mt. Cook (NZ) from the run with $\mu = 0.15$ and $\xi = 4000$ m s$^{-1}$ (highest correlation coefficient). (a) Maximum flow depths reach 80 m at an early stage of the avalanche but generally are not much higher than 36 m. (b) Maximum velocities are close to 100 m s$^{-1}$ over most of the avalanche track. (c) Overlapping flow depths for selected time steps (see Figure 13 for a more detailed view). (d) Momentum-dependent erosion was only allowed for the glacierized area. The Plateau Hut (PH) is marked with a white star. AP is Anzac Peak, and R is release area.

occupied Plateau Hut (Figures 4 and 11). After 2–3 min, a total volume of estimated 60–80 × $10^6$ m$^3$ [*McSaveney*, 2002] was deposited on Tasman Glacier as far as 6800 m in horizontal distance $L_d$, and 2720 m in height $H_d$ (resulting in an $H_d/L_d$ ratio of 0.4). The ice content of the material increased from only 10 vol % in the initial mass to approximately 80 vol % in the final deposit (Table 1). The avalanche path was mainly over firn and glacier ice above 2000 m asl, flowed through an ice fall with large seracs between 2000 and 1200 m asl, and then over the mostly debris-covered surface of the Tasman Glacier below 1200 m asl. Around 2300 m asl, a lateral branch of the avalanche ran 200 m up the orographic right side of the valley sidewall and overflowed a crest line to continue down to the boundary of Tasman Glacier [*McSaveney*, 2002].

### 5.2. Model Application

[46] The release area was defined as an elongated polygon with a slope normal average thickness of 42 m. The total release volume was 11.8 × $10^6$ m$^3$, corresponding to the estimate made by *McSaveney* [2002]. Because the amount of rock is estimated to be slightly higher than at Iliamna, the density of the avalanche was set to an average of 1100 kg m$^{-3}$ for a mix of snow, firn, ice and rock. This value also corresponds to the deposit density some days after the event reported by *McSaveney* [2002], excluding large rock boulders. We assume that the density during motion is lower, but including larger rock components the average density of 1100 kg m$^{-3}$ is plausible. The average density of the erodible layers of snow, firn and ice was assumed to be similar to the one on Red Glacier in Alaska (600 kg m$^{-3}$). An erosion factor $k_2$ = 0.25 was found to scale erosion of the glacier surface resulting in a deposition volume of 36 × $10^6$ m$^3$ that is smaller than but still within the precision of the estimate by *McSaveney* [2002] (M. J. McSaveney, personal communication, 2009). The difference of a factor two between reported and modeled deposition volumes is significant and definitively influences the momentum, kinetic energy, frictional work rate, and deposition thickness. However, model results with final volumes between 60 and 80 × $10^6$ m$^3$ have shown deposit thickness which did not match the pictures and reports from *McSaveney* [2002] while total work rate plots still maintained the basic shape with the three peaks. We therefore decided to assume a lower deposition volume. Applied friction values for the Aoraki/Mt. Cook avalanche ranged from 0.06 to 0.17 for $\mu$ and from 900 to 7000 m s$^{-2}$ for $\xi$ (Figure 6).

### 5.3. Model Results and Relation to Seismic Data

[47] The best results concerning spatial extent of the avalanche were found for $\mu$ between 0.09 and 0.15, and $\xi$ between 1300 and 4000 m s$^{-2}$. Features like the southern smaller branch, runup to Anzac Peak, and a late reverse flow from Anzac Peak to the plateau with subsequent deposition are also observable in each simulation. Figure 12 gives an overview over 4 different RAMMS model outputs for a single simulation. Because the geometric results of various simulations with different $\mu\xi$ combinations fit well the mapped outlines from *McSaveney* [2002], we first focus on the dynamic characteristics of the modeled avalanche. The avalanche seismogram of the closest station Erewhon (EWZ) has 3 distinct pulses of energy (Figure 13a), which are also well visible in the filtered absolute amplitude of the seismogram (Figure 13b). The calculated momentum and kinetic energy plots in Figures 13c and 13d show only two distinct peaks in amplitude (peaks I and III). These two peaks correspond to the potential energy that is transformed into kinetic energy during

the initial fall on the 55° slope, up to the moment before most parts of the moving mass reach the relatively flat Grand Plateau (peak I), and again when it crosses the steep Hochstetter icefall (peak III). Because a higher kinetic energy for a given mass is induced by higher velocities, the frictional resistance forces do also increase ($\xi$ term according to equation (4a) and (4b)) and lead to a higher frictional work rate (maxima I and III in Figure 13e and equation (7c)). The maxima I and III in Figures 13c, 13d, and 13e are separated by approximately 50 s which is similar for the peaks I and III in Figures 13a and 13b. This allowed fitting of the calculated curves to the seismic records.

[48] Peak number II is missing in the modeled total momentum and total kinetic energy plots because the avalanche loses momentum and kinetic energy on the flat part of the Grand Plateau. The total frictional work rate in Figure 13e, however, shows a third peak (peak II) between the others, exactly where the seismic signal has the highest amplitudes. This peak is related to an increased friction on a less inclined slope, leading to an enhanced frictional work rate and a strong loss of kinetic energy and momentum. The correlation analysis between the seismic data and all model results revealed low correlation coefficients $R^2$ from 0.357 to 0.569 for the total momentum, and 0.545 to 0.647 for the total kinetic energy (Table 3). In contrast to this, the $R^2$ values for the total frictional work rate are much better and range from 0.651 to 0.862. As at Iliamna, correlation of seismic data with model runs having larger $\mu\xi$ combinations show better correlation coefficients (best fit with $\mu = 0.15$ and $\xi = 4000$ is shown in Figure 14).

[49] Modeled maximum flow depths, maximum velocities, instantaneous flow depths, and erosion in Figure 12 are those from the run with the best fit to the seismic data. Flow depths are between 10 and 20 m with some extreme values up to 60 m. The modeled main deposit on Tasman Glacier has a maximum thickness of 36 m, but most of it is thinner than 18 m. The simulated avalanche reached the furthest point after 120 s (see also Figure 15g). For a horizontal runout distance of 6800 m, this leads to a horizontal average velocity component of ~56 m s$^{-1}$ while the maximum slope-parallel velocities were between 80 and 100 m s$^{-1}$ for extended sections. Erosion of snow, firn, ice, and debris cover on the glacier surfaces, for which erosion was allowed, reach 5–10 m in the steeper parts, where the avalanche is moving fast, and show a maximum of ~30 m on the orographically left side below Hochstetter Icefall, where the debris is piled up on the steep sidewall. The concentration of erosion on this site is due to the momentum-dependent erosion, that means where the largest momentum appears, the strongest erosion occurs. These results are in general agreement with the findings and photos of *McSaveney* [2002].

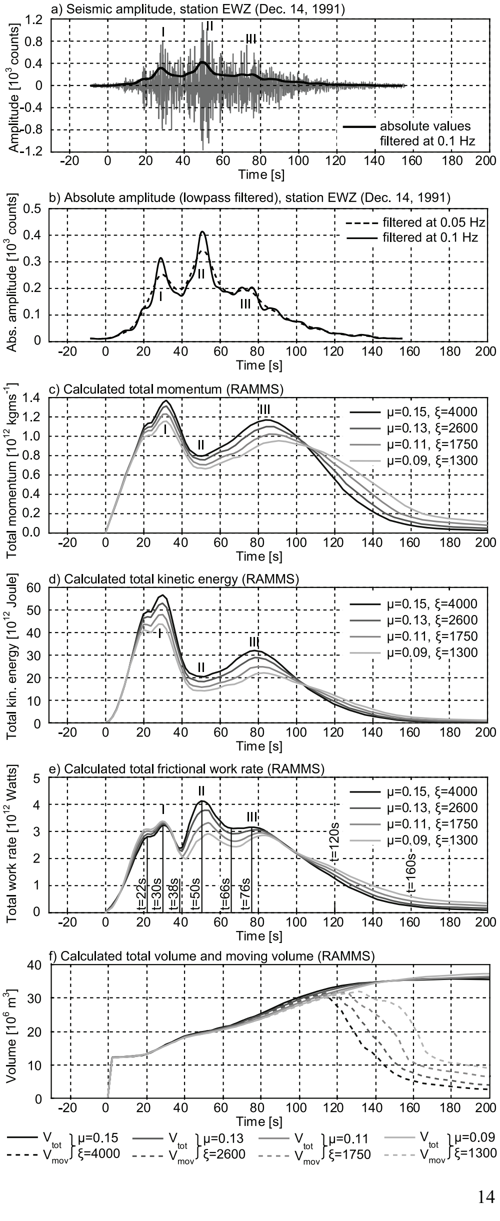

**Figure 13.** Comparison of seismic records of the 14 December 1991 Aoraki/Mt. Cook avalanche (NZ) with RAMMS model calculations. (a) Seismogram for station EWZ and filtered absolute values. The initiation of the avalanche shows low signal amplitude and cannot be clearly seen, probably due to almost free fall conditions. (b) Absolute amplitude low-pass filtered at 0.1 Hz (10 s) and 0.05 Hz (20 s). (c) Total momentum, (d) total kinetic energy, and (e) total frictional work rate for different $\mu\xi$ combinations calculated with RAMMS. (f) Evolution of the total volume of the avalanche due to erosion and the part which is still moving according to a defined threshold value. Note the similarity of absolute amplitude filtered at 0.1 Hz (Figure 13b) and calculated total frictional work rate for $\mu = 0.15$ and $\xi = 4000$ m s$^{-2}$ (Figure 13e). Time steps for local maxima and minima of this run are highlighted in Figure 13e, and specific avalanche flow depths for each corresponding time step are shown in Figure 12.

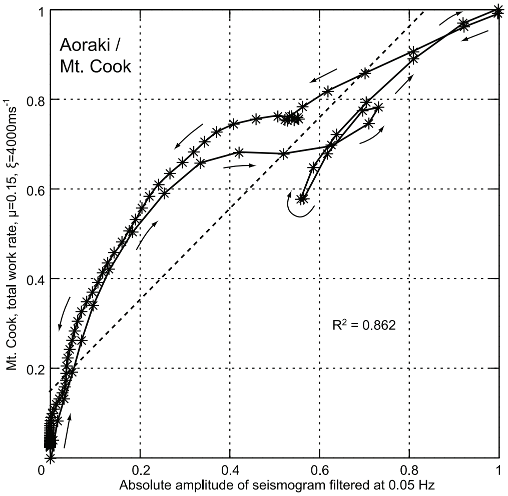

**Figure 14.** Plot of the best fit result of the correlation analysis between normalized seismic data and simulated avalanche parameters of Aoraki/Mt. Cook from Table 3 (sampled to 2 s steps between $t = 0$ s and $t = 200$ s). Best fit results are achieved for comparisons of the seismograms filtered at 0.05 Hz (20 s) with the total frictional work rate that was modeled with relatively high $\mu$–$\xi$ parameter values ($\mu = 0.15$, $\xi = 4000$). Arrows indicate the time direction, and the start and end are situated at the lower left. The linear regression is shown by the dashed line.

[50] Figure 15 shows a more detailed RAMMS output time series of the instantaneous flow depth taken from Figure 12c. Each plot relates to the time when the avalanche reaches a local minimum or maximum in the total frictional work rate curve from Figure 13e. We can see that the avalanche's frictional work rate is at a local maximum when the kinetic energy is very high (after crossing a steep part, e.g., at $t = 22$ s, 30 s and 76 s), as well as when the avalanche is running fast over a less inclined surface and frictional resistance forces are increased (after crossing a flat part, e.g., at $t = 50$ s). The longer the avalanche is running, the more the mass gets distributed along the flow path and the described effects become less clear. This might be the reason why the second major step in topography at Hochstetter Icefall appears less pronounced in the seismogram and the calculated work rate plots, than the initial fall when the mass is still very compact.

## 6. Discussion

### 6.1. Performance of the Numerical Model

[51] Commonly, avalanche model parameters are evaluated by fitting to the observed runout distance. However, a mass movement model should not only reproduce correct runout distances, but simultaneously fit geometric, energetic, and dynamic observations. Although the model is not able to exactly match every characteristic of the avalanche, the total level of fit suggests that the model adequately represents the real process.

[52] Uncertainties of the detachment volumes often are within a range of 10–20% or more, but uncertainties about erosion and the final volume are much larger. Within the analysis strategy to fit the runout distance, the uncertainty in erosion affects the frictional parameters. In turn, erosion and deposition depths/volumes are affected by the friction parameters. Independent data are needed to validate the model quantitatively. The simplest independent variable we used was the lateral expansion of the avalanche (entire outline geometry). The model fails when the lateral deposition of the avalanche is significantly different from the mapped real extent. Another variable could be the deposition thickness including the final volume, but unfortunately, a lack of data required us to verify erosion and deposition qualitatively according to the available photographs and field reports. We used the seismograms as another independent semiquantitative source to validate the energetic and dynamic fit of the model results. We call seismograms semiquantitative validation sources because site and path effects are difficult to quantify and may have a significant effect on the appearance of the seismic signal at large distances [*Deparis et al.*, 2008].

[53] Some differences between modeled and observed avalanches can be explained by a number of simplifications that were made, such as constant average friction parameters which are too large for an avalanche running over pure ice but also too small for a debris covered glacier surface. Because the model uses constant flow density, the avalanche density was adjusted for the deposits while real flow densities might have varied during downstream movement, generally being lower than defined within the input variables but being higher for the unbroken release mass. However, flow density is only used for flow pressure calculations and does not affect the propagation of the flow. Likewise, the average erosion density is too high if erosion is only superficial, but too low if erosion is deep or includes denser rock fragments. The application of momentum-dependent erosion is a further approximation of the real erosion process, and testing other erosion models is suggested.

[54] The accuracy and resolution of the DTM is crucial for all model calculations and it should stand in a reasonable relation to the avalanche size. While SRTM-1 is a sufficient resolution for an avalanche of several million cubic meters flowing many kilometers, it is too coarse for much smaller events [*Christen et al.*, 2010a; *Schneider et al.*, 2008]. However, the problem of DTM quality in glacial environments is often more due to topographic changes between the DTM acquisition time and the avalanche event. Therefore, the availability of preevent and postevent DTMs representing the topography shortly before and after the event is an important factor for the success of retrospective modeling. It further helps to calculate the erosion and deposition, and hence the volume of the avalanche, to better fit the geometric criteria.

[55] We generally used higher $\mu\xi$ combinations than, e.g., *Hungr and Evans* [1996] used for modeling the 27 March 1964 avalanche on Sherman Glacier ($\mu = 0.03$, $\xi = 1000$ m s$^{-1}$), *Sosio et al.* [2008] based on an analysis of the 18 September, 2004 Thurwieser rock avalanche on Zebrù Glacier for rock-ice avalanches in general ($\mu = 0.03$–$0.1$, $\xi = 1000$ m s$^{-1}$), or *Lipovsky et al.* [2008] for the 24 July, 2007 Mt. Steele rock-ice avalanche ($\mu = 0.052$, $\xi = 1525$ m s$^{-1}$). A reason is that modeled process durations to reach the full runout distance might be too high in certain cases where low $\mu\xi$ combinations

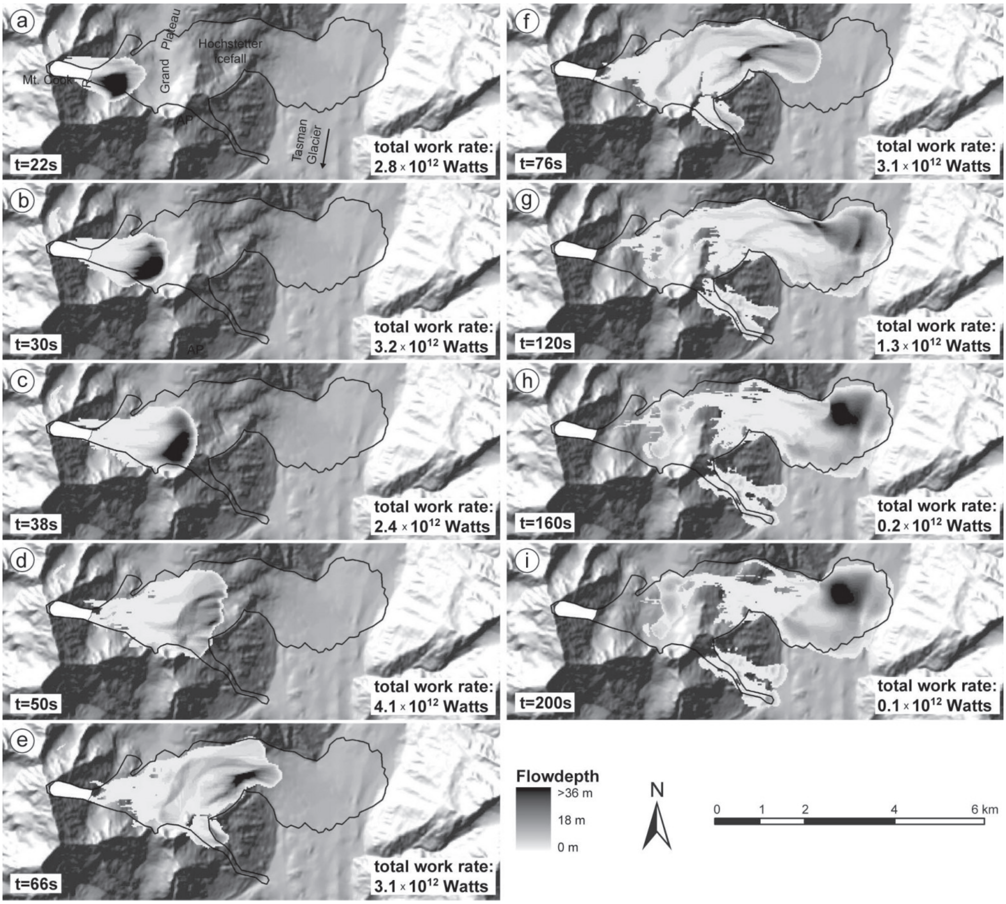

**Figure 15.** (a–i) RAMMS output time series of the instantaneous flow depth of the 14 December 1991 Aoraki/Mt. Cook avalanche (NZ) with friction parameters $\mu = 0.15$ and $\xi = 4000$ ms$^{-1}$. Selected time steps correspond to the local maxima and minima of the total frictional work rate indicated in Figure 14e. Total frictional work rate for all time steps is given in Watts (J s$^{-1}$). Figure 15i can also be seen as the deposition height because the total kinetic energy is lower than 1% of the maximum kinetic energy. The release area is the white polygon on the left side of the images.

were used. Very low Coulomb friction coefficients $\mu$ below 0.05 still allow a slow, largely velocity-independent sliding on a slope of only 3° far distant from the source (*arctan* $\mu$ = 2.86°). Even on ice this is a very low value for a dry granular mass; however, it is realistic if the mass movement transforms to a debris flow and enough water has been incorporated (or melted snow/ice due to frictional heating). This has been observed, e.g., at the rock-ice avalanches from Huascarán, Peru [*Evans et al.*, 2009a], or at Kolka-Karmadon, Russian Caucasus [*Evans et al.*, 2009b; *Huggel et al.*, 2005]. As soon as the avalanche reaches a slope with inclinations smaller than *arctan* $\mu$, frictional forces are higher than gravitational acceleration and the avalanche starts decelerating. The only thing defining that an avalanche can reach a more distant point is the avalanche momentum before deceleration starts. Frictional processes have to dissipate all the kinetic energy available from that point on. If we increase the turbulent friction coefficients $\xi$, the avalanche will accelerate faster in the early phase of failure in steep terrain, where high velocities are reached anyway. High $\xi$ values reduce the turbulent friction term significantly during higher velocities, leading to less frictional resistance and higher velocities again (equations (4a) and (4b) and Figures 9 and 13). At low velocities, this term anyway approximates zero and $\xi$ is no longer relevant. Higher $\mu\xi$ combinations therefore lead to higher peak velocities, faster stopping mechanisms, and hence to shorter process durations which are supported by the seismograms used in this study. Abrupt stopping was also observed from rock avalanches triggered by nuclear explosions at the Russian Novaya Zemlya test site [*Adushkin*, 2006].

### 6.2. Contribution of Seismic Data

[56] Seismic recordings often are the only evidence for the energetic and dynamic evolution of large avalanches. In the modeled total momentum, kinetic energy, and frictional work rate we found three parameters which should generally correlate with the seismograms. The calculated total frictional work rate shows the best correlation values ($R^2$) and is hence recommended for qualitative comparison with seismic data from nearby stations to evaluate the model results and to get a better insight into avalanche dynamics.

[57] The total frictional work rate calculated by the model depends on the frictional rheology but is largely controlled by the topography over which the avalanche is flowing. Topographic features such as major flat and steep parts should be evident in both the modeled frictional work rate and in the seismograms [see also *Favreau et al.*, 2009]. If three-component seismic data are available within a short distance from the source, calculations of the total received energy might be more representative than only horizontally polarized signals. However, many stations still record only vertical components, and *Suriñach et al.* [2001] have shown that the absolute amplitudes in three-component signals can be different, while seismic energy and frequency content are similarly distributed. Because our analysis is based only on the shape of the seismograms (amplitude envelopes, Figures 3 and 5) and not on the magnitudes, the vertical component should sufficiently well represent the information needed for comparison with modeling results.

[58] We expect differences in the amplitude of horizontal and vertical seismic waves depending on the azimuth direction of the seismic station in relation to the avalanche site and direction of movement [*Suriñach et al.*, 2001] (see stations EWZ, LMZ and BWZ at Aoraki/Mt. Cook). Acceleration or deceleration of a mass, e.g., in west-east direction might cause a stronger WE signal than the NS component. The Z component in turn, will better reflect vertical impacts of mass, such as after a near free fall on a topographic step like at Aoraki/Mt. Cook or the vertical impact component of granular random kinetic energy in the basal shear layer [*Buser and Bartelt*, 2009]. Thus, the seismic Z component could also be a measure for random kinetic energy which was proposed by *Buser and Bartelt* [2009]. According to their work, the random kinetic energy is a function of the frictional work rate done by the avalanche. The good correlation between the vertical seismic data and the total frictional work rate therefore supports a possible relation between the avalanche's random kinetic energy, its frictional work rate, and the seismic data. We expect that the frictional work rate is better represented by short-period stations (which have to be close) than by long-period stations (which can also be remote), because frictional interaction and random kinetic energy should be largely of high frequency. Low-frequency signals are more related to loading and unloading of the source area, the path, and the deposition area, that cannot be simulated directly with the used model. A fast degrading short-period signal can further be an advantage in terms of reducing disturbance by other seismic sources such as the beat of the sea which can strongly affect long-period signals [*McSaveney*, 2002].

[59] A landslide or avalanche event is usually captured by more than one seismic station, but path effects are likely to have a greater effect on more distal seismograms. *Deparis et al.* [2008] used a seismic network of up to 21 stations in the French Alps to analyze seismograms of rockfall avalanches with volumes between $2 \times 10^3$ and $1.75 \times 10^6$ $m^3$. The stations were within distances of 10–250 km, and due to the rapid degradation of the signal with distance they concentrated on the closest station for each event (usually between 10 and 25 km). *Weichert et al.* [1994] worked with stations between 60 and 250 km from the 1990 Brenda mine collapse and 1965 Hope rockslides in British Columbia, Canada, to differentiate between seismic signals from earthquakes and landslides. They interpreted the short-period signal as characteristic of the rockslide and stated that this signal was only recorded to a few hundred kilometers. In contrast to this, *Brodsky et al.* [2003] used the far reaching long-period signal of large landslides at epicentral distances of up to 7000 km to estimate basal friction. In the case of the Iliamna avalanche, the closest stations within 8 km were all saturated. Because all sensors were short period at the time of the avalanche and due to the reasons above, we suggest using the nearest least saturated signal. Station ILS at 8 km distance was saturated for ~20 s while the signal at the next station RSO (51 km distance) had a much lower signal-to-noise ratio. The signal was also compared to other stations with similar distances and azimuth ranges and high consistence was found (Figure 3b).

[60] Similarities and deviations between the theoretical values (total frictional work rate calculation) and the measurements (seismogram) can enhance the general understanding of the energetic and dynamic characteristics of a mass movement, such as major changes in the topographic geometry of the runout path, frictional conditions, and centrifugal effects can be identified in both the calculation and the seismogram. An evaluation of the model results by finding the best fitting frictional work rate compared to the seismogram, either qualitatively or quantitatively by correlation, helps to determine the exact timing of the failure (in detail by shifting the time axis of one data set to best fit the other data set) and to better constrain the range of the input friction parameters. Additionally, identification of single, multiple and progressive failure is possible. If more than one individual failure occurs (e.g., within 20–200 s), we are currently unable to simulate this process with the model but can recognize this in the much longer seismic signal compared to the simulated process duration of a single failure. The seismic waves of the individual failures will be superimposed and mixed, making the seismogram useless for comparison with the frictional work rate plots.

[61] A delicate point when using seismic signals is that the efficiency of seismic energy conversion seems to be very low. *Berrocal et al.* [1978] have shown that 1% of the potential energy of the 1974 Mantaro slide in Peru was converted into kinetic energy, of which only 0.01% was again converted into seismic energy. This results in an efficiency of seismic energy conversion of only $10^{-6}$ for this case [see also *Weichert et al.*, 1994]. For the presented case studies we do expect a somewhat higher efficiency in the conversion of potential to kinetic energy due to the low-friction surface on glacier ice. How-

ever, the efficiency in converting kinetic energy into seismic energy might be lower due to restraining effects of the underlying glacier. Hence, small changes in the efficiency of converting potential to kinetic energy as well as in converting kinetic into seismic energy during an avalanche event can have a strong influence on the resulting signal amplitudes. With respect to this, the good correlation between the seismic signals and the modeled total frictional work rate is remarkable and a predominantly constant seismic efficiency can be assumed for the two presented case studies. A comparison of any other modeled avalanche data with seismograms can only be successful if the seismic efficiency is largely constant.

[62] We evaluated several possibilities of combining seismic data and numerical model calculations, first on the very simple topography at Iliamna volcano in Alaska as a kind of "natural laboratory" and then in a much more spatially variable terrain such as at Aoraki/Mt. Cook (NZ). Despite the above mentioned simplifications and some uncertainties, the combination of seismic data with simulation results of the RAMMS model are promising and should be tested with other models and frictional rheologies at different study sites and for a broad variety of avalanche volumes and types. Particularly for large avalanches, the problem of sparse data is crucial and some characteristics like flow velocities may be well reconstructed with seismic data and any dynamic model capable of calculating momentum, kinetic energy, and frictional work rate.

## 7. Conclusions

[63] This work illustrates how seismic recordings can be used as independent data to better constrain the range of appropriate input parameters of a numerical avalanche model. Higher reliability of the model results in turn can lead to better insights into rock-ice avalanche dynamics. The main findings are as follows.

[64] 1. Model optimization and evaluation (e.g., determination of appropriate friction parameters) should be done systematically using geometric, energetic, and dynamic aspects of the avalanche.

[65] 2. For very large avalanches, seismic recordings are often the only data available for characterizing dynamic aspects. Such data may be obtained even for remote areas and are largely independent of weather conditions.

[66] 3. Dynamic model results should be compared to the seismic pattern of an avalanche event so that the model results are dynamically consistent with the seismic data over the entire displacement process and not only in the final resting state (deposition geometry and total duration).

[67] 4. Among different dynamic parameters, the total frictional work rate was found to best correlate with the seismic signal. The frictional work rate describes the rate of energy loss by the avalanche due to friction, and we suggest that the energy captured by the seismograph represents a small but proportional fraction of this energy loss.

[68] 5. Differences between the seismic data and the modeled total frictional work rate indicate source site, path, and recorder site effects, or departures of the model from reality (e.g., no single failure, wrong frictional properties). Such findings can in turn be used to assess the model quality or to optimize the choice of frictional parameters and other variables used for modeling.

## Notation

| | |
|---|---|
| $A$ | cell area, m$^2$. |
| $g$ | gravitational acceleration, m s$^{-2}$. |
| $g_x$ | gravitational acceleration component in $x$ direction, m s$^{-2}$. |
| $g_y$ | gravitational acceleration component in $y$ direction, m s$^{-2}$. |
| $g_z$ | gravitational acceleration component in $z$ direction, m s$^{-2}$. |
| $h$ | entrainment depth, m. |
| $H$ | flow depth, m. |
| $H_d$ | vertical distance, m. |
| $H_i$ | flow depth at cell $i$, m. |
| $i$ | cell number, dimensionless. |
| $k_{tot}$ | total kinetic energy, J. |
| $k_1$ | erosion factor for velocity-dependent entrainment, dimensionless. |
| $k_2$ | erosion factor for momentum-dependent entrainment, m$^{-1}$. |
| $L_d$ | horizontal distance, m. |
| $m$ | mass, kg. |
| $n$ | number of cells affected by the avalanche, dimensionless. |
| $p$ | momentum, kg ms$^{-1}$. |
| $p_{tot}$ | total momentum, kg ms$^{-1}$. |
| $Q$ | entrainment rate, m s$^{-1}$. |
| $Q_p$ | momentum-dependent entrainment rate, m s$^{-1}$. |
| $Q_U$ | velocity-dependent entrainment rate, m s$^{-1}$. |
| $S_{fx}$ | frictional deceleration force in x direction, m$^2$ s$^{-2}$. |
| $S_{fy}$ | frictional deceleration force in y direction, m$^2$ s$^{-2}$. |
| $S_{gx}$ | gravitational acceleration force in x direction, m$^2$ s$^{-2}$. |
| $S_{gy}$ | gravitational acceleration force in y direction, m$^2$ s$^{-2}$. |
| $t$ | time, s. |
| $U$ | velocity, m s$^{-1}$. |
| $U_i$ | velocity at cell $i$, m s$^{-1}$. |
| $U_x$ | depth averaged avalanche velocity in x direction, m s$^{-1}$. |
| $U_y$ | depth averaged avalanche velocity in y direction, m s$^{-1}$. |
| $V_{tot}$ | total volume of avalanche, m$^3$. |
| $V_{mov}$ | moving volume of avalanche, m$^3$. |
| $W_{tot}$ | total frictional work rate, J s$^{-1}$. |
| $x$ | local surface-parallel direction, m. |
| $y$ | local surface-parallel direction, m. |
| $z$ | local surface-normal direction, m. |
| $\alpha$ | slope, deg. |
| $\mu$ | Coulomb friction, dimensionless. |
| $\xi$ | turbulent friction, m s$^{-2}$. |
| $\rho_a$ | density of avalanche, kg m$^{-3}$. |
| $\rho_e$ | density of erodible layer, kg m$^{-3}$. |

[69] **Acknowledgments.** This work was supported by the Swiss National Foundation grant NF 200021-121823/1 (Rock-ice avalanches: A systematic investigation of the influence of ice). We are deeply grateful to Mauri J. McSaveney's essential conceptual contributions and thorough review. The reviews of Stephen G. Evans, two other unknown reviewers, and the associate editor, as well as from the editor Michael Church, helped to improve the manuscript significantly. We further thank Julia Kowalski, Simon Allen, Wilfried Haeberli, and Stefanie Gubler for their support.

## References

Adushkin, V. V. (2006), Mobility of rock avalanches triggered by underground nuclear explosions, in *Landslides From Massive Rock Slope Failures*, edited by S. G. Evans et al., pp. 267–284, doi:10.1007/978-1-4020-4037-5_15, Springer, Netherlands.

Aki, K., and B. Chouet (1975), Origin of coda waves: Source, attenuation and scattering effects, *J. Geophys. Res.*, *80*(23), 3322–3342, doi:10.1029/JB080i023p03322.

Alean, J. (1984), Untersuchungen über Entstehungsbedingungen und Reichweiten von Eislawinen, PhD thesis, 217 pp., Swiss Fed. Inst. of Technol., VAW/ETH Zurich, Zurich.

Allen, S., D. Schneider, and I. F. Owens (2009), First approaches towards modelling glacial hazards in the Mount Cook region of New Zealand's Southern Alps, *Nat. Hazard. Earth Syst. Sci.*, *9*(2), 481–499, doi:10.5194/nhess-9-481-2009.

Armento, M. C., R. Genevois, and P. R. Tecca (2008), Comparison of numerical models of two debris flows in the Cortina d'Ampezzo area, Dolomites, Italy, *Landslides*, *5*, 143–150, doi:10.1007/s10346-007-0111-2.

Bartelt, P., and O. Buser (2009), Frictional relaxation in avalanches, *Ann. Glaciol.*, *51*(54), 1–5.

Bartelt, P., B. Salm, and U. Gruber (1999), Calculating dense-snow avalanche runout using a Voellmy-fluid model with active/passive longitudinal straining, *J. Glaciol.*, *45*(150), 242–254.

Bartelt, P., O. Buser, and K. Platzer (2007), Starving avalanches: Frictional mechanisms at the tails of finite-sized mass movements, *Geophys. Res. Lett.*, *34*, L20407, doi:10.1029/2007GL031352.

Berrocal, J., A. F. Espinosa, and J. Galdos (1978), Seismological and geological aspects of the Mantaro landslide in Peru, *Nature*, *275*, 533–536, doi:10.1038/275533a0.

Bottino, G., M. Chiarle, A. Joly, and G. Mortara (2002), Modelling rock avalanches and their relation to permafrost degradation in glacial environments, *Permafrost Periglacial Processes*, *13*(4), 283–288, doi:10.1002/ppp.432.

Bouchut, F., E. D. Fernández-Nieto, A. Mangeney, and P.-Y. Lagrée (2008), On new erosion models of Savage-Hutter type for avalanches, *Acta Mech.*, *199*(1–4), 181–208, doi:10.1007/s00707-007-0534-9.

Brodsky, E. E., E. Gordeev, and H. Kanamori (2003), Landslide basal friction as measured by seismic waves, *Geophys. Res. Lett.*, *30*(24), 2236, doi:10.1029/2003GL018485.

Buser, O., and P. Bartelt (2009), Production and decay of random kinetic energy in granular snow avalanches, *J. Glaciol.*, *55*(189), 3–12, doi:10.3189/002214309788608859.

Buser, O., and H. Frutiger (1980), Observed maximum run-out distance of snow avalanches and the determination of the friction coefficients $\mu$ and $\xi$, *J. Glaciol.*, *26*(94), 121–130.

Caplan-Auerbach, J., and C. Huggel (2007), Precursory seismicity associated with frequent, large ice avalanches on Iliamna volcano, Alaska, USA, *J. Glaciol.*, *53*(180), 128–140, doi:10.3189/172756507781833866.

Caplan-Auerbach, J., S. Prejean, and J. A. Power (2004), Seismic recordings of ice and debris avalanches of Iliamna Volcano, Alaska, *Acta Vulcanol.*, *16*(1–2), 9–20.

Cherepanov, G., and I. E. Esparragoza (2008), A fracture-entrainment model for snow avalanches, *J. Glaciol.*, *54*(184), 182–188, doi:10.3189/002214308784409071.

Christen, M., P. Bartelt, and J. Kowalski (2010a), Back calculation of the *In den Arelen* avalanche with RAMMS: Interpretation of model results, *Ann. Glaciol.*, *51*(54), 161–168, doi:10.3189/172756410791386553.

Christen, M., J. Kowalski, and P. Bartelt (2010b), RAMMS: Numerical simulation of dense snow avalanches in three-dimensional terrain, *Cold Reg. Sci. Technol.*, *63*, 1–14, doi:10.1016/j.coldregions.2010.04.005.

Crosta, G. B., H. Chen, and D. F. Lee (2004), Replay of the 1987 Val Pola Landslide, Italian Alps, *Geomorphology*, *60*, 127–146, doi:10.1016/j.geomorph.2003.07.015.

Crosta, G. B., P. Frattini, and N. Fusi (2007), Fragmentation in the Val Pola rock avalanche, Italian Alps, *J. Geophys. Res.*, *112*, F01006, doi:10.1029/2005JF000455.

Crosta, G. B., S. Imposimato, and D. Roddeman (2009), Numerical modelling of entrainment/deposition in rock and debris-avalanches, *Eng. Geol. Amsterdam*, *109*, 135–145, doi:10.1016/j.enggeo.2008.10.004.

Davies, M. C. R., O. Hamza, and C. Harris (2001), The effect of rise in mean annual temperature on the stability of rock slopes containing ice-filled discontinuities, *Permafrost Periglacial Processes*, *12*, 137–144, doi:10.1002/ppp.378.

Davies, T. R. H., and M. J. McSaveney (1999), Runout of dry granular avalanches, *Can. Geotech. J.*, *36*, 313–320, doi:10.1139/cgj-36-2-313.

Davies, T. R. H., M. J. McSaveney, and A. M. Deganutti (2007), Dynamic fragmentation causes low rock-on-rock friction, paper presented at 1st Canada-U.S. Rock Mechanics Symposium, Can. Rock Mech. Assoc., Vancouver, 27–31 May.

Deline, P. (2001), Recent Brenva rock avalanches (Valley of Aosta): New chapter in an old story?, *Geogr. Fis. Din. Quat.*, *5*, 55–63.

Deparis, J., D. Jongmans, F. Cotton, L. Baillet, F. Thouvenot, and D. Hantz (2008), Analysis of rock-fall and rock-fall avalanche seismograms in the French Alps, *Bull. Seismol. Soc. Am.*, *98*(4), 1781–1796, doi:10.1785/0120070082.

Detterman, R. L., and B. L. Reed (1980), Stratigraphy, structure, and economic geology of the Iliamna Quadrangle, Alaska, *U.S. Geol. Surv. Bull.*, *1368-B*, 86 pp.

Evans, S. G., and J. J. Clague (1988), Catastrophic rock avalanches in glacial environments, *Proceedings of the 5th International Symposium on Landslides, Lausanne, Switzerland, 10–15 July 1988*, vol. 2, pp. 1153–1158, A. A. Balkema, Rotterdamn, Netherlands.

Evans, S. G., and J. J. Clague (1998), Rock avalanche from Mount Munday, Waddington Range, British Columbia, Canada, *Landslide News*, *11*, 23–25.

Evans, S. G., N. F. Bishop, L. F. Smoll, P. Valderrama Murillo, K. B. Delaney, and A. Oliver-Smith (2009a), A re-examination of the mechanism and human impact of catastrophic mass flows originating on Nevado Huascarán, Cordillera Blanca, Peru in 1962 and 1970, *Eng. Geol. Amsterdam*, *108*(1–2), 96–118, doi:10.1016/j.enggeo.2009.06.020.

Evans, S. G., O. V. Tutubalina, V. N. Drobyshev, S. S. Chernomorets, S. McDougall, D. Petrakov, and O. Hungr (2009b), Catastrophic detachment and high-velocity long-runout flow of Kolka Glacier, Caucasus Mountains, Russia in 2002, *Geomorphology*, *105*, 314–321, doi:10.1016/j.geomorph.2008.10.008.

Fagents, S. A., and S. M. Baloga (2006), Toward a model for the bulking and debulking of lahars, *J. Geophys. Res.*, *111*, B10201, doi:10.1029/2005JB003986.

Farr, T. G., et al. (2007), The shuttle radar topography mission, *Rev. Geophys.*, *45*, RG2004, doi:10.1029/2005RG000183.

Favreau, P., A. Mangeney, A. Lucas, N. M. Shapiro, G. B. Crosta, F. Bouchut, and O. Hungr (2009), Numerical modeling of landslide generated seismic waves, *Eos Trans. AGU*, *90*(52), Fall Meet. Suppl., Abstract S24A-04.

Fischer, L., and C. Huggel (2008), Methodical design for stability assessments of permafrost affected high-mountain rock walls, in *Proceedings of the Ninth International Conference on Permafrost, Fairbanks, Alaska, 29 June–3 July 2008*, vol. 1, edited by D. L. Kane and K. M. Hinkel, pp. 439–444, Univ. of Alaska Fairbanks, Fairbanks, Alaska.

Giani, G. P., S. Silvano, and G. Zanon (2001), Avalanche of 18 January 1997 on Brenva glacier, Mont Blanc Group, Western Italian Alps: An unusual process of formation, *Ann. Glaciol.*, *32*(1), 333–338, doi:10.3189/172756401781819157.

Gruber, S., and W. Haeberli (2007), Permafrost in steep bedrock slopes and its temperature-related destabilization following climate change, *J. Geophys. Res.*, *112*, F02S18, doi:10.1029/2006JF000547.

Haeberli, W., and R. Hohmann (2008), Climate, glaciers and permafrost in the Swiss Alps 2050: Scenarios, consequences and recommendations, in *Proceedings of the Ninth International Conference on Permafrost, Fairbanks, Alaska, 29 June–3 July 2008*, vol. 1, edited by D. L. Kane and K. M. Hinkel, pp. 607–612, Univ. of Alaska Fairbanks, Fairbanks, Alaska.

Haeberli, W., C. Huggel, A. Kääb, S. Zgraggen-Oswald, A. Polkvoj, I. Galushkin, I. Zotikov, and N. Osokin (2004), The Kolka-Karmadon rock/ice slide of 20 September 2002: An extraordinary event of historical dimensions in North Ossetia, Russian Caucasus, *J. Glaciol.*, *50*(171), 533–546, doi:10.3189/172756504781829710.

Hewitt, K. (1999), Quaternary moraines vs catastrophic rock avalanches in the Karakoram Himalaya, Northern Pakistan, *Quat. Res.*, *51*(3), 220–237, doi:10.1006/qres.1999.2033.

Hewitt, K. (2009), Rock avalanches that travel onto glaciers and related developments, Karakoram Himalaya, Inner Asia, *Geomorphology*, *103*, 66–79, doi:10.1016/j.geomorph.2007.10.017.

Hsu, L., W. E. Dietrich, and L. S. Sklar (2008), Experimental study of bedrock erosion by granular flows, *J. Geophys. Res.*, *113*, F02001, doi:10.1029/2007JF000778.

Huggel, C. (2009), Recent extreme slope failures in glacial environments: Effects of thermal perturbation, *Quat. Sci. Rev.*, *28*, 1119–1130, doi:10.1016/j.quascirev.2008.06.007.

Huggel, C., S. Zgraggen-Oswald, W. Haeberli, A. Kääb, A. Polkvoj, I. Galushkin, and S. G. Evans (2005), The 2002 rock/ice avalanche at Kolka/Karmadon, Russian Caucasus: Assessment of extraordinary avalanche formation and mobility, and application of QuickBird satellite imagery, *Nat. Hazard. Earth Syst. Sci.*, *5*, 173–187, doi:10.5194/nhess-5-173-2005.

Huggel, C., J. Caplan-Auerbach, C. F. Waythomas, and R. L. Wessels (2007), Monitoring and modeling ice-rock avalanches from ice-capped volcanoes: A case study of frequent large avalanches on Iliamna Volcano, Alaska, *J. Volcanol. Geotherm. Res.*, *168*(1–4), 114–136, doi:10.1016/j.jvolgeores.2007.08.009.

Huggel, C., S. Gruber, J. Caplan-Auerbach, R. L. Wessels, and B. F. Molnia (2008a), The 2005 Mt. Steller, Alaska, rock-ice avalanche: What does it tell us about large slope failures in cold permafrost?, in *Proceedings of the Ninth International Conference on Permafrost, Fairbanks, Alaska, 29 June–3 July 2008*, vol. 1, edited by D. L. Kane and K. M. Hinkel, pp. 747–752, Univ. of Alaska Fairbanks, Fairbanks, Alaska.

Huggel, C., J. Caplan-Auerbach, and R. L. Wessels (2008b), Recent extreme avalanches: Triggered by climate change?, *Eos Trans. AGU*, *89*(47), doi:10.1029/2008EO470001.

Hungr, O., and S. G. Evans (1996), Rock avalanche runout prediction using a dynamic model, in *Proceedings of the 7th International Symposium on*

*Landslides, Trondheim, Norway, 17–21 June 1996*, vol. 1, edited by K. Senneset, pp. 223–238, A. A. Balkema, Rotterdamn, Netherlands.

Hungr, O., and S. G. Evans (2004), Entrainment of debris in rock avalanches: An analysis of a long run-out mechanism, *Geol. Soc. Am. Bull.*, *116*(9), 1240–1252, doi:10.1130/B25362.1.

Hungr, O., and S. McDougall (2009), Two numerical models for landslide dynamic analysis, *Comput. Geosci.*, *35*, 978–992, doi:10.1016/j.cageo.2007.12.003.

Iverson, R. M., and R. P. Denlinger (2001), Flow of variably fluidized granular masses across three-dimensional terrain: 1. Coulomb mixture theory, *J. Geophys. Res.*, *106*(B1), 537–552, doi:10.1029/2000JB900329.

Kääb, A., et al. (2005), Remote sensing of glacier- and permafrost-related hazards in high mountains: An overview, *Nat. Hazards Earth Syst. Sci.*, *5*, 527–554, doi:10.5194/nhess-5-527-2005.

Kanamori, H., and J. W. Given (1982), Analysis of long-period seismic waves excited by the May 18, 1980, eruption of Mount St. Helens: A terrestrial monopole?, *J. Geophys. Res.*, *87*(B7), 5422–5432, doi:10.1029/JB087iB07p05422.

Kawakatsu, H. (1989), Centroid single force inversion of seismic waves generated by landslides, *J. Geophys. Res.*, *94*(B9), 12,363–12,374, doi:10.1029/JB094iB09p12363.

Kelfoun, K., and T. H. Druitt (2005), Numerical modeling of the emplacement of Socompa rock avalanche, Chile, *J. Geophys. Res.*, *110*, B12202, doi:10.1029/2005JB003758.

Kern, M., P. Bartelt, B. Sovilla, and O. Buser (2009), Measured shear rates in dry and wet snow avalanches, *J. Glaciol.*, *55*(190), 327–338, doi:10.3189/002214309788608714.

Körner, H. J. (1976), Reichweite und Geschwindigkeit von Bergstürzen und Fliessschneelawinen, *Rock Mech.*, *8*(4), 225–256, doi:10.1007/BF01259363.

Körner, H. J. (1983), Zur Mechanik der Bergsturzströme vom Huascarán, Perú, in *Die Berg- und Gletscherstürze vom Huascarán, Cordillera Blanca, Perú*, edited by G. Patzelt, pp. 71–110, Wagner Univ. Press, Innsbruck, Austria.

Korup, O. (2005), Large landslides and their effect on sediment flux in South Westland, New Zealand, *Earth Surf. Processes Landforms*, *30*, 305–323, doi:10.1002/esp.1143.

Kotlyakov, V. M., O. V. Rototaeva, and G. A. Nosenko (2004), The September 2002 Kolka Glacier catastrophe in north Ossetia, Russian Federation: Evidence and analysis, *Mt. Res. Dev.*, *24*(1), 78–83, doi:10.1659/0276-4741(2004)024[0078:TSKGCI]2.0.CO;2.

Kowalski, J. (2008), Two-phase modeling of debris flows, Ph.D. thesis, 136 pp., Swiss Fed. Inst. of Technol., ETH Zurich, Zurich, Switzerland.

Lipovsky, P. S., et al. (2008), The July 2007 rock and ice avalanches at Mount Steele, St. Elias Mountains, Yukon, Canada, *Landslides*, *5*(4), 445–455, doi:10.1007/s10346-008-0133-4.

Locat, P., R. Couture, S. Leroueil, J. Locat, and M. Jaboyedoff (2006), Fragmentation energy in rock avalanches, *Can. Geotech. J.*, *43*, 830–851, doi:10.1139/T06-045.

Mangeney, A., L. S. Tsimring, D. Volfson, I. S. Aranson, and F. Bouchut (2007), Avalanche mobility induced by the presence of an erodible bed and associated entrainment, *Geophys. Res. Lett.*, *34*, L22401, doi:10.1029/2007GL031348.

Margreth, S., and M. Funk (1999), Hazard mapping for ice and combined snow/ice avalanches—Two case studies from the Swiss and Italian Alps, *Cold Reg. Sci. Technol.*, *30*(1–3), 159–173, doi:10.1016/S0165-232X(99)00027-0.

McDougall, S., and O. Hungr (2005), Dynamic modelling of entrainment in rapid landslides, *Can. Geotech. J.*, *42*, 1437–1448, doi:10.1139/t05-064.

McSaveney, M. J. (2002), Recent rockfalls and rock avalanches in Mount Cook National Park, New Zealand, in *Catastrophic Landslides: Effects, Occurrence, and Mechanism*, *Rev. Eng. Geol.*, vol. 15, edited by S. G. Evans and J. V. DeGraff, pp. 35–70, Geol. Soc. of Am., Boulder, Colo.

McSaveney, M. J., and G. Downes (2002), Application of landslide seismology to some New Zealand rock avalanches, in *Landslides*, edited by J. Rybář, J. Stemberk, and P. Wagner, pp. 649–654, Swets Zeitlinger, Lisse, Netherlands.

Perla, R., T. T. Cheng, and D. M. McClung (1980), A two-parameter model of snow-avalanche motion, *J. Glaciol.*, *26*(94), 197–207.

Pirulli, M., and G. Sorbino (2008), Assessing potential debris flow runout: A comparison of two simulation models, *Nat. Hazards Earth Syst. Sci.*, *8*, 961–971, doi:10.5194/nhess-8-961-2008.

Plafker, G., and G. E. Ericksen (1978), Nevados Huascarán avalanches, Peru, in *Rockslides and Avalanches: 1. Natural Phenomena*, edited by B. Voight, pp. 277–314, Elsevier, Amsterdam.

Preuth, T., P. Bartelt, O. Korup, and B. W. McArdell (2010), A random kinetic energy model for rock avalanches: Eight case studies, *J. Geophys. Res.*, *115*, F03036, doi:10.1029/2009JF001640.

Rabus, B., M. Eineder, A. Roth, and R. Bamler (2003), The shuttle radar topography mission—A new class of digital elevation models acquired by spaceborne radar, *ISPRS J. Photogramm. Remote Sens.*, *57*, 241–262, doi:10.1016/S0924-2716(02)00124-7.

Sabot, F., M. Naaim, F. Granada, E. Suriñach, P. Planet, and G. Furdada (1998), Study of avalanche dynamics by seismic methods, image-processing techniques and numerical models, *Ann. Glaciol.*, *26*, 319–323.

Salm, B. (1993), Flow, flow transition and runout distances of flowing avalanches, *Ann. Glaciol.*, *18*, 221–226.

Schneider, D., H. Delgado Granados, C. Huggel, and A. Kääb (2008), Assessing lahars from ice-capped volcanoes using ASTER satellite data, the SRTM DTM and two different flow models: Case study on Iztaccíhuatl (Central Mexico), *Nat. Hazards Earth Syst. Sci.*, *8*(3), 559–571, doi:10.5194/nhess-8-559-2008.

Schneider, J. F. (2006), Risk assessment of remote geohazards in Western Pamir, GBAO, Tajikistan, in Proceedings of the International Conference on High Mountaing Hazard Prevention, Vladikavkaz-Moscow, June 23–26, 2004, pp. 252–267, Swiss Agency for Dev. and Coop., Vladikavkaz, Russia.

Sosio, R., G. B. Crosta, and O. Hungr (2008), Complete dynamic modeling calibration for the Thurwieser rock avalanche (Italian Central Alps), *Eng. Geol. Amsterdam*, *100*, 11–26, doi:10.1016/j.enggeo.2008.02.012.

Sovilla, B., P. Burlando, and P. Bartelt (2006), Field experiments and numerical modeling of mass entrainment in snow avalanches, *J. Geophys. Res.*, *111*, F03007, doi:10.1029/2005JF000391.

Sovilla, B., S. Margreth, and P. Bartelt (2007), On snow entrainment in avalanche dynamics calculations, *Cold Reg. Sci. Technol.*, *47*(1–2), 69–79, doi:10.1016/j.coldregions.2006.08.012.

Suriñach, E., F. Sabot, G. Furdada, and J. M. Vilaplana (2000), Study of seismic signals of artificially released snow avalanches for monitoring purposes, *Phys. Chem. Earth*, *25*(9), 721–727.

Suriñach, E., G. Furdada, F. Sabot, B. Biescas, and J. M. Vilaplana (2001), On the characterization of seismic signals generated by snow avalanches for monitoring purposes, *Ann. Glaciol.*, *32*, 268–274, doi:10.3189/172756401781819634.

Suriñach, E., I. Vilajosana, G. Khazaradze, B. Biescas, G. Furdada, and J. M. Vilaplana (2005), Seismic detection and characterization of landslides and other mass movements, *Nat. Hazards Earth Syst. Sci.*, *5*(6), 791–798, doi:10.5194/nhess-5-791-2005.

Trabant, D. C. (1999), Perennial snow and ice volumes on Iliamna volcano, Alaska, estimated with ice radar and volume modeling, *Water Res. Invest. Rep. 99-4176*, U.S. Geol. Surv., Anchorage, Alaska.

Voellmy, A. (1955), Über die Zerstörungskraft von Lawinen, *Schweiz. Bauztg.*, *73*(15), 212–217.

Waythomas, C. F., T. P. Miller, and J. E. Beget (2000), Record of Late Holocene debris avalanches and lahars at Iliamna Volcano, Alaska, *J. Volcanol. Geotherm. Res.*, *104*(1–4), 97–130, doi:10.1016/S0377-0273(00)00202-X.

Weichert, D., R. B. Horner, and S. G. Evans (1994), Seismic signatures of landslides: The 1990 Brenda mine collapse and the 1965 Hope rockslides, *Bull. Seismol. Soc. Am.*, *84*(5), 1523–1532.

---

P. Bartelt and M. Christen, WSL Institute for Snow and Avalanche Research SLF, Flüelastr. 11, Davos-Dorf CH-7260, Switzerland.

J. Caplan-Auerbach, Geology Department, Western Washington University, 516 High St., MS 9080, Bellingham, WA 98225, USA.

C. Huggel and D. Schneider, Department of Geography, University of Zurich, Winterthurerstr. 190, Zurich CH-8057, Switzerland. (demian.schneider@geo.uzh.ch)

B. W. McArdell, Swiss Federal Institute for Forest, Snow and Landscape Research WSL, Zuercherstr. 111, Birmensdorf CH-8903, Switzerland.

# Paper V

Cold Regions Science and Technology 69 (2011) 70–90

Contents lists available at ScienceDirect

Cold Regions Science and Technology

journal homepage: www.elsevier.com/locate/coldregions

# Frictional behavior of granular gravel–ice mixtures in vertically rotating drum experiments and implications for rock–ice avalanches

D. Schneider [a],*, R. Kaitna [b], W.E. Dietrich [c], L. Hsu [c], C. Huggel [a], B.W. McArdell [d]

[a] Department of Geography, University of Zurich, Zurich, Switzerland
[b] Institute of Mountain Risk Engineering, University of Natural Resources and Life Sciences (BOKU), Vienna, Austria
[c] Department of Earth and Planetary Science, University of California, Berkeley, California, USA
[d] Swiss Federal Institute for Forest, Snow and Landscape Research WSL, Birmensdorf, Switzerland

ARTICLE INFO

*Article history:*
Received 24 January 2011
Accepted 5 July 2011

*Keywords:*
Rock–ice avalanche
Friction
Debris-flow
Physical experiments
Rotating drum
Flow transformation
Hazard assessment

ABSTRACT

Rapid mass movements involving large proportions of ice and snow can travel significantly further downslope than pure rock avalanches and may transform into debris-flows as the ice melts and as water from the stream network or water-saturated debris is incorporated. Currently, ice is thought to have three distinctive effects: 1) reduction of the friction within the moving mass itself, 2) increase of pore pressure as the ice melts and consequent reduction of the shear resistance of the flowing material, and 3) reduction of boundary friction where the failing mass travels on a glacier. However, measurement-based evidence to support these hypotheses is largely missing. In this study, laboratory experiments on the first two mechanisms were carried out in two partially-filled large rotating drums, one in Vienna (Austria) and a second in Berkeley (USA). Varying proportions of cold gravel and gravel-sized ice were mixed and added to the rotating drum running at constant rotational velocity until all ice had melted. Flow behavior was recorded with flow depth, normal force, shear force, pore-water pressure, and temperature sensors. The bulk friction coefficient was found to decrease linearly with increasing ice content by ~20% in the early phase of the experiments, before significant portions of the ice transformed into water. For ice contents larger than 40% by volume, the transformation from a dry granular flow to debris-flow-like movement or hyperconcentrated flow was observed when pore-water pressures rose and approached the normal forces along the flow profile. Pore-water pressure from melting ice developed within several minutes after the start of the experiments and, as it increased, progressively reduced the friction coefficient. The results emphasize that the presence of ice in granular moving material can significantly reduce the friction coefficient of both dry and partially-saturated debris. Due to size effects and the absence of other factors reducing friction (e.g. surfaces with low friction and rock comminution), the absolute measured friction coefficients from the laboratory experiments were larger than those found from natural events. However, the relative changes in friction coefficients depending on the ice and water content may also be considered in real-scale hazard assessments of rapid mass movements in high mountain environments.

## 1. Introduction

Cryospheric systems are sensitive to climate change and generally respond quickly (Haeberli et al., 1997; Noetzli and Gruber, 2009; Salzmann et al., 2007). The decay of glaciers and degradation of permafrost can cause slope instabilities and large rapid mass movements in steep high mountain areas (Davies et al., 2001; Dramis et al., 1995; Geertsema et al., 2006; Gruber and Haeberli, 2007; Haeberli et al., 1997; Haeberli et al., 2003; Harris et al., 2001; Harris et al., 2003). The number of large slope failures in glaciated high mountain areas has increased in the last two decades as compared to the 20th century and may further increase in future (Fischer, 2009; Geertsema et al., 2006; Huggel et al., 2010; Van Der Woerd et al., 2004). While there is a broad variety of possible effects causing high mobility of large rapid mass movements (see discussion in Erismann and Abele, 2001; Korup et al., in press), slope failures from glacial environments are often subject to an additionally enhanced mobility for several reasons (e.g. Evans and Clague, 1988): 1) due to their origin, the moving mass usually contains or entrains a considerable proportion of snow and ice which reduces friction within the moving mass, 2) the transported snow and ice continuously supply meltwater due to frictional heating and convective mixing with non-frozen ground material and air, reducing the shear resistance of the flowing material as it reaches lower regions, and 3) propagation over a glacier which serves as a low friction surface can strongly increase the avalanche velocity and hence its momentum, resulting in an extended runout distance.

The rock avalanches on Sherman glacier on March 27, 1964 (Shreve, 1966), from Mt. Munday around June, 1997 (Evans and Clague, 1998), from Aoraki/Mt. Cook in 1991 (McSaveney, 2002), and the earthquake-triggered large multiple landslides and rock avalanches at Black Rapids on

---

* Corresponding author at: Tel.: +41 446355157.
*E-mail address:* demian.schneider@geo.uzh.ch (D. Schneider).

0165-232X/$ – see front matter © 2011 Elsevier B.V. All rights reserved.
doi:10.1016/j.coldregions.2011.07.001

November 3, 2002 (Jibson et al., 2006) are a few examples for large and/or long-runout events on glacial surfaces. The enormous rock and ice masses which detached from Huascarán in Peru on January 10, 1962 and May 31, 1970 have caused a total death toll of 7000 people ((Evans et al., 2009a), with older estimations reaching as high as 22,000 casualties (Plafker and Ericksen, 1978)), and have dramatically shown the catastrophic potential of combined rock–ice avalanches if they reach populated regions. On September 22, 2002, the extreme mobility of gravel-ice mixtures was again tragically demonstrated by the Kolka glacier failure in the Russian Caucasus (Evans et al., 2009b; Kotlyakov et al., 2004). Both events were characterized by extremely high velocities, high ice contents, and flow transformations (multi-phase movement) along the flow path, to debris-flows that traveled a great distance downstream (Petrakov et al., 2008). The unexpected and sudden initiation of large rock–ice avalanches makes any direct physical measurements in the field impossible. Therefore, the current knowledge of rock–ice avalanches is largely based on post-event documentation, using remote sensing data and some field investigations of the source zone, travel path, and deposition area. While a broad range of case studies exist, there is no physical quantification of the effects of ice on frictional characteristics available.

In this study we focus on the frictional characteristics of different gravel–ice mixtures and on the development of an inter-granular fluid (water) phase by using two large rotating drums. The first aspect considers the influence of the proportion of granular ice on the bulk friction coefficient (tangent of friction angle) while the second aspect concentrates on the time-evolution of the friction angle when the ice is melting, mimicking the evolution of a rock–ice avalanche during its runout. Rotating drums have been used for debris-flow rheology studies (Huizinga, 1996; Kaitna and Rickenmann, 2007b), measurements of bedrock erosion by debris-flows (Hsu et al., 2007; 2008), abrasion of fluvially transported grains (Kodama, 1994; Mikoš and Jaeggi, 1995), observations of grain-size segregation (Henein et al., 1985; Hsu, 2010), and for investigations on flow characteristics of dry granular material (Chou and Lee, 2009), but not for granular flow experiments containing gravel and ice. An advantage of drum experiments is that experimental devices allow measurements for pre-defined time spans at a given rotational velocity and enable long periods of observation so that flow transformations related to the melting of ice can be observed. The experimental setup in rotating drums is suited to study the flow process in a quasi-stationary regime, but neither initiation nor deposition.

## 2. Experimental design

### 2.1. Drum characteristics and velocity scaling

Because full dynamic similarity for geometrically similar flows at different sizes is probably impossible to achieve (Iverson et al., 2010), the best way to reduce this problem is to use the largest possible scale (Hsu, 2010). The laboratory experiments were performed in two similar vertically rotating drums with diameters of 246 cm in Vienna and 399 cm in Berkeley (Fig. 1 and Table 1). Each drum had its own advantages: The rotational drum in Berkeley was the largest facility available, while the smaller drum in Vienna has additional and redundant instruments. In addition, because of its smaller size and consequently reduced effort needed to set up and document flows, more experiments can be conducted in the smaller drum. The ratio of diameters of the smaller drum to the larger drum is 0.62. This value served for linear geometrical scaling of most parameters between the two drums. The width of both drums is given and cannot be changed, however the proportionality factor of 0.56 is very close to 0.62.

To prevent sliding on the otherwise smooth drum bed, in the larger drum 25 mm high risers were placed every 20 cm along the bed, while on the bottom of the smaller drum a 10 × 10 mm PVC grid with a height of approximately 2 mm was fixed. Hence, the proportion of the height of the different roughness elements between the two drums is only 0.08 compared to 0.62 for geometry in general. Because individual grains are caught between the risers of the larger drum as well as in the PVC grid at the bottom of the smaller drum, the effective sliding surface during the experiments largely consisted of grains from the mixture. This roughening of the boundary ensured that a basal resistance similar to that of a flow over a natural rough boundary was established.

The volumes of the mixtures were scaled by identical percentage fills to be comparable between the two different drums as proposed by Henein et al. (1983b). Our goal was to use a volume of material that created flows significantly thicker than the maximum grain diameter, but minimized the infilling of the drum to reduce bed curvature effects. In the larger drum we used a volume of 0.4 $m^3$ that corresponds to a percentage fill of 4.00% with a radius of 1.994 m and a drum width of 0.8 m. Applying the same percentage fill to the radius and width of the smaller drum led to the volume of 0.0856 $m^3$ that was used there.

We were using the same liquids in the laboratory as in nature (air and water), so that full dynamical scaling which includes Froude- and Reynolds-similarity was impossible (see discussion by Paola et al., 2009). For geometrical length scales $\lambda_L$ in the order of ~100 between real events and experiments, Reynolds scaling would consequently have required velocities many times larger than in natural flows (having average velocities often around 50 m/s), which was impossible in the laboratory. Furthermore, Reynolds scaling is more appropriate for questions related to the relative importance of inertial and viscous forces, and field evidence, e.g. the presence of turbulence, suggests that inertial forces dominate. Froude scaling, which we use in this study, has been applied with some success to other mass movements (e.g. for some aspects of debris-flows, Rickenmann, 1999; Kaitna, 2006; Paola et al., 2009), where the relative importance of gravitational and inertial forces is expected to be relevant. Accordingly, the target rotational velocities $u_{drum}$ (equal to average flow velocity relative to the channel bed) in the two drums were

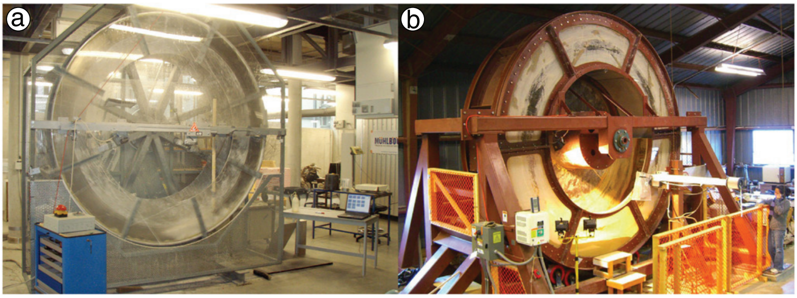

**Fig. 1.** Smaller rotating drum in Vienna (a) and larger rotating drum in Berkeley (b).

**Table 1**
Given and target characteristics of the smaller drum (V) and larger drum (B). The proportions of individual parameters of the smaller to the larger drum are indicated with V:B.

| | Smaller drum (V) | Larger drum (B) | V:B |
|---|---|---|---|
| Diameter ($d$) | 246 cm | 399 cm | 0.62 |
| Width ($w$) | 45 cm | 80 cm | 0.56 |
| Percentage fill | 4.00% | 4.00% | 1.00 |
| Roughness | 2 mm | 25 mm | 0.08 |
| Max segment height ($h_{max}$) | 20.5 cm | 33.2 cm | 0.62 |
| Max centripetal acc. ($a_{c,max}$) | 2.19 m/s$^2$ | 2.19 m/s$^2$ | 1.00 |
| Target volume ($V$) | 0.0856 m$^3$ | 0.4000 m$^3$ | 0.21 |
| Target rotational velocity ($u_{drum}$) | 1.64 m/s | 2.09 m/s<br>(B13-050[a]:<br>1.27 m/s) | 0.78 |
| Target rotational Froude number ($Fr_{rot}$) | 0.22 | 0.22 | 1.00 |
| Target hydraulic Froude number ($Fr_{hyd}$) | 1.16 | 1.16 | 1.00 |
| $D_{50}$ gravel | 9.1 mm[b] | 6 mm[c]<br>5.6 mm[d]<br>16 mm[e] | 1.52<br>1.63<br>0.57 |
| $D_{50}$ ice | 11 mm | 20 mm | 0.55 |
| Internal static friction coefficient of dry gravel ($\mu_{stat}$) | 0.88 (41.5°)[b] | 0.84 (40.0°)[c]<br>0.75 (37.0°)[d]<br>0.80 (38.5°)[e] | – |
| Internal static friction coefficient of granular ice at −10 °C ($\mu_{stat}$) | 0.54 (28.5°) | 0.55 (29.0°) | – |

[a] B13-050 stands for Berkeley-experiment #13 with 50% ice by volume (see Table 2).
[b] Quartz.
[c] Angular basalt.
[d] Rounded basalt.
[e] Dacitic andesite.

scaled after Henein et al. (1983a; 1983b) by making use of the Froude numbers $Fr$:

$$[Fr]_V\left[\frac{d}{D_{50}}\right]_V^{\frac{1}{2}}=[Fr]_B\left[\frac{d}{D_{50}}\right]_B^{\frac{1}{2}} \tag{1}$$

where $d$ is the drum diameter, and $D_{50}$ the median particle size. The indices $V$ and $B$ refer to Vienna and Berkeley. Because Froude numbers should be the same in models of different sizes and in nature we needed to linearly scale $D_{50}$ to $d$ (see Section 2.2). After Ding et al. (2002), the rotational Froude number $Fr_{rot}$ is calculated as following:

$$[Fr_{rot}]_V=[Fr_{rot}]_B=\omega^2\frac{r}{g} \tag{2}$$

where $\omega$ is the angular velocity (rad/s), $r$ the drum radius (m) and $g$ the gravitational acceleration (m/s$^2$). In the larger drum we found an angular velocity of 1.047 rad/s (10 rpm, 2.09 m/s) to be appropriate because this was close to the upper limit of possible velocities where measurements were still reasonable before the flow became too splashy and unsteady to make any useful flow depth or normal force measurements. This resulted in $Fr_{rot}=0.22$ for the larger drum that was used to calculate a target angular velocity of 1.333 rad/s (12.75 rpm, 1.64 m/s) for the smaller drum to achieve the same rotational Froude number there.

Because we later aim to compare the flows in the two drums to rock–ice avalanche events in nature, we used the hydraulic Froude number $Fr_{hyd}$ (Henderson, 1966) that includes the velocity $u$, the gravitational acceleration $g$, and the characteristic length $h$:

$$Fr_{hyd}=\frac{u}{\sqrt{gh}} \tag{3}$$

The Froude number $Fr_{hyd}$ is widely used to characterize debris-flows (e.g. Fraccarollo and Papa, 2000; Huebl et al., 2009), snow avalanches (Kern et al., 2009), and was already applied to describe the flow of natural debris-flow material in the smaller drum (Kaitna et al., 2007). Numerical modeling results of rock ice avalanche events at Aoraki/Mt. Cook in New Zealand and at Iliamna Volcano in Alaska (Schneider et al., 2010) revealed hydraulic Froude numbers between 4 and 6 for characteristic velocities $u$ and flow heights $h$ (see also Section 5.3). These values are consistent with estimates of $Fr_{hyd}$ from the Huascarán and Kolka events, which both are around 5. The values are clearly above 1, indicating that supercritical flow conditions should be achieved in the drum experiments.

Before starting with the experiments, we needed to ensure that $Fr_{hyd}>1$ for the experimental flows. For a given velocity, the lowest possible Froude number $Fr_{hyd}$ along the flow profile of a drum experiment is reached where $h$ has the largest value. Therefore we used $u=u_{drum}=2.09$ m/s and $h=h_{max}$ from the static wetted segment of 0.4 m$^3$ material in the standing larger drum (Table 1). The resulting value $Fr_{hyd}=1.16$ for the maximum flow height was still larger than the threshold value of 1 for critical flow, and hence ensured that supercritical flow was maintained through the entire experiment in all cases. The corresponding target rotational velocity for the smaller drum was 12.75 rpm (1.64 m/s) as previously calculated from the rotational Froude number in Eq. 2.

Finally, the maximum centripetal acceleration $a_{c,max}$ if a grain at the flume bottom moves at the same speed of the drum was calculated by:

$$a_{c,\,max}=\frac{u_{drum}^2}{r} \tag{4}$$

where $r$ is the drum radius and $u_{drum}$ the rotational velocity of the drum bottom. The centripetal acceleration is with 2.19 m/s$^2$ identical for the two drums and corresponds to 22% of the gravitational acceleration. The maximum centripetal acceleration should be as small as possible because it gives an upper limit of the centrifugal effect on all grains moving on a curved path. The real centripetal acceleration during the experiments is expected to be much lower and depends on the shear rates which are largely unknown for the inner flow.

### 2.2. Granular mixtures

To find appropriate grain-sizes and distributions, preliminary experiments were performed in the smaller drum. Mixtures including grains around the sand fraction (<2 mm) and smaller tended to rapidly develop a clumpy mass which moved as a coherent plug or developed a nonstationary slumping flow behavior (stick–slip effects; Mair et al., 2002). Because large rapid mass movements usually behave like granular flows (e.g. Legros, 2002) we tried to maintain granular flow behavior in the rotating drums as well. This was achieved by sieving to remove the fines (sand, silt, and clay). The upper boundary for the clasts was set to approximately one tenth of the maximum flow height and the selected gravel and ice was also restricted by the availability of different gravel and ice types. Hence, the first five experiments in the larger drum were performed with a range of varying gravel and ice contents consisting of fine basalt gravel ($D_{50}=6$ mm) and much larger ice shards ($D_{50}=20$ mm). For the subsequent three experiments we used the same gravel but with rounded and hence slightly smaller grains ($D_{50}=5.6$ mm; see Table 2). For the next five experiments, a coarser dacitic andesite (probably metamorphic) gravel with $D_{50}=16$ mm was used. Because the ice shards were reduced in size much faster than the gravel (due to breakage, rounding and melting) it was reasonable to use larger grain-sizes for the ice at the start of the experiment, so that we had comparable median grain-sizes for the first 5–10 min of the experiment.

We linearly scaled the grain-sizes of the gravel and ice for the smaller drum from the coarse gravel and ice used in the larger drum. For the smaller drum we used $D_{50}$-values of 9.1 mm and 11 mm for the quartz gravel and ice, respectively. This results in proportions of

0.57 for the gravel and 0.55 for the ice (Table 1, Fig. 2), which is close to the desired value of 0.62 used for geometric scaling of the two drums. The strength of basalt is somewhat lower than that of quartz (Prinz, 1997), and together with the higher rotational velocity and volume this resulted in a rounding and fragmentation of the grains within the experiment duration of 23–37 min (Fig. 2d, f and 3). Due to the higher strength of the quartz grains, the abrasion in the smaller drum was negligible. Another reason for the diminished wear of the grains in the smaller drum was that we only analyzed the first 5 min due to strong mass losses when the ice started to melt (leakage). Fig. 3 shows the grain-size distributions of the components, including pre- and post-experimental grain-size curves for the gravel which was used for the long-duration experiments in the larger drum and the size distribution of the gravel and ice in the smaller drum. The ranges for the grain-size were 4–16 mm and 6.3–16 mm for the gravel and ice, respectively, in the smaller drum with standard deviations of the sieve curves $\varsigma = (D_{84}/D_{16})^{0.5}$ around 1.3 (Strużyński et al., 2011). For the experiments in the larger drum, the fine gravel range was 3.35–11.2 mm ($\varsigma \approx 1.3$), the coarse gravel 6.7–26.5 mm ($\varsigma \approx 1.3$), and the ice 6.7–45 mm ($\varsigma \approx 1.5$). The small values of $\varsigma$ indicate that the grain size distribution is restricted to a relatively narrow range.

The ice and gravel were stored in a cold room at −10 °C (±1.5 °C). Densities of both materials as well as for water and air are comparable or identical in the model and in real events, leading to a scaling factor for density $\lambda_\rho = 1$ which is a prerequisite that affects scaling of several other parameters, such as mass, forces and energies. The length scale $\lambda_L$ between real events and the drum experiments varies between 50 and 500 (derived from flow depths and volumes with $\lambda_L$ and $\lambda_L^3$ respectively), and fracture toughness $K$ [Pa $\mathrm{m}^{0.5}$] should accordingly be scaled by $\lambda_K = \lambda_\rho{}^*\lambda_L^{1.5}$, leading to $\lambda_K$-values between ~350 and ~11,000. This means that the material used for the laboratory experiments should be $10^2$ to $10^4$ times weaker than the one of real events. However, we used the same material as in natural events, resulting in $\lambda_K = 1$. Consequently rock and ice comminution must be strongly reduced in the rotating drums compared to real events. Because the focus of the study is on the effects of ice and the melting thereof, we did not substitute the materials with others having lower strengths. Therefore, rock comminution would have to be studied separately (see e.g. Davies and McSaveney, 2009; Imre et al., 2010; Phillips and Davies, 1991).

Before each run, the slowly rotating drum was cooled by ~25 kg (smaller drum) and ~40 kg (larger drum) of pure crushed ice over more than 45 min which was removed before the start of each experiment. This method reduced the temperature of the inner drum surface to approximately 0 °C and prevented significant melting of the ice grains during the early phase of the experiment. The laboratory temperature, however, could not be adjusted to subzero degrees and was around 20 °C for all runs. While this setting differs from the conditions around the starting zones of natural rock–ice avalanches, in some cases it represents the warmer lower elevation regions which are often reached by larger events.

## 3. Instrumentation and data processing

### 3.1. Smaller drum (Vienna)

Measurements at the smaller drum in Vienna (Fig. 4) include torque at the drum axis, flow depth (via 2 lasers), normal and shear force (via 4 load cells), temperature of the mixture and rotational velocity of the drum. The lasers and load cells were arranged in two identical sensor groups called *'left'* and *'right'* (Fig. 4) and the signals of all sensors are recorded at a frequency of 800 Hz. Additionally, a video camera is installed near the drum axis to record the frontal region of the flow. More details of the instrumentation can be found in Kaitna and Rickenmann (2007a; 2007b) and in Kaitna et al. (2006, 2007).

#### 3.1.1. Torque

The torque was measured by a flange which is installed at the rotation axis between the bearing and the engine. The net-torque $Trq_{net}$ is calculated by:

$$Trq_{net} = Trq_{gross} - Trq_{tare} \tag{5}$$

where $Trq_{gross}$ is the torque measured during the experiments ranging from 320 Nm for pure ice to 980 Nm for gravel only, and $Trq_{tare}$ is the mean torque measured during several runs with an empty drum (34.6 Nm). The accuracy of the measurement is specified to 0.05% of the nominal torque, which corresponds to ~13–41 g at the drum bed in 3 o'clock position, depending on the ice and rock content. The standard deviations of the torque measurements $s_{trq}$ are around 25 Nm for all experiments.

#### 3.1.2. Lasers (flow height)

The laser sensors are installed at the channel center directly above the normal and shear force measurement units, so that for each rotation, two individual laser profiles were recorded. The supplier (Baumer Electronics Ltd.) specifies a resolution of 0.09–1.15 mm. We aggregated the laser data of both instruments for 11 full rotations within a one-minute period to get a total of ~266 data points for every full degree ±0.5°. Then we calculated, for each angular degree-interval $\alpha$ and time span $t = 1$ min, the mean flow height $h_{mean}(\alpha,t)$, median flow height $h_{median}(\alpha,t)$, and the standard deviation $s_h(\alpha,t)$ (Fig. 5a). The resampling to 1°-intervals reduced the sample frequency from 800 Hz to the equivalent of 75.9 Hz (with $u_{drum} = 12.7$ rpm). Finally, we applied a Butterworth filter (lowpass filter) at a cutoff frequency of one tenth of the previously reduced sample frequency (7.59 Hz), which can also be called lowpass filtering at 10° (periods shorter than 10° were not of interest for this study).

**Table 2**
Overview of experiments and some characteristics of the gravel in the smaller and larger drum. 'V' relates to 'Vienna' and 'B' to 'Berkeley', followed by a chronological number according to the temporal order of the runs, and a second number relating to the ice content in percent by volume.

| Grain-size $D_{50}$ [mm] | Rotational velocity | Lithology | Shape | Ice content [vol-%] | | | | | | | | | | |
|---|---|---|---|---|---|---|---|---|---|---|---|---|---|---|
| | $u_{drum}$ [m/s] | | | 0 | 10 | 20 | 30 | 40 | 50 | 60 | 70 | 80 | 90 | 100 |
| Smaller drum (Vienna) | | | | | | | | | | | | | | |
| 9.1 | 1.64 | Quartz | Angular | V09-000 | V08-010 | V06-020 | V05-030 | V02-040 | V01-050<br>V10-050 | V03-060 | V04-070 | V07-080 | V11-090 | V12-100 |
| Larger drum (Berkeley) | | | | | | | | | | | | | | |
| 6 | 2.09 | Basalt | Angular | | B04-010 | | B02-030 | | B01-050 | | B03-070 | | B05-090 | |
| 5.6 | 2.09 | Basalt | Rounded | | | | | B07-040 | B06-050 | B08-060 | | | | |
| 16 | 2.09 | Dacitic andesite | Angular | | | | | B11-040 | B09-050 | B10-060 | B12-070 | | | |
| 16 | 1.27 | Dacitic andesite | Angular | | | | | | B13-050 | | | | | |

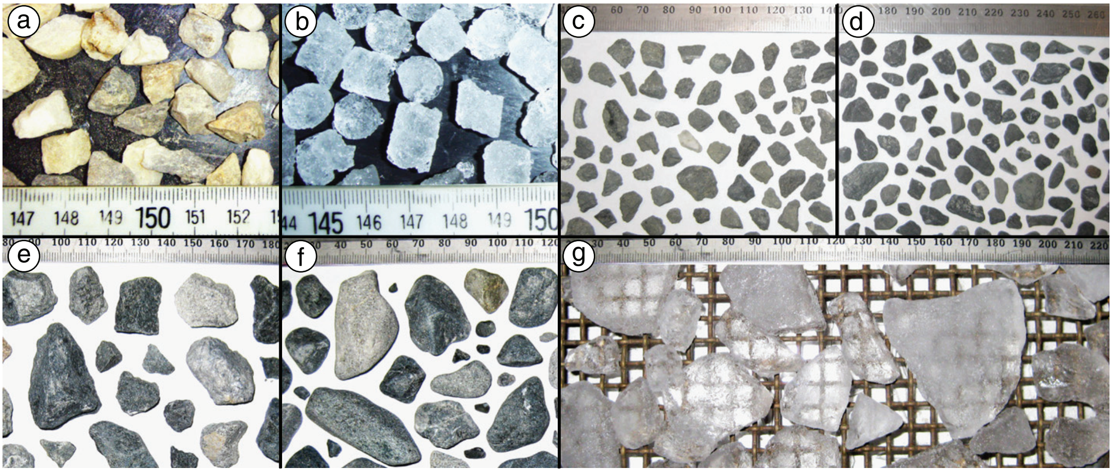

**Fig. 2.** Gravel and ice which were used for the experiments in the smaller drum (a, b) and in the larger drum (c–g). a) Pre-experiment angular quartz-gravel, 4–16 mm, $D_{50} = 9.1$ mm. b) Cylindrical ice-pellets, −10 °C, 6.3–16 mm, $D_{50} = 11$ mm. c) Pre-experiment fine angular basalt-gravel, 3.35–11.2 mm, $D_{50} = 6$ mm. d) Post-experiment fine rounded basalt-gravel, $D_{50} = 5.6$ mm. e) Pre-experiment coarse angular dacitic basalt-gravel, 6.7–26.5 mm, $D_{50} = 16$ mm. f) Post-experiment coarse rounded andesite basalt-gravel, $D_{50} = 14.5$ mm. g) Ice-shards, −10 °C, 6.7–26.5 mm, $D_{50} = 20$ mm.

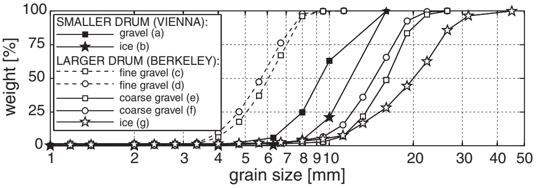

**Fig. 3.** Cumulative grain-size distribution of the gravel and ice from sieve analysis. Letters a–g in legend correspond to the grains shown in Fig. 2.

### 3.1.3. Load cells (basal normal and basal shear stress)

Two pairs of single-point load cells to measure basal normal and shear stress are placed within the middle third of the channel width and at the same angular position like the lasers (Fig. 4, smaller drum, letters b and c). This resulted in two individual profiles per rotation for the basal normal stress $\sigma_{bas}(\alpha,t)$ and basal shear stress $\tau_{bas}(\alpha,t)$ of the flow lobe. The plates are 60 mm in diameter and roughened by the same PVC grid as at the surrounding flume bottom. To prevent water loss and sediment intruding into the sensors, the edges of the plates were sealed with a very thin coating of silicone so that free movement of the plates was still possible. The distributor (HBM Ltd.) specifies an accuracy of the load cells of 0.5 g. Because the load cell measurements

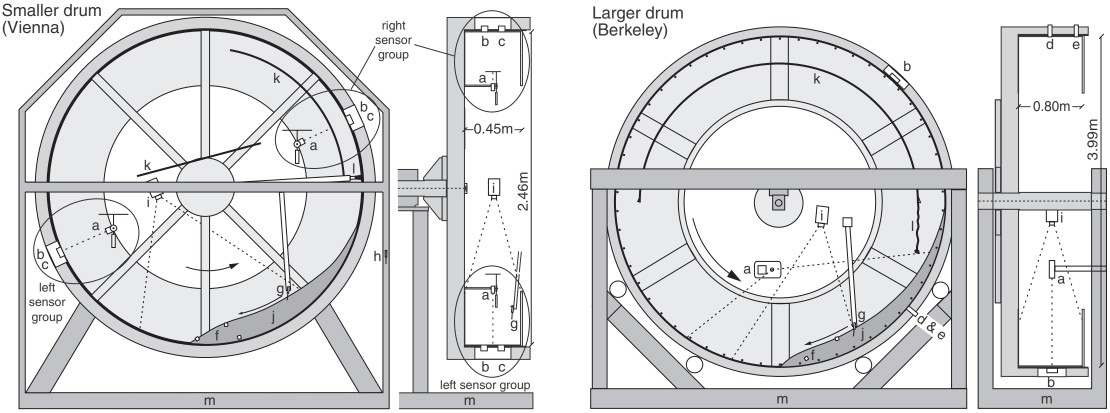

**Fig. 4.** Smaller and larger rotating drums in Vienna and Berkeley. a) Laser (measurement range is indicated for the larger drum), b) load cell, c) shear cell, d) pore-water pressure, center, e) pore-water pressure, side, f) in-flow temperature loggers, g) in-flow thermocouples, h) thermocouple for laboratory temperature, i) camera (view angle is indicated), j) gravel–ice mixture flow lobe, k) roof (drop protection), l) brush/curtain (splash protection), m) steel frame. Note the two sensor groups in the smaller drum which are called 'left' and 'right'.

Adapted from Kaitna and Rickenmann (2007a) and Hsu (2010).

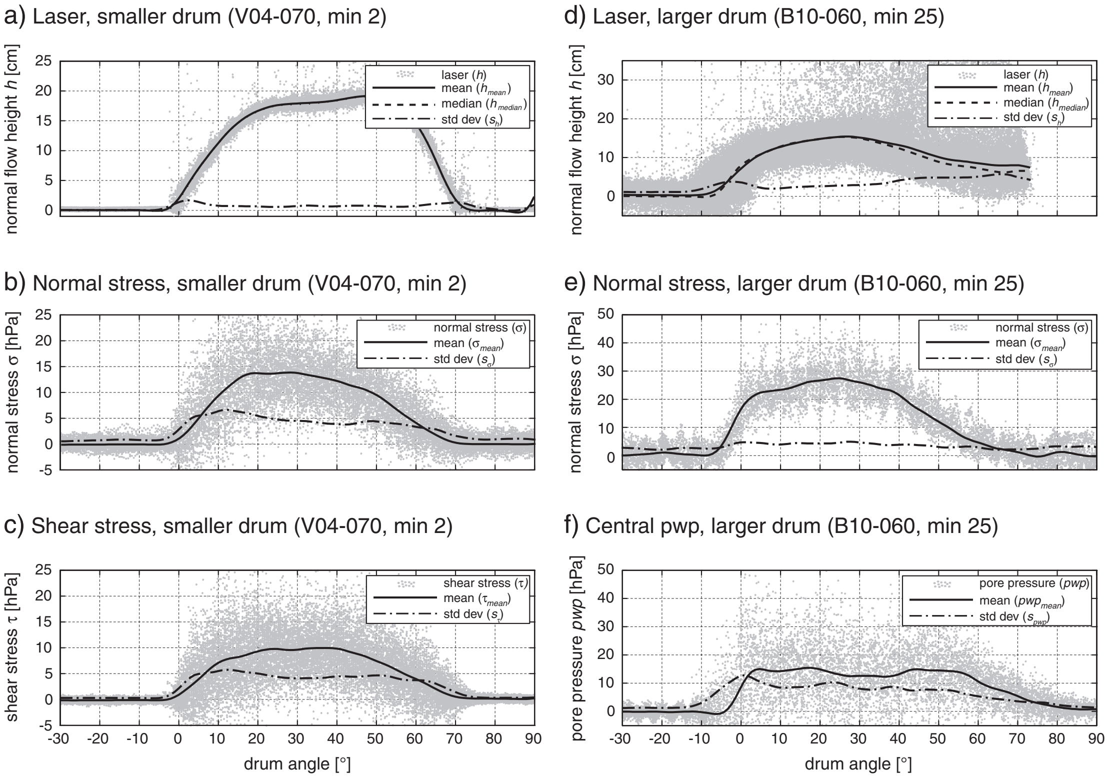

**Fig. 5.** Example for measured data during one early minute in the smaller drum and a late minute in the larger drum. The data from the smaller drum (a–c) is from the left and right sensor group resulting in 2 × 11 complete rotations, while the data from the larger drum (d–f) contains 5 complete drum rotations for normal stress and pore-water pressure, and 300 laser sweeps. Datapoints are binned to 1° intervals to calculate the mean, median and standard deviation profiles. Furthermore, all profiles were smoothed by lowpass filtering at 10°. Note that mean and median for the laser data in the smaller drum (a) is nearly identical so that the individual lines are not distinguishable on this scale. In the larger drum, the mean and median of the laser data (d) diverges to the tail where the flow surface gets more disturbed by drops and splashes.

were affected by superimposed sine waves, having the frequency of the time needed for a complete drum rotation, these low frequency signals needed to be removed. The data were smoothed and a sine function was fitted by means of two turning points and a minimum for each rotation and measurement to be subtracted from the original signal. While this method generally produced satisfactory results, the sine wave sometimes did not fit well. Therefore, sine wave corrected data of individual rotations showing shifts from the x-axis above a threshold value were ignored for the following data processing. The corrected normal and shear stress data from the '*left*' and '*right*' sensor groups were aggregated for all 11 full rotations within a minute and averaged to 1° intervals (at approximately 266 data points each). The profiles of $\sigma_{mean}(\alpha,t)$ and $\tau_{mean}(\alpha,t)$ resulted after lowpass filtering at 10° (7.59 Hz). The standard deviations $s_\sigma(\alpha,t)$ and $s_\tau(\alpha,t)$ of the load cells are relatively larger and reach up to 50% of the peak values of $\sigma_{mean}(\alpha,t)$ and $\tau_{mean}(\alpha,t)$.

### 3.1.4. Temperature and rotational velocity

Two thermocouples constantly measured the laboratory temperature $T_{tc,lab}(t)$ and the flow temperature with an accuracy of ± 1 °C (Fig. 4). One thermocouple was attached to a mechanism which could be manually adjusted so that the foremost 2–4 cm of the needle dipped into the flow to measure the flow temperature $T_{tc,flow}(t)$. Additionally, 1–3 miniature temperature loggers were added to the moving mass out of which the mean temperature $T_{cubes}(t)$ was calculated. The loggers had a side length of 3.1 cm, weight of 24 g, resolution of 0.1 °C, and measured at one-second intervals.

The rotational velocity was measured by means of a sliced ring fixed at the axis and a static photo-electric sensor which registered an impulse every degree of rotation and enabled determination of the exact rotational velocity for every position. The measured mean velocities $u_{drum}$ of the smaller drum experiments are between 1.58 and 1.64 m/s with standard deviations $s_u$ of 0.01–0.03 m/s over the entire duration of each individual experiment (Fig. 6).

### 3.2. Larger drum (Berkeley)

The instrumentation of the larger drum includes a laser sensor (flow depth), a load cell (normal force), two pore-water pressure sensors (*pwp*), temperature measurement and a video camera inside the drum (Fig. 4). All data except the temperature and video are recorded at a frequency of 1000 Hz. In the following, we explain some details of the sensors in the larger drum and the processing of the data. Further information can be found in Hsu et al. (2007) and Hsu (2010).

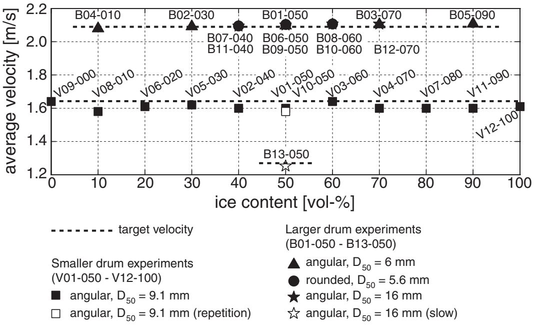

**Fig. 6.** Measured average velocities $u_{drum}$ of all experiments compared to the target rotational velocity from Table 1. Note that some markers of the velocities from the larger drum are printed on top of each other.

### 3.2.1. Laser (flow height)

A 2-D laser sensor was positioned over the center of the flow channel and fixed by means of a boom outside the drum on the laboratory floor (Fig. 4). The rotating mirror swept a laser beam over a longitudinal profile along the centerline of the channel, at a speed of 5 rotations per second. Hence, a total of 300 sweeps were recorded per minute. The data were processed like for the smaller drum, resulting in new equivalent frequencies of 60 Hz due to binning the data to 1°-intervals (experimental runs B01-050 to B12-070 with $u_{drum}=$ 2.09 m/s; see Table 2) and 36 Hz (experimental run B13-050 with $u_{drum}=1.27$ m/s), while the number of data points per 1°-interval was at ~167 for all velocities. To maintain geometrical comparability between the smaller and larger drums as well as between different velocities, lowpass filtering of the derived values was again performed at 10° (cutoff frequencies 6 and 3.6 Hz for the fast and slow runs respectively). Fig. 5d shows the mean $h_{mean}(\alpha,t)$, median $h_{median}(\alpha,t)$, and standard deviation $s_h(\alpha,t)$ of the flow height derived from the raw laser data, as well as the cutoff at the tail of the flow due to laser shadow (around 70°) which was caused by the curtain near the 3 o'clock position (Fig. 4). The curtain was needed to protect the laser instrument from splashes but as a consequence we do not have any laser measurements for the very rear of the flow.

### 3.2.2. Load cell (basal normal stress)

The 15 cm × 15 cm load cell was installed at the center of the flume channel having a loading capacity of 22,000 N (Fig. 4). The edges of the plate were sealed and surrounded by flexible foam to prevent water and sediment loss. With this setup we were able to measure one basal normal stress profile $\sigma_{bas}(\alpha,t)$ of the flow for each rotation. The profile length was always 315° from the −45° to the 270° position in the drum, where the drum is rotating counter clockwise and 0° is at the 6 o'clock position. Due to the shorter profile lengths we found that simulating a sine wave for the given mass of the load cell, which was then subtracted from the original data (Hsu, 2010) led to better results than the method with the turning points described for the smaller drum. The velocity-dependent offset due to centripetal acceleration forces of the new curve is then subtracted by using the mean value within a permanent non-flow region between −30° and −40°. Then we calculated the mean normal stress $\sigma_{mean}(\alpha,t)$ and standard deviation $s_\sigma(\alpha,t)$ for 1°-bins and each minute of run time. The data were finally lowpass filtered over an angular distance of 10° (6 Hz and 3.6 Hz for the fast and slow runs respectively; Fig. 5e).

### 3.2.3. Basal pore-water pressure

To measure basal pore-water pressure (*pwp*), two sensors as described by Kaitna and Rickenmann (2007b) were used. Both sensors were installed at the same angular positions and shifted −86.3° relatively to the load cell, one at the center of the channel and the other one 10 cm from the side (Fig. 4, larger drum, letters d and e). A steel mesh with 2 mm wide gaps on the level of the flume bottom protected an elastic membrane which transferred the pressure via an oil filled reservoir onto the pressure transducer. Creation of a sine wave for data correction was not feasible as described for the load cell because the tare weight acting on the pressure sensor was not known accurately enough. Therefore we needed to apply the method as described for the smaller drum and fitted sine waves by means of two turning points (−90° and 90° positions) and one minima (180° position) derived from the smoothed data which was recorded between the −131.3° and the 183.7° position of the drum. The following processing of the *pwp*-profiles was done as described above for the load cell data and finally resulted in the filtered basal pore-water pressure $pwp_{mean}(\alpha,t)$ and its standard deviation $s_{pwp}(\alpha,t)$ for each degree of the flow.

### 3.2.4. Temperature and rotational velocity

A thermostat with a needle dipping into the moving mass was used for real-time control of the current flow temperature, however, the device could not be connected to the recording system and only served to stop the experiment when all ice had melted and the temperature of the mixture rose to 2–5 ° C. 1–3 miniature cube temperature loggers recorded the in-flow temperature $T_{cubes}$ as described for the smaller drum experiments.

The rotational velocity of the larger drum in Berkeley was governed by the input frequency for the 20-kilowatt induction motor. The exact rotational velocity was derived by using the amount of data points which were recorded at 1000 Hz during one sweep over 315° (10.930 m). Fig. 6 shows that experiments B01-050 to B12-070 have mean velocities $u_{drum}$ between 2.08 and 2.11 m/s (±0.01–0.02 m/s), while $u_{drum}$ of the slower run B13-050 is 1.25 m/s (±0.01 m/s). Hence, all velocities are very close to the target velocities (Table 1 and Fig. 6).

### 3.3. Friction and density calculations (smaller drum)

Because this study aims to quantify the frictional characteristics of different gravel–ice mixtures, we need to derive average friction coefficients $\mu$ from the recorded data. The broad range of instruments in the smaller drum gives us the opportunity to test several different calculation methods. The force plate measurements during the running experiments enable calculation of the local dynamic bulk friction coefficient from shear and normal forces $\mu_{\tau/\sigma}$ at every degree position $\alpha$ and time $t$ along the flow profile, while the calculation methods using the center of mass or torque relate to dynamic average bulk friction coefficients ($\mu_\theta$ and $\mu_{trq}$) acting at time $t$ on the entire moving mass. All friction coefficients include Coulomb basal friction if the flow was moving like a rigid plug, and internal friction resulting from flow resistance due to enduring frictional contacts between grains (quasi-static), or due to short term collisional impacts of individual grains (grain inertial) within the sheared flow body (Iverson and Denlinger, 2001; Savage, 1984). The static internal friction coefficient $\mu_{stat}$, was derived from the tangent of the steepest possible stable slope angle of a static pile of the corresponding granular material (values are given in Table 1). All the above friction coefficients can be compared to the apparent friction coefficient $\mu_{app}$ of natural rapid mass movements which describes the ratio of $H/L$ where $H$ is the drop height and $L$ the travel distance of the mass (such as used e.g. by Goren and Aharonov, 2007 and many others; see Section 5.3 for comparison with natural events).

### 3.3.1. Local dynamic bulk friction from shear and normal forces

In the smaller drum we derived the local dynamic bulk friction coefficients from shear and normal forces measured at the base $\mu_{\tau/\sigma}(\alpha,t)$

for each angular position $\alpha$ and minute $t$ by building the ratio of basal shear stress $\tau_{bas}(\alpha,t)$ to basal normal stress $\sigma_{bas}(\alpha,t)$ (e.g. Kaitna et al., 2007; McArdell et al., 2007):

$$\mu_{\tau/\sigma}(\alpha,t) = \frac{\tau_{bas}(\alpha,t)}{\sigma_{bas}(\alpha,t)}. \tag{6}$$

This results in friction profiles which vary from the front to the end of the flow lobe. Because centripetal acceleration leads to larger measurement values for both, shear and normal forces, the derived dynamic bulk friction profiles from shear and normal forces measured at the base are not affected by centrifugal effects.

#### 3.3.2. Dynamic average bulk friction from center of mass

In a vertical rotating drum, the position of the center of mass (*COM*) has been used to approximate the mean slope of the entire moving mass (Kaitna et al., 2007; Kaitna and Rickenmann, 2007b). As shown in Fig. 7 we calculated angle $\theta$, where the *COM* acts on the channel bottom. Assuming that the mass in the rotating drum usually is in steady state, we used $\theta$ as the mean slope and hence as the dynamic average bulk friction angle of the entire mixture.

If we calculate the *COM* by using the flow height $h_{median}(\alpha,t)$ from the laser data, this results in the centroid (geometric center of the area) of the flow body, which does not account for any density variations along the profile. Therefore, to account for the density variations along the profile, the *COM* can be calculated from the normal stress data $\sigma_{mean}(\alpha,t)$. For each degree $\alpha$ we calculate a representative flow height $h_\sigma(\alpha,t)$ from the normal stress data as following:

$$h_\sigma(\alpha,t) = \frac{\sigma_{mean}(\alpha,t)}{\rho_{dyn}(t)\cdot g\cdot \cos\alpha(t)}. \tag{7}$$

The average dynamic bulk density $\rho_{dyn}(t)$ for the entire moving mixture during each minute $t$ was calculated by iterative adjustment of the static mix density $\rho_{stat}$ (measured prior to the experiment) until the volume of $V_\sigma(t)$ below the curve of $h_\sigma(\alpha,t)$ was identical to $V_h(t)$ calculated from $h_{median}(\alpha,t)$ (Fig. 7). The real *COM* then was calculated for the $h_\sigma(\alpha,t)$-curve and is usually closer to the front than the centroid from the laser data $h_{median}(\alpha,t)$. The position of the *COM* is defined by its cartesian x-coordinate $x_{COM}(t)$ and y-coordinate $y_{COM}(t)$, the drum radius is given by $r$, and the dynamic average bulk friction coefficient $\mu_\theta(t)$ of the moving mass averaged over one minute $t$, finally was calculated by (Fig. 7 shows the geometrical origin of Eq. 8):

$$\mu_\theta(t) = \tan\left(\arcsin\left(\frac{x_{COM}(t)}{r}\right)\right) = \tan\theta(t). \tag{8}$$

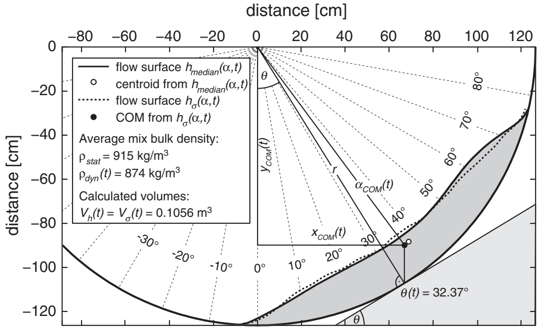

**Fig. 7.** Calculation of the centroid derived from the laser data $h_{median}(\alpha,t)$ and the center of mass (COM) from the flow height derived from the normal stress data $h_\sigma(\alpha)$ for the first minute of experiment V03-060 with 60% ice by volume. The slope which is used as a reference is angle $\theta(t)$. $x_{COM}(t)$ and $y_{COM}(t)$ are the cartesian coordinates of the COM, $\alpha_{COM}(t)$ its angular position, and r the drum radius. If the $h_\sigma(\alpha,t)$-curve is higher than the one for $h_{median}(\alpha,t)$ the local apparent bulk density $\rho_{bulk}(\alpha,t)$ is higher than the average dynamic apparent bulk density $\rho_{dyn}(t)$.

#### 3.3.3. Dynamic average bulk friction from torque data

We also used the net torque $Trq_{net}$ from the measurements to calculate the mean shear stress by assuming an equal shear stress distribution at the channel bed surface $A_{bed}$ covered by the mass (Kaitna and Rickenmann, 2007a; 2007b). In this case, we neglected any friction acting on the side walls because the roughness is several orders of magnitude smaller than at the bottom and we visually observed only a small influence (see Fig. 8). We then calculated the torque-derived average shear stress $\tau_{trq}$ for each minute $t$ as follows:

$$\tau_{trq}(t) = \frac{Trq_{net}(t)}{A_{bed}(t)\cdot r}. \tag{9}$$

Using the average basal normal stress of the entire flow profile $\sigma_{avg}(t)$, we calculated the alternative dynamic average bulk friction coefficient $\mu_{trq}(t)$ which was derived from the torque data:

$$\mu_{trq}(t) = \frac{\tau_{trq}(t)}{\sigma_{avg}(t)}. \tag{10}$$

#### 3.3.4. Apparent dynamic local bulk density

The depth-averaged dynamic local bulk density for each angle and minute $\rho_{bulk}(\alpha,t)$ was calculated by:

$$\rho_{bulk}(\alpha,t) = \frac{\sigma_{bas}(\alpha,t)}{\left(g + a_{c,avg}\right)\cdot h_{median}(\alpha,t)\cdot\cos\alpha}, \tag{11}$$

where $g$ is the gravitational acceleration and $a_{c,avg}$ the depth-averaged centripetal acceleration of all individual grains within 1°. We can only estimate the maximum centripetal acceleration $a_{c,max}$ for grains having the full rotational velocity of the drum $u_{drum}$ at the flume bottom (see Table 1 and Eq. 4) and have no information on the velocity profiles within the moving mass. Therefore we set $a_{c,avg}=0$ being aware that we only measure an apparent dynamic local bulk density which is somewhat overestimated. Eq. 4 and Table 1 show that $a_{c,max}$ is 22%, and therefore $\rho_{bulk}(\alpha,t)$ can also be overestimated by a maximum of 22%, but more likely much less.

### 3.4. Friction, density and liquefaction calculations (larger drum)

The larger drum lacks any direct shear force and torque measurements. Therefore we calculated the dynamic bulk friction coefficients from the center of mass (COM). Furthermore, the local bulk densities and liquefaction ratios were derived from the flow height, normal stress, and pore-water pressure data.

#### 3.4.1. Dynamic average bulk friction from center of mass

In the larger drum experiments, in contrast to the smaller drum experiments, the density adjustment by the volumes $V_h(t)$ and $V_\sigma(t)$ needed for the *COM* calculation could only be done over the part of the flow, where the laser data $h_{median}(\alpha,t)$ were available. For $\alpha > 68°$, the curtain first affected, and then disabled laser measurement of the flow height (Fig. 5d). Because only a minor part of the flow volume was missed, the effect on the results by using this method was only marginal. The friction coefficient $\mu_\theta(t)$ then was again calculated according to Eq. 8.

#### 3.4.2. Apparent dynamic local bulk density

We calculated the depth-averaged apparent dynamic local bulk density $\rho_{bulk}(\alpha,t)$ for each angle and minute, as in the smaller drum

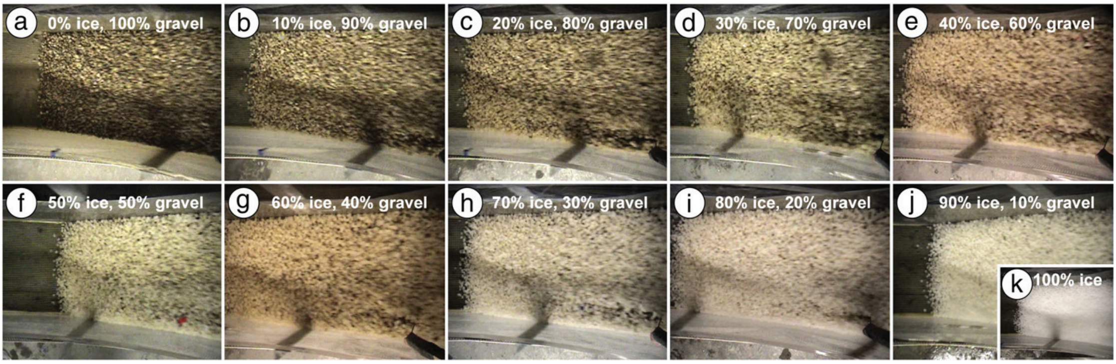

**Fig. 8.** Images from the video camera of the first minute of 11 experiments in the smaller drum. On some images, the thermocouple sticking into the moving mass is visible at the lower right (e.g. in subfigure g). Flow direction is from right to left while the drum rotated the opposite direction. Note that the view angles of the camera are only similar but not identical.

(Eq. 11). Eq. 4 and Table 1 show that the maximum centripetal acceleration $a_{c,max}$ was again around 22% of the gravitational acceleration. We expect that only a small part of $a_{c,max}$ was effective because the majority of the grains moved at significantly lower speeds than at full drum velocity, leading to a slight overestimation of $\rho_{bulk}(\alpha,t)$ compared to real local densities.

### 3.4.3. Liquefaction ratio

The average liquefaction ratio $Lq(t)$ for each minute $t$ measures how much of the granular part of the entire mass was supported by the liquid part (see also Major and Iverson, 1999):

$$Lq(t) = \frac{pwp_{sum}(t)}{\sigma_{sum}(t)} \tag{12}$$

with the sum of the 1°-bins of the pore-water pressure values

$$pwp_{sum}(t) = \sum_{\alpha=1}^{n} pwp_{mean}(\alpha, t) \tag{13}$$

and the sum of the 1°-bins of the basal normal stress values

$$\sigma_{sum}(t) = \sum_{\alpha=1}^{n} \sigma_{mean}(\alpha, t) \tag{14}$$

where $\alpha = 1$ is the first degree affected by the flow and $n$ the amount of degrees where material is flowing.

## 4. Results and interpretation

### 4.1. Smaller drum (Vienna)

### 4.1.1. Measured and observed flow characteristics

Here we present and discuss the results for the first 5 min of 12 experiments in the smaller drum in Vienna (V01-050 to V12-100) with ice contents between 0 and 100% by volume. The experiment numbers increase chronologically followed by a number representing the ice content (see also Table 2). We focused on the frictional behavior during the first 5 min when the flow was largely dry. Fig. 8 shows images from the video camera in the drum (see Fig. 4, letter *i*) for all runs with varying ice contents and the first minute. At the early phase of each experiment, the flow was largely dry, granular, steady and symmetrical (in the *rolling* to *cascading* mode after Henein et al. (1983b) and Mikoš and Jaeggi (1995)). The laterally almost straight front (Fig. 8) indicates that the influence of the sidewalls was marginal and similar for all experiments. The strong sliding component on the sides of the flow was also apparent in the photographs and videos made through the acrylic glass on the side of the rotating drums.

Fig. 9 gives an overview of all recorded and processed data over the first 5 min for a selected typical run in the smaller drum (run V10-050 with 50% ice content by volume). The data from the laser, normal- and shear stress sensors as well as the corresponding standard deviations show that the flow was steady during the individual 1-minute averages. The only trend is that the volume (derived from flow height) was reduced by 7% during the first 5 min. The volume loss is because some rock and ice grains were captured by the bottom mesh, as well as due to rounding and fragmentation of the grains (mainly ice). The density increase in that time however was only marginal (Fig. 9i), indicating that most of the volume loss must have been due to grains lost to the bottom mesh. The volume decrease led both the flow front to move slightly up-slope and the tail to move down-slope. The consequence was that the *COM* which is calculated from the normal stress data $\sigma_{mean}(\alpha,t)$ remained nearly at the same degree position over the entire 5 min but migrated slightly to the channel bottom (Fig. 9m).

Dynamic bulk friction coefficient profiles $\mu_{\tau/\sigma}(\alpha,t)$ from $\tau_{bas}(\alpha,t)$ and $\sigma_{bas}(\alpha,t)$ and apparent dynamic bulk density profiles $\rho_{bulk}(\alpha,t)$ are both consistent over the first 5 min, but there are artifacts in the data at the front and tail of the flow due to small measurement values (extremely small and large values; Fig. 9g and i). The fact that the normal and shear stress sensors were at the same degree position but placed side by side led to small variations in loading. In general, the dynamic bulk friction tended to increase from the front to the tail (Fig. 9g). The apparent bulk density profiles indicate the largest densities around 10° after a low-density front (including grain-spray), and a tendency of decreasing densities towards the tail (Fig. 9i). This may have been because at the very tail, the grains were close to falling and more dilated than at the main body of the flow where the flow was less agitated and more densely packed. Segregation of the rock and ice grains was not relevant during these experiments because the mass appeared well mixed on the videos and photos (Fig. 8). The reason therefore is that the grain-size distribution and the density differences of gravel and ice were not large enough to allow strong segregation as reported by Hsu (2010). Because the ice grain-size reduced due to melting, the median grain-size of the ice was chosen to be slightly larger than the one of the gravel (see Fig. 3), and therefore, ice and gravel grain-sizes were comparable during the first minutes of the experiments. Preliminary tests have shown that wider grain-size distributions of the gravel and ice fractions — particularly mixtures with higher contents of fines — led to stronger segregation and to stick-slip effects after 2–3 min when some of the ice has melted and the mass was not yet saturated.

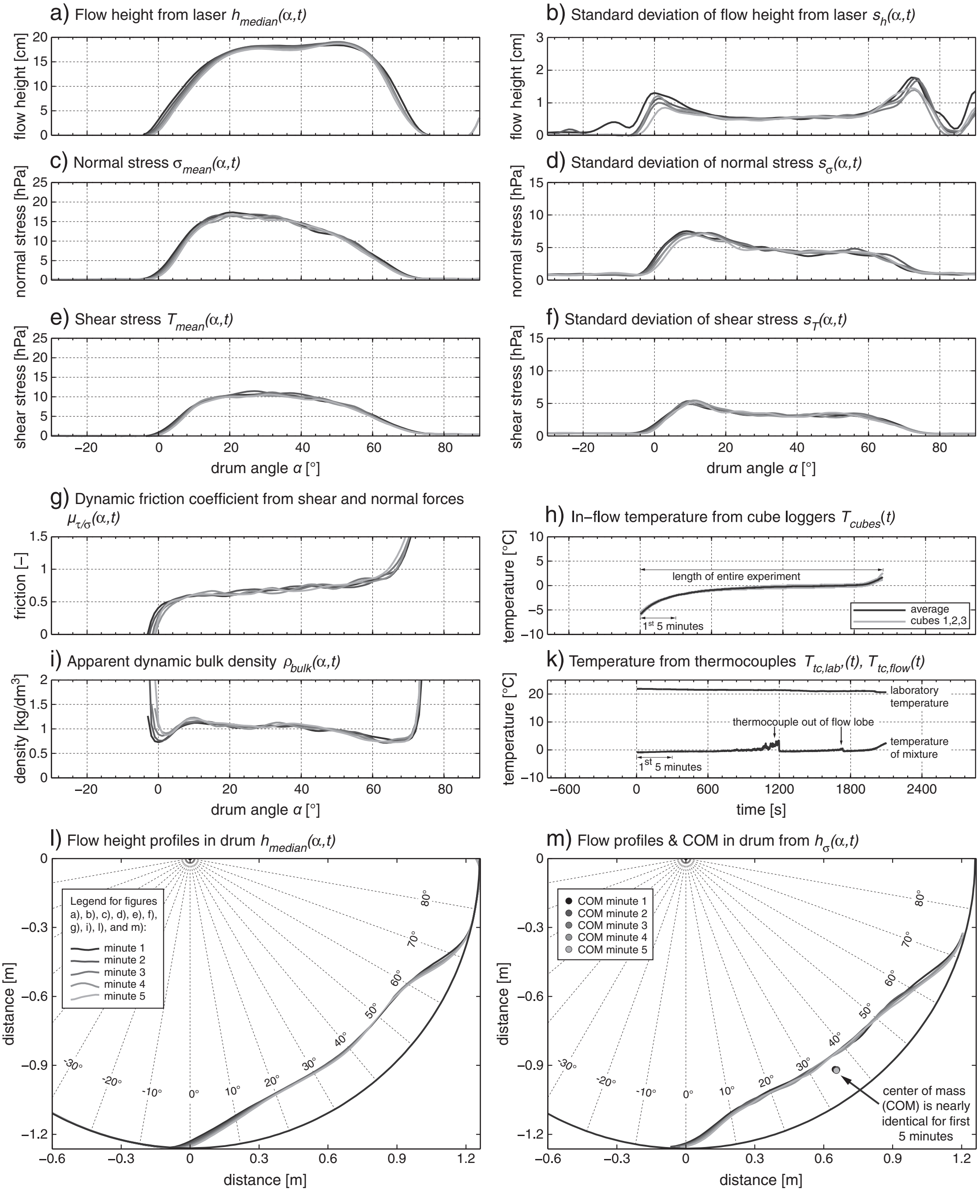

**Fig. 9.** Overview of measurements and some derived data from experiment V10-050 in the smaller drum in Vienna with 50% ice by volume and for the first 5 min.

The temperature data from the cube loggers show clearly negative temperatures between −6 °C and −2 °C for the first 5 min (Fig. 9h). In contrast to this, the very fast responding (<0.1 s) thermocouple measured temperatures near the melting point from the first minute and as long as there was some ice left in the mixture. This is because the sensitive Copper/Nickel wire was situated at the tip of a 2 mm hollow needle of the thermocouple where icy meltwater having a temperature of 0 °C was already taken up during the cooling runs previous to the experiment. The probe could not be entirely dried and the fluid did not refreeze even when dipped into subzero degree cold granular ice and rock. As soon as all ice had melted, the temperature measurements of the cube loggers and thermocouple started to rise sharply (see Fig. 9h and k at $t = 1920$ s). Due to the decreasing flow height during an experiment, the thermocouple was not always submerged in the flow and needed to be manually adjusted into the flow again (see Fig. 9k around $t = 1200$ s and 1700 s). Comparison between the two measurement methods shows that the delay of the cube loggers is not significant, because the measured cube logger temperatures rise simultaneously with the thermocouple measurement (in Fig. 9h and k at $t = 1920$s).

Fig. 9l shows the geometries of the moving mass in the rotating drum as measured by the flow heights $h_{median}(\alpha,t)$ from the laser instrument. The geometries of the representative flow heights $h_{\sigma}(\alpha,t)$ which were derived from normal stress data (Eq. 7; Fig. 7) and needed to calculate the *COM* are plotted in Fig. 9m.

### 4.1.2. Frictional effects of granular ice

The dynamic bulk friction coefficients $\mu_{\theta}(t)$ derived from the angle $\theta$ of the *COM* (Eq. 8) reveal a linear dependence on the ice content (Fig. 10, upper curves): the larger the ice content, the smaller the friction. In the smaller drum, $\mu_{\theta}(t)$ of the first 5 min (min 1–5) can be described as a linear function by the following equation:

$$\mu_{\theta(a)}(\text{min } 1\text{–}5) = 0.7321 - 0.0015x. \quad (15)$$

The intercept of 0.7321 corresponds to the dynamic bulk friction coefficient $\mu_{\theta}$ of pure gravel in the rotating drum and $x$ is the ice content in percent by volume. To compare and corroborate the results, we use the second independent calculation method which is derived from the torque data $\mu_{trq}(t)$ (Eq. 10), resulting in another linear function:

$$\mu_{trq(b)}(\text{min } 1\text{–}5) = 0.6752 - 0.0014x. \quad (16)$$

Indices *(a)* and *(b)* are for differentiation from Eqs. 17–19, and the linear correlation coefficients for the 55 data points are $R^2_{(a)} = 0.98$ for the $\mu_{\theta}$-values and $R^2_{(b)} = 0.94$ for the $\mu_{trq}$-values. Eqs. 15–16 and Fig. 10 show that the two independent calculation methods result in nearly parallel lines, but shifted by a $\mu$-value of ~0.06 (at a slope of 30° this corresponds to a shift of ~2.5°). The systematic shift between the two calculation methods indicates the measurement uncertainty and limits of the applicability of $\mu_{\theta}(t)$ and $\mu_{trq}(t)$ as average friction coefficients, however, the absolute change in friction depending on the ice content is consistent for both methods and describes a reduction of the dynamic bulk friction coefficient by ~20% for dry granular ice compared to dry granular rock.

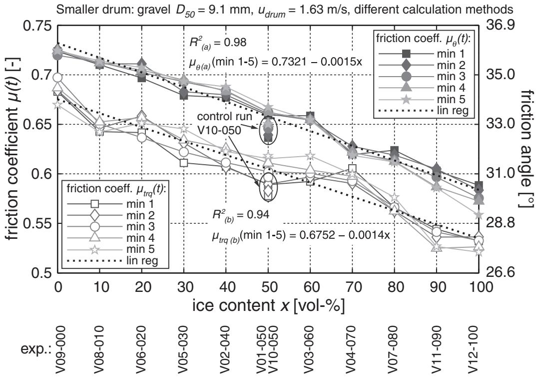

**Fig. 10.** Dependence of dynamic average bulk friction coefficients on ice content during the first 5 min (min 1–5) of all experiments in the smaller drum (Vienna) and from two different calculation methods. The upper curve results from $\mu_{\theta}(t)$ (Eq. 8) and the lower curve results from $\mu_{trq}(t)$ (Eq. 10). Control run V10-050 was performed after 9 previous experiments, so that the lower values may result from a lower friction due to abrasion of the bed roughness. $R^2$ is the linear correlation coefficient of all data points, and indices (a) and (b) for differentiation between Eqs. 15 and 16.

Dynamic bulk friction coefficients usually are smaller than the static internal ones ($\mu_{stat}$) measured from the steepest stable slope angle of a dry pile of the corresponding gravel or ice (Meriam and Kraige, 2006; Straub, 1997; Table 1). The dynamic average bulk friction coefficients of run V09-000 without any ice are with $\mu_{\theta} = 0.73$ and $\mu_{trq} = 0.68$ clearly below the measured 41.5° ($\mu_{stat} = 0.88$) for the static internal friction angle of the used dry gravel. The measured static internal friction angle of pure ice is 28.5° ($\mu_{stat} = 0.54$) at −10 °C and situated between the dynamic average friction coefficients $\mu_{\theta} = 0.58$ and $\mu_{trq} = 0.53$ of pure ice derived from experiment V12-100. We suppose that the surfaces of the ice grains thawed from the beginning of the experiment and led to a larger dynamic friction than would be expected from the dry static measurement values due to the development of an intergranular water film and related cohesion effects (Casassa et al., 1991; Chevoir et al., 2009; Iverson et al., 2004).

Experiments V01-050 and V10-050 were identical and served as control runs. For both calculation methods smaller friction coefficients were calculated for run V10-050 ($\mu_{\theta} = 0.64$ and $\mu_{trq} = 0.59$) compared to the first run V01-050 ($\mu_{\theta} = 0.67$ and $\mu_{trq} = 0.61$). Analysis of the bed PVC grid showed that experiments with high gravel contents abraded the grid and likely reduced the bed friction slightly. The difference between run V01-050 and V10-050 hence is a measure of the influence of bed friction wear within the ten first experiments. Experiments V11-090 and V12-100 were performed last, and due to their low gravel content caused little additional wear of the PVC grid resistance elements.

The third method is to derive average friction values from the profiles of the dynamic bulk friction coefficient from shear and normal forces measured at the base $\mu_{\tau/\sigma}(\alpha,t)$ (Fig. 9g and Eq. 6). We avoided local effects at the beginning and end of the flow lobe (Fig. 9g) and calculated the median friction $\mu_{\tau/\sigma,med}$ along the profiles at minute intervals and then used the mean of the first 5 min for comparison with the other two methods. Averaged over the first 5 min $t = 1$–5, run V10-050 with 50% ice by volume e.g. results in a median friction $\mu_{\tau/\sigma,med}(t)$ derived from the dynamic bulk friction profiles $\mu_{\tau/\sigma}(\alpha,t)$ of 0.68. This is slightly larger than the other calculated friction values in Fig. 10. The standard deviation of the median data within the first 5 min is 0.07 which is similar to the shift between $\mu_{\theta}(t)$ and $\mu_{trq}(t)$, but much less stable than the values of the first 5 min of each individual calculation method shown in Fig. 10. In general, the magnitudes of $\mu_{\tau/\sigma,med}(t)$ of all experiments are close to the $\mu_{\theta}$-curve in Fig. 10, but somewhat larger and having a larger scatter. A reason for the inconsistency of the load cell data can be that the shear force plate measurements might have been affected by grains which were temporally jammed at the edges. Some blocked grains were observed during the unloading of the material after each experiment. This makes a comparison of the friction coefficients $\mu_{\tau/\sigma,med}(t)$ between different experiments difficult, while a relative analysis within an individual profile of one experiment is still possible. The magnitude of the grain jamming effect is similar to the effect of changing ice content on the friction coefficient, so this third measurement method is best regarded as an estimation of the average friction which in general corroborates the values calculated by $\mu_{\theta}(t)$ and $\mu_{trq}(t)$ (Fig. 10).

## 4.2. Larger drum (Berkeley)

We conducted 13 experiments in the larger drum in Berkeley (B01-050 to B13-050) with ice contents between 10 and 90% by volume, different gravel angularity, grain-size, and drum rotation velocities (Table 2). An example of all recorded and processed datasets is shown in Fig. 11.

During the early phase of the experiments we generally observed very similar characteristics to that observed in the smaller drum, such as a largely dry, granular, and steady flow behavior. We extended our

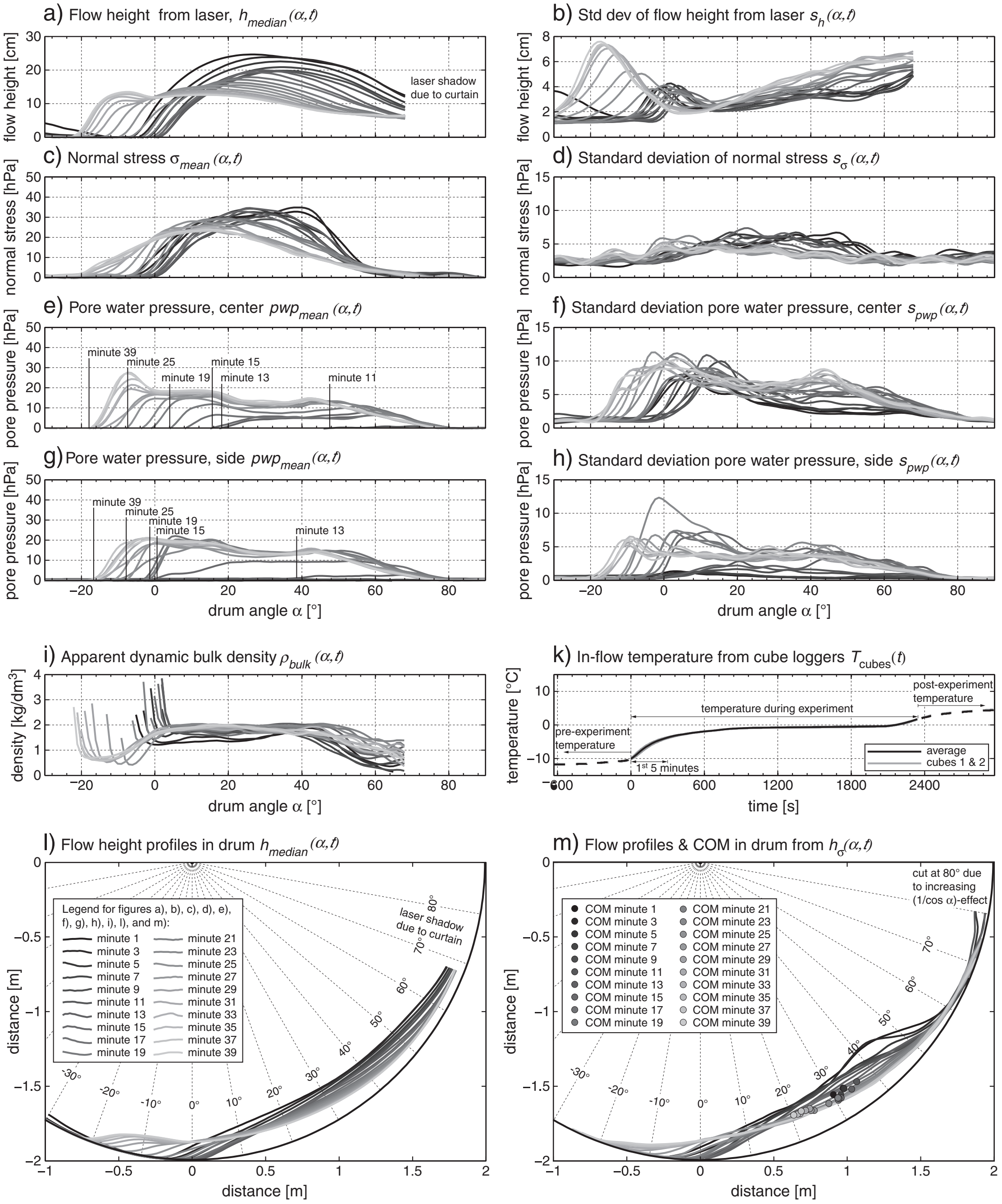

**Fig. 11.** Overview of measurements and some derived data from experiment B12-070 in the larger drum in Berkeley with 70% ice by volume and for all recorded minutes 1–39.

interest also to the later phase of the experiments which was characterized by flow transformations related to increasing pore-water pressures. Therefore, each of the two phases is treated separately in the next two sections.

### 4.2.1. Early phase: frictional effects of granular ice

The dark black lines in Fig. 11 show the measurement profiles of the early minutes from the flow heights $h_{median}(\alpha,t)$ and the normal stress $\sigma_{mean}(\alpha,t)$ as well as from the derived apparent dynamic bulk densities $\rho_{bulk}(\alpha,t)$. More specifically, we describe here only to the first 5 min which are represented by the 1st, 3rd and 5th minute and the following minutes are described in the next section (4.2.2.) about the late phase of the experiment. The largest flow depths during the early phase are reached around the 30° position in the drum while the maximum normal stresses are around 40°. The *pwp*-sensors at the center and side of the flow do not measure any pore-water pressures during the early phase (no dark lines in Fig. 11e and g) and hence prove that the early flow is clearly unsaturated at the beginning of the experiment. In contrast to the smaller drum, the apparent dynamic bulk density profiles $\rho_{bulk}(\alpha,t)$ increase slightly from the front to the 40° position, where the normal stress profiles do also show a maximum.

Fig. 12 shows the average dynamic bulk friction coefficients $\mu_\theta(t)$ derived from the location of the *COM* for each minute and all 13 experiments. The two experimental series with varying ice contents and fine gravel ($D_{50}=6$ mm and 5.6 mm) at a rotational velocity of 2.09 m/s for two different grain shapes (angular and rounded) are presented in Fig. 12a. We observe a somewhat stronger dependence of the friction coefficient on the ice content than detected by the smaller drum in Fig. 10 and Eq. 15, but also stronger variations between individual minutes and experiments. For example, B04-010 shows smaller friction values than B02-030 with higher ice content. Because we found a clear linear relationship between the friction coefficient and the ice content in the smaller drum, we assume that the relationship should also be linear in the larger drum (despite the outliers from run B04-010). A direct comparison might be slightly obscured because different gravel lithologies were used and grain abrasion was only relevant for the experiments with basalt/dacitic andesite in the larger drum. However, within the first 5 min which were included in Fig. 12, significant abrasion was not observed and therefore Fig. 10 and 12 are comparable. The linear correlation coefficient for the 15 data points from the fine angular gravel (B01-050 to B05-090 in Fig. 12a) therefore is $R^2_{(c)}=0.81$, and the linear function describing the dependence of the dynamic average bulk friction coefficient over the first 5 min $\mu_\theta(\text{min }1,3,5)$ on the ice content $x$ in percent by volume is given by:

$$\mu_{\theta(c)}(\text{min }1,3,5) = 0.7289 - 0.0020x \tag{17}$$

Index *(c)* and the following indices *(d)* and *(e)* in Eqs. 18–19 are for differentiation of the various equations given for $\mu_\theta(\text{min }1,3,5)$. The experimental series exemplifies the limitations and uncertainty of the calculation method by using $h_\sigma(\alpha,t)$ and the COM to calculate the friction coefficient $\mu_\theta(t)$, because it is strongly sensitive to measured normal stresses larger than zero near the tail of the flow at 3 o'clock position, which strongly influence the resulting $\mu_\theta(t)$-values. The problem is visible in Fig. 11m at drum positions between 70° and 80° where the representative flow heights $h_\sigma(\alpha,t)$ starts to rise again due to the flow height transformation which includes a factor of 1/cos α. This is also the reason that the profiles of $h_\sigma(\alpha,t)$ were cut behind 80°. On the other hand, the measurement method seems to be sensitive enough to detect expected smaller friction coefficients for experiments with fine rounded grains (B06-050 to B08-060 in Fig. 12a):

$$\mu_{\theta(d)}(\text{min }1,3,5) = 0.6339 - 0.0008x \tag{18}$$

where the correlation coefficient $R^2$ is 0.86 and the inclination of the curve reduced, but the data range is much less.

The results of the experiments with varying ice contents and coarse angular gravel ($D_{50}=16$ mm) at two different velocities are shown in Fig. 12b. We again observe a clear trend to smaller friction values for higher ice contents. The series shows a steeper curve with a correlation coefficient $R^2$ of 0.90, suggesting stronger dependence on ice content for the larger grains that could have important implications for natural real scale events with larger characteristic grain-sizes:

$$\mu_{\theta(e)}(\text{min }1,3,5) = 0.8151 - 0.0041x. \tag{19}$$

The three experimental series in the larger drum revealed reductions of the bulk friction angles of 27% (fine angular grains), 13% (fine rounded grains), and 50% (coarse angular grains) for pure granular ice runs compared to pure gravel runs. However, the restricted variation of the ice content in the three experimental series in the larger drum leads to larger uncertainties related to the strength of the dependence of the friction coefficients on the ice content. Therefore, the only conclusion about the influence of different grain characteristics is that they can be relevant.

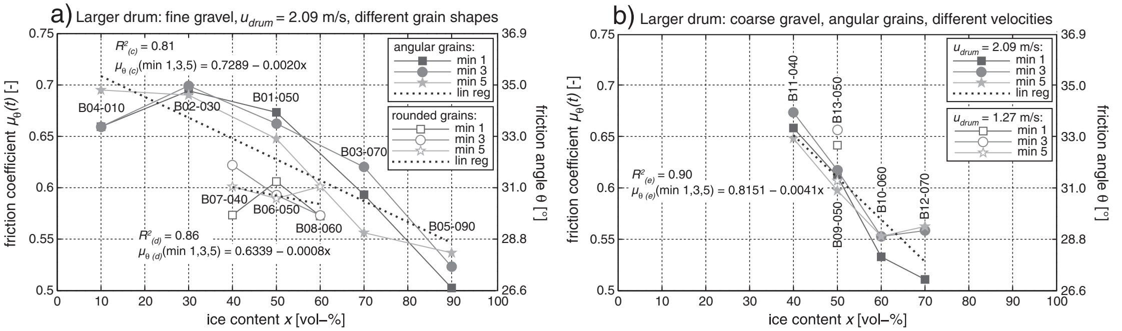

**Fig. 12.** Dependence of dynamic average bulk friction coefficients on ice content during the early minutes 1, 3, and 5 of all experiments in the larger drum (Berkeley) as derived from $\mu\theta(t)$. a) fine gravel at a rotational velocity of 2.09 m/s for angular grains ($D_{50}=6$ mm) and for slightly rounded grains ($D_{50}=5.6$ mm). b) Coarse gravel ($D_{50}=14$ mm) at a rotational velocity of 2.09 m/s and 1.27 m/s. $R^2$ is the linear correlation coefficient of all data points, and indices (c), (d), and (e) for differentiation of Eqs. 17–19.

Run B13-050 was performed to have a rough estimate of possible effects by different drum velocities. The run was performed at a velocity of 1.27 m/s compared to the 2.09 m/s for the previous 12 runs. This experiment shows larger friction values, suggesting that the dynamic average bulk friction coefficients decline with increasing velocity. Despite a single run is not representative and velocity-dependence needs to be further investigated with additional runs at varying velocities, this effect indicates that the measured friction coefficients include internal friction components besides possible basal slip which should be independent of sliding velocity (Coulomb's law of friction; Coulomb, 1773). From visual interpretation we can confirm that basal slip was not obvious and therefore suppose that internal friction from flow resistance caused by long-term frictional contacts between individual grains (quasi-static regime) may have played a role, but short-term collisional impacts of individual grains (grain inertial regime) within the sheared flow body also became significant (Iverson and Denlinger, 2001; Savage, 1984; see also Section 5.2).

### *4.2.2. Late phase: flow transformations and effects of water*

Because mass loss was negligible, we can analyze the temporal development of the flow characteristics within each run as well as between the different experiments for the entire experiment lengths reaching up to 55 min. In the laboratory experiments, the longer experimental duration may compensate for the lower rates of melting — that is, we may reach overall similar magnitudes of melting in the experiments as over the course of natural events. All runs having ice contents larger than 40% by volume showed a transformation from a dry granular mass to a much more liquid debris-flow-like movement. This flow transformation was visually observed and accompanied by a shift downslope of the position of the flow front (Fig. 13). At first, as the grains were moistened, an intergranular water film developed and in certain cases led to a slightly retreating frontal position (cohesion effects). This was supported by volumetric decrease due to grain fragmentation and melting of ice. As soon as partial saturation started from the tail, grain to grain contact forces were reduced and the friction was significantly decreased, finally resulting in partial or nearly complete liquefaction where most grains are supposed to have been supported by the liquid phase (Fig. 13h–j).

Fig. 11e and g show the evolution of the pore-water pressure from the tail to the front of the flow at both sensors. In general, the central *pwp* sensor shows larger values than the one at the side. However, at certain irregular stages with intermediate water contents (e.g. around minutes 15 and 19 in Fig. 11e and g), the flow was affected by a large asymmetric lateral component (also reported by Hsu, 2010) for a while and then became steady again. One of these unsteady moments is captured in Fig. 13f. This has to do with laterally unbalanced water input from the drop-protection roof back into the flow (Fig. 4, larger drum, letter ‘k’). The normal force and central *pwp* measurements were not much influenced by such asymmetries, because they were measuring at the centerline. In contrast, the *pwp* sensor near the side wall was strongly affected and could reach larger values than at the central *pwp* sensor within these phases (see labeled minutes in Fig. 11e and g).

Due to the different locations of the *pwp* and normal stress sensors, the flow conditions were not exactly the same. For example, if the mixture became much diluted at a later stage of the experiment, both *pwp* sensors tended to measure pore pressures at the front greater than the measured normal stress of the total load. On the load cell there is no roughness bar and consequently the smooth surface of the plate caused some local flow surge. This surge led to some of the water splashing directly onto the *pwp* sensors before they disappeared below the surge front of each rotation. The consequence is that the flows with high water contents can achieve liquefaction ratios slightly larger than 1 at late stages. In this situation, *pwp* measurements a short distance back from the flow front are more accurate because they were less affected by splashing water.

The development of the friction coefficients from the four experimental series against time is shown in Fig. 14a–d. Despite certain fluctuations we can see that (1) there is a direct dependence of the friction coefficient on ice content during the first 5 min as previously shown in Fig. 12 that particularly can be seen in Fig. 14a where curves with higher ice contents are situated lower, (2) a slight effect of rising friction due to the development of an intergranular water film and related cohesion effects when ice starts melting between $t \approx 5$–15 min, and (3) strong reduction of the friction and increased flow liquefaction when pore-water pressures are rising.

The liquefaction ratios calculated by Eq. 12 are shown in Fig. 14e–h. The onset and reduction of the friction coefficients depend on the onset and increase of the liquefaction ratios. Both, the decrease of the friction values and increase of the liquefaction ratios propagate nearly linear with time. This trend was only attenuated and finally stopped when almost all ice has melted. Those runs with more than 40% ice by volume achieved half or even complete liquefaction after ~30 min. The measured and visually observed behavior of these flow-states finally is similar to the one of hyperconcentrated flows. According to Pierson (2005), hyperconcentrated flows have sediment concentrations between 20 and 60 by volume, while for debris-flows the sediment concentration needs to be above 60% by volume. Because we

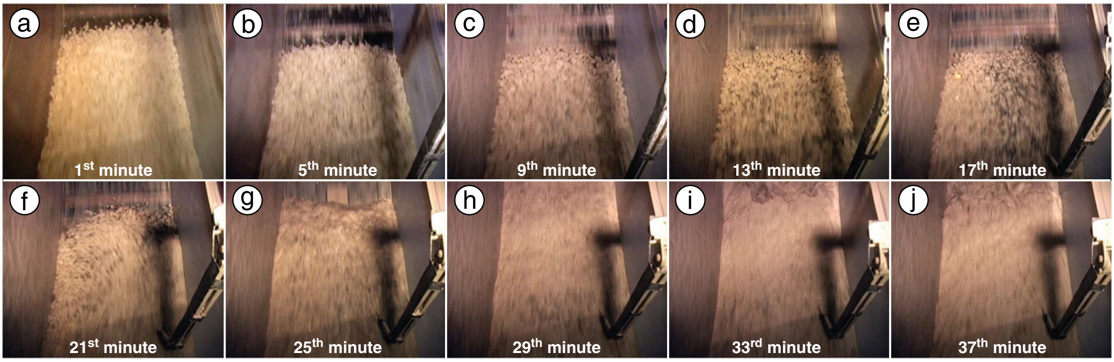

**Fig. 13.** Images from the video camera of every 4th minute of experiment B12-070 with 70% ice content in the larger drum show the flow transformation from a dry granular mixture (a–b) to a debris-flow-like movement (c–g), and finally to a hyperconcentrated flow-like behavior (h–j). On the right side, the thermostat sticking into the moving mass is visible. In (g), the normal force plate is visible right before the liquid front of the flow. Flow direction is from bottom to top while the drum rotated the opposite direction. Note that on these images, the view angles of the camera are identical.

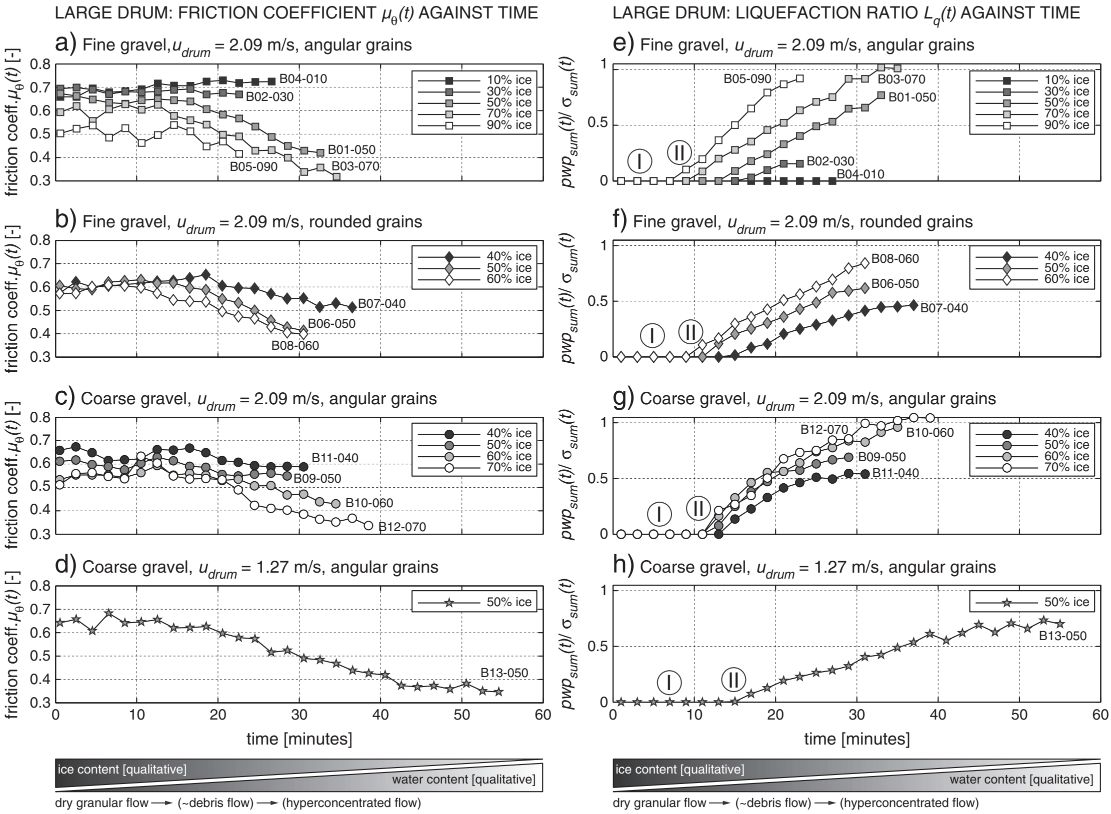

**Fig. 14.** Subfigures a–d show the dependence of the dynamic average bulk friction coefficient $\mu_\theta$ on ice and water content over time for all experiments in the larger drum. The friction is calculated by Eq. 8 (see Fig. 7). Experiments were stopped when all ice had melted or if the flow became highly unsteady. Subfigures e–h show the liquefaction ratio from Eq. 12. During the initial 5–15 min, water was retained as an intergranular water film (I). After ~10 min (II), the flow body got increasingly saturated and developed a debris-flow-like movement. If the water contribution from melting ice was large enough, a hyperconcentrated flow formed after ~30 min.

used a narrow grain-size distribution, the pore spaces of the gravel constituted 39–45% by volume so that the sediment concentration never rose above 55–61% by volume (Table 3) and a considerable part of the pore space was filled with air initially or during the entire experiment. Due to the lack of fines we never had real debris-flow conditions as in nature and as soon as the gravel was fully saturated,

**Table 3**

Calculation of static pore space, excess water and sediment concentrations for the larger drum experiments. All density values are based on static measurements of the basalt/dacitic andesite gravel and the total volume of the mixtures at the beginning of the experiments (0.400 $m^3$).

| Experiment number | B04-010 | B02-030 | B01-050 | B03-070 | B05-090 | B07-040 | B06-050 | B08-060 | B11-040 | B09-050 | B10-060 | B12-070 | B13-050 |
|---|---|---|---|---|---|---|---|---|---|---|---|---|---|
| Ice content [vol-%] | 10 | 30 | 50 | 70 | 90 | 40 | 50 | 60 | 40 | 50 | 60 | 70 | 50 |
| Static ice bulk density [kg/$m^3$] | | | 565 | | | | 565 | | | 565 | | | 565 |
| Static gravel bulk density start [kg/$m^3$] | | | 1500 | | | | 1600 | | | 1550 | | | 1550 |
| Static gravel bulk density end [kg/$m^3$] | | | 1600 | | | | 1650 | | | 1640 | | | 1640 |
| Density of solid rock [kg/$m^3$] | | | 2800 | | | | 2800 | | | 2740 | | | 2740 |
| Ice and water weight [kg] | 22.6 | 67.8 | 113.0 | 158.2 | 203.4 | 90.4 | 113.0 | 135.6 | 90.4 | 113.0 | 135.6 | 158.2 | 113.0 |
| Rock weight [kg] | 540.0 | 420.0 | 300.0 | 180.0 | 60.0 | 384.0 | 320.0 | 256.0 | 372.0 | 310.0 | 248.0 | 186.0 | 310.0 |
| Static pore space in gravel [L] | 144.6 | 112.5 | 80.4 | 48.2 | 16.1 | 95.6 | 79.7 | 63.7 | 91.1 | 75.9 | 60.7 | 45.5 | 75.9 |
| Excess water when all pores filled [L] | – 122.0[a] | – 44.7[a] | 32.6 | 110.0 | 187.3 | – 5.2[a] | 33.3 | 71.9 | – 0.7[a] | 37.1 | 74.9 | 112.7 | 37.1 |
| Sediment concentration when all ice had melted [vol-%] | 57[a] | 57[a] | 46[b] | 28[b] | 9 | 59[a] | 49[b] | 39[b] | 60[a] | 48[a] | 39[b] | 29[b] | 48[b] |

[a] These runs do not reach full saturation and air-filled pore space is still available (negative excess water values). The sediment concentration cannot be higher than the tightest packing of the grains allows.

[b] Hyperconcentrated flow from a later phase until all ice has melted can be expected from calculated values (note that real excess water can be less due to water loss to the inner drum surface). Transition includes debris-flow-like movement.

the water content of the mixture was already as high as the one of hyperconcentrated flows. However, the flow conditions always varied along the profile and to the sides as well as the ice and rock grains were fragmenting and reducing in size (ice also due to melting) and a small quantity of fines was produced successively. Measurements of the dirty water after the entire experiment resulted in a maximum water density of 1.198 kg/L for the run with 40% ice and around 1.100 kg/L for higher ice contents. We therefore expect that the fluid viscosity might have increased slightly, supporting development of debris-flow- and hyperconcentrated flow-like behavior. In those runs where enough water was available, most of the grains were carried by the liquid phase despite the low densities of the water and the monodisperse grain-size distribution (Figs. 14e–h). Hence, we relate the suspension of the larger grains rather to effects from fluid turbulence and grain agitation than to the necessarily large density of a muddy matrix and assume that debris-flow-like conditions were reached at least temporally and for certain flow sections as an intermediate state before hyperconcentrated flow-like behavior developed during those runs with 60% ice by volume and more (Fig. 13e–g).

Comparisons between theoretic excess water values given in Table 3 and the measured liquefaction ratios in Fig. 14e–h show a certain disparity. The measured maximum liquefaction was always lower than it would be expected from the theoretic excess water, because considerable amounts of water were lost despite the drum has been leak proof. Alone the inner drum surface including the drop protection roof and sidewalls have an area of approximately 35 m$^2$ on which wetting by a 1 mm thick water film requires 35 L of water. Additionally, some water splashed out of the drum and a part of the water must have evaporated during the experiments which usually were longer than 30 min. We estimate that the total water loss after more than 30 min may have been in the order of 50 L which is 12.5% of the starting volume or between 9 and 19% of the mass, depending on the ice content. Therefore, the mixtures required an ice content of a least 60% by volume to reach full liquefaction as shown in Fig. 14e–h.

The friction coefficients and liquefaction ratios between fine and coarse gravel in Fig. 14 develop similarly through time. The increasing friction due to cohesion effects (Chevoir et al., 2009; Iverson et al., 2004) has its peak after 10 min and can be best observed for the runs in Fig. 14b with fine rounded grains. This is because larger and more angular grains may be less affected by this effect. A part of the friction reduction in Fig. 14 may also result from grain abrasion over longer time periods (up to 54 min). The effects of grain shapes on the friction coefficients can be estimated from the difference between the two experimental series in Fig. 12a, where the previously used and rounded gravel shows friction coefficients which are at least 0.05 smaller than those of angular grains.

The lower rotational velocity of run B13-050 leads to a slower liquefaction process and hence a slower reduction of the friction coefficient. Velocity is therefore an important factor influencing the melting rate of ice due to frictional heating and mixing of drum material with material having positive temperatures (only air in the laboratory; air and eroded basal material in natural events).

## 5. Discussion

### 5.1. Comparison of drum experiments and natural events

A major difference between the rotating flume and straight chute experiments or natural events is related to the longitudinal flow characteristics. Kern et al. (2009) found supercritical flow behavior (Fr>1) for snow avalanche fronts and subcritical behavior (Fr<1) for the avalanche tails. This is not possible in rotating drums, because the avalanche tail is artificially held at the same velocity by higher inclination angles. Instead, the shear rates and Froude numbers rise to the tail due to the smaller flow heights at the same velocity. While natural avalanches tend to stretch and continuously loose material by deposition at the tail (Bartelt et al., 2007), the mass in the drum is forced to keep its geometry constant (the changing geometry through time in the presented experiments is due to grain fragmentation and melting ice).

To assess similitude between mean values of the different experimental series and natural events, physical parameters and dimensionless numbers were compared (Table 4). The Froude numbers $Fr_{hyd}$ in the rotating drum experiments slightly differ from those in Table 1 because $h_{avg}$ was used instead of $h_{max}$ in Eq. 3. The values are lower for the drum experiments than for natural flows, but reaching larger Froude numbers was not possible in the drums because flow heights of 0.13–0.21 m were needed in relation to the mean grain-size and larger velocities were not possible due to technical and flow instability reasons, as well as to reduce effects from centripetal acceleration (Eq. 4). However, the aim was to reach supercritical Froude numbers (>1) in the laboratory (except for run B13-050; see Table 4).

The ratio of inertial grain stress to viscous shear stress is described by the dimensionless Bagnold number $N_B$ (Iverson, 1997):

$$N_B = \frac{\upsilon_s \rho_s \delta^2 \dot{\gamma}}{\upsilon_f \eta} \tag{20}$$

where $\nu_s$ and $\nu_f$ ($=1-\nu_s$) are the solid and fluid volume fractions, $\rho_s$ the mean density of solids, $\delta$ the characteristic grain diameter where we used the weighted mean of the median grain-sizes $D_{50}$ of the corresponding gravel and ice fractions, $\eta$ the fluid viscosity, and $\dot{\gamma}$ the shear rate as calculated from $2 * u_{drum}/h_{avg}$ for the drum experiments and $u_{typ}/h_{avg}$ for the natural events where $u_{typ}$ is their typical velocity (corresponding to the median velocity). The values between $10^5$ and $10^6$ for the dry stage of the experimental flows indicate that viscous forces are not relevant when the granular mass is largely dry (Savage, 1984). This seems also to be the case in natural flows where the inertial stresses clearly dominate, however, Bagnold numbers are 1–3 orders of magnitude larger than in the experiments (Table 4). Considering that the Aoraki/Mt. Cook-, Kolka-, and Iliamna-events contained high water contents shortly before deposition, the approximately 100 times higher fluid viscosities $\eta$ of water compared to air would lead to accordingly lower Bagnold numbers for the saturated stage of the events.

The Savage number describes the ratio of inter-granular collisional stress to quasi-static shear stress associated with the weight and friction of the mass (Iverson and Denlinger, 2001):

$$N_S = \frac{\rho_s \delta^2 \dot{\gamma}^2}{\left(\rho_s - \rho_f\right) g h_{avg}}. \tag{21}$$

All values of $N_s$ in Table 4 are within a range of 0.010 and 0.120. This is close to the threshold value of 0.1 found by Savage and Hutter (1989), above which collisional stresses start to affect flow dynamics significantly. During the first minutes, the flows accordingly were in the transitional regime between the frictional (quasi-static regime) and the collisional (grain inertial) regimes (Savage, 1984). The values confirm that the experimental flows reached conditions similar to those of rapid granular avalanches where short-term collisions rather than long-term frictional contacts dominate intergranular momentum transport (Iverson and Denlinger, 2001). Using larger fluid densities $\rho_f$ for water instead of air to assess later stages of the flows, $N_s$ is somewhat larger.

**Table 4**
Physical parameters and dimensionless numbers for the beginning of the rotating drum experiments and for some natural events. Note that the values of the drum experiments and natural events only relate to the dry stage when no water was available. The numbers may change considerably when ice is progressively melting.

| | | Rotating drum experiments (dry stage)[a] | | | | Natural events (dry stage) | | | |
|---|---|---|---|---|---|---|---|---|---|
| | | Smaller drum | Larger drum | Larger drum | Larger drum | Elm[b] | Aoraki/ Mt. Cook[c] | Kolka[d] | Iliamna Red Glacier[c] |
| | | V01-050 V12-100 | B01-050 B08-060 | B09-050 B12-070 | B13-050 | | | | |
| Volume ($m^3$) | $V$ | $8.56\times10^{-2}$ | $4\times10^{-1}$ | $4\times10^{-1}$ | $4\times10^{-1}$ | $1\times10^{7}$ | $6\times10^{7}$ | $1.3\times10^{8}$ | $1.6\times10^{7}$ |
| Ice content (vol-%) | $x$ | 0–100 | 30–90 | 40–70 | 50 | 0 | 50 | 60 | 80 |
| Characteristic grain diameter (m) | $\delta$ | 0.01 | 0.007–0.019 | 0.018–0.019 | 0.018 | 1 | 0.3 | 1 | 0.2 |
| Avg flow height (m) | $h_{avg}$ | 0.13–0.15 | 0.15–0.20 | 0.18 | 0.21 | 10 | 13.3 | 26.7 | 6.7 |
| Avg normal stress (Pa) | $\sigma_{avg}$ | 700–2000 | 1200–2600 | 1500–2000 | 1800 | 120,000 | 140,000 | 270,000 | 70,000 |
| Velocity (m/s) | $u$ | 1.64 | 2.09 | 2.09 | 1.27 | 50 | 55 | 50 | 50 |
| Shear rate for $h_{avg}$ ($s^{-1}$)[e] | $\dot{\gamma}$ | 22–25 | 21–28 | 23–24 | 12 | 5 | 1.8 | 1.3 | 3.3 |
| Avg density of solids ($kg/m^3$) | $\rho_s$ | 900–2700 | 1100–2600 | 1500–2000 | 1800 | 2800 | 1900 | 1100 | 1700 |
| Fluid density ($kg/m^3$) [f] | $\rho_f$ | 1.2 | 1.2 | 1.2 | 1.2 | 2 | 2 | 2 | 2 |
| Avg dynamic bulk density of rock–ice mixture ($kg/m^3$) | $\rho_{dyn}$ | 400–1050 | 920–1530 | 1150–1560 | 940 | 1500 | 1100 | 950 | 1,000 |
| Fluid viscosity (Pa s)[f] | $\eta$ | $1.7\times10^{-5}$ | $1.7\times10^{-5}$ | $1.7\times10^{-5}$ | $1.7\times10^{-5}$ | $2\times10^{-5}$ | $2\times10^{-5}$ | $2\times10^{-5}$ | $2\times10^{-5}$ |
| Volume fraction solid (dimensionless) | $\nu_s$ | 0.56 | 0.56 | 0.58 | 0.58 | 0.6 | 0.6 | 0.6 | 0.6 |
| Volume fraction fluid (dimensionless) | $\nu_f$ | 0.44 | 0.44 | 0.42 | 0.42 | 0.4 | 0.4 | 0.4 | 0.4 |
| Froude number[g] | $Fr_{hyd}$ | 1.3–1.5 | 1.5–1.8 | 1.6 | 0.9 | 5.1 | 3.2 | 2.5 | 4.1 |
| Reynolds number | $N_R$ | 141–187 | 80–619 | 485–560 | 274 | 500,000 | 17,000 | 125,000 | 13,000 |
| Bagnold number | $N_B$ | $1.9–4.0\times10^{5}$ | $2.0–8.4\times10^{5}$ | $1.0–1.1\times10^{6}$ | $5.8\times10^{5}$ | $1.1\times10^{9}$ | $2.3\times10^{7}$ | $1.0\times10^{8}$ | $1.7\times10^{7}$ |
| Savage number | $N_S$ | 0.036–0.045 | 0.013–0.145 | 0.088–0.112 | 0.024 | 0.231 | 0.001 | 0.004 | 0.003 |
| Mass number | $N_M$ | 1000–2800 | 1400–2500 | 1700–2300 | 2100 | 2100 | 1391 | 824 | 1,250 |
| Friction coefficients | $\mu_\theta$ | 0.58–0.72 | 0.50–0.70 | 0.51–0.67 | 0.63 | — | — | — | — |
| | $\mu_{app}$ | — | — | — | — | 0.29 | 0.4 | 0.08–0.15 | 0.2 |

[a] Value ranges are related to the range of ice content used in the corresponding series.
[b] Hsü (1978) and Iverson and Denlinger (2001).
[c] Schneider et al. (2010).
[d] Huggel et al. (2005).
[e] Shear rate for drum experiments was calculated by $2*u_{drum}/h_{avg}$ and for natural events by $u_{typ}/h_{avg}$.
[f] Fluid density and viscosity for air was used for the drum experiments, and the values of dusty air for the natural events respectively.
[g] Froude number values are slightly higher than those in Table 1 because $h_{avg}$ was used instead of $h_{max}$.

The ratio of solid inertia to fluid inertia is given by the mass number $N_M$ (Iverson, 1997):

$$N_M = \frac{\upsilon_s \rho_s}{(1-\upsilon_s)\rho_f}. \tag{22}$$

As expected, the values in Table 4 are large (1000–2800) because solid inertia clearly dominates as long as no water is available. The 500–800 times larger fluid density of water compared to air and dusty air reduces $N_M$ significantly so that fluid forces become more relevant when ice is melting, however, solid forces still dominate.

Finally, the ratio of fluid inertia to its viscous shear stresses is described by a version of the Reynolds number $N_R$ that can also be expressed as the ratio of $N_B$ to $N_M$ (Iverson, 1997):

$$N_R = \frac{\rho_f \dot{\gamma} \delta^2}{\eta}. \tag{23}$$

$N_R$ is usually in the order of $10^6$ for natural geophysical flows and $10^4$–$10^5$ in the presented examples (Table 4), indicating that inertial forces dominate in large flows. When the same fluids (air and water) are used for small and large scales, viscous forces will be more important in the smaller ones due to simple scaling laws (e.g. Henderson, 1966). As expected due to Froude scaling (see Section 2.1), Reynolds numbers were 2–3 orders of magnitude smaller in the experiments, but they still indicate the dominance of inertial forces and are large enough so that the exact values probably do not strongly influence the overall dynamics (Paola et al., 2009).

Even though all flows are highly complex and the effects of pore-water or the fraction of fine grains are difficult to assess, we conclude that the dimensionless numbers indicate some similarities between the experimental series and natural flows to permit extrapolation of the influence of ice on flow behavior. However, important effects which may enhance the mobility of rapid mass movements such as dynamic grain fragmentation (Davies et al., 2010; McSaveney and Davies, 2007) and enhanced melting of the ice under large pressures are likely to be present only in nature (Davies and McSaveney, 1999) so that an additional reduction of the friction coefficients must be expected for very large events.

Friction angles of very large rapid mass movements have never been directly measured but estimated values for events above $1\times10^6$ $m^3$ are usually smaller than the ones for smaller-volume events (Erismann and Abele, 2001; Favreau et al., 2010; Legros, 2002). However, for smaller natural events of related process forms some direct measurements exist: Dent et al. (1998) measured dynamic bulk friction coefficients of 0.42 for the main body of a dry-snow avalanche. This is somewhat smaller than measured in our pure ice runs, and possibly related to volume effects (e.g. Davies, 1982; Legros, 2002). McArdell et al. (2007) calculated bulk friction angles of 26° ($\mu_{\tau/\sigma}=0.49$) for a natural debris-flow in a torrent channel. Such a value is reached in all experiments in the larger drum with ice content larger than 50% by volume around 20–25 min after the start of the experiment when much ice has melted. In nature, debris-flow fronts are often dry and followed by a more liquid body and tail (e.g. Major and Iverson, 1999). This is also the case for those runs in the drum experiments with more than 50% ice by volume and after ~25 min: pore-water pressures evolve from the back to the front (Fig. 11e) and only saturate the front if enough melt water is available to saturate the leading edge of the front, thereby producing a flow which more closely resembles a debris-flood or hyperconcentrated flow. The measured bulk densities around 2000 $kg/m^3$ during the debris-flow-like movement in the drum are close to the measured 2000–2250 $kg/m^3$ by McArdell et al. (2007) for a real debris-flow. The small portion of fine particles however does not allow larger densities.

The calculated dynamic average bulk friction coefficient $\mu_\theta$ for pure gravel in the rotating drums ($\mu_\theta \approx 0.72 \approx 36°$) is somewhat smaller, but still close to static internal friction angles $\mu_{stat}$ of the same gravel ($\mu_{stat} \approx 0.8 \approx 38.5°$), which is in the range of typical $\mu_{stat}$ of natural materials ($\mu_{stat} > 0.58$; $> 30°$) (Favreau et al., 2010). These values are relatively large compared to the apparent coefficients of friction $\mu_{app}$ observed in natural events with volumes above $1 \times 10^6$ m$^3$ which are often much below 0.36 (20°; see Table 4). Reasons for the often smaller apparent friction coefficients $\mu_{app}$ in nature – which are also used for retrospective and scenario-based modeling – compared to the rotational drum results, are largely the previously described volume effects and greatly intensified rock comminution in large events (see also Section 2.2). This includes the influence of the particle size on runout distance: for a given volume, $\mu_{app}$ is expected to be smaller for smaller particle sizes (Campbell et al., 1995; Legros, 2002). The particles used in the experiments are large compared to the volumes, however this was necessary to minimize cohesion (as described previously) which would have led to stick–slip effects (Mair et al., 2002) when ice melted, possibly increasing $\mu_\theta$. Another argument is that rapid mass movements that include large portions of ice often also travel over glaciers, which as basal low friction surfaces possibly have much stronger consequences on $\mu_{app}$ (Cleary and Campbell, 1993; see also ice–ice friction values far below 0.1 as measured by Maeno et al., 2003) than incorporated ice. This boundary effect was not included in our experiments. Instead, the basal roughness of both drums captures a thin layer of particles from the moving material rising the boundary friction $\mu$ consequently close to the static internal friction $\mu_{stat}$ (but still somewhat smaller due to the movement of the granules). Water can have a much stronger effect on reducing friction if it is concentrated in thin layers. (e.g. Maeno et al., 2003; Prager et al., 2006). This requires relatively impermeable material which overrides saturated debris which was not the case with the relatively permeable gravel used in the experiments. Finally, comminution of ice and rock was strongly limited in the experiments (see scaling of fracture toughness in Section 2.2). Dynamic fragmentation reduces effective shear stress by carrying a dispersive pressure due to failing individual grains (release of elastic energy) and the mechanism is intensified for reduced material strengths (Davies et al., 2007; 2010). This may explain that volcanic debris avalanches comprising weakened, hydrothermally altered rock with a lower mechanical strength usually have a higher mobility compared to non-volcanic events (Davies et al., 2010; Korup et al., in press). The strength of ice is much lower than the one of volcanic material, so it is possible that dynamic fragmentation could be significantly intensified in large natural rock–ice avalanches, causing a further reduction of the friction coefficient and consequently longer runout distance of the material. However more detailed investigations will have to be performed to verify if the dynamic fragmentation hypothesis can be extended to ice.

Therefore we suggest that ice as part of the moving mass (argument 1 from Introduction) and as a supplier of meltwater (argument 2) may be a significant, but possibly not the most important reason for the high mobility of rapid mass movements from glacial environments. Argument 3 which states that underlying glacier ice serves as a low friction surface for overriding rapid mass movements may be the dominant factor, particularly during the early acceleration phase in steep terrain, where kinetic energy greatly increases (Schneider et al., in press).

### 5.2. Implications for hazard assessment

The results quantitatively show that granular ice can significantly reduce the friction coefficient as part of a granular moving mass. Therefore, hazard assessments of slope instability where ice may be involved need to consider a higher mobility of possible rock–ice avalanches as proposed by others (e.g. Evans and Clague, 1988). This can be done by applying smaller friction values in numerical modeling of failure and flow propagation scenarios (e.g. Bottino et al., 2002). When different ice contents are considered, Fig. 10 and 12 can be used to estimate the expected decrease in friction for numerical modeling: a rough estimate from the laboratory experiments is, that the friction coefficient of a constant volume of a moving mass may be reduced by ~20% for pure dry granular ice compared to pure dry granular rock (however, variations can be strong as presented in Section 4.2). Hence, the friction of a dry granular rock–ice avalanche with 50% ice content by volume may have a friction that is 10% smaller than a pure dry granular rock avalanche of the same volume. This effect is significant, but not large enough to entirely explain the small apparent friction coefficients observed in nature.

The reduction of friction related to flow transformations (e.g. due to melting ice and consequent increases in pore pressure if the flow is undrained, e.g. Fig. 14) could also be used in scenario generation for model simulations for hazard assessment. This can be useful either for rock–ice avalanches where the ice may be the main contributor of water, but also for dry rock avalanches which could erode saturated soil along the flow path to form a more mobile debris-flow (Hungr and Evans, 2004), or when the debris is continuously diluted on its downstream path (Pierson and Scott, 1985). Melting water caused a reduction of the friction coefficient by more than 50% (in our experiments reduction of the friction coefficient from 0.72 to 0.31 from a dry to a fully saturated flow) which is much more effective than the effect of ice measured in this study but also requires much more time to become relevant.

The friction values presented herein should not be used directly and need to be adapted to the corresponding avalanche volume and environmental setting, such as topography (e.g. runup, lateral swash, and deviations, where additional energy is dissipated), surface characteristics (e.g. low friction glacial surface vs. high friction surface with large roughness elements), geological material properties (e.g. grain-size distribution, lithology, clay content), and erosion potential (availability of erodible material). Therefore, the *relative* reduction of the friction related to ice and pore-water pressure effects as suggested may be better suited to estimate the possible influence of ice and water on rapid granular mass movements than the *absolute* values from the laboratory.

The influence of ice on the frictional behavior may be enhanced for larger events, and positive feedbacks can further reduce the friction coefficients. For example, a rock–ice avalanche traveling over a glacier may increase its velocity significantly. If more kinetic energy is dissipated (e.g. when the mass reaches regions with a larger boundary friction), larger amounts of water may be melted in shorter time periods and possibly concentrated in thin shear layers, with a consequent increase in runout distance. Our data may serve as a minimum estimate of the influence of granular ice and water on friction and help in modeling different scenarios of varying ice and water contents in a rapid mass movement and related flow transformations.

## 6. Conclusions

The main objective of this study was to quantify the influence of ice on friction in rapid granular mass movements and on related phase transitions when ice is melting. The experiments provide new laboratory evidence to illustrate these effects and our results suggest that the presence of ice in the moving mass is important both as a part of the moving material and as supplier of water for the flow itself. However, scale effects are difficult to quantify and need to be considered if friction values are extrapolated to natural flows. The data from the laboratory experiments are leading to two individual conclusions:

(1) The friction coefficient of granular gravel–ice mixtures in the rotating drums is linearly related to volumetric ice content: the larger the ice content, the smaller the friction. The friction of the experimental series with the broadest variation of the ice content was reduced by approximately 20% for pure granular ice compared to gravel only. Different grain-sizes and grain shapes can influence this value.

(2) The runs with initial ice contents larger than 40% by volume were affected by liquefaction due to increasing contents of melt water during the later phase, around 15 min after the beginning of the experiments and later. Pore-water pressures developed from the rear to the snout, causing the liquefaction ratios to rise. Concomitantly, the friction coefficients were reduced and flow phase transitions from a dry granular mass to a debris-flood or debris-flow-like movement and finally to a hyperconcentrated flow evolved. Flow transformations are directly related to the water content and corresponding changes in the friction coefficient.

Future challenges remain in finding reasonable friction coefficients corresponding to certain topographic and geologic settings that can be applied for scenario modeling. It is important to note that natural events usually have smaller friction coefficients than found in the laboratory experiments. This is likely due to other effects reducing the friction of a rapid mass movement, such as sliding on low friction surfaces (e.g. glacier ice), volume- or size effects, dynamic fragmentation, wider grain size distributions, and the concentration of lubricants (e.g. water) to thin layers which further reduce the friction coefficient and need to be considered additionally. While the presented laboratory experiments help to determine friction coefficients on a relative basis for rapid mass movement scenarios containing different amounts of ice and water, the role of the mentioned other processes was not assessed and therefore is proposed to be investigated in more detail in future studies.

*Notation*

| | |
|---|---|
| $A_{bed}$ | area on drum bed which is covered by flow [m$^2$] |
| $a_{c,avg}$ | depth-averaged centripetal acceleration [m/s$^2$] |
| $a_{c,max}$ | maximum centripetal acceleration [m/s$^2$] |
| $COM$ | center of mass |
| $d$ | drum diameter [m] |
| $D_{16}$ | 16%-percentile of grain-size distribution [mm] |
| $D_{50}$ | median grain-size [mm] |
| $D_{84}$ | 84%-percentile of grain-size distribution [mm] |
| $Fr$ | Froude number [−] |
| $Fr_{rot}$ | rotational Froude number [−] |
| $Fr_{hyd}$ | hydraulic Froude number [−] |
| $g$ | gravitational acceleration [m/s$^2$] |
| $H$ | drop height [m] |
| $h$ | characteristic height for Froude number [m] |
| $h_{avg}$ | average flow height of entire flow profile [m] |
| $h_{max}$ | maximum flow height of entire flow profile [m] |
| $h_{mean}$ | filtered mean flow height within one angular degree [m] |
| $h_{median}$ | filtered median flow height within one angular degree [m] |
| $h_{\sigma}$ | representative flow height derived from normal stress data $\sigma_{mean}$ [m] |
| $K$ | fracture toughness [Pa m$^{0.5}$] |
| $L$ | travel distance [m] |
| $Lq$ | average liquefaction ratio of entire flow [−] |
| $N_B$ | Bagnold number [−] |
| $N_R$ | Reynolds number [−] |
| $N_S$ | Savage number [−] |
| $N_M$ | Mass number [−] |
| $pwp$ | basal pore-water pressure [Pa] |
| $pwp_{mean}$ | filtered basal pore-water pressure within one angular degree [Pa] |
| $pwp_{sum}$ | sum of the 1°-bins of the pore-water pressure values of the entire profile [Pa] |
| $r$ | inner drum radius [m] |
| $rpm$ | rounds per minute |
| $s_h$ | standard deviation of $h_{mean}$ [m] |
| $s_{pwp}$ | standard deviation of $pwp_{mean}$ [Pa] |
| $s_u$ | standard deviation of $u_{drum}$ [m/s] |
| $s_{trq}$ | standard deviation of $trq_{net}$ [Nm] |
| $s_{\sigma}$ | standard deviation of $\sigma_{mean}$ [Pa] |
| $s_{\tau}$ | standard deviation of $\tau_{mean}$ [Pa] |
| $t$ | time [min] |
| $T_{cubes}$ | mean flow temperature from all cube loggers [°C] |
| $T_{tc,lab}$ | laboratory temperature from thermocouple [°C] |
| $T_{tc,flow}$ | flow temperature from thermocouple [°C] |
| $Trq_{net}$ | torque (net) [Nm] |
| $Trq_{gross}$ | torque (gross) [Nm] |
| $Trq_{tare}$ | torque (tare) [Nm] |
| $u$ | velocity [m/s] |
| $u_{drum}$ | rotational velocity at bottom of drum [m/s, rpm] |
| $u_{typ}$ | typical velocity of a natural event [m/s] |
| $V$ | volume of mixture [m$^3$] |
| $V_h$ | volume derived from $h_{median}$ [m$^3$] |
| $V_{\sigma}$ | volume derived from $h_{\sigma}$ [m$^3$] |
| $w$ | drum width [m] |
| $x$ | ice content [vol-%] |
| $x_{COM}$ | x-coordinate of COM [m] |
| $y_{COM}$ | y-coordinate of COM [m] |
| $\alpha$ | drum angle (position) [°] |
| $\alpha_{COM}$ | deflection angle of center of mass [°] |
| $\dot{\gamma}$ | shear rate for $h_{avg}$ [s$^{-1}$] |
| $\Delta H$ | height difference [m] |
| $\delta$ | characteristic grain diameter [m] |
| $\theta$ | vertically projected angle of center of mass [°] |
| $\lambda_K$ | fracture toughness scale [−] |
| $\lambda_L$ | length scale [−] |
| $\lambda_{\rho}$ | density scale [−] |
| $\mu$ | friction coefficient [−] |
| $\mu_{app}$ | apparent friction coefficient [−] |
| $\mu_{\tau/\sigma}$ | dynamic bulk friction coefficient from $\tau_{bas}$ and $\sigma_{bas}$ [−] |
| $\mu_{\tau/\sigma,med}$ | median of $\mu_{\tau/\sigma}$ along the entire flow profile [−] |
| $\mu_{stat}$ | static internal friction coefficient [−] |
| $\mu_{trq}$ | dynamic average bulk friction coefficient from $\tau_{trq}$ and $\sigma_{avg}$ [−] |
| $\mu_{\theta}$ | dynamic average bulk friction coefficient from tan $\theta$ [−] |
| $\nu_f$ | fluid volume fraction [−] |
| $\nu_s$ | solid volume fraction [−] |
| $\rho_{bulk}$ | (apparent) dynamic bulk density [kg/m$^3$] |
| $\rho_{dyn}$ | average dynamic bulk density of entire mixture [kg/m$^3$] |
| $\rho_f$ | average density of fluid (air, dusty air or water) [kg/m$^3$] |
| $\rho_s$ | average density of solids (rock and ice) [kg/m$^3$] |
| $\rho_{stat}$ | average static bulk density of entire mixture [kg/m$^3$] |
| $\varsigma$ | standard deviation of the grain-size distribution as calculated from $(D_{84}/D_{16})^{0.5}$ [−] |
| $\sigma_{avg}$ | average basal normal stress of entire flow profile [Pa] |
| $\sigma_{bas}$ | basal normal stress [Pa] |
| $\sigma_{mean}$ | filtered mean basal normal stress within one angular degree [Pa] |
| $\sigma_{sum}$ | sum of the 1°-bins of the basal normal stress values of the entire profile [Pa] |
| $\tau_{bas}$ | basal shear stress [Pa] |
| $\tau_{mean}$ | filtered mean basal shear stress within one angular degree [Pa] |
| $\tau_{trq}$ | average shear stress from torque measurement [Pa] |
| $\eta$ | fluid viscosity [Pa s] |
| $\omega$ | angular velocity [rad/s] |

## Acknowledgments

This work was financially supported by the Swiss National Foundation grant NF 200021-121823/1 (Rock–ice avalanches: A systematic investigation of the influence of ice) and the Austrian

Science Foundation grant J2837-N10. The rotational drums were provided by the Department of Earth and Planetary Science at the University of California Berkeley (UCB) in cooperation with the National Center for Earth-surface Dynamics (NCED) and by the Institute of Mountain Risk Engineering (IAN) at the University of Natural Resources and Life Sciences in Vienna (BOKU). We particularly would like to thank Stuart Foster, Fritz Zott, Leonard Sklar, Wilfried Haeberli, Johannes Hübl, and Dieter Rickenmann who all heavily supported this work.

## References

Bartelt, P., Buser, O., Platzer, K., 2007. Starving avalanches: frictional mechanisms at the tails of finite-sized mass movements. Geophysical Research Letters 34 (L20407), 1–6.

Bottino, G., Chiarle, M., Joly, A., Mortara, G., 2002. Modelling rock avalanches and their relation to permafrost degradation in glacial environments. Permafrost and Periglacial Processes 13 (4), 283–288.

Campbell, C.S., Cleary, P.W., Hopkins, M., 1995. Large-scale landslide simulations: global deformation, velocities and basal friction. Journal of Geophysical Research 100 (B5), 8267–8283.

Casassa, G., Narita, H., Maeno, N., 1991. Shear cell experiments of snow and ice friction. Journal of Applied Physics 69 (6), 3745–3756.

Chevoir, F., Roux, J.-N., da Cruz, F., Rognon, P.G., Koval Jr., G., 2009. Friction law in dense granular flows. Powder Technology 190 (1–2), 264–268.

Chou, H.-T., Lee, C.-F., 2009. Cross-sectional and axial flow characteristics of dry granular material in rotating drums. Granular Matter 11, 13–32.

Cleary, P.W., Campbell, C.S., 1993. Self-lubrication for long runout landslides: examination by computer simulation. Journal of Geophysical Research 98 (B12), 21911–21924.

Coulomb, C.A., 1773. Sur une application des règles de maximis & minimus a quelques problèmes de statique, relatifs a l'architecture, Memoires de Mathématique et de Physique. Imp. R. Acad. Sci., Paris: Presentes à l'Académie Royale des Sciences, Paris, pp. 343–384.

Davies, T.R.H., 1982. Spreading of rock avalanche debris by mechanical fluidization. Rock Mechanics 15 (1), 9–24.

Davies, T.R.H., McSaveney, M.J., 1999. Runout of dry granular avalanches. Canadian Geotechnical Journal 36, 313–320.

Davies, T.R.H., McSaveney, M.J., 2009. The role of rock fragmentation in the motion of large landslides. Engineering Geology 109, 67–79.

Davies, M.C.R., Hamza, O., Harris, C., 2001. The effect of rise in mean annual temperature on the stability of rock slopes containing ice-filled discontinuities. Permafrost and Periglacial Processes 12, 137–144.

Davies, T.R.H., McSaveney, M.J., Deganutti, A.M., 2007. Dynamic fragmentation causes low rock-on-rock friction. 1st Canada—U.S. Rock Mechanics Symposium, Vancouver, pp. 1–8.

Davies, T.R.H., McSaveney, M.J., Kelfoun, K., 2010. Runout of the Socompa volcanic debris avalanche, Chile: a mechanical explanation for low basal shear resistance. Bulletin of Volcanology 72, 933–944.

Dent, J.D., Burrell, K.J., Schmidt, D.S., Louge, M.Y., Adams, E.E., Jazbutis, T.G., 1998. Density, velocity and friction measurements in a dry-snow avalanche. Journal of Glaciology 26, 247–252.

Ding, Y.L., Forster, R., Seville, J.P.K., Parker, D.J., 2002. Granular motion in rotating drums: bed turnover time and slumping–rolling transition. Powder Technology 124 (1–2), 18–27.

Dramis, F., Govi, M., Guglielmin, M., Mortara, G., 1995. Mountain permafrost and slope instability in the Italian Alps: the Val Pola landslide. Permafrost and Periglacial Processes 6 (1), 73–81.

Erismann, T.H., Abele, G., 2001. Dynamics of Rockslides and Rockfalls. Springer, Heidelberg. 316 pp.

Evans, S.G., Clague, J.J., 1988. Catastrophic rock avalanches in glacial environments. In: Bonnard, C. (Ed.), Landslides — Proceedings of the Fifth International Symposium on Landslides, Lausanne, Switzerland, pp. 1153–1158.

Evans, S.G., Clague, J.J., 1998. Rock avalanche from Mount Munday, Waddington Range, British Columbia, Canada. Landslide News 11, 23–25.

Evans, S.G., Bishop, N.F., Smoll, L.F., Valderrama Murillo, P., Delaney, K.B., Oliver-Smith, A., 2009a. A re-examination of the mechanism and human impact of catastrophic mass flows originating on Nevado Huascarán, Cordillera Blanca, Peru in 1962 and 1970. Engineering Geology 108 (1–2), 96–118.

Evans, S.G., Tutubalina, O.V., Drobyshev, V.N., Chernomorets, S.S., McDougall, S., Petrakov, D., Hungr, O., 2009b. Catastrophic detachment and high-velocity long-runout flow of Kolka Glacier, Caucasus Mountains, Russia in 2002. Geomorphology 105, 314–321.

Favreau, P., Mangeney, A., Lucas, A., Crosta, G., Bouchut, F., 2010. Numerical modeling of landquakes. Geophysical Research Letters 37 (L15305).

Fischer, L., 2009. Slope Instabilites on Perennially Frozen and Glacierised Rock Walls: Multi-scale Observations, Analyses and Modelling. University of Zurich, Zurich. 81 pp.

Fraccarollo, L., Papa, M., 2000. Numerical simulation of real debris-flow events. Physics and Chemistry of the Earth 25 (9), 757–763.

Geertsema, M., Clague, J.J., Schwab, J.W., Evans, S.G., 2006. An overview of recent large catastrophic landslides in northern British Columbia, Canada. Engineering Geology 83, 120–143.

Goren, L., Aharonov, E., 2007. Long runout landslides: the role of frictional heating and hydraulic diffusivity. Geophysical Research Letters 34 (L07301), 1–7.

Gruber, S., Haeberli, W., 2007. Permafrost in steep bedrock slopes and its temperature-related destabilization following climate change. Journal of Geophysical Research 112 (F02S18), 1–10.

Haeberli, W., Wegmann, M., Vonder Mühll, D., 1997. Slope stability problems related to glacier shrinkage and permafrost degradation in the Alps. Eclogae Geologicae Helveticae 90, 407–414.

Haeberli, W., Huggel, C., Kääb, A., Polkvoj, A., Zotikov, I., Osokin, N., 2003. Permafrost conditions in the starting zone of the Kolka–Karmadon rock/ice slide of 20 September 2002 in North Osetia (Russian Caucasus), extended abstracts reporting current research and new information. Eight International Conference on Permafrost, Zurich, Switzerland, pp. 49–50.

Harris, C., Davies, M.C.R., Etzelmueller, B., 2001. The assessment of potential geotechnical hazards associated with mountain permafrost in a warming global climate. Permafrost and Periglacial Processes 12, 145–156.

Harris, C., Vonder Muhll, D., Isaksen, K., Haeberli, W., Sollid, J.L., King, L., Holmlund, P., Dramis, F., Guglielmin, M., Palacios, D., 2003. Warming permafrost in European mountains. Global and Planetary Change 39 (3–4), 215–225.

Henderson, F.M., 1966. Open Channel Flow. Macmillan Publishing Co., Inc., New York. 522 pp.

Henein, H., Brimacombe, J.K., Watkinson, A.P., 1983a. Experimental study of transverse bed motion in rotary kilns. Metallurgical and Materials Transactions B 14 (2), 191–205.

Henein, H., Brimacombe, J.K., Watkinson, A.P., 1983b. The modeling of transverse solids motion in rotary kilns. Metallurgical and Materials Transactions B 14 (2), 207–220.

Henein, H., Brimacombe, J.K., Watkinson, A.P., 1985. An experimental study of segregation in rotary kilns. Metallurgical and Materials Transactions B 16 (4), 763–774.

Hsu, L., 2010. Bedrock Erosion by Granular Flow. University of California, Berkeley. 190 pp.

Hsü, K.J., 1978. Albert Heim: observations on landslides and relevance to modern interpretations. In: Voight, B. (Ed.), Rockslides and Avalanches, 1: Natural Phenomena. Elsevier, Amsterdam, pp. 71–93.

Hsu, L., Dietrich, W.E., Sklar, L.S., 2007. Normal stresses, longitudinal profiles, and bedrock surface erosion by debris-flows: initial findings from a large, vertically rotating drum. In: Chen, C.L., Major, J.J. (Eds.), Debris-Flow Hazards Mitigation: Mechanics, Prediction, and Assessment: Proceedings 4th International DFHM Conference. Millpress, Amsterdam, Chengdu, China, p. 11.

Hsu, L., Dietrich, W.E., Sklar, L.S., 2008. Experimental study of bedrock erosion by granular flows. Journal of Geophysical Research 113 (F02001), 1–21.

Huebl, J., Suda, J., Proske, D., Kaitna, R., Scheidl, C., 2009. Debris-flow Impact Estimation, International Symposium on Water Management and Hydraulic Engineering, Ohrid, Macedonia, pp. 137–148.

Huggel, C., Zgraggen-Oswald, S., Haeberli, W., Kääb, A., Polkvoj, A., Galushkin, I., Evans, S.G., 2005. The 2002 rock/ice avalanche at Kolka/Karmadon, Russian Caucasus: assessment of extraordinary avalanche formation and mobility, and application of QuickBird satellite imagery. Natural Hazards and Earth System Sciences 5, 173–187.

Huggel, C., Salzmann, N., Allen, S., Caplan-Auerbach, J., Fischer, L., Haeberli, W., Larsen, C., Schneider, D., Wessels, R., 2010. Recent and future warm extreme events and high-mountain slope stability. Philosophical Transactions of the Royal Society A 368, 2435–2459.

Huizinga, R.J., 1996. Verification of vertically rotating flume using non-newtonian fluids. Journal of Hydraulic Engineering 122 (8), 456–459.

Hungr, O., Evans, S.G., 2004. Entrainment of debris in rock avalanches: an analysis of a long run-out mechanism. GSA Bulletin 116 (9/10), 1240–1252.

Imre, B., Laue, J., Springman, S.M., 2010. Fractal fragmentation of rocks within sturzstroms: insight derived from physical experiments within the ETH geotechnical drum centrifuge. Granular Matter 12, 267–285.

Iverson, R.M., 1997. The physics of debris-flows. Reviews of Geophysics 35 (3), 245–296.

Iverson, R.M., Denlinger, R.P., 2001. Flow of variably fluidized granular masses across three-dimensional terrain — 1. Coulomb mixture theory. Journal of Geophysical Research 106 (B1), 537–552.

Iverson, R.M., Logan, M., Denlinger, R.P., 2004. Granular avalanches across irregular three-dimensional terrain: 2. Experimental tests. Journal of Geophysical Research 109 (F01015), 1–16.

Iverson, R.M., Logan, M., LaHusen, R.G., Berti, M., 2010. The perfect debris-flow? Aggregated results from 28 large-scale experiments. Journal of Geophysical Research 115 (F03005), 1–29.

Jibson, R.W., Harp, E.L., Schulz, W., Keefer, D.K., 2006. Large rock avalanches triggered by the M 7.9 Denali Fault, Alaska, earthquake of 3 November 2002. Engineering Geology 83 (1–3), 144–160.

Kaitna, R., 2006. Debris-flow experiments in a rotating drum. PhD thesis, Universität für Bodenkultur, Vienna, 170 pp.

Kaitna, R., Rickenmann, D., 2007a. Flow of Different Material Mixtures in a Rotating Drum, Fourth International DFHM Conference: Mechanics, Prediction and Assessment, Chengdu.

Kaitna, R., Rickenmann, D., 2007b. A new experimental facility for laboratory debris-flow investigation. Journal of Hydraulic Research 45 (6), 797–810.

Kaitna, R., Rickenmann, D., Schneiderbauer, S., 2006. Comparative rheologic investigations in a vertically rotating flume and a 'moving-bed' conveyor belt flume. In: Lorenzini, G., Brebbia, C.A., Emmanouloudis, D.E. (Eds.), Monitoring, Simulation, Prevention and Remediation of Dense and Debris-flows. WIT Press, Rhodos, pp. 89–98.

Kaitna, R., Rickenmann, D., Schatzmann, M., 2007. Experimental study on rheologic behaviour of debris-flow material. Acta Geotechnica 2, 71–85.

Kern, M., Bartelt, P., Sovilla, B., Buser, O., 2009. Measured shear rates in dry and wet snow avalanches. Journal of Glaciology 55 (190), 327–338.

Kodama, Y., 1994. Experimental study of abrasion and its role in producing downstream fining in gravel-bed rivers. Journal of Sedimentary Research A64 (1), 76–85.

Korup, O., Schneider, D., Huggel, C., Dufresne, A., in press. Long-runout landslides. In: J. Shroder, R. Marston and M. Stoffel (Editors), Treatise on Geomorphology. Academic Press, San Diego, CA, 7.

Kotlyakov, V.M., Rototaeva, O.V., Nosenko, G.A., 2004. The September 2002 Kolka glacier catastrophe in North Ossetia, Russian Federation: evidence and analysis. Mountain Research and Development 24 (1), 78–83.

Legros, F., 2002. The mobility of long-runout landslides. Engineering Geology 63, 301–331.

Maeno, N., Arakawa, M., Yasutome, A., Mizukami, N., Kanazawa, S., 2003. Ice–ice friction measurements, and water lubrication and adhesion-shear mechanisms. Canadian Journal of Physics 81 (1–2), 241–249.

Mair, K., Frye, K.M., Marone, C., 2002. Influence of grain characteristics on the friction of granular shear zones. Journal of Geophysical Research 107 (B10), 9.

Major, J., Iverson, R.M., 1999. Debris-flow deposition: effects of pore-fluid pressure and friction concentrated at flow margins. Geological Society of America Bulletin 110, 1424–1434.

McArdell, B.W., Bartelt, P., Kowalski, J., 2007. Field observations of basal forces and fluid pore pressure in a debris-flow. Geophysical Research Letters 34 (L07406).

McSaveney, M.J., 2002. Recent rockfalls and rock avalanches in Mount Cook National Park, New Zealand. In: Evans, S.G., DeGraff, J.V. (Eds.), Catastrophic Landslides: Effects, Occurrence and Mechanism. Geological Society of America, Reviews in Engineering Geology. Geological Society of America Reviews in Engineering Geology, Boulder, Colorado, pp. 35–70.

McSaveney, M.J., Davies, T.R.H., 2007. Rockslides and their motion. In: Sassa, K., Fukuoka, H., Wang, F., Wang, G. (Eds.), Progress in Landslide Science. Springer, pp. 113–133.

Meriam, J.L., Kraige, L.G., 2006. Engineering Mechanics: Statics. Wiley and Sons.

Mikoš, M., Jaeggi, M.N.R., 1995. Experiments on motion of sediment mixtures in a tumbling mill to study fluvial abrasion. Journal of Hydraulic Research 33 (6), 751–772.

Noetzli, J., Gruber, S., 2009. Transient thermal effects in Alpine permafrost. The Cryosphere 3, 85–99.

Paola, C., Straub, K., Mohrig, D., Reinhardt, L., 2009. The "unreasonable effectiveness" of stratigraphic and geomorphic experiments. Earth-Science Reviews 97, 1–43.

Petrakov, D.A., Chernomorets, S.S., Evans, S.G., Tutubalina, O.V., 2008. Catastrophic glacial multi-phase mass movements: a special type of glacial hazard. Advances in Geosciences 14, 211–218.

Phillips, C.J., Davies, T.R.H., 1991. Determining rheological parameters of debris-flow material. Geomorphology 4 (2), 101–110.

Pierson, T.C., 2005. Hyperconcentrated flow — transitional process between water flow and debris-flow. In: Jakob, M., Hungr, O. (Eds.), Debris-flow Hazards and Related Phenomena. Springer, Berlin Heidelberg, pp. 159–202.

Pierson, T.C., Scott, K.M., 1985. Downstream dilution of a lahar: transition from debris-flow to hyperconcentrated streamflow. Water Resources Research 21 (10), 1511–1524.

Plafker, G., Ericksen, G.E., 1978. Nevados Huascarán avalanches, Peru. In: Voight, B. (Ed.), Rockslides and Avalanches, 1: Natural Phenomena. Elsevier, Amsterdam, pp. 277–314.

Prager, C., Krainer, K., Seidl, V., Chwatal, W., 2006. Spatial features of holocene sturzstrom-deposits inferred from subsurface investigations (Fernpass rockslide, Tyrol, Austria). Geo. Alp 3, 147–166.

Prinz, H., 1997. Abriss der Ingenieurgeologie. Ferdinand Enke Verlag, Stuttgart. 546 pp.

Rickenmann, D., 1999. Empirical relationships for debris-flows. Natural Hazards 19, 47–77.

Salzmann, N., Frei, C., Vidale, P.-L., Hoelzle, M., 2007. The application of Regional Climate Model output for the simulation of high-mountain permafrost scenarios. Global and Planetary Change 56 (1–2), 188.

Savage, S.B., 1984. The mechanics of rapid granular flows. Advances in Applied Mechanics 24, 289–366.

Savage, S.B., Hutter, K., 1989. The motion of a finite mass of granular material down a rough incline. Journal of Fluid Mechanics 199, 177–215.

Schneider, D., Bartelt, P., Caplan-Auerbach, J., Christen, M., Huggel, C., McArdell, B.W., 2010. Insights into rock–ice avalanche dynamics by combined analysis of seismic recordings and a numerical avalanche model. Journal of Geophysical Research 115 (F04026), 1–20.

Schneider, D., Huggel, C., Haeberli, W., Kaitna, R., in press. Unraveling driving factors for large rock–ice avalanche mobility. Earth Surface Processes and Landforms.

Shreve, R.L., 1966. Sherman Landslide, Alaska. Science 154 (3757), 1639–1643.

Straub, S., 1997. Predictability of long runout landslide motion: implications from granular flow mechanics. Geologische Rundschau 86 (2), 415–425.

Strużyński, A., Wyrębek, M., Strutyński, M., Kulesza, K., 2011. Cross-section changes in the lower part of a mountain river after the flood in spring 2010, as Presented by means of CCHE2D program. In: Rowinski, P. (Ed.), Experimental Methods in Hydraulic Research. Geoplanet: Earth and Planetary Sciences. Springer, Berlin Heidelberg, pp. 287–297.

Van Der Woerd, J., Owen, L.A., Tapponnier, P., Xiwei, X., Kervyn, F., Finkel, R.C., Barnard, P.L., 2004. Giant, M8 earthquake-triggered ice avalanches in the eastern Kunlun Shan, northern Tibet: characteristics, nature and dynamics. GSA Bulletin 116 (3/4), 394–406.

# Paper VI

EARTH SURFACE PROCESSES AND LANDFORMS
*Earth Surf. Process. Landforms* **36**, 1948–1966 (2011)

(wileyonlinelibrary.com) DOI: 10.1002/esp.2218

# Unraveling driving factors for large rock–ice avalanche mobility

**D. Schneider,[1]* C. Huggel,[1] W. Haeberli[1] and R. Kaitna[2]**
[1] Department of Geography, University of Zurich, Zurich, Switzerland
[2] Institute of Mountain Risk Engineering, University of Natural Resources and Life Sciences (BOKU), Vienna, Austria

Received 9 March 2011; Revised 16 July 2011; Accepted 26 July 2011

*Correspondence to: D, Schneider, Department of Geography, University of Zurich, Zurich, Switzerland. E-mail: demian.schneider@geo.uzh.ch

ESPL
Earth Surface Processes and Landforms

ABSTRACT: Large rock–ice avalanches have attracted attention from scientists for decades and some of these events have caused high numbers of fatalities. A relation between rock slope instabilities in cold high mountain areas and climate change is currently becoming more evident and questions about possible consequences and hazard scenarios in densely populated high mountain regions leading beyond historical precedence are rising. To improve hazard assessment of potential rock–ice avalanches, their mobility is a critical factor. This contribution is an attempt to unravel driving factors for the mobility of large rock–ice avalanches by synthesizing results from physical laboratory experiments and empirical data from 64 rock–ice avalanches with volumes $>1\text{x}10^6$ m$^3$ from glacierized high mountain regions around the world. The influence of avalanche volume, water and ice content, low-friction surfaces, and topography on the apparent coefficient of friction (as a measure of mobility) is assessed. In laboratory experiments granular ice in the moving mass was found to reduce bulk friction up to 20% while water led to a reduction around 50% for completely saturated material compared with dry flows. Evidence for the effects of water as a key driving factor to enhance mobility was also found in the empirical data, while the influence of the ice content could not be confirmed to be of much relevance in nature. Besides liquefaction, it was confirmed that mobility increases with volumes and that frictional surface characteristics such as flow paths over glaciers are also dominant variables determining mass movement mobility. Effects of the topography along the flow path as well as channeling are assumed to be other critical factors. The results provide an empirical basis to roughly account for different path and flow characteristics of large rock–ice avalanches and to find appropriate ranges for friction parameters for scenario modeling and hazard assessments. Copyright © 2011 John Wiley & Sons, Ltd.

KEYWORDS: rock–ice avalanche; mobility; glacial and periglacial high mountain environment; climate change; hazard assessment

## Introduction

Destabilization, mobilization, transport and deposition of material are part of the natural equilibrium between tectonic uplift and erosion processes over a wide range of time and volume scales. Owing to the changing climate, highly sensitive glacial and periglacial areas are currently undergoing dramatic changes, and most likely will do so even more in the near future (O'Connor and Costa, 1993; Haeberli and Hohmann, 2008; Hewitt *et al*., 2008; Radic and Hock, 2011). The most obvious changes are the decrease in thickness and area of glaciers leading to stress redistributions (debuttressing) and more or less deep seated slope instabilities such as the relatively slow collapse of the eastern Eiger flank in summer 2006 in the Swiss Alps (Oppikofer *et al*., 2008) or the rapid failure of large rock and ice masses in 1992 from Mt Fletcher in New Zealand (Evans and Clague, 1994). Rising mean annual air temperatures are causing enduring progressive permafrost degradation (Harris *et al*., 2003; Noetzli and Gruber, 2009; Ravanel *et al*., 2010) while percolation of melted water can advectively penetrate into bedrock along joints and therefore lead to thermal perturbation and fast modification of the mechanical conditions at depth (Gruber and Haeberli, 2007; Hasler *et al*., in revision). Such observations give evidence that the observed increase in frequency and magnitude of mass movements in glacial environments have a relation to climate change (Davies *et al*., 2001; Geertsema *et al*., 2006; Huggel *et al*., 2010).

The most hazardous and spectacular forms of slope instabilities in glacierized high mountains are far reaching rapid large rock and ice avalanches. In view of rising population pressure (e.g. in the European Alps and Andes), concern related to the hazard potential from such events is rising. The most disastrous historical events in high-mountain glacial and permafrost enviroments were the huge rock–ice avalanches from Nevado Huascarán in Peru in 1962 and 1970 with an estimated total death toll of 7000 to 22 000 people (Evans *et al*., 2009a; Plafker and Ericksen, 1978). In 2002, a similar event occurred in the Russian Caucasus where an enormous mass of 100–130 × $10^6$ m$^3$ of ice, rock, debris and soil rushed 20 km downstream at peak velocities of 90 m/s and caused 125 fatalities (Evans *et al*., 2009b; Haeberli *et al*., 2004; Huggel *et al*., 2005; Kotlyakov *et al*., 2004). The most well-known examples in the European Alps are the Altels ice avalanche which killed six people and 169 head of cattle in 1895 (Faillettaz *et al*., 2011), the collapse of retreating Allalin Glacier that caused 88 casualties on a hydropower construction site in 1965 (Röthlisberger, 1977), the Brenva rock–ice avalanche where two skiers died in 1997 and that also reached very close to the Mont Blanc tunnel entrance (Deline, 2009), and the Thurwieser rock avalanche in 2004 that travelled over a glacier and fortunately did not cause any loss of lives but was the first large event filmed by mountaineers (Rozman *et al.*, 2004; Sosio *et al.*, 2008). An inventory of glacial disasters in the Swiss Alps has documented 21 minor and major events and a total number of 440 casualties since the year 1595, of which the majority was related to glacial avalanches and debris flows (Raymond *et al.*, 2003; see also Glacierhazards, 2011). A database of a variety of glacier and permafrost disasters is also available on a global level (Flubacher *et al.*, 2007), but rock–ice avalanches are not yet consistently captured.

Such disastrous events together with the current and expected climatic developments call for more detailed studies on rapid large mass movements in glacial environments, particularly because no systematic analysis of their characteristics and flow behavior has been performed – apart from individual case studies – since the constitutive work of Evans and Clague (1988). In this contribution we analyze various factors affecting the apparent friction coefficient of rock–ice avalanches and try to extract the key variables determining their mobility.

## Theoretical Background

### Long runout mechanisms

The question why many large landslides (> 1 million m$^3$) reach runout distances exceeding those expected from conventional friction physics (Heim, 1932; Hsü, 1975; Davies and McSaveney, 1999; Erismann and Abele, 2001; Legros, 2002) has concerned scientists for decades and a variety of theories has been developed to explain this phenomenon. We first give an overview of these theories which are relevant for rapid mass movement dynamics (including rock–ice avalanches).

#### Volume effect

Heim (1932) found that the apparent friction coefficients $\mu_{app}$ (maximum drop height $\Delta H$ divided by maximum horizontal travel distance $L_{hor}$) for landslides progressively decrease with increasing volumes. Many other authors extended the dataset differentiating between various types of mass movements, such as debris flows/debris avalanches/rock avalanches/landslides (Scheidegger, 1973; Hsü, 1975; Okura *et al.*, 2003; Rickenmann, 2005), and different environmental settings like volcanic/non-volcanic (Dade and Huppert, 1998), glacial/non-glacial (Alean, 1985; Evans and Clague, 1988), subaerial/submarine (Legros, 2002), or Earth/Moon/Mars (Collins and Melosh, 2003; Harrison and Grimm, 2003), largely confirming this trend. At first sight this may seem astonishing because the runout distance in a simple sliding block model is independent of volume, however, disintegrated rapidly moving granular masses apparently behave differently.

Legros (2002) proposed that the velocity and hence the reach of a rapid granular mass movement depends on the slope and flow thickness. Indeed, flow resistance forces are determined by the slope and frictional characteristics of the interacting materials which together define the shear gradient that in turn controls the rate of deposition at the base. As soon as deposition starts, the shear layer moves progressively upwards (slope normally) to let the mass movement run out of material and stop entirely (see also Van Gassen and Cruden, 1989; Bartelt *et al.*, 2007). In other words, the forces acting against gravitational acceleration and previously gained momentum (frictional and viscous resistance) need to stop one layer after another from the base to the top. The stopping mechanism consequently takes more time for thicker mass movements than for thin and less voluminous ones. This time can be used to travel further and elongate the deposition lobe (Straub, 1997). In fact, the friction coefficient of the center of mass $\mu_{com}$ rather than the apparent friction coefficient $\mu_{app}$ defines the energy balance, and excess runout can only be achieved by corresponding early deposition of material (Figure 1; Straub, 1997; Davies, 1982; Campbell *et al.*, 1995). Okura *et al.* (2000) have experimentally confirmed the decrease of $\mu_{app}$ with increasing volume but also found $\mu_{com}$ to increase, possibly due to more frequent collisions between blocks (for number of particles $1 \leq n \leq 1000$ and volumes $0.001 \leq V \leq 1$ m$^3$). While the decrease of $\mu_{app}$ with increasing volume can be widely confirmed for large natural rapid mass movements, $\mu_{com}$ remains much more difficult to determine and precise field data is largely missing.

If friction at the base is reduced by any of the mechanisms presented in the following sections, the shear gradient gets sharper (thinner shear layer) and hence its upward migration (Imre *et al.*, 2010) that finally stops the flow is retarded. The consequence is endured preservation of the movement resulting in an enhanced runout in addition to the volume effect.

#### Theories related to dispersive pressure

In a granular mass that destabilizes and starts moving, the static friction coefficient reduces to a significantly lower dynamic friction (Straub, 1997). With increasing velocity, the mass leaves the frictional flow regime in which energy is dissipated by long-lasting frictional contacts and reaches the collisional flow regime where energy dissipates predominantly by short-lived collisional contacts between individual grains (Bagnold, 1954; Savage, 1984; Iverson and Denlinger, 2001) and the particle behavior resembles that of individual molecules in a gas (Campbell, 1990; Iverson *et al.*, 1997). The *granular agitation* energy is causing a randomly driven dispersive pressure which is also called *granular temperature* (due to the linkage to thermodynamics) or *random kinetic energy* (Bartelt *et al.*, 2006). This is expected to result in a volume increase (dilatation) and a further reduction of the internal shear resistance within the shear layer. The so-called *mechanical fluidization* (Davies, 1982) hence is driven by the avalanche movement itself (loss of potential energy) and the work done to overcome friction (frictional work rate). When the avalanche is thinning or decelerating, the production of random kinetic energy and its effect to reduce the friction coefficient starve (Bartelt *et al.*, 2007). This also explains the often observed abrupt stopping and sharp boundaries of rapid mass movements as well as the formation

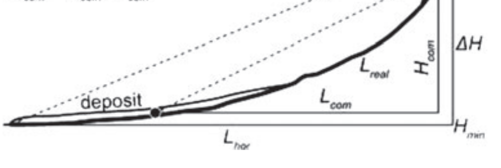

**Figure 1.** Schematic profile with different measures of the friction coefficients. Centres of mass are indicated by black dots. $\mu_{app}$, apparent coefficient of friction [−]; $\mu_{com}$, coefficient of friction of the center of mass [−]; $H_{max}$, maximum failure altitude [m a.s.l.]; $H_{min}$, minimum deposition altitude of [m a.s.l.]; $\Delta H$, total drop height ($H_{max}$ - $H_{min}$) [m]; $L_{hor}$, total horizontal runout distance [m]; $H_{com}$, drop height of center of mass [m]; $L_{com}$, horizontal runout distance of center of mass [m]; $L_{real}$, length of the real inclined path [m].

of pressure ridges (Davies, 1982; Eisbacher and Clague, 1984; Campbell, 1989; Hewitt, 2002).

A similar decrease of the shear resistance due to grain dilatation may be externally induced by the oscillating ground during an earthquake, such as hypothesized by McSaveney (1978) to be a reason for the extremely long runout of the Sherman Glacier rock-avalanche during the Alaskan earthquake of 1964, and as shown in small-scale laboratory experiments by Davies (1982). However, many long runout events do not occur during earthquakes. Melosh (1979) proposed that the energy needed to cause grain fluctuations may result from an acoustic source and called the effect *acoustic fluidization*. The initial collapse and subsequent flow of the rock material are assumed to generate high frequency pressure fluctuations which locally relieve overburden stresses, reducing frictional resistance (Collins and Melosh, 2003).

The *dynamic fragmentation* theory infers that dispersive pressure can also be generated by the rapid breakage of rock particles within force chains (or so-called grain bridges; Davies *et al.*, 1999, 2010; Campbell, 2002; Mair and Hazzard, 2007; Davies and McSaveney, 2009). Thereby, the elastic strain energy increases until the particle crushes and the stored energy converts into kinetic energy (pressure energy) and heat. The crushed fragments move away from the original center of mass, reducing the friction between these grains. This is also possible within a strongly confined shear layer and the resulting effective shear stress is a function of the overburden stress (flow thickness) and the strength of the intact material. That gives support to the observed volume effects as well as to the generally higher mobility of volcanic debris avalanches which comprise much more weakened material compared with non-volcanic events (Davies *et al.*, 2010).

All these mechanism do not require the presence of any lubricants such as water, air or molten rock, and therefore could also explain long runout landslides on Moon, Mars, Venus and other planets.

### Lubrication and fluidization

On Earth, most rapid mass movements are not completely dry and the presence of liquids strongly influences flow dynamics. Thereby we distinguish *lubrication* that is restricted on a thin basal layer and *fluidization* that affects larger parts of the flow body.

Kent (1966) and Shreve (1968) proposed air lubrication where rapid landslides may slide on a thin layer of compressed air after topographic jumps. However, the dynamic air pressures needed to support the overburden stresses are unrealistically high (Erismann and Abele, 2001), and agitated particles are relatively permeable so that air is likely to leak largely unhindered through the debris. Lubrication by water is much more realistic due to its incompressibility, as well as its higher density and viscosity (Legros, 2002). High water concentrations can be reached at the base of landslides e.g. by initial shearing within a highly saturated water-rich layer, entrainment of river water, shallow lakes, or water-saturated valley-fill deposits (Voight and Sousa, 1994; Hungr and Evans, 2004; Kelfoun and Druitt, 2005; Prager *et al.*, 2006; McSaveney and Davies, 2007). This may force pore water to support at least part of the landslide's weight and occasionally lead to hydroplaning (Voight and Sousa, 1994).

Evidence for lubrication by frictional heating was provided when layers of molten rock (frictionites) were found in several rock-avalanche deposits (Erismann, 1979; Legros *et al.*, 2000; De Blasio and Elverhoi, 2008; Weidinger and Korup, 2009). Refrozen snow observed at the base of snow avalanches gave further support to the relevance of frictional heating (Bartelt *et al.*, 2006; De Blasio and Elverhoi, 2008). Goguel (1978) even discussed steam generation along thin sliding planes which may elevate pore pressure and reduce shear resistance if permeability and diffusion rates of the overlying substrate are low enough (Goren and Aharonov, 2007). However, measured shear layers are often much thicker than they would be required to concentrate the frictional heat energy sufficiently to enable steam production (Davies *et al.*, 2006).

If water is not concentrated on a thin layer but affects the entire avalanche body, partial or complete saturation may evolve. Under unsaturated conditions water can stabilize soil and debris due to cohesion (particularly in combination with clays; McSaveney and Davies, 2007), but as soon as the pores become saturated, buoyancy forces strongly increase and support parts of the debris, reducing internal friction and finally fluidizing the mass. This effect can liquefy large amounts of friable material to form far reaching debris avalanches, debris flows or lahars, and has already been verified theoretically (Iverson, 2005), experimentally in artificial debris flow flumes (Iverson *et al.*, 2010a; Schneider *et al.*, 2011), as well as observed in natural debris flows (McArdell *et al.*, 2007). Water is therefore seen as one of the most important reasons for excess runout of rapid mass movements (Legros, 2006).

## Rapid mass movements in glacial environments

Evans and Clague (1988) stated that glacial environments can significantly enhance the runout distance of rapid mass movements by travelling on low-friction surfaces such as on glaciers, by melting of ice and snow due to frictional heating that causes pore pressure effects at the base of the moving mass or fluidizes the entire flow body, and by channeling or air-launching the debris by moraines. By means of numerical simulations, Bottino *et al.* (2002) quantified the observed runout distances of rock–ice avalanches in glacial environments to exceed predicted ones for pure rock avlanches by 30%. Sosio *et al.* (2008) compiled typical friction coefficients for different flow rheologies and avalanche types from retrospective numerical modeling in literature, where rock–ice avalanches ranged among the lowest values.

While it is evident that glacial environments increase the runout distance of rapid mass movements, individual involved processes are difficult to separate. Besides the mentioned interactions at the boundary, snow and ice also have effects on internal friction when they are incorporated into the granular mass either as ice or water (Schneider *et al.*, 2011). Three general possibilities exist about how ice can be incorporated in the moving mass, while most events include combinations of them:

- Failure of steep glaciers. Ice content is high to very high but debris may be eroded along the downstream path (Figure 2 (a)–(c)).
- Failure within bedrock or rock debris. Ice content ranges from high if entire overlying glaciers are entrained to low if permafrost from cleft systems or pore spaces is involved (Figure 2(d)–(f))
- Entrainment of snow, ice and frozen debris by rock-/debris avalanche passing over glaciers, snow or debris covered areas with seasonal frost or permafrost (potentially degraded). The amount of eroded ice strongly varies depending on the erosion rate and the entrained material (Figure 2 (g)–(i))

Hewitt (2002, 2009) classified rock avalanches in glacial environments according to topographic effects and related to their origin, and deposition areas. We define rock–ice

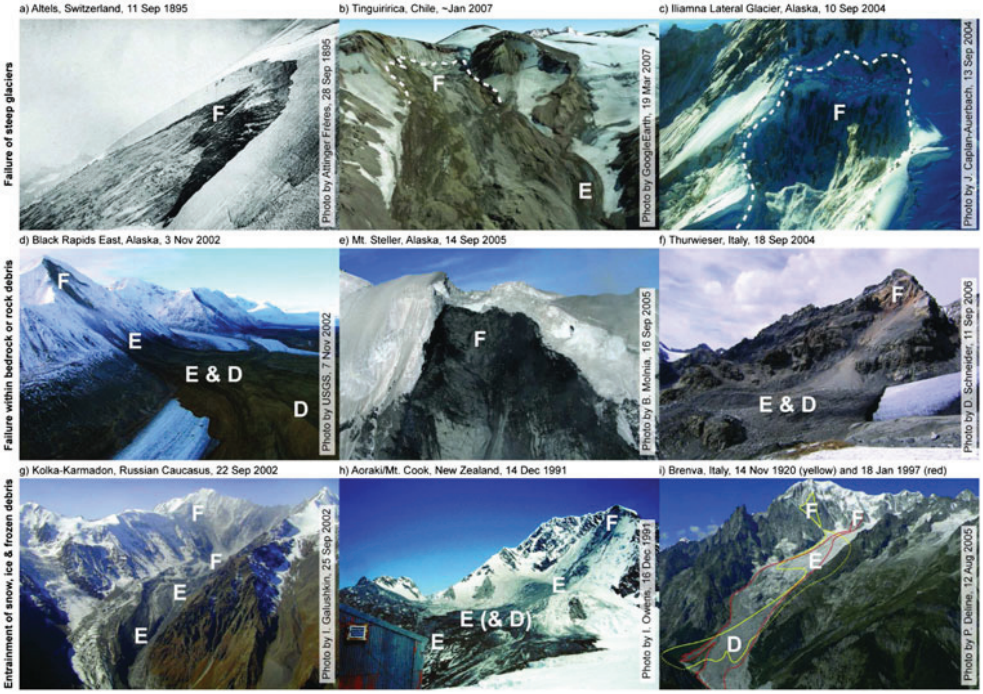

**Figure 2.** Rough classification of three different possibilities how ice can be involved in large rapid mass movements. Scar from failure zone in (b) and (c) is highlighted by white dashed line. F: failure zone; E: entrainment zone; D: deposition zone. Figure 2i is from Deline (2009). This figure is available in colour online at wileyonlinelibrary.com/journal/espl

avalanches generally as rapid mass movement events where ice is supposed to have influenced the runout dynamics either as underlying surface or as part of the moving mass. This includes a broad variety of rapid mass movement types, such as rock-, ice-, and debris avalanches, and debris flows. Many of the events discussed herein are difficult to classify in such a scheme because they have shown continuous flow transformations or involved process chains (Petrakov *et al*., 2008).

## Data and Method

### Observed events

To analyze individual processes involved, a list of rock–ice avalanche events around the globe was compiled and selected empirical parameters were extracted or derived (Table I). To restrict the dataset we used the following criteria for rapid mass movement events to be included:

- interaction with ice/snow: runout over glacial surface/significant snow cover, and/or ice was a considerable part of the moving mass;
- size: $V > 1 \times 10^6\,\mathrm{m}^3$ and $L_{hor} > 1\,\mathrm{km}$;
- flow dynamics: rapid, disintegrated, granular, avalanche-like movement;
- documentation and data availability;
- recent occurrence (primarily 20th and 21th century, some exceptions if well documented).

The table does not aim for a complete list of large rock–ice avalanches, but provides an overview of 64 well documented events and their key characteristics. We suppose that the smaller the volume (closer to $1 \times 10^6\,\mathrm{m}^3$), the older the date, and the more remote the location, the less complete is the dataset.

As a measure of the event size, we generally used deposit volumes and calculated mean values if they varied in different literature sources. Volumes of mass movements in literature usually are estimations and subject to considerable errors so that the precision of the estimates can be seen to be around ±50%. Likewise the ice and water content was scarcely quantified in literature and usually needed to be estimated from images and descriptions of the source area, travel path, and deposits. We estimate the error of the ice content to ±20% by volume and that of water to ±1 qualitative category, corresponding to ±20% (water content was classified in five qualitative categories). A further problem relates to strong variations of certain characteristics along the flow path. In these cases we used *characteristic values* which are assumed to best represent the event along the entire flow path and for the total duration (similar to a mode value).

To estimate the influence of topography-induced horizontal and vertical deflections of the moving mass, we derived a path deviation index $i_{pd}$ as a quantitative value:

$$i_{pd} = \frac{L_{real}}{L_{dir}} \tag{1}$$

where $L_{real}$ is the length of the real curved and inclined path of the avalanche and $L_{dir}$ the direct diagonal connection between highest and lowest points of the avalanche path (Figure 3). Simple flow lines corresponding to the position of the center of mass were reconstructed by means of available photos, maps and GoogleEarth®. Then they were exported into a GIS-environment to derive the needed length variables $L_{real}$, $L_{hor}$,

**Table I.** Overview and characteristics of 64 large rock-ice avalanches

| Country & date | Name of event | Abbreviation | Latitude [dec °] | Longitude [dec °] | Ice cont. [vol-%] | $H_{max}$ [m a.s.l.] | $H_{min}$ [m a.s.l.] | $L_{hor}$ [m] | $\mu_{app}$ [–] | $i_{pd}$ [–] | $W/L_{real}$ [–] | Ice content [–] | Qualitative liquefaction [–] | $i_g$ [–] | $i_{gd}$ [–] | $V$ [$10^6$ m$^3$] | Reference |
|---|---|---|---|---|---|---|---|---|---|---|---|---|---|---|---|---|---|
| Alps, Switzerland | | | | | | | | | | | | | | | | | |
| 27 Dec 1819 | Bisglacier | Bis1 | 46.1014 | 7.7219 | 100 | 4100 | 1602 | 5490 | 0.46 | 1.08 | 0.05 | 1.0 | very low | 0.53 | 0.53 | 13 | [1], [2] |
| ~20 Jul 1977 | Bisglacier | Bis2 | 46.1014 | 7.7219 | 100 | 4100 | 1602 | 5490 | 0.46 | 1.08 | 0.06 | 1.0 | very low | 0.53 | 0.53 | 1.5 | [3] |
| 19 Mar 1901 | Fletschhorn | Flho | 46.1703 | 8.0044 | 30 | 3775 | 1470 | 6001 | 0.38 | 1.16 | 0.04 | 0.3 | very low | 0.38 | 0.62 | 5 | [3], [5], [6], [7], [8] |
| 11 Sep 1895 | Altels | Alte | 46.4319 | 7.6744 | 100 | 3308 | 2154 | 3907 | 0.30 | 1.09 | 0.09 | 1.0 | very low | 0.00 | 0.00 | 5 | [3], [4] |
| 12 Sep 1973 | Balmhorn | Balm | 46.4328 | 7.6917 | 100 | 3000 | 1388 | 3127 | 0.52 | 1.11 | 0.06 | 1.0 | very low | 0.28 | 0.36 | 2 | [3] |
| Alps, Italy | | | | | | | | | | | | | | | | | |
| 12 Sep 1717 | Triolet | Trlt | 45.8917 | 7.0042 | 50 | 3400 | 1743 | 7450 | 0.22 | 1.78 | 0.06 | 0.5 | medium | 0.59 | 0.80 | 12 | [5], [8], [9], [10], [11] |
| 14 Nov 1920 | Brenva Gl. | Brv1 | 45.8283 | 6.8803 | 75 | 4200 | 1540 | 5621 | 0.47 | 1.19 | 0.09 | 0.8 | very low | 0.28 | 0.48 | 10 | [8], [9], [11], [12] |
| 18 Jan 1997 | Brenva Gl. | Brv2 | 45.8369 | 6.8833 | 70 | 3725 | 1400 | 5849 | 0.40 | 1.07 | 0.08 | 0.7 | very low | 0.41 | 0.81 | 6.5 | [8], [9], [11], [12] |
| 18 Sep 2004 | Thurwieser | Thrw | 46.4950 | 10.5256 | 10 | 3570 | 2274 | 2697 | 0.48 | 1.15 | 0.19 | 0.1 | very low | 0.14 | 0.14 | 2.5 | [13], [14] |
| Aug 2005 | Monte Rosa east face | Moro | 45.9364 | 7.8814 | 100 | 3700 | 2066 | 3438 | 0.48 | 1.04 | 0.13 | 1.0 | very low | 0.48 | 0.65 | 2.5 | [15] |
| Caucasus, Russia | | | | | | | | | | | | | | | | | |
| 20 Sep 2002 | Kolka-Karmadon | Kolk | 42.7322 | 44.4269 | 90 | 3368 | 1321 | 19379 | 0.11 | 1.16 | 0.03 | 0.9 | very high | 0.16 | 0.16 | 130 | [16], [17], [18], [19], [20], [21] |
| Alaska, USA | | | | | | | | | | | | | | | | | |
| 1960 | Iliamna Red Gl. | Ilr1 | 60.0281 | −153.0703 | 60 | 2125 | 653 | 5498 | 0.27 | 1.01 | 0.16 | 0.6 | low | 0.66 | 0.93 | 5 | [22] |
| 1978 | Iliamna Red Gl. | Ilr2 | 60.0281 | −153.0763 | 60 | 2310 | 528 | 7691 | 0.23 | 1.01 | 0.15 | 0.6 | low | 0.58 | 0.91 | 17 | [22] |
| 1980 | Iliamna Red Gl. | Ilr3 | 60.0281 | −153.0731 | 60 | 2193 | 514 | 7806 | 0.22 | 1.01 | 0.15 | 0.6 | low | 0.59 | 0.94 | 28 | [22] |
| 1994 | Iliamna Red Gl. | Ilr4 | 60.0281 | 153.0742 | 60 | 2230 | 434 | 9993 | 0.18 | 1.01 | 0.12 | 0.6 | low | 0.47 | 0.95 | 17 | [22] |
| 19 May 1997 | Iliamna Red Gl. | Ilr5 | 60.0281 | 153.0742 | 60 | 2230 | 524 | 7694 | 0.22 | 1.01 | 0.15 | 0.6 | low | 0.60 | 0.92 | 14 | [22] |
| 8 Aug 2000 | Iliamna Red Gl. | Ilr6 | 60.0281 | −153.0761 | 60 | 2310 | 478 | 8890 | 0.21 | 1.01 | 0.13 | 0.6 | low | 0.54 | 0.94 | 15 | [22] |
| 25 Jul 2003 | Iliamna Red Gl. | Ilr7 | 60.0281 | −153.0750 | 60 | 2256 | 487 | 8556 | 0.21 | 1.01 | 0.14 | 0.6 | low | 0.53 | 0.93 | 16 | [22] |
| 9 Feb 2004 | Iliamna Umbrella Gl. | Ilum | 60.0253 | −153.0872 | 50 | 2406 | 641 | 6036 | 0.29 | 1.04 | 0.05 | 0.5 | low | 0.67 | 0.92 | 4 | [22] |
| 10 Sep 2004 | Iliamna Lateral Gl. | Illa | 60.0356 | −153.0786 | 95 | 2560 | 820 | 5178 | 0.34 | 1.08 | 0.05 | 1.0 | low | 0.97 | 0.97 | 5 | [22] |
| 25 Sep 2008 | Iliamna Red Gl. | Ilr8 | 60.0281 | −153.0750 | 80 | 2256 | 548 | 7447 | 0.23 | 1.01 | 0.09 | 0.8 | low | 0.61 | 0.94 | 11 | [23] |
| 27 Mar 1964 | Sherman Gl. | Sher | 60.5328 | −145.1083 | 40 | 1224 | 246 | 5962 | 0.16 | 1.13 | 0.40 | 0.4 | very low | 0.90 | 0.90 | 12 | [24], [25], [26], [27], [28] |
| 27 Mar 1964 | Schwan Gl. | Schw | 60.8475 | −145.1503 | 40 | 2136 | 751 | 6476 | 0.21 | 1.05 | 0.29 | 0.4 | very low | 0.88 | 0.88 | 9 | [26] |
| 27 Mar 1964 | Steller Gl. 1 | Stg1 | 60.5492 | −143.2947 | 40 | 2900 | 1439 | 6846 | 0.21 | 1.05 | 0.21 | 0.4 | very low | 0.97 | 0.97 | 20 | [26] |
| 27 Mar 1964 | Bering Gl. 1 | Beg1 | 60.5483 | −143.2933 | 40 | 2841 | 959 | 5703 | 0.33 | 1.10 | 0.10 | 0.4 | very low | 0.82 | 0.82 | 8 | [26] |
| 27 Mar 1964 | Bering Gl. 2 | Beg2 | 60.5414 | −143.1706 | 40 | 2828 | 821 | 6748 | 0.30 | 1.09 | 0.10 | 0.4 | very low | 0.55 | 0.84 | 10 | [26] |

(*Continues*)

**Table 1.** (Continued)

| Country & date | Name of event | Abbreviation | Latitude [dec °] | Longitude [dec °] | Ice cont. [vol-%] | $H_{max}$ [m a.s.l.] | $H_{min}$ [m a.s.l.] | $L_{hor}$ [m] | $\mu_{app}$ [–] | $i_{pd}$ [–] | $W/L_{real}$ [–] | Ice content [–] | Qualitative liquefaction [–] | $i_g$ [–] | $i_{gd}$ [–] | $V$ [$10^6$ m$^3$] | Reference |
|---|---|---|---|---|---|---|---|---|---|---|---|---|---|---|---|---|---|
| 27 Mar 1964 | Bering Gl. 3 | Beg3 | 60.5178 | −143.1003 | 40 | 3054 | 775 | 5664 | 0.40 | 1.06 | 0.08 | 0.4 | very low | 0.60 | 0.85 | 6 | [26] |
| 1964 or 1965 | Allen | Alln | 60.7361 | −144.9711 | 40 | 1814 | 698 | 7659 | 0.15 | 1.03 | 0.16 | 0.4 | very low | 0.96 | 0.96 | 23 | [26] |
| 1965 | Fairweather | Fair | 58.9142 | −137.5597 | 40 | 4050 | 700 | 10197 | 0.33 | 1.13 | 0.09 | 0.4 | low | 0.53 | 0.76 | 26 | [26] |
| Jul 1983 | Marvine | Marv | 60.1056 | −140.3136 | 70 | 1650 | 790 | 3144 | 0.27 | 1.05 | 0.15 | 0.7 | very low | 0.65 | 0.65 | 3 | [3] |
| 3 Nov 2002 | McGinnis Peak North | Ginn | 63.5533 | −146.2697 | 30 | 2743 | 1025 | 10960 | 0.16 | 1.25 | 0.06 | 0.3 | low | 0.49 | 0.92 | 20 | [29] |
| 3 Nov 2002 | McGinnis Peak South | Gins | 63.5308 | −146.2661 | 30 | 2879 | 975 | 11463 | 0.17 | 1.10 | 0.06 | 0.3 | low | 0.53 | 0.88 | 11 | [29] |
| 3 Nov 2002 | Black Rapids East | Blke | 63.4383 | −146.1825 | 30 | 2181 | 1184 | 4605 | 0.22 | 1.33 | 0.41 | 0.3 | low | 0.43 | 0.65 | 14 | [29] |
| 3 Nov 2002 | Black Rapids Middle | Blkm | 63.4486 | −146.2539 | 30 | 2051 | 1224 | 4478 | 0.18 | 1.25 | 0.53 | 0.3 | low | 0.54 | 0.69 | 14 | [29] |
| 3 Nov 2002 | Black Rapids West | Blkw | 63.4519 | −146.2794 | 30 | 2034 | 1310 | 3307 | 0.22 | 1.04 | 0.48 | 0.3 | low | 0.53 | 0.63 | 10 | [29] |
| 3 Nov 2002 | West Fork Gl. North | Wfrn | 63.4492 | −147.4481 | 30 | 1867 | 1130 | 3296 | 0.22 | 1.16 | 0.23 | 0.3 | low | 0.35 | 0.70 | 4 | [29] |
| 3 Nov 2002 | West Fork Gl. South | Wfrs | 63.4372 | −147.4272 | 30 | 2086 | 1081 | 4249 | 0.24 | 1.06 | 0.18 | 0.3 | low | 0.41 | 0.63 | 5 | [29] |
| 14 Sep 2005 | Mt. Steller | Stel | 60.5186 | −143.0889 | 30 | 3100 | 667 | 9009 | 0.27 | 1.06 | 0.15 | 0.3 | low | 0.82 | 0.96 | 50 | [30] |
| Jul 2008 | Mt. Steller north 1 | Stn1 | 60.5442 | 142.9939 | 30 | 2300 | 1478 | 1767 | 0.47 | 1.04 | 0.17 | 0.3 | very low | 0.62 | 0.62 | 1.5 | [31] |
| Jul 2008 | Mt. Steller north 2 | Stn2 | 60.5533 | 143.0086 | 30 | 1932 | 1456 | 2200 | 0.22 | 1.09 | 0.21 | 0.3 | very low | 0.84 | 0.84 | 1.5 | [31] |
| 6 Aug 2008 | Mt. Miller | Mill | 60.4711 | 142.2189 |  | 2200 | 1290 | 4507 | 0.20 | 1.06 | 0.31 | 0.5 | very low | 0.81 | 0.81 | 22 | [31] |
| British Columbia, Canada |  |  |  |  |  |  |  |  |  |  |  |  |  |  |  |  |  |
| 1959 or 1960 | Pandemonium Creek | Pand | 51.9903 | −125.8011 | 50 | 2600 | 660 | 8105 | 0.24 | 1.32 | 0.05 | 0.5 | high | 0.08 | 0.08 | 6 | [28], [32] |
| 22 Jul 1975 | Devastation Gl. | Devs | 50.6014 | −123.5306 | 50 | 2010 | 840 | 6568 | 0.18 | 1.37 | 0.07 | 0.5 | high | 0.12 | 0.12 | 12 | [32] |
| 1986 | North Creek | Nocr | 50.6650 | −123.2328 | 30 | 1980 | 1235 | 2683 | 0.28 | 1.19 | 0.05 | 0.3 | medium | 0.39 | 0.59 | 2 | [32] |
| Jun 1997 | Mt. Munday | Mund | 51.3217 | −125.2194 | 20 | 3000 | 2100 | 4545 | 0.20 | 1.15 | 0.11 | 0.2 | very low | 0.91 | 0.91 | 5 | [32], [33] |
| 14 Sep 2000 | Tsar Mountain | Tsar | 52.0664 | −117.8011 | 40 | 2778 | 2110 | 2546 | 0.24 | 1.07 | 0.34 | 0.4 | very low | 0.65 | 0.75 | 4 | [34] |
| 24 Jul 2007 | Mt. Steele, Yukon | Stee | 61.1017 | −140.3050 | 30 | 4640 | 2788 | 5996 | 0.36 | 1.12 | 0.42 | 0.3 | low | 0.59 | 0.59 | 27 | [35] |
| 6 Aug 2010 | Capricorn Gl. | Capr | 50.6275 | −123.5017 | 10 | 2500 | 390 | 11315 | 0.21 | 1.27 | 0.03 | 0.1 | very high | 0.04 | 0.04 | 40 | [36] |
| Cascade volcanoes, Washington, USA |  |  |  |  |  |  |  |  |  |  |  |  |  |  |  |  |  |
| 6 Dec 1963 | Little Tahoma Peak | Lita | 46.8514 | −121.7106 | 20 | 3092 | 1437 | 6798 | 0.24 | 1.08 | 0.14 | 0.2 | low | 0.67 | 0.77 | 1 | [37], [38] |
| 31 Aug 1997 | Mt. Adams | Adm1 | 46.2006 | −121.4947 | 90 | 3650 | 2089 | 3995 | 0.39 | 1.05 | 0.06 | 0.9 | medium | 0.31 | 0.31 | 5 | [39] |
| 20 Oct 1997 | Mt. Adams | Adm2 | 46.2008 | −121.4803 | 80 | 3369 | 1686 | 4472 | 0.38 | 1.03 | 0.03 | 0.8 | medium | 0.22 | 0.47 | 4 | [39] |
| Cordillera Blanca, Peru |  |  |  |  |  |  |  |  |  |  |  |  |  |  |  |  |  |
| 10 Jan 1962 | Huascarán | Hua1 | −9.1036 | −77.6236 | 35 | 6396 | 2430 | 16880 | 0.23 | 1.12 | 0.05 | 0.4 | very high | 0.14 | 0.20 | 16 | [19], [27], [40], [41], [42] |
| 31 May 1970 | Huascarán | Hua2 | −9.1036 | −77.6236 | 30 | 6396 | 2430 | 16880 | 0.23 | 1.12 | 0.05 | 0.3 | very high | 0.14 | 0.20 | 58 | [20], [28], [40], [39], [42] |

(*Continues*)

**Table 1.** (Continued)

| Country & date | Name of event | Abbreviation | Latitude [dec °] | Longitude [dec °] | Ice cont. [vol-%] | $H_{max}$ [m a.s.l.] | $H_{min}$ [m a.s.l.] | $L_{hor}$ [m] | $\mu_{app}$ [–] | $i_{pd}$ [–] | $W/L_{real}$ [–] | Ice content [–] | Qualitative liquefaction [–] | $i_g$ [–] | $i_{gd}$ [–] | $V$ [$10^6$ m$^3$] | Reference |
|---|---|---|---|---|---|---|---|---|---|---|---|---|---|---|---|---|---|
| Chile | | | | | | | | | | | | | | | | | |
| 29 Nov 1987 | Estero Parraguirre | Parr | −33.3061 | −70.0139 | 40 | 4350 | 2104 | 17981 | 0.12 | 1.21 | 0.01 | 0.4 | very high | 0.00 | 0.08 | 15 | [43] |
| ~Jan 2007 | Tinguiririca | Ting | −34.8292 | −70.3478 | 70 | 3903 | 2477 | 8287 | 0.17 | 1.15 | 0.06 | 0.7 | medium | 0.11 | 0.11 | 14 | [44] |
| South Georgia | | | | | | | | | | | | | | | | | |
| 6 Sep 1975 | Lyell Gl. | Lygl | −54.3406 | −36.6619 | 90 | 1840 | 268 | 5171 | 0.30 | 1.10 | 0.09 | 0.9 | very low | 0.90 | 0.90 | 4 | [11], [45] |
| Pamir, Tajikistan | | | | | | | | | | | | | | | | | |
| 2002 | Vanch valley, Pamir | Vnch | 38.7928 | 72.0764 | 30 | 4726 | 3177 | 9138 | 0.17 | 1.29 | 0.06 | 0.3 | medium | 0.77 | 1.00 | 8 | [46] |
| Cashmir, Pakistan | | | | | | | | | | | | | | | | | |
| 29 Jul 1986 | Bualtar I | Bual | 36.1481 | 74.7219 | 10 | 4450 | 2960 | 4808 | 0.31 | 1.13 | 0.10 | 0.1 | very low | 0.59 | 0.59 | 10 | [47], [48] |
| Eastern Kunlun Shan, China | | | | | | | | | | | | | | | | | |
| 14 Nov 2001 | Burhan Budai Shan B2 | Bbs2 | 35.6639 | 94.2531 | 95 | 5675 | 4339 | 6000 | 0.22 | 1.06 | 0.04 | 1.0 | low | 0.60 | 0.60 | 4 | [49] |
| 14 Nov 2001 | Burhan Budai Shan B4 | Bbs4 | 35.6542 | 94.2064 | 95 | 5550 | 4520 | 4914 | 0.21 | 1.09 | 0.05 | 1.0 | low | 0.59 | 0.59 | 4 | [49] |
| 14 Nov 2001 | Kunlun Pass K2 | Kupa | 35.7525 | 93.5311 | 95 | 5390 | 5050 | 1552 | 0.22 | 1.05 | 0.09 | 1.0 | low | 0.00 | 0.00 | 2 | [49] |
| Southern Alps, New Zealand | | | | | | | | | | | | | | | | | |
| 1984 | Beelzebub Gl. | Blzb | −43.3028 | 170.7125 | 10 | 2206 | 1804 | 1012 | 0.40 | 1.26 | 0.44 | 0.1 | very low | 0.69 | 0.69 | 2 | [50] |
| 14 Dec 1991 | Aoraki/Mt. Cook | Cook | −43.5950 | 170.1419 | 50 | 3754 | 1034 | 7008 | 0.39 | 1.12 | 0.19 | 0.5 | low | 0.63 | 0.81 | 60 | [51] |
| 2 May 1992 & 16 Sep 1992 | Mt. Fletcher | Fltc | −43.4431 | 170.4944 | 20 | 2411 | 1047 | 3806 | 0.36 | 1.33 | 0.14 | 0.2 | very low | 0.47 | 0.64 | 10 | [51] |

$H_{max}$, maximum altitude of detachment area; $H_{min}$, minimum altitude of deposited material; $L_{hor}$, length of horizontally projected runout path; $\mu_{app}$, apparent coefficient of friction $((H_{max}\text{-}H_{min})/L_{hor})$; $i_{pd}$, path deviation index; $i_g$, ratio of glacier trajectory without significant debris cover $L_g$ to the real inclined path $L_{real}$; $i_{gd}$, ratio of glacier trajectory including significant debris cover $L_{gd}$ to the real inclined path $L_{real}$; $V$, deposition volume (incl. entrainment).

References: [1] Hanke (1966); [2] Raymond *et al.* (2003); [3] Alean (1984); [4] Faillettaz et al. 2011; [5] Eisbacher and Clague (1984); [6] Coaz (1910); [7] Noetzli *et al.* (2003); [8] Noetzli *et al.* (2006); [9] Bottino *et al.* (2002); [10] Deline and Kirkbride (2009); [11] Deline (2009); [12] Deline (2001); [13] Sosio *et al.* (2008); [14] Rozman *et al.* (2004); [15] Fischer *et al.* (2006); [16] Haeberli *et al.* (2003); [17] Haeberli *et al.* (2004); [18] Kotlyakov *et al.* (2004); [19] Huggel *et al.* (2005); [20] Petrakov *et al.* (2008); [21] Evans *et al.* (2009b); [22] Huggel *et al.* (2007); [23] Estimations from photos by G. McGimsey (USGS); [24] Shreve (1966); [25] Marangunic and Bull (1968); [26] Post (1968); [27] McSaveney (1978); [28] Erismann and Abele (2001); [29] Jibson *et al.* (2006); [30] Huggel et al. (2008a); [31] Huggel *et al.* (2010); [32] Evans and Clague (1988); [33] Delaney and Evans (2008); [34] Jiskoot (2010); [35] Lipovsky *et al.* (2008); [36] http://daveslandslideblog.blogspot.com/search?q=meager; [37] Crandell and Fahnestock (1965); [38] Sheridan *et al.* (2005); [39] Iverson (1997); [40] Plafker and Ericksen (1978); [41] Körner (1983); [42] Evans et al. (2009a); [43] Hauser (2002); [44] Iribarren Anacona and Bodin (2010); [45] Gordon *et al.* (1978); [46] Schneider (2006); [47] Hewitt (1988); [48] Hewitt (2009); [49] Van der Woerd *et al.* (2004); [50] Korup (2005); [51] McSaveney (2002).

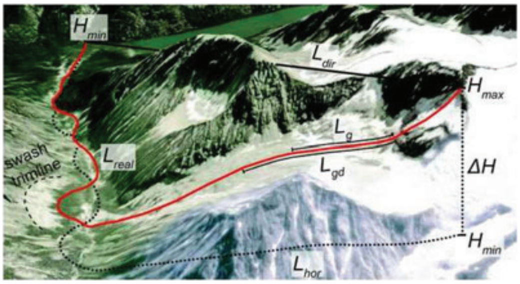

**Figure 3.** Different measures of path lengths (Pandemonium Creek avalanche, 1959 or 1960, perspective view). Dotted lines are subsurface, red line is on the surface, and full black line is the air-line. $L_{dir}$, direct diagonal connection between highest and lowest points of the avalanche path [m]; $L_g$, length of glacier trajectory without significant debris cover [m]; $L_{gd}$, length of glacier trajectory including significant debris cover [m]. See Fig. 1 for additional explanations. Background image by GoogleEarth®. This figure is available in colour online at wileyonlinelibrary.com/journal/espl

and $L_{dir}$ on the basis of the SRTM90-DEM (Shuttle Radar Topography Mission Digital Elevation Model at 90 m resolution). Additionally, the approximate characteristic width $W$ (in this study $W$ is equivalent to a median width) of the avalanches was estimated to calculate the width to length ratio $W/L_{real}$.

The path deviation index is assumed to be robust because $L_{real}$ and $L_{dir}$ are well defined and the measurement method based on the SRTM90-DEM is consistent. However, $L_{real}$ can be underestimated if the flow path is affected by strong topographic variations smaller than the grid size of 90 m, leading to lower $i_{pd}$. Because the characteristic width cannot be determined precisely, the width to length ratio probably involves larger uncertainties than $i_{pd}$. The error range of both parameters cannot be assessed accurately without any more precise DEM and flow path data. Nevertheless, we estimate the error of the path deviation index to be in the order of ±10% and that of the width to length ratio to be around ±20%.

The role of the glacier as low-friction surface was captured by the debris-free glacier path index $i_g$ and the debris-covered glacier path index $i_{gd}$:

$$i_g = \frac{L_g}{L_{real}} \tag{2}$$

and

$$i_{gd} = \frac{L_{gd}}{L_{real}} \tag{3}$$

where $L_g$ and $L_{gd}$ are the length of the runout path over glacier (glacier trajectory) without significant debris cover and the length including debris cover, respectively (Figure 3). This was also done with GoogleEarth® and by means of photos. Errors herein largely account for difficulties in determination of the boundary non-debris-covered/debris-covered glacier as well as in defining the end of the glacier, and are estimated to be smaller than ±10%.

## Laboratory data

We use laboratory data as a basis for the quantification of the effects of ice and water content on the bulk friction coefficient of gravel–ice mixtures for comparison with the previously described empirical data. Laboratory experiments with gravel–ice mixtures of varying fractions were performed in two vertically rotating drums, one with 2.4 m diameter in Vienna (Austria) and a second one with 4 m diameter in Berkeley (USA) (Schneider *et al.*, 2011). The two laboratory devices are described by Kaitna and Rickenmann (2007) and by Hsu *et al.* (2007), and the experiments with the gravel–ice mixtures by Schneider *et al.* (2011). Herein we used measurements of the dynamic bulk friction coefficients of cold ($T \approx -5\,°C$) and dry granular gravel–ice mixtures with varying volumetric ice contents (0.0856 $m^3$ material in the smaller drum and 0.4 $m^3$ in the larger drum). The data was recorded within the first 5 min of each series of predefined ice content. Therefore, no significant melting of the ice occurred and the effect of the amount of granular ice in the moving mass on the dynamic bulk friction can be assessed.

Furthermore we used the changing dynamic bulk friction coefficients of increasingly water saturated gravel–ice–water mixtures for longer experiment durations where the ice started melting and progressively saturated the remaining gravel–ice mixture (the longest run took 55 min to melt all ice). Water was detected by two pore water pressure sensors (*pwp*) as described by Kaitna and Rickenmann (2007) and the *pwp*-data was processed together with data from a normal load cell to the liquefaction ratio $Lq(t)$ depending on time $t$:

$$Lq(t) = \frac{pwp_{\mathrm{int}}(t)}{\sigma_{\mathrm{int}}(t)} \tag{4}$$

where $pwp_{int}(t)$ is the integrated pore water pressure and $\sigma_{int}(t)$ the integrated basal total normal stress along the entire flow profile in the rotating drum (Figure 4). The continuous data was reduced to 1-min averages for every second minute (minute 1, 3, 5, etc.). $Lq(t) = 1$ means that all grains (gravel and ice if still available) were supported by meltwater while $Lq(t) = 0$ says that no saturated pores are present along the flow profile. However, adhesive water can already be present in the granular mass.

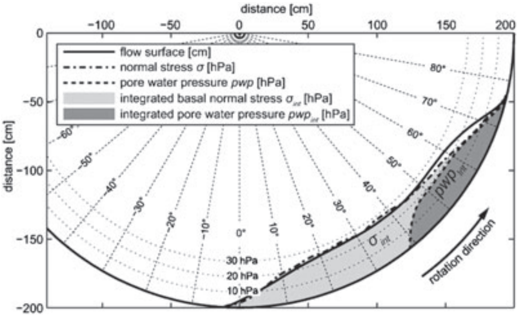

**Figure 4.** Measurements of a rock–ice mixture at time $t = 15$ min when some of the ice has melted in the larger rotating drum (Berkeley, USA, 50% ice by volume). Normal stress and pore water pressure pwp were recorded with corresponding instruments which were built in the drum and passed below the moving material once per rotation to record a profile. The flow surface was captured by a laser. Integrated pore water pressure pwpint and integrated basal total normal stress σint were calculated from the sum along each profile (σint includes the area which is overlaid by pwpint) and the liquefaction ratio Lq is given by pwpint/σint. Pore water pressure was only measured where the flow was entirely saturated and usually progressed from the tail to the front. Note that the units of σ and pwp are h Pa and the scale is adjusted to fit the laser data given in cm.

## Results and Discussion

### Spatial distribution of rock-ice avalanches

The rock–ice avalanches presented in Table I are distributed over most glacierized regions around the world as indicated in Figure 5(a). They seem to be clustered around north-western America and the European Alps which however may be related to bias in the data availability and documentation. Despite the climatically strongly varying regions, the altitudes of the highest elevations of the failure zones $H_{max}$ to latitude show a parabolic distribution (Figure 5(b)), which mirrors the general latitude distribution of the high-mountain cryosphere worldwide.

### Volume

To some degree the previously described trend of decreasing friction with increasing volumes is visible in Figure 6. However, the restricted volume range between 1 and $130 \times 10^6\,\mathrm{m}^3$ and large scatter in the y-direction make conclusions difficult. The correlation coefficient is low ($R = -0.291$) and for this reason, regression lines of the data were not plotted. Instead, regressions from Evans and Clague (1988) are shown for comparison. Most events plot around this regression curve for glacial events, but many of them are also much lower. On the other hand several events exhibit even higher apparent friction coefficients than could be expected for non-glacial events (circles above dotted line). In hazard assessments, percentiles and worst-case scenarios depending on the risk acceptance are usually more important than average values. Therefore, the 75, 90, and 100% percentiles of this data projected from the regression of the Evans and Clague (1988) glacial events (where 25, 10, and 0% of the 64 events are falling below) and the lowest boundary for apparent coefficients of friction depending on volumes that can be expected solely from this data for worst-case rock–ice avalanches are indicated.

The colors of the circles indicate a marginal trend of a reduced friction for longer glacial trajectories while the squares scatter around the lowest friction values with travelling only over relatively short distances on glacier surfaces. On that account we treat the latter group separately and relate it to events with special characteristics in the following. As suggested by Straub (1997) we assume that besides the errors included in the volumes the scatter may be induced by other factors some of which might be quantified or qualitatively captured.

### Topography

Despite rapid mass movements becoming less sensitive to topographic features with increasing velocity and volume, topography remains the most important driving factor for their propagation and spreading behavior (Alean, 1985; Nicoletti and Sorriso-Valvo, 1991; Legros, 2002). The runout paths of large rock or rock–ice avalanches can be unconstrained but often are affected by more or less abrupt slope changes, interfluve overflows, caroming or swash effects (Hewitt, 2002; Hewitt *et al.*, 2008). We used the path deviation index $i_{pd}$ described by Equation 1 to quantitatively assess the topographic characteristics along the flow paths. The underlying hypothesis is that events with higher apparent friction coefficients might have higher path deviation indices, meaning that major vertical and horizontal changes in flow direction (meandering) imply an energy loss. Such a trend is not obvious in Figure 7(a) so that we also did not plot regression lines, but it is remarkable that most events have runout paths which usually are 101–120% of the direct diagonal connection between the highest and lowest points $L_{dir}$. The Triolet event of 1717 (Italy) has an exceptionally high path deviation index $i_{pd}$ due to its nearly 180° turn but it still reached a relatively low apparent coefficient of friction. This exceptionally high path deviation index could also suggest that the location of the source area, which was only based on toponymy, is incorrect. The avalanche scar of 1717 may have been located in the central or eastern part of the Triolet upper basin instead of the west part, thereby reducing $i_{pd}$ significantly (but it would remain higher than 1.30 because such a path still includes at least a 90° turn).

Due to the lack of a strong trend in this plot, we conclude that such a topographic influence is not predominant on the

**Figure 5.** (a) Distribution of compiled large rock–ice avalanche events in the world. (b) Latitude versus altitude of avalanche source areas with regression line (dashed line). Clusters are regionally named and individual events labeled according to Table I. AK: Alaska (USA); BC: British Columbia (Canada); AL: European Alps; WA: Washington State (USA).

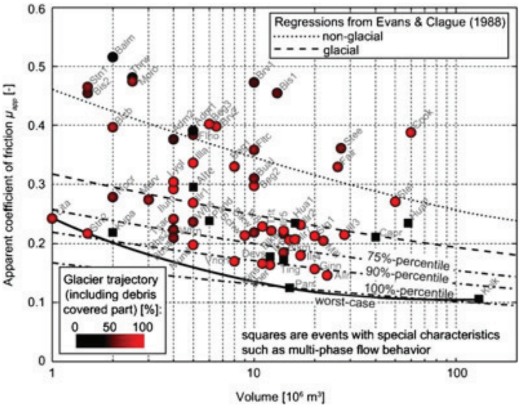

**Figure 6.** Relation of rock–ice avalanche volumes to apparent coefficient of friction (semi-logarithmic plot). Note that uncertainties of volumes are around ±50%. Squares indicate events with special characteristics (e.g. multi-phase flow behavior) and circles relate to all other events from Table I. Colorcodes of the data points relate to the relative length of the glacier trajectory. 75, 90, and 100% percentiles of this data are projected from the Evans and Clague (1988) regression for glacial events. Furthermore, the lower limit for empirical worst case scenarios according to the presented data is indicated. This figure is available in colour online at wileyonlinelibrary.com/journal/espl

measured scale. The 90 m x 90 m grid size of the SRTM90-DEM excludes smaller terrain variations which might be important for abrupt energy losses. Extremes, such as instantaneous vertical and horizontal deflections close to 90°, can absorb most of the kinetic energy (Nicoletti and Sorriso-Valvo, 1991). The consequence is a drop of the kinetic energy where the mass is decelerated or stopped completely (Okura *et al.*, 2003; see also energy line concept by Sheridan, 1979). The amount of this drop strongly depends on the strength of the break in slope – a single break of 30° has a much stronger impact than two smaller breaks each with 15° (Perla *et al.*, 1980; Alean, 1984). Strong and sharp breaks in slope are smoothed in the SRTM90-DEM topography and their effects are therefore underestimated in the presented path deviation index. The sensitivity of rapid mass movement on terrain variations generally decreases with increasing volumes (Christen *et al.*, 2010). However, we suggest that sharp small-scale terrain variations ($10^0$–$10^1$ m) possibly have a stronger influence on flow dynamics of large rapid mass movements than relatively smooth large-scale terrain variations ($10^2$–$10^3$ m) within the flow path. Further studies using high-resolution DEMs (and/or less accurate versions) may help on this issue.

Evans and Clague (1988) have found that channelizing effects of Neoglacial lateral moraines below current glacier limits funnel the moving mass and lead to a velocity increase. Nicoletti and Sorriso-Valvo (1991) have shown that any topographic structure preventing the moving material from spreading (mainly the form of the valley cross-section) can enhance runout because it reduces mechanical energy dissipation by keeping flow depths high (Legros, 2002; see Chapter 2.1). However, very narrow channels can in turn lead to a more efficient transmission of frictional resistance forces into the core of the avalanche comparable to a decreasing hydraulic radius (Chow, 1959). The most efficient channels consequently should be U-shaped but also require a considerable flow depth. V-shaped valleys can also be quite efficient while on laterally unconfined slopes the material thins and stops much earlier. Because this influence was too difficult to measure and quantify for all events, we used the width to length ratio of the entire flow path to characterize how much channeled the flows were (Figure 7(b)). Many flows hence reached more than 10 times further than their characteristic widths ($W/L_{real} \leq 0.1$), which is an indicator for the degree of channeling. The most channelized flows are those of Kolka-Karmadon and Estero Parraguirre which reached runout distances of 40 and 90 times the characteristic width, respectively. However, there are also some highly mobile flows that were very wide ($W/L_{real} > 0.3$), such as the Sherman and Black Rapids avalanches, which possibly would have reached much further if they had been more confined. On the other hand, the effect of very narrow channels to decelerate avalanches can be seen preferentially for smaller avalanches such as for those from Bisglacier and Balmhorn, the latter of which also included a vertical step of nearly 400 m. As a result, we again do not observe a clear dependence of the apparent coefficient of friction on the width to length ratio and suppose that it is hidden by other effects. Some examples with different flow path topographies are given in Figure 8(a)–(c).

The path deviation index could be improved by applying more accurate DEMs so that terrain variations are better represented. For a comparison between different events, a consistent DEM source and resolution is required that makes today ASTER G-DEM (global DEM from Advanced Spaceborne Thermal Emission and Reflection Radiometer stereo imagery) the only alternative on a global scale having a somewhat higher resolution than the SRTM90-DEM (Hayakawa *et al.*, 2008) while on national scales much higher resolutions are

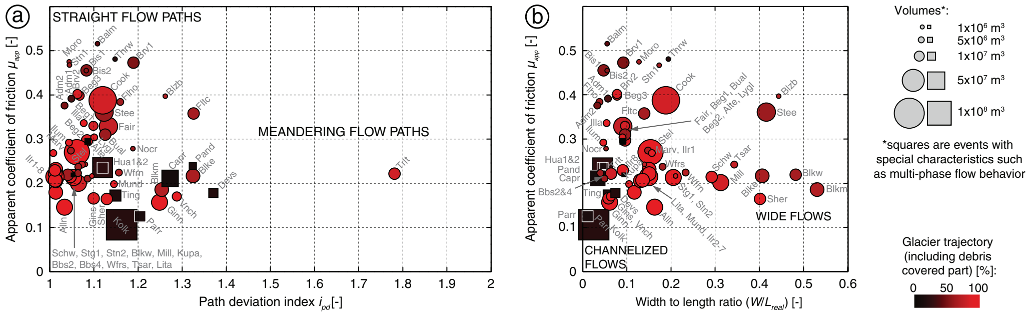

**Figure 7.** Influence of topography on apparent friction coefficient. (a) Path deviation index $i_{pd} = L_{real}/L_{dir}$ derived from SRTM90-DEM data as a measure of the deviation of the real flow path from a perfect straight incline and (b) width to length ratio $W/L_{real}$ as a measure of lateral confinement. Regression lines are not indicated due to low correlation coefficients ($R < 0.234$). This figure is available in colour online at wileyonlinelibrary.com/journal/espl

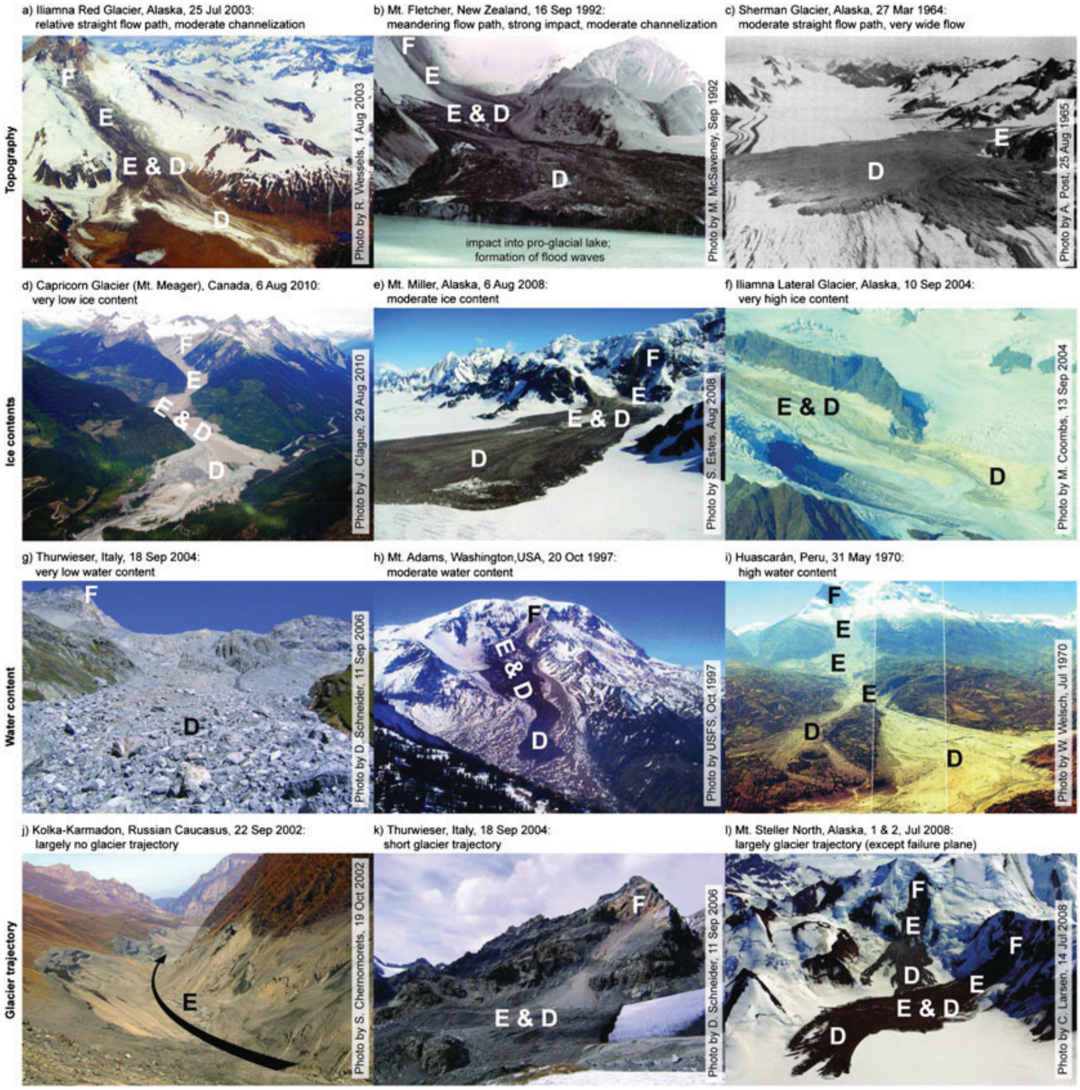

a) Iliamna Red Glacier, Alaska, 25 Jul 2003: relative straight flow path, moderate channelization

b) Mt. Fletcher, New Zealand, 16 Sep 1992: meandering flow path, strong impact, moderate channelization

c) Sherman Glacier, Alaska, 27 Mar 1964: moderate straight flow path, very wide flow

d) Capricorn Glacier (Mt. Meager), Canada, 6 Aug 2010: very low ice content

e) Mt. Miller, Alaska, 6 Aug 2008: moderate ice content

f) Iliamna Lateral Glacier, Alaska, 10 Sep 2004: very high ice content

g) Thurwieser, Italy, 18 Sep 2004: very low water content

h) Mt. Adams, Washington,USA, 20 Oct 1997: moderate water content

i) Huascarán, Peru, 31 May 1970: high water content

j) Kolka-Karmadon, Russian Caucasus, 22 Sep 2002: largely no glacier trajectory

k) Thurwieser, Italy, 18 Sep 2004: short glacier trajectory

l) Mt. Steller North, Alaska, 1 & 2, Jul 2008: largely glacier trajectory (except failure plane)

**Figure 8.** Examples for the factors topography, ice content, water content, and glacier trajectory. Note that in all examples more than a single factor is relevant. F: failure zone; E: entrainment zone; D: deposition zone; USFS: United States Forest Service. This figure is available in colour online at wileyonlinelibrary.com/journal/espl

sometimes available. The width to length ratio is a possible measure of lateral confinement but subject to uncertainties related to the method by which the characteristic width *W* is determined (e.g. mean, median, mode and based on calculations or estimations).

## Ice content

The apparent coefficient of friction describes the reach of a rapid mass movement and is related to the internal and boundary friction (bulk friction) which are depending on the material properties such as grain size (including clay content), angularity, and material (water content is treated in the next section). The only factor varying for different events that we can roughly estimate is the ice content as a material with frictional properties strongly different from those of any other lithology (Figure 8(d)–(f)). Furthermore we have quantified the influence of the ice content on the friction coefficients in a number of laboratory experiments (Schneider *et al.*, 2011) that can be used for comparison with the real events.

The rotating drum experiments revealed bulk friction values between 0.50 and 0.72 for varying volumetric ice contents while real events having an estimated ice content of 10–100% reach much lower apparent coefficients of friction between 0.11 and 0.52 (Figure 9). The friction coefficient in the laboratory experiments linearly decreases with increasing ice content, leading to a ~20% reduction of the friction for dry granular pure ice compared with gravel only (Schneider *et al.*, 2011). The field data again does not obviously reveal such a trend except for the events with multi-phase flow behavior (squares) where a slight trend for lower apparent coefficients of friction with higher ice contents could be

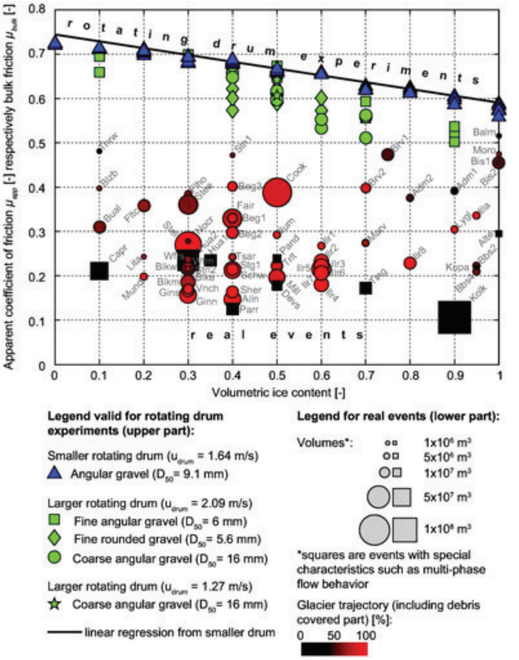

**Figure 9.** Influence of volumetric ice content on apparent coefficient of friction. Results from laboratory experiments are shown in the upper part of the figure, in blue for the smaller rotating drum and in green for the larger rotating drum. The black line represents the linear regression of the smaller drum experiments ($R = -0.99$). The strength of the effect of ice on reducing the friction in the smaller rotating drum thereby is at 20% for pure ice compared with gravel only. Empirical data from real events are presented in the lower section of the figure and colored from black to red depending on the relative length of the trajectory over glacier surface. Regression line is not indicated due to low correlation coefficient ($R < 0.295$). $D_{50}$ is the median grain size.

demonstrated. However, such a statement remains vague in view of the large observed scatter.

## Pore water pressure

A special category of rapid mass movements in glacial environments are those which evolve from sliding to turbulent avalanche-like movement and later transform into highly mobile debris flows either due to (1) strong water saturation of the failing mass (Evans *et al.*, 2007), (2) impacts in natural or artificial lakes followed by flood waves and lake outburst (Clague and Evans, 2000), (3) entrainment of water saturated valley fills (McDougall and Hungr, 2005), (4) mixing with water from the stream network (Pierson, 1986), (5) meltwater generation from entrained ice and snow due to frictional heating (Huggel *et al.*, 2005; Goren and Aharonov, 2007), and (6) a combination of all factors. Petrakov *et al.* (2008) proposed the term *catastrophic glacier multi-phase mass movements* for these highly hazardous events. However, water already has an effect on landslide mobility before complete liquefaction occurs and the transition between dry rock avalanches or landslides to saturated debris flows is gradual (Figure 8(g)–(i); Legros, 2006).

Pore water saturation and ongoing liquefaction were measured in the laboratory experiments. Figure 10 (upper part) reveals a strong dependency of the bulk friction coefficient on the liquefaction ratio. The complete liquefied mass reveals a bulk friction coefficient which is reduced by nearly 50% compared to the friction values of the dry flows (on the very left side in Figure 10). For the data of real events which were classified to five qualitative liquefaction classes we see that all events with strong or very strong liquefaction reached low apparent friction coefficients below 0.25 while only some of those with low and very low liquefaction were that mobile (Figure 10, lower part). Hence we can conclude that strongly liquefied flows are always very mobile, but dryer flows can be mobile as well if other factors are reducing the friction. This can, for example, include low-friction surfaces such as described in the next section.

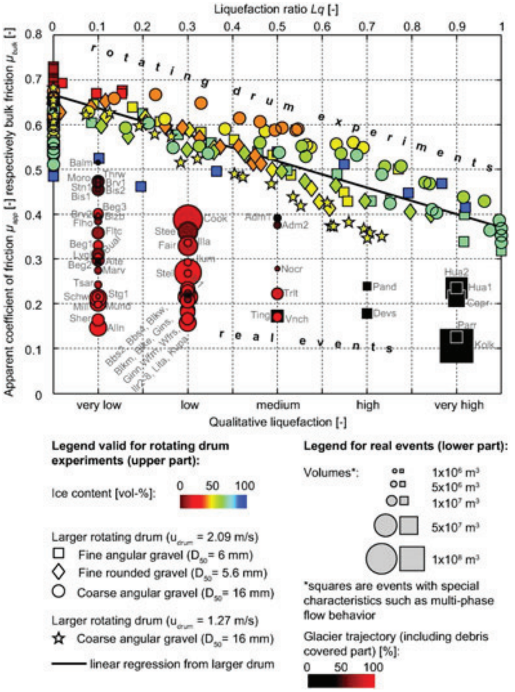

**Figure 10.** Influence of water on apparent coefficient of friction. Results from the larger rotating drum are in the upper part of the figure and colored from dark red to dark blue. The liquefaction ratio gives the amount of the entire material that is saturated (fully supported by liquid phase). Full liquefaction in the rotating drum reduced friction by approximately 50% compared to the friction of the dry mixtures. Qualitative liquefaction of the empirical data from real events is based on estimations according to descriptions in literature, reports and photos, and shown in the lower part of the figure. The data points are colored in black to red depending on the relative length of the trajectory over glacier surface. The qualitative data can be roughly compared to the quantitative laboratory data. However, regression lines are not shown because of the qualitative character of the data. $D_{50}$ is the median grain size.

## Low-friction surfaces

In rapid granular flows, higher surface roughness increases the size of the shear zone and finally leads to shorter runout distances (Cleary and Campbell, 1993). In glacial environments, glaciers usually provide surfaces with low friction (however, the friction can be significantly increased on debris covered glaciers and in highly crevassed zones until debris or terrain irregularities have been removed by entrainment or deposition). This may be due to the low friction of ice or due to a continuous supply of water at the bottom of the avalanche by frictional melting of ice (Huggel *et al.*, 2005). The effects of glaciers as a low-friction sliding surface for rock, ice and debris was best demonstrated by the 1964 Alaskan earthquake when dozens of very large rock avalanches were triggered in the Chugach Mountains (National Research Council, 1968). Some of them slid many kilometers over relatively flat glacier surfaces, such as the famous Sherman Glacier avalanche and those on Schwan, Steller, and Bering Glaciers (Post, 1968).

Figures 8(j)–(l) show some examples of shorter and longer glacier trajectories and Figure 11 gives an overview concerning the quantitative influence of the glaciers as low-friction surfaces on the apparent coefficient of friction. We distinguish between the relative path lengths leading over glacier (glacier trajectory) with and without the debris covered part (left and right subfigures), and ice and water content (upper and lower subfigures). By excluding those events with special characteristics, such as multi-phase flow behavior (squares), we find some moderate correlation coefficients of −0.650 for the glacier trajectories including debris cover and −0.448 for glacial trajectories without any significant debris cover. This indicates that glaciers reduce the boundary friction nearly independently of their debris cover, probably due to sudden entrainment of the mostly thin debris covers by an overflowing rapid mass movement.

We do not find any trends in the distribution of the ice content in Figure 11(a) and 11(b) that suggests the ice content to be not dominant. In contrast to this, the water content in Figure 11(c) and 11(d) clearly separates the events with high and very high water contents from those with medium to very low water contents. This fact and the differences in flow behavior which are described in the corresponding references (see Table I) led us to separate them from those data points which are depicted as circles. Most of the events shown as squares have multi-phase flow behavior such as described by Petrakov *et al.* (2008). It is remarkable that multi-phase flows usually do not pass much over glacial trajectories but are among the events with the highest mobilities. Three events that did not show clear multi-phase flow behavior were included in this group: Altels, Tinguiririca, and Kunlun Pass. They have shown exceptionally high mobility despite very low water contents and without flowing over a glacier. For the Altels and Tinguiririca cases, we assume that the surface-parallel bedding planes and the smooth rock surface provided low-friction surfaces as well (see also Figure 2(a) and 2(b)). The Kunlun Pass avalanche data is sparse and we did not find an obvious reason for its high mobility but it might be related to the relative straight and channelized flow path or to the earthquake. Figure 11(c) and 11(d) therefore show that the apparent coefficients of friction of rapid mass movement events involving medium to very low water contents significantly depend on the relative lengths of their flow paths leading over glacier surfaces and that even debris covered surfaces have the potential to increase runout distances. It needs to be noted that for most events, the failure zone represents a considerable part of the flow path which usually consists of bedrock and therefore does not count as glacier surface. This means that for many events, the section which is not leading over glaciers is at the upper part of the flow path rather than at the distal end, and hence, most flows remain within glacial limits. On the

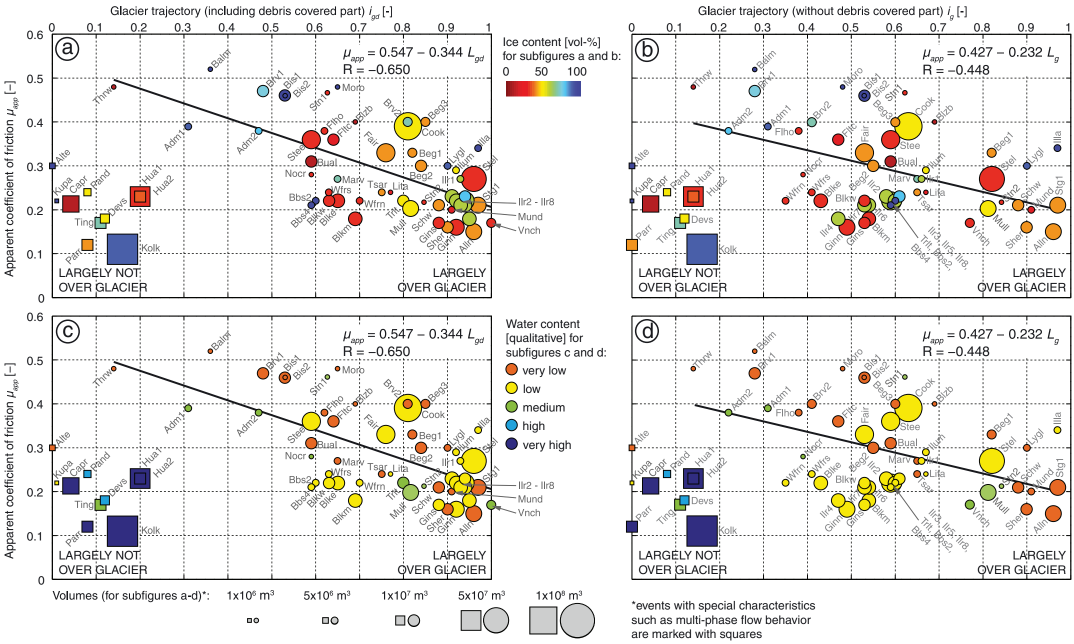

*events with special characteristics such as multi-phase flow behavior are marked with squares

**Figure 11.** Influence of glacier trajectories on apparent coefficients of friction. Colors of individual events depict the estimated volumetric ice content (a, b), and qualitative water content (c, d). For subfigures (a) and (c), the debris covered parts were included in the path length while they were excluded in (b) and (d). Black lines represent the linear regressions; corresponding equations for $\mu_{app}$ and the correlation coefficients *R* are indicated (for all events plotted as circles). The events plotted as squares exhibit low apparent coefficient of friction values despite that their flow paths predominantly did not lead over glaciers. Subfigures (c) and (d) indicate that most of them had much higher water contents while descriptions in the corresponding references reveal that they clearly involved multi-phase flow behavior and therefore are treated separately.

other hand, Figure 11(a) and 11(b) also indicate that if events are passing beyond glacial limits, they often turn into multiphase flow behavior and reach very high mobilities.

## General Discussion

### Importance of analyzed parameters

We have seen that large rock–ice avalanches occur in glacial regions all around the world, although the number of unreported cases might be high (but decreasing for increasing event magnitude). It is difficult to separate individual processes that influence avalanche mobility due to the diversity of the processes, their complex interlacing, and uncertainties related to many parameters. Measurement and estimation errors as well as the variation of parameters during the event (in space and time) complicate the derivation of characteristic values. However, we can say that glacier trajectory, water content and possibly the volume are among the strongest parameters determining rock–ice avalanche mobility and that most of the presented parameters have the potential to be enhanced by improvements of the datasets (Figure 12). For example, the path deviation index could be improved by using DEMs with higher resolution than the SRTM90-DEM, so that terrain variations in the order of some decameters which are still relevant for rock–ice avalanches of volumes between $10^6$ and $10^8\,m^3$, would be better represented. The volume effect also could be better quantified, either with more precise volume estimations or by including a larger number of smaller and larger events than used in this dataset. Other effects like grain size distribution, angularity, strong impacts, and other low-/high-friction surfaces were not analyzed, but some of the presented parameters represent extreme cases of the mentioned categories and therefore mark the upper boundary of a possible influence (ice content is a material property such as the lithology; glacier trajectory is a special type of a low-friction surface). Within an improved dataset, a third dimension could be introduced in Figure 12 for those cases with relatively high correlation coefficients: e.g. the slope of a linear correlation which describes strength of each effect on the apparent coefficient of friction.

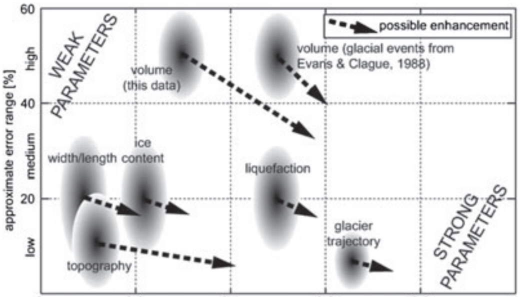

**Figure 12.** Classification of the presented parameters according to their error ranges and the signal strength (empirical data). Their location can be seen with respect to their strength/weakness to affect the apparent coefficient of friction. Gradients indicate the approximate fuzziness of the estimated error ranges and corresponding influence on the correlation coefficients. Possible enhancements of the parameters by more precise data are indicated by dashed arrows where the lengths of the arrows represent the maximal expected degree of improvement. Volumetric data from Evans and Clague (1988) achieves a higher correlation coefficient due to a wider volume range of the included events.

Effects of topography are likely to be underestimated by the presented parameters and are supposed to be a dominant factor if impacts and strong deviations could be adequately included. For example, the effects of topographic features smaller than the DEM grid size, such as smaller moraines of a few decameters in width and height or large boulders in the downstream path are not adequately included in the SRTM90-DEM (Christen *et al.*, 2010; Huggel *et al.*, 2008b). On the other hand, the surface can be significantly modified by the mass movement itself, particularly on glaciers and friable material. Larger rapid mass movements are likely to erode debris cover on ice, entirely remove serac zones, and fill crevasses with material so that smoother surfaces are generated and the boundary roughness is additionally reduced. This effect is also of great importance for potential subsequent mass movement events (Alean, 1985). Whether, entrainment enhances or decreases the mobility of the mass movement depends on the eroded material (e.g. water content, internal static friction angle), the slope angle, and the availability of erodible material (Hungr and Evans, 2004; Iverson *et al.*, 2010b; Mangeney *et al.*, 2010). Entrainment and deposition can directly affect the frictional characteristics of the surface that has been found to be a dominant factor if they are much different from 'normal' friction, such as over glaciers or sometimes also smooth bedrock. Glacier trajectories can therefore be seen as extremely low friction surfaces having major impacts on mass movement mobility.

The ice content was found to have a significant influence on the bulk friction coefficient in the laboratory experiments where most other variables were held constant. Nevertheless, this effect could not be clearly verified for the natural events probably because its effect is actually limited and/or overprinted by other factors. In view of the abundance of individual parameters and the corresponding uncertainties it is remarkable to see effects of individual factors at all. In turn, the lack of obvious trends for a specific factor in the database is no evidence for the absence of any effects but indicates at least a restricted influence of the corresponding factor (e.g. ice content).

The high mobility of the multi-phase flows without any long trajectories over glaciers is remarkable and most likely to be related to the high water content. These flows pose critical threats because they can reach far below glacial and periglacial limits into inhabited regions. Liquid water as a dominant factor for mass movement mobility gets more abundant in lower areas because it is stored as ground and pore water in erodible sediments as well as incorporated ice in the moving mass melts more efficiently by advective mixing with entrained debris having temperatures above 0 °C and due to frictional heating. These effects can provide a continuous supply of water in order that high pore pressures can be reached and maintained over longer distances.

The drum experiments involved monodisperse angular grains and volumes that were $10^7$–$10^9$ times smaller than the real events. We applied Froude-scaling and found a variety of dimensionless numbers to be not far from those of several case studies (Schneider *et al.*, 2011). However, full dynamic similarity is not possible and the projection of the laboratory experiment to real events remains delicate. Nevertheless, laboratory experiments are helpful tools to assess the influence of individual factors that is not possible in nature. The generally higher friction coefficients from the rotating drum experiments (Figures 9 and 10) are supposed to be due to the described volume effects on the one hand, but on the other hand also likely to be a consequence of the lack of other effects that might reduce friction further, such as low friction surfaces or dispersive pressure effects. If the influence of ice or water needs to be projected on natural events, the reduction of the friction coefficients need to be done on a relative rather than on an absolute basis.

## Relevance of dispersive pressure theories

Theories related to dispersive pressure could not be analyzed because these processes are extremely difficult to quantify for that many events but they definitively play an important role in large rapid mass movements. A key to enhance the understanding of the processes at the base of flows, such as caused by granular agitation (e.g. by random kinetic energy or dynamic fragmentation), might be the analysis of seismograms of rapid mass movements that are likely to be linked to the frictional work rate and topographic effects (Favreau *et al.*, 2010; Schneider *et al.*, 2010). The underlying hypothesis is that the emitted seismic energy is proportional to the frictional work rate done by the avalanche as well as it reflects strong impacts of the mass. The frictional work rate controls the dispersive pressure in the shear layer and hence steers how much the internal frictional resistance is reduced either by random kinetic energy (Bartelt *et al.*, 2006), or by dynamic fragmentation (Davies *et al.*, 2010). Therefore, seismic data could also help to validate dispersive pressure theories and to quantify the amount of energy absorption due to topographic impacts.

We assume that the presence of water generally damps the effects of dispersive pressure. Related to dynamic fragmentation, Davies and McSaveney (2009) concluded that these effects are probably marginal and might be overtopped by the effect of water to enhance mobility. Figure 10 provides evidence that high water contents necessarily reduce friction but in turn are not necessarily needed for high mobility which is likely due to the presence of dispersive pressure effects.

Because rock strength is a driving parameter within the dynamic fragmentation theory (Davies *et al.*, 2010), the low strength of ice in rock–ice avalanches might also increase mobility similar to the weak material commonly present in volcanic debris avalanches of high mobility. Compressive strength of ice is strongly temperature-dependent, but in the range 5–10 MPa for temperatures between 0 °C and −5 °C (Petrovic, 2003). This is about 25–50 times lower than the strength of intact rock (~250 MPa; Davies *et al.*, 2010) while the density of snow and ice which affects the overburden pressure is 3–8 times lower compared with rock and debris. The influence of rock strength and material density on avalanche and landslide mobility will require intensive further investigations. Ice could thereby be a well suited material due to its significantly reduced strength and density.

Other types that reach high mobility are very turbulent rapid mass movements in the highly collisional regime and those flowing over smooth glacier surfaces without any strong steps, deflections, and runups. Many of these events were triggered by strong earthquakes so that friction might have been additionally reduced by extended ground vibrations (McSaveney, 1978). We conclude that the lowest friction values can only be achieved by combinations of several of the described factors. One of the most extreme examples is the Kolka-Karmadon event where a huge volume of 130 x $10^6$ m$^3$ of primarily ice and water ran partially over a glacier which was incorporated into the moving mass and strongly channelized on a relative straight flow path until the mass was blocked by a narrow gorge (Haeberli *et al.*, 2004; Huggel *et al.*, 2005). On the other side, the Thurwieser event involved a much smaller volume of nearly pure dry rock that fell and spread unchannelled over a short part of glacier to be partially air launched, impacted, and finally blocked in a small bouldery funnel-shaped side valley (Sosio *et al.*, 2008).

## Implications for hazard assessments

The presented point clouds in Figures 6, 7, 9, 10, and 11 mirror the natural variability, measurement precision, and current knowledge of some characteristics of large rock–ice avalanches. Low correlations of individual parameters make it difficult to find robust threshold values and to achieve reasonable predictions such as by means of numerical avalanche models. Figure 6 includes lower boundaries for the apparent coefficients of friction of worst-case scenarios depending on event volumes and the 75%, 90%, and 100% percentiles projected from the Evans and Clague (1988) regression of rapid mass movements in glacial environments that might be used in hazard assessments. Note that these percentiles might underestimate friction coefficients particularly in the volume-range between 1 and 10 million m$^3$ where corresponding extremely mobile real events are rare or missing in the presented database (left part between the 90% and 100% percentile lines in Figure 6). In contrast to this, the indicated worst-case scenario line delineates the lower boundary of friction coefficients of the most mobile events for all volume categories. In fact, authorities need to consider local risk acceptance for high magnitude/low frequency events and apply cost-benefit analysis to decide for an appropriate level of risk. In a first step, the empirical data in Figure 6 can help to find a basis for the mobility of a potential large rock–ice avalanche with a given volume. As our results suggest, it is important to narrow the range of possible apparent friction coefficients in following steps by estimating the influence of ice, water, glacier trajectory, and possible other effects. Figures 9–11 thereby provide a (semi-) quantitative basis to decide for higher or lower friction values depending on the assumed characteristics of the potential rock–ice avalanche. Numerical dynamic avalanche models then need to be adjusted so that the modeled maximum runout fits the determined apparent coefficient of friction based on the empirical data.

If full dynamic similarity of a numerically modeled dynamic avalanche to a real event is required (rather for retrospective modeling and process understanding than for hazard assessments), friction parameters need to be adjusted for individual flow path sections. This can mainly be done on a relative basis according to changes in surface friction and of the flowing material such as varying contents of rock, ice and water or different grain characteristics (lithology, angularity, size).

In future work, an extension of the database, more precise data and further differentiation of individual event types could serve as a basis for an improved multifactor analysis. If the influence of individual factors could be quantified more precisely, rock–ice avalanche runout predictions as needed for hazard maps or during emergency hazard assessments could be further improved. However, to be realistic, isolating individual factors in natural large-scale avalanches will continue to be much more difficult compared with controlled laboratory conditions. Thus, the presented figures provide a first (semi-) quantitative basis that is very useful to estimate the mobility of large rock–ice avalanches under the current level of understanding.

Recent studies have found an increase in volumes and frequencies of rapid mass movements in high mountain areas that is supposed to be related to atmospheric warming, permafrost degradation, glacial recession and associated debuttressing. Such developments have consequences in high mountain areas, particularly where they are populated or developed. In hazard assessments, it also needs to be considered that the new hazard situations generally reduce the applicability of empirical historic information as a basis for future events (Haeberli and Beniston, 1998). The mobility of rock–ice avalanches might be reduced by increasingly smaller glaciers (low-friction surfaces), but could be enhanced by other effects such as higher altitudes of detachment zones, stronger water saturation of failing and erodible materials e.g. in extraordinarily warm summers, and the generally more abundant erodible debris. The largest hazard potential is expected from process chains, such as from rock or rock–ice avalanches falling into existing or future lakes that generate flood waves leading to failure or progressive erosion of moraine, ice or landslide dams and possibly causing subsequent debris flows which can reach much further (Clague and Evans, 2000; Korup and Tweed, 2007; Haeberli and Hohmann, 2008; Frey *et al.*, 2010).

## Conclusions

The mobility of large rock–ice avalanches is assumed to be controlled by many factors, including the volume, topography, ice and water content, and the frictional characteristics of the surface over which the avalanche is flowing (particularly glacial surfaces). As shown by many other authors, we could confirm in the present study that larger volumes tend to increase mobility, however, scatter is large due to the high variability of flow and surface characteristics. Surprisingly, the downstream topography was not found to significantly influence mobility but is still likely to be a key factor because the path deviation index as parameterized in this study probably underestimates the effects of strong impacts. Lateral confinement is also a relevant factor for mobility but difficult to quantify. The presented width to length ratio is an attempt to measure channelization but quantification on the basis of the hydraulic radius concept for individual channel sections may lead to more representative results. However, this is time-intensive for a large number of events and requires more precise data.

According to the laboratory experiments, the ice content in the moving mass reduced bulk friction by about 20%. This effect is not visible in the empirical data so that it might not be a dominant but more likely a secondary factor in reducing bulk friction which is blurred by other effects. In the same laboratory experiments, increasing water content reduced the bulk friction coefficient by nearly 50% for completely liquefied flows compared with dry granular masses. In contrast to the ice content, the effect of the water content could also be observed in the empirical data: events with high water contents reach much further while those with low water contents are usually less mobile. However, the mobility of dry rapid mass movements can also be enhanced by other factors.

The effect of low-friction surfaces on extending runout distances was analyzed using the percentage of the flow path leading over glacier surfaces (ratio of glacier trajectory). We found that the avalanche mobility significantly increased for events with larger ratios of the glacier trajectory ($i_g$ or $i_{gd}$). Debris cover on glaciers is not relevant, probably due to rapid entrainment of the debris layer. It is important to note that low-friction surfaces may also be provided by smooth bedrock planes and that multi-phase flows can also reach high mobilities without extended glacial trajectories.

Most of the parameters analyzed may be significantly enhanced by improvements of the dataset. A reduction of uncertainties could help in separating individual factors which influence rapid mass movement mobility. In future studies, other effects such as dispersive pressure-related mechanisms and corresponding friction reduction should be considered in addition to the presented parameters. They are much more difficult to be quantified but seismic data may provide deeper insights to these mechanisms.

For hazard assessments of future events, dynamic avalanche models should be adjusted to fit empirical apparent coefficients of friction from events having similarities to the considered scenario. Figures 6, 7, 9, 10, and 11 provide a first semi-quantitative basis to assess the mobility of potential large rock–ice avalanches with given characteristics. Thereby, scenarios going beyond historical evidence need to be considered to account for new hazard situations from glacial and periglacial areas due to climate change. Reduced slope stability can be related to permafrost degradation and glacial debuttressing while new glacial lake formations provide a potential for chain reactions such as avalanche impact waves leading to subsequent debris flows (flow transformations). This includes large rock–ice avalanches passing glacial limits and evolving to events with multi-phase flow behavior reaching much further and having an extremely destructive potential. Such events usually involve many factors that enhance mobility, such as large volumes, water and ice contents, glacier trajectories or smooth bedrock, and lateral confinement (catastrophic glacier multi-phase mass movements; Petrakov *et al.*, 2008). Several tragic events have demonstrated the potential for extreme runout of large rapid mass movements if certain conditions are fulfilled. In a changing climate, such scenarios need to be considered more carefully.

## NOTATION

| | |
|---|---|
| $D_{50}$ | median grain size [mm] |
| $H_{max}$ | maximum altitude of detachment area [m a.s.l.] |
| $H_{min}$ | minimum altitude of deposited material [m a.s.l.] |
| $i_g$ | ratio of glacier trajectory without significant debris cover $L_g$ to the real inclined path $L_{real}$ [–] |
| $i_{gd}$ | ratio of glacier trajectory including significant debris cover $L_{gd}$ to the real inclined path $L_{real}$ [–] |
| $i_{pd}$ | path deviation index [–] |
| $L_{dir}$ | direct diagonal connection between highest and lowest points of the avalanche path [m] |
| $L_g$ | length of glacier trajectory without significant debris cover [m] |
| $L_{gd}$ | length of glacier trajectory including significant debris cover [m] |
| $L_{hor}$ | length of horizontally projected runout path [m] |
| $L_{real}$ | length of the real curved and inclined path of the avalanche [m] |
| $Lq$ | liquefaction ratio [–] |
| $pwp_{int}$ | integrated pore water pressure of entire profile [Pa] |
| $V$ | deposit volume (incl. entrainment) [$10^6$ m$^3$] |
| $W$ | characteristic width of the avalanche [m] |
| $\Delta H$ | drop height of the avlanche [m] |
| $\mu_{app}$ | apparent coefficient of friction [–] |
| $\mu_{bulk}$ | bulk friction coefficient [–] |
| $\mu_{com}$ | coefficient of friction of the center of mass [–] |
| $\sigma_{int}$ | integrated basal total normal stress of entire profile [Pa] |

*Acknowledgements*—This work was supported financially by the Swiss National Foundation grant NF 200021-121823/1 (Rock–ice avalanches: a systematic investigation of the influence of ice) and the Austrian Science Foundation grant J2837-N10. The rotational drums were provided by the Department of Earth and Planetary Science at the University of California Berkeley (UCB) in cooperation with the National Center for Earth-surface Dynamics (NCED) and by the Institute of Mountain Risk Engineering (IAN) at the University of Natural Resources and Life Sciences in Vienna (BOKU). The laboratory experiments were heavily supported by William Dietrich, Leslie Hsu, Stuart Foster, Fritz Zott, Dieter Rickenmann, Johannes Hübl, Brian McArdell, and Perry Bartelt. We also would like to acknowledge the very helpful reviews of Philip Deline and another anonymous reviewer.

## References

Alean J. 1984. *Untersuchungen über die Entstehungsbedingungen und Reichweiten von Eislawinen. Mitteilungen der Versuchsanstalt für Wasserbau, Hydrologie und Glaziologie*. VAW/ETH: Zürich Vol. **74**, 217 pages.

Alean J. 1985. Ice avalanches: some empirical information about their formation and reach. *Journal of Glaciology* **31**(109): 324–333.

Bagnold RA. 1954. Experiments on a gravity-free dispersion of large solid spheres in a Newtonian fluid under shear. *Royal Society of London* **225**: 49–63.

Bartelt P, Buser O, Platzer K. 2006. Fluctuation-dissipation relations for granular snow avalanches. *Journal of Glaciology* **52**(179): 631–643.

Bartelt P, Buser O, Platzer K. 2007. Starving avalanches: Frictional mechanisms at the tails of finite-sized mass movements. *Geophysical Research Letters* **34**(L20407): 1–6.

Bottino G, Chiarle M, Joly A, Mortara G. 2002. Modelling rock avalanches and their relation to permafrost degradation in glacial environments. *Permafrost and Periglacial Processes* **13**(4): 283–288.

Campbell CS. 1989. Self-lubrication for long runout landslides. *Journal of Geology* **97**(6): 653–665.

Campbell CS. 1990. Rapid granular flows. *Annual Review of Fluid Mechanics* **22**: 57–92.

Campbell CS. 2002. Granular shear flows at the elastic limit. *Journal of Fluid Mechanics* **465**: 261–291.

Campbell CS, Cleary PW, Hopkins M. 1995. Large-scale landslide simulations: Global deformation, velocities and basal friction. *Journal of Geophysical Research* **100**(B5): 8267–8283.

Chow VT. 1959. *Open-Channel Hydraulics*. McGraw-Hill: New York.

Christen M, Bartelt P, Kowalski J. 2010. Back calculation of the *In den Arelen* avalanche with RAMMS: interpretation of model results. *Annals of Glaciology* **51**(54): 161–168.

Clague JJ, Evans SG. 2000. A review of catastrophic drainage of moraine-dammed lakes in British Columbia. *Quaternary Science Reviews* **19**: 1763–1783.

Cleary PW, Campbell CS. 1993. Self-lubrication for long runout landslides: examination by computer simulation. *Journal of Geophysical Research* **98**(B12): 21911–21924.

Coaz JWF. 1910. *Statistik und Verbau der Lawinen in den Schweizeralpen*. Stämpfli: Bern, Switzerland.

Collins GS, Melosh HJ. 2003. Acoustic fluidization and the extraordinary mobility of sturzstroms. *Journal Of Geophysical Research* **108**(B10): 2473–2487.

Crandell DR, Fahnestock RK. 1965. Rockfalls and avalanches from Little Tahoma Peak on Mount Rainier Washington, Geological Survey Bulletin.

Dade WB, Huppert HE. 1998. Long-runout rockfalls. *Geology* **26**(9): 803–806.

Davies TRH. 1982. Spreading of rock avalanche debris by mechanical fluidization. *Rock Mechanics* **15**(1): 9–24.

Davies TRH, McSaveney MJ. 1999. Runout of dry granular avalanches. *Canadian Geotechnical Journal* **36**: 313–320.

Davies TRH, McSaveney MJ. 2009. The role of rock fragmentation in the motion of large landslides. *Engineering Geology* **109**: 67–79.

Davies MCR, Hamza O, Harris C. 2001. The effect of rise in mean annual temperature on the stability of rock slopes containing ice-filled discontinuities. *Permafrost and Periglacial Processes* **12**: 137–144.

Davies TRH, McSaveney MJ, Beetham RD. 2006. Rapid block glides: slide-surface fragmentation in New Zealand's Waikaremoana landslide. *Quarterly Journal of Engineering Geology & Hydrogeology* **39**: 115–129.

Davies TRH, McSaveney MJ, Hodgson KA. 1999. A fragmentation-spreading model for long-runout rock avalanches. *Canadian Geotechnical Journal* **36**: 1096–1110.

Davies TRH, McSaveney MJ, Kelfoun K. 2010. Runout of the Socompa volcanic debris avalanche, Chile: a mechanical explanation for low basal shear resistance. *Bulletin of Volcanology* **72**: 933–944.

De Blasio FV, Elverhoi A. 2008. A model for frictional melt production beneath large rock avalanches. *Journal of Geophysical Research* **113**(F02014): 1–13.

Delaney KB, Evans SG. 2008. Application of digital cartographic techniques in the characterization and analysis of catastrophic landslides; the case of the 1997 Mount Munday rock avalanche, British Columbia. In *4th Canadian Conference on Geohazards: From Cause to Management*, Locat J, Perret D, Turmel D, Demers D, Leroueil S (eds). Presse de l'Université Laval, University Laval: Québec, Canada; 141–146.

Deline P. 2001. Recent Brenva rock avalanches (Valley of Aosta): new chapter in an old story? *Geografia Fisica e Dinamica Quaternaria* **V**: 55–63.

Deline P. 2009. Interactions between rock avalanches and glaciers in the Mont Blanc massif during late Holocene. *Quaternary Science Reviews* **28**(11–12): 1070–1083.

Deline P, Kirkbride MP. 2009. Rock avalanches on a glacier and morainic complex in Haut Val Ferret (Mont Blanc Massif, Italy). *Geomorphology* **103**(1): 80–92.

Eisbacher H, Clague JJ. 1984. Destructive mass movements in high mountains: hazard and management. Geological Survey of Canada Paper 84–16, Ottawa.

Erismann TH. 1979. Mechanics of large landslides. *Rock Mechanics* **12**(1): 15–46.

Erismann TH, Abele G. 2001. *Dynamics of Rockslides and Rockfalls*. Springer: Heidelberg.

Evans SG, Clague JJ. 1988. Catastrophic rock avalanches in glacial environments. In *Landslides - Proceedings of the Fifth International Symposium on Landslides*, Bonnard C (ed.). A.A.Balkema/Rotterdam/Brookfield: Switzerland. 1153–1158.

Evans SG, Clague JJ. 1994. Recent climatic change and catastrophic geomorphic processes in mountain environments. *Geomorphology* **10**(1–4): 107–128.

Evans SG, Bishop NF, Smoll LF, Valderrama Murillo P, Delaney KB, Oliver-Smith A. 2009a. A re-examination of the mechanism and human impact of catastrophic mass flows originating on Nevado Huascarán, Cordillera Blanca, Peru in 1962 and 1970. *Engineering Geology* **108**(1–2): 96–118.

Evans SG, Guthrie RH, Roberts NJ, Bishop NF. 2007. The disastrous 17 February 2006 rockslide-debris avalanche on Leyte Island, Philippines: a catastrophic landslide in tropical mountain terrain. *Natural Hazards and Earth System Sciences* **7**: 89–101.

Evans SG, Tutubalina OV, Drobyshev VN, Chernomorets SS, McDougall S, Petrakov D, Hungr O. 2009b. Catastrophic detachment and high-velocity long-runout flow of Kolka Glacier, Caucasus Mountains, Russia in 2002. *Geomorphology* **105**: 314–321.

Faillettaz J, Sornette D, Funk M. 2011. Numerical modeling of a gravity-driven instability of a cold hanging glacier: reanalysis of the 1895 break-off of Altelsgletscher, Switzerland. *Journal of Glaciology* **57** (205): 817–831.

Favreau P, Mangeney A, Lucas A, Crosta G, Bouchut F. 2010. Numerical modeling of landquakes. *Geophysical Research Letters* **37**(L15305).

Fischer L, Kääb A, Huggel C, Noetzli J. 2006. Geology, glacier retreat and permafrost degradation as controlling factors of slope instabilities in a high-mountain rock wall: the Monte Rosa east face. *Natural Hazards and Earth System Sciences* **6**: 761–772.

Flubacher M, Huggel C, Kääb A, Zemp M. 2007. Web-based database on worldwide glacier and permafrost disasters. *Geophysical Research Abstracts* **9**(04374).

Frey H, Haeberli W, Linsbauer A, Huggel C, Paul F. 2010. A multi-level strategy for anticipating future glacier lake formation and associated hazard potentials. *Natural Hazards and Earth System Sciences* **10**: 339–352.

Geertsema M, Clague JJ, Schwab JW, Evans SG. 2006. An overview of recent large catastrophic landslides in northern British Columbia, Canada. *Engineering Geology* **83**: 120–143.

Glacierhazards. 2011. Glacier hazards database, www.glacierhazards.ch, University of Zurich, Switzerland, last accessed March 2011.

Goguel J. 1978. Scale-dependent rockslide mechanisms, with emphasis on the role of pore fluid vaporization. In *Rockslides and Avalanches, 1: Natural Phenomena*, Voight B (ed.). Elsevier: Amsterdam; 693–705.

Gordon JE, Birnie R, Timmis R. 1978. A major rockfall and debris slide on the Lyell Glacier, South Georgia. *Arctic and Alpine Research* **10**: 49–60.

Goren L, Aharonov E. 2007. Long runout landslides: the role of frictional heating and hydraulic diffusivity. *Geophysical Research Letters* **34**(L07301): 1–7.

Gruber S, Haeberli W. 2007. Permafrost in steep bedrock slopes and its temperature-related destabilization following climate change. *Journal of Geophysical Research* **112**(F02S18): 1–10.

Haeberli W, Beniston M. 1998. Climate change and its impacts on glaciers and permafrost in the Alps. *Ambio* **27**(4): 258–265.

Haeberli W, Hohmann R. 2008. Climate, glaciers and permafrost in the Swiss Alps 2050: scenarios, consequences and recommendations. In *Ninth International Conference on Permafrost*, Kane DL, Hinkel KM (eds). University of Alaska, Fairbanks: Fairbanks, Alaska; 607–612.

Haeberli W, Huggel C, Kääb A, Polkvoj A, Zotikov I, Osokin N. 2003. Permafrost conditions in the starting zone of the Kolka-Karmadon rock/ice slide of 20 September 2002 in North Osetia (Russian Caucasus), Extended Abstracts Reporting Current Research and New Information. *Eighth International Conference on Permafrost*, Zurich, Switzerland: 49–50.

Haeberli W, Huggel C, Kääb A, Zgraggen-Oswald S, Polkvoj A, Galushkin I, Zotikov I, Osokin N. 2004. The Kolka-Karmadon rock/ice slide of 20 September 2002: an extraordinary event of historical dimensions in North Ossetia, Russian Caucasus. *Journal of Glaciology* **50**(171): 533–546.

Hanke H. 1966. *Gletscherkatastrophen*. Der Bergsteiger, 33.

Harris C, Vonder Muhll D, Isaksen K, Haeberli W, Sollid JL, King L, Holmlund P, Dramis F, Guglielmin M, Palacios D. 2003. Warming permafrost in European mountains. *Global and Planetary Change* **39**(3–4): 215–225.

Harrison KP, Grimm RE. 2003. Rheological constraints on martian landslides. *Icarus* **163**(2): 347–362.

Hasler A, Gruber S, Font M, Dubois A. In revision. Advective heat transport in frozen rock clefts - conceptual model, laboratory experiments and numerical simulation. *Permafrost and Periglacial Processes*.

Hauser A. 2002. Rock avalanche and resulting debris flow in Estero Parraguirre and Río Colorado, Región Metropolitana, Chile. In *Catastrophic Landslides: Effects, Occurrence, and Mechanisms*, Evans SG, DeGraff (eds). Geological Society of America Reviews in Engineering Geology: Boulder, CO; 135–148.

Hayakawa YS, Oguchi T, Lin Z. 2008. Comparison of new and existing global digital elevation models: ASTER G-DEM and SRTM-3. *Geophysical Research Letters* **35**: L17404.

Heim A. 1932. Bergsturz und Menschenleben. *Beiblatt zur Vierteljahrsschrift der Naturforschenden Gesellschaft Zürich* **20**: 217.

Hewitt K. 1988. Catastrophic landslide deposits in the Karakoram Himalaya. *Science* **242**: 64–67.

Hewitt K (ed.). 2002. Styles of rock-avalanche depositional complexes conditioned by very rugged terrain, Karakoram Himalaya, Pakistan. Reviews in Engineering Geology, XV. The Geological Society of America: Boulder, CO; 345–377.

Hewitt K. 2009. Rock avalanches that travel onto glaciers and related developments, Karakoram Himalaya, Inner Asia. *Geomorphology* **103**: 66–79.

Hewitt K, Clague JJ, Orwin JF. 2008. Legacies of catastrophic rock slope failures in mountain landscapes. *Earth-Science Reviews* **87**: 1–38.

Hsü KJ. 1975. Catastrophic debris streams (Sturzstroms) generated by rockfalls. *Geological Society of America Bulletin* **86**: 129–140.

Hsu L, Dietrich WE, Sklar LS. 2007. Normal stresses, longitudinal profiles, and bedrock surface erosion by debris flows: initial findings from a large, vertically rotating drum. In *Debris-Flow Hazards Mitigation: Mechanics, Prediction, and Assessment: Proceedings 4th International DFHM Conference*, Chen CL, Major JJ (eds). Millpress: AmsterdaBm; Chengdu: China.

Huggel C, Caplan-Auerbach J, Waythomas CF, Wessels RL. 2007. Monitoring and modeling ice-rock avalanches from ice-capped volcanoes: a case study of frequent large avalanches on Iliamna Volcano, Alaska. *Journal of Volcanology and Geothermal Research* **168**(1–4): 114–136.

Huggel C, Gruber S, Caplan-Auerbach J, Wessels RL, Molnia BF. 2008a. The 2005 Mt. Steller, Alaska, rock–ice avalanche: what does it tell us about large slope failures in cold permafrost? In *Ninth International Conference on Permafrost*, Kane DL, Hinkel KM (eds). University of Alaska: Fairbanks, Alaska; 747–752.

Huggel C, Salzmann N, Allen S, Caplan-Auerbach J, Fischer L, Haeberli W, Larsen C, Schneider D, Wessels R. 2010. Recent and future warm extreme events and high-mountain slope stability. *Philosophical Transactions of the Royal Society* **A368**: 2435–2459.

Huggel C, Schneider D, Julio P, Delgado H, Kääb A. 2008b. Evaluation of ASTER and SRTM DEM data for lahar modeling: a case study on lahars from Popocatépetl Volcano, Mexico. *Journal of Volcanology and Geothermal Research* **170**(1–2): 99–110.

Huggel C, Zgraggen-Oswald S, Haeberli W, Kääb A, Polkvoj A, Galushkin I, Evans SG. 2005. The 2002 rock/ice avalanche at Kolka/Karmadon, Russian Caucasus: assessment of extraordinary avalanche formation and mobility, and application of QuickBird satellite imagery. *Natural Hazards and Earth System Sciences* **5**: 173–187.

Hungr O, Evans SG. 2004. Entrainment of debris in rock avalanches: An analysis of a long run-out mechanism. *GSA Bulletin* **116**(9/10): 1240–1252.

Imre B, Laue J, Springman SM. 2010. Fractal fragmentation of rocks within sturzstroms: insight derived from physical experiments within the ETH geotechnical drum centrifuge. *Granular Matter* **12**: 267–285.

Iribarren Anacona P, Bodin X. 2010. Geomorphic consequences of two large glacier and rock glacier destabilizations in the Central and Northern Chilean Andes. *Geophysical Research Abstracts* **12**: 7162–7165.

Iverson R. 1997. Mount Adams, Washington 1997 debris avalanches. Internet source: http://vulcan.wr.usgs.gov/Volcanoes/Adams/DebrisAval/DebrisAval1997/framework.html (last access June 15, 2011).

Iverson RM. 2005. Regulation of landslide motion by dilatancy and pore pressure feedback. *Journal of Geophysical Research* **110**(F02015): 1–16.

Iverson RM, Denlinger RP. 2001. Flow of variably fluidized granular masses across three-dimensional terrain - 1. *Coulomb mixture theory. Journal of Geophysical Research* **106**(B1): 537–552.

Iverson RM, Logan M, LaHusen RG, Berti M. 2010a. The perfect debris flow? Aggregated results from 28 large-scale experiments. *Journal of Geophysical Research* **115**(F03005): 1–29.

Iverson RM, Reid ME, LaHusen RG. 1997. Debris-flow mobilization from landslides. *Annual Review of Earth and Planetary Sciences* **25**: 85–138.

Iverson RM, Reid ME, Logan M, LaHusen RG, Godt JW, Griswold JP. 2010b. Positive feedback and momentum growth during debris-flow entrainment of wet bed sediment. *Nature Geoscience* **4**: 1–6.

Jibson RW, Harp EL, Schulz W, Keefer DK. 2006. Large rock avalanches triggered by the M 7.9 Denali Fault, Alaska, earthquake of 3 November 2002. *Engineering Geology* **83**(1–3): 144–160.

Jiskoot H. 2010. Long-runout rockslide on glacier at Tsar Mountain, Canadian Rocky Mountains: potential triggers, seismic and glaciological implications. *Earth Surface Processes and Landforms* **14**: 203–216.

Kaitna R, Rickenmann D. 2007. A new experimental facility for laboratory debris flow investigation. *Journal of Hydraulic Research* **45**(6): 797–810.

Kelfoun K, Druitt TH. 2005. Numerical modeling of the emplacement of Socompa rock avalanche, Chile. *Journal of Geophysical Research* **110**: 1–13.

Kent PE. 1966. The transport mechanism in catastrophic rock falls. *Journal of Geology* **74**: 79–83.

Körner HJ. 1983. Zur Mechanik der Bergsturzströme vom Huascarán, Perú. In *Die Berg- und Gletscherstürze vom Huascarán, Cordillera Blanca, Perú*, Patzelt G (ed.). Universitätsverlag Wagner: Innsbruck; 71–110.

Korup O. 2005. Large landslides and their effect on sediment flux in South Westland, New Zealand. *Earth Surface Processes and Landforms* **30**: 305–323.

Korup O, Tweed F. 2007. Ice, moraine, and landslide dams in mountainous terrain. *Quaternary Science Reviews* **26**(25–28): 3406–3422.

Kotlyakov VM, Rototaeva OV, Nosenko GA. 2004. The September 2002 Kolka Glacier Catastrophe in North Ossetia, Russian Federation: evidence and Analysis. *Mountain Research and Development* **24**(1): 78–83.

Legros F. 2002. The mobility of long-runout landslides. *Engineering Geology* **63**: 301–331.

Legros F. 2006. Landslide mobility and the role of water. In *Advanced Research Workshop: Landslides from Massive Rock Slope Failure*, Evans SG, Scarascia Mugnozza G, Strom AL, Hermanns RL (eds). NATO Science Series, IV Earth and Environmental Sciences, June 16–21, 2002, Celano, Italy. Springer: 233–242.

Legros F, Cantagrel J-M, Bertrand D. 2000. Pseudotachylyte (frictionite) at the base of the Arequipa volcanic landslide deposit (Peru): Implications for emplacement mechanisms. *Journal of Geology* **108**: 601–611.

Lipovsky PS, Evans SG, Clague JJ, Hopkinson C, Couture R, Bobrowsky P, Ekström G, Demuth MN, Delaney KB, Roberts NJ, Clarke G, Schaeffer A. 2008. The July 2007 rock and ice avalanches at Mount Steele, St. Elias Mountains, Yukon, Canada. *Landslides* **5**(4): 445–455.

Mair K, Hazzard JF. 2007. Nature of stress accommodation in sheared granular material: Insights from 3D numerical modeling. *Earth and Planetary Science Letters* **259**(3–4): 469–485.

Mangeney A, Roche O, Hungr O, Mangold N, Faccanoni G, Lucas A. 2010. Erosion and mobility in granular collapse over sloping beds. *Journal of Geophysical Research* **115**(F03040): 1–21.

Marangunic C, Bull C. 1968. *The Landslide on the Sherman Glacier, The Great Alaska Earthquake of 1964, Hydrology*. National Academy of Sciences: Washington DC; 383–394.

McArdell BW, Bartelt P, Kowalski J. 2007. Field observations of basal forces and fluid pore pressure in a debris flow. *Geophysical Research Letters* **34**(L07406).

McDougall S, Hungr O. 2005. Dynamic modelling of entrainment in rapid landslides. *Canadian Geotechniqual Journal* **42**: 1437–1448.

McSaveney MJ. 1978. Sherman Glacier rock avalanche, Alaska, U.S.A. In *Rockslides and Avalanches, 1; Natural Phenomena*, Voight B (ed.). Elsevier: Amsterdam; 197–258.

McSaveney MJ. 2002. Recent rockfalls and rock avalanches in Mount Cook National Park, New Zealand. In *Catastrophic Landslides: Effects, Occurrence and Mechanism*, Evans SG, DeGraff JV (eds). Geological Society of America, Reviews in Engineering Geology: Boulder, CO; 35–70.

McSaveney MJ, Davies TRH. 2007. Rockslides and their motion. In *Progress in Landslide Science*, Sassa K, Fukuoka H, Wang F, Wang G (eds). Springer: Berlin Heidelberg New York; 113–133.

Melosh HJ. 1979. Acoustic fluidization: A new geologic process? *Journal of Geophysical Research* **84**(B13): 7513–7520.

National Research Council. 1968. The Great Alaska Earthquake of 1964, Hydrology, 3. Committee on the Alaska Earthquake, National Academy of Sciences, Publication 1603,Washington D.C.

Nicoletti PG, Sorriso-Valvo M. 1991. Geomorphic controls of the shape and mobility of rock avalanches. *Geological Society of America Bulletin* **103**: 1365–1373.

Noetzli J, Gruber S. 2009. Transient thermal effects in Alpine permafrost. *The Cryosphere* **3**: 85–99.

Noetzli J, Hoelzle M, Haeberli W. 2003. Mountain permafrost and recent Alpine rock-fall events: a GIS-based approach to determine critical factors. In *8th International Conference on Permafrost*, Phillips M, Springman S, Arenson L (eds). Swets & Zeitlinger: Lisse, Zurich; 827–832.

Noetzli J, Huggel C, Hoelzle M, Haeberli W. 2006. GIS-based modelling of rock–ice avalanches from Alpine permafrost areas. *Computational Geosciences* **10**(2): 161–178.

O'Connor JE, Costa JE. 1993. Geologic and hydrologic hazards in glacierized basins in North America resulting from 19th and 20th century global warming. *Natural Hazards* **8**(2): 121–140.

Okura Y, Kitahara H, Kawanami A, Kurokawa U. 2003. Topography and volume effects on travel distance of surface failure. *Engineering Geology* **67**(3–4): 243.

Okura Y, Kitahara H, Sammori T, Kawanami A. 2000. The effects of rockfall volume on runout distance. *Engineering Geology* **58**(2): 109.

Oppikofer T, Jaboyedoff M, Keusen H-R. 2008. Collapse at the eastern Eiger flank in the Swiss Alps. *Nature Geoscience* **1**(8): 531–535.

Perla R, Cheng TT, McClung DM. 1980. A two-parameter model of snow-avalanche motion. *Journal of Glaciology* **26**(94): 197–207.

Petrakov DA, Chernomorets SS, Evans SG, Tutubalina OV. 2008. Catastrophic glacial multi-phase mass movements: a special type of glacial hazard. *Advances in Geosciences* **14**: 211–218.

Petrovic JJ. 2003. Review: mechanical properties of ice and snow. *Journal of Materials Science* **38**: 1–6.

Pierson TC. 1986. Flow behaviour of channelized debris flows, Mount St. Helens, Washington. In *Hillslope Processes*, Abrahams AD (ed). Allen & Unwin: Winchester; 269–296.

Plafker G, Ericksen GE. 1978. Nevados Huascarán avalanches, Peru. In *Rockslides and Avalanches, 1: Natural Phenomena*. Voight B (ed). Elsevier: Amsterdam; 277–314.

Post A. 1968. *Effects on Glaciers, The Great Alaska Earthquake of 1964, Hydrology*. National Academy of Sciences: Washington DC; 266–308.

Prager C, Krainer K, Seidl V, Chwatal W. 2006. Spatial features of holocene sturzstrom-deposits inferred from subsurface investigations (Fernpass rockslide, Tyrol, Austria). *Geo.Alp* **3**: 147–166.

Radic V, Hock R. 2011. Regionally differentiated contribution of mountain glaciers and ice caps to future sea-level rise. *Nature Geoscience* **4**(2): 91–94.

Ravanel L, Allignol F, Deline P, Gruber S, Ravello M. 2010. Rock falls in the Mont Blanc Massif in 2007 and 2008. *Landslides* **7**: 493–501.

Raymond M, Wegmann M, Funk M. 2003. *Inventar gefährlicher Gletscher in der Schweiz*. Laboratory of Hydraulics, Hydrology and Glaciology: Zurich; 182.

Rickenmann D. 2005. Runout prediction methods. In *Debris-flow Hazards and Related Phenomena*, Jakob M, Hungr O (eds). Springer: Berlin/Heidelberg; 305–324.

Röthlisberger H. 1977. Ice avalanches. *Journal of Glaciology* **19**(81): 669–671.

Rozman J, Rožič A, Budkovič A, Budkovič T. 2004. Rockfall in the southern wall of Punta Thurwieser (Italy) on September 18, 2004. *Geologija* **47**(2): 221–232.

Savage SB. 1984. The mechanics of rapid granular flows. *Advances in Applied Mechanics* **24**: 289–366.

Scheidegger AE. 1973. On the prediction of the reach and velocity of catastrophic landslides. *Rock Mechanics* **5**: 231–236.

Schneider JF. 2006. Risk assessment of remote geohazards in Western Pamir, GBAO, Tajikistan. In *Proceedings of the International Conference on High Mountain Hazard Prevention*, Haeberli W et al. (eds). Swiss Agency for Development and Cooperation: Vladikavkaz/Moscow. 252–267.

Schneider D, Bartelt P, Caplan-Auerbach J, Christen M, Huggel C, McArdell BW. 2010. Insights into rock–ice avalanche dynamics by combined analysis of seismic recordings and a numerical avalanche model. *Journal of Geophysical Research* **115**(F04026): 1–20.

Schneider D, Kaitna R, Dietrich WE, Hsu L, Huggel C, McArdell BW. 2011. Frictional behavior of granular gravel-ice mixtures in vertically rotating drum experiments and implications for rock–ice avalanches. *Cold Regions Science and Technology*. **69**(1): 70–90.

Sheridan MF. 1979. Emplacement of pyroclastic flows: a review. In *Ash-Flow Tuffs*, Chapin CE, Elston WE (eds). Geological Society of America, Special Paper; 125–136.

Sheridan MF, Stinton AJ, Patra A, Pitman EB, Bauer A, Nichita CC. 2005. Evaluating Titan2D mass-flow model using the 1963 Little Tahoma Peak avalanches, Mount Rainier, Washington. *Journal of Volcanology and Geothermal Research* **139**(1–2): 89–102.

Shreve RL. 1966. Sherman landslide, Alaska. *Science* **154**(3757): 1639–1643.

Shreve RL. 1968. Leakage and fluidization in air-layer lubricated avalanches. *Geological Society of America Bulletin* **79**: 653–658.

Sosio R, Crosta GB, Hungr O. 2008. Complete dynamic modeling calibration for the Thurwieser rock avalanche (Italian Central Alps). *Engineering Geology* **100**: 11–26.

Straub S. 1997. Predictability of long runout landslide motion: implications from granular flow mechanics. *Geologische Rundschau* **86**(2): 415–425.

Van Der Woerd J, Owen LA, Tapponnier P, Xiwei X, Kervyn F, Finkel RC, Barnard PL. 2004. Giant, ~M8 earthquake-triggered ice avalanches in the eastern Kunlun Shan, northern Tibet: characteristics, nature and dynamics. *GSA Bulletin* **116**(3/4): 394–406.

Van Gassen W, Cruden DM. 1989. Momentum transfer and friction in the debris of rock avalanches. *Canadian Geotechniqual Journal* **26**: 623–628.

Voight B, Sousa J. 1994. Lessons from Ontake-san: A comparative analysis of debris avalanche dynamics. *Engineering Geology* **38**: 261–297.

Weidinger JT, Korup O. 2009. Frictionite as evidence for a large Late Quaternary rockslide near Kanchenjunga, Sikkim Himalayas, India – implications for extreme events in mountain relief destruction. *Geomorphology* **103**(1): 57–65.

# Curriculum Vitae (short version)

| | |
|---|---|
| Last name | SCHNEIDER |
| First name | Demian Raffael Gian |
| Date of birth | November 6, 1978 |
| Hometown | Luzern LU / Suhr AG |
| Address | Dynamostrasse 15, CH-5400 Baden |
| E-mail | demian.schneider@geo.uzh.ch |

## Education

| | |
|---|---|
| 1995 - 1999 | Highschool Wettingen, University entrance certificate, type PSG |
| Oct. 2000 – Jan. 2006 | Studies of Physical Geography at the University of Zurich, Switzerland. Diploma thesis: “Modeling of lahar hazard potentials on glacier covered volcanoes: Iztaccíhuatl, Mexico”, supervised by Prof. Dr. Andreas Kääb, Dr. Christian Huggel, Prof. Dr. Hugo Delgado Granados and Prof. Dr. Wilfried Haeberli |
| Since June 2006 | Department of Geography, Physical Geography, Glaciology, Geomorphodynamics & Geochronology Group, University of Zurich (GIUZ): Assistant/PhD candidate (preparative work) |
| Since June 2006 | Swiss Federal Institute for Forest, Snow and Landscape Research (WSL/SLF, Birmensdorf/Davos): internship and academic guest |
| Sept. 2007 – April 2011 | Department of Geography, Physical Geography, Glaciology, Geomorphodynamics & Geochronology Group, University of Zurich (GIUZ): Dissertation: PhD thesis “On characteristics and flow dynamics of large rapid mass movements in glacial environments” |

## Tasks

Numerical modeling, laboratory experiments, cases study analysis, field visits, supervision of diploma-, bachelor-, and master thesis, teaching, field courses, meeting organization.

## Employment

Internal assistant position, Swiss National Science Foundation, TajHaz-Project (FOCUS Humanitarian Assistance/Aga Khan Development Network/Swiss Agency for Development and Cooperation SDC/British Department for International Development DFID), June 2006 – April 2011.

## Publications & presentations

See *Personal Bibliography*, pp. 77-79.